

AD 723823

ENCLOSURE  
70024751

NR68H-434

VOLUME I

INTERNAL AERODYNAMICS MANUAL

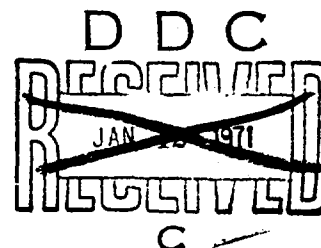
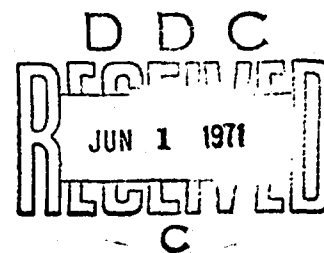
June 1970

Prepared for  
NAVAL AIR SYSTEMS COMMAND  
WASHINGTON, D.C.

CONTRACT NOW66-0460-d

REPRODUCED BY  
NATIONAL TECHNICAL  
INFORMATION SERVICE  
SPRINGFIELD, VA.

Prepared by  
COLUMBUS DIVISION  
NORTH AMERICAN ROCKWELL CORPORATION  
COLUMBUS, OHIO 43216



Reproduced by  
NATIONAL TECHNICAL  
INFORMATION SERVICE  
Springfield, Va. 22151

423

INTERNAL AERODYNAMICS MANUAL

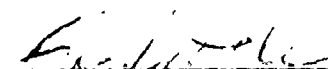
Prepared for  
NAVAL AIR SYSTEMS COMMAND  
WASHINGTON, D.C.


CONTRACT NOW66-0460-d


APPROVED FOR IN LEO FORMATE;  
DISTRIBUTION UNLIMITED


Prepared by  
COLUMBUS DIVISION  
NORTH AMERICAN ROCKWELL CORPORATION  
COLUMBUS, OHIO 43216

APPROVED BY

  
F. K. Little  
Manager  
Thermodynamics & Propulsion

  
M. Schweiger  
Manager  
Aero-Thermo

  
R. H. Gulcher  
Chief Engineer  
Aircraft Research  
and Engineering

  
J. R. Bartfield  
Aircraft R&D

June 1970

### ABSTRACT

The Internal Aerodynamics Handbook has been developed in order to provide a convenient, accurate and reliable internal aerodynamics design manual which enables rapid determination of the internal airflow effects on airplane performance. It also enables the computation of internal airflow systems performance by developed theoretical and empirical methods. The scope of the design manual relates specifically to internal aerodynamics for the complete aircraft speed range up to and including Mach 3.5. In addition to the detailed data and methods presentation, an extensive bibliography is provided.

### KEY WORDS

Additive Drag  
Airflow  
Control System  
Cooling  
Diffuser  
Ejector  
Exhaust Nozzle  
High Bypass Ratio  
Inlet  
Instability  
Installation Loss  
Jet Effects  
Thermodynamics  
Thrust  
Thrust Reverser

## TABLE OF CONTENTS

<u>Section</u>	<u>Title</u>	<u>Page</u>
	List of Figures	xii
	Introduction	xxxii
1.0	Inlet Design Considerations	1-1
	1.1 Inlet Sizing	1-2
	1.2 Inlet Location	1-3
	1.3 Method of Pre-Compression	1-3
	1.4 Compression Surface Orientation	1-5
	1.5 Boundary Layer Removal Provisions	1-5
2.0	Air Induction System Loss Determination	2-1
	2.1 Inlet Lip Losses - Sharp Lips	2-1
	2.2 Inlet Lip Losses - Rounded Lips	2-2
	2.3 Low Speed Inlet Loss Calculation Method	2-3
	2.4 Inflow Losses at Subsonic Speeds; Mass-Flow-Ratio Less Than 1.0	2-5
	2.5 Shock Loss Determination	2-5
	2.5.1 Normal Shock Loss	2-5
	2.5.2 Two-Dimensional Oblique Shock Wave Analysis	2-6
	2.5.3 Axisymmetric or Three-Dimensional Oblique Shock Wave Analysis	2-8
	2.6 Internal Ducting Losses	2-10
	2.6.1 Principles of Ducting Loss Analysis	2-10
	2.6.1.1 Sources of Losses	2-10
	2.6.1.2 Correlation of Duct Component Pressure Loss Data	2-11
	2.6.1.3 Evaluation of Overall Inlet System Loss	2-13
	2.6.2 Subsonic Diffusion Losses	2-14
	2.6.2.1 General Considerations	2-14
	2.6.2.2 Conical Diffuser Losses	2-16
	2.6.2.3 Non-Conical Diffuser Losses	2-17
	2.6.2.4 Boundary Layer Control Provisions	2-17



<u>Section</u>	<u>Title</u>	<u>Page</u>
	2.6.3 Miscellaneous Losses	2-18
	2.6.3.1 Elbows	2-18
	2.6.3.2 Constant Area Ducts	2-19
	2.6.3.3 Screens	2-20
	2.6.4 Effects of Losses on Pressure Recovery	2-20
	2.6.5 Pressure Distortion Effects	2-21
	2.6.6 Subsonic Duct Loss Calculation Method	2-22
3.0	Boundary Layer Considerations	3-1
	3.1 Boundary Layer Thickness	3-1
	3.2 Boundary Layer Profiles	3-2
	3.3 Fuselage Boundary Layer Removal	3-3
	3.4 Compression Surface Boundary Layer Removal	3-4
4.0	Additive Drag	4-1
	4.1 Theoretical Additive Drag	4-1
	4.2 Subsonic Additive Drag	4-7
	4.3 Supersonic Additive Drag	4-7
	4.3.1 Two-Dimensional Inlets	4-11
	4.3.2 Three-Dimensional Inlets	4-12
	4.4 Terminal Shock Wave Position	4-14
	4.5 Additive Drag Correction	4-16
5.0	Inlet Instability and Unsteady Flow Phenomena	5-1
	5.1 Unsteady Flow at Static and Subsonic Flight Conditions	5-1
	5.2 Duct Rumble and Twin Duct Instability	5-2
	5.3 Supersonic Unsteady Flow Phenomena	5-3
	5.3.1 Supersonic Normal Shock Oscillation	5-3
	5.3.2 Inlet Buzz	5-4
	5.4 Inlet/Engine Dynamic Interaction	5-5

<u>Section</u>	<u>Title</u>	<u>Page</u>
6.0	Inlet Control Considerations	6-1
6.1	Requirements for an Air Inlet Control System	6-2
6.1.1	Inlet Control System Performance	6-3
6.1.2	Inlet Off-Design Point Penalties	6-4
6.1.3	Inlet-Engine Airflow Matching	6-5
6.1.4	Inlet Transients, Buzz and Distortion Limits	6-5
6.2	Configuration of Variable Geometry Inlets	6-6
6.2.1	Two-Dimensional Inlets (2-D)	6-6
6.2.1.1	Ramps	6-6
6.2.1.1.1	Ramp Location	6-7
6.2.1.1.2	By-Pass Ring or Doors	6-7
6.2.1.1.2.1	By-Pass Ring	6-8
6.2.1.1.2.2	By-Pass Doors	6-8
6.2.2	Axially Symmetric (3-D) Inlets	6-8
6.2.2.1	Spike	6-9
6.2.2.1.1	Translating Spike	6-9
6.2.2.1.2	Collapsible Spikes	6-9
6.3	Comparison of 2-D and 3-D Inlet Control Systems	6-10
6.4	Inlet Control System	6-10
6.4.1	Closed vs Open Loop Systems	6-11
6.4.2	Considerations for Inlet Control System Selection	6-12
6.4.2.1	Signals	6-13
6.4.2.2	Manual Control	6-14
6.4.2.3	Flexibility	6-14
6.4.2.4	Complexity	6-14
6.4.2.5	Installation	6-15
6.4.2.6	Power Consumption	6-15
6.4.2.7	Weight	6-15
6.5	Sensors	6-15
6.5.1	Mechanical Sensors	6-16

<u>Section</u>	<u>Title</u>	<u>Page</u>
	6.5.1.1 Jet Pipe Concept	6-16
	6.5.1.2 Hydro-Mechanical Vector Sensor	6-16
	6.5.1.3 Force Balancing Beam Concept	6-17
6.5.2	Electronic Sensors	6-17
6.5.3	Pure Fluid Amplifiers	6-18
6.6	Servo Valve	6-19
6.6.1	Output Power of Servo Valve	6-21
6.6.1.1	Two-Stage Hydraulic Servo Valves	6-22
6.7	Actuators	6-23
6.7.1	Design Considerations	6-24
6.7.2	Weight Formulae and Curves	6-25
6.7.3	Design Summary	6-26
6.8	Linkages	6-27
6.8.1	Power Linkages	6-27
6.8.2	Follow-up Linkages	6-27
6.9	Error Analysis	6-28
6.9.1	Control System Errors	6-28
6.9.1.1	Sensor Characteristics	6-28
6.9.1.2	Computer Characteristics	6-29
6.9.1.3	Feedback Characteristics	6-30
6.9.2	Sample Error Analysis	6-30
6.9.2.1	Local Mach Sensor Error	6-30
6.9.2.2	Scheduling Cam Error	6-30
6.9.2.3	Control Shifts	6-31
6.9.2.4	Feedback Error	6-32
6.9.3	Vehicle Impact	6-32
6.9.4	Type III Characteristics (Mach 2.5 and Above)	6-33

<u>Section</u>	<u>Title</u>	<u>Page</u>
7.0	Secondary Airflow Systems Performance	7-1
7.1	Introduction	7-1
7.1.1	Definition of Secondary Airflow	7-1
7.1.2	Purposes	7-1
7.2	Engine Cooling	7-1
7.2.1	Cooling Configurations	7-1
7.2.2	Structural Temperatures	7-2
7.3	Inlet Matching	7-2
7.4	Nozzle Performance	7-3
7.4.1	Effects of Secondary Airflow	7-3
7.4.2	Engine Compartment Pressure	7-4
7.5	Estimating Secondary Airflow Quantities	7-6
7.5.1	Method of Calculation with Overboard Dump	7-6
7.5.2	Method of Calculation with Flow Through Compartment	7-10
7.5.3	Engine Compartment Bursting Loads	7-12
7.5.4	Overboard Exits	7-12
7.6	Secondary Airflow Losses	7-14
7.6.1	Inlets and Diffusers	7-14
7.6.1.1	Flush Inlet Losses	7-15
7.6.1.2	Flush Slots	7-17
7.6.1.3	Ram Scoops	7-18
7.7	Heat Exchanger Drag	7-19
7.7.1	Heat Exchanger Types	7-19
7.7.2	Heat Exchanger Drag Estimation	7-20
7.8	Auxiliary Cooling Drag	7-24
7.9	Boundary Layer Bleed Drag	7-24
7.10	Boundary Layer Diverter	7-27
7.10.1	Sizing Considerations	7-27
7.10.2	Drag Estimation	7-28
7.11	By-Pass Door Drag	7-29
7.12	Miscellaneous Drag	7-29

<u>Section</u>	<u>Title</u>	<u>Page</u>
	7.12.1 Screen Drag	7-29
	7.13 Internal Ducting Losses	7-30
8.0	Exhaust Nozzle Performance	8-1
	8.0.1 Introduction	8-1
	8.0.2 Thermodynamic Background	8-2
	8.1 Theoretical Performance	8-4
	8.1.1 Theoretical Thrust Types	8-4
	8.1.2 Convergent Nozzle Thrust Parameter Derivation	8-4
	8.1.2.1 Derivation for Un-Choked Nozzle	8-4
	8.1.2.2 Derivation for Choked Nozzle	8-6
	8.1.3 Optimum Thrust Parameter Derivations	8-7
	8.1.3.1 Derivation of $\frac{F_1}{W T_T}$	8-8
	8.1.3.2 Derivation of $\frac{F_1}{A^* P_T}$	8-10
	8.1.4 Area Ratio	8-15
	8.1.4.1 Optimum Thrust Area Ratio	8-15
	8.1.4.2 Non-Optimum Area Ratio	8-15
	8.2 Coefficients	8-18
	8.2.1 Basic Coefficients	8-18
	8.2.2 Nozzle Efficiency Terms	8-20
	8.3 Discussion and Experimental Performance of Various Nozzle Types	8-22
	8.3.1 Convergent Nozzles	8-22
	8.3.1.1 Simple Convergent	8-22
	8.3.1.2 Annular (For Fan Air)	8-22
	8.3.2 Performance Characteristics of Convergent-Divergent Nozzles	8-25

<u>Section</u>	<u>Title</u>	<u>Page</u>
8.3.3	Convergent Divergent Ejector Nozzles	8-31
8.3.3.1	Experimental Results	8-31
8.3.3.2	Exhaust Angularity	8-35
8.3.3.3	Pumping and Flow Characteristics	8-36
8.3.3.3.1	Nozzle Flow Characteristics	8-36
8.3.3.3.2	Nozzle Flow Instability	8-39
8.3.3.3.3	Nozzle Pumping	8-43
8.3.3.3.4	Characteristic Estimation	8-50
8.3.3.4	Ejector Gross Thrust Estimation	8-52
8.3.3.4	Nozzle Flow Separation	8-52
8.3.3.4.1	Base Nozzle Flow Consideration	8-52
8.3.3.4.2	Nozzle Stalled Thrust Performance	8-54
8.3.3.5	External Aerodynamic Effects on Nozzles	8-56
8.3.4	Plug Nozzles	8-60
8.3.4.1	Introduction	8-60
8.3.4.2	Quiescent Air Testing	8-60
8.3.4.3	Supersonic Expansion	8-60
8.3.4.3.1	Isentropic Plug	8-60
8.3.4.3.2	Conical Plug	8-65
8.3.4.3.3	Convergent-Divergent Plug Nozzle Configuration	8-65
8.3.4.4	Non-Supersonic Expansion	8-66
8.3.4.4.1	Aerodynamic Boattail Nozzle	8-66
8.3.4.4.2	Convergent Plug Nozzle	8-68
8.3.5	Blow-In-Door Ejector Nozzles	8-72
8.3.6	Expansion-Deflection Nozzle	8-75
8.4	Comparison of Nozzle Performance	8-77

<u>Section</u>	<u>Title</u>	<u>Page</u>
	8.4.1 Introduction	8-77
	8.4.2 Nozzle Types	8-78
	8.4.3 Integration and Evaluation	8-80
8.5	Thrust Reversers	8-82
	8.5.1 Aircraft Applications for Reverse Thrust	8-82
	8.5.2 Configurations of Thrust Reversers	8-83
	8.5.3 Performance of Thrust Reversers	8-85
	Symbols	8-89
	References	8-92
9.0	Afterbody and Exhaust System Drag	9-1
9.1	Afterbody Drag	9-4
9.1.1	Skin Friction Drag Component	9-4
	9.1.1.1 Two-Dimensional Bodies	9-7
	9.1.1.2 Three-Dimensional Bodies	9-8
	9.1.1.3 Effects of Wall Temperature	9-9
	9.1.1.4 Effects of Surface Roughness	9-11
9.1.2	Pressure Drag Component	9-18
	9.1.2.1 Subsonic-Transonic Speeds	9-18
	9.1.2.2 Supersonic Speeds	9-19
	9.1.2.2.1 Two-Dimensional Afterbodies	9-20
	9.1.2.2.2 Three-Dimensional Afterbodies	9-21
	9.1.2.3 Bodies of Arbitrary Cross-Section	9-23
9.2	Base Drag	9-24
9.2.1	Two-Dimensional Base Drag	9-24
	9.2.1.1 Base Flow Characteristics and Flow Analogy	9-24
	9.2.1.2 Effects of Afterbody Boattailing	9-27
	9.2.1.2.1 Subsonic Speeds	9-27
	9.2.1.2.2 Supersonic Speeds	9-28
	9.2.1.3 Effect of Angle of Attack	9-32

<u>Section</u>	<u>Title</u>	<u>Page</u>
9.2.2	Axisymmetric Base Drag	9-33
9.2.2.1	Three-Dimensional Wake Characteristics	9-33
9.2.2.2	Effects of Afterbody Boattailing	9-34
9.2.2.2.1	Subsonic-Transonic Speeds	9-34
9.2.2.2.2	Supersonic Speeds	9-36
9.2.2.3	Effect of Angle of Attack	9-38
9.3	Jet Interference Effects on Afterbody and Base Drag	9-39
9.3.1	Description of Jet Interference Flow Phenomena	9-40
9.3.1.1	Analytical Flow Model	9-40
9.3.1.2	Criterion for Incipient Separation	9-44
9.3.1.3	Pressure Rise Across Reattachment Region	9-47
9.3.2	Calculation Procedures	9-48
9.3.3	Test Results	9-54
9.3.3.1	Afterbody Shaping	9-54
9.3.3.2	Test Model Design	9-55
9.3.3.3	Analysis of Results	9-55
9.3.3.3.1	Consider Drag at Subsonic Mach Numbers for Configuration with Non-Augmented Nozzles	9-56
9.3.3.3.2	Consider Drag at Subsonic Mach Numbers for Configurations with Augmented Setting Nozzles	9-58
9.3.3.3.3	Consider Drag for Low Supersonic Mach Numbers and Configurations with Augmented Nozzles	9-59
9.3.3.4	Conclusions	
10.0	High Bypass Ratio Turbofan Installation	10-1
10.1	Introduction	10-1
10.2	High Bypass Ratio Turbofan Installation Considerations	10-5



<u>Section</u>	<u>Title</u>	<u>Page</u>
	10.2.1 Windmilling Performance	10-5
	10.2.2 Exhaust Path Design	10-5
	10.2.3 Cooling	10-7
	10.2.4 Miscellaneous	10-7
10.3	Installation Loss Breakdown	10-7
	10.3.1 External Losses	10-7
	10.3.1.1 Additive Drag	10-8
	10.3.1.2 Fan Cowl Friction	10-8
	10.3.1.3 Boattail Drag	10-8
	10.3.1.4 Scrubbing and Interference Drag	10-10
	10.3.1.5 Testing Methods	10-12
	10.3.2 Internal Losses	10-14
10.4	Performance Summary	10-15
10.5	Thrust Reverser Installation	10-17
Appendices		
	Appendix A. Basic Thermodynamic Relationships	A1
	Appendix B. Normal Shock Wave Parameters	B1
	Appendix C. Two-Dimensional Shock Wave Analysis	C1
	Appendix D. Three-Dimensional Shock Wave Analysis	D1
	Appendix E. Corrected Weight Flow Parameters	E1
	Appendix F. Parameters for Thrust Calculation	F1

# LIST OF FIGURES

<u>Figure No.</u>	<u>Title</u>	<u>Page</u>
1-1	Typical Variation of Corrected Airflow.	1-8
1-2	Typical Pressure Recovery Schedule.	1-9
1-3	Typical Variation of Freestream Tube Area.	1-10
1-4	Example of Relationship of $A_0$ to $A_c$ .	1-11
1-5	Local Flow Conditions on a Body.	1-12
1-6	Inlet Local Angle of Attack and Mach Number as Measured in Flight, Side Inlet Location.	1-3
2-1	Theoretical Sharp Lip Inlet Total Pressure Recovery.	2-26
2-2	Low Speed Lip Loss Correlation. $M_0 = 0.166$	2-27
2-3	Ratio of Experimental Lip Suction Coefficient to Coefficient Required to Make Lip Loss Vanish. $IFR = 1.0$ $M_0 = 0-0.4$	2-28
2-4	Lip Suction Coefficient, $K$ , Required to Make Lip Loss Vanish. $M_0 = 0$	2-29
2-5	Lip Suction Coefficient, $K$ , Required to Make Lip Loss Vanish.	2-30
2-6	Inlet Lip Loss Correlation.	2-31
2-7	Inlet Lip Loss Correlation. $M_0 = 0.237$	2-32
2-8	Inlet Lip Loss Correlation Elliptical Profiles. $M_0 = 0.237$	2-33
2-9	Examples of Normal Shocks.	2-34
2-10	Normal Shock Wave Parameter.	2-35
2-11	Oblique Shock Wave Velocity Relationships.	2-36
2-12	Optimum Pressure Recovery for 2, 3 And 4-Shock, 2-Dimensional Inlet.	2-37
2-13	Optimum Deflection Angles for 2-Shock, 2-Dimensional Inlet.	2-38
2-14	Optimum Deflection Angles for 3-Shock, 2-Dimensional Inlet.	2-39
2-15	Optimum Deflection Angles for 4-Shock, 2-Dimensional Inlets.	2-40
2-16	Shock Wave Angles Corresponding to Optimum Deflection Angles for 2-Shock, 2-Dimensional Inlet.	2-41
2-17	Shock Wave Angles Corresponding to Optimum Deflection Angles for 3-Shock, 2-Dimensional Inlet.	2-42
2-18	Shock Wave Angles Corresponding to Optimum Deflection Angles for 4-Shock, 2-Dimensional Inlet.	2-43

<u>Figure No.</u>	<u>Title</u>	<u>Page</u>
2-19	Downstream Mach Numbers Corresponding to Optimum Deflection Angles for 2-Shock, 2-Dimensional Inlet.	2-44
2-20	Downstream Mach Numbers Corresponding to Optimum Deflection Angles for 3-Shock, 2-Dimensional Inlet.	2-45
2-21	Downstream Mach Numbers Corresponding to Optimum Deflection Angles for 4-Shock, 2-Dimensional Inlet.	2-46
2-22	Deflection Angles for Shock Detachment and Sonic Flow, 2-Dimensional.	2-47
2-23	Double Cone in Supersonic Flow.	2-48
2-24	Optimum Deflection Angles for Axisymmetric 2 and 3-Shock Inlets.	2-49
2-24	Turbulent Boundary Layer Thickness and Friction Criteria. (References 10 and 11)	2-50
2-25	Compressibility Effects in Diffusers. (Reference 16)	2-51
2-27	Effect of Diffuser Divergence Angle on Length.	2-52
2-27	Diffuser Momentum and Turbulence Loss Criteria. (Reference 16)	2-53
2-29	Diffuser Friction Loss Criteria.	2-54
2-30	Typical Conical Diffuser Losses.	2-55
2-3	Typical Losses for Various Types of Diffusers. (Reference 16)	2-56
2-32	Typical Supersonic Shock Compression Boundary Layer Control.	2-57
2-33	Typical Boundary Layer Control Provisions for Annular Subsonic Diffusers.	2-58
2-34	Elbow Pressure Losses. (Reference 14)	2-59
2-35	Screen Pressure Losses. (Reference 20 and 24)	2-60
2-36	Effect of Subsonic Losses on Inlet Pressure Recovery.	2-61
2-37	Inlet Flow Mach Number Parameters.	2-62
3-1	Variation of Reynolds Number with Mach Number at Various Altitudes, Standard Atmosphere.	3-6
3-2	Boundary Layer Thickness Data, Fuselage Station 221, Lower Surface.	3-7
3-3	Boundary Layer Thickness Data, Fuselage Station 274, Altitude 40,000 Ft.	3-8
3-4	Boundary Layer Thickness Data, Fuselage Station 258, Altitude 40,000 Ft.	3-9
3-5	Theoretical Performance of Inlets in the Presence of a Boundary Layer Without Precompression.	3-10
3-6	Theoretical Performance of Inlets in the Presence of a Boundary Layer Without Compression.	3-11
3-7	Theoretical Performance of Inlets in the Presence of a Boundary Layer Without Compression.	3-12
3-8	Theoretical Performance of Inlets in the Presence of a Boundary Layer Without Compression.	3-13

<u>Figure No.</u>	<u>Title</u>	<u>Page</u>
3-9	Theoretical Performance of Inlets in the Presence of a Boundary Layer Without Compression.	3-14
3-10	Theoretical Performance of Inlets in the Presence of a Boundary Layer Without Compression.	3-15
3-11	Theoretical Performance of Inlets in the Presence of a Boundary Layer Without Compression.	3-16
3-12	Theoretical Performance of Inlets in the Presence of a Boundary Layer Without Compression.	3-17
3-13	Theoretical Performance of Inlets in the Presence of a Boundary Layer Without Compression.	3-18
3-14	Theoretical Performance of Inlets in the Presence of a Boundary Layer Without Compression.	3-19
3-15	Theoretical Performance of Inlets in the Presence of a Boundary Layer Without Compression.	3-20
3-16	Theoretical Performance of Inlets in the Presence of a Boundary Layer Without Compression.	3-21
3-17	Typical Boundary Layer Diverter on a Two-Dimensional Horizontal Ramp Inlet.	3-22
3-18	Typical Boundary Layer Diverter on a Two-Dimensional Vertical Ramp Inlet.	3-23
3-19	Diverter Static Pressure Distribution - $M_0 = 0.9$ .	3-24
3-20	Diverter Static Pressure Distribution - $M_0 = 1.57$ .	3-25
3-21	Diverter Static Pressure Distribution - $M_0 = 1.97$ .	3-26
3-22	Compression Surface Boundary Layer Control.	3-27
3-23	Effect of Compression Surface Bleed on Inlet Performance and Distortion - $M_0 = 2.05$ .	3-28
3-24	Summary of Bleed Effectiveness - $M_0 = 2.05$ .	3-29
3-25	Effect of Mach Number on Bleed Flow.	3-30
4-1	Illustration of Meaning of Additive Drag.	4-19
4-2	Schematic Representation of Forces Acting on a Typical Propulsion System - Using Stations 1 and e.	4-20
4-3	Schematic Representation of Forces Acting on a Typical Propulsion System - Using Stations 0 and e.	4-21
4-4	Illustration of Inlet Spillage.	4-22
4-5	Illustration of a Control Volume Used to Calculate Additive Drag.	4-23
4-6	Example for Theoretical Additive Drag Calculation.	4-24
4-7	Open Nose Inlet at Mass Flow Ratio Less Than 1.0.	4-25
4-8	Theoretical Additive Drag Coefficient - Open Nose Inlet.	4-26
4-9	Illustration of Stagnation Point Movement With Mass Flow Variation for a Blunt-Tipped Inlet. (a) Stagnation Stream-Tube Area Variation (b) Mathematical Approximation	4-27

<u>Figure No.</u>	<u>Title</u>	<u>Page</u>
4-10	Example of Inlet Surface Velocity Distribution and Stagnation Point Movement for an Axisymmetric Inlet_Potential Flow Simulation.	4-28
4-11	Flow Patterns for Sharp-Lip Inlet.	4-29
4-12.	Theoretical Additive Drag for a Sharp Lip (Supersonic) Operating at Subsonic Speeds.	4-30
4-13	Illustration of Terminal Shock Wave Position and Approximation Used in Theoretical Additive Drag Calculations.	4-31
4-14	Theoretical Additive Drag Coefficient for 2-Shock, All-External Inlet or Mixed Compression Inlet with Single External Shock.	4-32
4-15	Theoretical Additive Drag Coefficient for 2-Shock, All-External Inlet or Mixed Compression Inlet with Single External Shock.	4-33
4-16	Theoretical Additive Drag Coefficient for 2-Shock, All-External Inlet or Mixed Compression Inlet with Single External Shock.	4-34
4-17	Theoretical Additive Drag Coefficient for 2-Shock, All-External Inlet or Mixed Compression Inlet with Single External Shock.	4-35
4-18	Theoretical Additive Drag Coefficient for 2-Shock, All-External Inlet or Mixed Compression Inlet with Single External Shock.	4-36
4-19	Theoretical Additive Drag Coefficient for 2-Shock, All-External Inlet or Mixed Compression Inlet with Single External Shock.	4-37
4-20	Theoretical Additive Drag Coefficient for 2-Shock, All-External Inlet or Mixed Compression Inlet with Single External Shock.	4-38
4-21	Theoretical Additive Drag Coefficient for 2-Shock, All-External Inlet or Mixed Compression Inlet with Single External Shock.	4-39
4-22	Illustration of 3-Shock Geometric Relationships.	4-40
4-23	Theoretical Additive Drag Coefficient for 3-Shock, All-External Inlet or Mixed Compression Inlet with Two-External Shocks.	4-41
4-24	Theoretical Additive Drag Coefficient for 3-Shock, All-External Inlet or Mixed Compression Inlet with Two-External Shocks.	4-42
4-25	Theoretical Additive Drag Coefficient for 3-Shock, All-External Inlet or Mixed Compression Inlet with Two-External Shocks.	4-43
4-26	Theoretical Additive Drag Coefficient for 3-Shock, All-External Inlet or Mixed Compression Inlet with Two-External Shocks.	4-44

<u>Figure No.</u>	<u>Title</u>	<u>Page</u>
4-27	Theoretical Additive Drag Coefficient for 3-Shock, All-External Inlet or Mixed Compression Inlet with Two-External Shocks.	4-45
4-28	Theoretical Additive Drag Coefficient for 3-Shock, All-External Inlet or Mixed Compression Inlet with Two-External Shocks.	4-46
4-29	Theoretical Additive Drag Coefficient for 3-Shock, All-External Inlet or Mixed Compression Inlet with Two-External Shocks.	4-47
4-30	Theoretical Additive Drag Coefficient for 3-Shock, All-External Inlet or Mixed Compression Inlet with Two-External Shocks.	4-48
4-31	Illustration of Additive Drag Calculation Path for an Axisymmetric Inlet.	4-49
4-32	Diagram Showing Conical Flow Field Streamline Construction.	4-50
4-33	Theoretical Additive Drag Design Charts for Axisymmetric (Single Cone) Inlets. Cone Semi-Vertex Angle $\theta_{r1} = 5^\circ$	4-51
4-34	Theoretical Additive Drag Design Charts for Axisymmetric (Single Cone) Inlets. Cone Semi-Vertex Angle $\theta_{r1} = 6^\circ$	4-52
4-35	Theoretical Additive Drag Design Charts for Axisymmetric (Single Cone) Inlets. Cone Semi-Vertex Angle $\theta_{r1} = 7^\circ$	4-53
4-36	Theoretical Additive Drag Design Charts for Axisymmetric (Single Cone) Inlets. Cone Semi-Vertex Angle $\theta_{r1} = 8^\circ$	4-54
4-37	Theoretical Additive Drag Design Charts for Axisymmetric (Single Cone) Inlets. Cone Semi-Vertex Angle $\theta_{r1} = 10^\circ$	4-55
4-38	Theoretical Additive Drag Design Charts for Axisymmetric (Single Cone) Inlets. Cone Semi-Vertex Angle $\theta_{r1} = 12.5^\circ$	4-56
4-39	Theoretical Additive Drag Design Charts for Axisymmetric (Single Cone) Inlets. Cone Semi-Vertex Angle $\theta_{r1} = 15^\circ$	4-57
4-40	Theoretical Additive Drag Design Charts for Axisymmetric (Single Cone) Inlets. Cone Semi-Vertex Angle $\theta_{r1} = 17.5^\circ$	4-58
4-41	Theoretical Additive Drag Design Charts for Axisymmetric (Single Cone) Inlets. Cone Semi-Vertex Angle $\theta_{r1} = 20^\circ$	4-59

<u>Figure No.</u>	<u>Title</u>	<u>Page</u>
4-42	Theoretical Additive Drag Design Charts for Axisymmetric (Single Cone) Inlets. Cone Semi-Vertex Angle $\theta_{r1} = 25^\circ$	4-60
4-43	Theoretical Additive Drag Design Charts for Axisymmetric (Single Cone) Inlets. Cone Semi-Vertex Angle $\theta_{r1} = 30^\circ$	4-61
4-44	Theoretical Additive Drag Design Charts for Axisymmetric (Single Cone) Inlets. Cone Semi-Vertex Angle $\theta_{r1} = 35^\circ$	4-62
4-45	Illustration of Double-Cone Inlet Flow Field.	4-63
4-46	Illustration of Two-Dimensional Detached Shock Wave Geometry.	4-64
4-47	Compilation and General Correlation of Data on Detachment Distance for Two-Dimensional and Axisymmetric Nose Shapes. (Reference 7)	4-65
4-48	Illustration of Theoretical $C_{Da}$ Variation Resulting From "Attached" Terminal Shock Position Assumption. Mach 2.4 Design Isentropic Ramp at Mach 2.4.	4-66
4-49	Illustration of Method Employed to Obtain Corrected Additive Drag.	4-67
4-50	Drag Variation With Mass Flow Ratio.	4-68
4-51	Drag Variation With Mass Flow Ratio.	4-69
4-52	Drag Variation With Mass Flow Ratio.	4-70
4-53	Variation of Corrected to Theoretical Additive Drag Ratio. $\theta_{r1}$ = Initial Ramp Angle - $\theta_{r2}$ = Second Ramp Angle (Reference 11)	4-71
5-1	Theoretical Diffuser Static Pressure Rise as a Function of Initial Mach Number - $\theta/2 = 2^\circ$ .	5-7
5-2	Theoretical Diffuser Static Pressure Rise as a Function of Initial Mach Number - $\theta/2 = 4^\circ$ .	5-8
5-3	Theoretical Diffuser Static Pressure Rise as a Function of Initial Mach Number - $\theta/2 = 6^\circ$ .	5-9
5-4	Sketch of Test Model.	5-10
5-5	Static Pressure Fluctuation Characteristics of Straight Diffuser Models.	5-11
5-6	Diffuser Exit Static Pressure Fluctuation Data	5-12
5-7	Representation of the Nature of Diffuser Total Pressure Fluctuations.	5-13
5-8	Amplitude and Frequency of Diffuser Exit Total Pressure of Sharp Lipped Inlet.	5-14
5-9	Amplitude and Frequency of Diffuser Exit Total Pressure of Round Lipped Inlet.	5-15

<u>Figure No.</u>	<u>Title</u>	<u>Page</u>
5-10	Theoretical Variation of Compressor Face Mach Number with Inlet Mach Number.	5-16
5-11	Streamtube at Low Inlet Mass-Flow-Ratios	5-17
5-12	Twin Duct Instability.	5-18
5-13	Typical Supersonic Inlet Performance Curve with Regions of Instability.	5-19
5-14	Schematics of Buzz Triggering Theories.	5-20
5-15	Effect of Inlet Pressure Fluctuation on Stall.	5-21
6-1	Inlet Compression.	6-35
6-2	Typical Inlet Performance Characteristics.	6-36
6-3	Engine Airflow Matching.	6-37
6-4	Off-Design Inlet Performance.	6-38
6-5	Off-Design Engine Performance.	6-39
6-6	Buzz and Distortion Regions with Varying Engine Airflow.	6-40
6-7	Typical Two-Dimensional Inlet Control System.	6-41
6-8	By-Pass Door Configuration.	6-42
6-9	Illustration of a Conical Spike Inlet Control System.	6-43
6-10	Inlet Control Concepts.	6-44
6-11	Signal With Ideal Control Characteristics.	6-45
6-12	Signal With Poor Control Characteristics.	6-46
6-13	Jet Pipe Pressure Ratio Sensor.	6-47
6-14	Force Vector - Pressure Ratio Sensor.	6-48
6-15	Pressure Ratio Sensor Block Diagram.	
	Compliments of AiResearch Mfg. Div.	6-49
6-16	Stretched Diaphragm Pressure Sensor.	6-50
6-17	Variable Capacitance Concentric Cylinder Pressure Sensor.	6-51
6-18	Pure Fluid Amplifiers.	6-52
6-19	Pressure Ratio Sensor.	6-53
6-20	General Configuration of Valve Ports Showing Control Dimensions.	6-54
6-21	Omitted	6-55
6-22	Omitted	6-56
6-23	Omitted	6-57
6-24	Illustration of Jet Pipe Valve Characteristics.	6-58
6-25	Idealized Characteristics of a Hydraulic Servo Valve.	6-59
6-26	Two-Stage Electrohydraulic Servo Valve. The First Stage is a Four-Way Flapper Valve With a Calibrated Pressure Output, Driving a Second Stage Spring-Loaded Four-Way Spool Valve.	6-60
6-27	Two-Stage Valve With Mechanical Feedback. The First Stage is a Three-Way Valve. The Second Stage is a Four-Way Spool Valve.	6-61
6-28	Two-Stage Valve With Mechanical Feedback. The First Stage is a Four-Way Flapper Valve. The Second Stage is a Four-Way Spool Valve. The extension of the 6-62 Flapper into a Leaf Spring Acts as the Feedback Element.	



<u>Figure No.</u>	<u>Title</u>	<u>Page</u>
6-29	Two-Stage Serv. Valve With a Jet-Pipe First Stage and Mechanical Feedback. The Second Stage is a Four-Way Spool Valve Attached to the First-Stage Nozzle by a Special Feedback Spring.	6-63
6-30	Actuation Geometry and Legend.	6-64
6-31	Actuator Force Vs Force Gradient - M/L.	6-65
6-32	Actuator Force Vs Force Gradient - M/L.	6-66
6-33	Actuator Force.	6-67
6-34	Actuator Stroke Vs Lever Arm and Deflection.	6-68
6-35	Weights of Plain, Single Rod End Actuator Assemblies.	6-69
6-36	Weights of Tandem or Parallel Actuators and Valves Assemblies.	6-70
6-37	Signal Variations	6-71
6-38	Local Mach Sensor - Pressure Ratio Error Vs $M_0$	6-72
6-39	Performance of Pressure Ratio Sensor	6-73
6-40	Bypass Door Control Loop Pressure Recovery Vs Signal Pressure Ratio	6-74
6-41	Bypass Door Control Loop - Typical Sensor Accuracy Requirements	6-75
6-42	Centerbody Control Loop - Sensor Accuracy Requirements	6-76
7-1	Typical Engine Compartment Cooling Configuration.	7-33
7-2	Estimated T2B Forward Engine Compartment Secondary Airflow.	7-34
7-3	Structural Temperature Variation With Secondary Airflow.	7-35
7-4	Inlet Optimization.	7-36
7-5	Typical Plot of Nozzle Gross Thrust Coefficient.	7-37
7-6	Sketch of Ejector Configurations.	7-38
7-7	Effect of Secondary Airflow on Ejector Performance - $M_0 = 0.9$ , 35000 Ft.	7-39
7-8	Effect of Secondary Airflow on Ejector Performance - $M_0 = 1.6$ , 35000 Ft.	7-40
7-9	Effect of Secondary Airflow on Ejector Performance - $M_0 = 2.0$ , 35000 Ft.	7-41
7-10	Comparison of Nozzle Gross Thrust Coefficients.	7-42
7-11	Nozzle Pumping Characteristics.	7-43
7-12	Engine Compartment Pressure at Mach No. = 2.0.	7-44
7-13	Engine Compartment Bursting Pressure Versus Power Setting.	7-45
7-14	Sketch of Cooling Configuration.	7-46
7-15	Secondary Airflow Matching.	7-47
7-16	Secondary Airflow Versus Gap Area.	7-48
7-17	Sketch of RA-5C Ground Cooling Configuration.	7-49
7-18	Ground Cooling Airflow Matching.	7-50
7-19	Engine Compartment Bursting Pressures.	7-51

<u>Figure No.</u>	<u>Title</u>	<u>Page</u>
7-20	Sketch of Interaction Between Exit Flow and Free Stream Flow.	7-52
7-21	Performance of the 15-Deg Oblique Exhaust Nozzle with External Flow.	7-53
7-22	Performance of the 30-Deg Oblique Exhaust Nozzle with External Flow.	7-54
7-23	Performance of the 45-Deg Oblique Exhaust Nozzle with External Flow.	7-55
7-24	Performance of the 60-Deg Oblique Exhaust Nozzle with External Flow.	7-56
7-25	Sketch of Flush and Shielded Exits.	7-57
7-26	Performance Comparison of Flush and Shielded Exits.	7-58
7-27	Sketch of RA-5C Engine Compartment Pressure Relief Door.	7-59
7-28	Flow Coefficients for RA-5C Engine Compartment Pressure Relief Door.	7-60
7-29	Correlated Characteristics of Drilled Materials in Normal Flow: $\ell/D_H \approx .64$ .	7-61
7-30	$g(\ell/D_H)$ and $f(\sigma_0)$ for Drilled Materials in Parallel Flow from Equation 1.	7-62
7-31	Nomenclature.	7-63
7-32	Sample Determination of $\sigma_0$ as a Function of $\overline{\Delta P}/\overline{P}_0$ for the Case of: $\frac{\overline{U}\sqrt{\overline{\rho}}}{\delta_0 A_0} = .010$ ; $\overline{H}_0 = 1.20$ ; $\ell/D_H = 1.00$	7-64
7-33	Recovery Characteristics of a Flush Rectangular Inlet. Reference: (NASA MEMO 12-21-58L).	7-65
7-34	Drag Characteristic of a Flush Rectangular Inlet. Reference: (NASA MEMO 12-21-58L).	7-66
7-35	Recovery Characteristic of a Flush Rectangular Inlet. Reference: (NASA MEMO 12-21-58L).	7-67
7-36	Drag Characteristic of a Flush Rectangular Inlet. Reference: (NASA MEMO 12-21-58L).	7-68
7-37	Recovery Characteristic of a Flush Rectangular Inlet. Reference: (NASA MEMO 12-21-58L).	7-69
7-38	Drag Characteristic of a Flush Rectangular Inlet. Reference: (NASA MEMO 12-21-58L).	7-70
7-39	Recovery Characteristic of a Flush Rectangular Inlet. Reference: (NASA MEMO 12-21-58L).	7-71
7-40	Drag Characteristic of a Flush Rectangular Inlet. Reference: (NASA MEMO 12-21-58L).	7-72
7-41	Recovery Characteristic of a Flush Rectangular Inlet. Reference: (NASA MEMO 12-21-58L).	7-73
7-42	Drag Characteristic of a Flush Rectangular Inlet. Reference: (NASA MEMO 12-21-58L).	7-74

<u>Figure No.</u>	<u>Title</u>	<u>Page</u>
7-44	Pressure Recovery Characteristic of Flush Rectangular Inlet Using a 7° Approach Ramp with Diverging Walls. (NACA Submerged Inlet.) Reference: (NASA MEMO 12-21-58L).	7-75
7-45	Drag Characteristics of a Flush Rectangular Inlet Using a 7° Approach Ramp with Diverging Walls. (NACA Submerged Inlet.) Reference: (NASA MEMO 12-21-58L).	7-76
4-46	Variation of Required Inlet Area with Mach Number for Operation at Equal Mass Flows and Minimum Drag for Each Flush Rectangular Inlet.	7-77
7-47	Mass Flow Ratio for Various Fractions of Boundary Layer Velocity Profile Parameter $M = 7$ . Reference: NACA TN 3533.	7-78
7-48	Total Momentum Ratio for Various Fractions of Boundary Layer Velocity Profile Parameter $M = 7$ . Reference: NACA TN 3533.	7-79
7-49	Momentum Ratio for Various Fractions of Boundary Layer Velocity Profile Parameter $M = 7$ . Reference: NACA TN 3533.	7-80
7-50	Total Pressure Recovery of Attached Rectangular Boundary Layer Inlets for Various Inlet Heights. Velocity Profile Parameter $M = 7$ . Reference: NACA TN 3533.	7-81
7-51	Test of Submerged and Scoop Inlet. Reference: NACA RM E53L28b.	7-82
7-52	Total Pressure Recovery of Submerged and Scoop Inlets. Reference: NACA RM E53L28b.	7-83
7-53	Mass Flow Characteristics of a Scoop Inlet.	7-84
7-54	Estimated Actual to Theoretical Mass Flow and Recovery Characteristics of a Scoop Inlet.	7-85
7-55	Typical Heat Exchanger Effectiveness Curves.	7-86
7-56	Typical Heat Exchanger Pressure Drops.	7-87
7-57	Pressure Loss Through Heat Exchanger used in Example.	7-88
7-58	Effect of Ramp Bleed on Inlet Duct Performance.	7-89
7-59	Ramp Bleed Flow Rates.	7-90
7-60	Boundary Layer Diverter Geometry.	7-91
7-61	Turbulent Boundary Layer Profile Characteristics.	7-92
7-62	Turbulent Boundary Layer Profile Characteristics.	7-93
7-63	Mach Number Function For Turbulent Boundary Layer.	7-94
7-64	Free-Stream Reynolds Number Per Unit Length.	7-95
7-65	Equivalent Flat Plate Distance For Turbulent Boundary Layers.	7-96
7-66	Wedge Diverter Pressure Drag Coefficient.	7-97
7-67	Wedge Diverter Pressure Drag Coefficient.	7-98
7-68	Wedge Diverter Pressure Drag Coefficient.	7-99
7-69	Wedge Diverter Skin-Friction Coefficient (Turbulent Flow)	7-100
7-70	Wedge Diverter Skin-Friction Multiplication Factor.	7-101
7-71	Comparison of Results to Experimental Data.	7-102

<u>Figure No.</u>	<u>Title</u>	<u>Page</u>
7-72	Total-Pressure-Loss Coefficient Design Chart for Screens for Values of Loss Coefficient from 0 to 1.0.	7-103
8-1	Turbojet Engine Cycle and Nozzle Process.	8-108
8-2	Isentropic Nozzle Expansion.	8-109
8-3	Real Nozzle Process.	8-110
8-4	Unchoked Convergent Nozzle.	8-111
8-5	Choked Convergent Nozzle.	8-112
8-6	Theoretical Convergent Nozzle Gross Thrust Parameter.	8-113
8-7	Theoretical Convergent Nozzle Gross Thrust Parameter.	8-114
8-8	Theoretical Convergent Nozzle Gross Thrust Parameter.	8-115
8-9	Optimum or Theoretical Maximum Gross Thrust Parameter.	8-116
8-10	Optimum or Theoretical Maximum Gross Thrust Parameter.	8-117
8-11	Optimum or Theoretical Maximum Gross Thrust Parameter.	8-118
8-12	Optimum or Theoretical Maximum Gross Thrust Parameter.	8-119
8-13	Converging Conical Nozzle, Gross Thrust.	8-120
8-14	Converging Conical Nozzle Gross Thrust.	8-121
8-15	Converging Conical Nozzle Gross Thrust.	8-122
8-16	Convergent Divergent Nozzle Terminology.	8-123
8-17	Optimum Nozzle Area Ratio.	8-124
8-18	Variable C-D Nozzle Thrust Coefficients.	8-125
8-19	Variable C-D Nozzle Discharge Coefficients.	8-126
8-20	Theoretical Thrust Variation from Optimum for Various Fixed Area Ratio Nozzles.	8-127
8-21	Theoretical Thrust Types.	8-128
8-22	Theoretical C-D Thrust Variation with Area Ratio and Pressure Ratio, $\gamma = 1.2$ .	8-129
8-23	Theoretical C-D Thrust Variation with Area Ratio and Pressure Ratio, $\gamma = 1.25$ .	8-130
8-24	Theoretical C-D Thrust Variation with Area Ratio and Pressure Ratio, $\gamma = 1.3$ .	8-131
8-25	Theoretical C-D Thrust Variation with Area Ratio and Pressure Ratio, $\gamma = 1.30$ .	8-132
8-26	Theoretical C-D Thrust Variation with Area Ratio and Pressure Ratio, $\gamma = 1.35$ .	8-133
8-27	Convergent Nozzle Thrust Coefficient.	8-134
8-28	Variable Convergent Nozzle Thrust Coefficient.	8-135
8-29	Estimated Performance of Convergent Nozzle with Blunt Base.	8-136
8-30	Effect of Lip Angle Variation on Gross Thrust Coefficient and Flow Coefficient of a Convergent Nozzle.	8-137
8-31	Effect of Lip Angle Variation at Two Inlet-to-Outlet Diameter Ratios on the Flow Coefficient.	8-138

<u>Figure No.</u>	<u>Title</u>	<u>Page</u>
8-32	Effect of Inlet-to Outlet Diameter Ratio on the Flow Coefficient at Various Lip Angles and at Two Jet Total Pressure Ratios.	8-139
8-33	Annular Nozzle Configurations.	8-140
8-34	Fan Air Exhaust Nozzle on Fan Engine.	8-141
8-35	Schematic Diagram of Jet-Exit Model Installed in 3- by 6-Foot Supersonic Wind Tunnel.	8-142
8-36	Installation of Nozzle in Test Chamber.	8-143
8-37	Thrust Coefficient Characteristics for Conical Nozzle.	8-144
8-38	Thrust Coefficients of Convergent-Divergent Conical Nozzles for Expansion Ratio of 2.65 and Divergent Angles of $7^{\circ}10'$ , $11^{\circ}50'$ , $24^{\circ}$ and $50^{\circ}$ .	8-145
8-39	Schematic Diagrams of Convergent-Divergent Conical Nozzles.	8-146
8-40	Nozzles Designed Conical and by Characteristics (All dimensions in inches).	8-147
8-41	Nozzles of Various Throat and Diffuser Geometry, Dimensions in Inches.	8-148
8-42	Variation of Thrust Coefficient with Various Contours.	8-149
8-43	Variation in Thrust Coefficient at a Nozzle Pressure Ratio of 2.0 with Divergence Angle for Nozzles of Various Design Pressure Ratios.	8-150
8-44	Generalized Pressure Distributions Along Divergent Walls of Several Convergent-Divergent Conical Nozzles Having Various Divergence Angles at a Nozzle Pressure Ratio of Approximately 4.	8-151
8-45	Variation of Thrust Coefficient for a Nozzle Designed by Characteristic Theory.	8-152
8-46	Thrust Coefficients for Two C-D Nozzles Having Different Throat Contours Downstream of Throat; Expansion Ratio, 1.8.	8-153
8-47	Thrust Coefficients for Nozzles Having Various Wall Angles; Expansion Ratio = 1.55; $l_d/D_t = .44$	8-154
8-48	Nozzle Thrust Coefficient Characteristics for a Range of Freestream Mach Numbers; Expansion Ratio = 1.39; Nozzle is Conical.	8-155
8-49	Nozzle Thrust Coefficient Characteristics for a Range of Freestream Mach Numbers; Expansion Ratio = 9.0; Nozzle is Conical.	8-156
8-50	Friction Effects on a Convergent-Divergent Conical Nozzle; Expansion Ratio, 1.39; Divergence Angle, $7^{\circ}10'$ .	8-157
8-51	Variation in Thrust Coefficient and Nozzle-Exit Area Resulting from Decreases in Divergent Angle.	8-158
8-52	Comparison of Theoretical and Experimental Thrust Variation.	8-159

<u>Figure No.</u>	<u>Title</u>	<u>Page</u>
8-53	Ejector Configurations of NACA RM E55G21a.	8-160
8-54	Test Results of Ejector 1 of NACA RM E55G21a.	8-161
8-55	Test Results of Ejector 2 of NACA RM E55G21a.	8-162
8-56	Test Results of Ejector 3 of NACA RM E55G21a.	8-163
8-57	Test Results of Ejector 4 of NACA RM E55G21a.	8-164
8-58	Test Results of Ejector 5 of NACA RM E55G21a.	8-165
8-59	Test Results of Ejector 6 of NACA RM E55G21a.	8-166
8-60	Test Results of Ejector 11 of NACA RM E55G21a.	8-167
8-61	Test Results of Ejector 12 of NACA RM E55G21a.	8-168
8-62	Ejector Geometry of NACA TN D-763.	8-169
8-63	Performance of Ejector 1 of NACA TN D-763.	8-170
8-64	Pumping Performance of Ejector 1 of NACA TN D-763.	8-171
8-65	Performance of Ejector 2 of NACA TN D-763.	8-172
8-66	Pumping Performance of Ejector 2 of NACA TN D-763.	8-173
8-67	Corrected Ejector Temperature Ratios For Typical Conditions.	8-174
8-68	Ejector Configurations, NACA RM E57F13.	8-175
8-69	Effect of Flow Divergence Angle on Thrust Coefficient at Design Pressure Ratio.	8-176
8-70	Performance of Ejector 1. Exit Diameter Ratio, 1.24; Throat Diameter Ratio, 1.08; Spacing Ratio, 0.33; Flow Divergence Angle, 13°; Shroud Divergence Angle, 15°.	8-177
8-71	Performance of Ejector 2. Exit Diameter Ratio, 1.24; Throat Diameter Ratio, 1.08; Spacing Ratio, 0.28; Flow Divergence Angle, 23°; Shroud Divergence Angle, 20°.	8-178
8-72	Performance of Ejector 3. Exit Diameter Ratio, 1.24; Throat Diameter Ratio, 1.08; Spacing Ratio, 0.22; Flow Divergence Angle, 28°; Shroud Divergence Angle, 25°.	8-179
8-73	Performance of Ejector 4. Exit Diameter Ratio, 1.46; Throat Diameter Ratio, 1.10; Spacing Ratio, 0.69; Flow Divergence Angle, 19°; Shroud Divergence Angle, 15°.	8-180
8-74	Performance of Ejector 5. Exit Diameter Ratio, 1.46; Throat Diameter Ratio, 1.10; Spacing Ratio, 0.51; Flow Divergence Angle, 25°; Shroud Divergence Angle, 20°.	8-181
8-75	Performance of Ejector 6. Exit Diameter Ratio, 1.46; Throat Diameter Ratio, 1.10; Spacing Ratio, 0.40; Flow Divergence Angle, 30°; Shroud Divergence Angle, 25°.	8-182
8-76	Comparison of Nozzle Performance for Two Nozzles with Different Shroud Divergence Angles.	8-183

<u>Figure No.</u>	<u>Title</u>	<u>Page</u>
8-77	Ejector Configuration.	8-184
8-78	Performance of Ejector at Weight-Flow Ratio of About .032. Exit Diameter Ratio, 1.8; Throat Diameter Ratio, 1.0.	8-185
8-79	Shroud Static Pressure Distribution for Various Primary Nozzle Pressure Ratios. Shroud Divergence = 15°. Corrected Weight Flow Ratio, = .032	8-186
8-80	Effect of Secondary Airflow on Nozzle Performance.	8-187
8-81	Shroud Static Pressure Distribution at Several Corrected Weight Flows.	8-188
8-82	Low Base Drag Nozzle Configuration.	8-189
8-83	Low Base Drag Nozzle Pressure Distributions.	8-190
8-84	Converging-Diverging Nozzle with Supersonic Convergence.	8-191
8-85	Typical Diverging Wall Pressures. Nozzle Pressure Ratio $\Delta = 2.336$ $\phi = 2.323$	8-192
8-86	Effect of Nozzle Misalignment on Nozzle Performance.	8-193
8-87	Axially Symmetric Compressible Nozzle Flow.	8-194
8-88	Compound-Compressible Flow in a Nozzle of Fixed Geometry.	8-195
8-89	Evolution of a One-Dimensional Compound-Wave.	8-196
8-90	Relationship of Flow Parameters in a Convergent- Divergent Nozzle.	8-197
8-91	Relationship of Flow Parameters During Choked Flow.	8-198
8-92	Stream Mach Numbers at the Nozzle Throat During Choked Flow.	8-199
8-93	Comparison of Compound Compressible Flow Theory with Experimental Results.	8-200
8-94	Schematic of Analytical Model Used in Computations.	8-201
8-95	Choked Pumping Characteristics - Two Flow Ejector $\gamma_1 = 1.3 \quad \gamma_2 = 1.4$	8-202
8-96	Two-Flow Nozzle Pumping Characteristics.	8-203
8-97	Two-Flow Nozzle Pumping Characteristics. $\gamma_1 = 1.3 \quad \gamma_2 = 1.4 \quad A^*/A_{EXIT} = 0.2$	8-204
8-98	Two-Flow Nozzle Pumping Characteristics. $\gamma_1 = 1.3 \quad \gamma_2 = 1.4 \quad A^*/A_{EXIT} = 0.3$	8-205
8-99	Two-Flow Nozzle Pumping Characteristics. $\gamma_1 = 1.3 \quad \gamma_2 = 1.4 \quad A^*/A_{EXIT} = 0.4$	8-206
8-100	Two-Flow Nozzle Pumping Characteristics. $\gamma_1 = 1.3 \quad \gamma_2 = 1.4 \quad A^*/A_{EXIT} = 0.5$	8-207
8-101	Two-Flow Nozzle Pumping Characteristics. $\gamma_1 = 1.3 \quad \gamma_2 = 1.4 \quad A^*/A_{EXIT} = 0.6$	8-208

<u>Figure No.</u>	<u>Title</u>	<u>Page</u>
8-102	Two-Flow Nozzle Pumping Characteristics. $\gamma_1 = 1.3 \quad \gamma_2 = 1.4 \quad A^*_1/A_{EXIT} = 0.7$	8-209
8-103	Two-Flow Nozzle Pumping Characteristics. $\gamma_1 = 1.3 \quad \gamma_2 = 1.4 \quad A^*_1/A_{EXIT} = 0.8$	8-210
8-104	Two-Flow Nozzle Pumping Characteristics. $\gamma_1 = 1.3 \quad \gamma_2 = 1.4 \quad A^*_1/A_{EXIT}$	8-211
8-105	Variation in $P_{t2}/P_{t1}$ with Primary Nozzle Pressure Ratio.	8-212
8-106	Comparison of Theoretical and Experimental Static Thrust Characteristics for One Ejector Operating Point.	8-213
8-107	Optimum Area Ratio and Thrust Trends for Converging-Diverging Nozzles (Reference 1).	8-214
8-108	Typical Operating Regimes for Conical Converging-Diverging Nozzles (References 2 and 3).	8-215
8-109	Convergent-Divergent Ejector Nozzle Flow Fields.	8-216
8-110	Effect of Exit-to-Primary Area Ratio on Divergent Shroud Nozzle Thrust (Reference 10).	8-217
8-111	Effect of Nozzle and Shroud Exit Spacing on Divergent Shroud Ejector Nozzle Thrust.	8-218
8-112	Effect of Secondary Flow on Divergent Shroud Ejector Nozzle Thrust.	8-219
8-113	External Aerodynamic Flow Effects on Nozzle Thrust (Reference 9)	8-220
8-114	Isentropic Plug Flow and Design Characteristics.	8-221
8-115	Comparison of Nozzle Performance.	8-222
8-116	Two Nozzle Configuration with a Design Pressure Ratio of 16.5.	8-223
8-117	Variation of Gross Thrust-Minus-Drag Coefficient with Jet Total Pressure Ratio.	8-224
8-118	Variation of Gross Thrust Coefficient with Jet Total-Pressure Ratio.	8-225
8-119	Gross Thrust-Minus-Drag and Gross Thrust Coefficients $v_2$ , Mach Number for Jet Total-Pressure Ratio Schedule.	8-226
8-120	Effect of Design Pressure Ratio on Gross Thrust Coefficient.	8-227
8-121	Afterbody Configurations.	8-228
8-122	Comparison of Conical Plug Performance to Isentropic Plug Performance.	8-229
8-123	Other Types of Plug Nozzles.	8-230
8-124	Aerodynamic Boattail Nozzle Configuration and Flow Pattern.	8-231
8-125	Effect of Jet Total-Pressure Ratio and Mach Number on Gross Thrust Coefficient.	8-232



<u>Figure No.</u>	<u>Title</u>	<u>Page</u>
8-126	Effect of Jet Total-Pressure Ratio and Mach Number on Gross Thrust-Minus-Drag Coefficient.	8-233
8-127	Effect of Truncation on Gross Thrust-Minus-Drag and Gross Thrust Coefficients vs. Mach Number at a Jet Total-Pressure Ratio Schedule.	8-234
8-128	Configuration of Convergent Plug Nozzle.	8-235
8-129	Blow-In-Door Ejector.	8-236
8-130	Effect of Mach Number on Ejector Performance.	8-237
8-131	Effect of Blow-In-Door Area on Ejector Performance.	8-238
8-132	Effect of Gross Section Geometry on Ejector Performance.	8-239
8-133	Variation of Gross Thrust Minus Boattail and Chroud Drag Performance with Primary Total-Pressure Ratio for Constant Corrected Weight-Flow Ratios and Mach Numbers.	8-240
134	Variation of Ejector Performance and External Drag Characteristics with Mach Number for a Scheduled Primary Total-Pressure Ratio and Corrected Weight-Flow Ratio.	8-241
8-135	Variation of Nozzle Performance and External Drag Characteristics as a Function of Nozzle Pressure Ratio.	8-242
8-136	Variation of Nozzle Performance and External Drag Characteristics with Mach Number for a Jet Total-Pressure Ratio Schedule.	8-243
8-137	Variation of Average Nozzle Performance Coefficient with Primary Total-Pressure Ratio, Mach No., $M = 1.70$ , $\alpha = 9.5^\circ$ (angle of attack).	8-244
8-138	Variation of Average Nozzle Performance Coefficient with Primary Total-Pressure Ratio; Mach No., 1.2; $\alpha, 2^\circ$ .	8-245
8-139	Propulsion System Weight.	8-246
8-140	Propulsion System Weight.	8-247
8-141	Nozzle Performance Comparison.	8-248
8-142	Nozzle and Afterbody Analysis Area.	8-249
8-143	Nozzle Types and Relationship.	8-250
8-144	Nozzle Variations.	8-251
8-145	Convergent Nozzles.	8-252
8-146	J79-10, 17 Convergent Divergent Nozzle, Guided Expansion.	8-253
8-147	J79-8, 15 Aerodynamic Ejector Nozzle.	8-254
8-148	Flow Diagrams for J79 Exhaust Nozzles.	8-255
8-149	Blow-In-Door Ejector.	8-256
8-150	Blow-In-Door Ejector Flow Diagram.	8-257
8-151	Isentropic Plug Nozzle.	8-258

<u>Figure No.</u>	<u>Title</u>	<u>Page</u>
8-152	Aerodynamic Boattail Nozzle.	8-259
8-153	Aerodynamic Boattail Nozzle with Aft Flap.	8-260
8-154	Performance of Convergent-Divergent Ejector Nozzles.	8-261
8-155	Blow-In-Door Ejector Nozzle.	8-262
8-156	Long-Cone Plug Nozzle, (ABN).	8-263
8-157	Fixed Ejector Exit Configuration.	8-264
8-158	Clustered Jet Exits.	8-265
8-159	Engine Interfairing Pressure Distributions, $M = 1.2$ .	8-266
8-160	Performance of Basic-and Extended-Interfairing Configurations, $M = 1.2$ .	8-267
8-161	Effect of Nozzle Efficiency on Sea Level Dash Fuel Requirements, $M = 0.85$ Sea Level.	8-268
8-162	Ratio of Gross to Net Thrust with Bypass Ratio.	8-269
8-163	Comparative Effectiveness of Thrust Reversers and Drag Parachutes for Ground Roll Distance Reduction.	8-270
8-164	Comparative Effectiveness of Thrust Reverser Speed Brakes for In-Flight Aircraft Deceleration.	8-271
8-165	Typical Types of Common Reversers.	8-272
8-166	Typical Thrust Reverser Static Performance.	8-273
8-167	Conical Clamshell Target Reverser Performance Trends.	8-274
8-168	Coannular E-D Nozzle.	8-275
8-169	E-D Nozzle Performance.	8-276
8-170	Sting in Base.	8-277
8-171	Base Vent Through Sting.	8-278
8-172	Base Bleed Through Sting.	8-279
8-173	Radial Base Bleed.	8-280
8-174	Axial Base Bleed.	8-281
8-175	Effectiveness of Sting Concepts in Increasing Base Thrust.	8-282
9-1	Transverse Curvature Effects of Turbulent Boundary Layer. (Reference 1)	9-64
9-2	Effect of Compressibility on Skin Friction to Smooth and "Completely Rough" Surfaces.	9-65
9-3	Increase of Skin Friction Due to Surface Roughness.	9-66
9-4	Superposition of Pressure Distribution. (Reference 3)	9-67
9-5	Subsonic Wave Drag of Conical Afterbodies.	9-68
9-6	Subsonic-Transonic Wave Drag of Circular Arc Afterbodies.	9-69
9-7	Conical Boattail Analogy. (Reference 8)	9-70
9-8	Supersonic Wave Drag of Wedge Afterbodies. (Reference 11)	9-71
9-9	Supersonic Wave Drag of Conical Afterbodies. (Reference 11)	9-72
9-10	Supersonic Wave Drag of Parabolic Afterbodies. (Reference 11)	9-73
9-11	Pressure Coefficients on Conical Afterbodies at Supersonic Speeds. (Reference 11)	9-74
9-12	Pressure Coefficients on Cylinder Behind Cone. (Reference 11)	9-75

<u>Figure No.</u>	<u>Title</u>	<u>Page</u>
9-13	Subsonic and Transonic Flow Past a Blunt-Trailing-Edge Section. (Reference 19)	9-76
9-14	Supersonic Flow Analogy.	9-77
9-15	Critical Pressure-Rise Coefficient for Turbulent Boundary Layer on Two-Dimensional Afterbodies.	9-78
9-16	Two-Dimensional Base Pressures ( $\alpha = \beta = 0^\circ$ , No Jet)	9-79
9-17	Two-Dimensional Wake Turning Angle.	9-80
9-18	Mach Number Notation.	9-81
9-19	Two-Dimensional Boattail Flow Conditions.	9-82
9-20	Two-Dimensional Boattail Separation Angle.	9-83
9-21	Two-Dimensional Afterbody at Angle of Attack.	9-84
9-22	Base Pressure Coefficient for Cylindrical Afterbodies.	9-85
9-23	Axisymmetric Wake Turning Angle. (Reference 8)	9-86
9-24	Subsonic-Transonic Base Pressures on Axisymmetric Boattails.	9-87
9-25	Axisymmetric Boattail Angle at Separation.	9-88
9-26	Axisymmetric Boattail Flow Conditions.	9-89
9-27	Pressure Rise Required for Separation of a Turbulent Boundary Layer on Afterbodies of Revolution. (Reference 6)	9-90
9-28	Supersonic Base Drag Coefficients on Axisymmetric Boattails. (Reference 6)	9-91
9-29a	Supersonic Base Drag Coefficients on Axisymmetric Boattails. (Reference 6)	9-92
9-29b	Supersonic Base Drag Coefficients on Axisymmetric Boattails. (Reference 6)	9-93
9-29c	Supersonic Base Drag Coefficients on Axisymmetric Boattails (Continued). (Reference 6)	9-94
9-29d	Supersonic Base Drag Coefficients on Axisymmetric Boattails (Continued). (Reference 6)	9-95
9-29e	Supersonic Base Drag Coefficients on Axisymmetric Boattails (Concluded). (Reference 6)	9-96
9-30	Schematic Diagram of Attached External Flow.	9-97
9-31	Schematic Diagram of Separated External Flow.	9-98
9-32a	Sequence of Events Denoting Jet Interference Effects on Afterbody (Reference 25)	9-99
9-32b	Sequence of Events Denoting Jet Interference Effects on Afterbody (Concluded) (Reference 25)	9-100
9-33	Plateau Pressure Rise Coefficient in Turbulent Separated Flow. (Reference 42)	9-101
9-34	Turning Angle Required to Compress Flow to Plateau Pressure Level. (Reference 25)	9-102
9-35	Height of Mach 1.4 Line in Turbulent Boundary Layer.	9-103
9-36	Effect of Pressure Feed-Back on Incipient Separation of Turbulent Boundary Layer. (Reference 32)	9-104
9-37	Flow Schematic of Jet Interference Problem with Attached Boundary Layer.	9-105

<u>Figure No.</u>	<u>Title</u>	<u>Page</u>
9-38	Calculated Requirements for Incipient Separation	9-106
9-39a	Effect of Jet Temperature Ratio on Wake-Pressure Ratio - Continued. (Reference 25)	9-107
9-39b	Effect of Jet Temperature Ratio on Wake-Pressure Ratio - Continued. (Reference 25)	9-108
9-39c	Effect of Jet Temperature Ratio on Wake-Pressure Ratio - Concluded. (Reference 25)	9-109
9-40	Effect of Mixing Length Ratio on Wake-Pressure Ratio. (Reference 25)	9-110
9-41	Effect of Internal Specific Heat Ratio on Wake-Pressure Ratio.	9-111
9-42	Extent of Separation Upstream of Disturbance for Turbulent Flow.	9-112
10-1	Turbofan Gas Flow Paths.	10-20
10-2	Propulsive Efficiency.	10-21
10-3	Specific Fuel Consumption.	10-22
10-4	Specific Thrust.	10-23
10-5	Thrust Lapse With Speed.	10-24
10-6	Cruise to Static Thrust Ratio.	10-25
10-7	JT9D-1 Cutaway.	10-26
10-8	RB.203 Trent Cutaway.	10-27
10-9	Estimated Windmilling Drag.	10-28
10-10	Typical Fan Exit Static Pressure Distortion.	10-29
10-11	Fan Cowl Comparison	10-30
10-12	Cowl Length Comparison	10-31
10-13	Typical Compartment Temperature Zones.	10-32
10-14	Typical High Bypass Turbofan Inlet Velocity Profile.	10-33
10-15	External Drag Breakdown.	10-34
10-16	Afterbody Boattail Drag Test Results.	10-35
10-17	Front Fan Nacelle.	10-36
10-18	Skin Friction Drag Coefficient Based on Surface Wetted Area	10-37
10-19	Reynolds Number	10-38
10-20	Effect of Mach Number on the Skin-Friction Coefficient.	10-39
10-21	Skin Friction Drag Coefficient.	10-40
10-22	Total Nacelle Scrubbing Drag.	10-41
10-23	Scrubbing Drag.	10-42
10-24	Change in Airplane Drag with Nacelle Position.	10-43
10-25	Nacelle Pressure Coefficients, Effect of Fuselage and Wing Proximity.	10-44
10-26	Flow-Through Nacelles.	10-45
10-27	Incremental Nacelle Drag Comparison.	10-46
10-28	Blowing Nacelle.	10-47
10-29	Afterbody Drag vs. Fan Gross Thrust.	10-48
10-30	Powered Fan Simulation.	10-49
10-31	Powered Fan Simulation Calibration.	10-50
10-32	Powered Fan Simulation Calibration Facility.	10-51

<u>Figure No.</u>	<u>Title</u>	<u>Page</u>
10-33	Powered Fan Simulator Performance.	10-52
10-34	Auxiliary Inlets.	10-53
10-35	Auxiliary Inlet Performance	10-54
10-36	Offset Fan Nozzle Velocity Coefficients.	10-55
10-37	Typical Nacelle Drag Breakdown.	10-56
10-38	Effect of Installation on Cruise SFC.	10-57
10-39	Total Installation Loss.	10-58
10-40	Typical Reverser Effectiveness.	10-59
10-41	Thrust Reverser Comparison.	10-60
10-42	Attached Flow Reingestion.	10-61
10-43	Inlet Pressure Recovery.	10-62
10-44	Inlet Distortion.	10-63
10-45	Average Inlet Air Temperature Rise.	10-64
10-46	Effect of Reingestion on Reverser Thrust.	10-65

## INTRODUCTION

Airbreathing vehicles have been developed for much of the flight spectrum applicable to their operation. In the twenty year history of turbojet operation, flight speeds have advanced from moderate subsonic to Mach 3 and beyond. Recently, new innovations have appeared such as high by-pass ratio turbofans with high air handling capacities which make induction system losses and associated drag more critical performance items than with conventional turbojets. Variable 3-dimensional inlets, translating spikes, and translating cowl are fairly recent innovations aimed at propulsion system optimization. New exhaust system techniques such as variable guided expansion ejector nozzles, blow-in-door nozzles and IP suppression plug nozzles are appearing on the scene to broaden the spectrum of performance trade-off to be accomplished.

A large quantity of data has been gathered on airbreathing propulsion system performance. Some of these data reside with this contractor in its several divisions, in publications of several governmental agencies and of other contractors. In the field of propulsion, inlet and exhaust flows and their effects on vehicle performance characteristics, there has existed a definite need to bring isolated, though related, items of data together to be correlated and interpreted in the light of known theory. The effort presented herein was developed as a tool by which future design evaluations can be made on the basis of a much more complete and comprehensive correlation of the large quantity of existing data than has been available in the past.

## 1.0 Inlet Design Considerations

In order to furnish the aero-thermodynamic design of an air induction system, a great deal of information must be known about the roles and missions of the aircraft and about the device/services that are to be supplied with air. The items that have to be considered as design features include size of the entry, location, method of precompression (if required), entry lip shape, orientation, cross-sectional shape, boundary layer removal provisions (if required), and secondary air-flow provisions.

### 1.1 Inlet Sizing

In high speed flight regimes, when the flight Mach number is greater than the inlet entrance Mach Number, the size of the freestream tube area occupied by the flow that is required by the total propulsion system is the most important criterion for selecting the size of the inlet capture area. This is particularly true if the aircraft is being designed to fly supersonically. This parameter varies with flight condition and hence, its variation must be considered over the design flight envelope of the aircraft.

The most important air requirement is, of course, for the engine. Other air requirements are minor percentages of the engine air requirement, usually between 5 and 25 percent. Therefore, an evaluation of the engine air freestream area requirement trends will serve to establish the requirement trend of the entire propulsion system. Figure 1-1 is a plot of the typical variation of corrected airflow versus Mach number in the stratosphere for a turbojet or turbofan engine. The corrected airflow parameter being used is  $W_2 \sqrt{t_2} / \delta t_2$ , where  $W_2$  is the engine airflow in pounds per second,  $\sqrt{t_2}$  is the square root of the ratio of the total temperature of the air to the standard total temperature of 518.688° R, and  $\delta t_2$  is the ratio of the engine face total pressure to the standard total pressure of 14.696 pounds per square inch.

Noting that the corrected airflow demand is expressed in a term that includes the engine face total pressure, it is apparent that the inlet size requirement is a function of the inlet performance. For purposes of this explanation, a typical inlet performance schedule will be assumed. This assumed schedule is plotted as Figure 1-2.

Corrected airflow divided by flow area,  $W \sqrt{\theta_t} / A \delta_t$ , is a function of Mach number. This is easily seen when we consider the familiar continuity expression,  $m = \rho AV$ .  $W \sqrt{\theta_t} / A \delta_t$  is tabulated in Appendix E and was used to generate the plot of  $A_0$  vs  $M$  corresponding to the airflow demand plotted on Figure 1-1. Appendix E also contains tabulations of corrected airflow  $W \sqrt{\theta_t} / A \delta_t$  versus the total to static pressure ratio  $P_t/P$  and another corrected airflow parameter,  $W \sqrt{T_t} / A P_t$ , versus Mach number.

Typically, the inlet capture area requirement is determined at the highest flight Mach number as one would expect from the  $A_0$  versus  $M$  trend of Figure 1-3. Figure 1-4 depicts the relationship of the freestream tube area,  $A_0$ , to the capture area,  $A_c$ . The ratio  $A_0/A_c$  is the mass-flow-ratio and is an important parameter in the capture area sizing equation. The equation can be expressed as

$$A_c = \frac{W_D \sqrt{\theta_2} / \delta_{t2}}{W \sqrt{\theta} / A_0 \delta_{t0}} \cdot \frac{\delta_{t2}}{\delta_{t0}} \cdot \frac{1}{A_0/A_c} \quad (1.1)$$

where  $W_D$  is the sum of the engine airflow demand plus the other flow requirements of the system such as boundary layer control bleed and secondary airflow.  $\delta_{t2}/\delta_{t0}$  is equal to  $P_{t2}/P_{t0}$ . If the expected operating mass-flow-ratio at the design point is not realized, a downward adjustment is required in the  $\delta_{t2}/\delta_{t0}$  term. This is accomplished by a downstream motion of the terminal shock to a larger area where the increased terminal shock Mach number will increase the shock loss.

The foregoing inlet sizing criteria are strictly true, only when the air induction system has variable geometry with sufficient authority to vary throat area to accommodate the high corrected airflow demand that the engine has at low speed. In the case of a fixed geometry inlet the sizing expression is written for the minimum or throat area as

$$A_1 = \frac{W_D \sqrt{\theta_2} / \delta_{t2}}{W \sqrt{\theta} / A_1 \delta_{t1}} \cdot \frac{\delta_{t2}}{\delta_{t1}} \quad (1.2)$$

where  $W \sqrt{\theta} / A_1 \delta_{t1}$  is at the desired throat Mach number at the operating point where engine corrected airflow demand is at a maximum. The critical sizing point may be in the low speed flight regime when the mass-flow-ratio or inlet velocity ratio is greater than 1.0. Selection of the desired inlet Mach number may then be



based on performance requirements. Inlet performance in the low speed flight regime is covered in the next section. (Section 2.0).

### 1.2 Inlet Location

The operating environment of an inlet is governed, in part, by its location. However, because of the requirement for compatibility with the overall arrangement of an aircraft, complete freedom in the selection of location is not usually available. The large radomes on most high performance military aircraft have made the nose location unavailable. Also aircraft length is often such that the duct would be unduly long with the inlet at the nose. Hence, the inlet is often located some place aft on the body. One then has the task of selecting the location around the periphery of the body.

Figure 1-5, which was taken from Reference 1 shows the flow characteristics about a body of revolution at moderate supersonic speeds. This set of characteristics indicates that the bottom quadrant is the more favored location, with the top running second best. Considerable angularity and increased local Mach number are indicated for the sides. However, most aircraft bodies are not bodies of revolution and for practical reasons, the sides are often selected for inlet location. The bottom of the body is shunned because of ingestion problems and possible foreign object damage to the engine. When inlets are located on top of the body and are far aft, there is considerable danger that they will be located in a separated region, particularly at angle of attack. The side location has been used with success in several applications. The flow angularity and freestream Mach number elevation measured in flight tests on a high performance aircraft with side inlets were quite moderate as shown on Figure 1-6.

There is no set method for evaluating the inlet location on an aircraft. The foregoing discussion was meant to point up the fact that location is a serious design consideration. In any development program, measurement of the inlet local environment should be given high priority.

### 1.3 Method of Pre-Compression

Pre-compression, prior to the terminal normal shock, in a supersonic inlet can vary in dimensionality, quantity, and complexity according to the requirements of the air vehicle. Pre-compression can be 2-dimensional (i.e., with ramp/ramps) or 3-dimensional (conical). The number of degrees through which the flow is forced to turn depends on the high speed requirements of the aircraft. The number

of oblique shock waves selected by the designer depends upon the required performance level. Isentropic compression may be used to achieve the required results in some cases. And finally, the pre-compression devices may be made to vary with speed in order to optimize performance and to permit better inlet-engine matching.

Aircraft requirements can vary in the following manner:

1. All Subsonic
2. Basic Mission - Sustained Supersonic
3. Subsonic and High Supersonic Mission Requirements
4. Basic Mission - Subsonic, Supersonic Performance Level Required
5. Subsonic and Moderate Supersonic Mission Requirements, High Supersonic Performance Level Required
6. Subsonic and Supersonic Mission Requirements with Emphasis on Low Level Operation

While detailed trade-off studies are required in the final selection of inlet type, the type selection is slanted a priori by the above stated aircraft requirements. It is easily recognized that the all subsonic aircraft does not need pre-compression. At the other end of the spectrum, the aircraft with a sustained high supersonic basic mission can well use a multi-shock, mixed external-internal compression inlet to maximize net propulsive effort and minimize specific fuel consumption. If the supersonic speed performance requirement is sufficiently high on the other four categories cited, mixed compression might be required. External turning limitations are cited in Reference 2. One criterion is that of shock structure requirements as they relate to satisfying equal pressure across the vortex sheet between internal and external flow. The other criterion relates to satisfying shock attachment of both external and internal flow in supercritical operation. This turning restriction is of little consequence below a Mach number of 2.5. The air induction system requirements of a highly maneuverable combat aircraft designed to operate up to this speed can be satisfied with all external inlet compression with less inlet control system complexity and fewer of the attendant technical risks. Aircraft designed to operate above Mach 2.5 may be required to have partially internal shock systems to satisfy performance requirements.

The 3-shock, two oblique, one normal, all external systems has been a fairly common choice in supersonic inlet design. A fixed leading edge wedge usually is used to generate the first oblique shock. Variable compression geometry on the second shock is quite simple to design into the system by allowing the second oblique shock to be generated by a hinged second wedge. Up to a Mach

number of about 2.0, near optimum compression is available from such a system. The deflection angle of the first wedge is often limited by consideration of shock detachment at low supersonic speeds. For instance, a 10 degree wedge generates a detached shock until a Mach number of 1.43. When the first wedge angle is thus limited, the strengths and static pressure ratios of the other two shocks tend to become excessive in the Mach 2.0 - 2.5 regime.

Isentropic compression, using a curved compression surface, can be used to improve performance and control shock strength in that Mach number regime.

The choice of 3-dimensional or 2-dimensional compression is often made by general arrangement considerations. A better overall configuration is probably achieved with 3-dimensional, axisymmetric compression if the engine is mounted in an isolated nacelle on a supersonic aircraft. Again it is stressed that detailed design studies are required to arrive at a final, satisfactory selection, and developmental testing is required to confirm the selection.

#### 1.4 Compression Surface Orientation

The question of whether or not 2-dimensional compression surfaces should be horizontally or vertically oriented faces the designer quite often. Intuitively it seems that the horizontal orientation, inherently, has a higher degree of attitude tolerance than the vertical. However, there have been vertical ramp inlets that have operated and are operating successfully at angle of attack. The development of attitude tolerance does, perhaps, provide more challenge in the case of the vertical ramp inlet. However, there are ways in which it can be accomplished. Some tolerance to angle of attack can be provided by canting the inlet centerline downward so that at high aircraft angles of attack, the inlet angle of attack is quite moderate. Angle of attack tolerance can also be increased by modifications to the upper and lower sideplate design. Therefore, suitability to the aircraft general arrangement should be the governing criterion for compression surface orientation.

#### 1.5 Boundary Layer Removal Provisions

High performance aircraft with the inlet located on the body or other surface on which boundary layer can build usually require some provision for diversion of all or part of the boundary layer. The reasons for this requirement vary with the aircraft and its flight regime.

Some purely subsonic aircraft require boundary layer diversion because the high static pressure gradient in the entering stream-tube at very low mass-flow-ratios tends to interact with fuselage boundary layer. The disturbance phenomenon that sometimes results is often referred to as "duct rumble" and will be discussed in a later section along with other unsteady flow phenomena.

Supersonic aircraft with precompression always require boundary layer diversion when boundary layer is present in order to operate satisfactorily. Ingested boundary layer would react with the initial shock and compound shock - boundary layer interaction problems with the subsequent shock waves.

Detailed attention needs to be paid to the design details of the boundary layer diversion device. The major problems that can occur are related to failure to give the intercepted boundary layer a sufficiently clear exit path. When this occurs, the flow blockage can feed upstream and an apparent local thickening of the boundary layer occurs.

For high performance and adequate inlet stability in the high supersonic flight regime, boundary layer bleed is applied to the compression surfaces and sometimes to the walls of an inlet. Distributed porosity has been demonstrated as being quite effective. However, slots which are more attractive from an ease of fabrication standpoint can be located so as to perform just as effectively. The design of a bleed system is somewhat of a cut and try process. The correct place to bleed is in the region of shock boundary layer interaction. Bleed slots or porosity can be located from just upstream to just downstream of the expected terminal shock position. During exploratory developmental testing, the various candidate bleed positions can be throttled down or shut off to determine the most effective location/locations.

#### References

1. Davis, W. F. and Scherrer, R., Aerodynamic Principles for the Design of Jet-Engine Induction Systems, NACA RM A55F16, February 27, 1956.
2. Connors, J. T. and Meyer, R. C., Design Criteria for Axisymmetric and Two-Dimensional Inlets and Exits, NACA TM 3589, January, 1956.

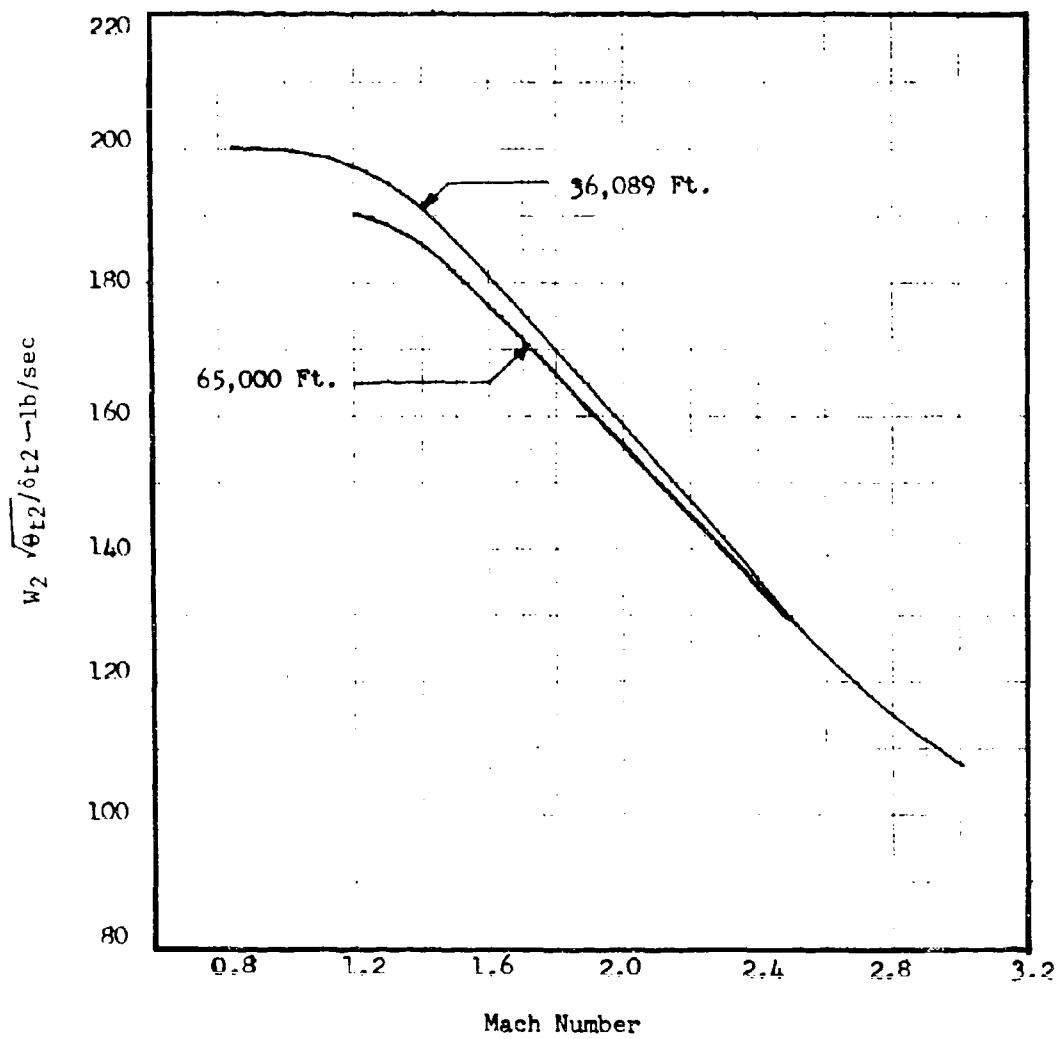


FIGURE 1-1. Typical Variation of Corrected Airflow.

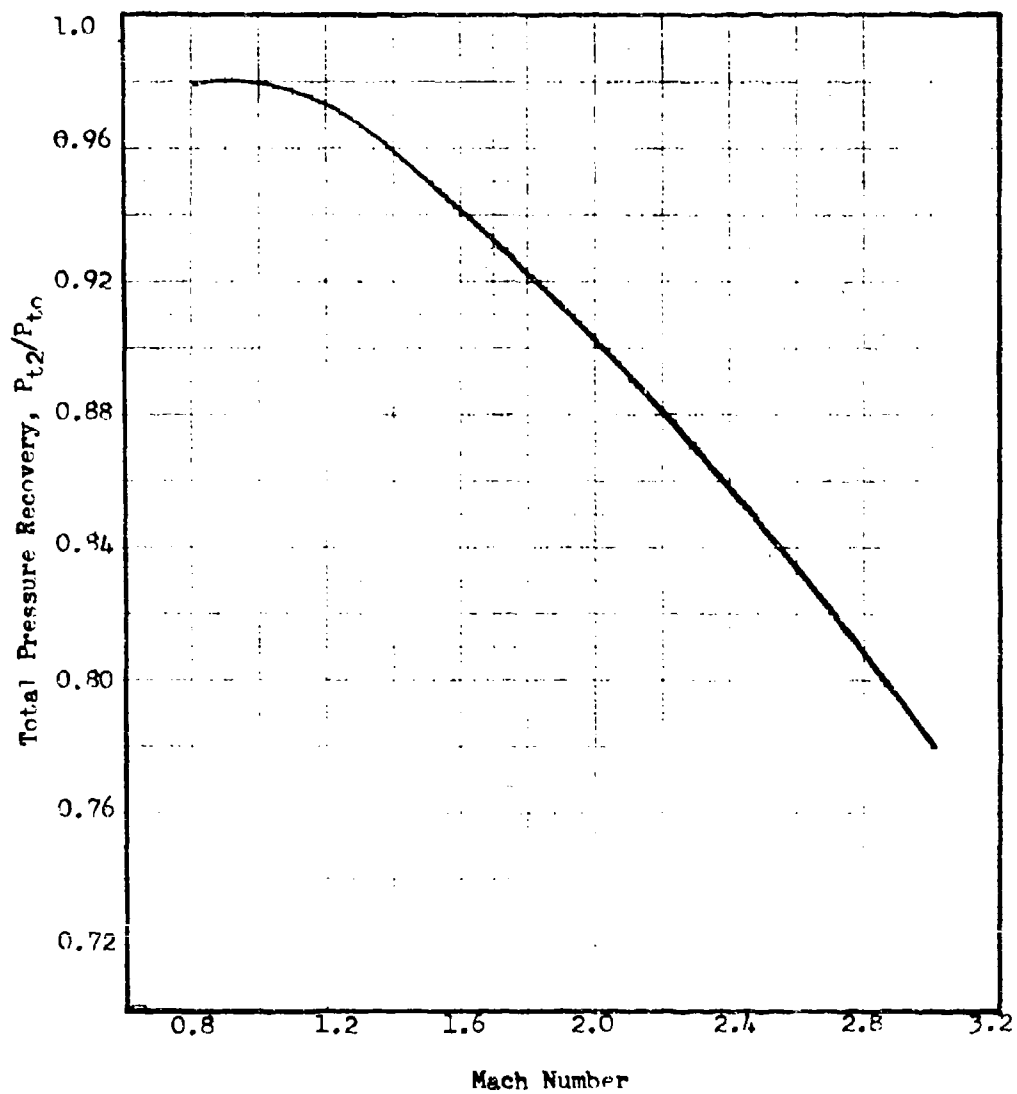


FIGURE 1-2. Typical Pressure Recovery Schedule.

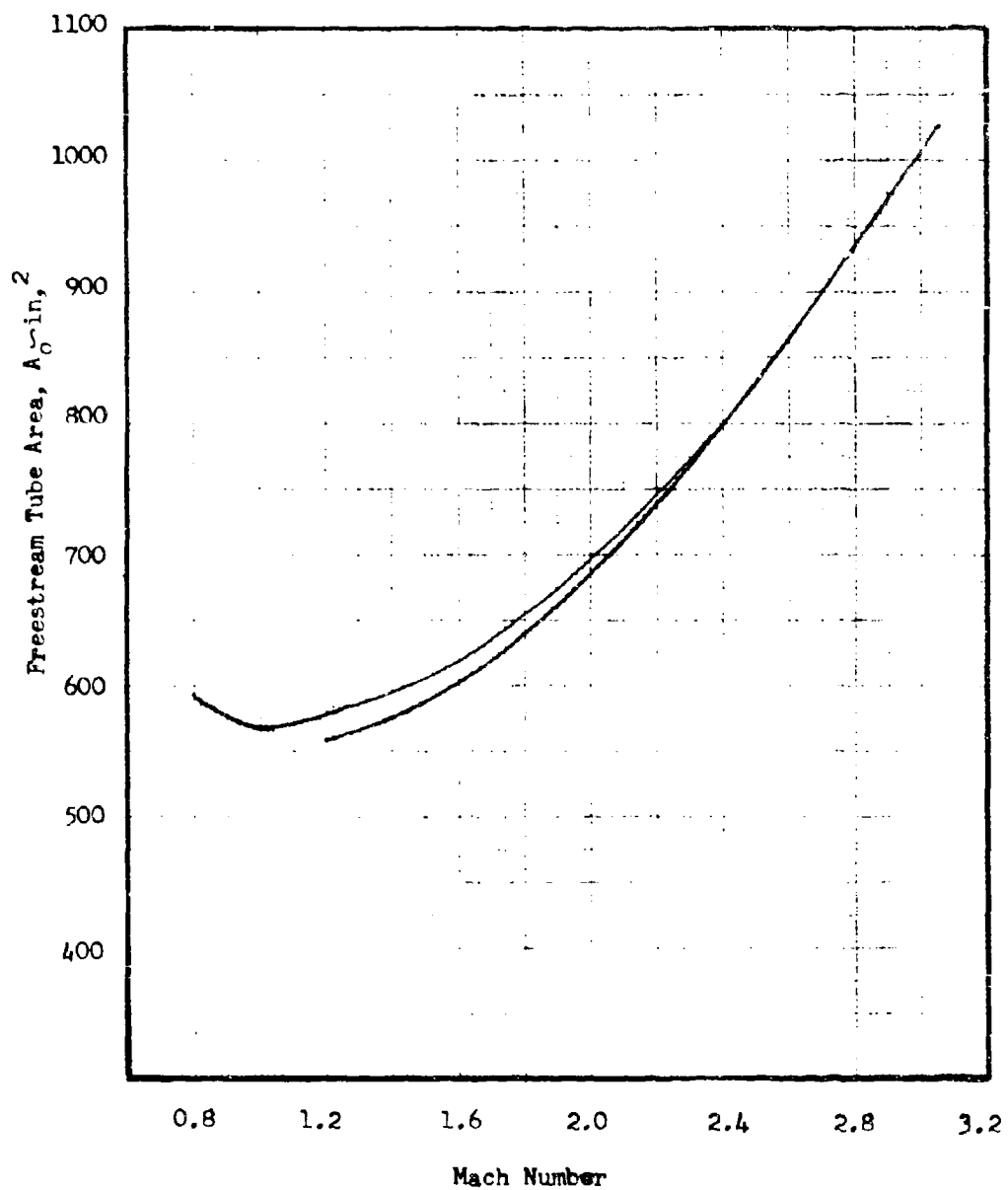


FIGURE 1-3. Typical Variation of Freestream Tube Area.



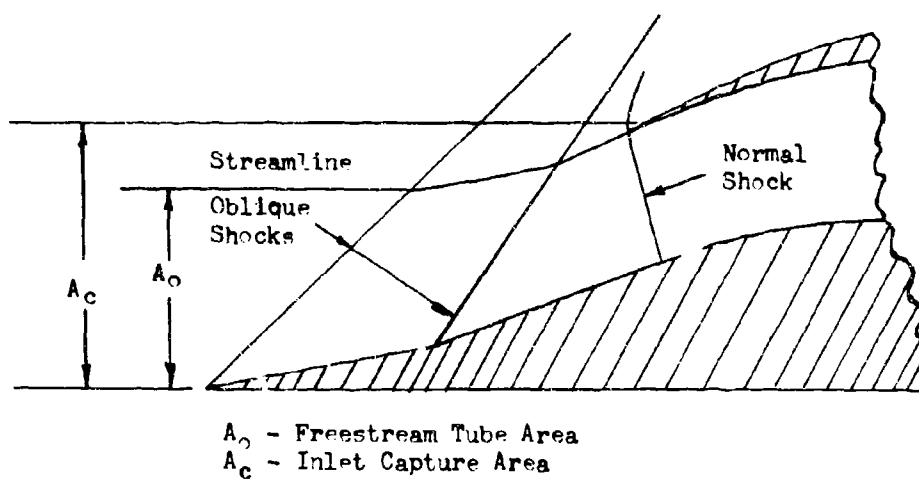


FIGURE 1-4. Example of Relationship of  $A_0$  to  $A_c$ .

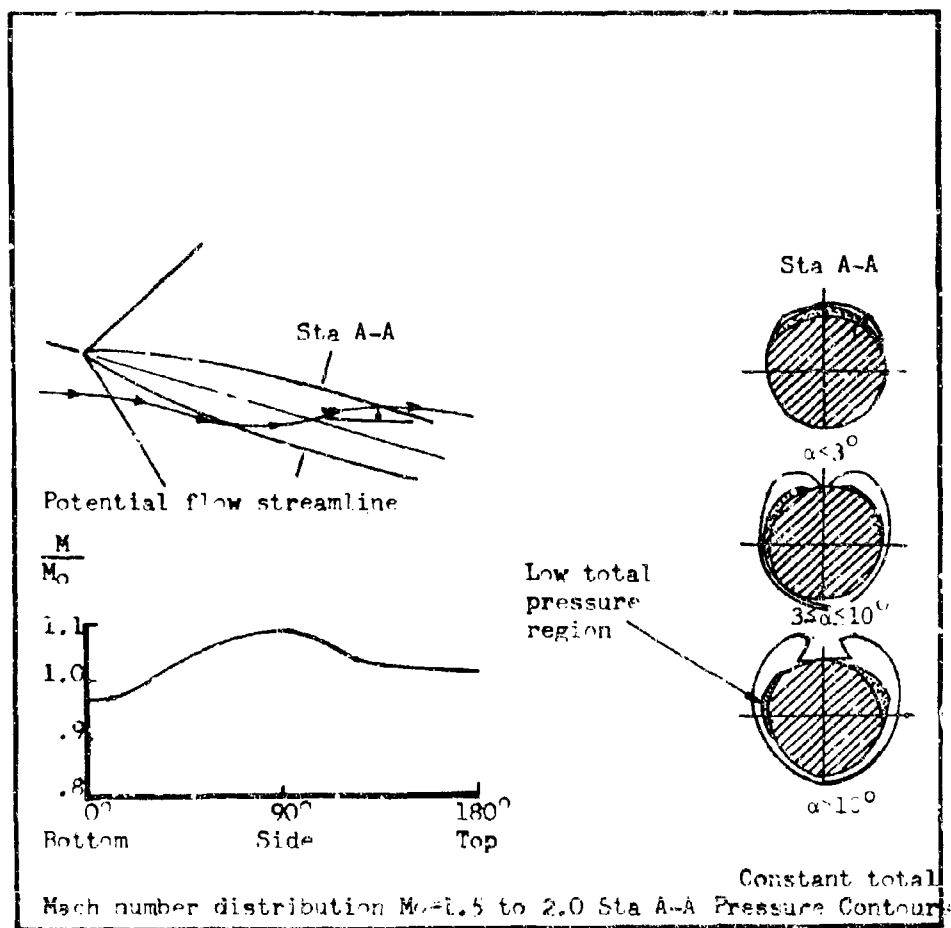


FIGURE 1-5. Local Flow Conditions on a Body.

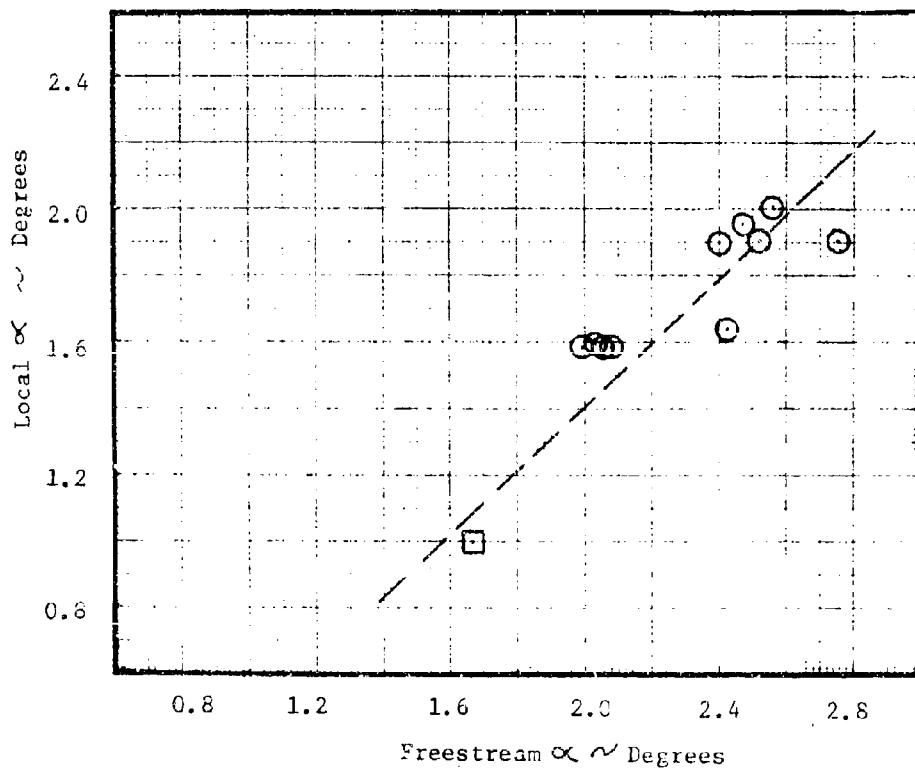
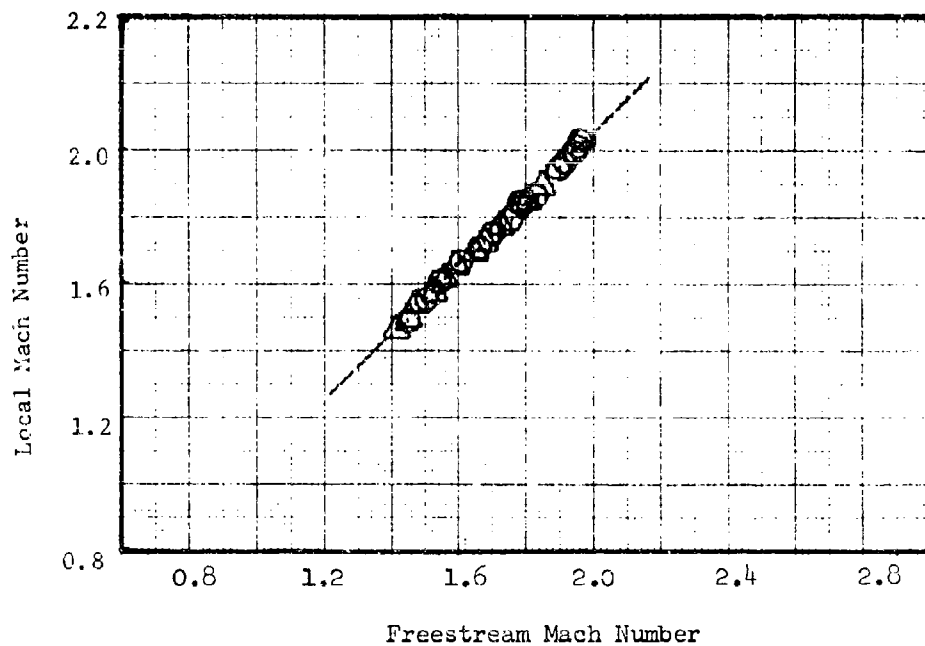


FIGURE 1 - 6. Inlet Local Angle of Attack and Mach Number as Measured in Flight, Side Inlet Location.

## 2.0 Air Induction System Loss Determination

The major contributing factors to the loss of total pressure in air induction systems vary with different flight regimes and operating conditions. There are three flight regimes within the scope of this study in which the makeup of the loss contributors differ. Common to all three of these is the loss due to the combined effects of fluid friction, diffusion, separation, and changes in shape and/or direction in that part of the system with purely subsonic flow most immediately forward of the engine face.

In the static and very low speed flight regime, the pressure losses due to flow around the inlet lips is usually the most significant loss contributor, particularly when the lips are fairly sharp and thin as on most high performance aircraft. In the supersonic flight regime, the losses associated with shock waves become significant contributors to the overall total pressure loss.

### 2.1 Inlet Lip Losses - Sharp Lips

Reference (1) is a classic theoretical presentation of the mechanism of the total pressure loss due to inlet flow over completely sharp lips at inlet velocity ratios in excess of unity. This theory is developed by use of a total momentum balance in which either a lip suction force or a loss in total pressure is required to satisfy conservation of momentum. In the case of a completely sharp cylindrical inlet which does not have lip frontal area to support a suction force, the necessary total pressure loss was readily theoretically predicted. This was done in Reference 1 by writing the momentum balance as

$$\phi_1 = \gamma P_1 M_1^2 A_1 + (P_1 - P_0) A_1 = \phi_0 = \gamma P_0 M_0^2 A_0 \quad (2.1)$$

and writing the continuity relation as

$$P_1 \left( M \frac{a}{a^*} \right)_1 A_1 = P_0 \left( M \frac{a}{a^*} \right)_0 A_0 \quad (2.2)$$

and considering that

$$\frac{P_{t1}}{P_{t0}} = \frac{P_1}{P_0} \frac{(P/P_t)_0}{(P/P_t)_1} \quad (2.3)$$

and combining equations to yield

$$\frac{P_{t1}}{P_{t0}} = \frac{(P/P_t)_0}{(P/P_t)_1 \left[ 1 + \gamma M_1^2 - \gamma M_0^2 \frac{\left( M \frac{a}{a^*} \right)_1}{\left( M \frac{a}{a^*} \right)_0} \right]} \quad (2.4)$$

This relationship is plotted as Figure 2-1. Data from Reference 2 for a sharp lipped inlet is plotted thereon, and shows reasonable substantiation. The reason for selection of Reference 2 data was the low diffuser loss level which makes the comparison near valid

without separation of the two loss contributors. While the agreement is very good at inlet Mach numbers up to about 0.7, premature choking is noted for the Reference 2 model. This is believed to be due to the approximately 1.5 diameters of constant area throat in the model. However, for inlet Mach numbers in the practical range, the method is shown to be valid for predicting losses incurred in flow into a sharp lipped inlet. A computer program has been written based on equation 2.4. A listing of the program is included as Figure 2-38.

The sharp lip losses derived in equation 2.4 are an inviscid phenomena. In the "real world" of viscous forces an additional sharp lip loss occurs due to separation of the internal flow at the sharp lip. This separation can be minimized by correct rounding of the internal lip shape (at the expense of internal contraction), however, it should be emphasized that the sharp lip losses calculated from equation 2.4 are the theoretical optimum performance that can be expected. Since equation 2.4 is derived assuming a zero external cowl thickness and since no improvement over this value can be derived from the internal cowl shape the next logical question is "What effect does the external cowl shape have on sharp lip losses". To find this effect, equation 2.1 is modified to include a force on the stagnation streamline (F)

$$\phi_0 = \phi_1 + F \text{ (F defined positive in the thrust direction)}$$

If this equation is now combined with equations 2.2 and 2.3 as before, the resulting equation is:

$$\frac{P_{t1}}{P_{t0}} = \frac{(P/P_t)_0}{(P/P_t)_1 \left[ 1 + \gamma M_1^2 - (\gamma M_0^2 - F/P_0) \frac{(M_{aa}^2)_1}{(M_{aa}^2)_0} \right]} \quad 2.4a$$

To determine the effect of the external cowl thickness on the force term consider the integration of the pressure along the stagnation streamline. As shown in Reference (1).

$$\int_{-\infty}^{\infty} (P - P_0) dA = 0$$

$$\text{Then } \int_S^{\infty} (P - P_0) dA = - \int_{-\infty}^S (P - P_0) dA = -F \quad 2.4b$$

where S is the stagnation point on the cowl. The term on the left hand side of equation 2.4b is just the pressure drag term of the cowl which will increase with increasing thickness. The negative sign in equation 2.4b shows that the integration along the stagnation streamline from freestream to the stagnation point, defined as F, will be in the thrust direction as defined. Therefore, from equation 2.4a, increasing the cowl thickness will increase the positive force term which will in turn increase the sharp lip losses. This again shows that the sharp lip losses of equation 2.4 are the theoretical optimum performance that can be expected.

## 2.2 Inlet Lip Losses - Rounded Lips

The theory for inflow losses with rounded lips, at mass flow ratios in excess of unity, is an extension of the theory for sharp lipped inlets. Reference 3 gives a similar expression to Equation (2.4) for the estimation of inlet total pressure recovery for a round lipped inlet; it is

$$\frac{P_{t1}}{P_{t0}} = \frac{1 + K (A_L/A_1)}{\frac{(P/P_t)_1}{(P/P_t)_0} \left[ 1 + \gamma M_1^2 - \gamma M_0^2 \frac{(M \frac{a}{a_0})_1}{(M \frac{a}{a_0})_0} \right]} \quad (2.5)$$

In the above expression, a value of K equal to unity represents a perfect vacuum acting on the inlet lip projected area  $A_L$ .

Reference 2 represented the most consistent set of data available for the performance of a family of inlet lip configurations which shared in common a relatively low loss subsonic diffuser. The subsonic diffuser loss was evaluated from test data taken with a bellmouth inlet installed and was considered to apply at a given inlet Mach number for the entire test range of free stream Mach numbers from 0 to 0.33.

The data available from Reference 2 included, in addition to the bellmouth case, a sharp lipped profile, round inlet lip profile shapes and elliptical profile shapes. Round inlet lip profiles with radii of 0.04, 0.08, 0.16, 0.24, and 0.32 inches were tested. The inner minor axes of the two elliptical profile shapes tested were 0.08 and 0.176 inches. The major axes of the elliptical profiles were 3.6 times the minor axes.

After isolating the lip loss from the subsonic diffuser loss by the use of data furnished for the bellmouth inlet, an analysis was conducted to determine the value of K in Equation (2.5). A determination was also made of the value of K that would be required to make the lip loss vanish. For the round lip inlets the two curves were found to have some similarity in shape characteristic. An example of this is shown in Figure 2-2. As a result of this study, an average set of values of the ratio of K to the K required to make the lip loss vanish was derived from the Reference 2 data and is shown on Figure 2-3. Values of  $K_{reqd}$  are plotted in Figures 2-4 and 2-5 for freestream Mach numbers up to 0.4. Since the values in Figure

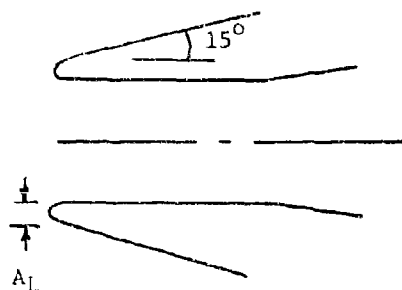
were derived from faired data and averaged, they were then used to calculate values for comparison with the data as published in Reference 2. This comparison is shown in Figures 2-6 and 2-7 and the agreement is shown to be quite reasonable.

Correlation of data for the elliptical profiles was quite good at the static test condition and the method for rounded inlet lip profiles can be used, with confidence, at static conditions for a variety of curved inlet lip profiles. However, at forward speeds, elliptical and circular lip profile data did not agree. This is because the lip loss is dependent upon the pressure force generated inboard of the stagnation streamline of the entering flow. At static condition, virtually the entire lip is within the stagnation streamline, while at forward speeds the point of impingement of the stagnation streamline varies with speed. Also at the point of impingement of the stagnation streamline the pressure is elevated locally, and this affects the lip suction force. The amount and extent of this effect is concluded to follow a less predictable pattern in the case of the elliptical profiles. This is believed to be caused by the fact that the elliptical profile has a varying radius of curvature as opposed to the constant radius of curvature of the circular profile.

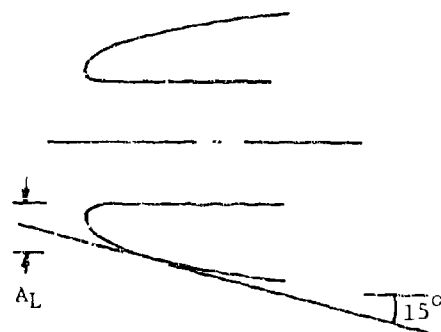
For arbitrary lip profile shapes, potential flow theory provides the analytical base on which predictions of lip forces can be made. However, this type of analysis is far too complex to fall within the scope of this present work. In order to provide some guidelines for modifying the answers obtained from the method given for circular profiles, examples of data taken with elliptical profiles is shown plotted with the corresponding calculated circular profile pressure recovery on Figure 2-8.

### 2.3 Low Speed Inlet Loss Calculation Method

Following is the suggested method for calculating the inflow portion of total pressure losses at mass flow ratios,  $m_1/m_0$ , greater than unity. In this method, the mass flow ratio term,  $m_1/m^*$ , the ratio of mass flowing in the inlet to the theoretical choking flow, is being used as the reference ratio.



$A_L$  used in correlation



$A_L$  suggested for arbitrary shape

1. Required basic geometric data is the ratio  $A_L/A_1$ . The method herein was correlated using the entire circular profile inside and out but ignoring the  $15^\circ$  cowl on the outside downstream of the lip. Therefore the suggested criterion is to assess the lip frontal to the  $15^\circ$  tangency point.
2. Select a range of low speed freestream Mach numbers to be analyzed.
3. Select a range of inlet Mach numbers to be analyzed.
4. Evaluate the corresponding values of total pressure ratio for completely sharp lips ( $P_{t1}/P_{t0}$  @  $A_L = 0$ ), from Equation (2.1) or read from Figure
5. The reciprocal of  $P_{t1}/P_{t0}$  @  $A_L = 0$  produces  $1.0 + K_R \left( \frac{A_L}{A_1} \right)$ . This can be readily derived from Equation (2.5).

6. Calculate the value of K required to make the lip loss vanish as

$$K_{\text{reqd or } K_R} = \frac{[1.0 + K_R (A_L/A_1)] - 1.0}{A_L/A_1}$$

The bracketed quantity was determined in Step 5 above.

7. If present correlation is acceptable for configuration in question, read  $K/K_R$  from Figure 2-3. The alternative being to resort to experimental methods or potential flow theory.
8. The ratio of the estimated total pressure ratio to the sharp lip total pressure ratio is then  $1.0 + K (A_L/A_1)$ .
9. After obtaining the estimated  $P_{t1}/P_{t0} = (P_{t1}/P_{t0})_{A_L=0} (1.0 + K (A_L/A_1))$   
the reference mass flow ratio,  $m/m^*$ , can be calculated for each point analyzed.
10. The mass flow ratio,  $m/m^* = 1.729 (P_{t1}/P_{t0}) (p/P_t)_1 M \frac{a}{a^*}$

The derivation of the above appears in Reference 1

Many tabulations of  $(p/P_t)$  are readily available and  $M \frac{a}{a^*}$  can be shown to be equal to  $M \sqrt{T_t/T}$ ,  $T_t/T$  being also readily available in tabulated form.



## 2.4 Inflow Losses at Subsonic Speeds; Mass Flow Ratios Less Than 1.0

At subsonic flight speeds and at mass flow ratios of 1.0 or less, there is no theoretical inflow loss. The losses in total pressure that occur in an air induction system in this flight regime can be accounted for as occurring from friction, diffusion, or other ducting loss. Methods for analysis of subsonic duct losses will appear in a later section of this report.

## 2.5 Shock Loss Determination

During air induction system operation at supersonic speeds, a loss in total pressure is incurred due to shock waves as the flow is reduced to subsonic speed. Depending upon the configuration, the shocks can be two or three dimensional. Another breakdown is into the categories of attached oblique, detached oblique, and normal. The latter is treated as a one dimensional phenomenon. There is no known rigorous theoretical method for the analysis of detached oblique shocks.

### 2.5.1 Normal Shock Loss

A normal shock is formed when a pitot entry is placed in a supersonic airstream or also can occur as the terminal shock in a compression chain downstream of oblique shocks or isentropic compression elements as shown in Figure 2-9.

Reference 4, gives the following expression for the total pressure ratio across a normal shock:

$$\begin{aligned} \frac{P_{t2}}{P_{t1}} &= \frac{P_{t2}}{P_{t1}} = e^{-\frac{\Delta S}{R}} \\ &= \left[ \frac{(\gamma + 1) M_1^2}{(\gamma - 1) M_1^2 + 2} \right]^{\frac{\gamma}{\gamma - 1}} \left[ \frac{\gamma + 1}{2 \gamma M_1^2 - (\gamma - 1)} \right]^{\frac{1}{\gamma - 1}} \quad (2.6) \end{aligned}$$

which for a value of the ratio of specific heats,  $\gamma$ , of 1.40 becomes:

$$\frac{P_{t2}}{P_{t1}} = \left( \frac{6 M_1^2}{M_1^2 + 5} \right)^{3.5} \left( \frac{6}{7 M_1^2 - 1} \right)^{2.5}$$

For most air induction system analyses in the flight spectrum covered by this present work, a value of  $\gamma = 1.4$  is acceptable. Values of normal shock total pressure ratio for  $\gamma = 1.4$  are plotted as Figure 2-10 along with other pertinent normal shock relationships and appear in Appendix B in tabulated form.

## 2.5.2 n-Dimensional Oblique Shock Wave Analysis

The expression for the total pressure ratio across an attached oblique shock is similar to that for a normal shock, the difference being that the upstream Mach number,  $M_1$ , is replaced by the component normal to the wave, i.e.,  $M_1$  is replaced in Equation (2.6) by  $M_1 \sin \theta_w$ , where  $\theta_w$  is the shock wave angle. Following is the expression for the total pressure ratio:

$$\begin{aligned} \frac{P_{t2}}{P_{t1}} &= \frac{\rho_{t2}}{\rho_{t1}} = e^{\frac{-\Delta S}{R}} \\ &= \left[ \frac{(\gamma + 1) M_1^2 \sin^2 \theta_w}{(\gamma - 1) M_1^2 \sin^2 \theta_w + 2} \right]^{\frac{\gamma}{\gamma - 1}} \left[ \frac{\gamma + 1}{2 \gamma M_1^2 \sin^2 \theta_w - (\gamma - 1)} \right]^{\frac{1}{\gamma - 1}} \quad (2.7) \end{aligned}$$

which for  $\gamma = 1.4$  becomes

$$\frac{P_{t2}}{P_{t1}} = \left( \frac{6 M_1^2 \sin^2 \theta_w}{M_1^2 \sin^2 \theta_w + 5} \right)^{3.5} \left( \frac{6}{7 M_1^2 \sin^2 \theta_w - 1} \right)^{2.5}$$

Equation (2.7) is valid for the total pressure ratio across any shock wave. For the normal shock the wave angle  $\theta_w$  is  $90^\circ$  and hence the sine is 1.0 and Equation (2.7) becomes identical to Equation (2.6). Figure 2-11 is a graphic presentation of oblique shock wave velocity relationships. The tangential components of the velocity are equal on the two sides of the shock wave. Equation (2.6) can be used to calculate the total pressure when the normal component of the upstream Mach number is employed. The expression is valid also for three dimensional attached oblique shock waves. The relationship between the surface deflection angle and wave angle is different for three dimensional waves, but the relationship between the total pressure ratio and the shock wave angle remains the same.

Reference 4, gives several expressions for the relationship between flow deflection angle,  $\delta$ , and shock wave angle,  $\theta_w$ . Two of these appear below:

$$\cot \delta = \tan \theta_w \left[ \frac{(\gamma + 1) M_1^2}{2 (M_1^2 \sin^2 \theta_w - 1)} - 1 \right] \quad (2.8)$$

which for  $\gamma = 1.4$  becomes

$$\cot \delta = \tan \theta_w \left[ \frac{6 M_1^2}{5 (M_1^2 \sin^2 \theta_w - 1)} - 1 \right]$$

and

$$\tan \delta = \frac{2 \cot \theta_w (M_1^2 \sin^2 \theta_w - 1)}{2 + M_1^2 (\gamma + 1 - 2 \sin^2 \theta_w)} \quad (2.9)$$

which for  $\gamma = 1.4$  becomes

$$\tan \delta = \frac{5 \cot \theta_w (M_1^2 \sin^2 \theta_w - 1)}{5 + M_1^2 (6 - 5 \sin^2 \theta_w)}$$

In multiple oblique shock systems, there are optimum combinations of deflection angles for each supersonic Mach number. The results of an analysis performed by K. Oswatitsch, the translation of which appears as Reference 6, give the optimum angles for two, three, and four shock two-dimensional systems. These systems have one, two, and three oblique shocks, respectively. Each has a terminal normal shock. Figure 2-12 presents the theoretical shock pressure recovery values for optimum two, three, and four shock inlets. Figures 2-13, 2-14, and 2-15 present curves of the optimum deflection angles for two, three, and four shock inlets. Figures 2-16, 2-17 and 2-18 present the corresponding shock wave angles and Figures 2-19, 2-20 and 2-21 present the corresponding Mach numbers. For the analysis of non-optimum multiple shock systems, tabulations appear in Appendix C from which theoretical performance of the shock systems can be analyzed. Such information usually is presented in graphical form, examples of which can be found in References 4 and 5, however it was felt that this tabular form would be both handier and more accurate. The range of deflection angles for which the calculations were made extends into the region of shock detachment. When this happened, a comment was printed. The conditions for shock detachment and also for the attainment of sonic flow appear as Figure 2-22. The program, from which the Appendix tabulation was calculated, makes an attempt to handle the

detached case. As was mentioned previously, the solution for the detached case is not theoretically rigorous. Test data results indicate that the answer in the tabulation for total pressure ratio in the detached case is conservative. Examples of this will be shown in a later subsection. Sample calculations and substantiating data for supersonic air induction system loss estimation will appear later when all the loss contributing items have been discussed.

### 2.5.3 Axisymmetric or Three-Dimensional Oblique Shock Wave Analysis

The analysis of the flow field downstream of an attached oblique shock wave generated by a right circular cone is considerably more complicated than that generated by a two-dimensional wedge. Equation (2.7) does, however, hold true for the total pressure ratio across the shock. The theoretical expression for supersonic conical flow is:

$$\begin{aligned}
 & - \frac{d^2 V_r}{d\omega^2} \left[ \frac{\gamma+1}{2} \left( \frac{d V_r}{d\omega} \right)^2 + \frac{\gamma-1}{2} (V_m^2 - V_r^2) \right] \\
 & - \frac{\gamma-1}{2} \left( \frac{d V_r}{d\omega} \right)^3 \cot \omega - \gamma V_r \left( \frac{d V_r}{d\omega} \right)^2 \\
 & + \frac{\gamma-1}{2} (V_m^2 - V_r^2) \frac{d V_r}{d\omega} \cot \omega \\
 & + (\gamma-1) V_r (V_m^2 - V_r^2) = 0
 \end{aligned} \tag{2.10}$$

where  $V_r$  is the velocity along a ray,  $\omega$  is the ray angle, and  $V_m$  is the maximum velocity attainable by adiabatic expansion to absolute zero temperature. This equation and its derivation appear in Reference 7. It can be solved numerically by the assumption of a surface velocity and the knowledge that  $d V_r/d\omega$  is zero at the surface. The other boundary condition is Equation (2.7) and the relationships shown on Figure 2-11 at the shock wave. Tabulations of some of the pertinent flow parameters of conical flow including shock total pressure ratio appear in Appendix D. Unlike the two-dimensional case, these tabulations are not adequate for the analysis of multiple shock conical systems.

A conical flow field is non-uniform. This is shown by a sample solution of Equation (2.10) which is included in Appendix D. When there are two external conical shocks, as depicted by Figure 2-23, the second wave is curved due to the non-uniform conical flow field. Reference 8 suggests that the second shock can be estimated as a two-dimensional shock in the average conical flow field. This is approximately correct when making an analysis of shock total pressure ratio. However, this does not define the shape of the wave and allow one to determine accurately the intersection of the two shocks and the relation of the second shock to the inlet lip. A more exact analysis was made of the second shock in which the orientation of the downstream flow field was checked by continuity considerations. A sample result is included in Appendix D and indicates that each element of flow in a conical flow field is turned through an angle equal to the surface turn. An additional accuracy check on the result was made by a total momentum integration to produce an additive drag coefficient very nearly equal to zero for the cylindrical control volume considered.

In addition to the conical flow field analysis results, EDPM logic listings are included in Appendix D so that internal aerodynamics manual users wishing to perform additional external conical flow field analyses on EDPM will have them available.

Another method of analysis that is often used for axisymmetric flow field analysis is the method of characteristics. Reference 9 presents a programmed method of characteristics write-up that is suitable for calculations of the flow field in cases where there is only one external shock. This program will accommodate multiple internal shocks, including reflected oblique shocks. However, sudden slope changes such as the second cone of a double cone inlet are treated by that program as generating shocks of zero strength.

There has been no optimization analysis performed for multiple shock axisymmetric inlets as extensive as that performed by Oswatitch for two-dimensional inlets. Reference 8 does, however, present values for optimum single and double cones which appear as Figure 2-24.

## 2.6 Internal Ducting Losses

### 2.6.1 Principles of Ducting Loss Analysis

#### 2.6.1.1 Sources of Losses

Pressure losses are caused by friction, momentum, and turbulence effects in the air flowing through ducting. Since air vehicle engine inlet ducting is relatively short, the friction losses are relatively small. However, friction can be the primary source of subsonic loss in straight inlet ducts with small divergence angles. Friction can also be a major factor in the loss of inlet ducts with bends or high divergence angles because the momentum and turbulence losses are affected by the duct velocity profiles produced by friction.

Frictional forces are generated when air flows along duct walls (or other solid surfaces). Except with rarified air (not encountered in engine inlets), there is no slip of air particles at walls, and duct flow causes shearing stresses in the air near walls. The walls therefore impose frictional forces opposite to the direction of air flow. The wall friction also builds up boundary layers with lower velocities than the primary duct flow. These boundary layers are an important factor relative to most of the momentum and turbulence pressure losses. Friction is the only source of subsonic pressure loss in straight ducts of uniform cross section.

Momentum forces are generated by the static pressure distribution imposed on the ducting walls (or other solid surfaces) by the flow pattern of the primary air stream (outside the boundary layer). Elbows impose momentum force components opposite to the direction of air flow because there is centrifugal acceleration of the air during turning. Screens impose momentum forces opposite to the direction of air flow because of the difference between windward and leeward surface pressures produced by the flow.

Turbulence losses occur when the primary flow separates from ducting walls and produces reverse and vortex flow near the walls. These spurious flows produce direct losses by turbulence, and the separation of the primary flow from the walls can also increase the momentum losses. Separation is most commonly encountered in regions of flow expansion or deceleration. These regions have adverse (positive) pressure gradients because the static pressure increases in the direction of flow. When the low velocity fluid within the boundary layer cannot cope with the increase of pressure produced by the primary flow stream, reverse flow will occur along the wall from the higher pressure regions further downstream. The primary flow is then separated from the wall by a region of reverse and vortex flow. The onset of flow separation is a function of the nature and thickness of the boundary layer as well as the magnitude of adverse pressure gradient (and other factors).

Separation is more likely with laminar than turbulent boundary layers and is most likely with thick boundary layers. Separation is an important consideration in subsonic diffusers because of the required adverse pressure gradients.

#### 2.6.1.2 Correlation of Duct Component Pressure Loss Data

Basic data are usually presented as a dimensionless loss coefficient defined in terms of duct dynamic pressure as shown below:

$$K_n = \Delta P_T / q = \text{loss coefficient of a specific ducting component (Section 2.5.4.2 and 2.5.4.3)}$$

$$\Delta P_T = \text{total pressure loss in ducting component}$$

$$q = \frac{\rho V^2}{2g} = \text{dynamic pressure at ducting component inlet}$$

$$\rho = \text{air density}$$

$$V = \text{air velocity}$$

$$g = \text{acceleration of gravity}$$

Most of the available loss coefficient data are in the form of total combined (friction, momentum, and turbulence) loss for a duct component when connected downstream of a pipe with fully developed turbulent flow. A duct length 25 to 100 times the duct diameter is required to obtain fully developed turbulent pipe flow (References 10 and 11). Engine inlet systems usually have lengths less than ten times their diameter, and their duct components will have undeveloped duct flow (boundary layers not extending to the centers of ducts). The friction loss of an engine inlet duct component will therefore be dependent on the characteristics of the local boundary layer.

The boundary layers would usually be thin and turbulent near the upstream end of engine inlet subsonic ducting. During supersonic flight, an inlet has one or more shocks upstream of the subsonic ducting. The interaction of shocks with boundary layers tends to produce transition to turbulent flow and thickening in boundary layers (References 12 and 13), but the thickening is usually suppressed with suction boundary layer control provisions on engine inlet systems. During subsonic flight, the throat (minimum cross sectional area) of an inlet will be a short distance downstream of the lip stagnation regions. The short flow distances along walls tend to produce boundary layer thicknesses which are small compared with the engine inlet throat size. However, the flow distances will usually be long enough to obtain relatively high (greater than  $10^5$ ) Reynolds number at the throat

(based on distance from leading edge). Transition to turbulent flow is likely in this Reynolds number range, particularly with the adverse (positive) pressure gradients downstream of the throat (References 10, 11 and 14).

Assuming a turbulent boundary layer on a smooth flat plate with no pressure gradient, the boundary layer growth can be approximately defined as shown below (Reference 10).

$$\delta^* = 0.04625 x / (R_x)^{0.2} = \text{local boundary layer displacement thickness} \quad (2.11)$$

$x$  = Distance downstream of the turbulent boundary layer origin

$R_x$  = Reynolds number based on the dimensional length downstream of the turbulent boundary layer origin.

The above flat plate equation can be used to estimate boundary layer growth along the inside of duct walls. Wall friction coefficients can be estimated from experimental data (Reference 11), which shows magnitudes similar to a flat plate near the duct inlet and magnitudes corresponding to fully developed pipe flow 25 to 100 diameters downstream of the duct inlet. Estimates on this basis (Figure 2-25) involve inaccuracies due to the assumption of a turbulent boundary layer, the assumption of a hydraulically smooth surface, and the neglect of pressure gradient effects on the boundary layer. The assumption of a turbulent boundary layer introduces little error in skin friction estimates because the laminar and transition flow lengths would be relatively small for engine inlet ducts. The assumption of smooth surfaces will cause pressure loss estimates to be somewhat lower than actual losses, but there is no practical general method of accounting for roughness. Neglect of pressure gradient effects could cause large errors in subsonic diffuser skin friction estimates for conditions approaching those of flow separation, but skin friction losses are small compared with momentum and turbulence losses for these conditions.

Boundary layer thickness is an important factor relative to subsonic diffuser momentum and turbulence losses. The skin friction coefficient has a direct effect on duct friction losses. The pressure loss of a ducting component can be correlated as the sum of the friction loss and the momentum and turbulence loss (References 15 and 16). The usual duct friction correlation factor is four times the friction coefficient (Reference 12). With turbulent boundary layers, the variation of friction loss factor is relatively small (Figure 2-25), and a typical loss factor of 0.02 is frequently assumed for pressure loss estimates (Reference 17).



The exact region of boundary layer transition to turbulent flow is an important factor in the subsonic performance of an engine inlet system. If transition does not occur near the engine inlet system throat, laminar separation could occur within the diverging duct. The loss usually would then be much greater than that due to friction. Inlet performance may be improved by a lip boundary layer trip when the operating Reynolds number is too low to assure early transition with a smooth surface. Roughness criteria for boundary layer tripping are available (Reference 18).

### 2.6.1.3 Evaluation of Overall Inlet System Loss

Total losses are evaluated as the sum of individual duct component losses. The most important loss is usually the subsonic diffuser because it contains an (adverse) expanding air stream with relatively high dynamic pressures. The losses are therefore added in the manner which yields an overall loss coefficient relative to the dynamic pressure at the throat of the subsonic diffuser. This involves correction for cross sectional flow area differences of various ducting components as shown below.

$$K_o = \sum (A_1/A_n)^2 K_n = \text{Overall engine inlet loss coefficient based on throat dynamic pressure (2.12)}$$

$$K_n = \text{loss coefficient of a specific ducting component (Section 2.5.4.2 and 2.5.4.3)}$$

$$A_1 = \text{area at the inlet of subsonic diffuser (throat of an engine inlet system)}$$

$$A_n = \text{area at the inlet of a specific ducting component}$$

The above relations are for incompressible flow, and they are exactly applicable only at low Mach numbers. Typical engine inlet systems have relatively low Mach numbers except at the throat (subsonic diffuser inlet). Pressure losses usually increase moderately with diffuser inlet Mach number except in the range near that for choking (Figure 2-26), but there are considerable scatter in the data (References 16 and 19). Test data indicate that choking occurs at an average Mach number somewhat lower than would be defined by the theory for the effect of boundary layer thickness (Figure 2-26), probably because of minor flow angularities at the section which chokes. Compressibility effects are usually neglected when computing engine inlet system pressure losses because there are no quantitative general analysis methods available. However, the compressibility effects always impose pressure losses which essentially limit engine inlet system air flows at high diffuser inlet Mach numbers.

## 2.6.2 Subsonic Diffusion Losses

### 2.6.2.1 General Considerations

A subsonic diffuser is a duct which increases in cross sectional area in the flow direction. Engine inlet diffusers frequently have complex contours not conforming with any geometric shape. Typical cross sections of interest are (approximately) round, rectangular, and annular. Rates of divergence are usually not uniform over the entire length of an engine inlet diffuser. These factors limit the generality attainable in geometric correlation of diffuser pressure loss data.

The rate of divergence in the direction of flow is an important factor relative to diffuser performance. Conical divergence is designated by the included wall angle ( $2\theta_w$ ), and this also provides a correlation of non-conical diffuser momentum and turbulence losses (Reference 16). Many other methods have been suggested for correlation of non-conical diffuser data (References 15, 16, 17, 19 and 20), the most general being in terms of an "equivalent conical diffuser". The specific designation is the included angle of a cone with the same inlet area, outlet area, and length as the non-conical diffuser.

$$2\theta_d = 2 \tan^{-1} \frac{\sqrt{A_2} - \sqrt{A_1}}{\sqrt{\pi} L_d} = \text{equivical conical angle} \quad (2.13)$$

$A_1$  = diffuser inlet area

$A_2$  = diffuser outlet area

$L_d$  = diffuser length

The equivalent conical diffuser angle provides a general indication of diffuser length required to achieve divergence from one cross sectional area to another (Figure 2-27), and it can be utilized to correlate diffuser friction losses. The diffuser inlet-to-outlet area ratio is also a factor in diffuser pressure losses, but the area ratio correlation for momentum and turbulence losses is different than for friction losses (References 15 and 16).

$$K_n = k_d' (1 - A_1/A_2)^2 + 4f k_d'' [1 - (A_1/A_2)^2] \quad (2.14)$$

$K_n$  = diffuser loss coefficient

$k_d'$  = reference momentum pressure loss coefficient for a specific type of diffuser (Figure 2-28)

$k_d''$  =  $0.1412 \sqrt{A/D_e} \tan \theta_c$  = reference friction pressure loss coefficient for a specific type of diffuser (Figure 2-29)

$\theta_c$  = equivalent conical half angle of diffuser divergence

$4f$  = duct friction loss coefficient (Figure 2-25)

$A_1$  = diffuser cross sectional inlet area

$A_2$  = diffuser cross sectional outlet area

$\sqrt{A}/D_e$  = a weighted average cross sectional shape factor based on diffuser area ( $A$ ) and equivalent diameter ( $D_e$ )

$D_e = 4A/p$  = equivalent duct diameter (hydraulic diameter)

$p$  = diffuser cross sectional perimeter

The reference friction loss coefficient is a coefficient normalized to a unity friction loss factor and to an infinitely small inlet-to-outlet diffuser area ratio. The ratio of square root of area and equivalent diameter accounts for the effect of cross sectional shape on friction (Figure 2-29). When a diffuser incorporates a change in shape (i.e. rectangular inlet and circular outlet cross sections), a weighted average value of the ratio can be used, the important weighting being assigned to the high velocity regions near the diffuser inlet.

The reference momentum and turbulence loss coefficient is a coefficient normalized to an infinitely small inlet-to-outlet diffuser area ratio. Since diffusers have adverse (positive) pressure gradients, boundary layer thickness is an important factor relative to the losses (particularly flow separation losses), and this is best correlated by a dimensionless boundary layer thickness parameter (Figure 2-28).

$\delta_1^*/R_1$  = boundary layer thickness parameter

$\delta_1^*$  = boundary layer displacement thickness at diffuser inlet

$R_1$  = diffuser inlet section radius  
(or other characteristic dimension)

The diffuser inlet section characteristic dimension  $R_1$  is half of the distance between diverging walls for all types of diffusers (conical, rectangular, and annulars), and this defines the radius of a conical diffuser. The boundary layer displacement thickness can be estimated for subsonic flight (Figure 2-25), but is usually dependent on the unknown effectiveness of the inlet boundary layer control provisions during supersonic flight. A boundary layer thickness parameter of 0.01 has been suggested as desirable for inlet boundary layer control (Reference 19), but this is not based on any quantitative theoretical or experimental data.

The diffuser loss criteria above would imply that increasing Reynolds number would produce decreasing friction loss (Figure 2-25) with no change of momentum and turbulence loss. The momentum and turbulence loss could theoretically increase with increasing Reynolds number because of boundary layer effects, and the actual diffuser loss trends with Reynolds number are not known (Reference 16). The exact effects of Reynolds number are believed to be dependent on what portion of the total loss is caused by skin friction. However, the magnitudes of these effects are believed to be relatively small.

#### 2.6.2.2 Conical Diffuser Losses

More data are available on conical diffusers than any other type, and the diffuser momentum and turbulence loss criteria (Figure 2-28) were developed from conical diffuser data. Application of this criteria for a selected thin boundary layer ( $\delta_1^*/R_1 = 0.01$ ) and addition of friction loss (Figure 2-29) for typical conditions ( $4f = 0.02$ ) yields conical diffuser loss trends (Figure 2-30).

With large divergences (small inlet-to-outlet area ratios), the overall losses are lowest for approximately 5 to 10 degree included angles. In this range the optimum compromise is obtained between the friction and the momentum and turbulence losses. Conical angles smaller than optimum are seldom of interest for engine inlet systems, but large conical angles are frequently desirable to obtain short diffusers. Conical diffuser losses increase very rapidly at included angles greater than approximately 20 to 25 degrees, and the losses are usually greater than for an abrupt expansion at angles greater than approximately 50 degrees. Zero length diffusers (abrupt expansion) are sometimes considered for engine inlet systems, particularly when high inlet-to-outlet area ratios make the absolute loss levels relatively small (Figure 2-30).

Diffuser momentum and turbulence losses increase with boundary layer thickness (Figure 2-28), and friction losses are a function of flight Reynolds number (Figure 2-25). Large (up to threefold) differences in the conical diffuser pressure loss trends with boundary layer thickness have been observed during individual experiments (Figure 2-30 and Reference 16). The reasons for these large differences are unknown, but boundary layer tripping techniques appear likely to be an important factor in the diffuser test data. Most of the diffuser tests involved boundary layer tripping, and undeveloped pipe flow tests have indicated that tripping can produce significant increases of friction not conforming with the conventional turbulent boundary layer theory (Reference 11). Although the boundary layer thickness correlation herein (Figure 2-28) is based on extensive test data (Reference 16), the accuracy of the correlation is known to be limited.

#### 2.6.2.3 Non-Conical Diffuser Losses

Because of the geometric aspects of two and three dimensional supersonic engine inlets, rectangular (or square) and annular diffuser cross sections are frequently of interest. Non-uniform divergence along diffusers is also of interest because lower pressure losses can be obtained than with constant divergence. The many geometric variables pertinent to engine inlet diffusers make exact general definition of non-conical diffuser losses impractical. Equivalent conical diffuser angle is the most general criteria for rate of divergence, but wall divergence angle has been found to provide better correlation of pressure loss data (Reference 16). For non-uniformly divergent diffusers, wall angles are defined arbitrarily in terms of angles subtended by the inlet and outlet cross sectional areas (with minor aerodynamic fairings near the diffuser inlet and/or outlet neglected).

Diffusers with uniformly divergent rectangular and annular cross sections have greater pressure losses than conical diffusers (Figure 2-31). There are larger momentum and turbulence losses when diffusion is not axially symmetric, and there are larger friction losses when ducts have greater wetted surface areas. Uniformly divergent diffusers have limited interest in engine inlet applications because lower pressure losses are attainable with non-uniform divergence.

The most efficient configurations of short diffusers involve non-uniform divergences commonly designated as trumpet shaped. Exact optimum shapes of such diffusers have not been defined. Diffusers with many arbitrary shapes (such as double truncated cones and various mathematically defined curves) have been tested (References 15, 16, 17 and 22). These diffusers have losses comparable with conical diffusers of lower divergence angles (Figure 2-31). The favorable variable divergence results have been obtained with round, square rectangular and annular diffuser cross sections. Exact losses in such diffusers cannot be predicted because of the complex geometric factors involved and the large scatter in the available specific test data. However, the typical overall gains with non-uniform divergence have been approximately 5 to 15 degree greater wall divergence angles than conical diffusers with approximately the same pressure losses.

#### 2.6.2.4 Boundary Layer Control Provisions

Boundary layer control is not normally required for subsonic air vehicles. Subsonic inlets generally permit attainment of optimum diffusion angles without excessive lengths, and the diffuser inlet boundary layers are generally thin. Supersonic inlets will usually have boundary layer control for any regions of shock impingement on surfaces upstream of subsonic diffusers and may also have boundary

layer control within subsonic diffusers. Boundary layer control is essential in regions of shock impingement to avoid large losses and thick subsonic diffuser inlet boundary layers. Boundary layer control in subsonic diffusers of supersonic inlets is sometimes desirable when large divergence angles are necessary to achieve practical diffuser lengths.

Wall suction is the type of supersonic boundary layer control employed for suppression of adverse shock interaction effects. Since supersonic shocks produce static pressure increases, wall suction is readily obtained by suitable overboard dumps (Figure 2-32). Prevention of bleed-back (in the subsonic portion of the boundary layer) is the most important effect of boundary layer removal by suction. Supersonic boundary layer control systems employ porous plates, flush slots, or projecting scoops for the wall boundary layer removal.

The four most common types of subsonic diffuser boundary layer control are wall suction, air injection, vortex generators, and turning vanes (Figure 2-33). All of these types of boundary layer control tend to delay flow separation in the diffuser, which decreases the pressure loss and improves the flow uniformity at the diffuser exit. Wall suction can be applied to remove the low energy boundary layer. High energy air injection through the walls can be applied to re-energize the boundary layer. Vanes or vortex generators can be applied to re-energize the boundary layer by mixing of the higher velocity central core air with the boundary layer air. Vortex generators have been the type of boundary layer control most frequently applied to subsonic diffusers.

The quantitative effects of boundary layer control on subsonic diffuser performance cannot be analytically predicted. Tests of specific arrangements are required, and these are best performed as overall inlet tests which include the boundary layer build-up and any supersonic compression effects upstream of the subsonic diffuser. Significant performance increments have been experimentally demonstrated for all four types of diffuser boundary layer control (Reference 16). Vortex generators have been found advantageous for the subsonic diffusers of supersonic inlets (References 22 and 24). Boundary layer control has been found more valuable in reducing pressure distortions than in reducing pressure losses.

### 2.6.3 Miscellaneous Losses

#### 2.6.3.1 Elbows

Elbows can produce significant losses, and careful design is required to incorporate them effectively in engine inlet systems. The most important design parameter is the radius ratio (ratio of elbow mean radius of curvature and duct depth). Engine inlet system elbows

sometimes have splitters to avoid adverse radius ratios. Splitters can reduce pressure losses and improve elbow exit flow uniformity.

Engine inlet systems frequently have duct offsets connected by two elbows (commonly designated a compound elbow). The turning in the first elbow is then reversed in the second elbow, and there is no net turning in the complete compound elbow. Pressure loss data are available only for ninety-degree compound elbows, which are of little interest in engine inlet systems. The best procedure available is to estimate compound elbow losses as the sum of individual elbow losses. The actual losses will be lower than estimated by this procedure, particularly for small elbow turning angles.

The incompressible pressure losses of elbows with round and rectangular cross sections can be readily computed for high Reynolds number flow conditions (Figure 2-34). Pressure losses increase very rapidly when radius ratios are reduced below approximately 1.5, and it is desirable to avoid these sharp bends if possible. Loss coefficients are relatively constant for radius ratios between 2 and 5 because of the compensating effects of the turning and duct friction losses (increased radius ratios requiring increased elbow lengths). For radius ratios greater than 6, the turning losses are small enough to neglect, and total losses can be estimated on the basis of duct friction.

Data are available for a range of Reynold's numbers with round, rectangular, and elliptical duct elbows (Reference 15). Despite certain discrepancies in the data from different sources, fairly reliable estimates can be made for elbow losses with incompressible flow. Engine inlet system elbows may operate at high Mach numbers, and compressibility effects can be significant. Data available on round duct elbows indicate compressible losses to be as much as two or three times the incompressible losses (Reference 15). However, these data are very limited, and tests of specific configurations are usually necessary for inlet systems with high Mach number elbows.

#### 2.6.3.2 Constant Area Ducts

Most engine inlet systems do not have long enough constant area ducting to contribute losses significant compared with diffusers and/or elbows. However, the incompressible friction losses can be evaluated from a loss coefficient defined as shown below:

$$K_n = 4f L/D_e \quad \text{duct loss coefficient} \quad (2.15)$$

$4f$  duct friction loss coefficient (Figure 2-25)

$L$  duct length

$D_e = 4 A/P$  - equivalent duct diameter (hydraulic diameter)

A = duct cross sectional area

p = duct cross sectional perimeter

The order of magnitude of duct loss can be computed by assuming a typical turbulent duct friction factor ( $4f = 0.02$ ). If duct friction losses are significant, more exact analysis may be desirable. Friction factors for fully developed duct flow can be evaluated as a function of Reynolds number and pipe roughness (Reference 12), but this approach does not account for the partially developed boundary layers typical for engine inlet systems (Reference 11). The uncertainties in friction factors will usually not introduce errors as large as those due to uncertainties about the effects of duct cross sectional shape.

Adapter ducts changing from rectangular to round cross sections are commonly required to connect two-dimensional supersonic inlets with engine faces. Adapter duct losses can be estimated on the basis of friction, but this is valid only when local duct divergence angles are small enough to avoid flow separation. No quantitative information is available on separation criteria for constant area ducts of changing cross sectional shape. However, separation does not occur in conical diffusers with divergence angles less than approximately 10 degrees despite the adverse pressure gradients present in diffusers. On this basis, 10 to 15 degree total included divergence angles are unlikely to produce separation in adapter ducts which do not have significant overall diffusion. When divergence angles are marginally large, inlet system model tests are necessary to evaluate adapter duct pressure losses.

#### 2.6.3.3 Screens

Pressure losses can be readily computed for incompressible flow through screens at high Reynolds numbers (Figure 2-35). Compressibility and viscous effects can also be evaluated for screens (Reference 24). The compressible flow limitations are usually significant for engine inlet screens. A screen downstream of a subsonic diffuser tends to reduce diffuser loss (Reference 15) and improve flow uniformity, but these effects would not be significant for low-loss engine inlet screens.

#### 2.6.4 Effects of Losses on Pressure Recovery

The primary index of engine inlet system performance is pressure recovery which is defined as the ratio of the engine face and free stream total pressures. Internal ducting pressure loss reduces the inlet system pressure recovery. The magnitude of this pressure recovery reduction is dependent on the Mach number at the inlet of the subsonic diffuser as well as the overall pressure loss coefficient (Figure 2-36). The subsonic diffuser inlet Mach number is dependent on many aspects of the inlet system design configuration and operating conditions.



With a subsonic engine inlet system, the minimum duct area is at the subsonic diffuser inlet, and internal ducting loss is the primary factor relative to inlet recovery. With supersonic inlet systems, shock compression loss is usually the primary factor relative to inlet recovery during supersonic flight. The subsonic diffuser in this case is downstream of the terminal normal shock, which is not necessarily at the minimum duct area. Supersonic inlet systems usually have variable geometry provisions which alter the subsonic diffuser inlet Mach number and area as a function of flight conditions. It is necessary to evaluate subsonic losses for all geometric variables of interest, including subsonic flight with a supersonic inlet system.

Friction losses are greatest for flight conditions producing the lowest Reynolds numbers (Figure 2-25). Subsonic engine inlet recovery therefore tends to be somewhat less at high than at low flight altitude. However, large variations of inlet system recovery with flight conditions are usually due to flow separation and/or compressibility effects.

#### 2.6.5 Pressure Distortion Effects

Non-uniformities in local total pressures over the engine inlet face are important relative to engine performance. Various aspects of the inlet ducting affect engine face pressure distortions.

An elbow will typically develop a low pressure region along the inside wall of the bend. This type of distortion can sometimes be reduced by the use of splitters, vanes, or vortex generators.

Subsonic diffusers will typically develop relatively thick low energy boundary layers, particularly along walls with high local flow divergence angles. Diffuser exit pressure distortions can be reduced by boundary layer control (References 16, 22 and 23). Boundary layer control may be applied to all walls or to the walls most critical relative to flow divergence. The degree of boundary layer control desirable may be established by flow distortion (such as use of vortex generators for reduced flow distortion when there is no corresponding reduction of diffuser pressure loss).

The pressure distortions downstream of an elbow or diffuser tend to decrease if the air subsequently flows through a straight duct. Although no general quantitative data are available, significant flow distortion improvements are likely with 1 to 3 diameters of duct length. Low divergence straight engine inlet ducts (with lengths 5 to 10 times their diameter) have engine face velocity distributions similar to fully developed turbulent duct flow. Screens are known to reduce pressure distortions, but little significant effect is likely with a low loss screen which would be considered for an engine inlet system. Engine inlet systems frequently have a moderate contraction (such as a bullet-nose in a constant area duct) immediately upstream of the engine face. This produces a favorable

(negative) pressure gradient which tends to suppress flow distortions.

The actual compressor face pressure distortion is also dependent on the flow arrangement of the specific engine. Some engines have an opening around the compressor face periphery to pass (secondary) cooling air through an engine bay to the exhaust nozzle ejector. The secondary flow in this case tends to remove the boundary layer from the inlet duct and greatly reduce the flow distortion over the compressor face.

Local discontinuities (such as bumps on duct walls) can cause local flow separations which produce pressure distortions. No general criteria are available for evaluating the effect of local discontinuities, but the probability of separation is known to be greatest with thick boundary layers and adverse (positive) pressure gradients. Evaluation of local discontinuities can be made only by qualitative study of the local flow field turning angles for favorability in terms of the duct boundary layer and pressure gradient conditions. Model tests are required for quantitative evaluation of local discontinuities.

#### 2.6.6 Subsonic Duct Loss Calculation Method

Following is the suggested method for calculating subsonic duct losses:

1. Plot the duct cross sectional area versus distance from the inlet of the subsonic diffuser duct (throat). Considering the appropriate area variations and the local duct configuration, divide the total duct into functional components (such as subsonic diffuser, elbow, constant area duct, adapter, and screen) and identify the upstream cross sectional area of each component. Most configurations require exercise of judgment relative to excluding fillets, fairings, protuberances, and other minor surface contours when selecting the ducting component break-down.
2. Compute individual ducting component pressure loss coefficients as shown below:
  - a. Evaluate the subsonic diffuser loss coefficient by one or (if possible) more than one method. For general approximate pressure loss ranges, apply Figure 2-31 to evaluate various types of diffusers. If the diffuser is nearly conical, apply Figure 2-30 for a typical thin boundary layer case. For arbitrary diffuser shapes and specific flight conditions, apply Equation (2.14). Use Equation (2.13) to define equivalent conical diffuser angle. Use Equation (2.11) or Figure 2-25 to define boundary layer displacement

thickness for subsonic inlet systems. Use a typical ( $\delta_1^*/R_1$ ) of 0.01 for supersonic inlet systems if exact boundary layer thickness is not known. Since the diffuser will usually be the most critical subsonic loss component, it should be evaluated as carefully as possible.

- b. Evaluate elbow loss coefficients from Figure 2-34.
  - c. Evaluate screen loss coefficients from Figure 2-35.
  - d. Evaluate constant area duct and adapter loss coefficients from Equation (2.15) with an assumed typical 0.02 friction loss factor or a loss factor from Figure 2-25. For duct contractions, apply the same procedure using a weighted average duct hydraulic diameter.
3. Combine the individual component loss coefficients by applying Equation (2.12) to define overall loss coefficient in terms of the inlet system throat flow conditions. Define these overall loss coefficients for all inlet variable geometry positions of interest in the specific propulsion system.
  4. Apply Figure 2-36 to evaluate reduction of inlet system pressure recoveries caused by subsonic losses. Evaluate recoveries in this manner for the flight range of Mach number, altitude, engine power setting, and inlet variable geometry.
  5. Evaluate qualitatively the effects of subsonic diffuser boundary layer control provisions on losses as discussed in Section 2.5.4.2.4.
  6. Evaluate qualitatively the geometric configuration and boundary layer control provisions in terms of pressure distortion effects as discussed in Section 2.5.4.5.

## References

1. Fradenburg, E. A. and Wyatt, D. D., Theoretical Performance of Sharp-Lip Inlets at Subsonic Speeds, NACA Report 1193, 1954
2. Blackaby, J. R. and Watson, E. C., an Experimental Investigation of the Effects of Lip Shape on the Drag and Pressure Recovery of a Nose in a Body of Revolution, NACA TN3170, April 1954
3. Moeckel, W. E., Estimation of Lip Forces at Subsonic and Supersonic Speeds, NACA TN3457, June 1955
4. Ames Research Staff, Equations, Tables, and Charts for Compressible Flow, NACA Report 1135, 1953
5. Dailey, C. L. and Wood, F. C., Computation Curves for Compressible Fluid Problems, John Wiley & Sons, Inc., 1949
6. Oswatitsch, K., Pressure Recovery for Missiles with Reaction Propulsion at High Supersonic Speeds (The Efficiency of Shock Diffusers), NACA TM1140, 1947
7. Shapiro, Ascher H., The Dynamics and Thermodynamics of Compressible Fluid Flow, Volume II, The Ronald Press Co., 1954
8. Conners, J. T. and Meyer, R. C., Design Criteria for Axisymmetric and Two-Dimensional Inlets and Exits, NACA TN3589, January 1956
9. Sorensen, V. L., Computer Program for Calculating Flow Fields in Supersonic Inlets, NASA TN D-2897, July 1965
10. Schlichting, Hermann, Boundary Layer Theory, McGraw-Hill Book Company, 1955
11. Shapiro, Ascher H. and Smith, R. Douglas, Friction Coefficients in the Inlet Length of a Smooth Round Tube, NACA Technical Note 1785, November 1948
12. Shapiro, Ascher H., The Dynamic and Thermodynamics of Compressible Fluid Flow, Volume I, The Ronald Press Company, 1953
13. Shapiro, Ascher H., The Dynamic and Thermodynamics of Compressible Fluid Flow, Volume II, The Ronald Press Company, 1954
14. Lin, C. C., Turbulent Flows and Heat Transfer, Princeton University Press, 1959
15. SAE Committee A-9, Aero-Space Applied Thermodynamics Manual, Society of Automotive Engineers, Inc., February 1960

## References

16. Henry, John R., Wood, Charles C., and Wilbur, Stafford, W., Summary of Subsonic - Diffuser Data, NACA Report No. RML 56F05, October 12, 1956
17. Henry, John R., Design of Power-Plant Installations Pressure Loss Characteristics of Duct Components, NACA Report No. ARR L4F26, June 1944
18. Braslow, Albert L. and Knox, Eugene C., Simplified Method for Determination of Critical Height of Distributed Roughness Particles for Boundary Layer Transition at Mach Numbers from Zero to Five, NACA Technical Note 4363, September 1958
19. Crossthwait, E. L., Kennon, I. G., Jr., and Roland, H. L., Preliminary Design Methodology for Air - Induction Systems, Air Force Systems Command Report SEG-TR-67-1, January 1967
20. Anon, Design Handbook for Submerged Engine Cooling Systems and Duct Systems, Contract NOa(s) 56-880-f, January 1958
21. Scherrer, Richard and Anderson, Warren E., Preliminary Investigations of a Family of Diffusers Designed for Near Sonic Inlet Velocities, NACA Technical Note 3668, February 1956
22. Brown, Alan C., Nawrocki, H. Franz, and Paley, Peter N., Subsonic Diffusers Designed Integrally with Vortex Generators, Paper No. 67-464, AIAA Third Propulsion Joint Specialist Conference, July 17-21, 1967
23. Sorensen, Norman E., Anderson, Warren E., Wong, Norman D., and Smeltzer, Donald B., Performance Summary of a Two-Dimensional and an Axisymmetric Supersonic-Inlet System NASA Report No. SP-124, Conference on Aircraft Aerodynamics, May 1966
24. Cornell, W. G., Losses in Flow Normal to Plane Screens, Transactions of the ASME, May 1958

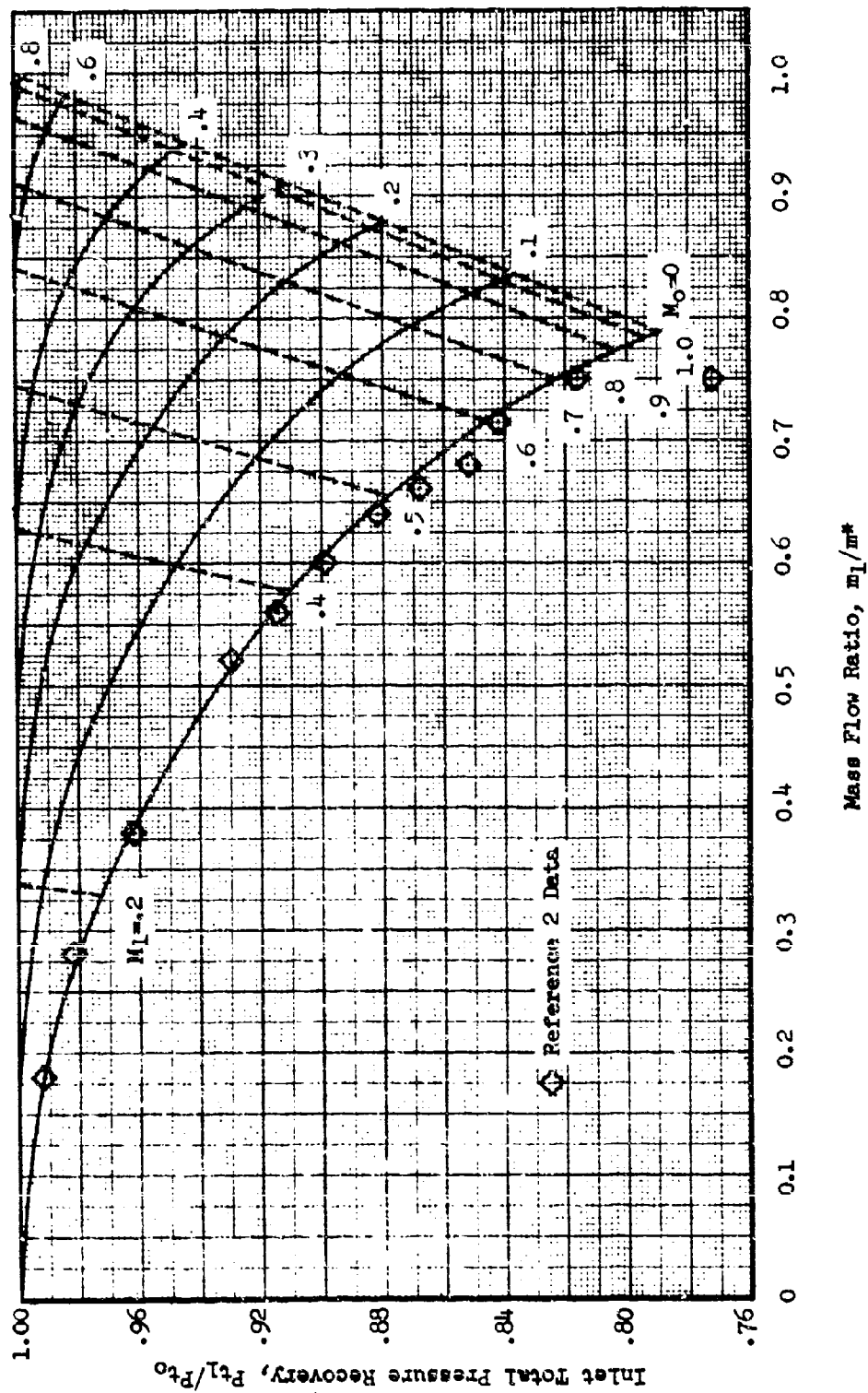


FIGURE 2-1. Theoretical Sharp Lip Inlet Total Pressure Recovery.

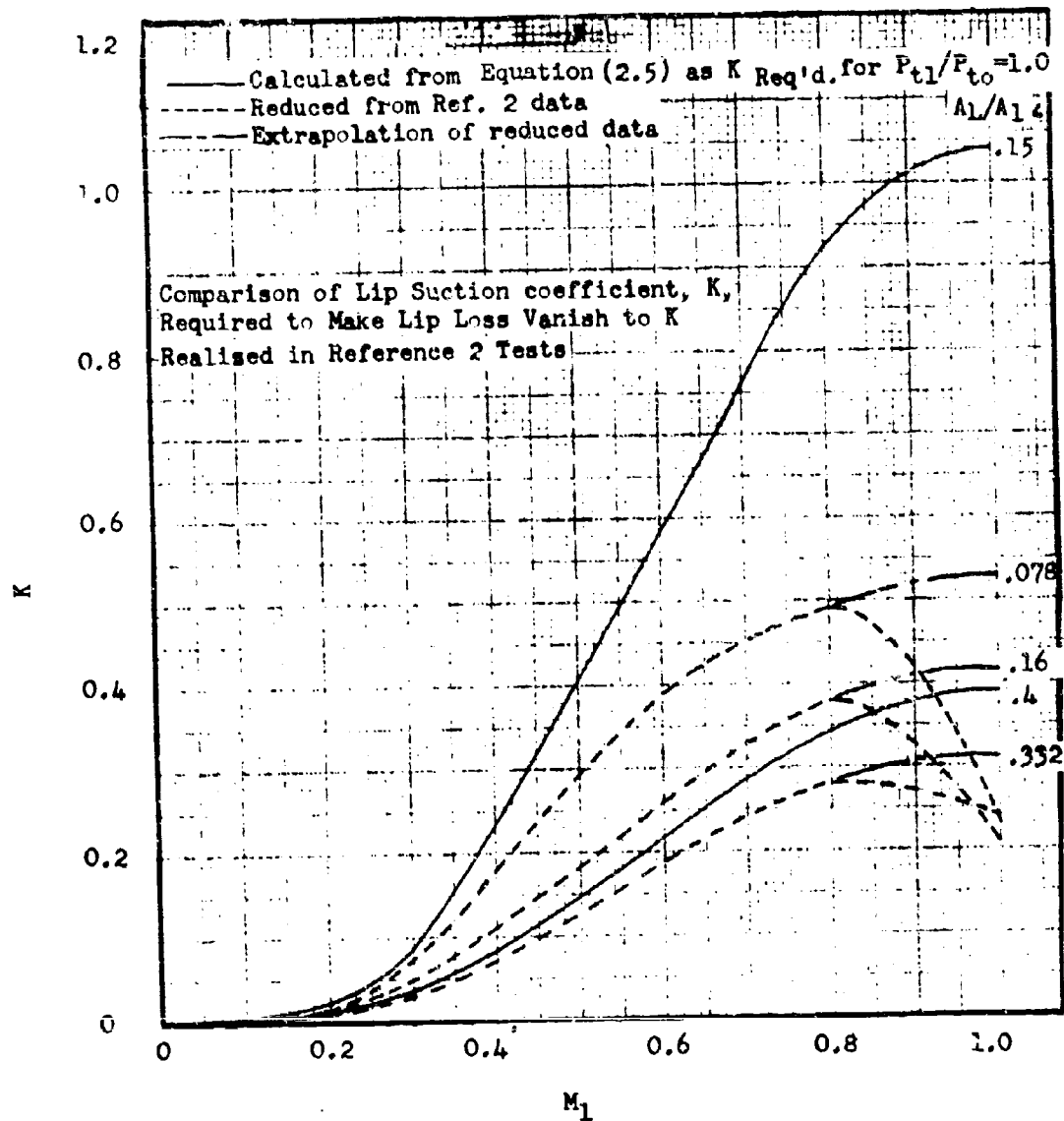


FIGURE 2-2. Low Speed Lip Loss Correlation.  
 $M_0=0.166$

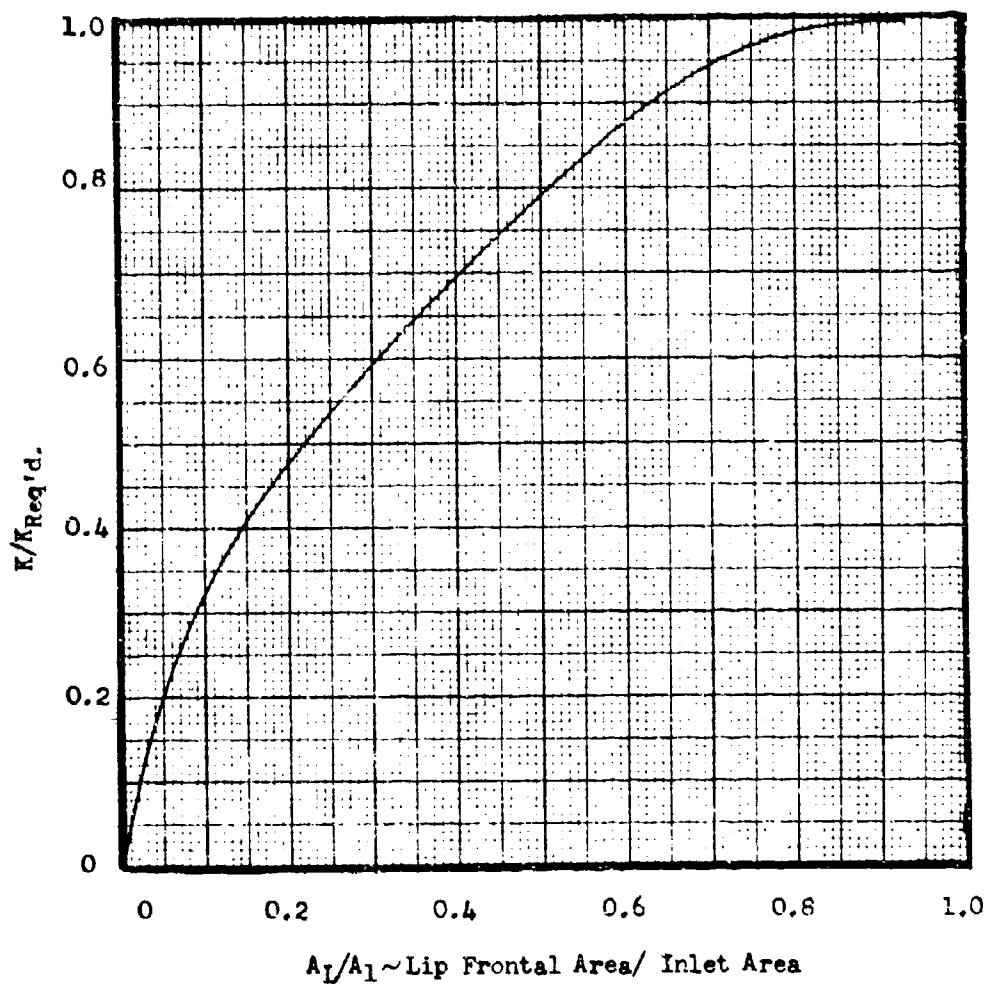


FIGURE 2-3. Ratio of Experimental Lip Suction Coefficient  
to Coefficient Required to Make Lip Loss Vanish

MFR = 1.0

$M_o = 0-0.4$



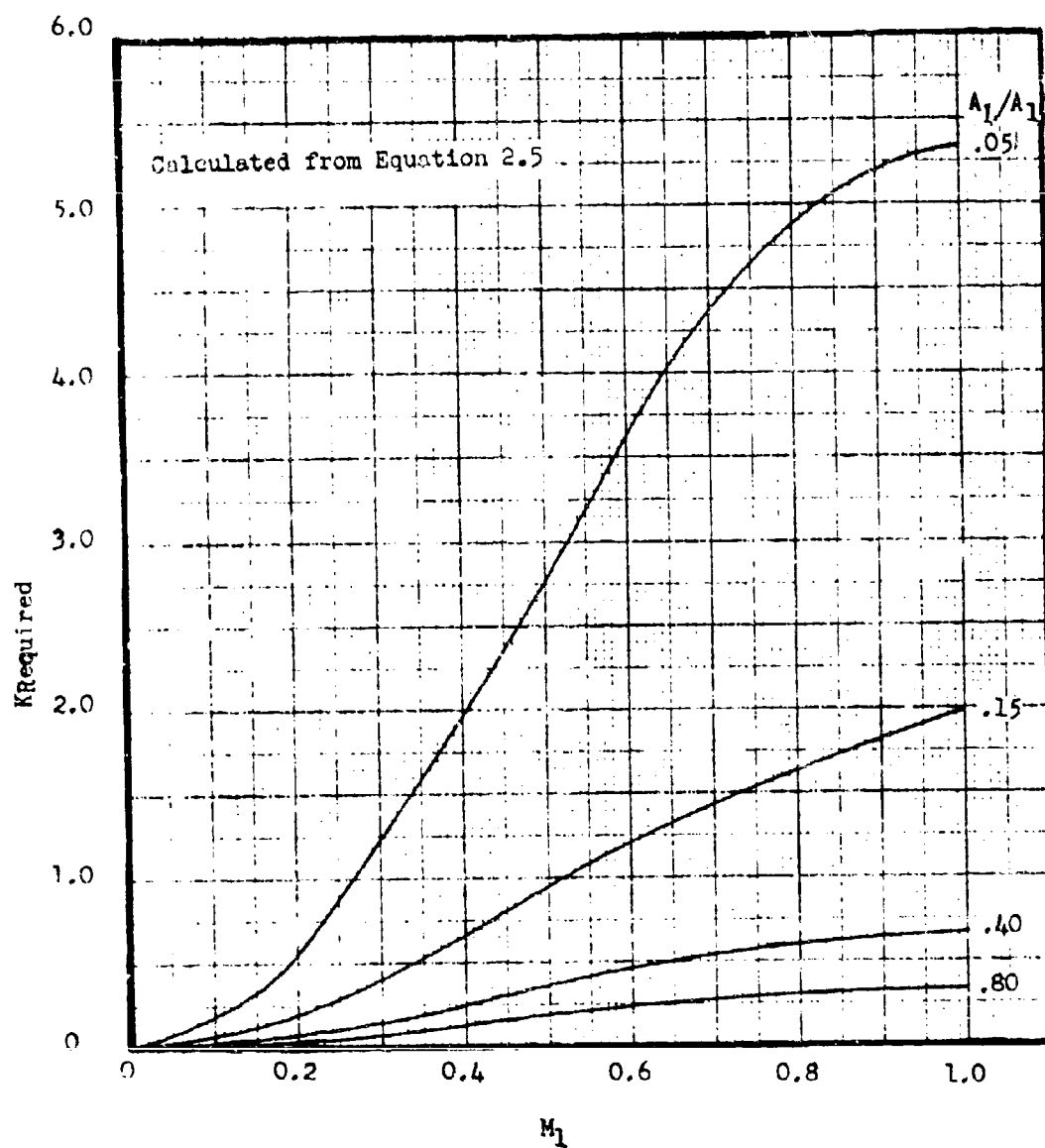


FIGURE 2-4. Lip Suction Coefficient,  $K$ , Required to Make Lip Loss Vanish.  
 $M_0=0$

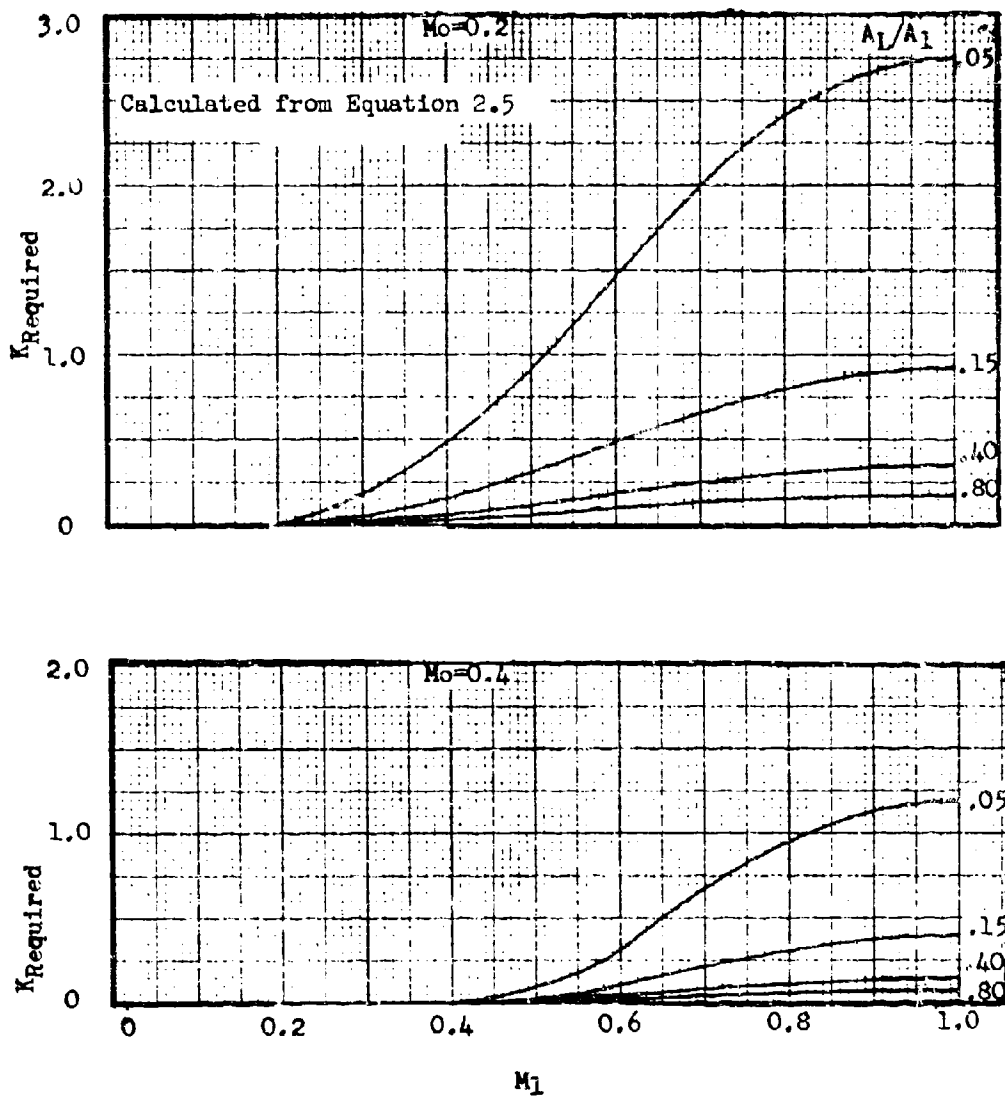


FIGURE 2-5. Lip Suction Coefficient,  $K$ , Required to Make Lip Loss Vanish.

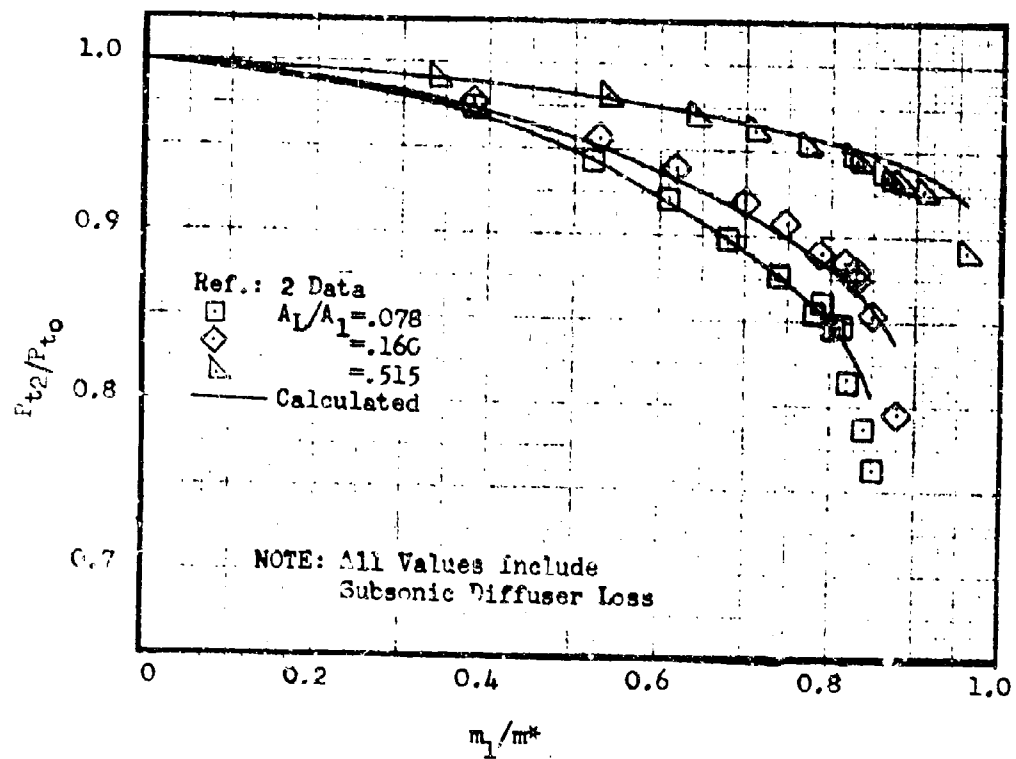


FIGURE 2-6. Inlet Lip Loss Correlation.

$$M_0 = 0$$

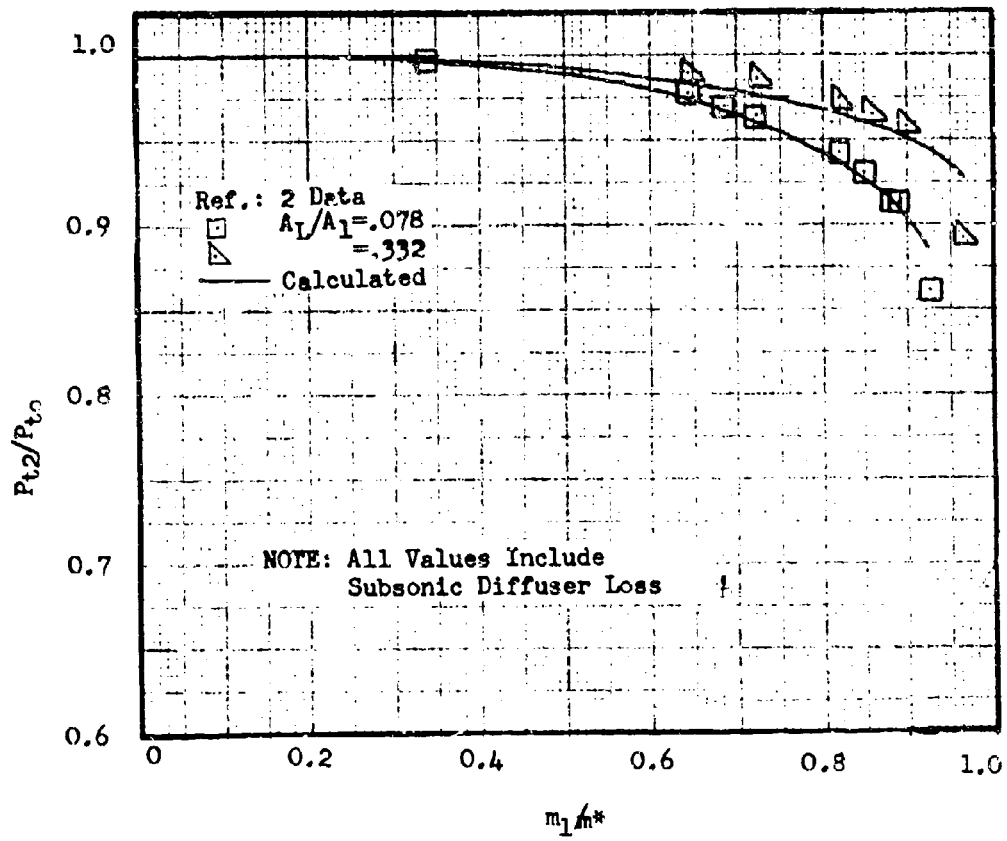


FIGURE 2-7. Inlet Lip Loss Correlation

$$M_0 = 0.237$$

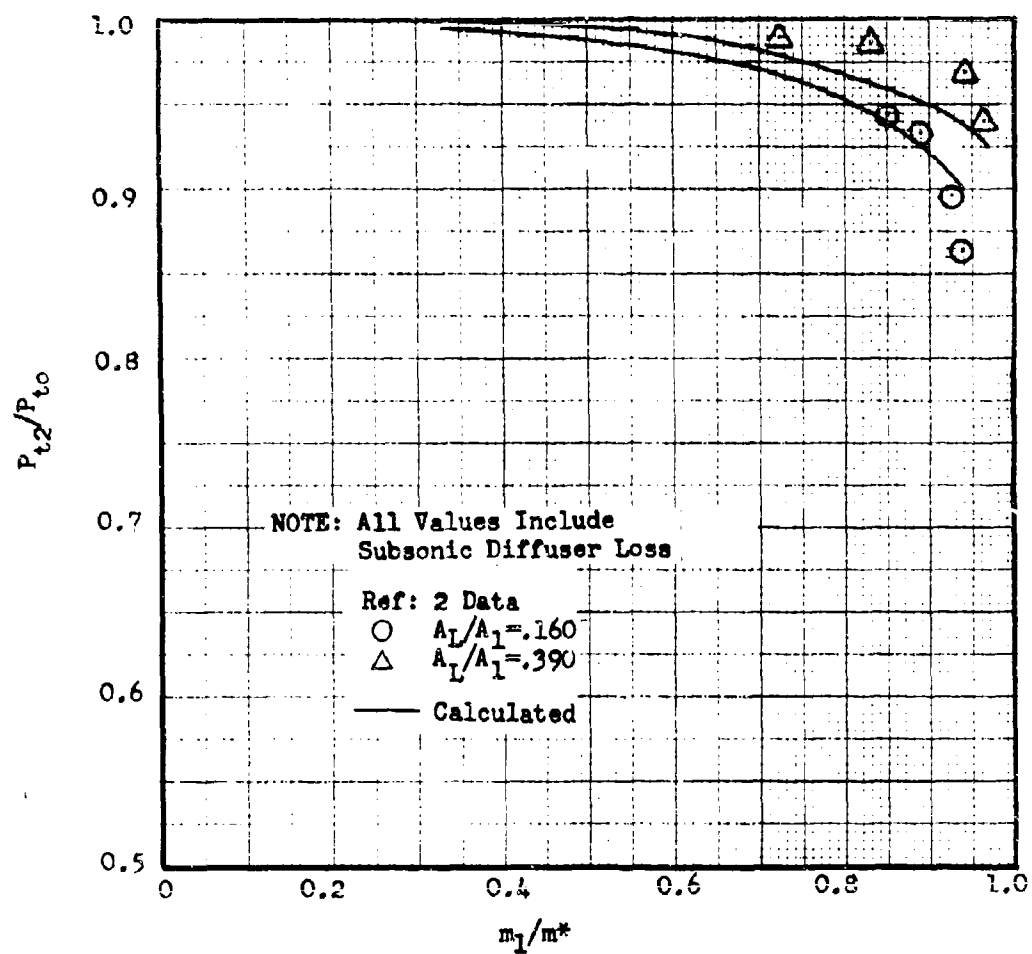


FIGURE 2-8. Inlet Lip Loss Correlation

Elliptical Profiles.

$$M_0 = 0.237$$

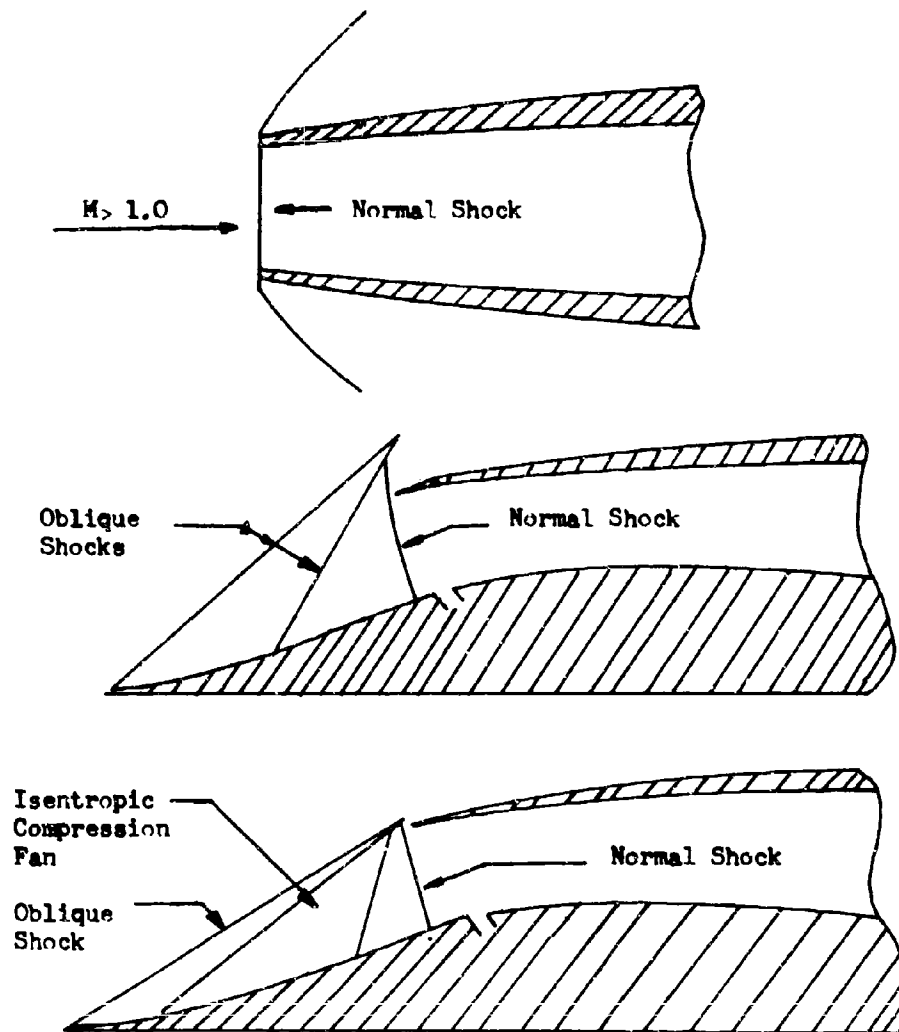


FIGURE 2-9. Examples of Normal Shocks.

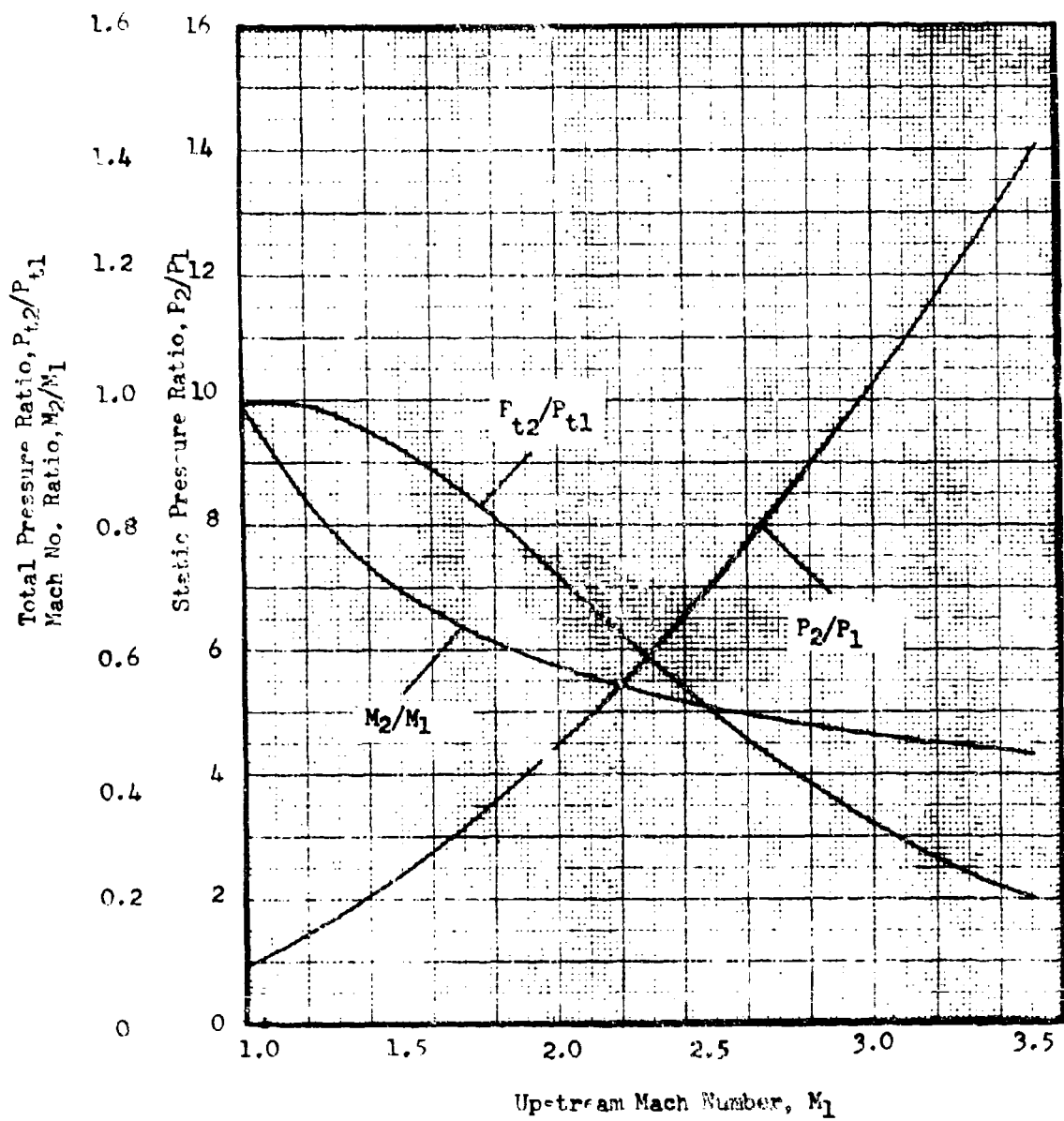
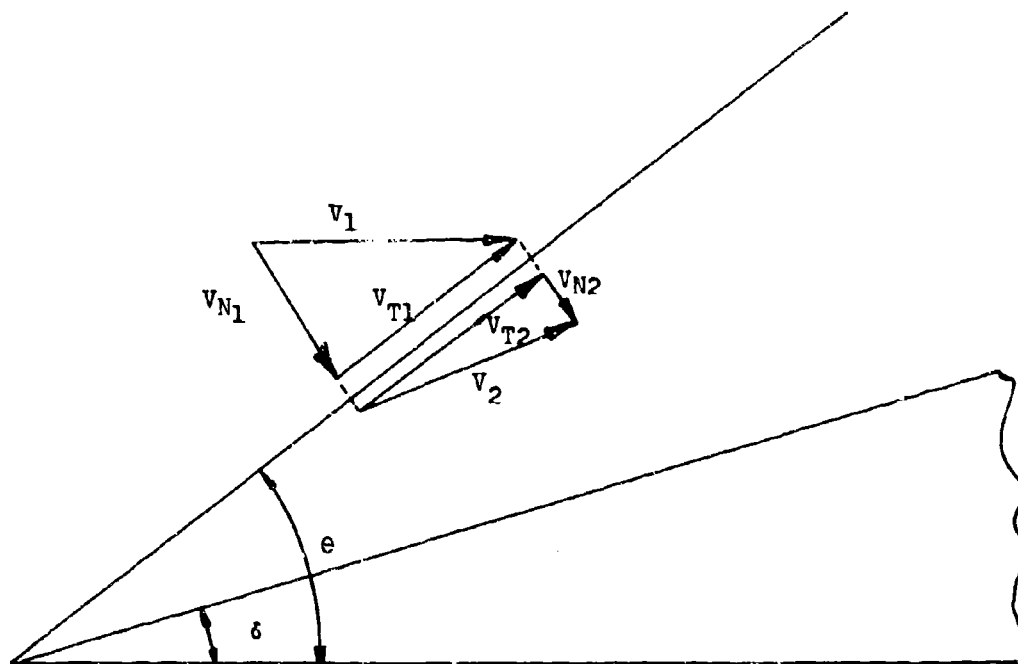


FIGURE 2-10. Normal Shock Wave Parameter.



$$v_{T1} = v_{T2}$$

$$v_{N1} = v_1 \sin \theta$$

$$v_{N2} = v_2 \sin (\theta - \delta)$$

FIGURE 2-11. Oblique Shock Wave Velocity Relationships.



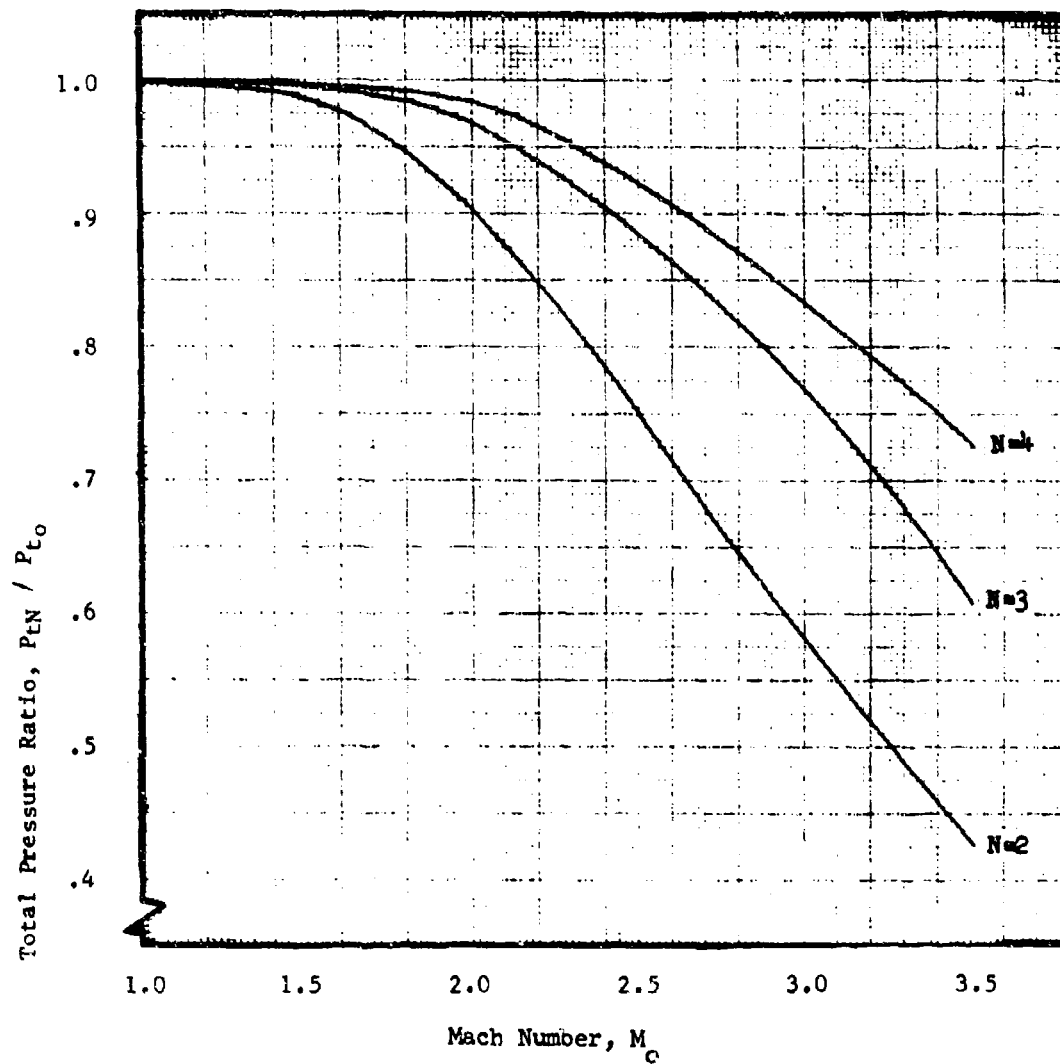


FIGURE 2-12. Optimum Pressure Recovery For 2, 3 And 4-Shock, 2-Dimensional Inlet.

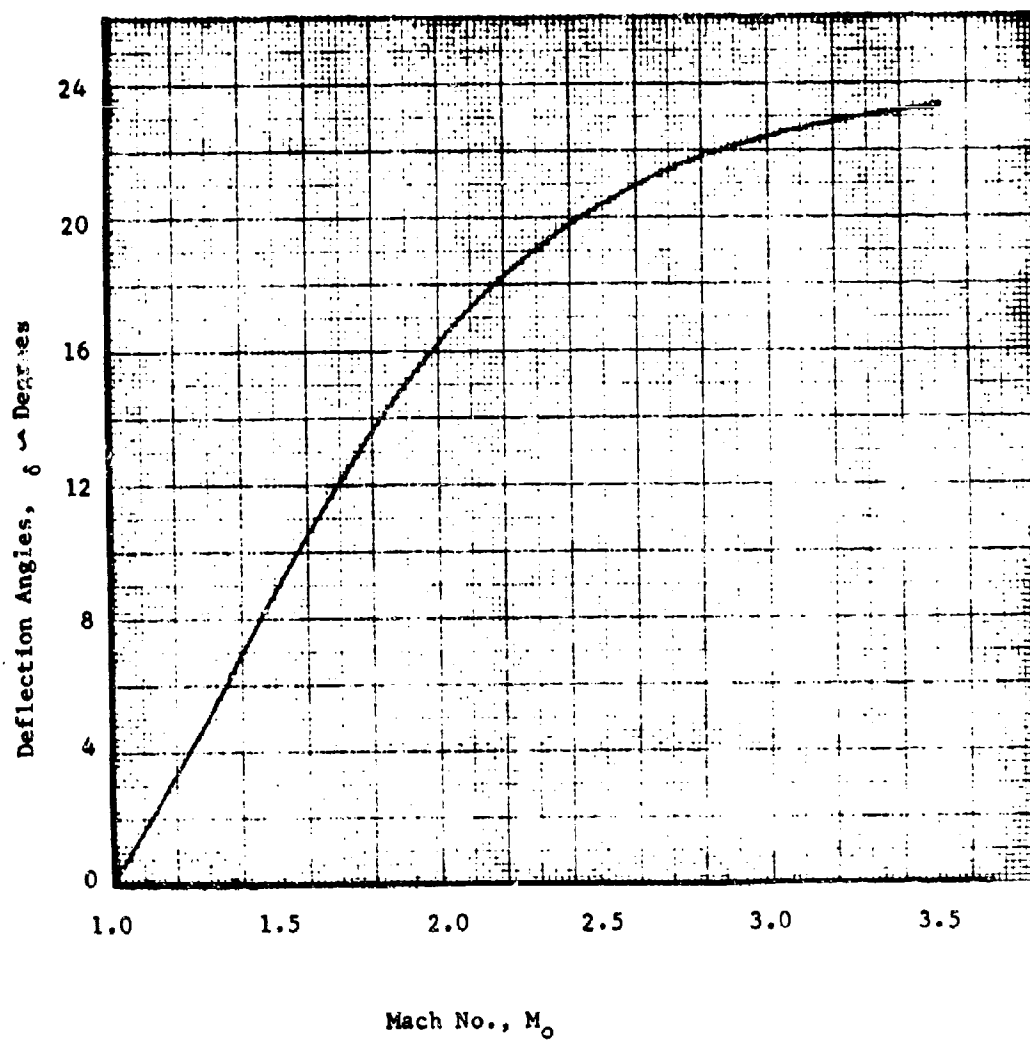


FIGURE 2-13. Optimum Deflection Angles for 2-Shock, 2-Dimensional Inlet

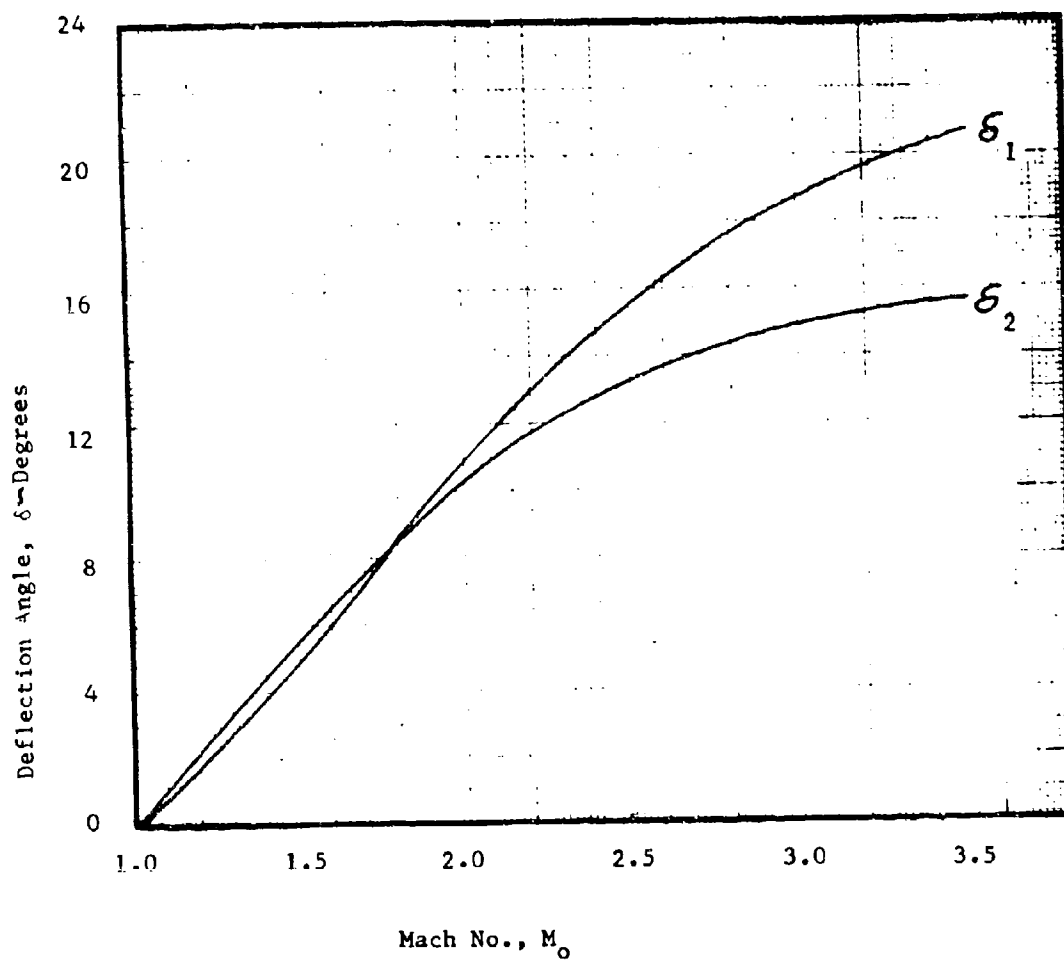


FIGURE 2-14. Optimum Deflection Angles for 3-Shock, 2-Dimensional Inlet

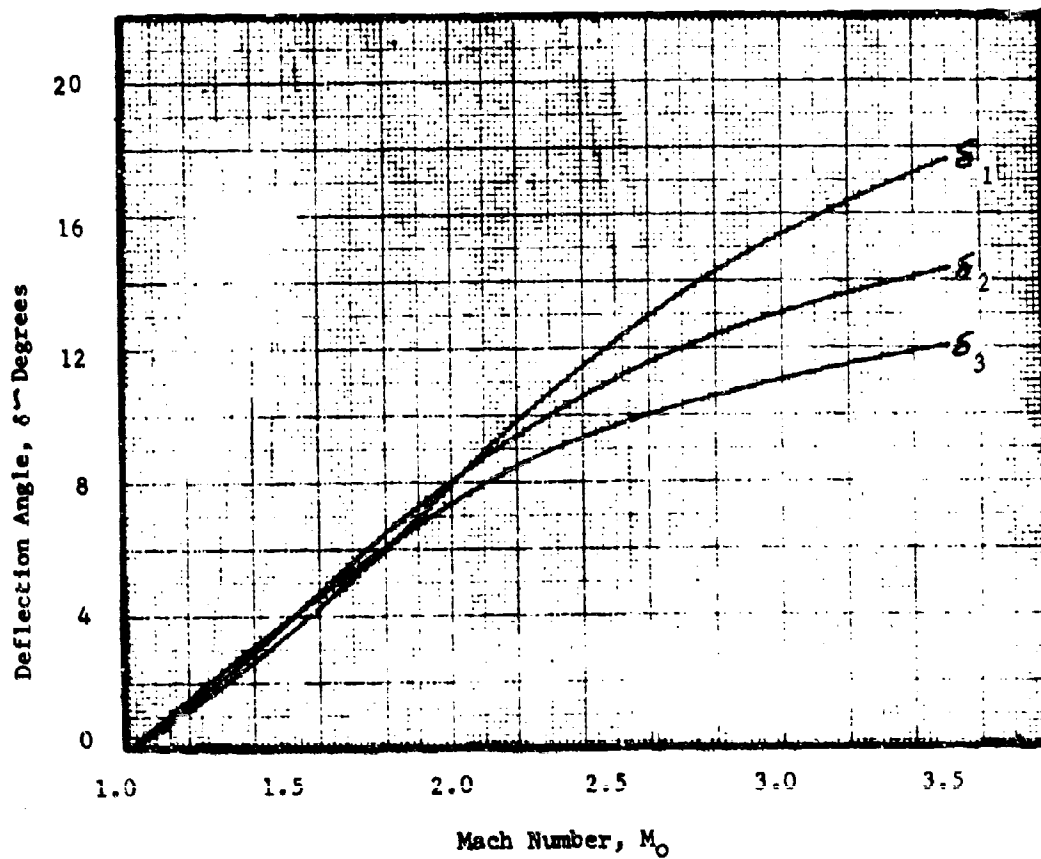


FIGURE 2-15. Optimum Deflection Angles For 4-Shock, 2-Dimensional Inlets

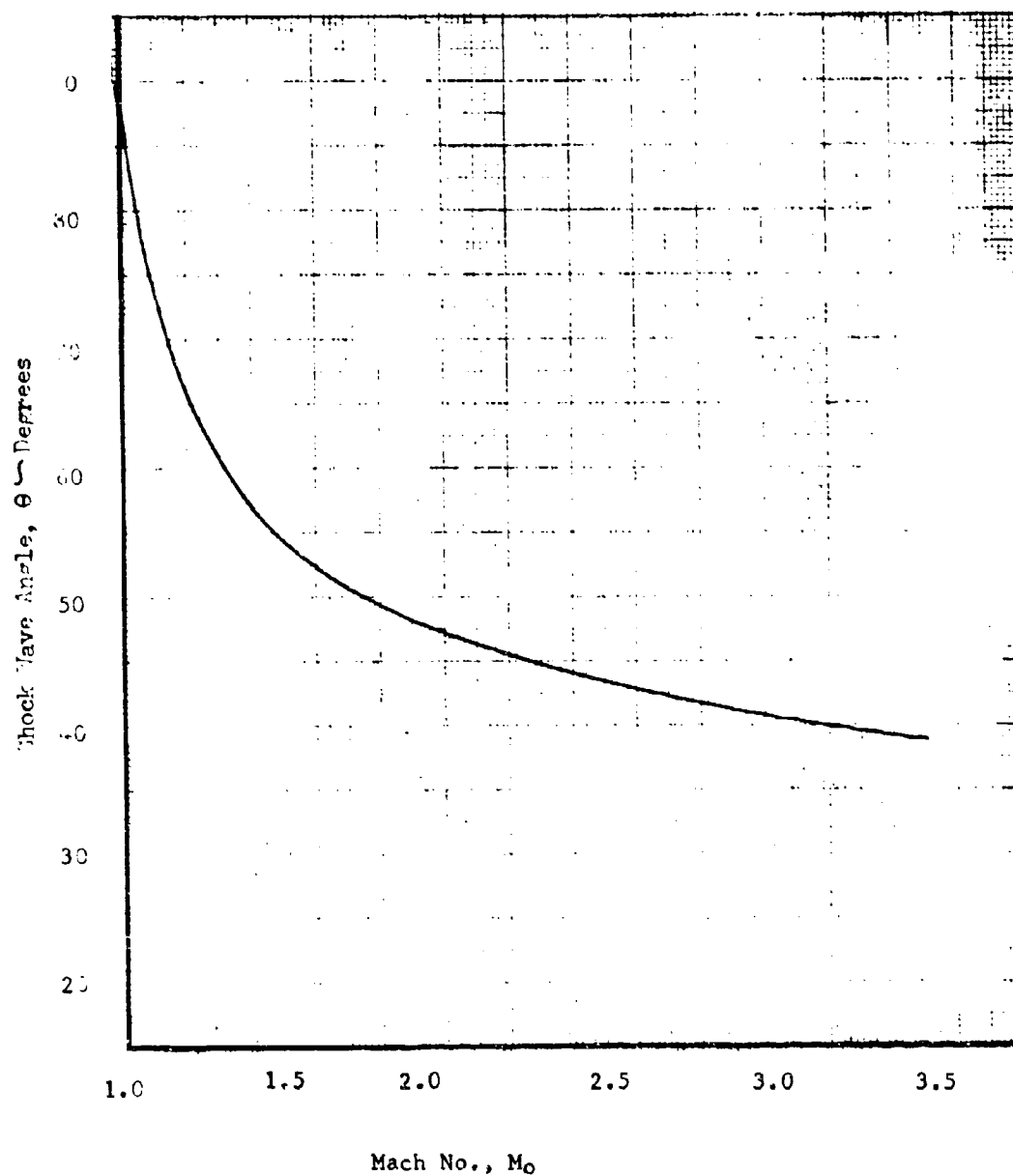


FIGURE 2-16. Shock Wave Angles Corresponding To Optimum Deflection Angles For 2-Shock, 2-Dimensional Inlet.

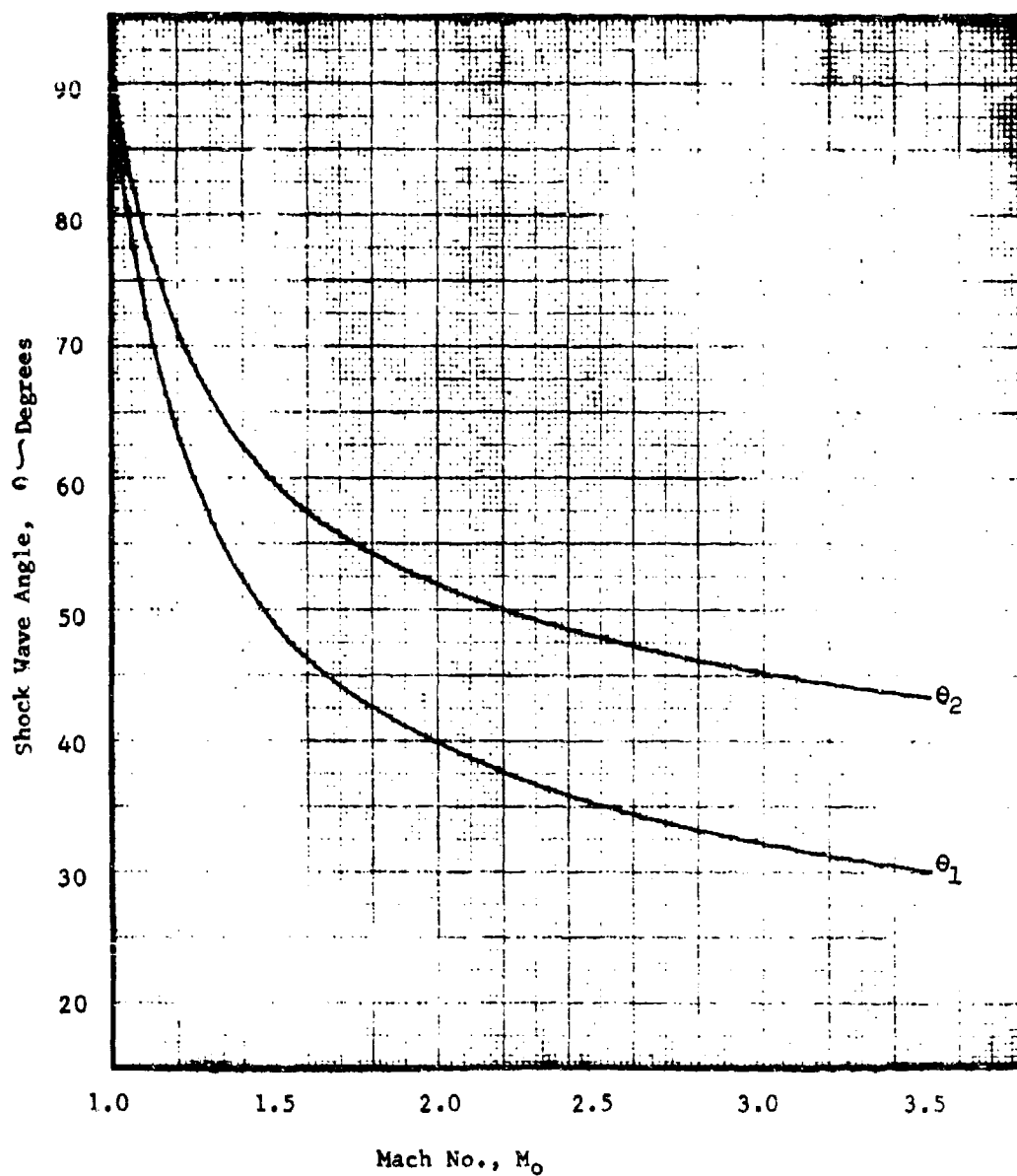


FIGURE 2-17. Shock Wave Angles Corresponding To Optimum Deflection Angles for 3-Shock, 2-Dimensional Inlet.

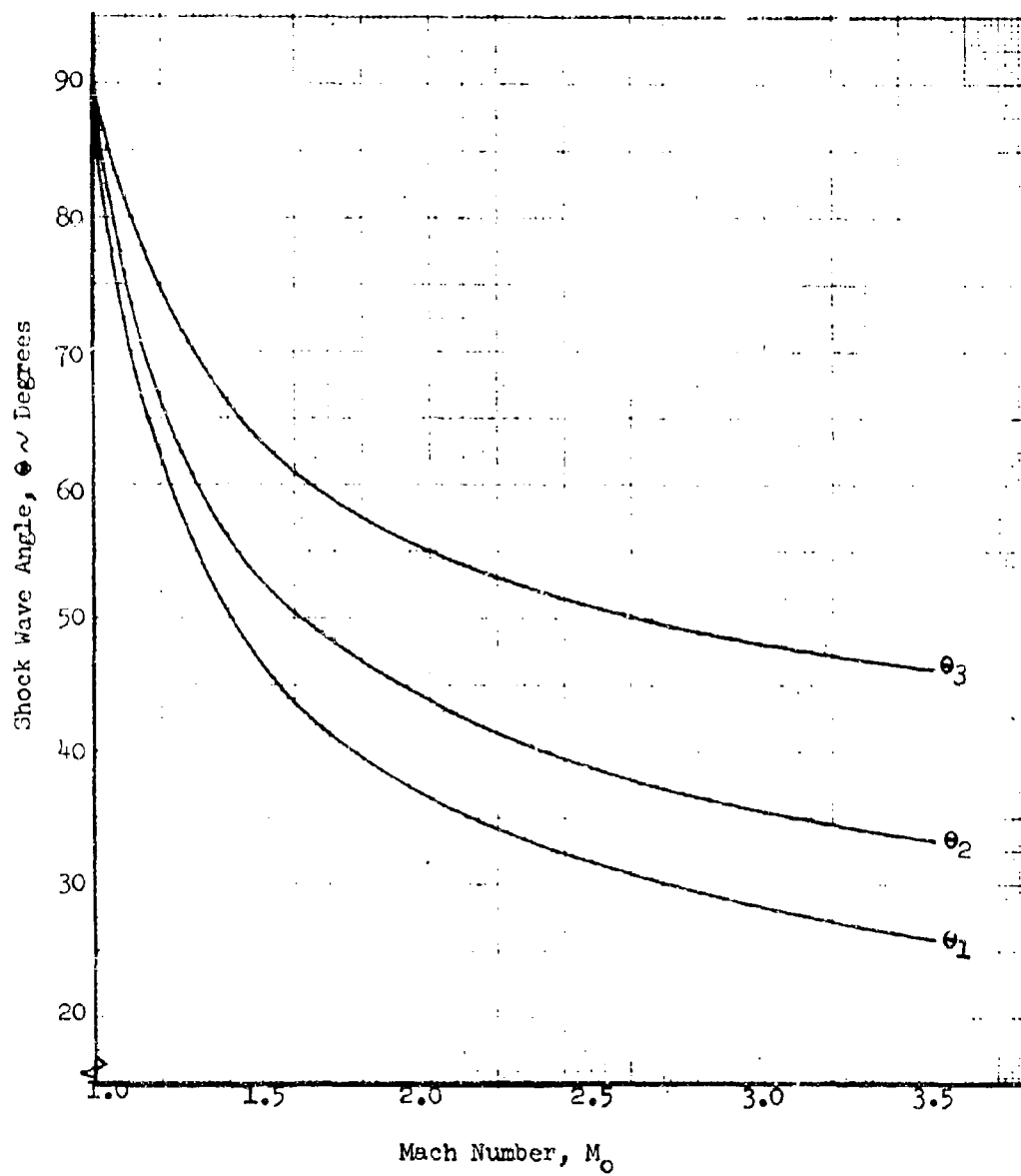


FIGURE 2 - 18. Shock Wave Angles Corresponding to Optimum Deflection Angles for 4-Shock, 2-Dimensional Inlet.

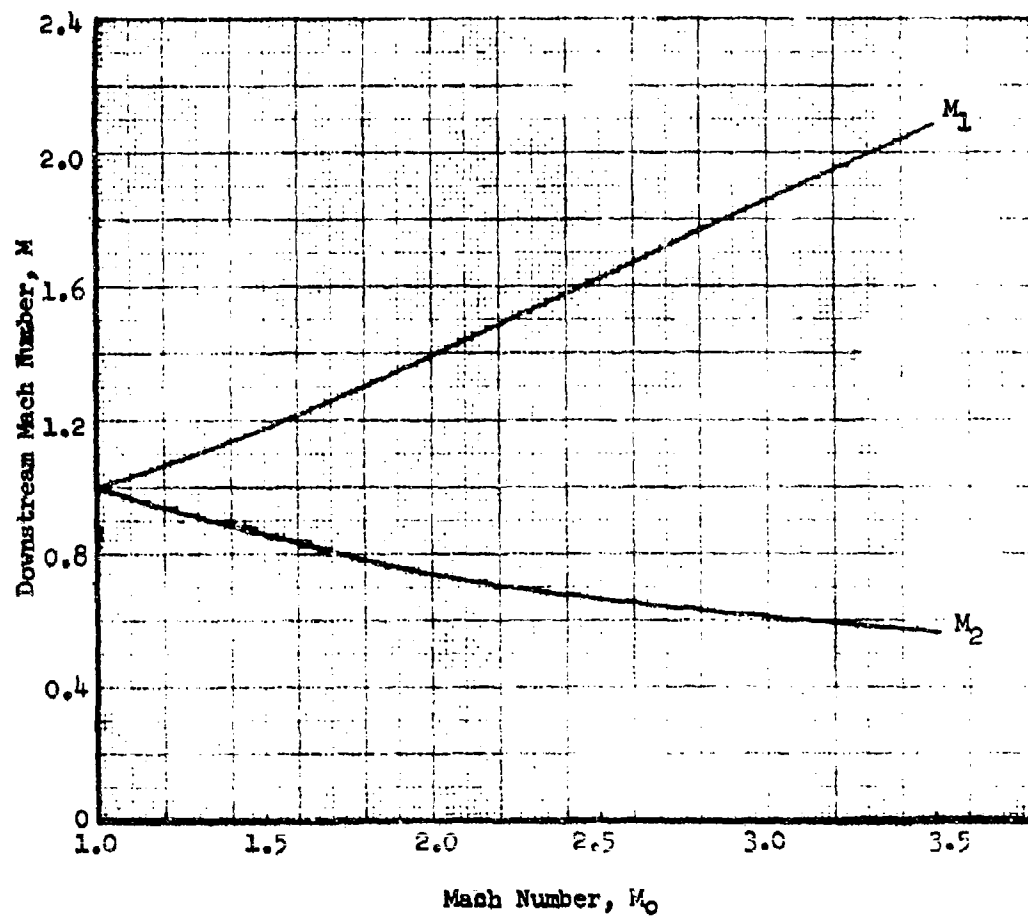


FIGURE 2 - 19. Downstream Mach Numbers Corresponding to Optimum Deflection Angles for 2-Shock, 2-Dimensional Inlet.



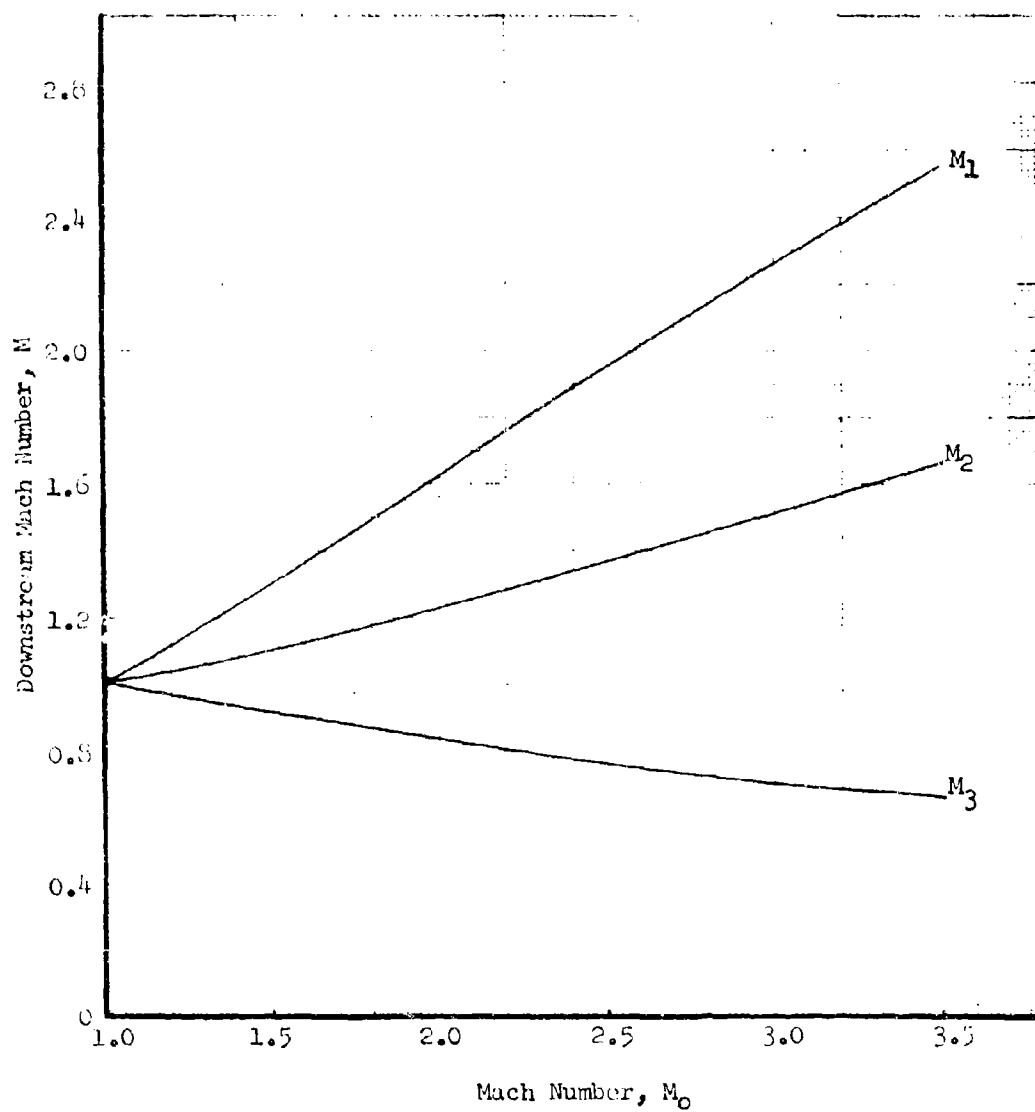


FIGURE 2 - 20. Downstream Mach Numbers Corresponding to Optimum Deflection Angles for 3-Shock, 2-Dimensional Inlet.

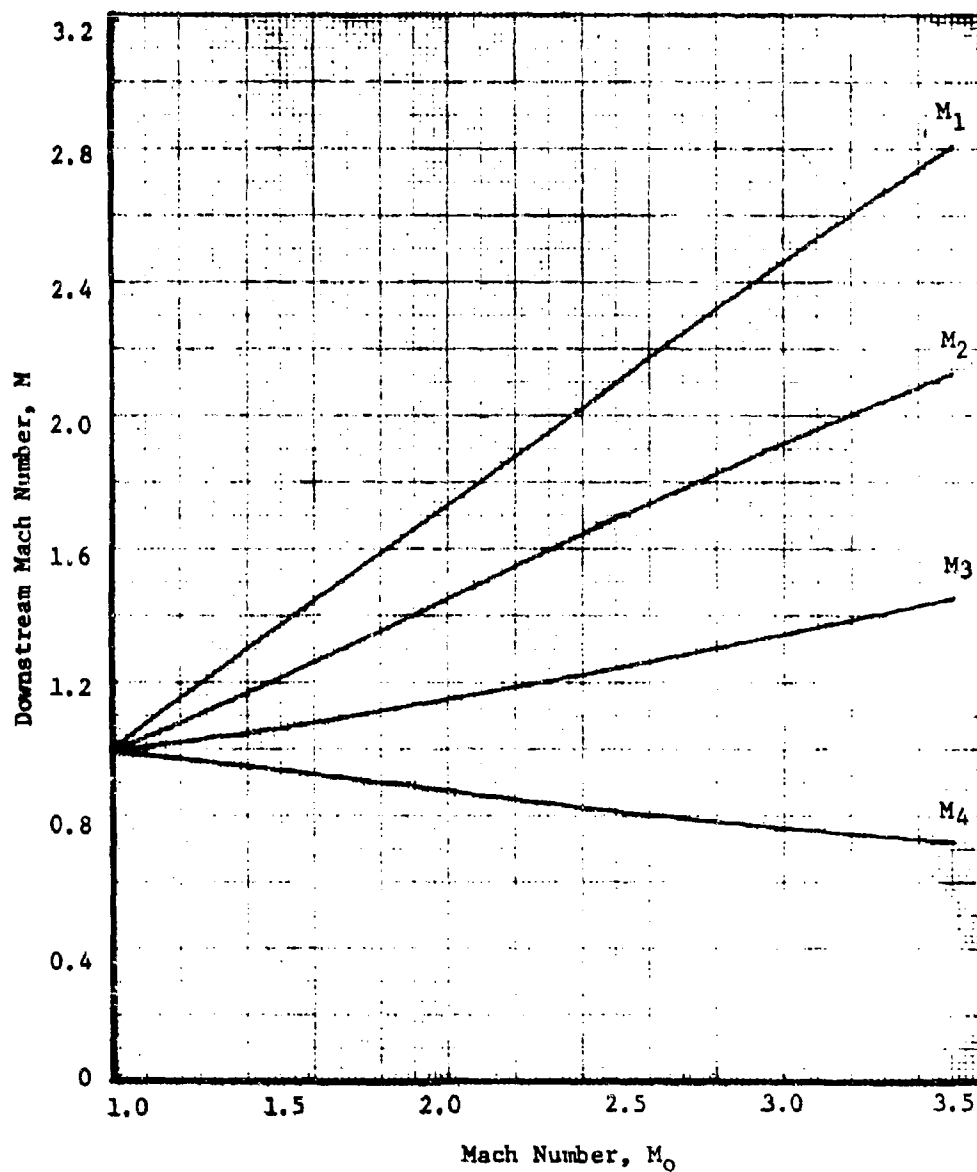


FIGURE 2 - 21. Downstream Mach Numbers Corresponding to Optimum Deflection Angles for 4-Shock, 2-Dimensional Inlet.

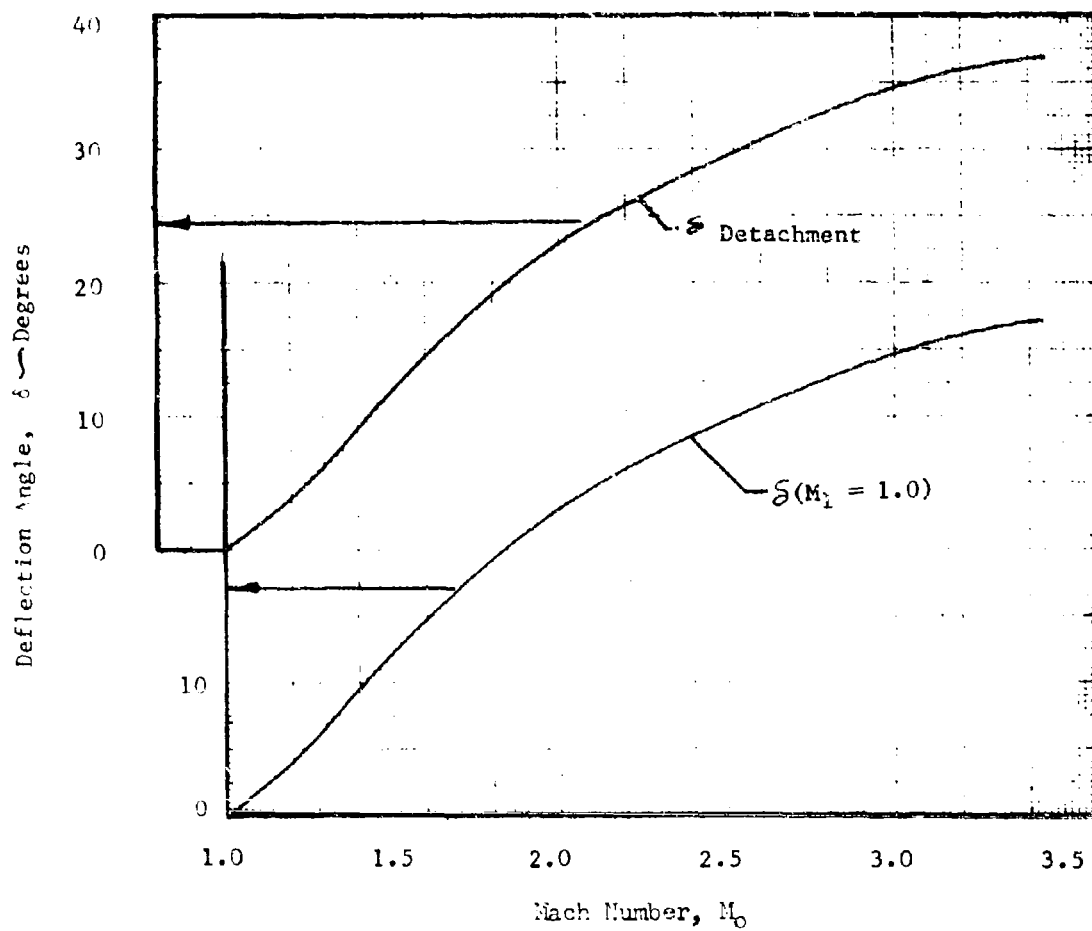


FIGURE 2-22. Deflection Angles For Shock Detachment and Sonic Flow, 2-Dimensional

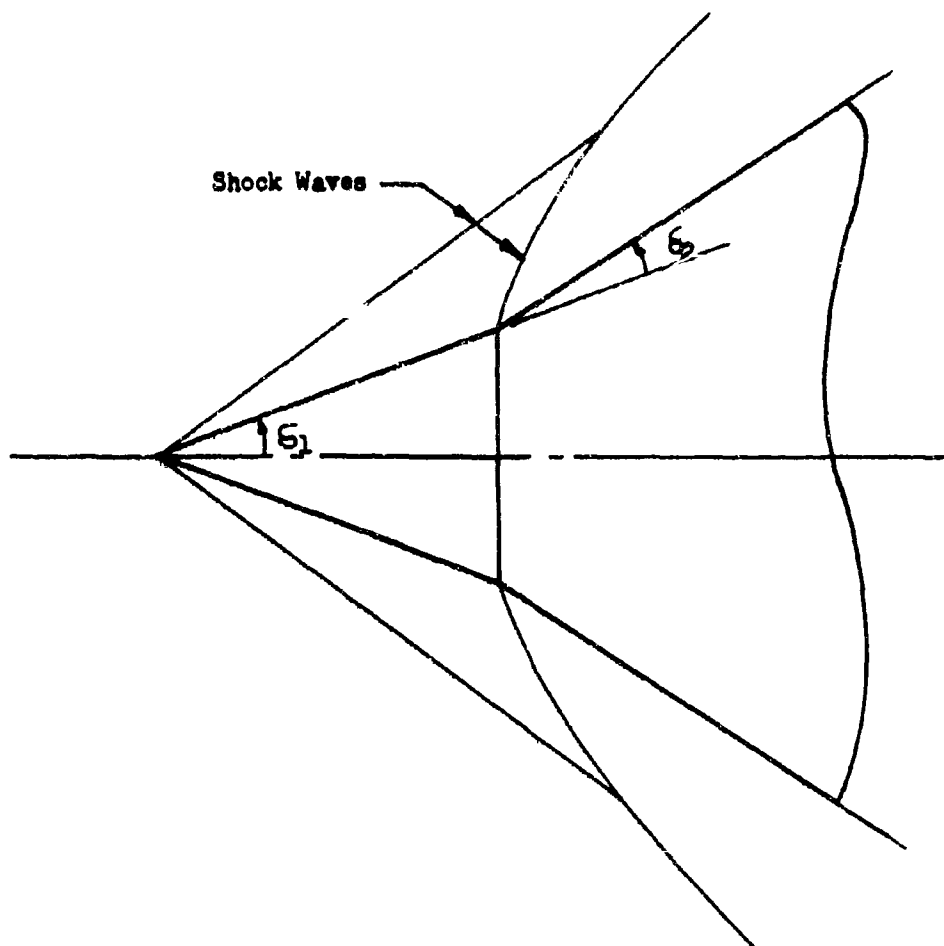


FIGURE 2 - 23. Double Cone in Supersonic Flow

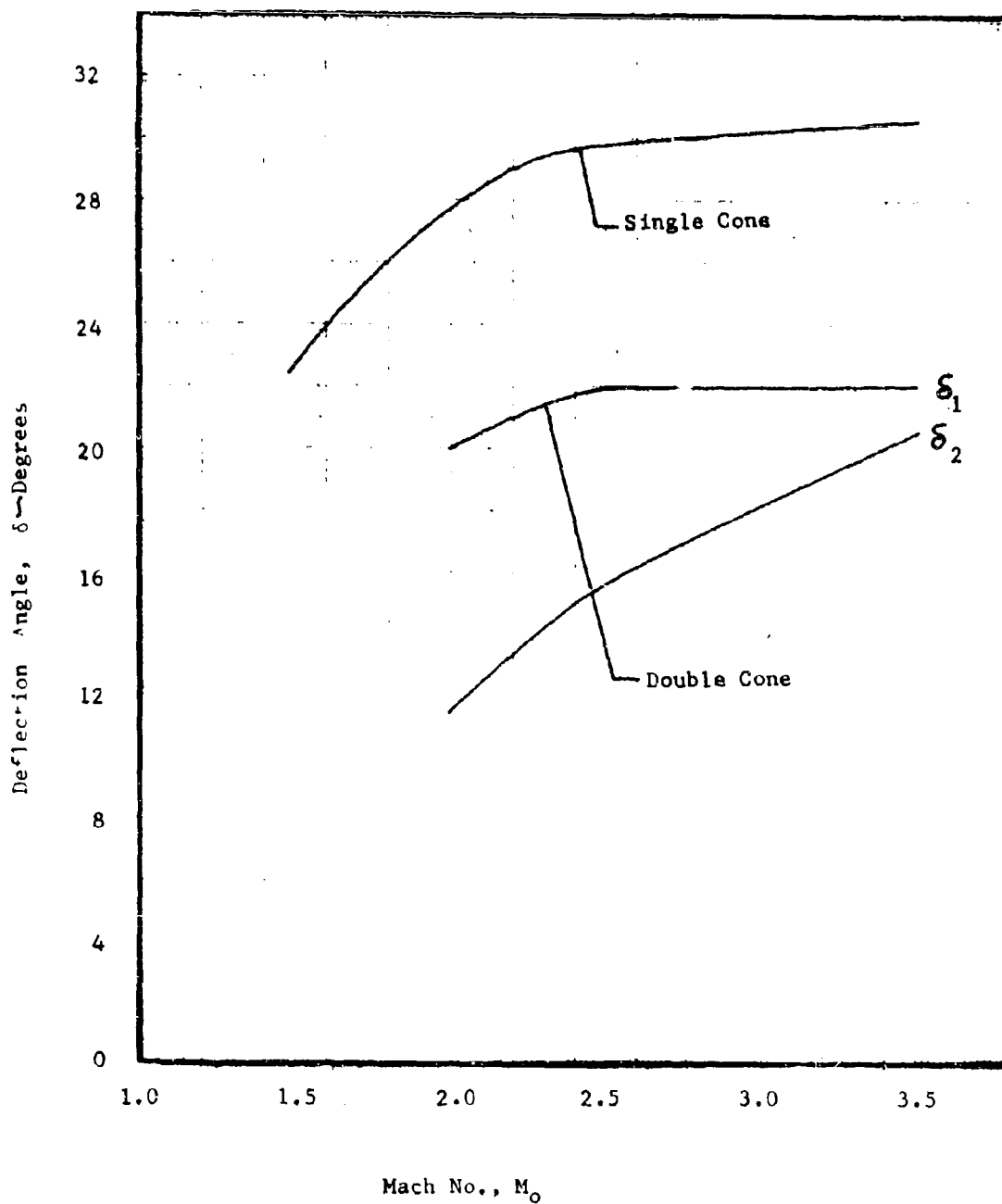


FIGURE 2-24. Optimum Deflection Angles for Axisymmetric 2 and 3-Shock Inlets

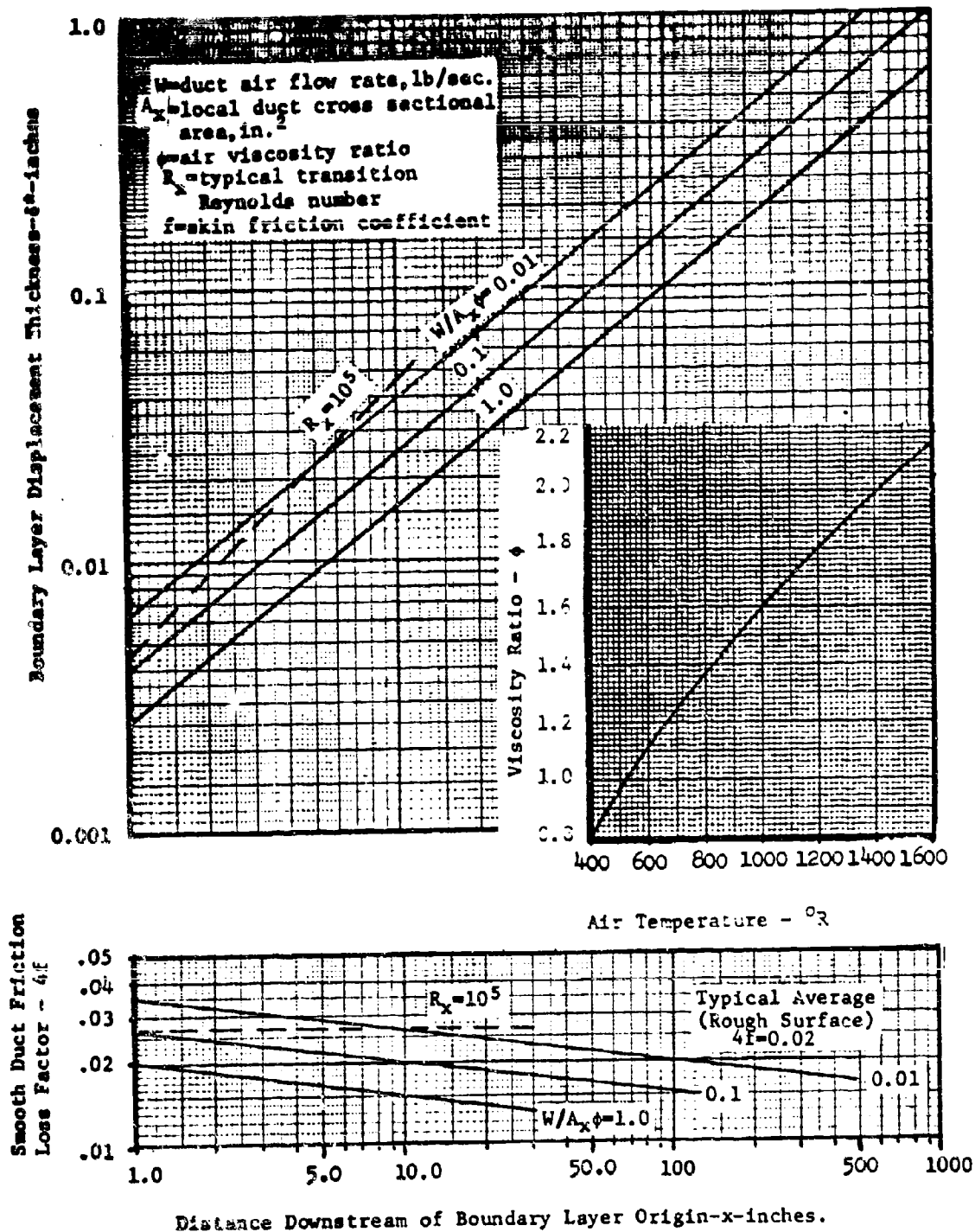


FIGURE 2-25. Turbulent Boundary Layer Thickness and Friction Criteria.  
(References 10 and 11)

# Choking Criteria

Average Diffuser Inlet Mach Number at Choke  
(Based on  $W\sqrt{\theta_T}/\delta_{T1}A_1$  from Figure 2-37.)

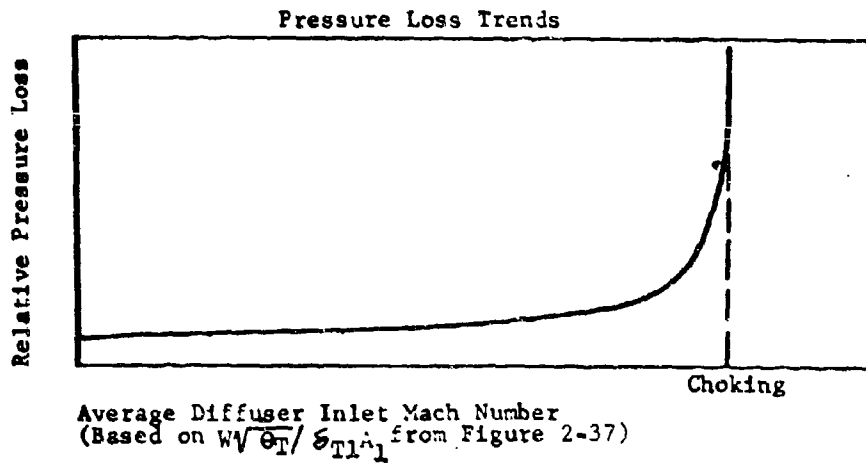
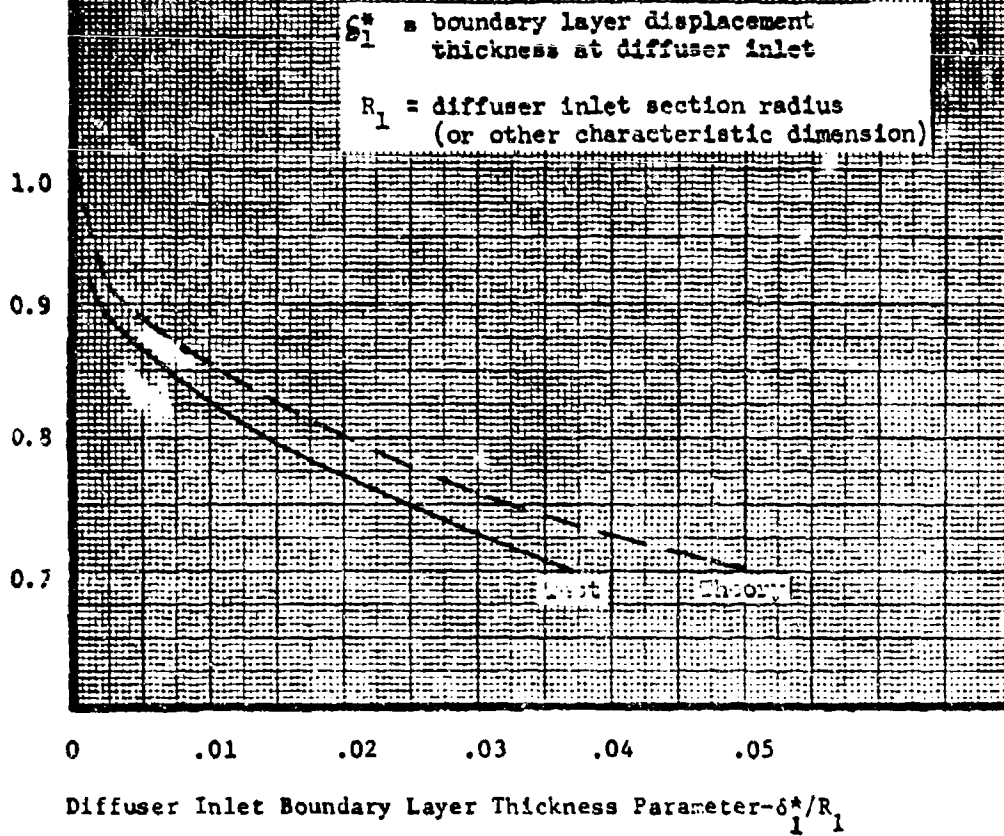


FIGURE 2-26. Compressibility Effects in Diffusers  
(Reference 16)

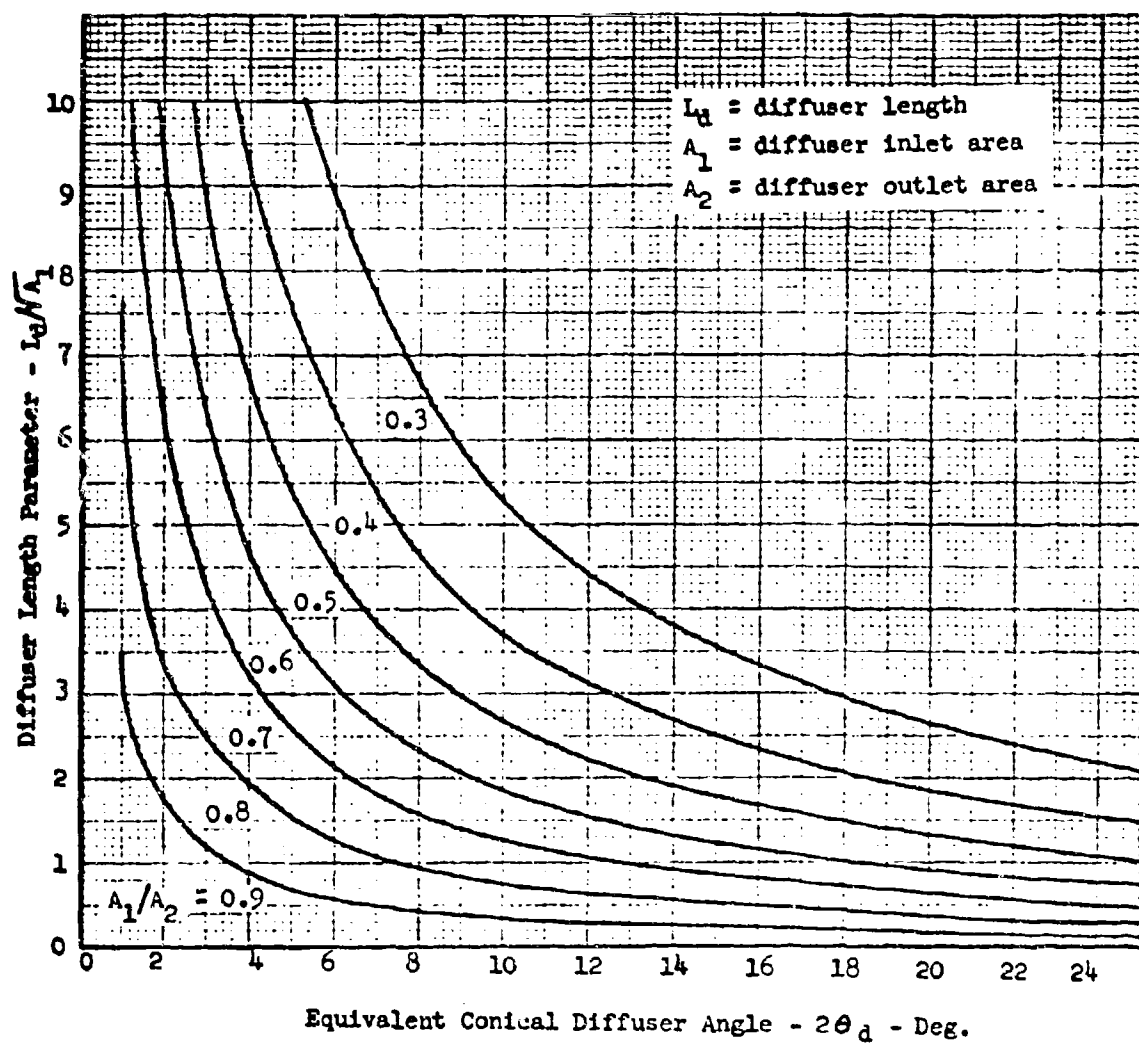


FIGURE 2-27. Effect of Diffuser Divergence Angle on Length



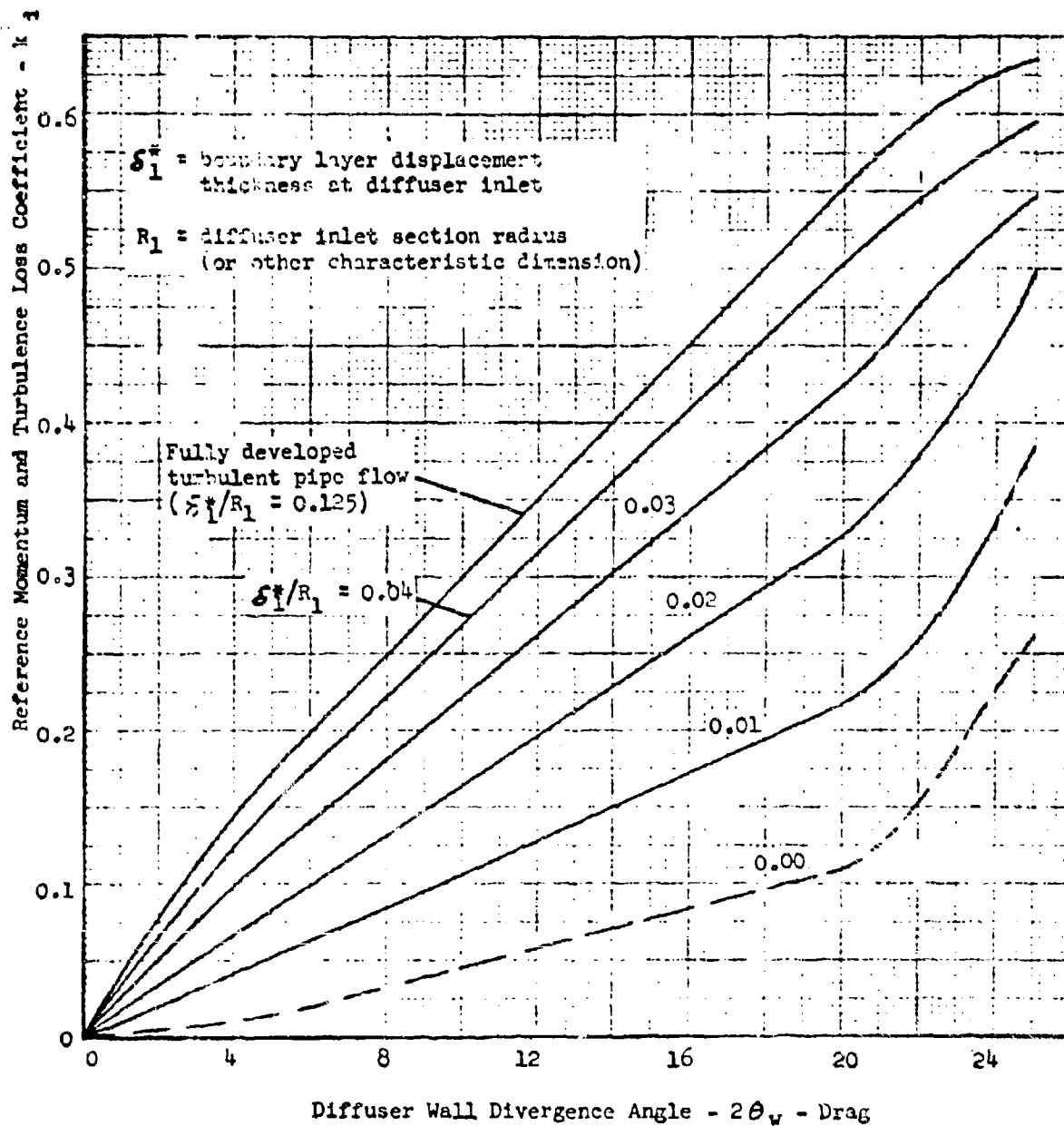


FIGURE 2-28. Diffuser Momentum and Turbulence Loss Criteria (Reference 16)

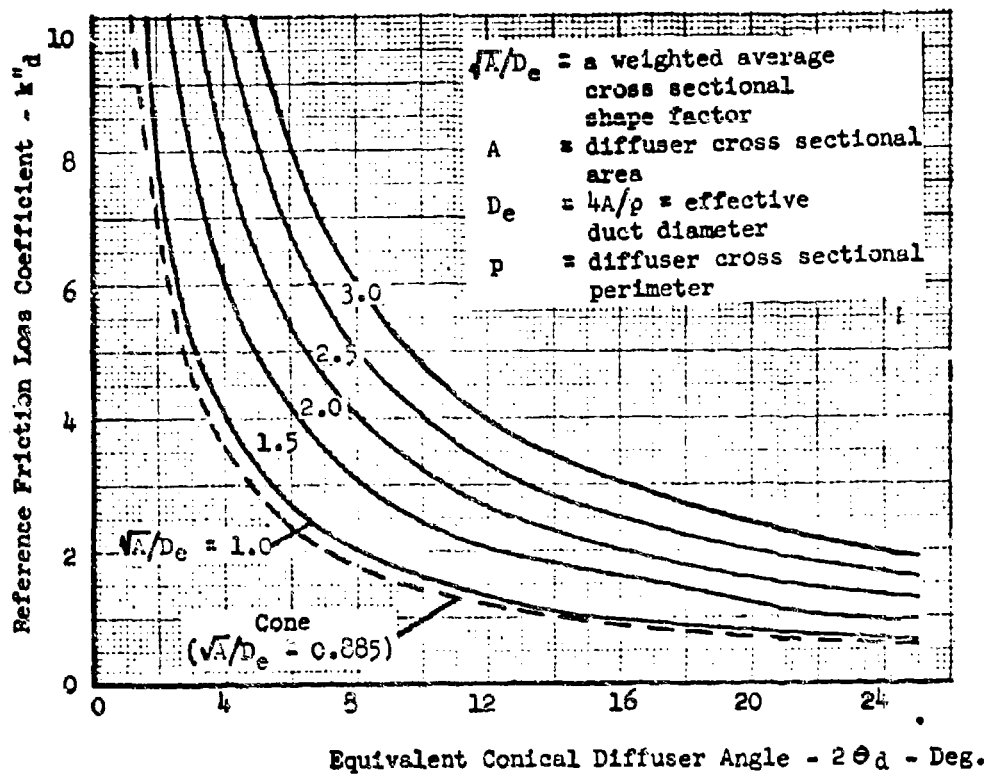


FIGURE 2-29. Diffuser Friction Loss Criteria

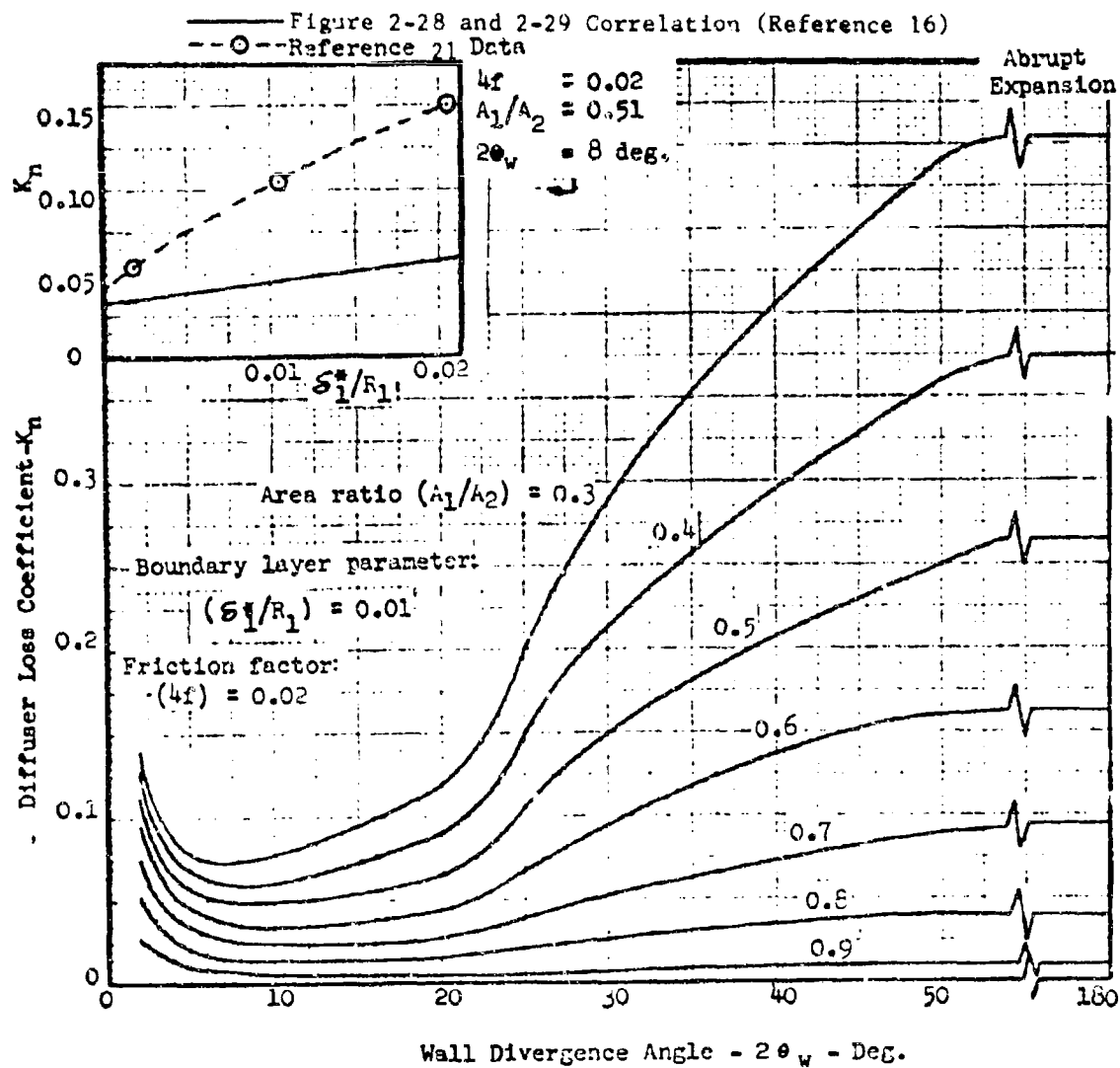


FIGURE 2-30. Typical Conical Diffuser Losses

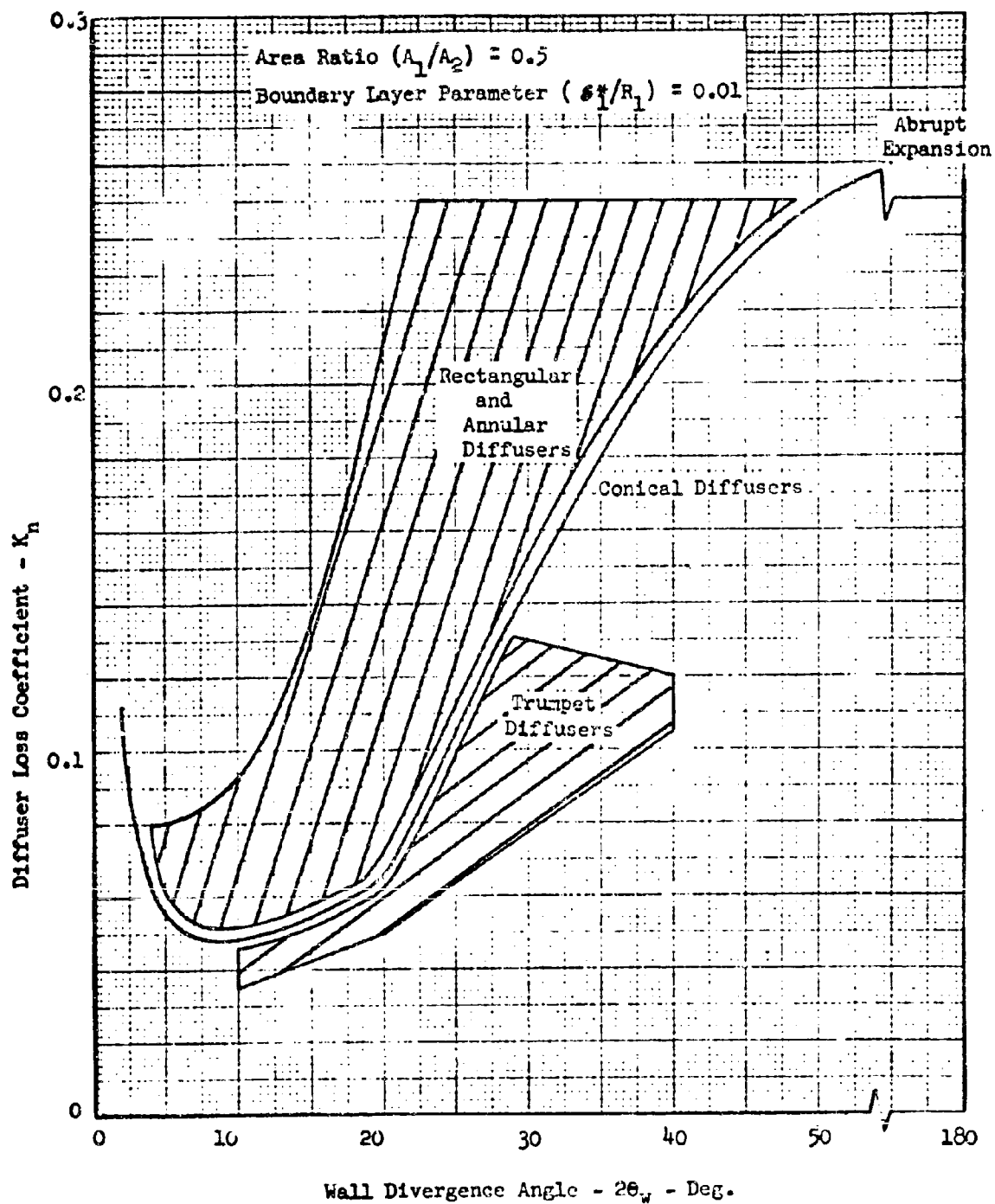
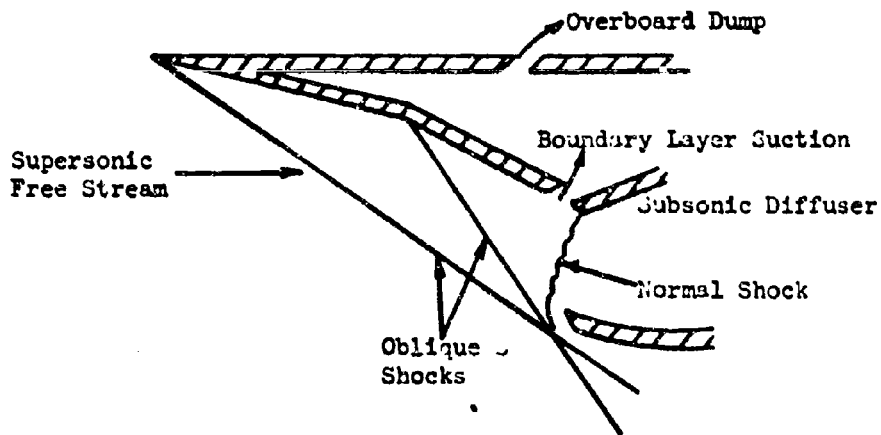
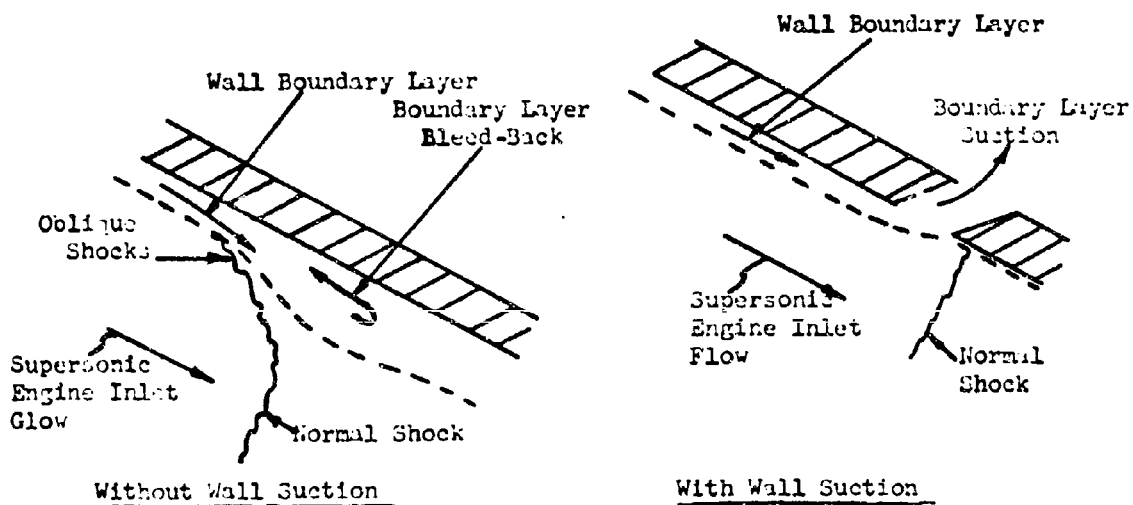


FIGURE 2-31. Typical Losses for Various Types of Diffusers  
(Reference 16)



Typical Suction Boundary Layer Control System



Typical Interactions of Shocks and Boundary Layers

FIGURE 2-32. Typical Supersonic Shock Compression Boundary Layer Control.

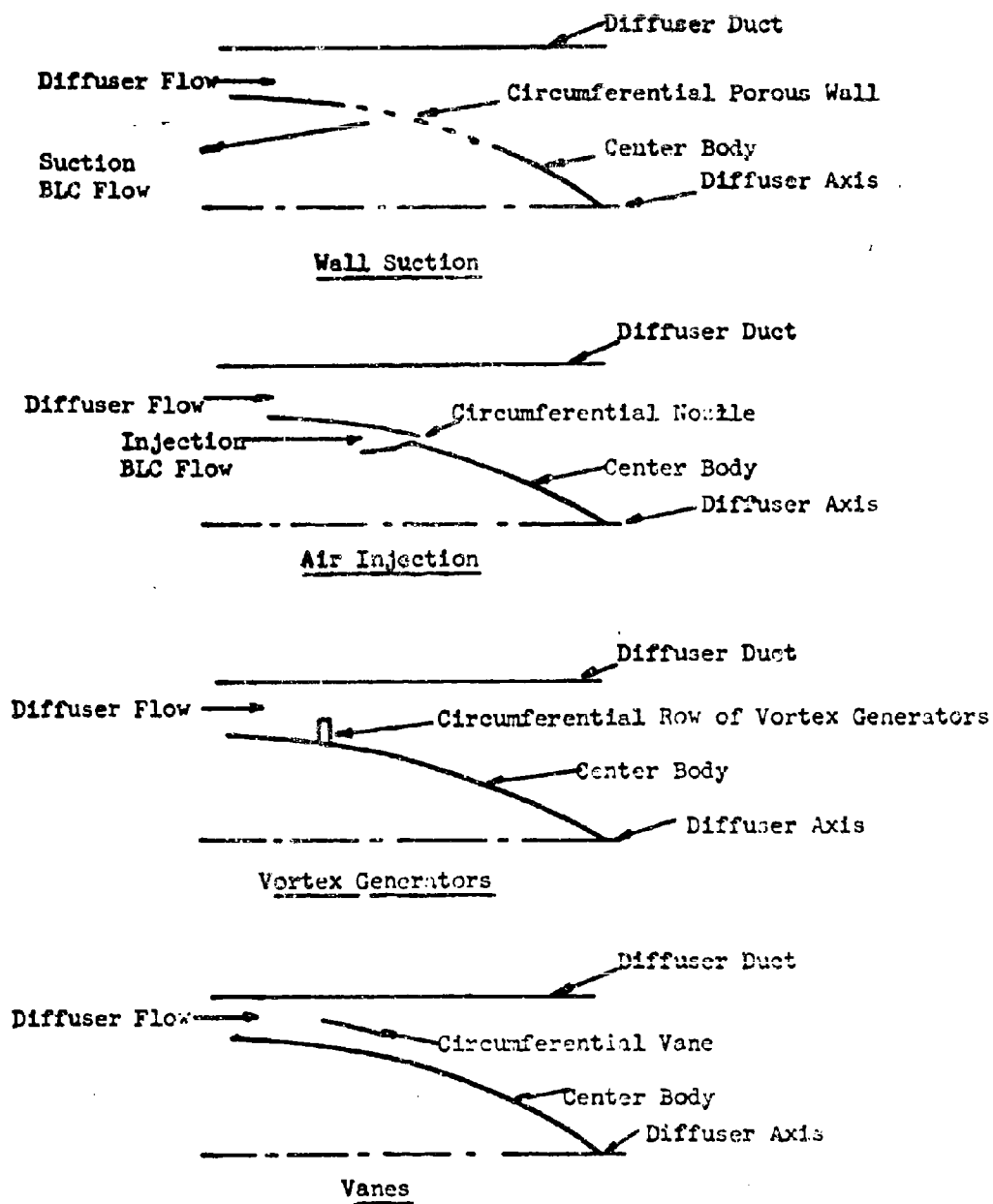


FIGURE 2-33. Typical Boundary Layer Control Provisions for Annular Subsonic Diffusers.

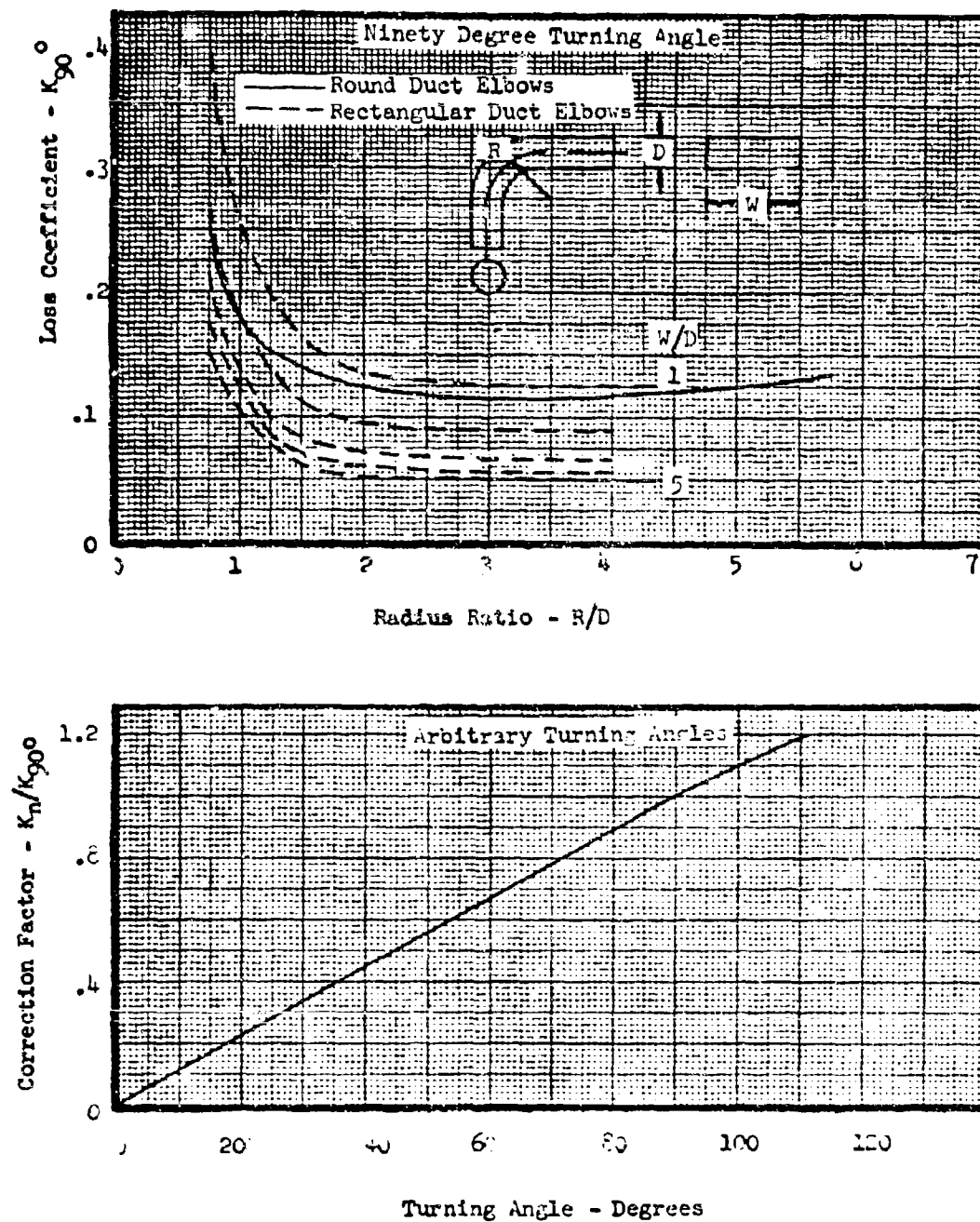


FIGURE 2-34. Elbow Pressure Losses (Reference 14)

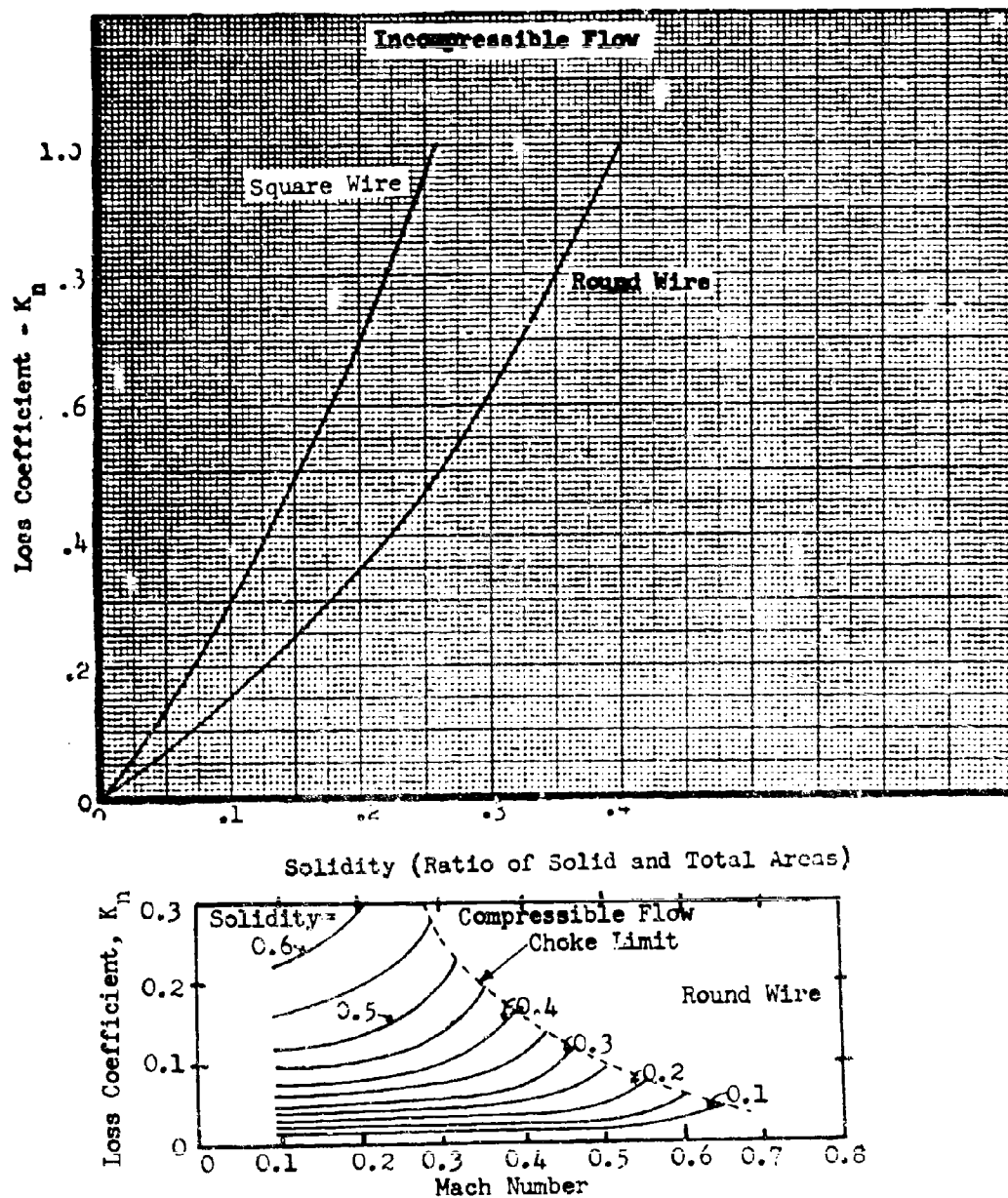
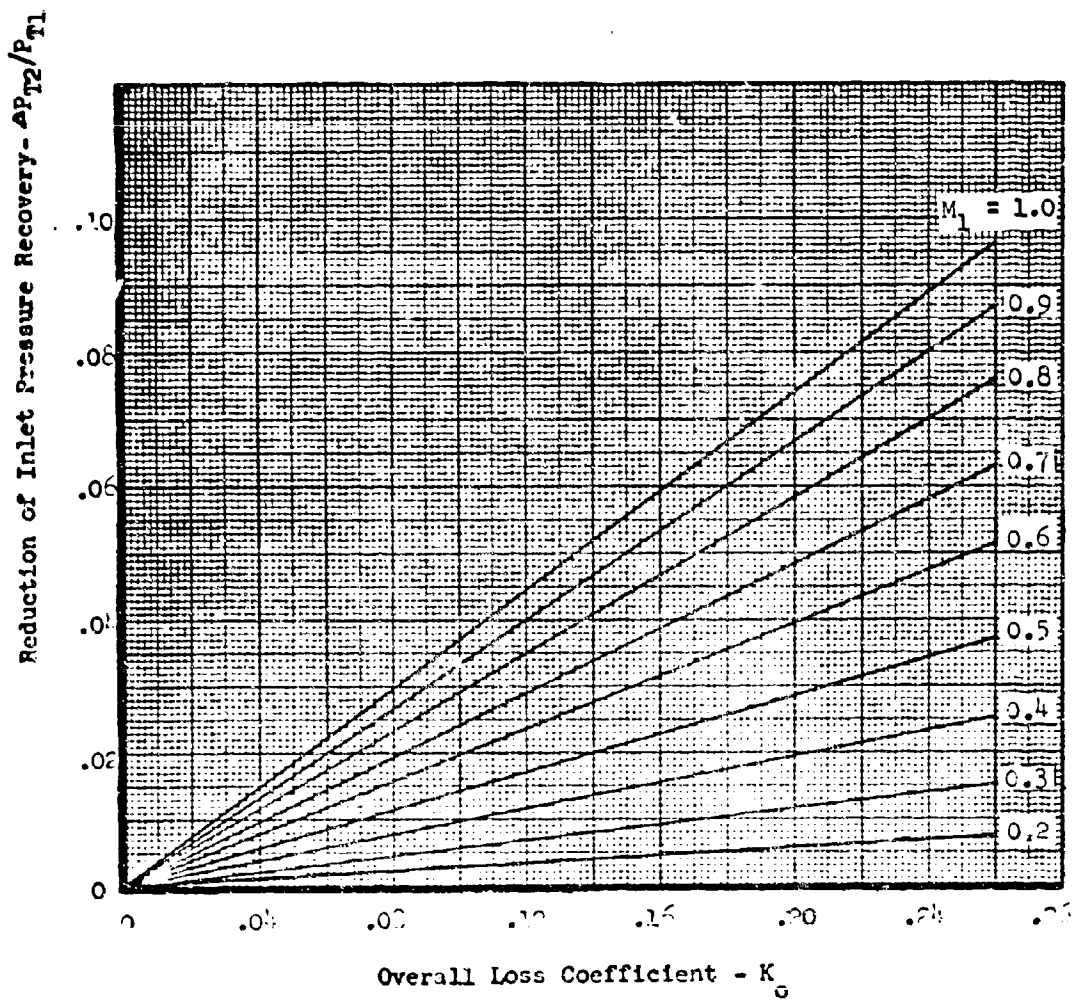


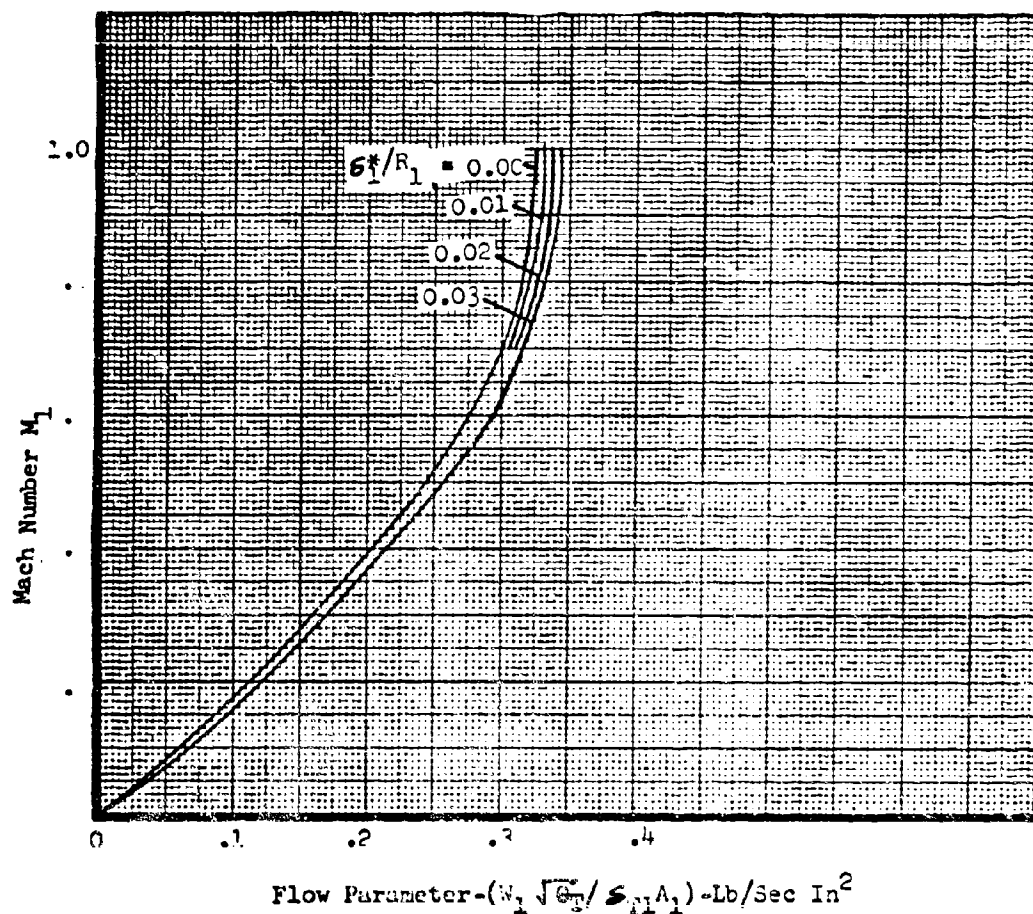
FIGURE 2-35. Screen Pressure Losses (Reference 23 and 24)





NOTE: See Figure 2-37 for inlet flow Mach number parameters.

FIGURE 2-36. Effect of Subsonic Losses on Inlet Pressure Recovery.



- $W_1$  = Air Flow, Lb/Sec  
 $A_1$  = Cross Sectional Area,  $\text{In}^2$   
 $\theta_T$  =  $T_T/519$   
 $T_T$  = Total Temperature,  $^{\circ}\text{R}$   
 $s_1$  =  $P_{T1}/14.7$   
 $P_{T1}$  = Total Pressure, PSIA  
 $\delta_1^*$  = Boundary Layer Displacement Thickness  
 $R_1$  = Inlet Radius (or other dimension)

FIGURE 2-37. Inlet Flow Mach Number Parameters

```

*18FTC RFI193
SUBROUTINE S1193(XM1,XM2,XMOXMS,PT2PT1,A1GA2,COA,XK,PT3PT1)
C
C THEORETICAL PERFORMANCE CHARACTERISTICS OF SHARP-LIP INLETS AT
C SURSONIC SPEEDS ** REFERENCE NACA REPORT 1193 ** DATED 1954
C HY E. A. FRADENBURGH AND D. D. WYATT
C
C FDFM DECK A1157
C
C PROGRAMMER ** R.W. WIRFS , OCTOBER, 1969
C
C PSOPT(A)=(1.0+0.2*A**2)**(-3.5)
C ADAT(A)=(1.0+0.2*A**2)**(-0.5)
C
C PT2PT1=PSOPT(XM1)/(PSOPT(XM2)*(1.4*XM2**2+1.0-1.4*XM1**2*((XM2*ADAT
2 T(XM1))/(XM1*ADAT(XM2))))
C IF(XM1 .GE. XM2) PT2PT1=1.0
C XMOXMS=1.72795*PT2PT1*PSOPT(XM2)*XM2/ADAT(XM2)
C IF(XM1 .FO. 0.0) GO TO 10
C A1GA2=0.578792*XMOXMS/(PSOPT(XM1)*XM1/ADAT(XM1))
C GO TO 15
10 A1GA2=0.0
15 IF(A1GA2 .LE. 1.0) GO TO 20
C COA=0.0
C RETURN
20 PS2PS1=PSOPT(XM2)/PSOPT(XM1)*PT2PT1
C COA=2.0/(1.4*XM1**2)*(1.4*XM2**2*PS2PS1+PS2PS1-1.0)-2.0*A1GA2
C DELPT=0.7*XK*PSOPT(XM2)*XM2**2
C PT3PT1=PT2PT1*(1.0-DELPT)
C RETURN
C END
A15700C0
A15700C5
A1570010
A1570015
A1570020
A1570025
A1570030
A1570035
A1570040
A1570045
A1570050
A1570055
A1570060
A1570065
A1570070
A1570075
A1570080
A1570085
A1570090
A1570095
A1570100
A1570105
A1570110
A1570115
A1570120
A1570125
A1570130
A1570135
A1570140
A1570145
A1570150
A1570155
A1570160

```

FIGURE 2-38 Subroutine Program for Calculation of Sharp Lip Losses

### 3.0 Boundary Layer Considerations

When the air induction system entrance is placed aft on the body or other aircraft component, boundary layer, unless completely removed, is part of the inlet's operating environment. The several items that have to be taken into consideration are:

1. The boundary layer thickness
2. The nature of the boundary layer profile
3. The amount of boundary layer that should be removed
4. The effectiveness of the boundary layer removal device
5. The energy level of the boundary layer flow if it is to be taken aboard
6. The drag incurred by the boundary layer removal device

Another serious consideration with regard to boundary layer control is the removal of compression surface boundary layer on supersonic inlets. This is done to alleviate shock-boundary layer interaction problems. The consequences of shock-boundary layer interaction can be in the form of increased losses, increased distortion at the duct exit, and/or increased turbulence.

#### 3.1 Boundary Layer Thickness

The majority of calculations that are made to determine fuselage boundary layer thickness are made using the familiar expression for the thickness of a turbulent boundary layer on a smooth flat plate at zero incidence. The expression, taken from Reference 1 is:

$$\delta/l = 0.37 R_l^{-0.2} \quad (3.1)$$

where  $\delta/l$  is the total thickness ratioed to the length back to the inlet station and  $R_l$  is the Reynolds number. The expression has both conservative and optimistic aspects. It is conservative in that it assumes transition to turbulent flow at the plate leading edge; the optimism lies in the fact that the plate is assumed smooth, flat, and at zero incidence. Some have suggested making a more precise calculation by considering an initial laminar boundary layer and then calculating the growth of the turbulent boundary layer from the point of transition. This is not considered advisable because a typical aircraft configuration does not fit the ideal picture on which the theoretical calculation would be based. Therefore, the use of Equation (3.1) is advised for purposes of calculating the theoretical value of boundary layer thickness. Values of Reynolds number are plotted as a function of Standard Day Mach number and altitude on Figure 3-1 to facilitate the calculation.

The theoretical trend, which shows decreasing boundary layer thickness with increasing flight Mach number at a given altitude, is not always borne out by in-flight measurement. Figures 3-2, 3-3, and 3-4 present data measured in flight test at various locations on a supersonic aircraft. The very exaggerated thickness that was observed at high Mach numbers at the Fuselage Station 274 measurement, which was near the inlet leading edge station, is believed to be due to influence from the boundary layer diverter downstream of the measuring station. Elevated pressures in the diverter were felt as an adverse pressure gradient in the boundary layer. This points up the advisability of obtaining a measured value of boundary layer thickness early in the development program of an air induction system.

### 3.2 Boundary Layer Profiles

In making analyses of boundary layers, it is sometimes necessary to know the shape of the velocity profile. The general theoretical expression for the shape of a turbulent boundary layer is

$$u/U_{\infty} = (y/\delta)^{1/N} \quad (3.2)$$

Where  $u$  is the local velocity,  $U_{\infty}$  is the freestream velocity,  $y$  is the distance from the wall corresponding to the velocity,  $u$  and  $\delta$  is the distance from the wall where the local velocity first becomes equal to freestream velocity.  $N$  is the profile shape factor and the most commonly assumed value is 7. However, the value can range from about 5 to 11. Another meaningful boundary layer definition is displacement thickness,  $\delta^*$ , which is defined as the distance from the wall that the potential flow is displaced by the velocity deficiency in the boundary layer. For a boundary layer profile with a shape conforming to Equation (3.2), the displacement thickness is defined by

$$\delta^*/\delta = 1/\left[1 + N\right] \quad (3.3)$$

The loss in momentum in the boundary layer can also be expressed by an equivalent thickness called the momentum thickness, the expression for which is

$$\theta/\delta = 1/\left[1 + N\right](2 + N) \quad (3.4)$$

Reference 2 gives a method for the theoretical evaluation of the loss in mass and momentum for an inlet partially or totally immersed in a turbulent boundary layer with a profile conforming to Equation (3.2). Included in this methodology is a method for estimating total pressure recovery. The method was programmed for making the calculations on an Electronic Data Processing Machine (EDPM) and results for a range of Mach numbers and dimensions are shown in Figures 3-5 through 3-16. With these results, one can assess the value of boundary layer removal.

### 3.3 Fuselage Boundary Layer Removal

Fuselage boundary layer removal devices are usually sized to remove from a half to all of the boundary layer thickness. The most common method of removal is by diversion with a wedge shaped device located between the fuselage surface and the inlet. Figures 3-17 and 3-18 show typical boundary layer diverter configurations for horizontal and vertical compression inlets respectively. Note in the front views that the channels are designed to diverge. This is to allow some pressure relief to the flow, preventing a buildup in pressure which could feed forward through the boundary layer and reduce the effectiveness of the diverter. Figures 3-19, 3-20 and 3-21 show boundary layer diverter static pressure data taken during model tests of a supersonic aircraft. Also shown on the figures is some data from full scale flight tests. The disagreement between the two sets of data, particularly at the highest test Mach number, is indicative of how drastic Reynolds number effects can be. Also sufficient methodology is not available for accurately predicting the drag contribution of full scale boundary layer diverters, particularly when scale effects have shown such a lack of predictability.

In addition to diversion of the boundary layer, the method of taking the air aboard via a scoop is also sometimes used. When this method is used, the problem of apparent boundary layer thickening can also take place as in the case of the diverter. If the exit path is such as to make the scoop operate subcritically, the result will be the apparent thickening of the boundary layer and impairment of the effectiveness of the removal device. Predicting the drag of a fuselage boundary layer scoop is more of an internal flow problem than in the case of the wedge diverter. The method of Section 3.2 could be used to predict the initial conditions where the flow is taken on board. Then Section 2.6 can be utilized for estimation of the internal ducting losses. If other resistances are in the system, such as heat exchangers, etc., they must also be taken into account. Finally the exiting momentum can be arrived at with the help of Section 7.0 if an oblique nozzle is used or Section 8.0 if a more conventional nozzle type is used.

### 3.4 Compression Surface Boundary Layer Removal

The removal of boundary layer from the compression surfaces of a supersonic inlet improve the performance and stability of the inlet. The most effective bleed location/locations are in the interaction region of the terminal shock. This is being stated in this way because, experimentally effective locations have been found which range from in front of to behind the terminal shock location.

The design of a compression surface bleed system with regard to exact location and quantity usually has to be aided by experimental development. Several candidate locations are selected for trial on the first wind tunnel model to be tested. These are controlled during the test by some variable throttling device to determine the effect of quantity on effectiveness. Sometimes certain bleed locations are sealed off to determine if the location is essential to performance and/or stable operation of the inlet. In subsequent tests at larger scale, the bleed configuration that proved to be the most satisfactory at small scale is usually used. However, the effect of quantity is reassessed because of possible scale effects.

Some typical bleed system configurations are depicted for two-dimensional external compression inlets on Figure 3-22. As is seen on the figure, it has been the practice to use both distributed porosity and slots.

In order to give an idea of bleed quantity requirements, some unpublished wind tunnel data is plotted on Figure 3-23. A summary plot of the same data for the points nearest the knee of the pressure recovery versus mass flow ratio curves is presented as Figure 3-24. It is to be noted that the greatest performance gain came with a small bleed quantity.

In general, bleed quantity is determined at the highest Mach number at which steady state operation of the aircraft is expected. The bleed system is usually of fixed geometry and the bleed quantity decreases with decreasing Mach number because of decreasing ram pressure ratio. Figure 3-25 is a comparison of bleed quantity at two test Mach numbers, where for the higher Mach number, some data shown on Figure 3-23 is repeated.

Bleed quantity requirements generally increase with increases in design Mach number so that preliminary estimates of quantity requirement for a higher design Mach number can be made by extrapolating existing experience curves.

#### References

1. Schlichting, Herman, Boundary Layer Theory, McGraw-Hill Book Company, 1955
2. Simon, P. C. and Kowalski, K. L., Charts of Boundary-Layer Mass Flow and Momentum for Inlet Performance Analysis, NACA TN 3583, November 1955



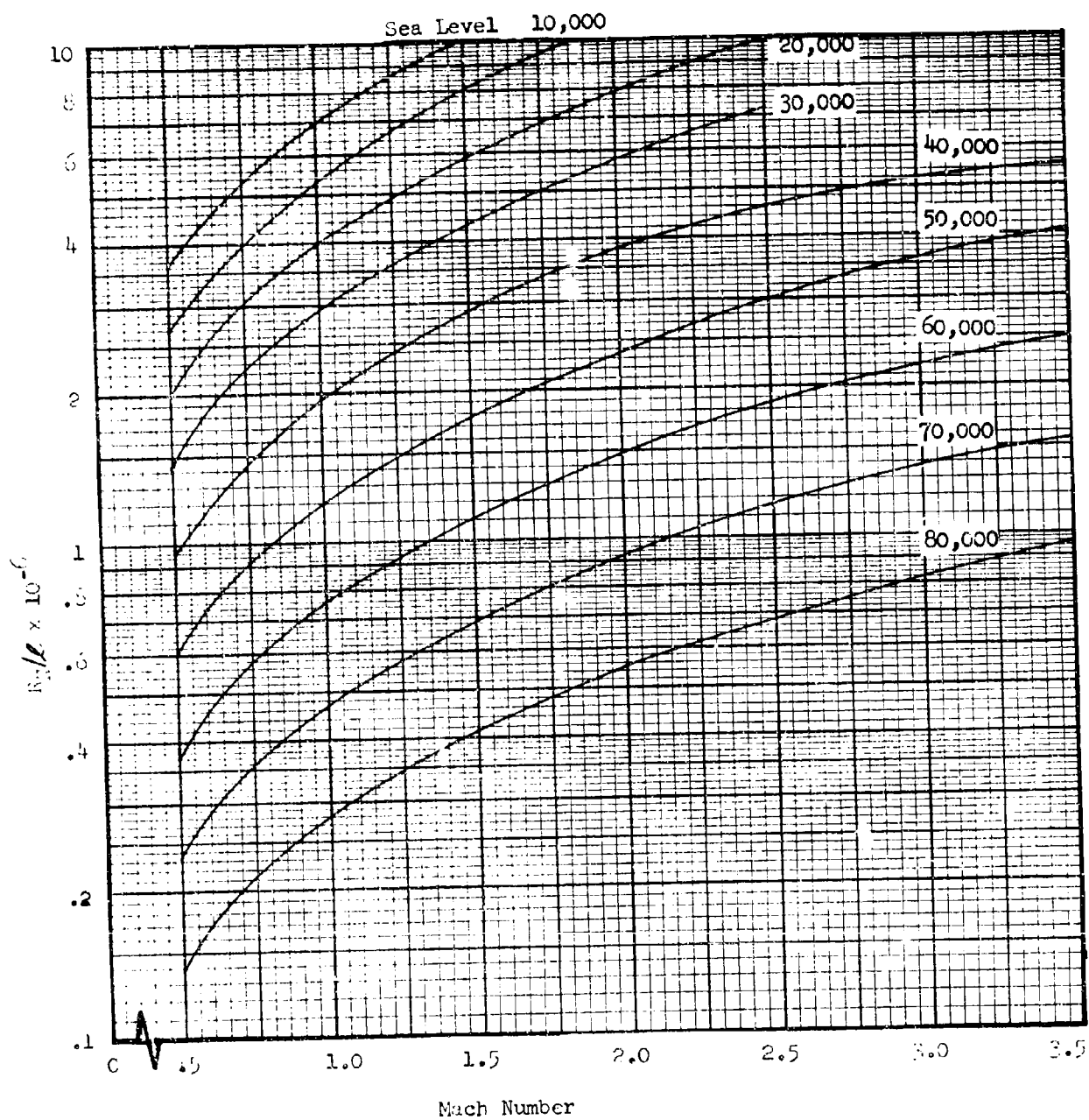


Figure 3 - 1. Variation of Reynolds Number with Mach Number at Various Altitudes, Standard Atmosphere.

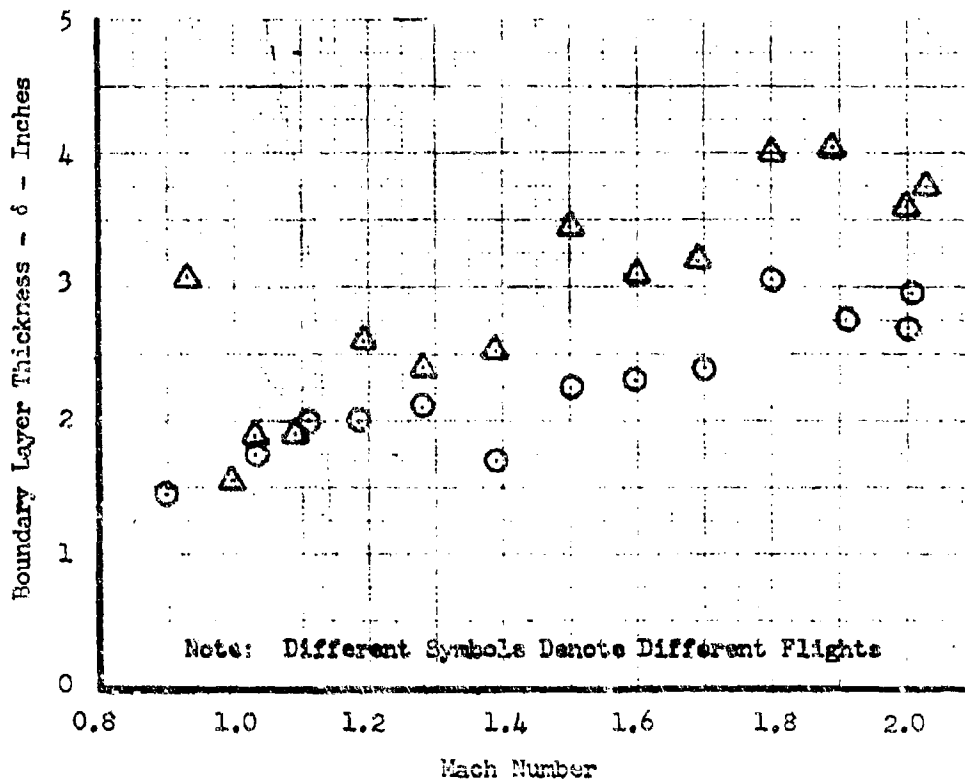


FIGURE 3-2. Boundary Layer Thickness Data  
Fuselage Station 221  
Lower Surface  
Altitude = 40,000 Feet

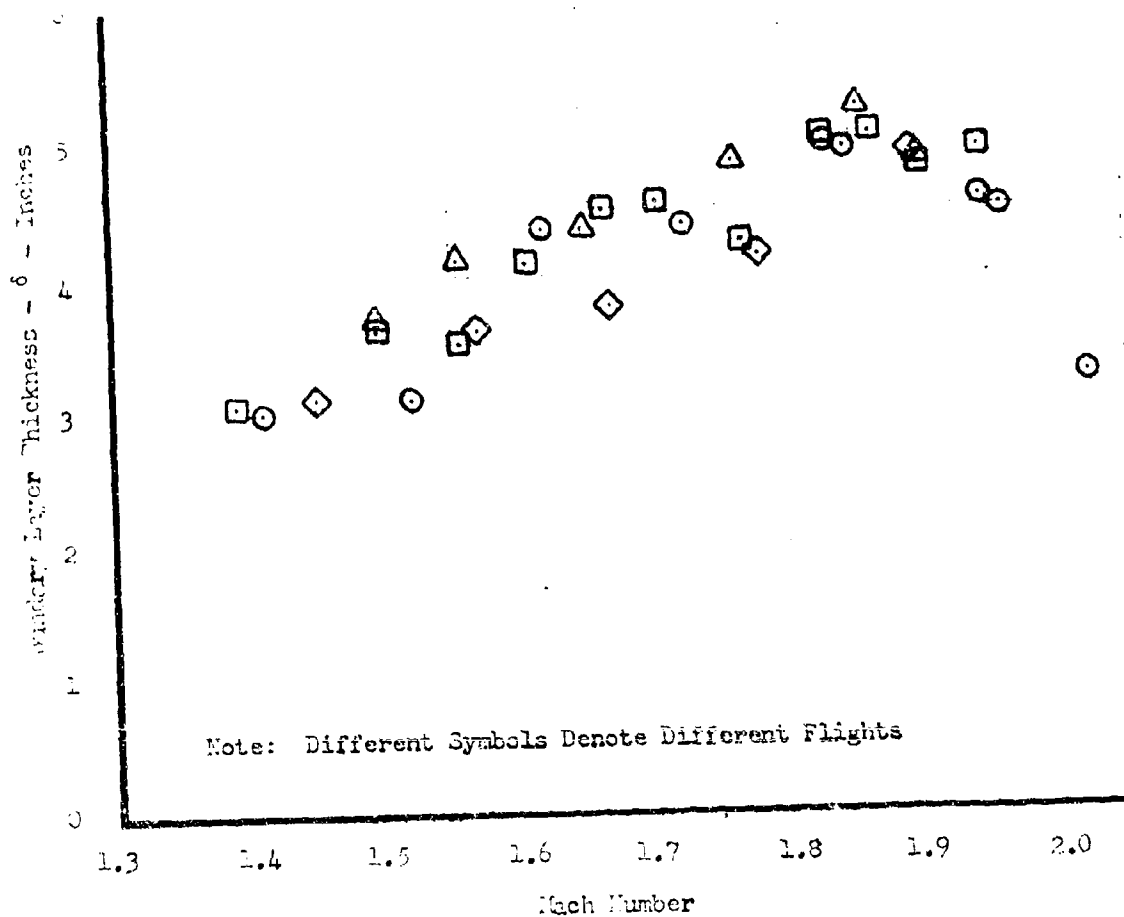


FIGURE 3-3. Boundary Layer Thickness Data  
Fuselage Station 274  
Altitude 40,000 Ft.

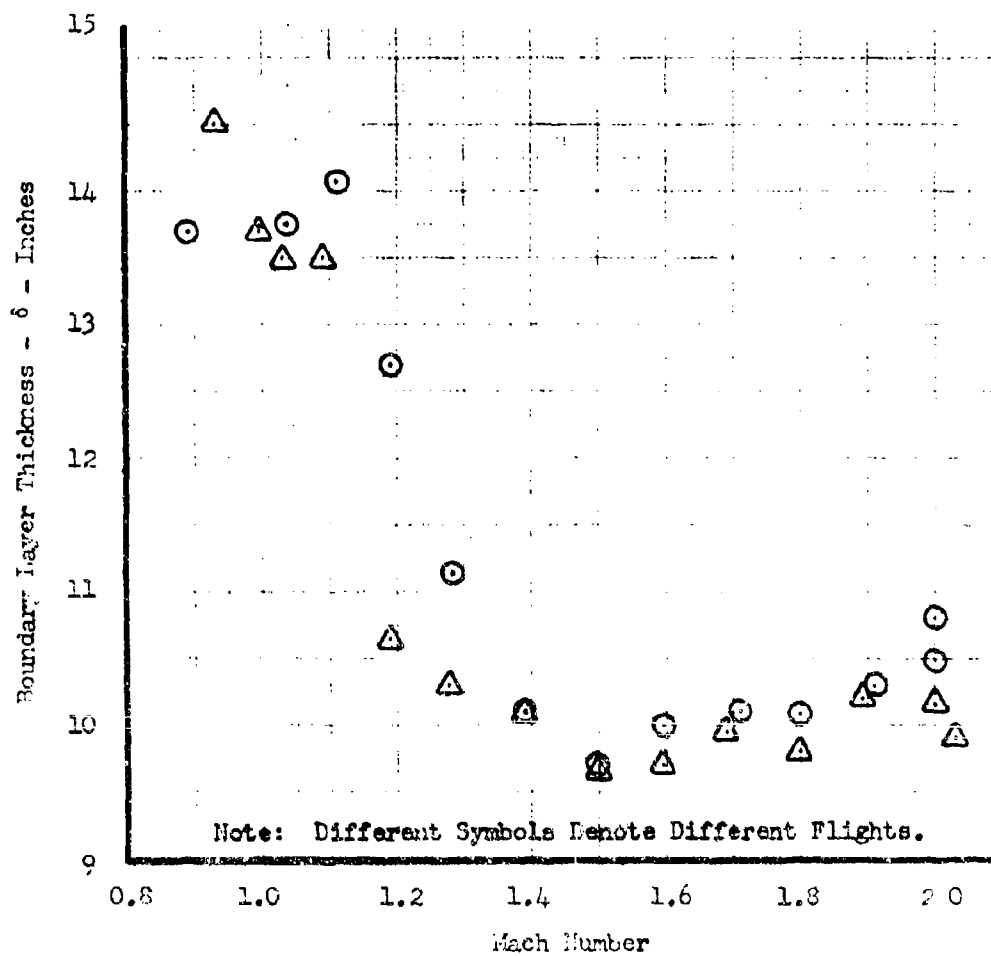


FIGURE 3-4. Boundary Layer Thickness Data  
Fuselage Station 528  
Altitude 40,000 Ft.

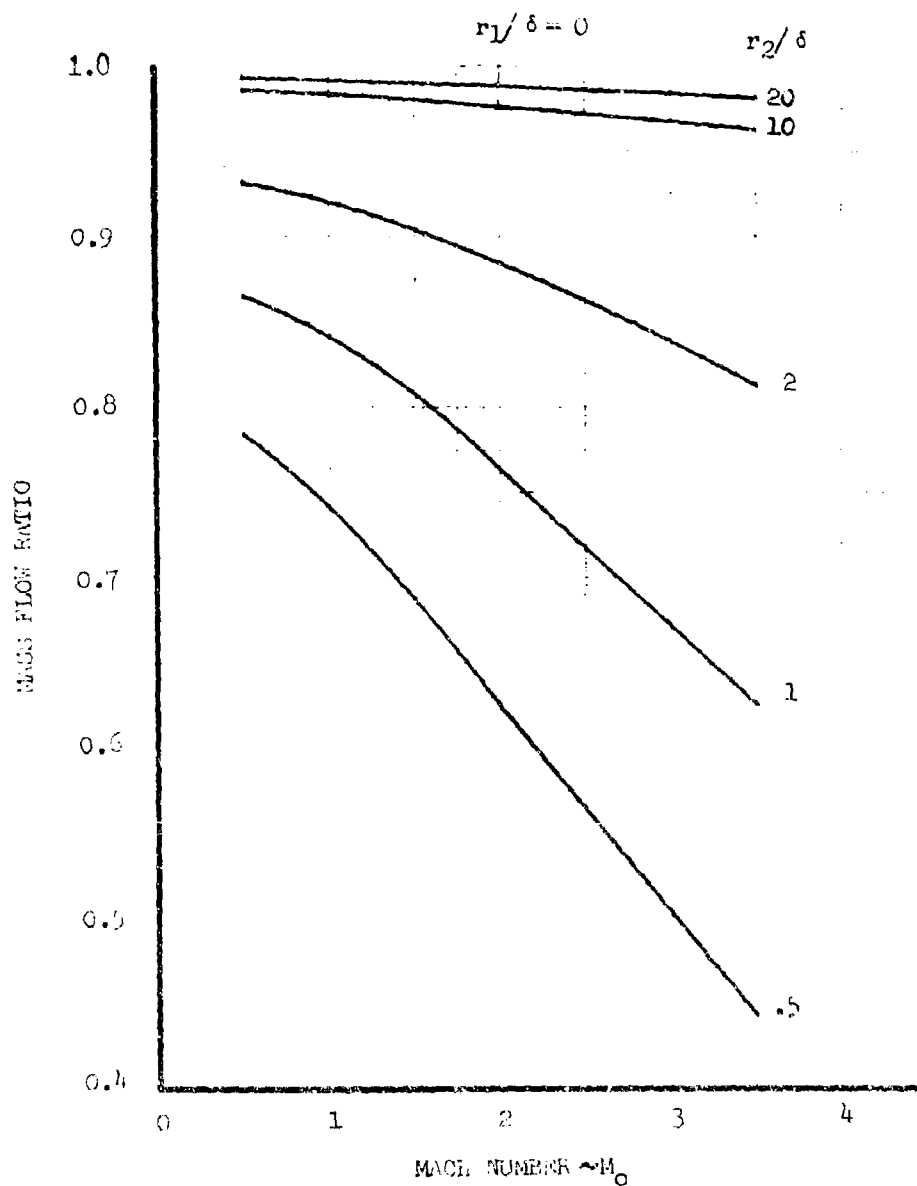
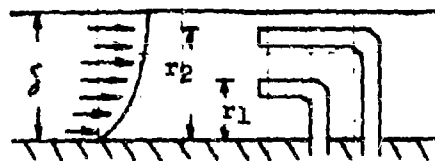


FIGURE 3-5. THEORETICAL PERFORMANCE OF INLETS IN THE PRESENCE OF A BOUNDARY LAYER WITHOUT PRECOMPRESSION

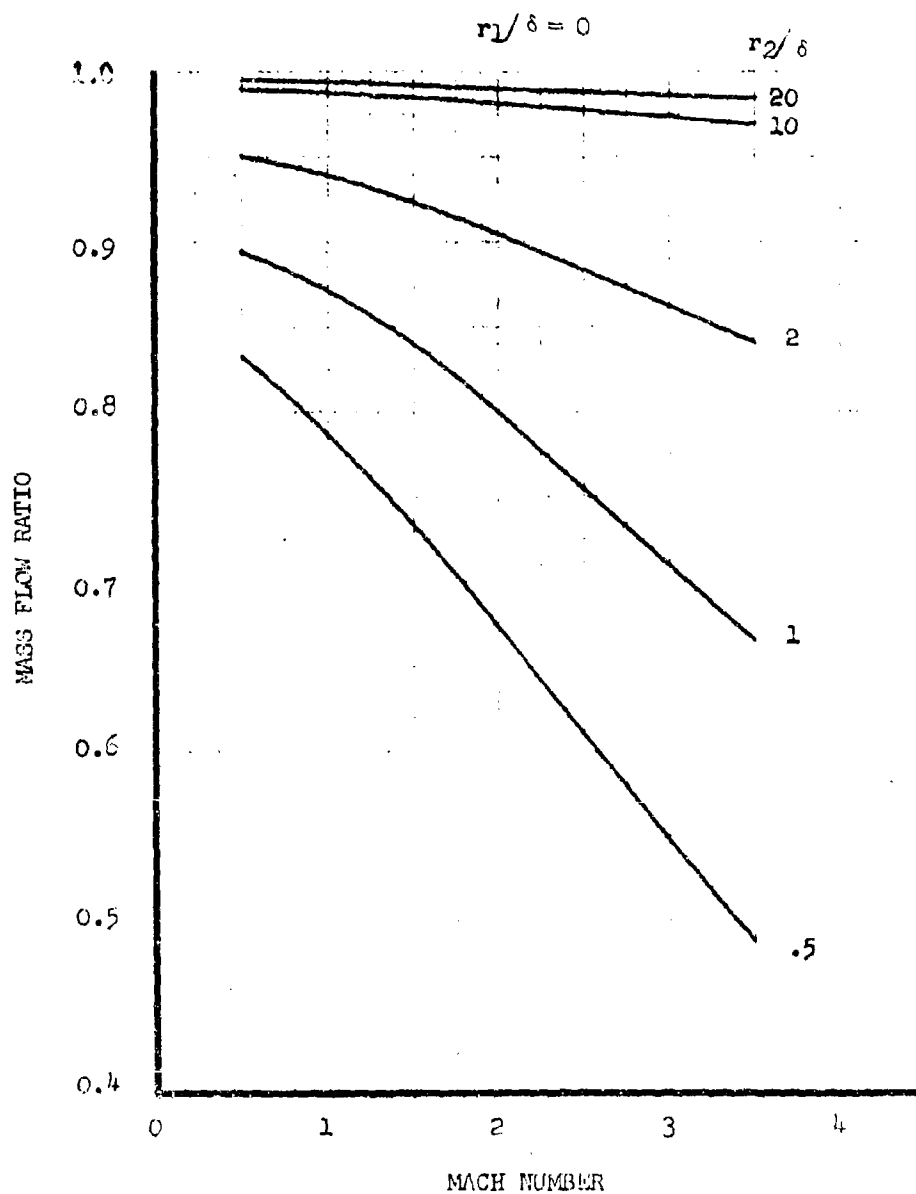
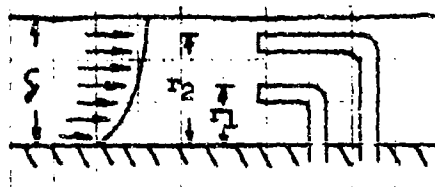


FIGURE 3-6. THEORETICAL PERFORMANCE OF INLETS IN THE PRESENCE OF A BOUNDARY LAYER WITHOUT COMPRESSION

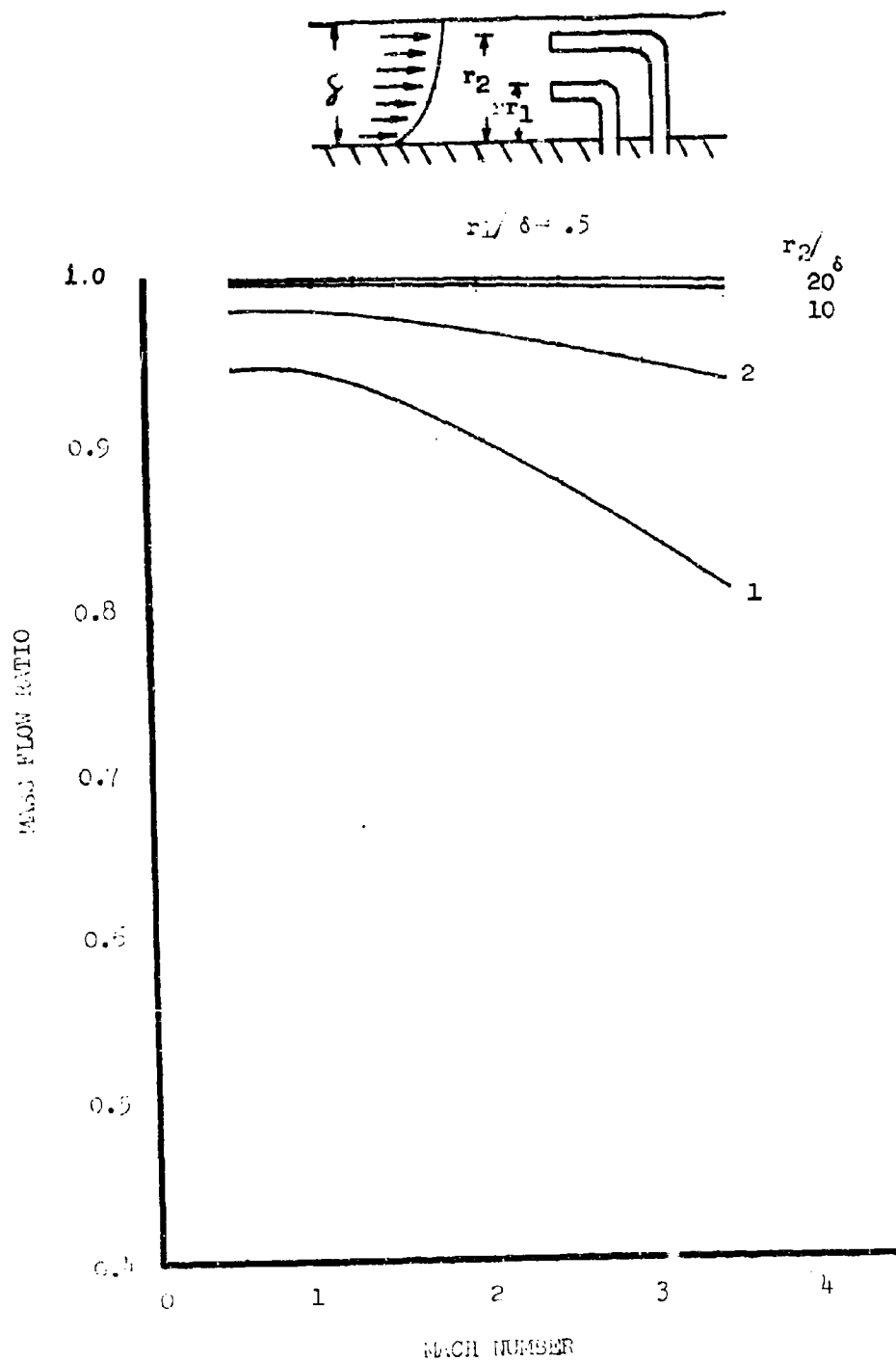


FIGURE 3-7. THEORETICAL PERFORMANCE OF INLETS IN THE PRESENCE OF A BOUNDARY LAYER WITHOUT COMPRESSION

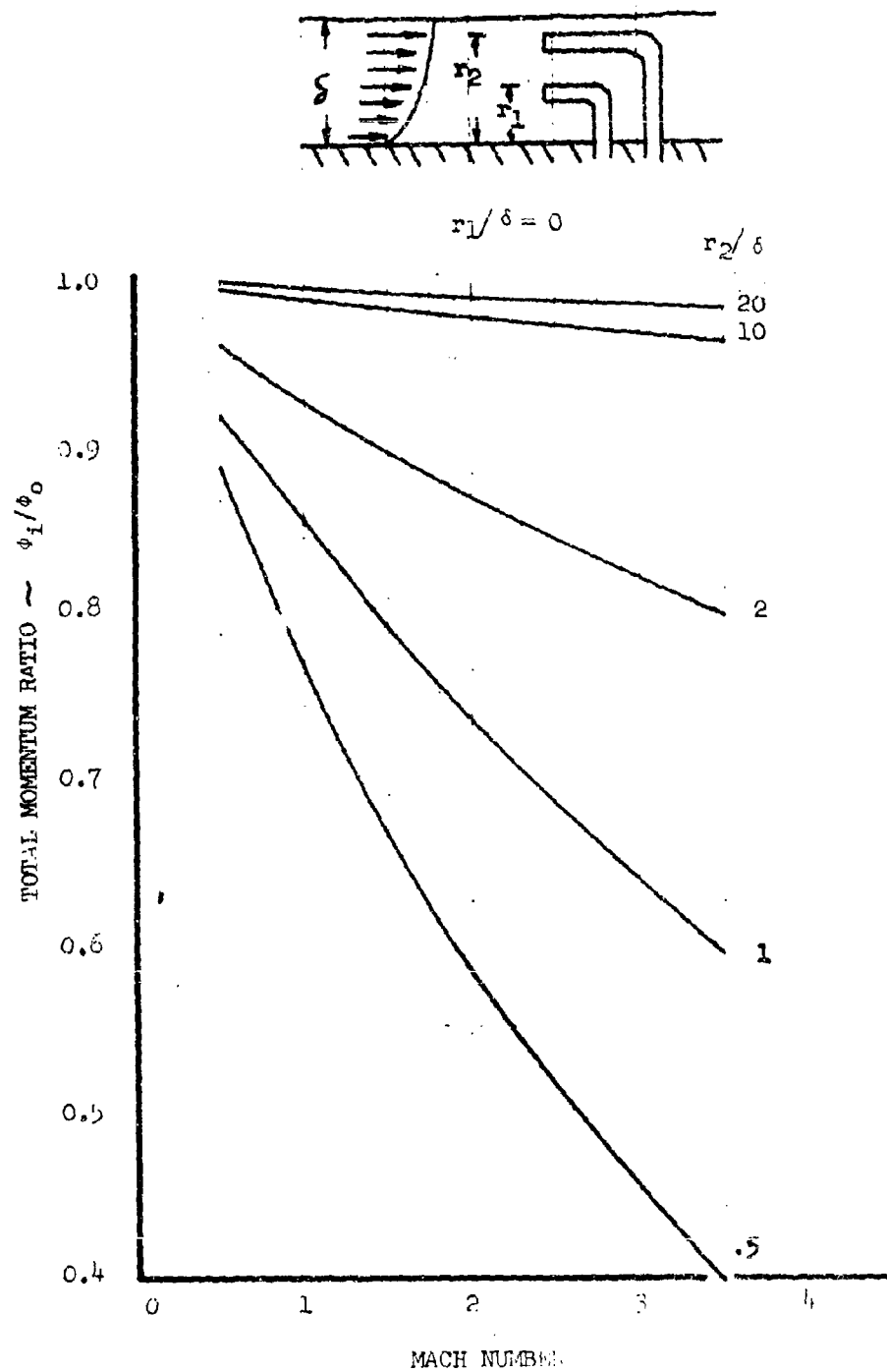
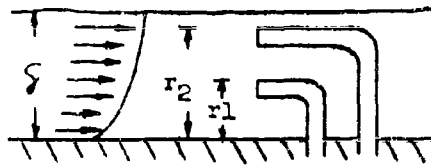


FIGURE 3-8. THEORETICAL PERFORMANCE OF INLET IN THE PRESENCE OF A BOUNDARY LAYER WITHOUT COMPRESSION





$$r_1/\delta = .1$$

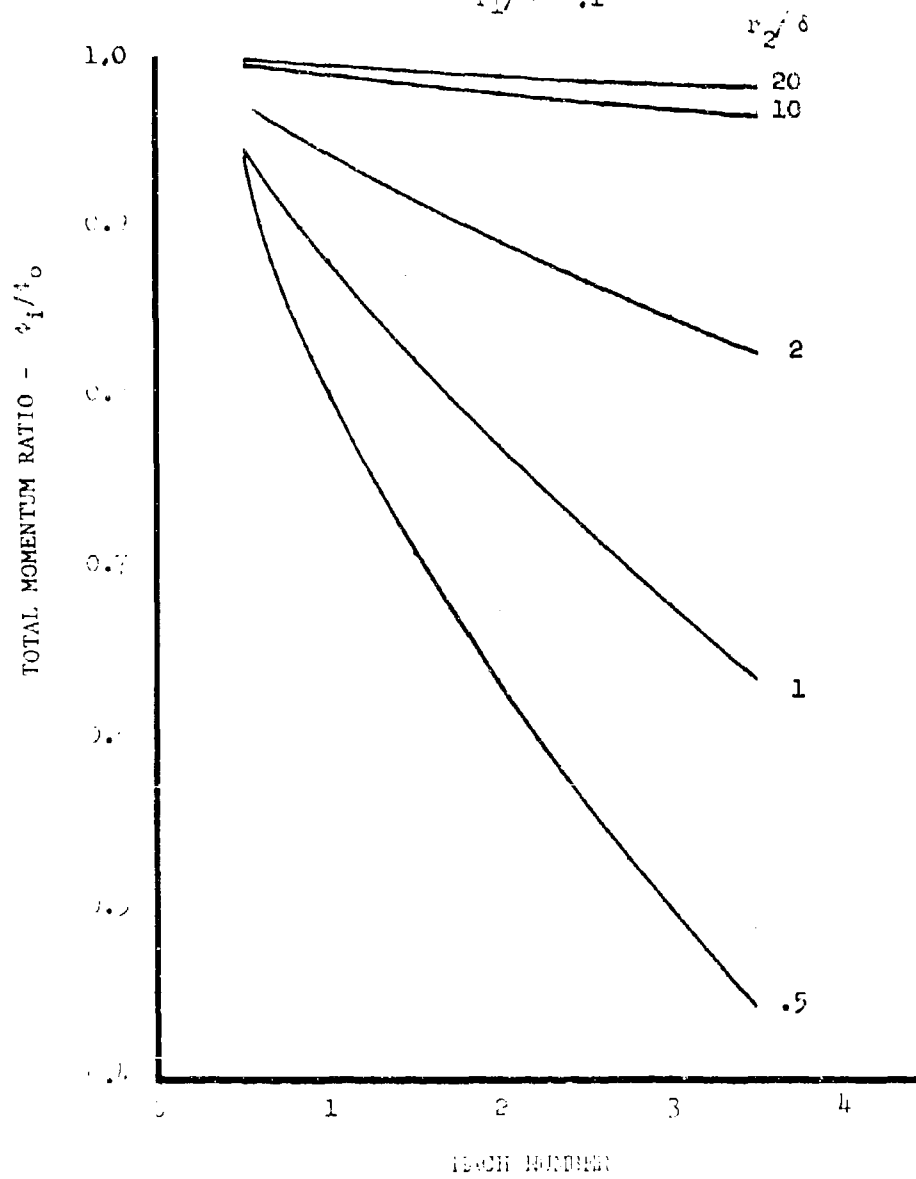


FIG. 3-4. MOMENTUM RATIO OF INLET IN THE PRESENCE OF A BOUNDARY LAYER WITHOUT PARALLEL FLOW

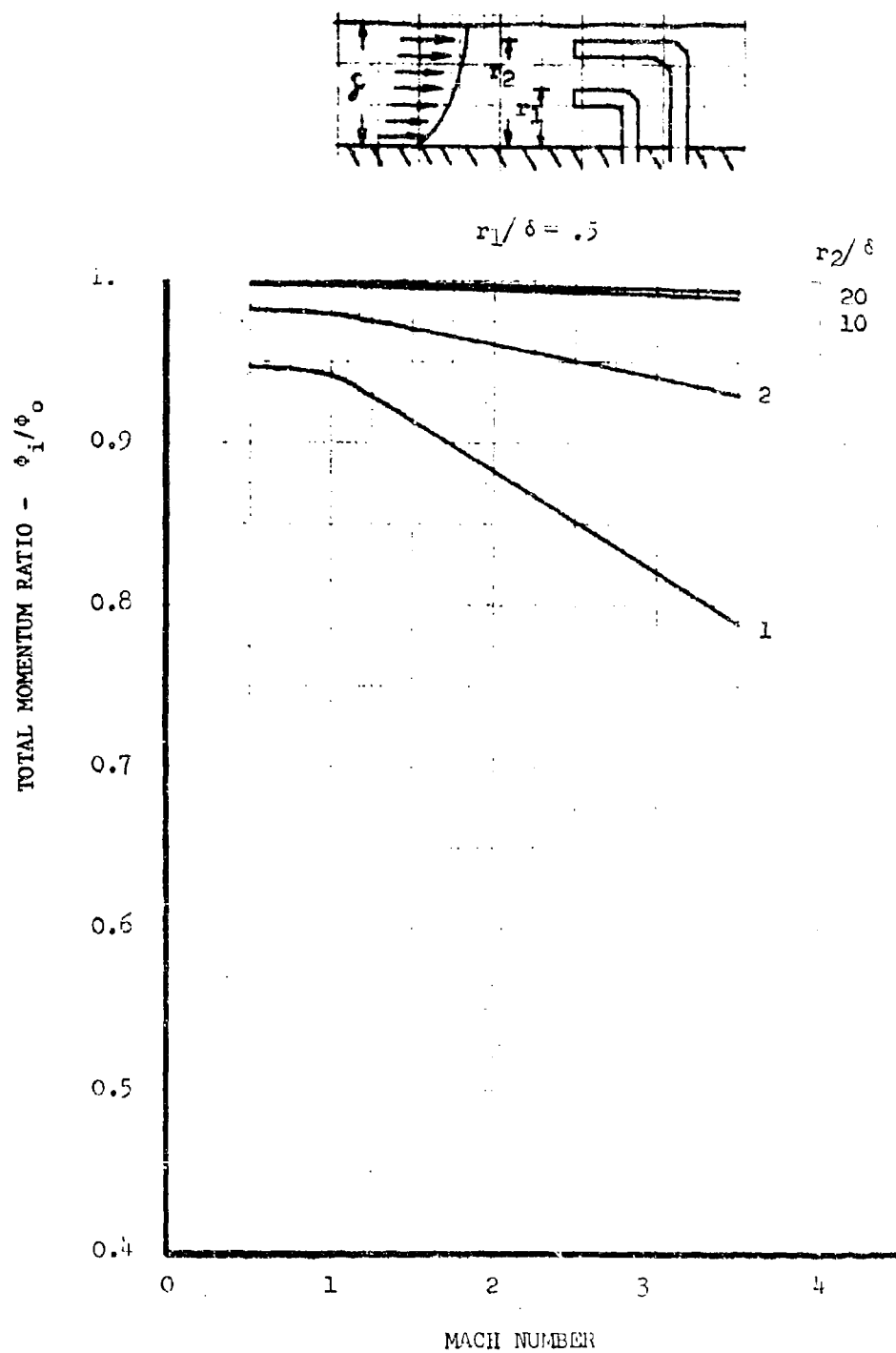


FIGURE 3-10. THEORETICAL PERFORMANCE OF INLETS IN THE PRESENCE OF A BOUNDARY LAYER WITHOUT COMPRESSION

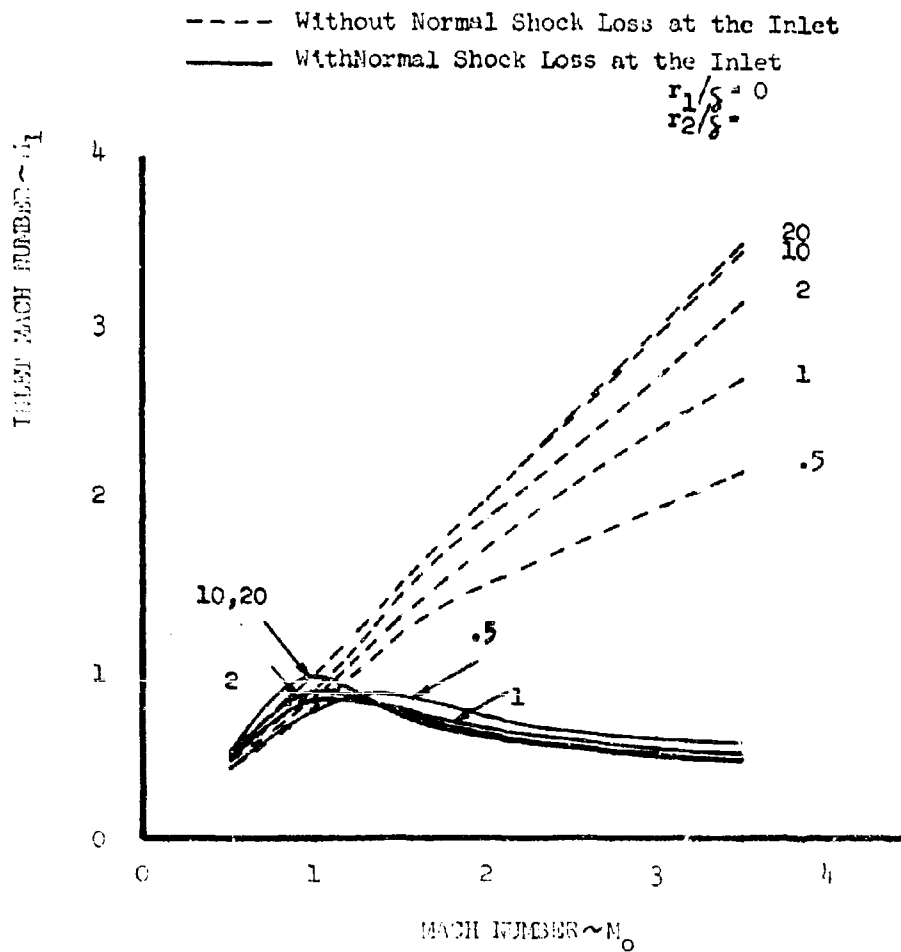
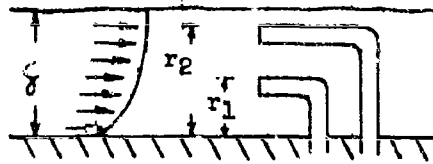


FIGURE 3-11. THEORETICAL PERFORMANCE OF INLETS IN  
 THE PRESENCE OF A BOUNDARY LAYER  
 WITHOUT CORRECTION

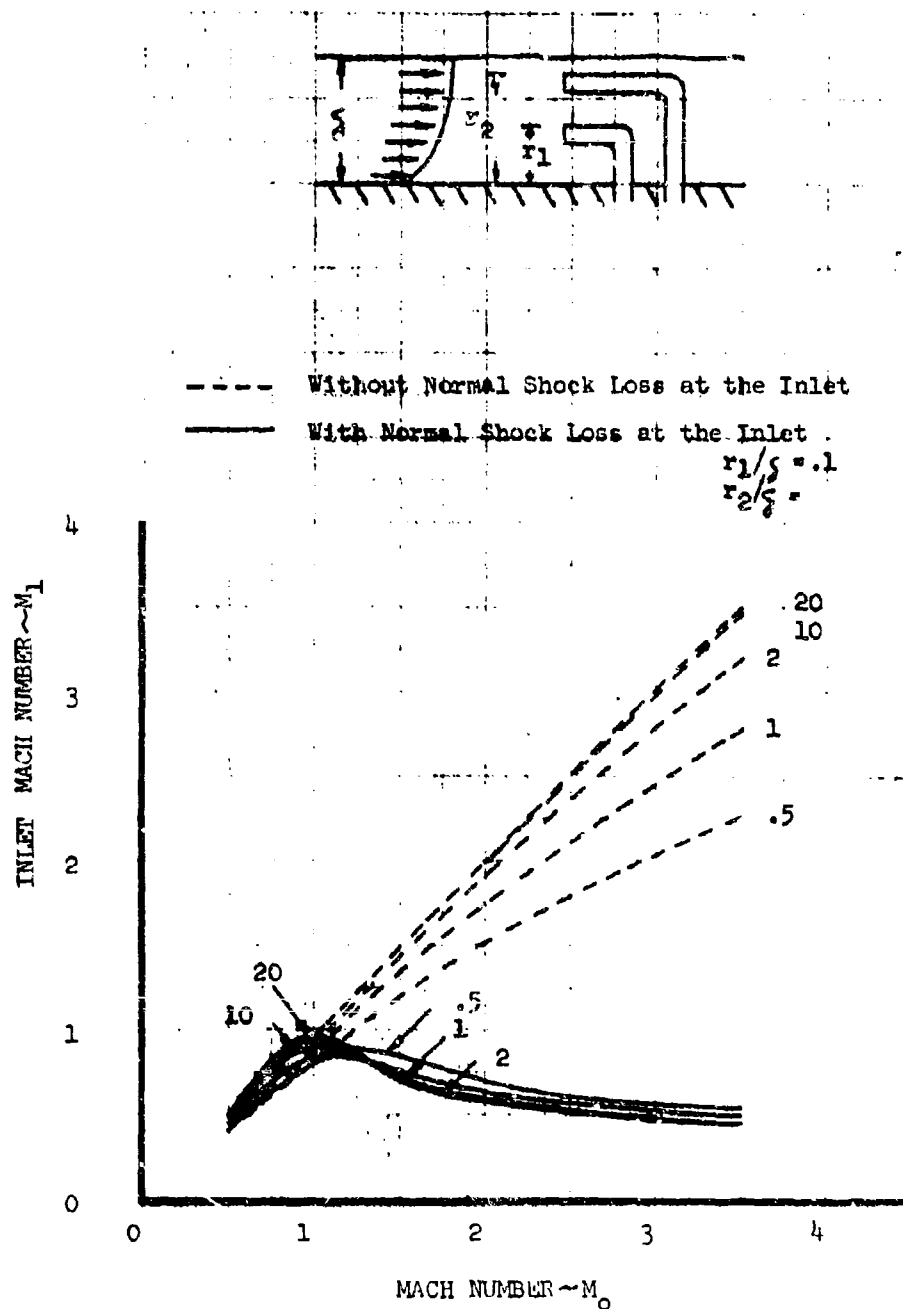


FIGURE 3-12. THEORETICAL PERFORMANCE OF INLETS IN THE PRESENCE OF A BOUNDARY LAYER WITHOUT COMPRESSION

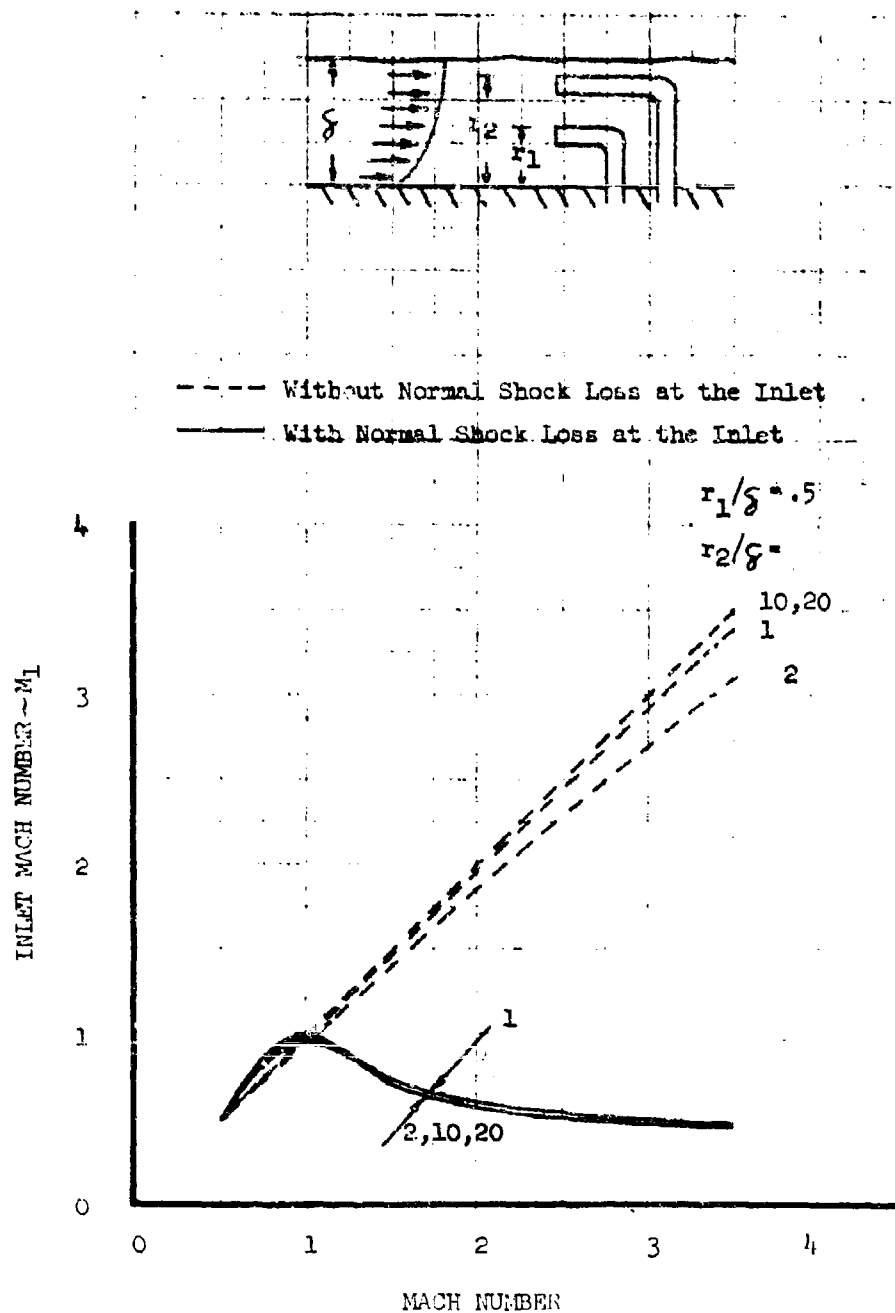


FIGURE 3-13. THEORETICAL PERFORMANCE OF INLETS IN THE PRESENCE OF A BOUNDARY LAYER WITHOUT COMPRESSION

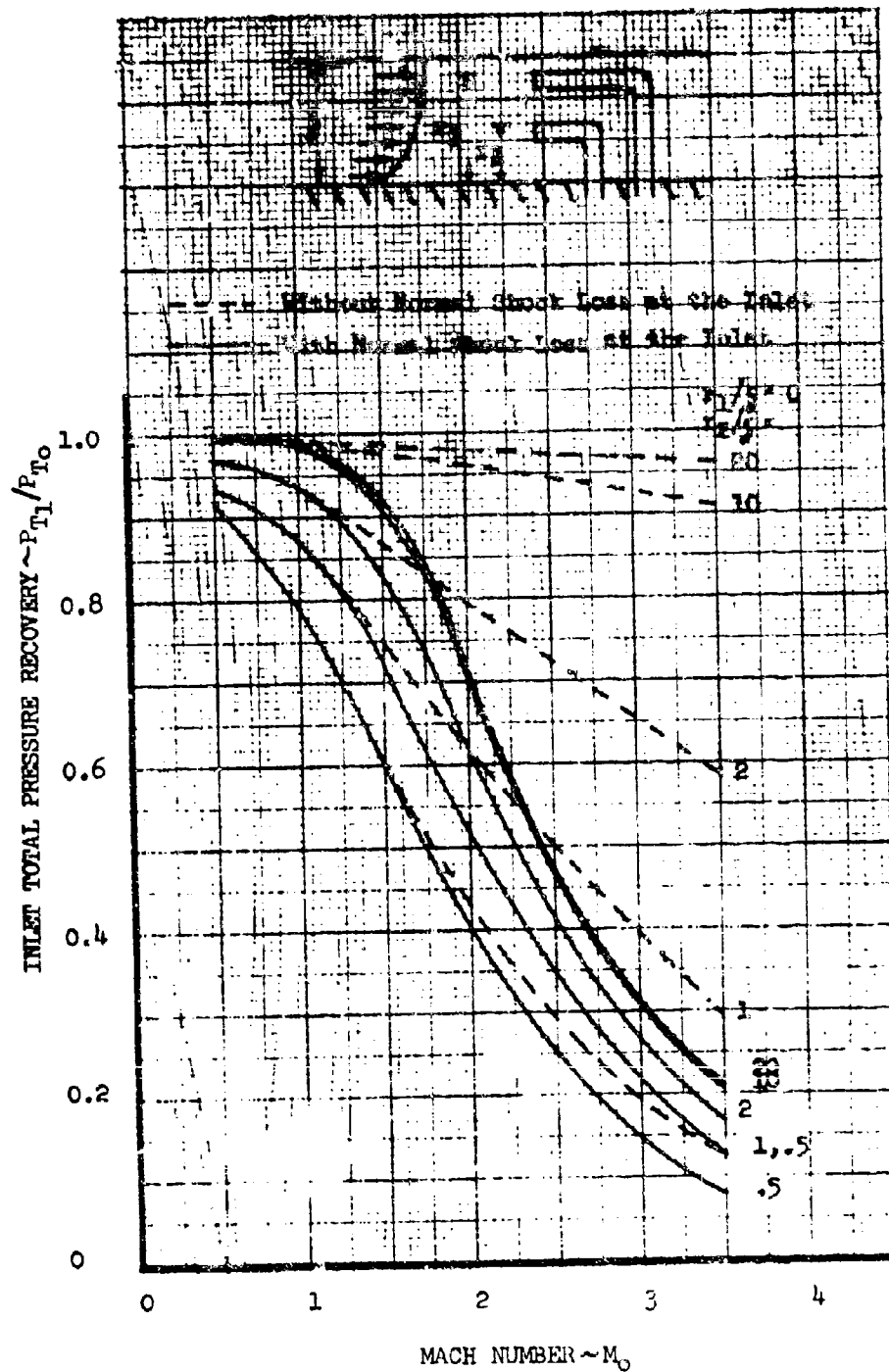


FIGURE 3-14. THEORETICAL PERFORMANCE OF INLETS IN THE PRESENCE OF A BOUNDARY LAYER WITHOUT COMPRESSION

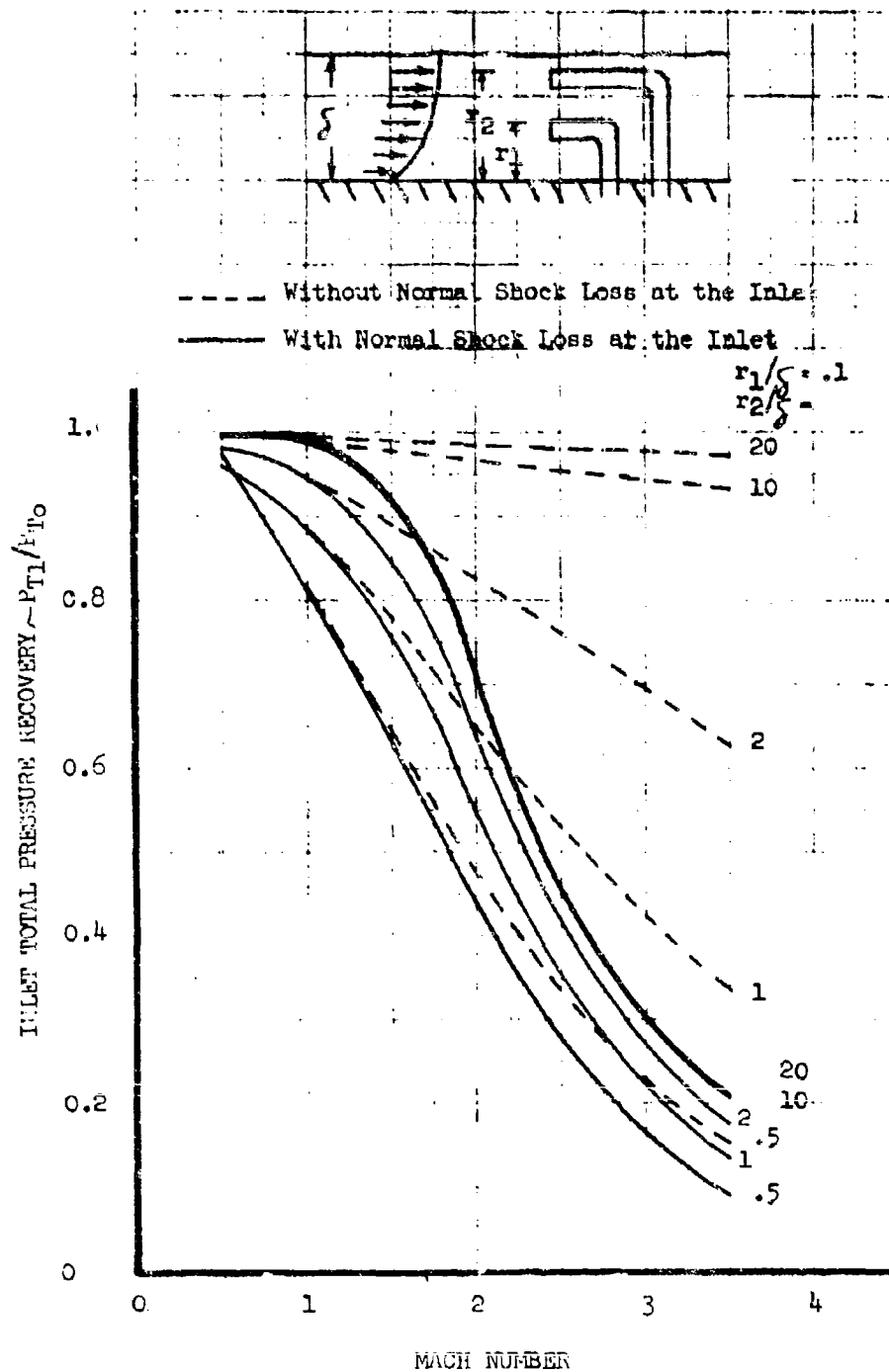


FIGURE 3-15. THEORETICAL PERFORMANCE OF INLETS IN THE PRESENCE OF A BOUNDARY LAYER WITHOUT COMPRESSION

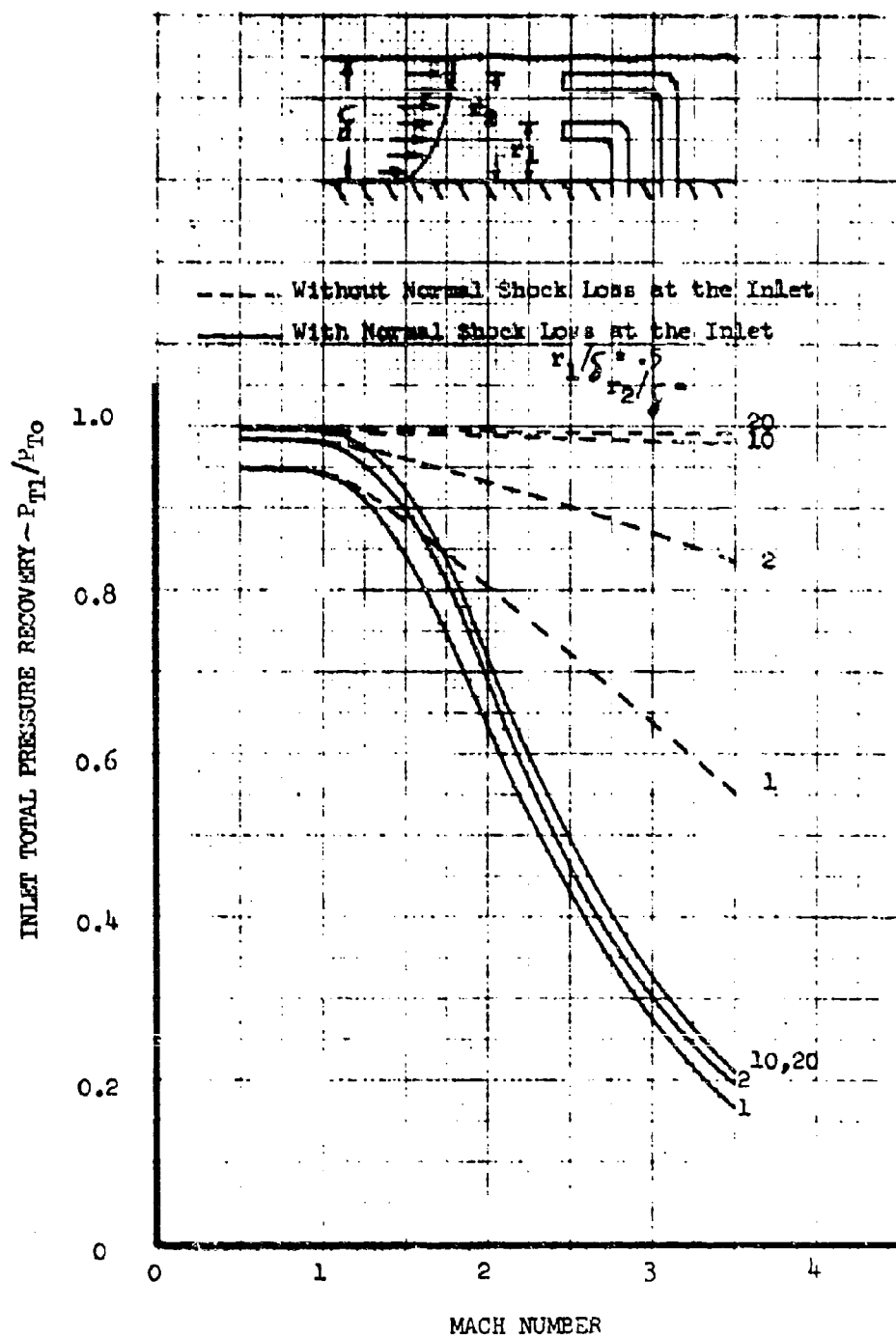


FIGURE 3-16. THEORETICAL PERFORMANCE OF INLETS IN THE PRESENCE OF A BOUNDARY LAYER WITHOUT COMPRESSION



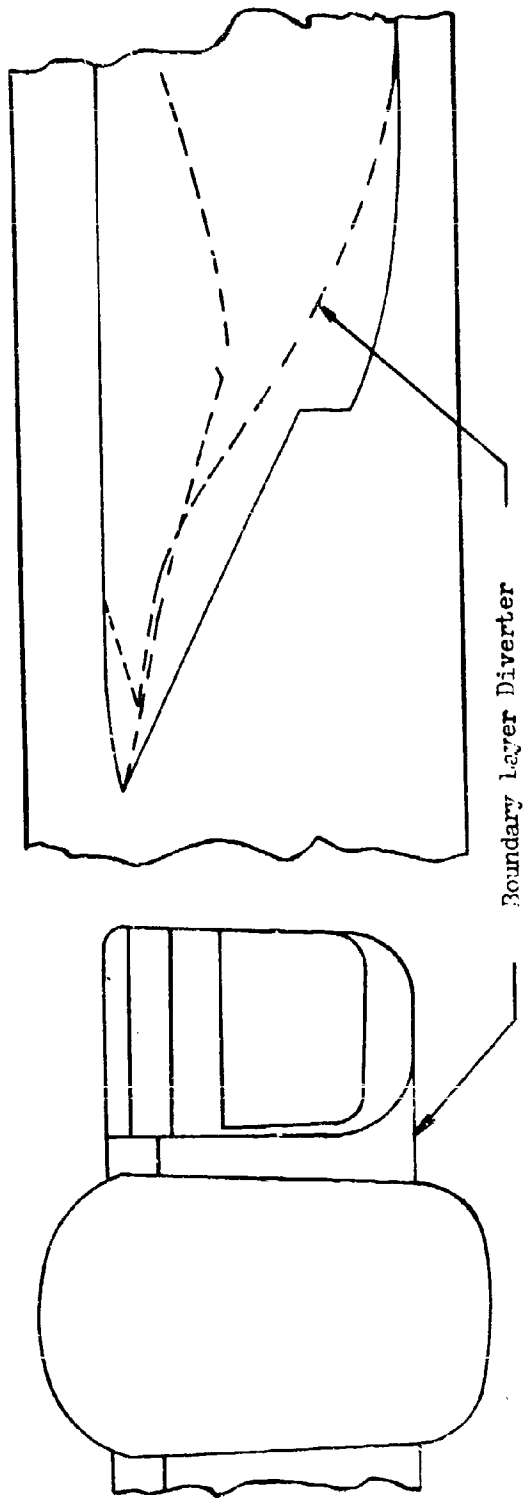


FIGURE 3-17. Typical Boundary Layer Diverter on a Two-Dimensional Horizontal Ramp Inlet

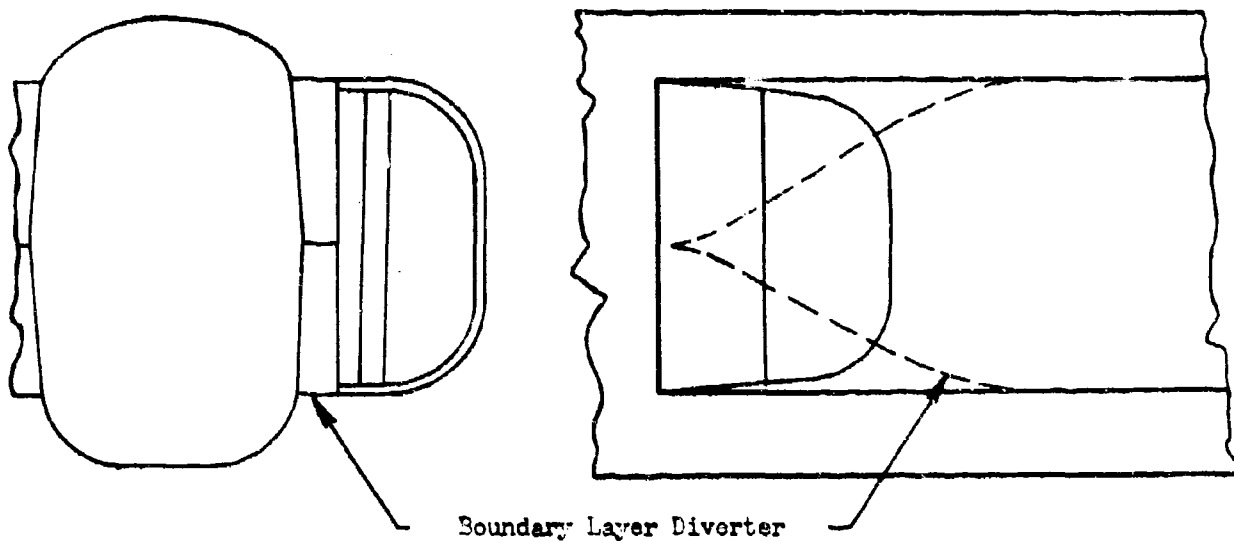


FIGURE 3-18. Typical Boundary Layer Diverter on a Two-Dimensional Vertical Ramp Inlet

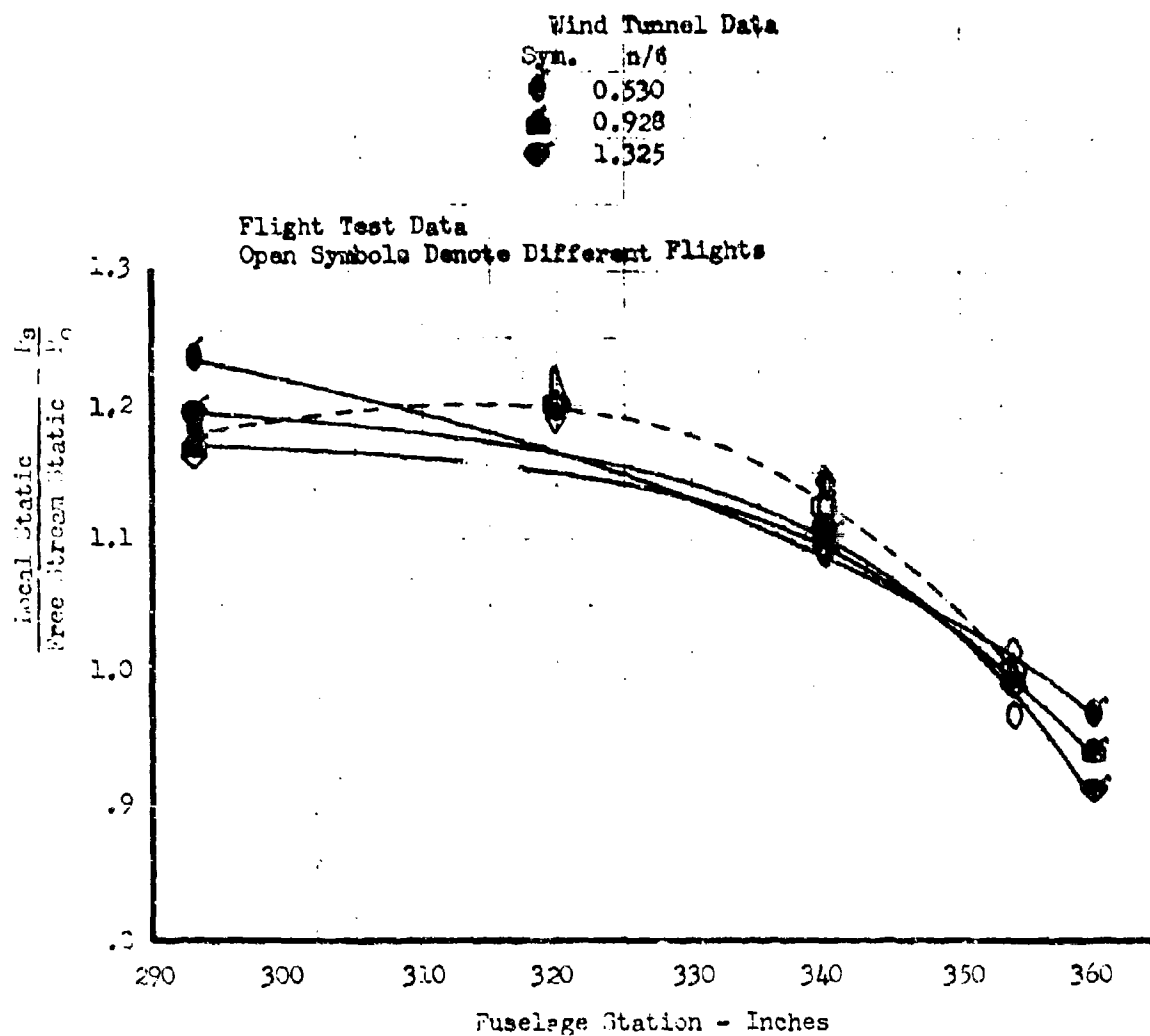


FIGURE 3-19. Diverter Static Pressure Distribution -  $M_0 = 0.9$

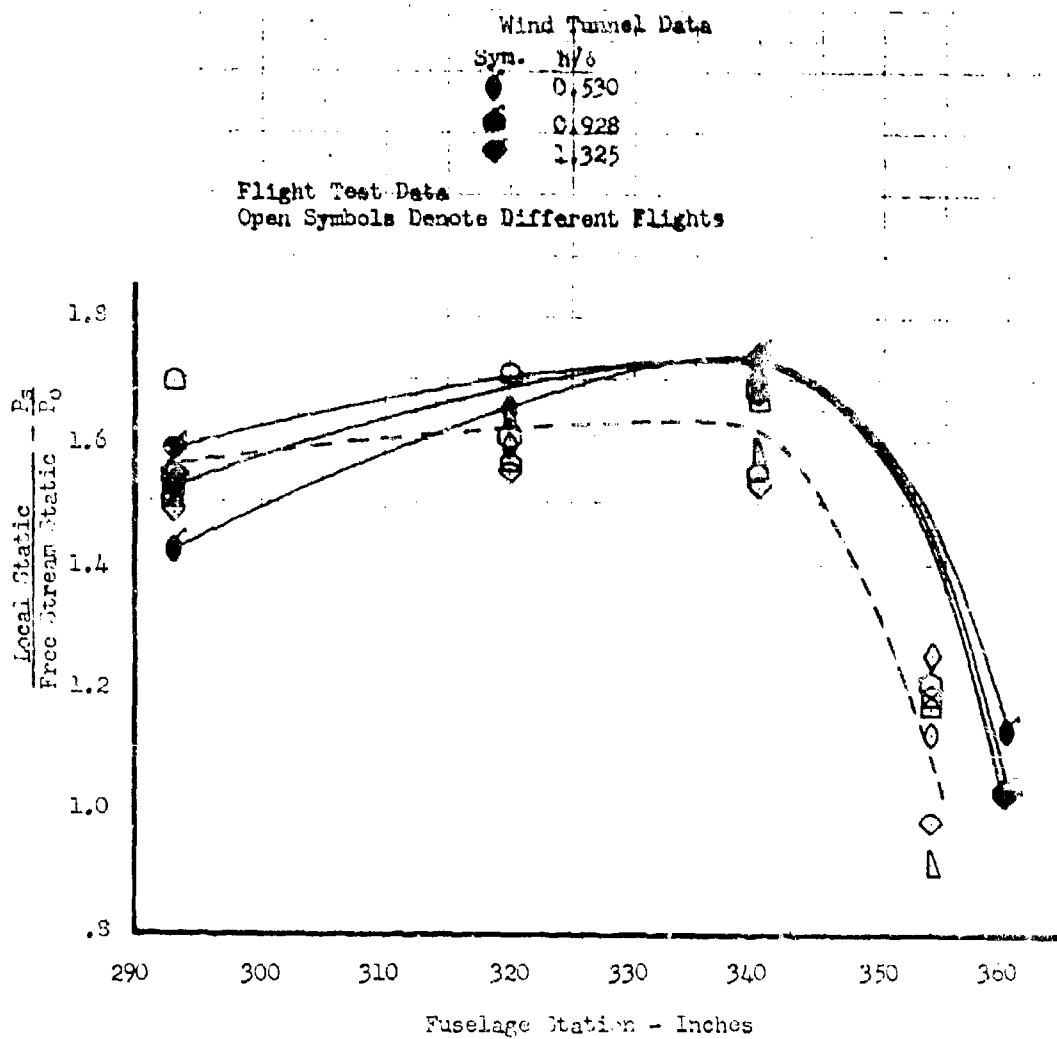


FIGURE 3-20. Diverter Static Pressure Distribution -  $M_0 = 1.57$

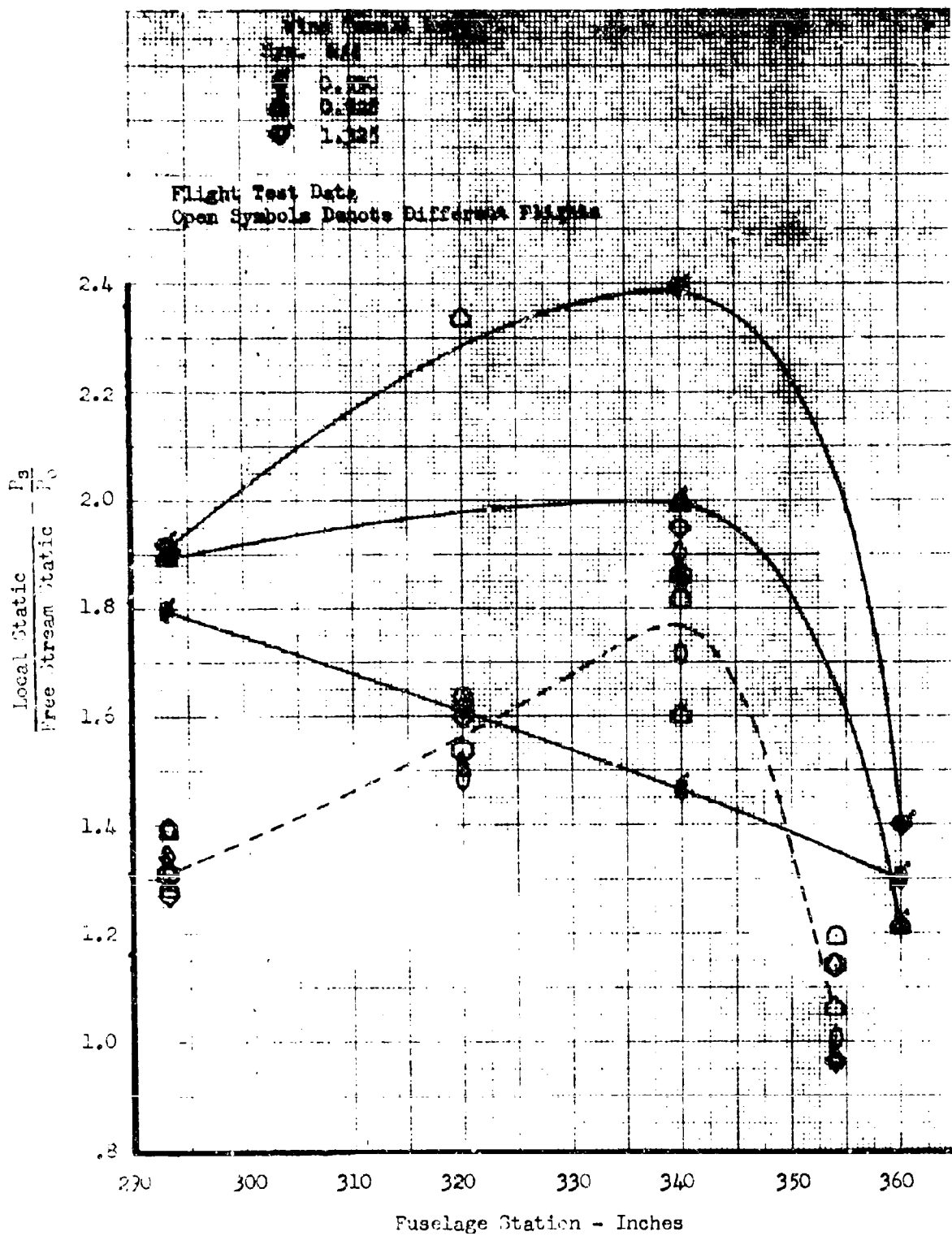


FIGURE 3-21. Diverter Static Pressure Distribution -  $M_0 = 1.97$

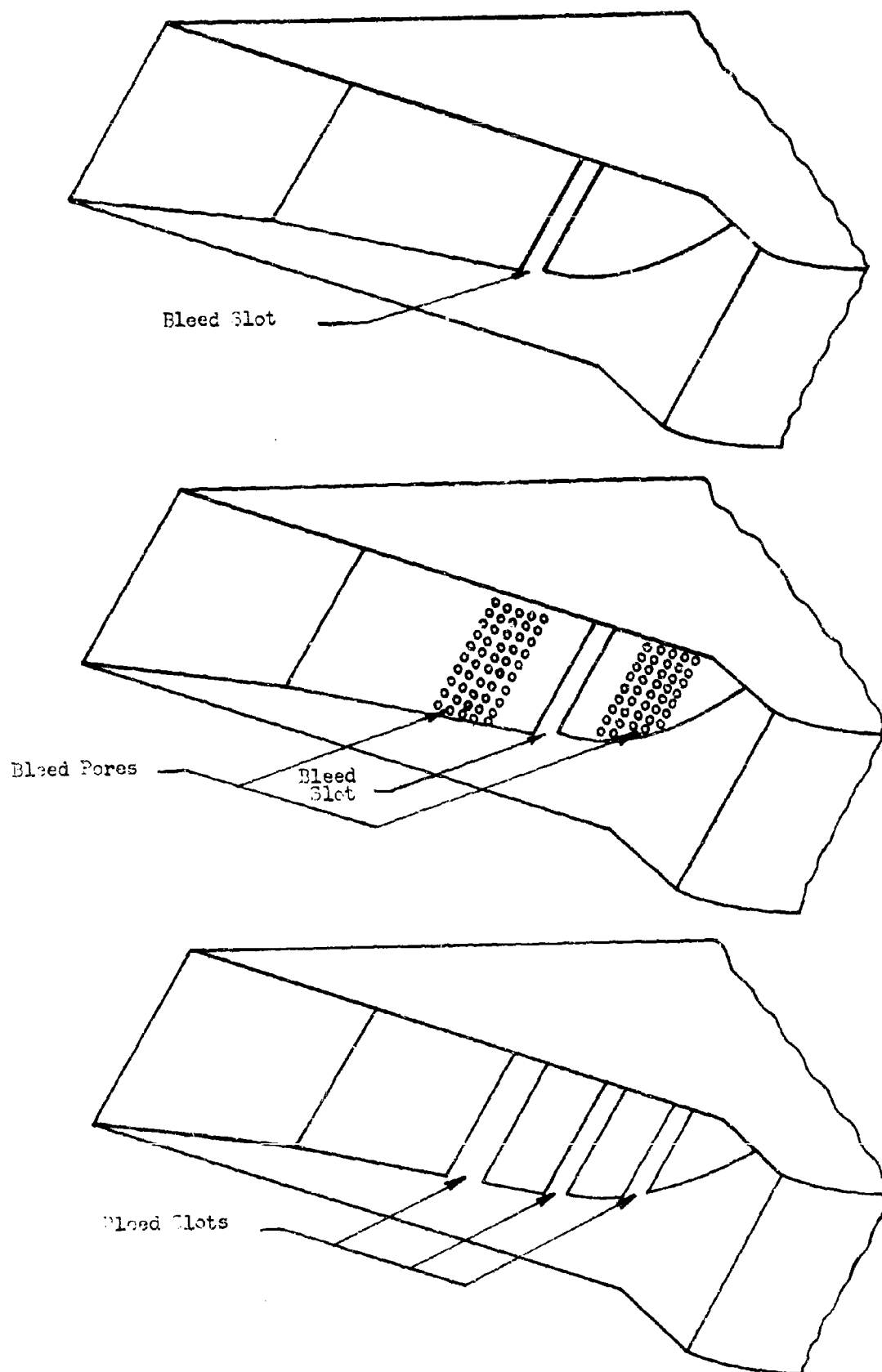


FIGURE 3-22. Compression Surface Boundary Layer Control

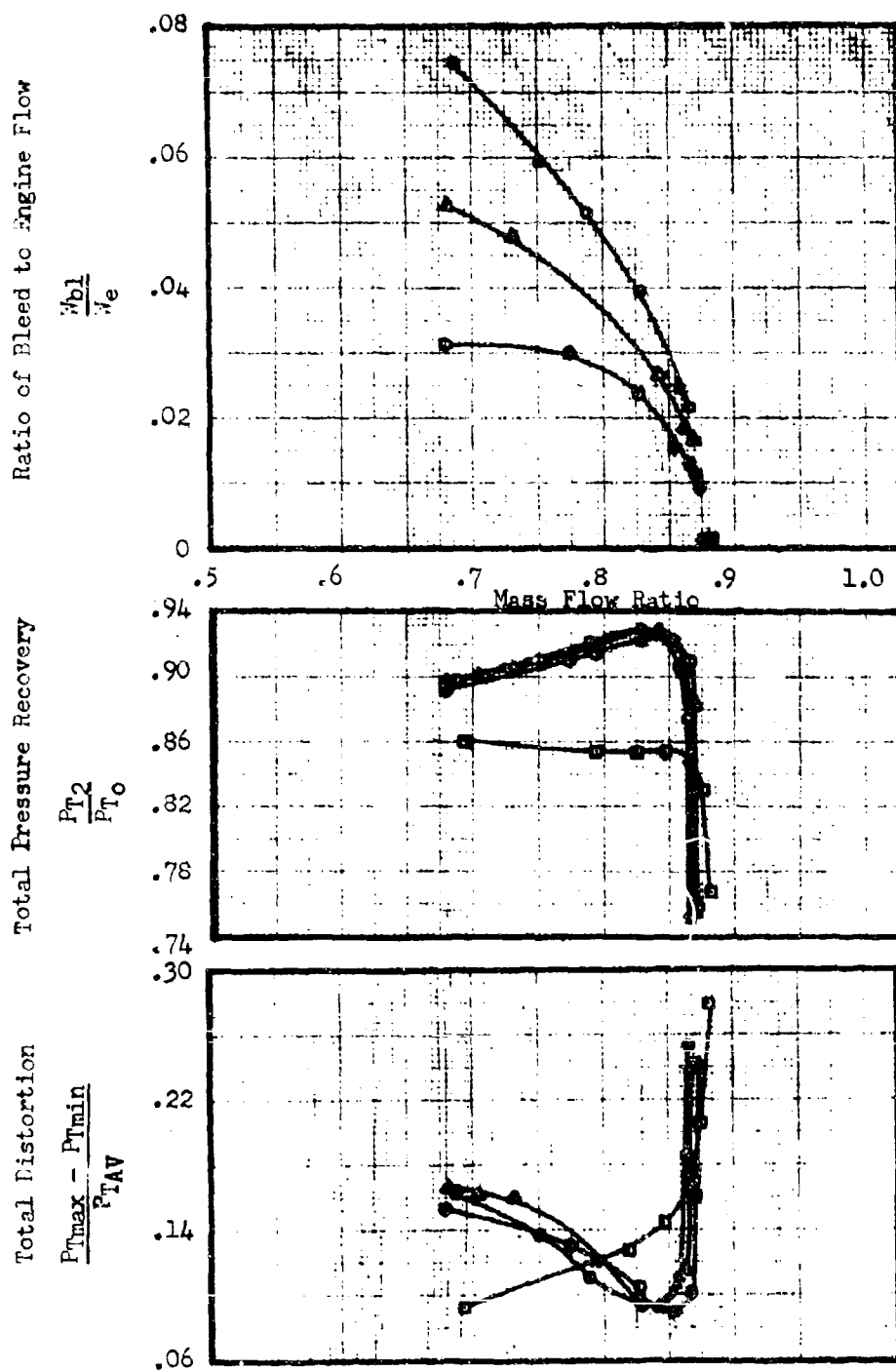


FIGURE 3-23. Effect of Compression Surface Bleed on Inlet Performance and Distortion -  $M_0 = 2.05$

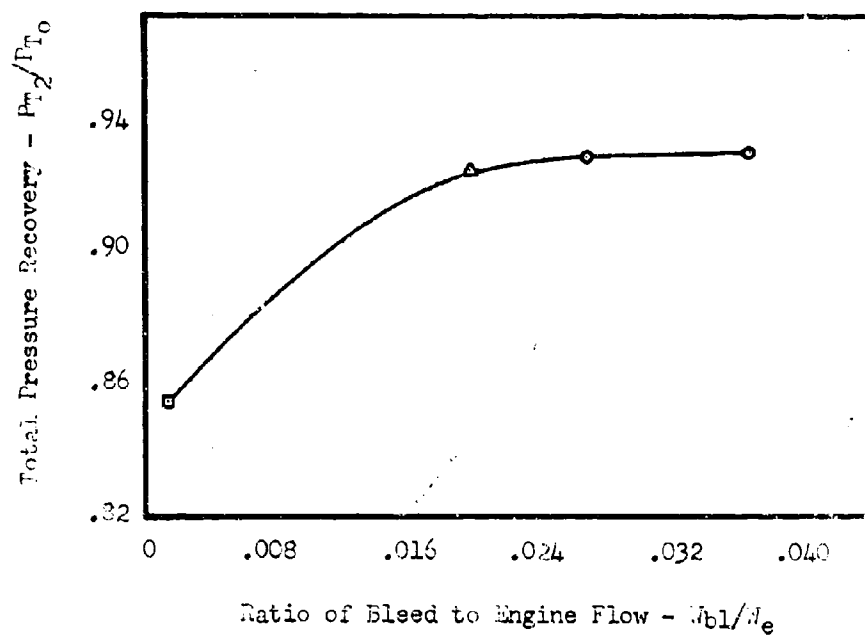
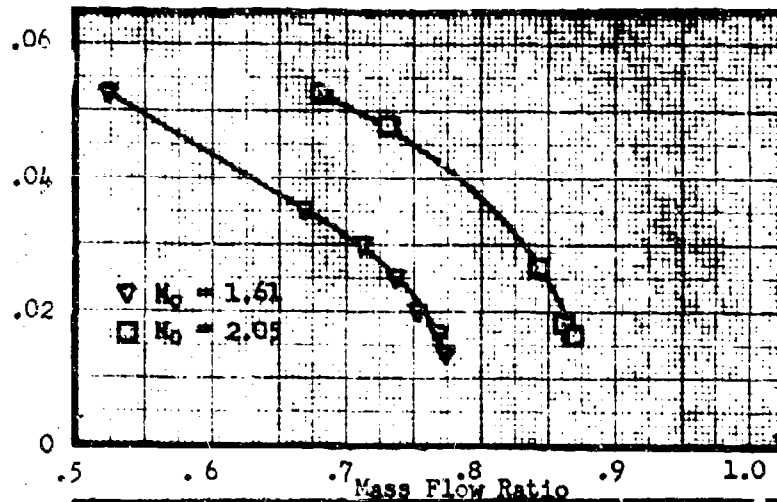


FIGURE 3-24. Summary of Bleed Effectiveness -  $M_0 = 2.05$



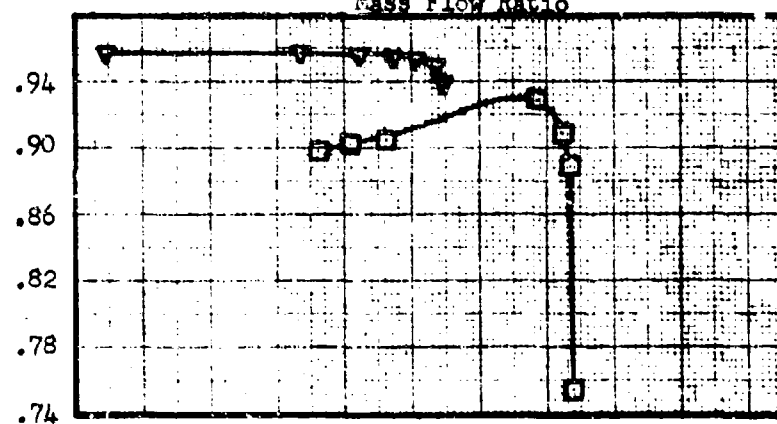
Ratio of Bleed to Engine Bleed

$$\frac{\dot{m}_{bl}}{\dot{m}_e}$$



Total Pressure Recovery

$$\frac{P_{t2}}{P_{t0}}$$



Total Distortion

$$\frac{P_{tmax} - P_{tmin}}{P_{tAV}}$$

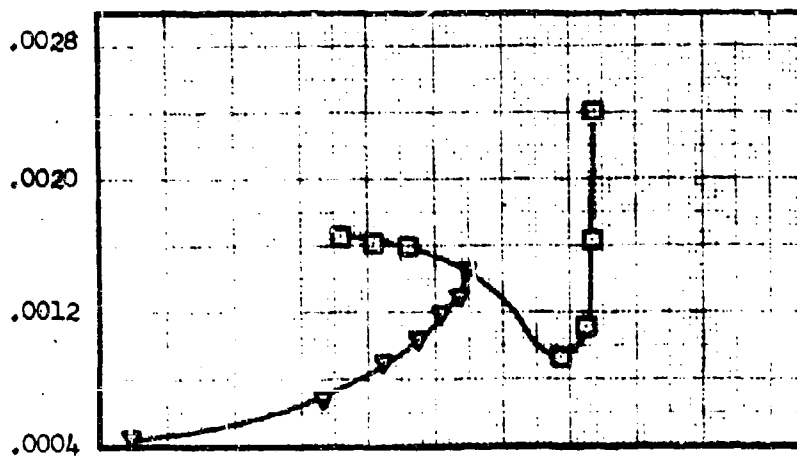


FIGURE 3-25. Effect of Mach Number on Bleed Flow

#### 4.0 Inlet Additive Drag

Additive drag is a correction term applied to the net propulsive effort of an aircraft. It is a consequence of the way in which net thrust is defined. For instance, net thrust is usually defined as the rate of change of total momentum of inlet airflow between the free-stream and the propulsion system exit. Momentum change between the inlet and the exit, however, is not equivalent to this definition when conditions at the inlet differ from those in the free-stream (i.e., at mass-flow-ratios less than 1.0). Figure 4 - 1 illustrates the foregoing for a simple isolated inlet in a subsonic airstream.

When the rate of momentum change between free-stream and the inlet is properly calculated, the result is called theoretical additive drag. Theoretical additive drag may be modified to reflect changes in external cowl drag with mass-flow-ratio and the result is considered to be the corrected additive drag (sometimes called spillage drag). The shape of the cowl lips, the cowl and the flight regime affect the cowl external pressure field and hence the correction to theoretical additive drag. Cowl lip suction force, as external cowl drag is sometimes called, can cancel theoretical additive drag for an inlet employing well rounded lips. As lip design becomes sharper and thinner and as flight Mach number increases, the full theoretical additive drag penalty becomes more likely.

#### 4.1 Calculation of Additive Drag

When inlet capture area intercepts an amount of air greater than the duct air required by the airplane, excess air is deflected or "spilled" around the inlet. Additive drag is the force required to divert this air from the path of the airplane. This force comes from the airplane and reduces net propulsive effort.

The net propulsive thrust of an engine at zero angle of attack is the resultant of the axial components of pressure and friction forces acting on the engine. Forces affecting a typical propulsion system are shown schematically in Figure 4 - 2. In this illustration, net propulsive thrust is replaced by an equal and opposite inertial force  $F_p$ . The forces are defined as positive in the directions shown by the force vectors.

Net internal thrust  $F_{n_i}$ , defined as the sum of pressure and friction forces acting on the interior of the propulsion system, can be calculated by considering the change in momentum between the inlet and the exit; Stations 1 and e, respectively, in Figure 4 - 2.

Thus,

$$F_{n1} = F_j - F_1 \quad (4.1)$$

where,

$$F_j = MV_j + A_c(P_e - P_o)$$

and,

$$F_1 = MV_1 + A_1(P_1 - P_o)$$

Then, if  $F_d$  is the sum of the forces acting on the external surfaces of the cowl,

$$F_p = F_{n1} - F_d \quad (4.2)$$

As stated earlier, engine performance is generally evaluated by considering the change in total momentum between the free-stream (Station 0) and the propulsion system exit. This momentum change is defined as the net thrust  $F_n$ . Using the notation of Figure 4 - 2,

$$F_n = F_j - F_o \quad (4.3)$$

where,

$$F_o = MV_o + A_o(P_o - P_o) = MV_o$$

Unlike Equation (4.2) and as illustrated in Figure 4 - 3,

$$F_p \neq F_n - F_d$$

In order to obtain the net propulsive thrust, momentum change between the free-stream and the inlet must be considered. Hence,

$$F_p = F_n - F_d - D_a \quad (4.4)$$

$D_a$  is called additive drag. By combining Equations (4.2) and (4.4), additive drag may be defined mathematically as,

$$D_a = F_n - F_{n1} = F_1 - F_o \quad (4.5)$$

An important interpretation of momentum change between the free-stream and the inlet can be realized from stream-flow relations. Consider a stream-tube which intercepts the cowl of an arbitrary inlet, as shown in Figure 4 - 4. From continuity requirements, it is apparent

that air entering this stream-tube in the free-stream must equal the duct air demand of the aircraft. If the "free-stream" tube area  $A_0$  is smaller than the capture area  $A_0$  intercepted by the inlet, then airflow entering Station 0 through  $A_1 - A_0$  must be deflected around the inlet.

The force required to divert the excess air can be evaluated by integrating pressure forces acting on the stream-tube. For an aircraft in steady, unaccelerated flight, the summation of forces acting on a control volume of air is zero. By applying this criterion to a control volume bounded by the stream-tube and the inlet entrance plane, as shown in Figure 4 - 5, it can be shown that the force acting on the stream tube is,

$$F_{ST} = F_1 - F_0$$

but,

$$F_{ST} = \int_{\text{Free-Stream}}^{\text{Inlet Lip}} (P - P_0) dA_x \quad (\text{Integration along the stream surface})$$

where  $dA_x$  is an area increment projected normal to the flight path. As noted in Reference (1), the "spillage" force  $F_{ST}$  is none other than the additive drag  $D_a$ . This can be substantiated by referring to Equation (4.5). Hence, the integral,

$$D_a = \int_{\text{Free Stream}}^{\text{Inlet Lip}} (P - P_0) dA_x \quad (4.6)$$

defines additive drag in general terms and is equivalent to the definition given earlier. Equation (4.6) is applicable to all types of inlet geometry - from an "open-nose" inlet to a ramp or spike inlet with a centerbody projected ahead of the inlet entrance station. As shown in the following example, a "control-volume" approach lends facility to the calculation of theoretical additive drag.

Figure 4 - 6 shows a two-dimensional inlet operating in a supersonic stream. This simple mathematical model was chosen to illustrate the principle of theoretical additive drag analysis. The inlet is assumed to be operating at a free-stream Mach number of 2.0 with an initial ramp angle of  $10^\circ$  and a total turning angle of  $20^\circ$ . It is to be shown here that any path from the free-stream to the inlet lip

(D to A in Figure 4 - 6) can be taken as a path of integration for the change in total momentum in the evaluation of theoretical additive drag. The alternate paths are listed below:

DCBA  
D'E'FGA  
DEFGA  
DC'F'GA  
DCFGA

First, to assess the theoretical additive drag by taking the path along DCBA; the most straightforward path from the definition given in Equation (4.6). Consider the difference in pressure on the two sides of the entering stream-tube and a projection of the stream-tube surface normal to the free-stream flow. Then, if the drag acting on the projected stream area is non-dimensionalized with inlet capture area  $A_C$  as the reference area and free-stream total pressure as the reference pressure, the resulting theoretical additive drag coefficient is given by,

$$C_{Da} = \frac{D_a}{P_{T0} A_C} = \frac{P_0}{P_{T0}} \left( \frac{A_{D-C}}{A_C} \right) \left( \frac{P_2 - P_0}{P_0} \right) + \frac{P_0}{P_{T0}} \left( \frac{A_{C-B}}{A_C} \right) \left( \frac{P_1 - P_0}{P_0} \right) \quad (4.7)$$

Again, a physical interpretation of the drag could be: the force that the spilled air exerts on the forward facing stream-tube surface.

The next path chosen for analysis, D'E'FGA, evaluates the total momentum  $\phi$  an infinitesimal distance downstream of the normal shock DE. Using D'E' to designate the use of properties on the downstream side of the normal shock, ramp pressure terms on E to F and F to G were calculated and free-stream momentum from G to A was subtracted from the sum of the other force terms. The expression for the drag coefficient is,

$$C_{Da} = \frac{D_a}{P_{T0} A_C} = \gamma \left( \frac{P_0}{P_{T0}} \right) \left( \frac{A_{D-E(FLW)}}{A_C} \right) \left( \frac{P_3}{P_0} \right) M_3^2 \cos(\delta_1 + \delta_2) + \left( \frac{P_0}{P_{T0}} \right) \left( \frac{A_{D-E}}{A_C} \right) \left( \frac{P_3 - P_0}{P_0} \right) + \left( \frac{P_0}{P_{T0}} \right) \left( \frac{A_{E-F}}{A_C} \right) \left( \frac{P_2 - P_0}{P_0} \right)$$

$$+ \left( \frac{P_o}{P_{To}} \right) \left( \frac{A_F - G}{A_C} \right) \left( \frac{P_1 - P_o}{P_o} \right) - \gamma \left( \frac{P_o}{P_{To}} \right) \left( \frac{A_C - A}{A_C} \right) \left( \frac{P_o}{P_o} \right) M_o^2 \quad (4.8)$$

Note here that the area used at the face of the normal shock was the flow area; then having calculated the momentum, the momentum component in the free-stream direction was calculated by multiplying by  $\cos(\delta_1 - \delta_2)$ . The area involved in the pressure-area term is the area projected perpendicular to free-stream. This important distinction will become more obvious when a path is taken involving CF and will be borne out by the numerical examples.

When the first two terms in Equation (4.8) are changed to reflect the Mach number and pressure in front of the normal shock plane, the equation for theoretical additive drag becomes,

$$\begin{aligned} C_{Da} = \frac{D_a}{P_{To} A_C} = & \gamma \left( \frac{P_o}{P_{To}} \right) \left( \frac{A_{D-E}(\text{FLOW})}{A_C} \right) \left( \frac{P_2}{P_o} \right) M_2^2 \cos(\delta_1 + \delta_2) \\ & + \left( \frac{P_o}{P_{To}} \right) \left( \frac{A_{D-E}}{A_C} \right) \left( \frac{P_2 - P_o}{P_o} \right) + \left( \frac{P_o}{P_{To}} \right) \left( \frac{A_{E-F}}{A_C} \right) \left( \frac{P_2 - P_o}{P_o} \right) \\ & + \left( \frac{P_o}{P_{To}} \right) \left( \frac{A_F - G}{A_C} \right) \left( \frac{P_1 - P_o}{P_o} \right) - \gamma \left( \frac{P_o}{P_{To}} \right) \left( \frac{A_C - A}{A_C} \right) \left( \frac{P_o}{P_o} \right) M_o^2 \quad (4.9) \end{aligned}$$

If the path DC'F'GA is chosen as the next path for analysis, the expression for the additive drag coefficient is,

$$\begin{aligned} C_{Da} = \frac{D_a}{P_{To} A_C} = & \frac{P_o}{P_{To}} \left( \frac{A_{D-C}}{A_C} \right) \left( \frac{P_2 - P_o}{P_o} \right) + \gamma \left( \frac{P_o}{P_{To}} \right) \left( \frac{A_{C'-F'}(\text{FLOW})}{A_C} \right) \\ & \left( \frac{P_2}{P_o} \right) M_2^2 \cos(\delta_1 + \delta_2) + \frac{P_o}{P_{To}} \left( \frac{A_{C-F}}{A_C} \right) \left( \frac{P_2 - P_o}{P_o} \right) \\ & + \frac{P_o}{P_{To}} \left( \frac{A_F - G}{A_C} \right) \left( \frac{P_1 - P_o}{P_o} \right) - \gamma \left( \frac{P_o}{P_{To}} \right) \left( \frac{A_C - A}{A_C} \right) \left( \frac{P_o}{P_o} \right) M_o^2 \quad (4.10) \end{aligned}$$

In Equation (4.9)  $A_{D-E}(\text{FLOW}) \cdot \cos(\delta_1 - \delta_2)$  was equal to  $A_{D-E}$ , both being equal to the projected area of the inlet opening. However, in Equation (4.10),  $A_{C'-F'}(\text{FLOW}) \cdot \cos(\delta_1 - \delta_2)$  is different from  $A_{C-F}$ . In either case (Equation (4.9) or (4.10)), the momentum term - mass times velocity - is being assessed and then having its axial component taken. The pressure-area term is simply the product of the pressure and the projected area.

If a final path DEFGA, passing an infinitesimally short distance in front of the second oblique wave, is chosen; the drag expression becomes,

$$C_{Da} = \frac{D_a}{P_{T0} A_C} = \frac{P_0}{P_{T0}} \left( \frac{A_{D-C}}{A_C} \right) \left( \frac{P_2 - P_0}{P_0} \right) + \gamma \left( \frac{P_0}{P_{T0}} \right) \left( \frac{A_{C-F(FLow)}}{A_C} \right) \left( \frac{P_1}{P_0} \right) M_1^2 \cos \delta_1$$

$$+ \left( \frac{P_0}{P_{T0}} \right) \left( \frac{A_{C-F}}{A_C} \right) \left( \frac{P_1 - P_0}{P_0} \right) + \frac{P_0}{P_{T0}} \left( \frac{A_{E-G}}{A_C} \right) \left( \frac{P_1 - P_0}{P_0} \right) - \gamma \left( \frac{P_0}{P_{T0}} \right) \left( \frac{A_{C-1}}{A_C} \right) \left( \frac{P_0}{P_0} \right) M_0^2$$

(4.11)

For the flow properties and geometry of the simple mathematical inlet model shown in Figure 4 - 6, numerical values of theoretical additive drag coefficient  $C_{Da}$  were calculated for each path of analysis using Equations (4.7) through (4.11). The values of  $C_{Da}$  are referenced to an  $A_C$  of 1.0 and were calculated at a maximum value of  $A_0$ . Calculation results are presented in tabular form below:

Path	Equation	Term 1	Term 2	Term 3	Term 4	Term 5	$C_{Da}$
DCBA	(4.7)	.0398	.0055				.0453
D'E'FGA	(4.8)	.2592	.2343	.0874	.0140	-.5496	.0453
DEFGA	(4.9)	.3860	.1075	.0874	.0140	-.5496	.0453
DE'F'GA	(4.10)	.0398	.3860	.1551	.0140	-.5496	.0453
DEFGA	(4.11)	.0398	.4805	.0608	.0140	-.5496	.0453

Note that the drag coefficients are all equal, as they should be. Also, excess air is spilled supersonically and the terminal (normal) shock wave remains attached.

The preceding discussion has shown that additive drag calculations can be simplified by the selection of a "proper" path of integration for Equation (4.6). This is equivalent to using any convenient control volume, bounded by the free-stream and a plane through the inlet lip station. This calculation technique is applicable to all flight regimes. In simpler systems, of course, there are not as many alternate paths.

In the case of a simple pitot intake, theoretical additive drag calculations are essentially unchanged for subsonic and supersonic operation; the only difference being the presence of a normal shock in the case of supersonic operation. An open nose inlet operating at a mass-flow-ratio less than 1.0 is shown schematically in Figure 4 - 7. The additive drag, from Equation (4.6), takes the form:

$$C_{Da} = \frac{D_a}{P_{T0} A_C} = \gamma \left( \frac{P_0}{P_{T0}} \right) \left( \frac{P_1}{P_0} \right) M_1^2 - \gamma \left( \frac{P_0}{P_{T0}} \right) \left( \frac{A_0}{A_1} \right) M_0^2 \quad (4.12)$$

where,

$$\frac{P_1}{P_0} = \frac{P_{T0}}{P_0} \frac{P_{T1}}{P_{T0}} \cdot \frac{P_1}{P_{T1}}$$

and,

$$\frac{P_{T1}}{P_{T0}} = 1.0 \quad (\text{Subsonic Flight})$$

$$\frac{P_{T1}}{P_{T0}} = \left( \frac{6M_0^2}{M_0^2 - 5} \right)^{3.5} \left( \frac{6}{7M_0^2 - 1} \right)^{2.5} \quad (\text{Supersonic Flight}) \quad \text{for } \gamma = 1.4$$

Normal shock wave total pressure recovery  $P_{T1}/P_{T0}$  as a function of upstream Mach number is tabulated in Appendix B. Figure 4 - 8 shows theoretical additive drag values calculated from Equation (4.12).

As has been shown, additive drag calculations depend on the evaluation of Equation (4.6) for an inlet and operating condition of interest. Calculation techniques depend largely on the flight speed. Often, subsonic and supersonic operation dictate the use of different assumptions and control volume calculation paths. These special considerations will be discussed in the following sections.

#### 4.2 Subsonic Additive Drag

Accurate theoretical additive drag calculations are critically dependent upon inlet flow field determination. Due to the complexity of subsonic flow calculations, inlet flow fields can, at best, only be approximated. The importance of stagnation point position on analysis techniques will be presented in the following discussion. In addition, supersonic (sharp lip) inlets operated at subsonic flight speeds will be evaluated.

Air induction systems designed for subsonic aircraft employ well rounded inlet lips. While providing reduced flow separation losses, this type of lip design enhances additive drag cancellation by increasing the frontal area over which lip suction forces can act. Unfortunately, a rounded lip permits the "stagnation" streamline, the streamline separating flow entering the inlet from that spilling over the cowl, to move about the leading edge of the lip as mass-flow-ratio is varied, see Figure 4 - 9. It is apparent, from the definition of additive drag, that the momentum change of interest occurs between free-stream and the lip stagnation point. Therefore, Equation (4.6) can be properly evaluated only if the path of integration varies with stagnation point movement.



Reference 2 has shown in detail that, based on potential flow theory, theoretical additive drag of a blunt lip inlet is zero at subsonic speeds and mass-flow-ratio greater than 1.0. Such is not the case for subcritical (mass-flow-ratio less than 1.0) inlet operation.

At present, potential flow theory is the most accurate means of calculating subcritical blunt lip performance. With this approach, it is possible to simulate angle of attack and mass-flow-ratio variation, see References 3 and 4. Further, stagnation point position can be determined as a function of mass-flow-ratio and cowl lip geometry. The variation of stagnation point position with mass flow for a typical axisymmetric inlet is illustrated in Figure 4 - 10. Note that in this figure the stagnation point occurs at a velocity ratio of  $V/V_0 = 0.0$ . If the inner surface of this inlet had a more rounded contour, stagnation point movement would have been apparent at high mass flow values.

The calculation technique used in this analysis involves a numerical integration of velocities and pressures at the plane of the stagnation point. With integrated properties at the "stagnation plane", total momentum  $\phi$  may be evaluated. Thus, for an open-nose inlet

$$C_{Da} = \frac{D_a}{P_{T0} A_C} = \frac{\phi_1 - \phi_0}{P_{T0} A_C} \quad (4.13)$$

where,

$$\begin{aligned} \phi_1 &= M\bar{V}_1 + A_{1SP}(\bar{P}_1 - P_0) = (\gamma \bar{P}_1 \bar{M}_1^2 + P_1 - P_0) A_{1SP} \\ \phi_0 &= M\bar{V}_0 = \gamma P_0 \bar{M}_0^2 A_0 \end{aligned}$$

$\bar{M}_1$ ,  $\bar{P}_1$ , and  $\bar{V}_1$  represent integrated flow properties. The flow area of the stagnation plane is denoted  $A_{1SP}$ .

In most preliminary design analyses, potential flow calculations are far too complex for easy use. Even Electronic Data Processing Machine (EDPM) programs can take an hour of computing time to solve a single case. Thus, one-dimensional flow approximations are usually employed to facilitate additive drag calculations. For example, Equation (4.12) is a one-dimensional approximation for the pitot inlet just described. In this approximate approach, the stagnation point is assumed stationary at the "highlight" or leading edge of the inlet lip.

Inlets designed for supersonic aircraft must, in general, employ sharp, thin lips if large wave drag penalties associated with blunt lips in supersonic flow are to be avoided. Since supersonic vehicles must take-off and land at subsonic speeds, it is important to be able to predict low speed performance of supersonic inlet systems.

Sharp lip performance of a cylindrical inlet at subsonic speeds is analyzed by the methods presented in Reference 2. An illustration of the flow pattern to be evaluated is presented in Figure 4 - 11. Lip suction force is denoted by the vector  $F$  and  $S$  defines a typical stagnation streamline.

At mass flow ratios greater than unity, actual inlet conditions are non-uniform. However, inlet flow may be approximated by equivalent one-dimensional flow; that is, flow of an equivalent mass flow, energy and momentum level.

Inlet momentum is equal to the free-stream value plus all forces exerted on the internal flow between free-stream and the stagnation point. These forces consist of a lip suction force  $F$  and the integral of the pressure increment along the stagnation streamline up to the stagnation point. Hence,

$$\phi_1 = \phi_0 + F + \int_{F.S.}^{S.P.} (P - P_0) dA_x \quad (\text{Mass Flow Ratio} > 1.0)$$

As shown in Reference 2, the pressure integral given above is zero at mass flow ratios greater than 1.0. Since the lip is assumed infinitely sharp, there is no lip area to support lip suction. Following this criterion, there is no change in total momentum between free-stream and the inlet. It is apparent that,

$$C_{D_a} = 0.0 \quad (\text{Sharp Lip Inlet at MFR} \geq 1.0) \quad (4.14)$$

For mass flow ratios less than 1.0, the only force exerted on the internal flow is the streamline pressure integral. In general, this term is not zero. Evaluation of the momentum change between the free-stream and the inlet leads to,

$$C_{D_a} = \frac{D_a}{P_{T0} A_C} = \frac{P_1}{P_{T0}} \left[ M_1^2 + 1 \right] - \frac{P_0}{P_{T0}} - \frac{2A_0}{P_{T0} A_1} \quad (4.15)$$

(Mass Flow Ratio < 1.0)

Subsonic additive drag values determined from this equation are presented in Figure 4 - 12.

In many instances, especially in the subsonic case, theoretical additive drag is calculated along shock generator surfaces (i.e. ramps or spikes) of the supersonic inlet. This integration path is selected because subsonic stagnation streamline properties are quite difficult to evaluate. While free-stream properties are defined by flight conditions and inlet conditions are specified by

engine and secondary airflow requirements; the variation of thermodynamic properties along the ramp is not easily determined. In practice, a linear variation of flow properties between the leading edge of the ramp and the inlet station is assumed. Ramp drag is then calculated by using an average pressure acting on the frontal area of the surface. Calculation errors incurred with this approach may result in negative additive drag values. The discussion in Section 4.5 will show how this deficiency may be corrected through the use of an additive drag correction term called  $K_{ADD}$ .

#### 4.3 Supersonic Additive Drag

Thermodynamic calculations required to evaluate Equation (4.6) for supersonic additive drag are generally quite straightforward. Primarily, this is a result of the "limited region of disturbance" nature of supersonic flow. The inlet flow field can usually be divided into regions bounded by shock waves and inlet surfaces, as shown in Figure 4 - 6. Cowl lip stagnation streamline properties and/or surface thermodynamics are then evaluated from region to region.

Theoretical additive drag coefficients for representative two and three-dimensional inlets will be presented herein. Before proceeding to these design charts, however, certain simplifying assumptions employed in calculating the drag values should be noted.

As must be apparent from the preceding discussion, friction forces have been neglected in the calculation of momentum terms along the shock generator (ramp) surface. While this approach may lead to low theoretical drag estimates at high mass flow and ramp surface Mach numbers, Section 4.5 presents an empirical correction technique which will account for friction forces and other discrepancies resulting from a simplified analysis. In a similar manner, boundary layer is not considered; inviscid pressure distributions are used to calculate inlet ramp drag. Another important approximation involves terminal shock wave position. An infinitely sharp cowl lip is assumed. The terminal shock wave is considered to remain attached to the rim of the cowl during critical and supercritical operation. In practice, the terminal wave stands slightly ahead of the lip, critically, due to finite rim bluntness. Subcritically, the terminal shock may be positioned large distances upstream of the lip. The detachment distance is largely a function of inlet mass-flow-ratio (a more complete discussion of this phenomenon is presented in Section 4.4). In the calculations of this section, subcritical shock position is considered to be an infinitesimal distance ahead of the inlet entrance plane as illustrated in Figure 4 - 13. Of course, this "fixed" terminal shock assumption will result in a low drag estimate at reduced inlet mass flow.

#### 4.3.1 Two-Dimensional Inlets

Theoretical additive drag coefficients have been calculated for a family of two and three-shock inlets. The calculation path is taken along D'E'FGA as shown in Figure 4 - 6. Based upon the assumptions above, flow is spilled supersonically.

Two-shock additive drag is presented in Figures 4 - 14 through 4 - 21. Note that the variable  $\lambda_s$  shown in these figures is called a lip position parameter. It is considered to be a primary characteristic of a given inlet configuration. The lip position parameter is defined as the acute angle between the free-stream flow direction and a line drawn between the leading edge of the ramp and the cowl lip. Mass flow variation is presented as the ratio  $MFR/MFR_{max}$ , where MFR is the operating mass-flow-ratio and  $MFR_{max}$  is the mass-flow-ratio corresponding to critical operation for a given configuration (typified by  $\lambda_s$ ). Ramp angles used for each Mach number correspond to optimum design according to Oswatitsch analysis techniques presented in Reference 5.

Three-shock additive drag is presented in terms of the same parameters used to describe two-shock values. Again, cowl lip position is specified by  $\lambda_s$ . Multiple shock inlet designs that achieve precompression by the use of three or more shocks can not be characterized by  $\lambda_s$  alone. That is, the position of the ramps with respect to one another and with respect to the cowl lip have a definite impact upon inlet performance. To incorporate this geometric influence in theoretical three-shock additive drag calculations - without introducing added complexity - the cowl lip is assumed to lie along a plane perpendicular to the aft ramp and passing through the intersection of the oblique shocks. This geometric restriction is illustrated in Figure 4 - 22. Three-shock additive drag values for Oswatitsch optimum turning are presented in Figures 4 - 23 to 4 - 30.

Theoretical two and three-shock additive drag levels presented above are clearly applicable to all-external compression inlets. They apply to mixed compression inlets as well, depending, of course, on the number of external shocks associated with a given internal-external compression field. For example, two-shock values can be used to approximate additive drag for a single external shock system. Likewise, three-shock all-external additive drag is equivalent to that for a mixed compression design with two external oblique shock waves. Mixed compression configurations with more than two external shocks are rarely used.

The equivalence between all-external and mixed compression inlet flow fields is clearly shown in an example of Section 4.1. Recall that

total momentum  $\Phi$  at the inlet entrance plane is constant whether evaluated upstream of the attached normal shock wave (along D-E in Figure 4 - 6) or downstream of the shock (along D'-E'). Thus, the presence of this terminal wave has no influence on theoretical additive drag. Since the terminal wave is treated as attached even at reduced mass flow, it could have been ignored. The flow field upstream of the normal shock, hence additive drag, is identical to that of a mixed compression inlet with two external oblique shock waves. Additive drag coefficients presented in Figures 4 - 14 to 4 - 30 are more rigorous for the mixed compression configuration because terminal shock position at reduced mass flow ratio does not influence the calculation as was the case for an all-external inlet.

#### 4.3.2 Three-Dimensional Inlets

A discussion of theoretical additive drag for three-dimensional inlets is presented herein. Design charts are shown for axisymmetric inlets employing right circular cones as shock generator surfaces (spikes). An analysis technique for a double-cone spike configuration is also included. Due to mathematical complexities associated with arbitrary three-dimensional inlet analyses, this discussion will be restricted to axisymmetric inlets.

Flow over the forward portion of an axisymmetric inlet with a conical spike is governed by the equation:

$$-\frac{\gamma V_r}{d\phi} \left[ \frac{\gamma+1}{2} \left( \frac{dV_r}{d\phi} \right)^2 - \frac{\gamma-1}{2} (V_{\max}^2 - V_r^2) \right] - \frac{\gamma-1}{2} \left( \frac{dV_r}{d\phi} \right)^3 \cot \phi \\ - \gamma V_r \left( \frac{dV_r}{d\phi} \right)^2 + \frac{\gamma-1}{2} (V_{\max}^2 - V_r^2) \frac{dV_r}{d\phi} \cot \phi + (\gamma-1) V_r (V_{\max}^2 - V_r^2) = 0 \quad (4.16)$$

with the additional restriction -

$$\frac{dV_r}{d\phi} = V_r$$

A definition of each variable in Equation (4.16) is contained in Appendix D. It is important to note that a non-uniform flow field results from the solution of this equation and that additive drag calculations are more complex than those associated with two-dimensional flow.

Static pressure along the spike surface is constant, hence, no added difficulty arises with the evaluation of ramp drag. Since flow at the inlet entrance is non-uniform, total momentum there must be integrated along a path from the spike to the cowl lip. Referring to Figure 4 - 31, inlet entrance total momentum is integrated along D-C.

Rather than evaluate theoretical additive drag by calculating along A-F-E-D-C (in Figure 4 - 31), a direct integration along the stagnation streamline (path A-B-C) is used. As shown in Reference 6, the streamline can be approximated by connecting a series of truncated conical flow surfaces between the free-stream and the cowl lip. A cross-sectional view of the stream surface construction is illustrated in Figure 4 - 32. The integration is treated in a stepwise manner and the relation for additive drag becomes,

$$C_{Da} = \frac{D_a}{P_{T_0} A_C} = \frac{P_0}{2P_{T_0} R_L^2} \sum_{j=2}^L \left( \frac{P_j}{P_0} - \frac{P_{j-1}}{P_0} - 2 \right) \left( R_j^2 - R_{j-1}^2 \right) \quad (4.17)$$

where,

$$\frac{P_j}{P_0} = \frac{P_1}{P_0} \left[ \frac{(P/P_T)_j}{(P/P_T)_1} \right]$$

The summation index  $j$  refers to a particular ray originating at the cone and passing within boundaries formed by the initial shock and the cone surface. Integration begins at the shock wave and ends with the ray  $L$  which intersects the cowl lip. Note that thermodynamic properties are constant along each ray.

Additive drag charts are presented in Figures 4 - 33 through 4 - 44. Each figure consists of two design charts derived from Reference 6. The first of the pair shows the variation of mass-flow-ratio with flight Mach number and lip position parameter  $\lambda_s$ . Once mass-flow-ratio has been determined, the second chart may be entered to obtain theoretical additive drag coefficient. Each set of curves corresponds to a given spike semi-vertex angle  $\theta_{R1}$ .

Since the analysis makes no provision for a detached terminal shock, additive drag coefficients obtained from Figures 4 - 33 to 4 - 44 are rigorous for critical or supercritical inlet operation only. Subcritical conditions may be approximated by entering the second chart of the set at the desired inlet mass-flow-ratio.

A double-cone spike configuration has been investigated and the results available to date are presented in Appendix D. While additive drag design charts have not been obtained, there are some aspects of the analysis that should be noted.

Flow over the forward cone is purely conical, hence, the path of the stagnation streamline in this region can be obtained from Equation (4.17). The aft cone (actually a truncated cone) generates a curved conical shock wave as shown in Figure 4 - 45. Flow properties downstream of the curved shock are non-uniform and do not satisfy conical flow equations. Region 2 (defined in Figure 4 - 45) flow is determined by the method of characteristics. The stagnation streamline may be defined in this region by tracing its path through the flow net in a stepwise manner similar to that used in conical flow. Additive drag is calculated by integrating numerically the pressure difference ( $P_{local} - P_0$ ) acting on the streamline.

#### 4.4 Terminal Shock Wave Position

Numerous simplifying assumptions are employed to facilitate theoretical additive drag calculations, each of which serve to degrade the estimate in varying degrees. Terminal shock wave position is one such assumption. Often a terminal wave can stand large distances ahead of the inlet entrance. The high pressure region behind this wave can increase the ramp drag contribution to additive drag appreciably above that obtained with an "attached" shock approximation. An extensive examination of simple concepts for predicting the shape and position of detached shock waves (Reference 7) has shown that a method proposed by Moeckel yields satisfactory results at supersonic speeds. This technique will be presented below and its influence on theoretical additive drag will be illustrated.

A terminal shock wave must stand ahead of the inlet lip when supersonic flow exists just upstream of the inlet entrance and duct air demand is below the critical value. A method for estimating shock location and shape as a function of mass flow that is spilled over the cowl is derived from Reference 8. It is assumed that the form of the shock between its foremost point and its sonic point is adequately represented by an hyperbola asymptotic to the free-stream Mach lines. Also, spillage is assumed to occur two-dimensionally — in the X-Y plane as shown in Figure 4 - 46 and locally two-dimensional in the case of an axisymmetric inlet.

Figure 4 - 46 presents the terms used in a two-dimensional calculation. The coordinate  $Y_m$  denotes the free-stream location of the streamline that separates the mass entering the inlet from that passing over the cowl. The intersection of this streamline with the detached shock wave is assumed to be the origin of the hyperbolic portion of that shock wave. In order to determine the quantity  $Y_s/Y_{sb}$ , the continuity equation is applied to the fluid passing the sonic line. The area  $A_s$  of Figure 4 - 46 must be determined such that spilled air can pass through it at sonic conditions. In most cases the cowl lip will be quite sharp, hence, the sonic point on the cowl lip can coincide with the leading edge. Using these criteria, the expression for the location of the vertex of the detached shock wave becomes:

$$\frac{\Delta X}{Y_{sb}} = \frac{\Delta X}{Y_{lip}} = \left( 1.0 - \frac{MFR}{MFR_{max}} \right) \left( C + B \cdot \sin(\delta_s) \right) \left( 1.0 - B \cdot \cos(\delta_s) \right)^{-1} \quad (4.18)$$

where,

$\delta_s$  = flow direction behind the shock angle  $\phi_s$  for which sonic velocity exists downstream at  $M_0$

$$B = (P_{T0}/P_{Ts})_c \cdot A^*/A_0$$

$\left( \frac{P_{T0}}{P_{Ts}} \right)_c$  = total pressure recovery at the centroid of the flow passing the sonic line

$$C = B \cdot \left( B \cdot \tan(\phi_s) - \sqrt{B^2 \cdot \tan^2(\phi_s) - 1.0} \right)$$

$$B = \sqrt{M_0^2 - 1.0}$$

The pressure recovery  $(P_{T0}/P_{Ts})_c$  varies with terminal shock strength and hence the Mach number ahead of the terminal shock. If the inlet flow field is not constant at large distances ahead of the lip (i.e., an isentropic compression surface), shock location must be iterated to reflect the proper value of  $(P_{T0}/P_{Ts})_c$ .

Spillage about an axially symmetric inlet tends to vary from locally two-dimensional at high inlet mass flow to that obtained with a closed body of revolution at low inlet flow. Since relatively low spillage values are of greatest interest, it is assumed that flow near the cowl lip is two-dimensional. With the same reasoning, a two-dimensional value of total-pressure recovery at the mass centroid (see definition of  $(P_{T0}/P_{Ts})_c$  above) will be used. Detachment distance for an axisymmetric inlet takes the form:



$$\frac{\Delta X}{Y_{sb}} = \frac{\Delta X}{Y_{lip}} \cdot \sqrt{\frac{1.0 - \left(\frac{MFR}{MFR_{max}}\right)^2 B \cos(\delta_s)}{1.0 - B \cos(\delta_s)}} \left[ C + \tan(\delta_s) \right] - C \frac{MFR}{MFR_{max}} - \tan(\delta_s) \quad (4.19)$$

where the terms employed in Equation (4.19) are as defined above or in Figure 4 - 46.

Experimental correlation with this shock prediction technique for blunt nosed bodies is presented in Reference 7. Figure 4 - 47 shows the results of this compilation and the excellent agreement provided by such an approach.

Reference 9 has incorporated the Moeckel technique in theoretical additive drag calculations for an isentropic compression surface. A comparison of additive drag coefficients obtained with a detached terminal shock and with a "fixed" (attached) terminal shock is presented in Figure 4 - 48. Discrepancies resulting from an attached normal shock assumption at reduced mass-flow-ratios are apparent in this figure.

#### 4.5 Additive Drag Correction

The full value of theoretical additive drag is rarely charged as a penalty to the airplane at low supersonic or subsonic speeds. Cowl and sideplate suction created by the spilled air tends to reduce the drag penalty. A method for correcting theoretical additive drag estimates is discussed in this section and a correlation factor  $K_{ADD}$  is presented.

External drag varies with inlet mass-flow-ratio since the amount of air spilled around the inlet affects the pressure field acting on the external surfaces of the airplane. To eliminate the effect of varying mass-flow-ratio on external drag levels, an external drag corresponding to the maximum inlet mass-flow-ratio is chosen to represent the external drag of the airplane. This reference drag level is assumed to remain constant with mass-flow-ratio. A correction is then applied to theoretical additive drag, to account for the change in the external pressure field with mass-flow-ratio.

Figure 4-49 illustrates the correction technique employed to obtain corrected additive drag. Curve X is the sum of model external drag and corrected additive drag obtained from a wind tunnel axial balance reading. The drag reading has been corrected for buoyancy effects, sting effects, base drag and internal drag. If a reference mass flow ratio is now established, the term  $K_{ADD}$  can be defined as

$$K_{ADD} = \frac{(\text{Corrected } D_{ADD}) \text{ MFR} - (\text{Corrected } D_{ADD}) \text{ Ref. MFR}}{(\text{Theoretical } D_{ADD}) \text{ MFR} - (\text{Theoretical } D_{ADD}) \text{ Ref. MFR}}$$

or

$$K_{ADD} = \frac{\Delta \text{Corrected } D_{ADD}}{\Delta \text{Theoretical } D_{ADD}}$$

Now from Figure 4-49, we see that

$$\begin{aligned} X_{\text{MFR}} - X_{\text{REF}} &= \left[ (\text{Corrected } D_{ADD}) \text{ MFR} + (\text{EXTERNAL-MODEL})_{\text{MFR}} \right] - \\ &\quad - \left[ (\text{Corrected } D_{ADD})_{\text{REF}} + (\text{EXTERNAL-MODEL})_{\text{REF}} \right] \end{aligned}$$

If the model is designed correctly, the external model drag will be independent of MFR; therefore,

$$X = \Delta \text{Corrected } D_{ADD}$$

or

$$K_{ADD} = \frac{X}{\Delta \text{Theoretical } D_{ADD}} = \frac{D_a'}{D_a}$$

To find the total aircraft drag the corrected additive drag is simply adjusted to pass through the reference external drag point, determined by aerodynamic force model tests, as shown in Figure 4-54. As Figure 4-54 points out, the reference MFR for the external drag point will not necessarily be the same as the reference MFR used in the  $K_{ADD}$  calculations. In many cases, the reference MFR for the external drag point is  $\text{MFR}=1$  in which case the corrected additive curve will probably (for inlets with external compression) have to be extrapolated to  $\text{MFR} = 1$ .

The corrected additive drag can be expected to vary with external cowl shape, cowl length, lip shape and thickness, ramp geometry, sideplate geometry and thickness, flight condition and mass-flow-ratio.

Several experimental studies have been conducted in an effort to empirically evaluate these interrelated effects. References 10-13 contain the results of these studies. Reference 10 concentrated

on two dimensional inlets with design Mach numbers from 2.2 to 3.0. Reference 11 was limited to development of the A3J-1 inlet. Reference 12 looked at a small matrix of open nose inlets while Reference 13 contains a fairly large matrix of inlets including open nose, single cone axisymmetric, F-4 type two dimensional and a uniquely designed opposed ramp two dimensional inlet. Each of these reports is useful in showing the effects of varying various inlet component configurations. Several curves from Reference 13 are included as Figures 4-55 through 4-58 to illustrate these effects. It should be pointed out here that extreme care should be exercised in using absolute drag values and in comparing data from one of these reports to another because of variation in definitions and differences in test procedures and equipment. It is felt that each report is, however, consistent within itself so that the effects of the various geometry changes are correctly evaluated. As might be expected, the correction factor  $K_{ADD}$  reflects the influence of these variables. Unfortunately,  $K_{ADD}$  is also affected by the approximations used in the calculation of theoretical additive drag.

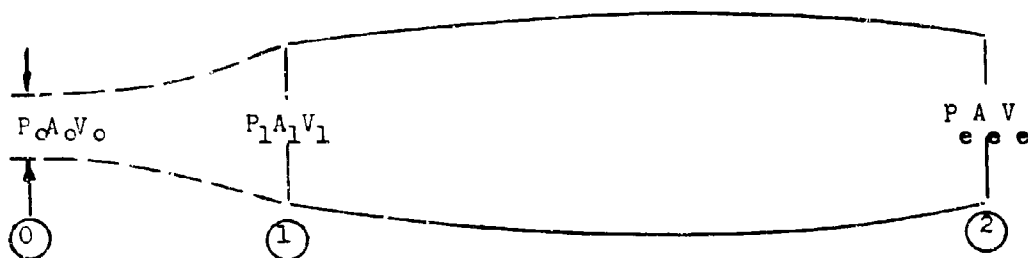
The preceding discussion leads one to believe that additive drag correction is complex beyond use. Until the spillage phenomenon is better understood, an uncompromising approach to actual additive drag prediction may be, in fact, useless. However, if a compromise is acceptable, an approximate additive drag correction obtained from Reference 11 data is available.

Data from Reference 11 is shown in Figures 4-50 through 4-52. These data are presented in the form illustrated in Figure 4-49 and are used to define the variation of  $K_{ADD}$  with Mach number found in Figure 4-53. Note here that the correction factor is invariant with mass-flow-ratio. While the  $K_{ADD}$  factors of Reference 10 do vary with mass-flow-ratio, a number of "average" correction factors were selected from this data and superimposed on Figure 4-53. As indicated, Reference 10 data shows good agreement with the 0.125 scale A-5A inlet model data of Reference 11.

At present, the additive drag correction factor shown in Figure 4-53 is the most useful correlation available. Although it is not completely rigorous, it should yield acceptable actual additive drag estimates for preliminary inlet analyses.

## References

1. Cibulkin, Merwin, Theoretical and Experimental Investigation of Additive Drag, NACA Report 1187, 1954.
2. Fradenburgh, D. A. and Wyatt, D. D., Theoretical Performance Characteristics of Sharp-Lip Inlets at Subsonic Speeds, NACA Report 1193, 1954.
3. Hess, J. L. and Smith, A. M. O., General Method for Calculating Low Speed Flow about Inlets, AGARD Specialists' Meeting on Aerodynamics of Powerplant Installation, October 25-27, 1965.
4. Smith, A. M. O. and Pierce, J., Exact Solution of the Neumann Problem, Calculation of Non-Circulatory Plane and Axially Symmetric Flows about or Within Arbitrary Boundaries, Douglas Aircraft Company, Incorporated, Report ES 26988, April, 1958.
5. Hermann, R., Supersonic Inlet Diffusers and Introduction to Internal Aerodynamics, Minneapolis-Honeywell Regulator Company, Minneapolis, 1956.
6. Mascitti, V. R., Charts of Additive Drag Coefficient and Mass-Flow-Ratio for Inlets Utilizing Right Circular Cones at Zero Angle of Attack, NACA TN D-3434, 1966.
7. Love, D. G., A Reexamination of the Use of Simple Concepts for Predicting the Shape and Location of Detached Shock Waves, NACA TN 4170, 1957.
8. Moeckel, W. T., Approximate Method for Predicting Form and Location of Detached Shock Waves Ahead of Plane or Axially Symmetric Bodies, NACA TN 1921, 1949.
9. Wires, R. W., Inlet Methodology, North American Rockwell Corporation, January, 1968.
10. Peterson, M. W. and Tamplin, G. C., Experimental Review of Transonic Spillage Drag of Rectangular Inlets, AFAPL-TR-66-30, 1966.
11. 0.125 Scale A3J-1 Inlet-Duct Model Results and Analysis of Lewis Test No. 2003, NA60H-265. (Unpublished)
12. Peterson, M. W., and Tamplin, G. C., Open Nose Additive Drag Test Results at Subsonic and Transonic Speeds, North American Rockwell Corp., NA64-921, September 1964.
13. McVey, F. D., Rejeske, J. V., Phillips, E. V., et.al., Experimental Evaluation of Inlet Drag Characteristics in the Transonic Mach Number Range, McDonnell Douglas Corp., AFAPL-TR-68-119, November 1968.



1. Net thrust by definition is the rate of change of momentum between stations 0 and 2

$$F_N = mV_e + A_e (P_e - P_o) - mV_o - A_o (P_o - P_o)$$

2. Propulsive force actually felt by body is

$$F_{NE} = mV_e + A_e (P_e - P_o) - mV_1 - A_1 (P_1 - P_o)$$

3.  $mV_1 + A_1 (P_1 - P_o) \neq mV_o + A_o (P_o - P_o)$

4. The difference is a force increment in the drag direction, called Additive Drag.

FIGURE 4-1 Illustration of Meaning of Additive Drag

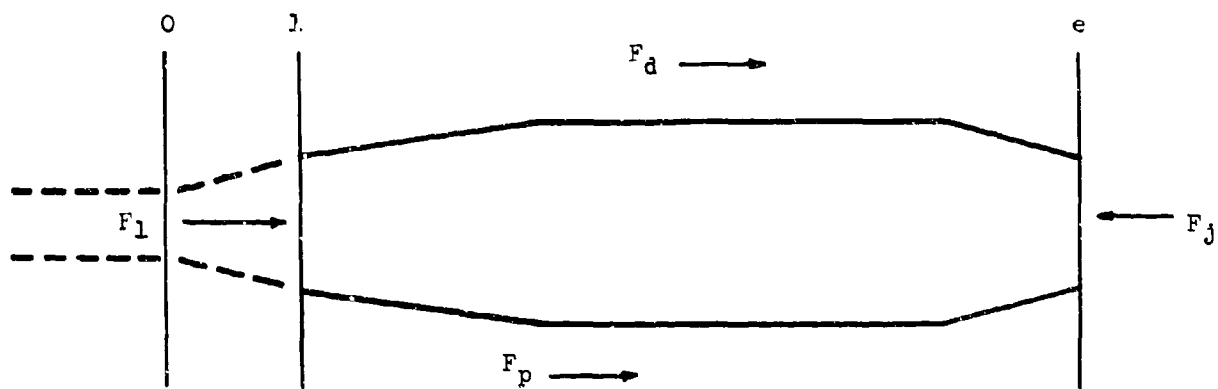


FIGURE 4-2. Schematic Representation of Forces Acting on a Typical Propulsion System — Using Stations 1 and e.

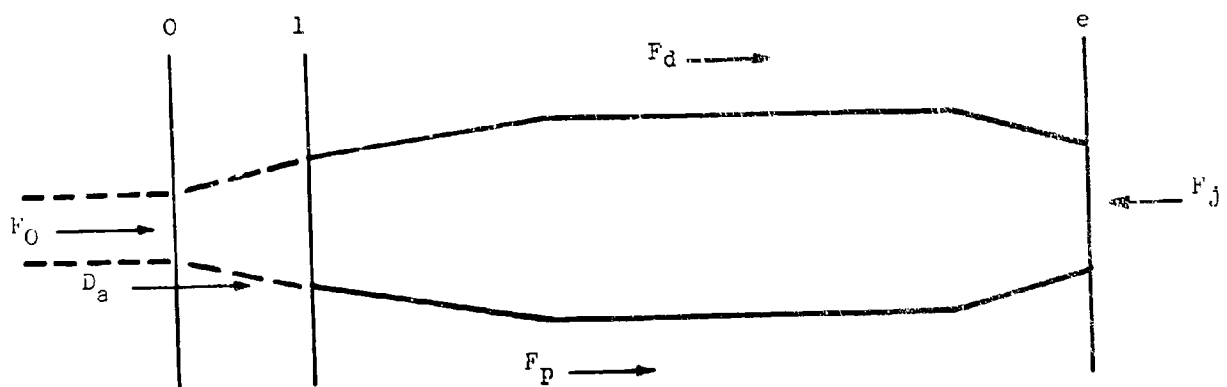


FIGURE 4-3. Schematic Representation of Forces Acting on a Typical Propulsion System — Using Stations 0 and e.

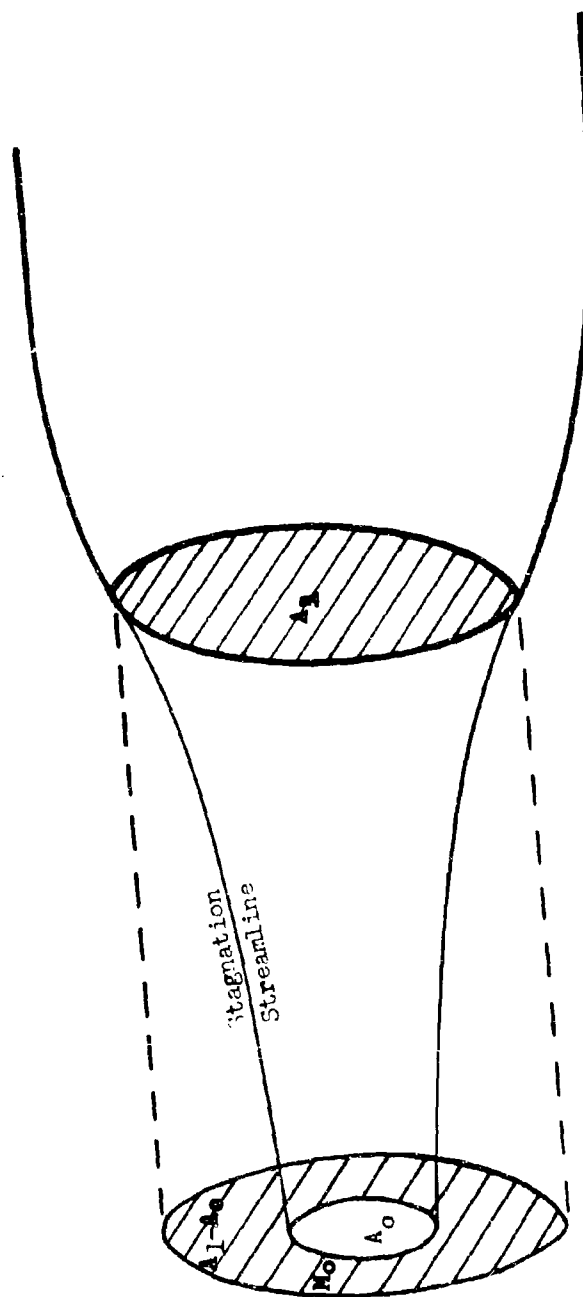


FIGURE 4-4. Illustration of Inlet Spillage



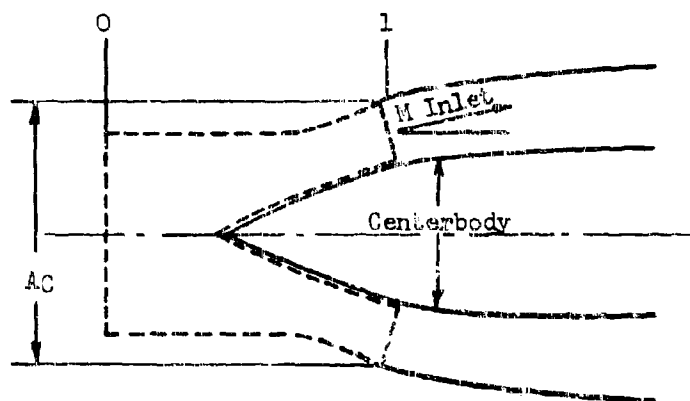


FIGURE 4-5. Illustration of a Control Volume Used to Calculate Additive Drag

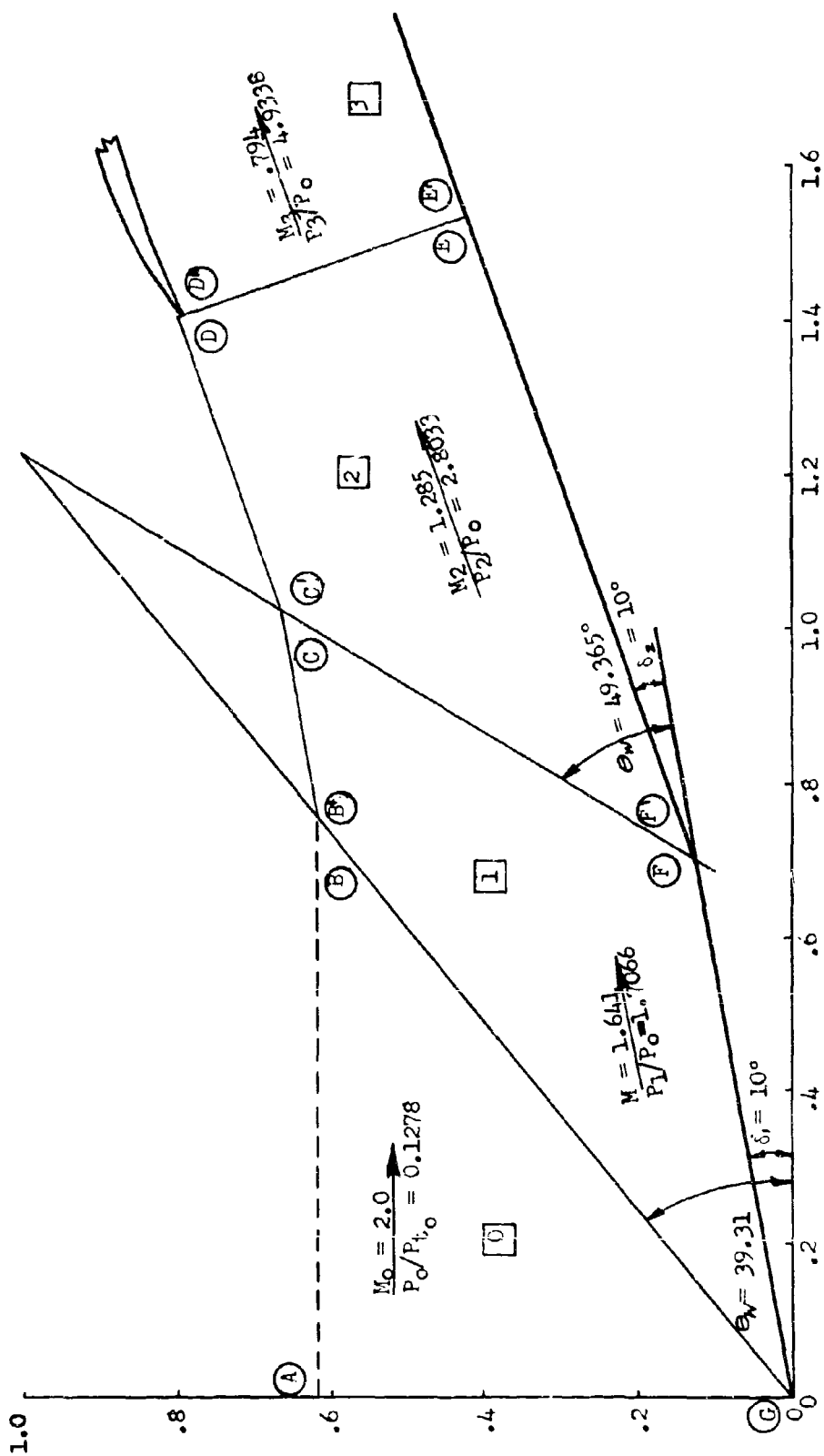
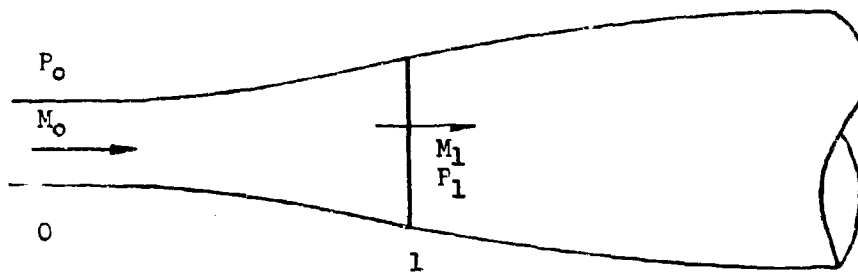
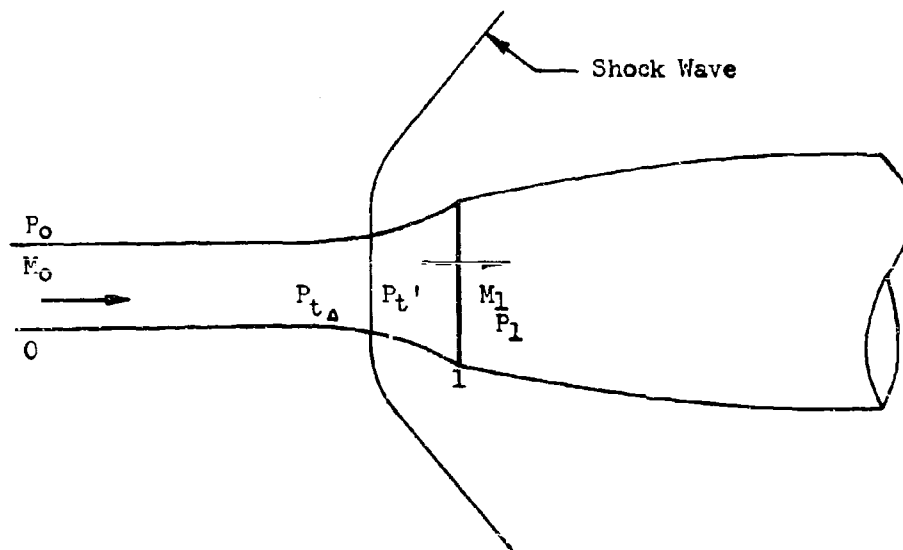


FIGURE 4-6. Example for Theoretical Additive Drag Calculation



Subsonic Operation



Supersonic Operation

FIGURE 4-7. Open Nose Inlet at Mass Flow Ratio Less Than 1.0

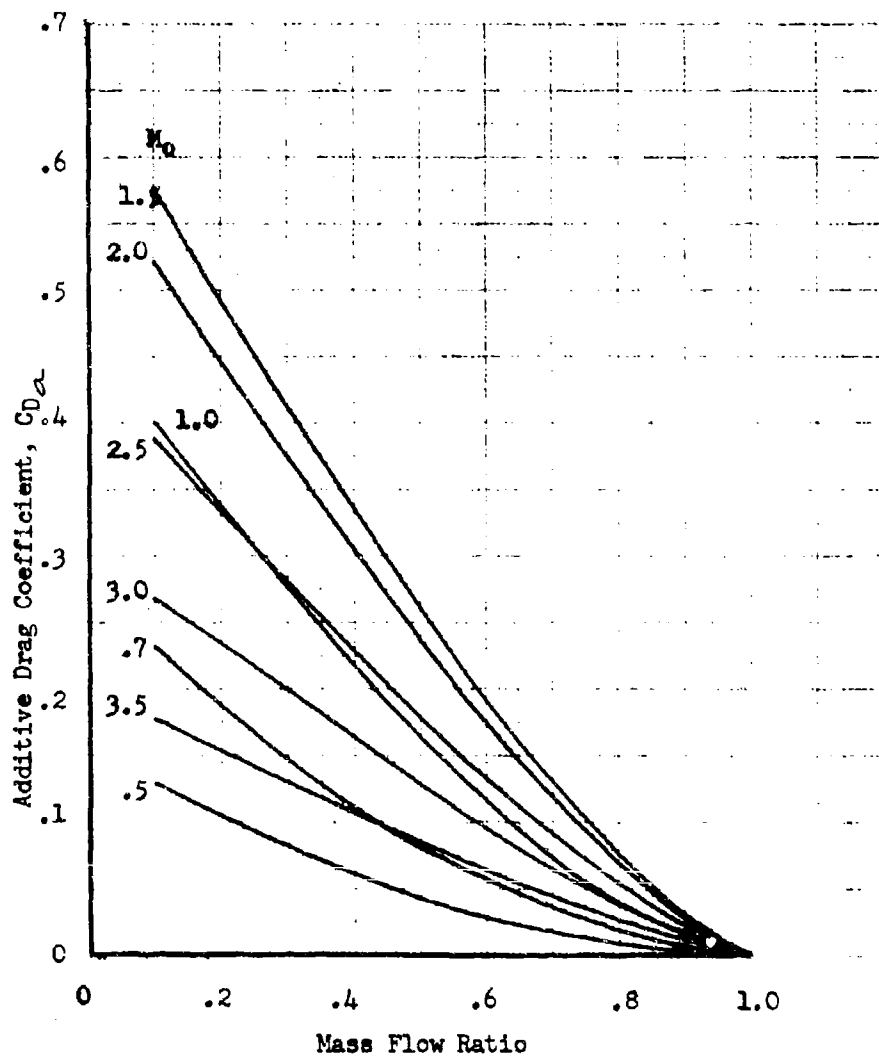


FIGURE 4-8. Theoretical Additive Drag Coefficient - Open Nose Inlet

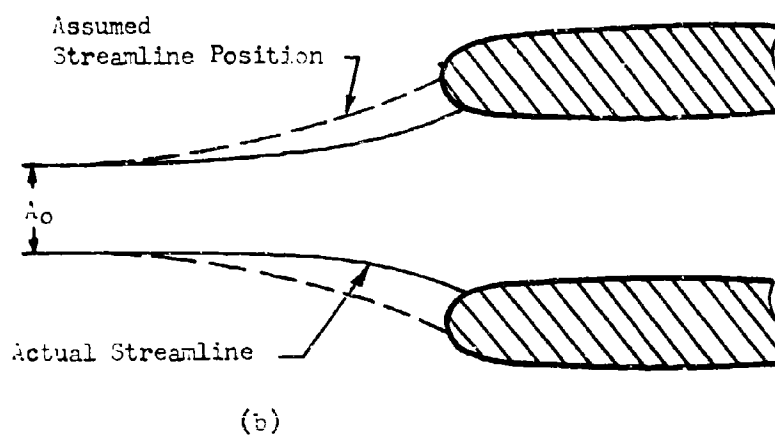
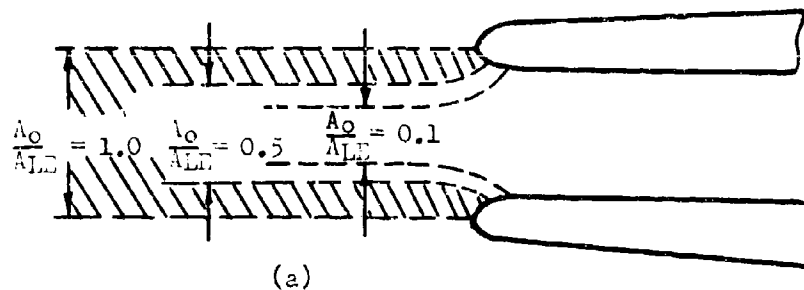


FIGURE 4-9. Illustration of Stagnation Point Movement With Mass Flow Variation for a Blunt-Lipped Inlet

(a) Stagnation Stream-Tube Area Variation

(b) Mathematical Approximation

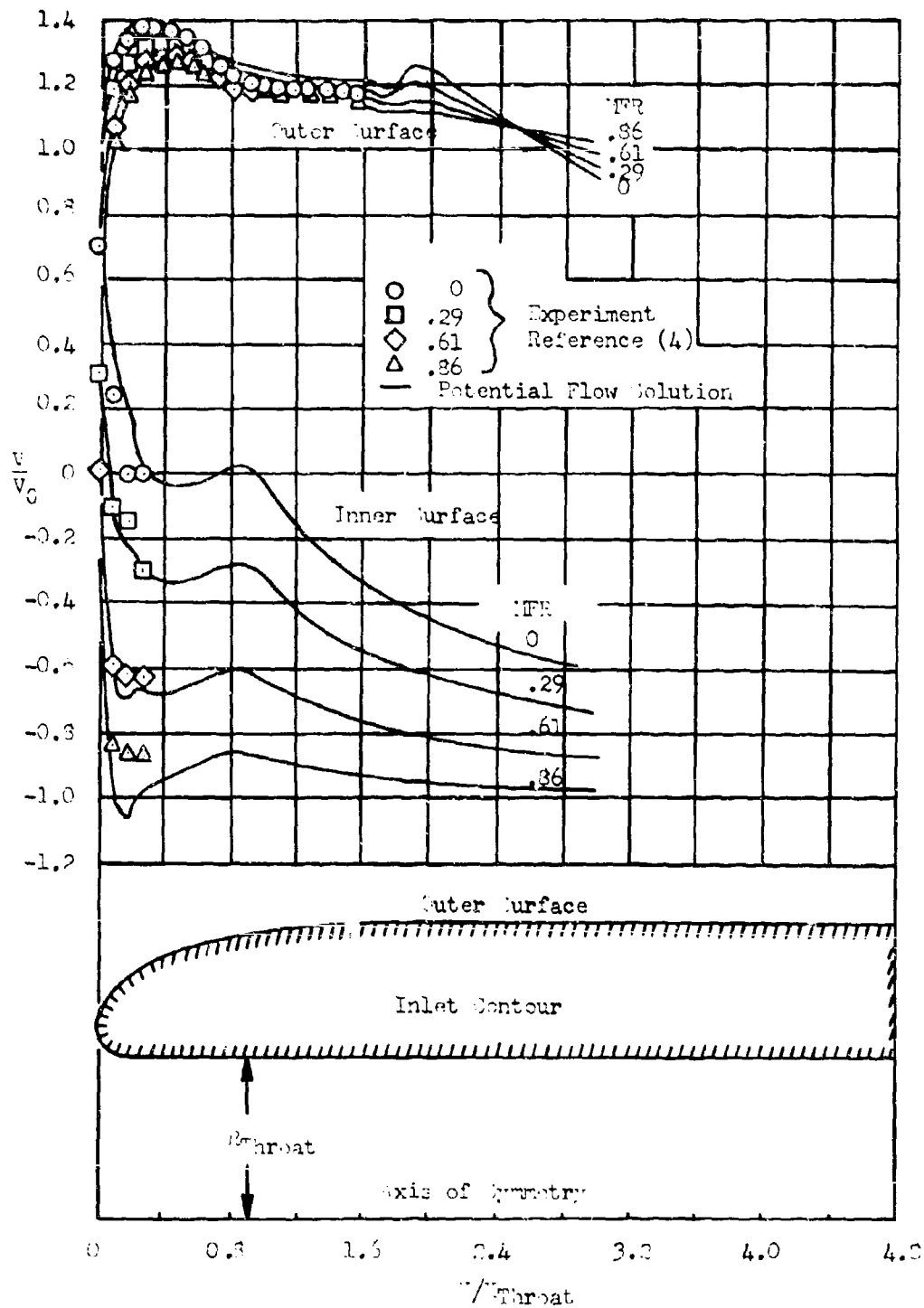
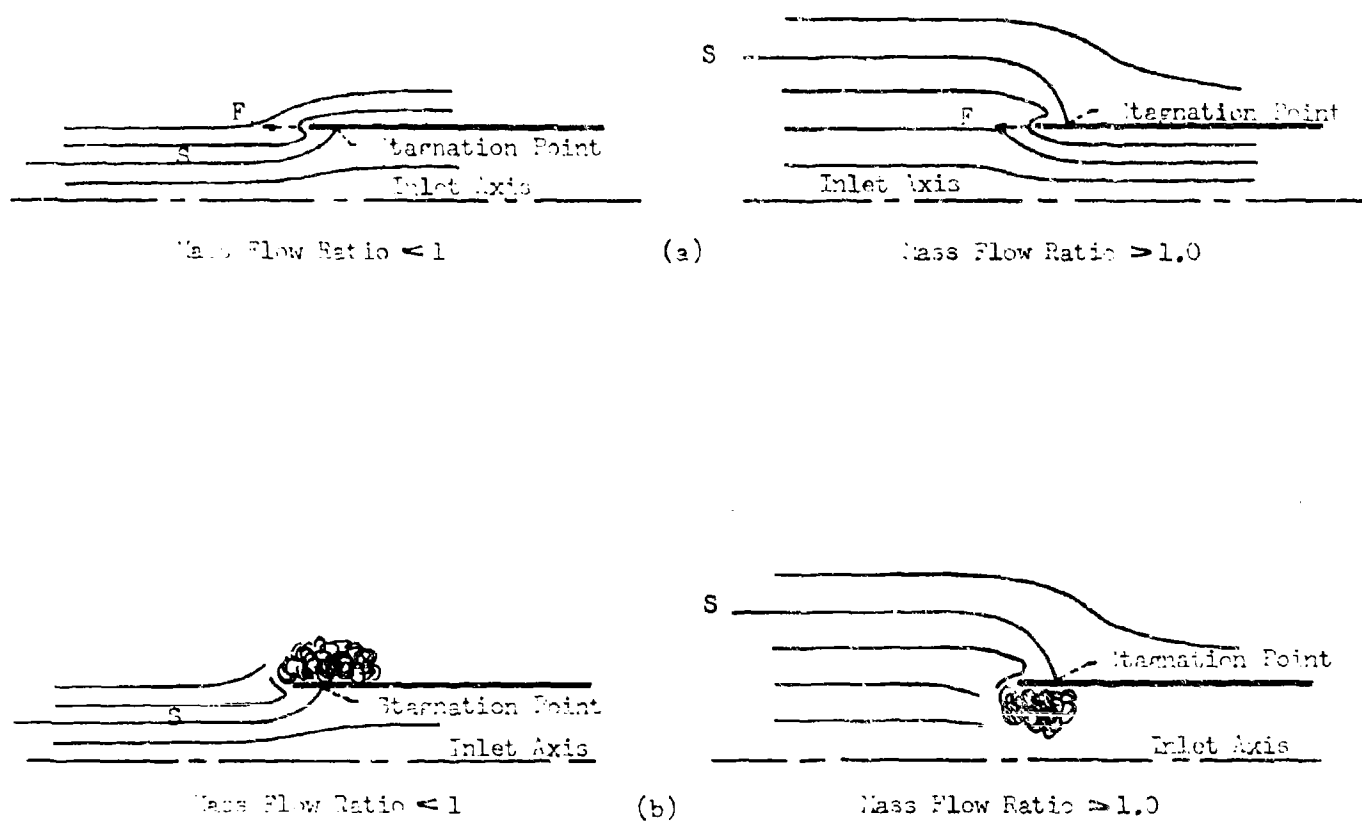


FIGURE 4-10. Example of Inlet Surface Velocity Distribution and Stagnation Point Movement for an Axisymmetric Inlet Potential Flow Simulation



- (a) Inviscid Potential Flow  
(b) Actual Flow

FIGURE 4-11. Flow Patterns for Sharp-Lip Inlet

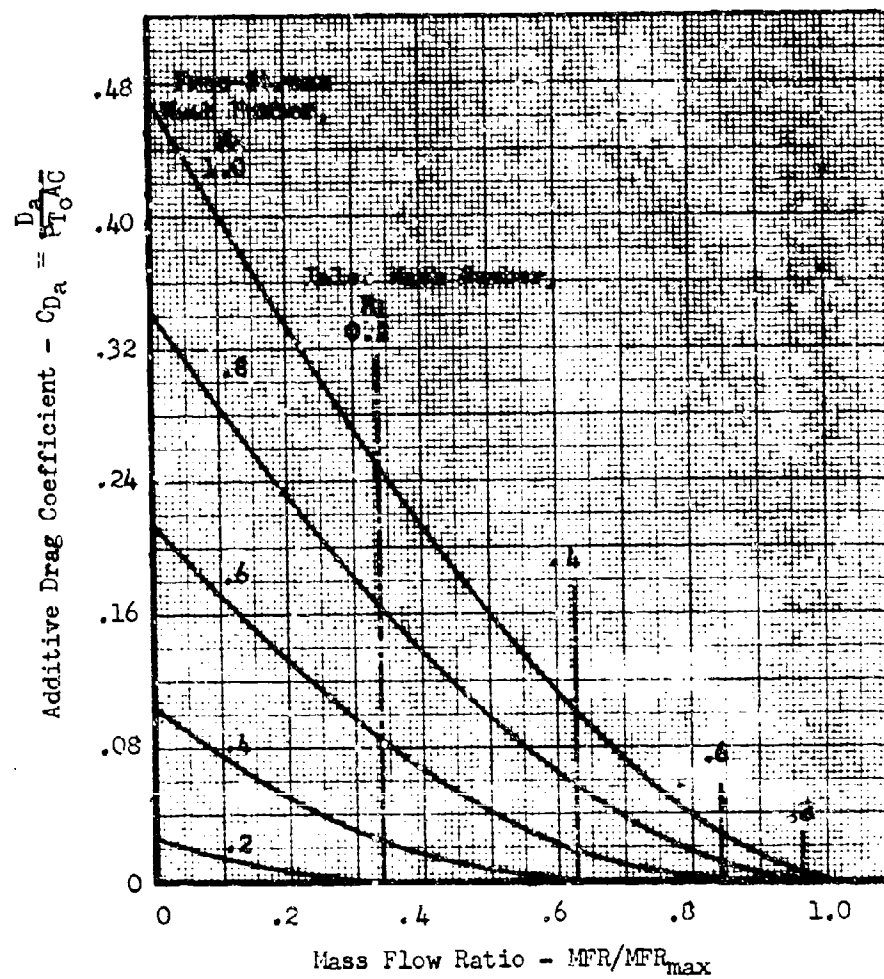


FIGURE 4-12. Theoretical Additive Drag for a Sharp Lip (Supersonic) Inlet Operating at Subsonic Speeds



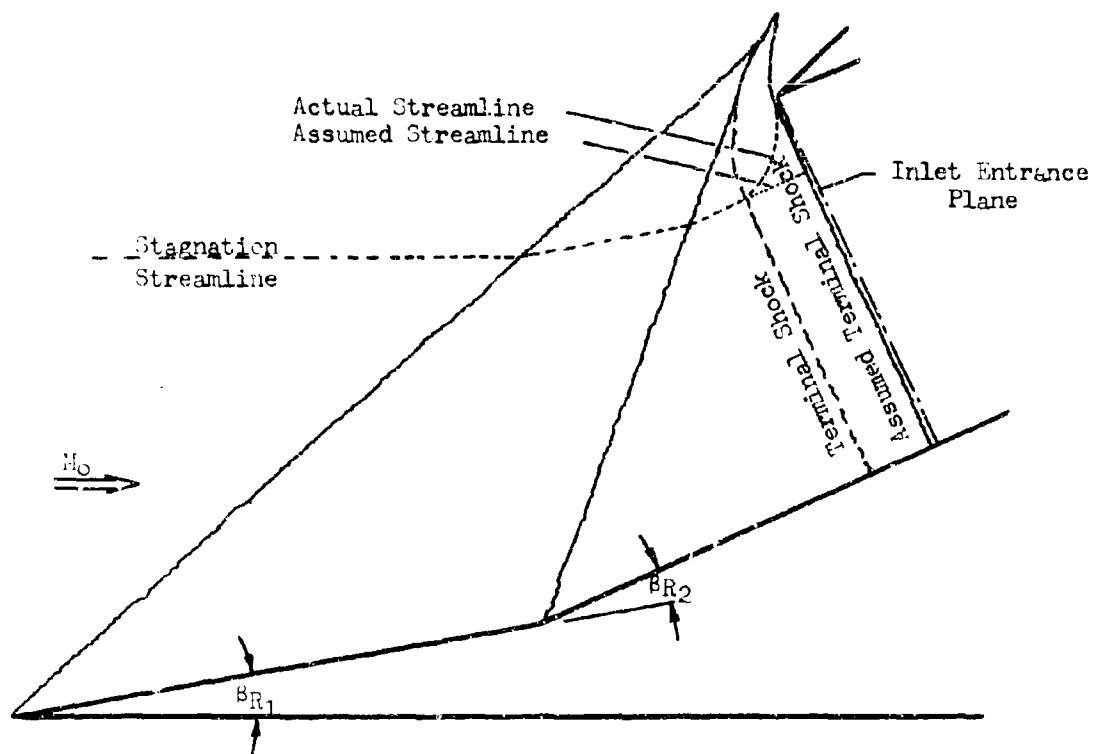


FIGURE 4-13. Illustration of Terminal Shock Wave Position and Approximation Used in Theoretical Additive Drag Calculations

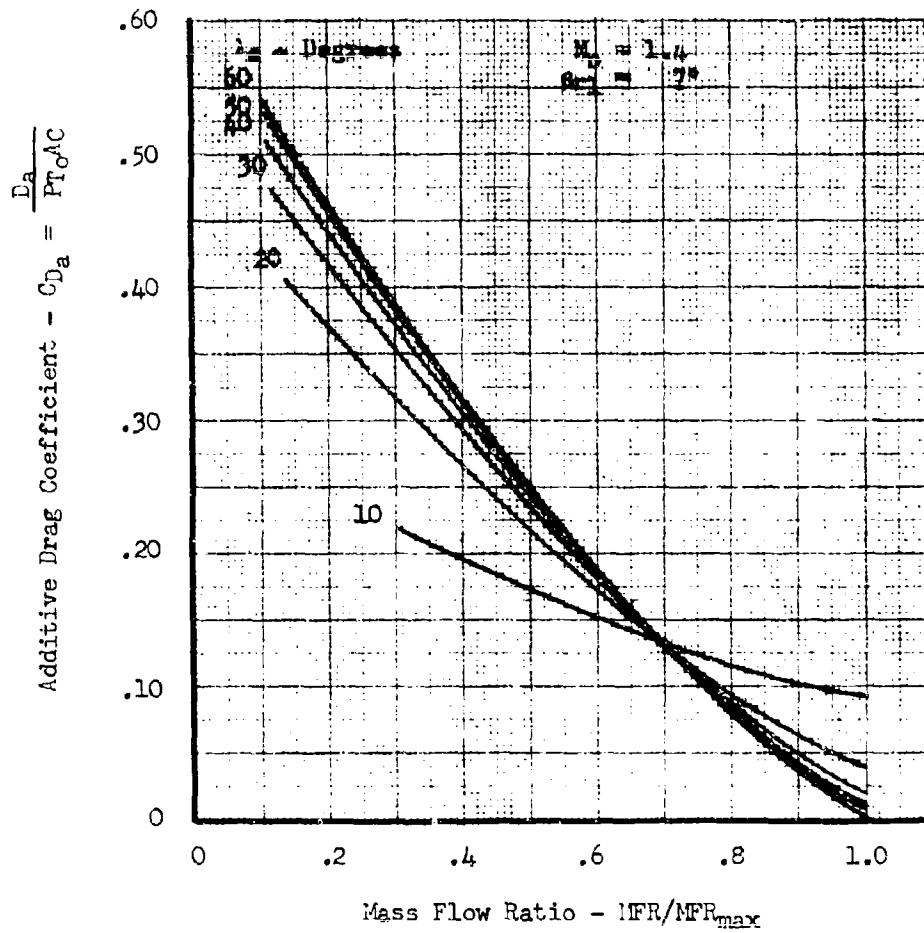


FIGURE 4-14. Theoretical Additive Drag Coefficient for 2-Shock, All-External Inlet or Mixed Compression Inlet with Single External Shock

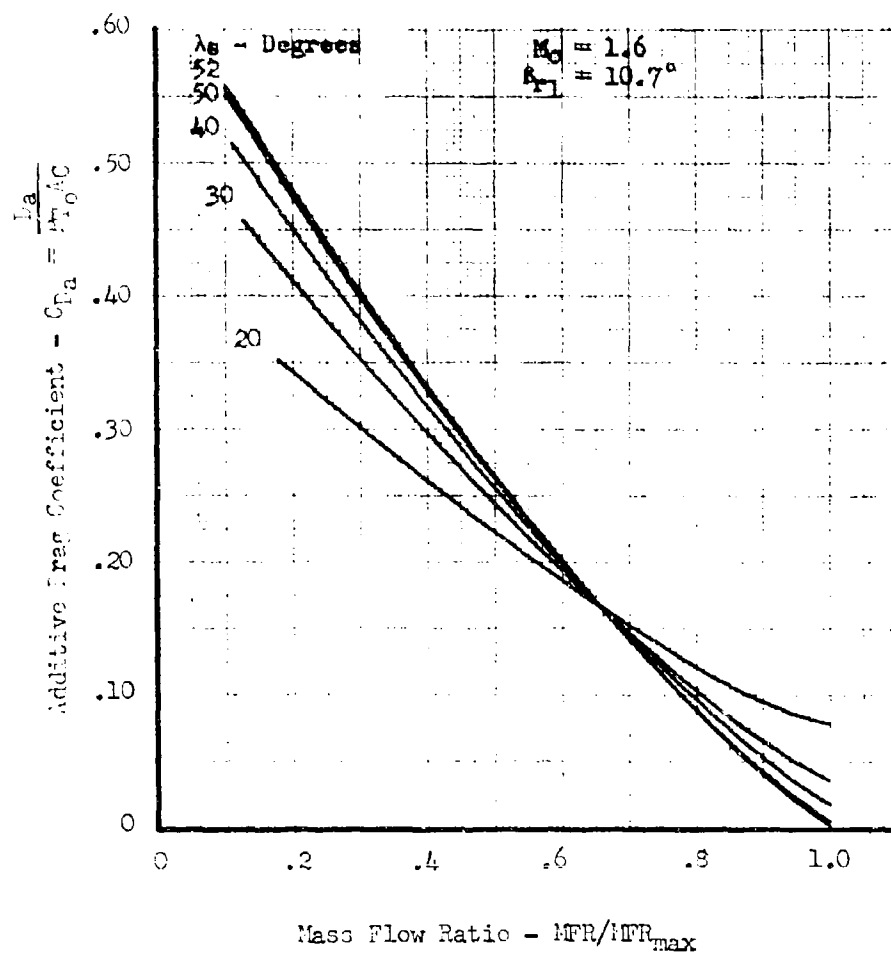


FIGURE 4-15. Theoretical Additive Drag Coefficient for 2-Shock, All-External Inlet or Mixed Compression Inlet with Single External Shock

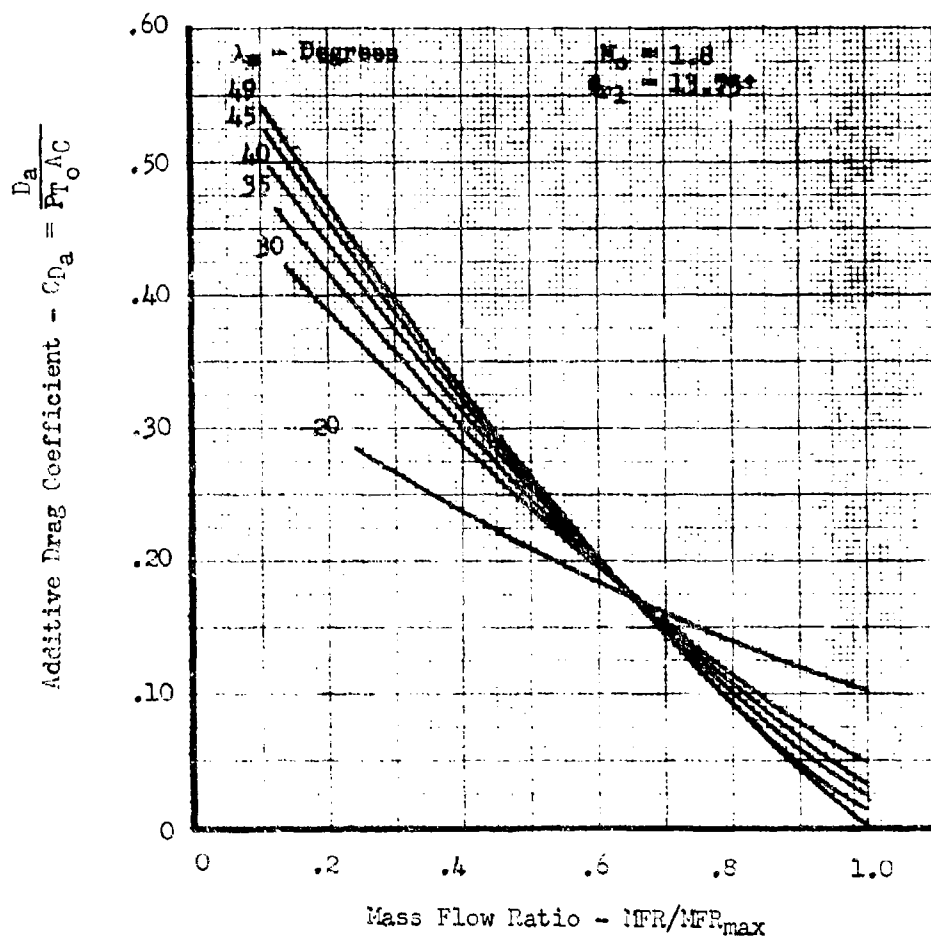


FIGURE 4-16. Theoretical Additive Drag Coefficient for 2-Shock, All-External Inlet or Mixed Compression Inlet with Single External Shock

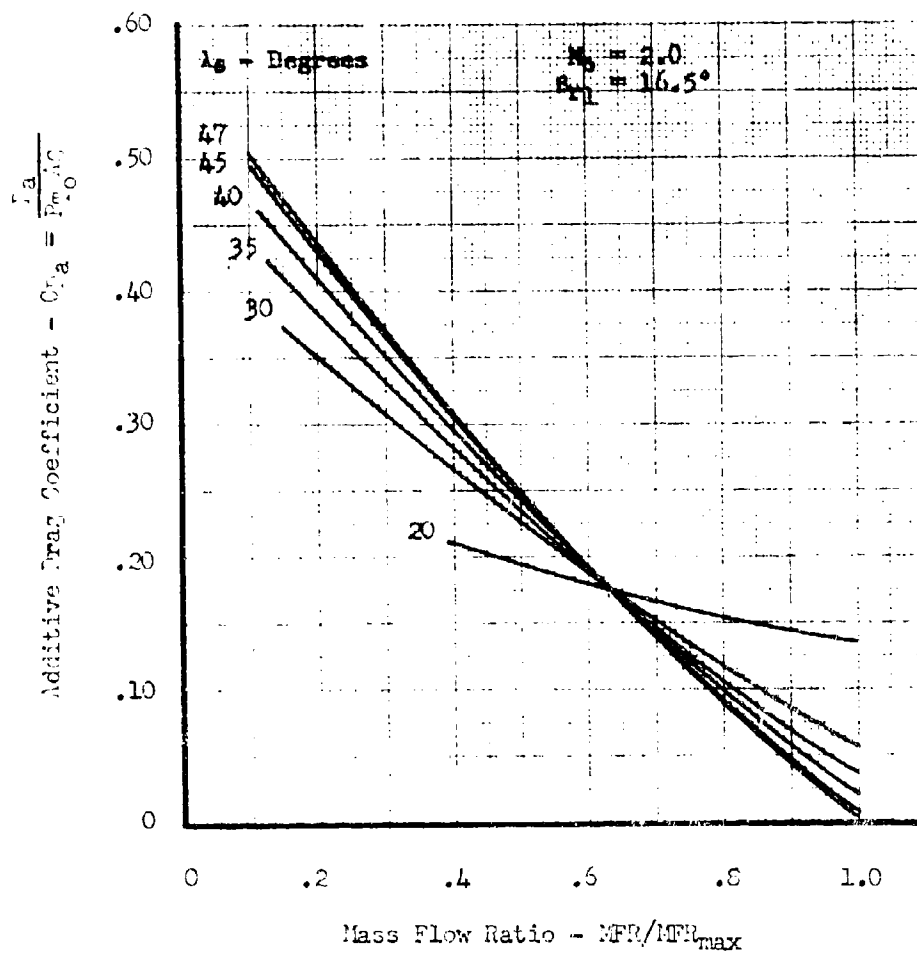


FIGURE 4-17. Theoretical Additive Drag Coefficient for 2-Shock, All-External Inlet or Mixed Compression Inlet with Single External Shock

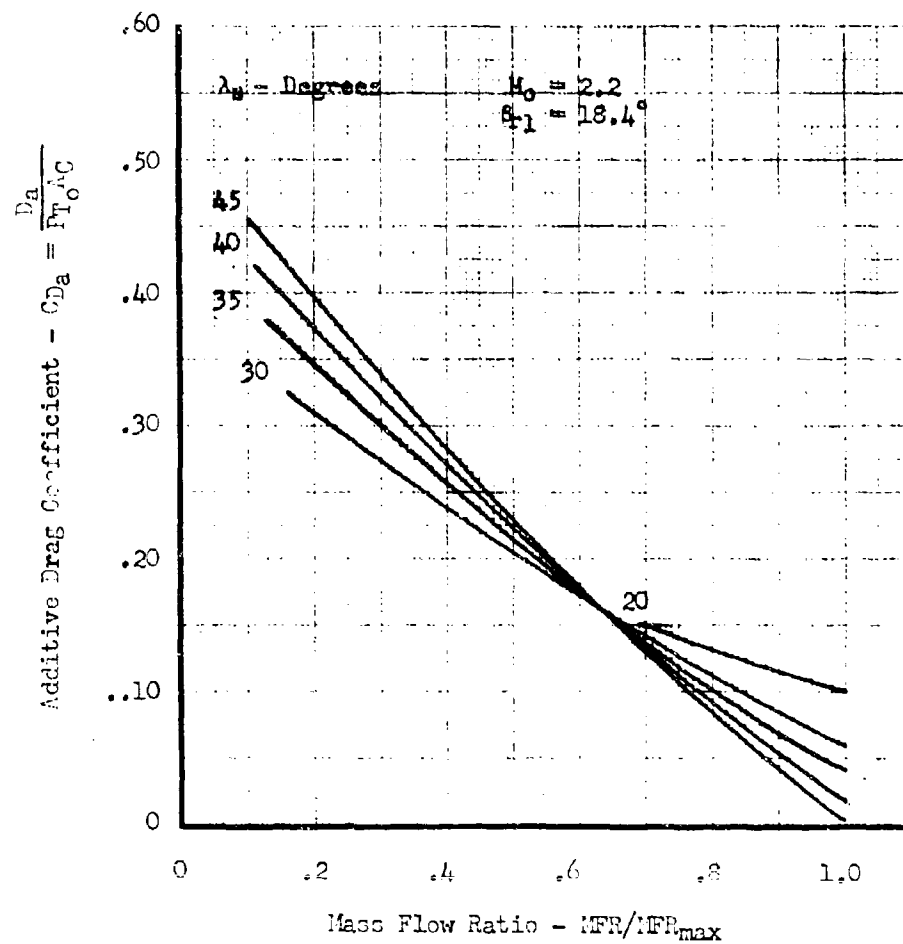


FIGURE 4-13. Theoretical Additive Drag Coefficient for 2-shock, All-External Inlet or Mixed Compression Inlet with Single External Shock

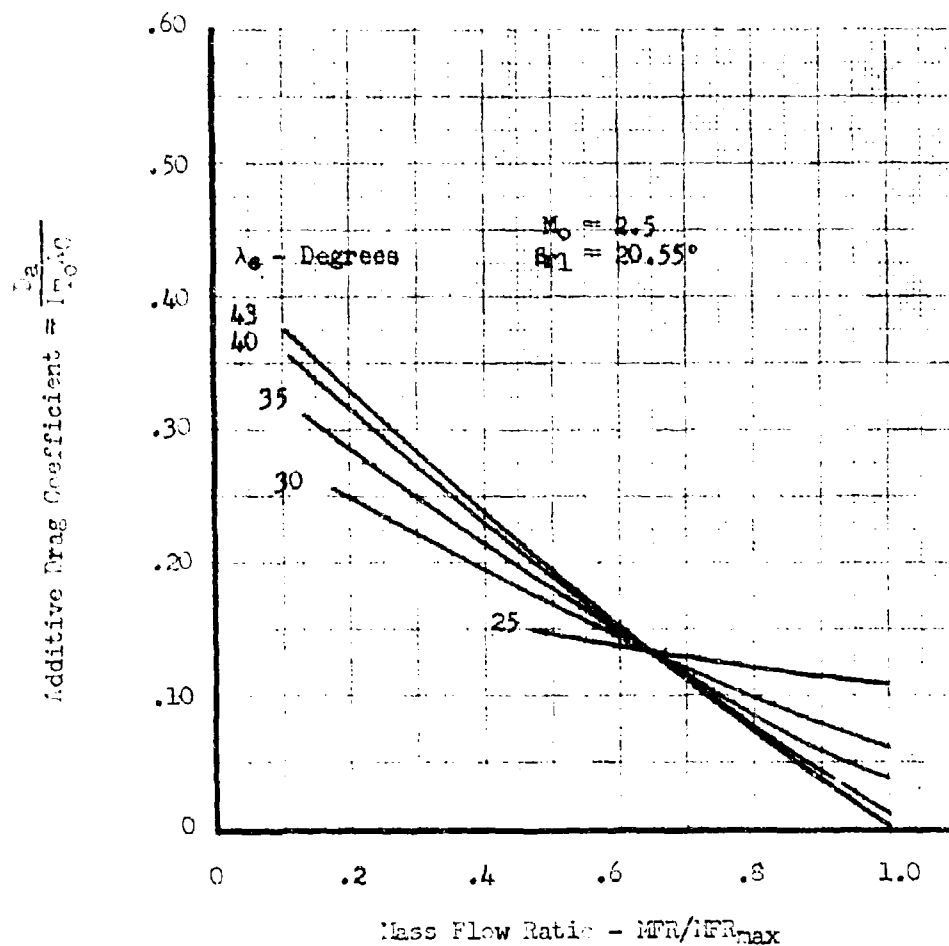


FIGURE 4-19. Theoretical Additive Drag Coefficient for 2-Shock, All-External Inlet or Mixed Compression Inlet with Single External Shock

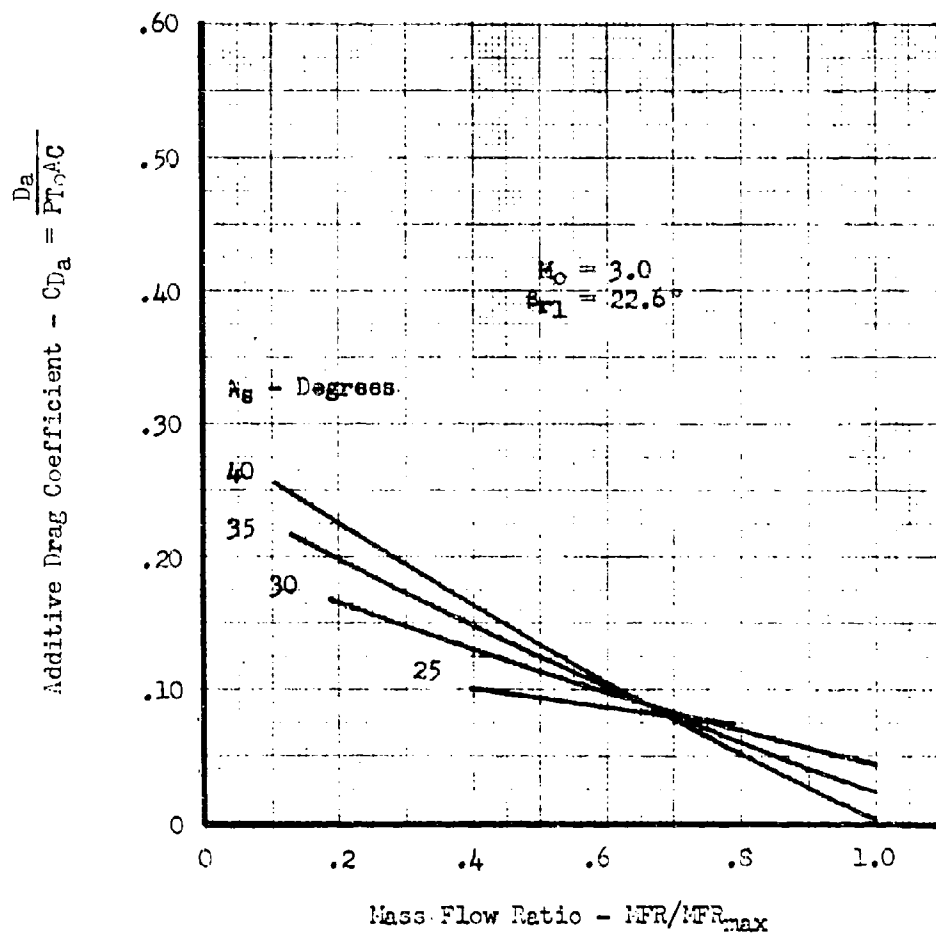


FIGURE 4-20. Theoretical Additive Drag Coefficient for 2-Shock, All-External Inlet or Mixed Compression Inlet with Single External Shock



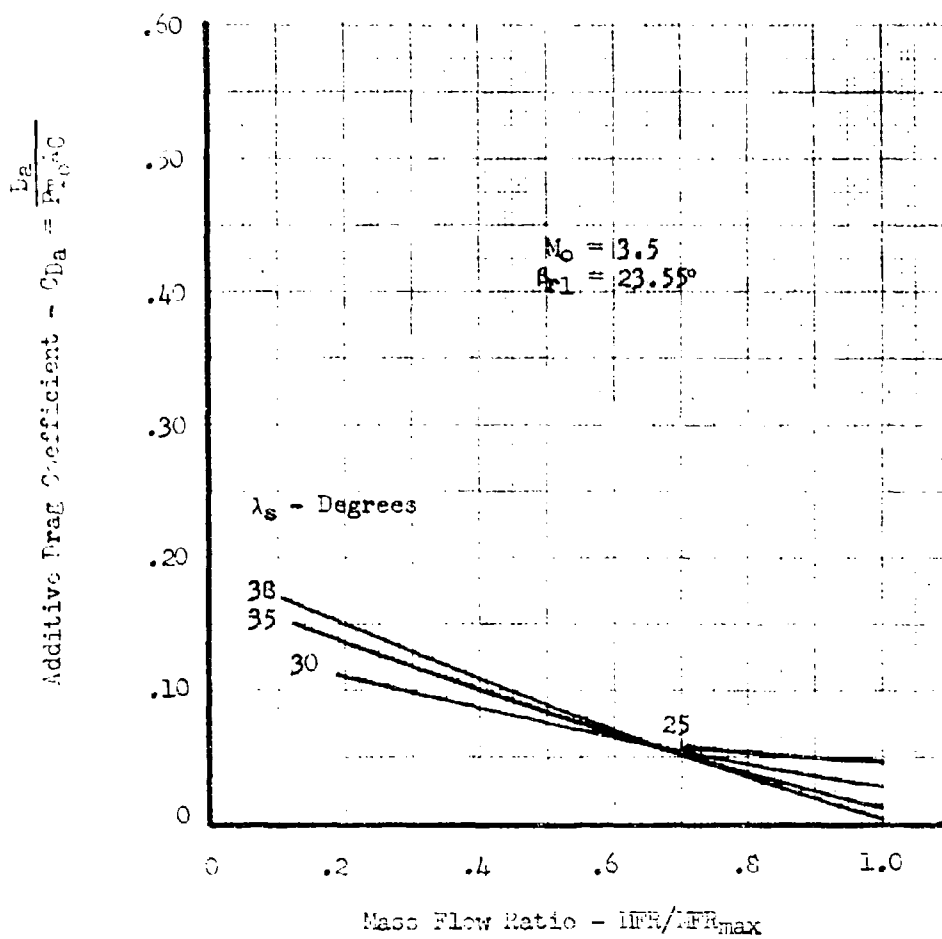


FIGURE 4-21. Theoretical Additive Drag Coefficient for 2-Shock, All-External Inlet or Mixed Compression Inlet with Single External Shock

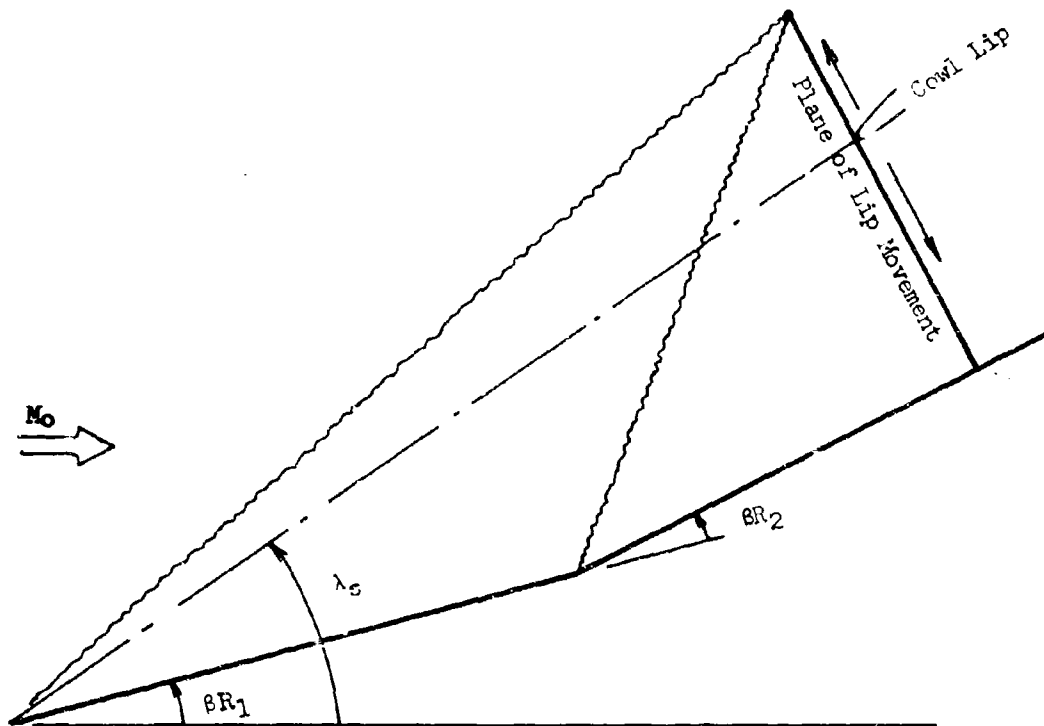


FIGURE 4-22. Illustration of 3-Shock Geometric Relationships

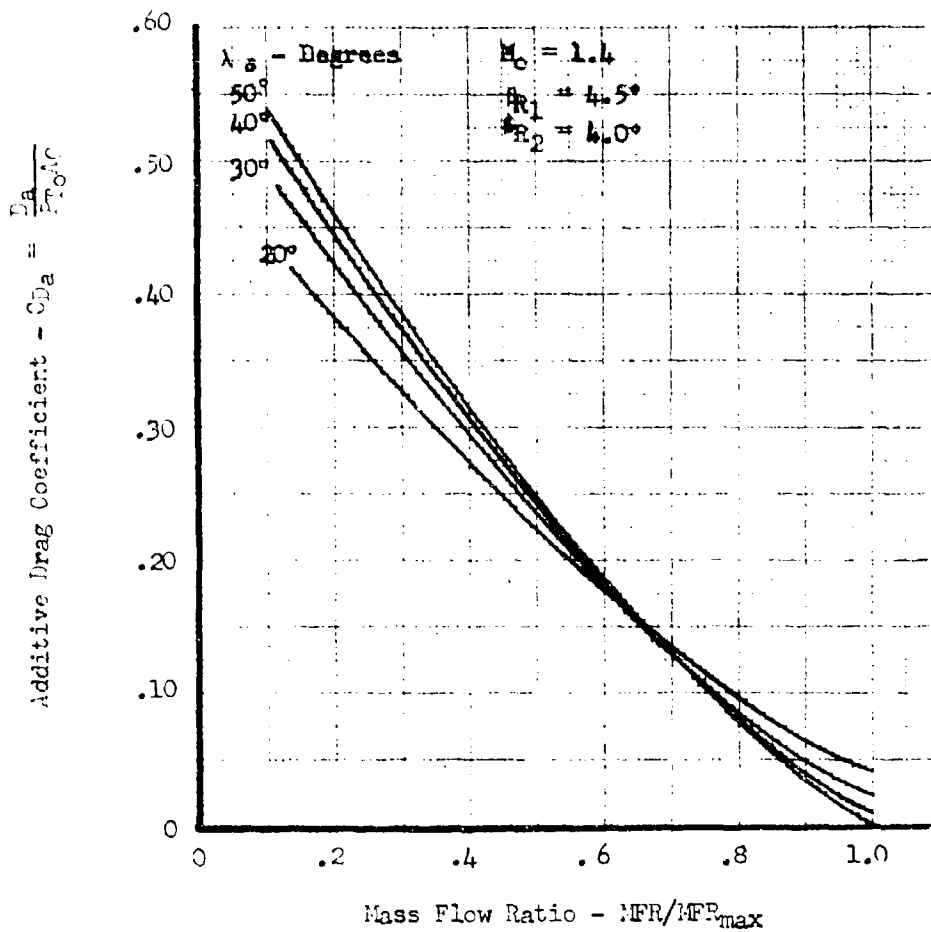


FIGURE 4-23. Theoretical Additive Drag Coefficient for 3-Shock, All-External Inlet or Mixed Compression Inlet with Two-External Shocks

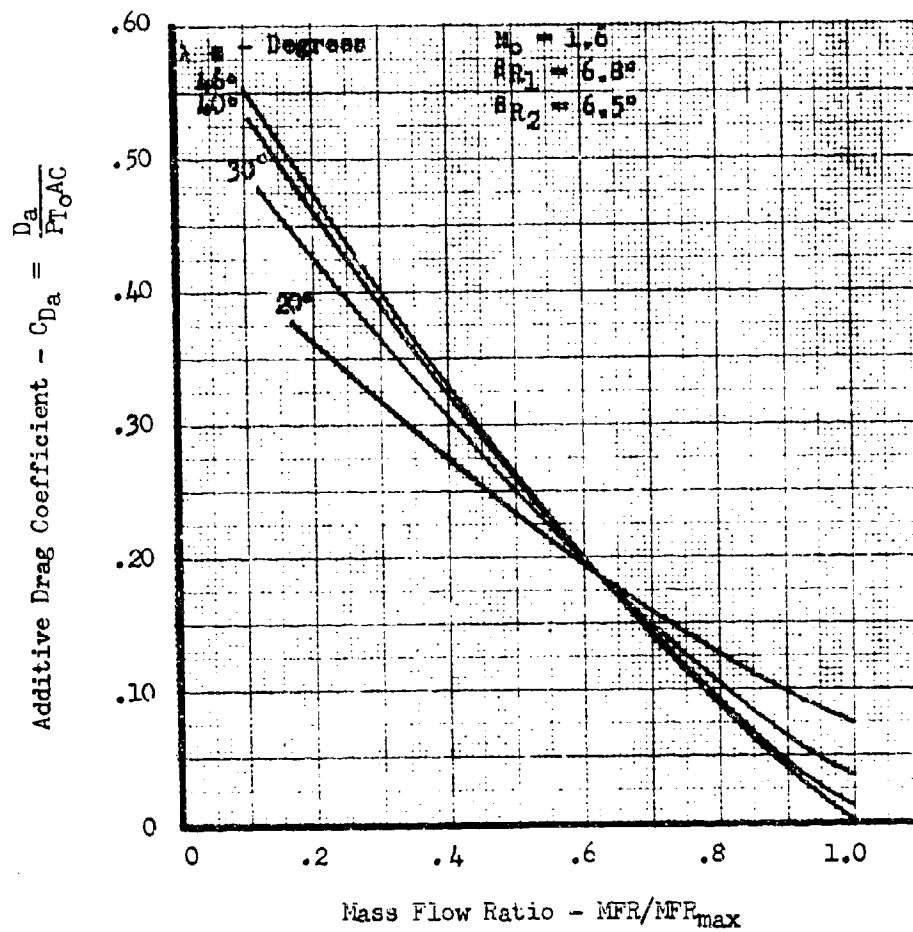


FIGURE 4-24. Theoretical Additive Drag Coefficient for 3-Shock, All-External Inlet or Mixed Compression Inlet with Two-External Shocks

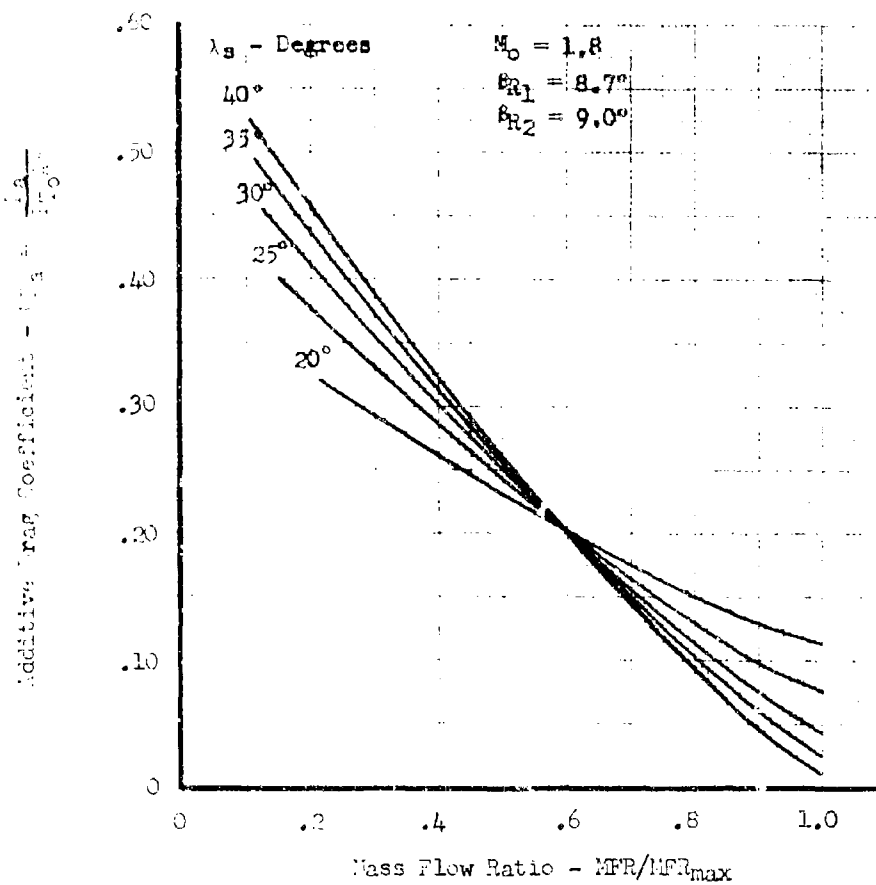


FIGURE 4-25. Theoretical Additive Drag Coefficient for 3-Shock, All-External Inlet or Mixed Compression Inlet with Two-External Shocks

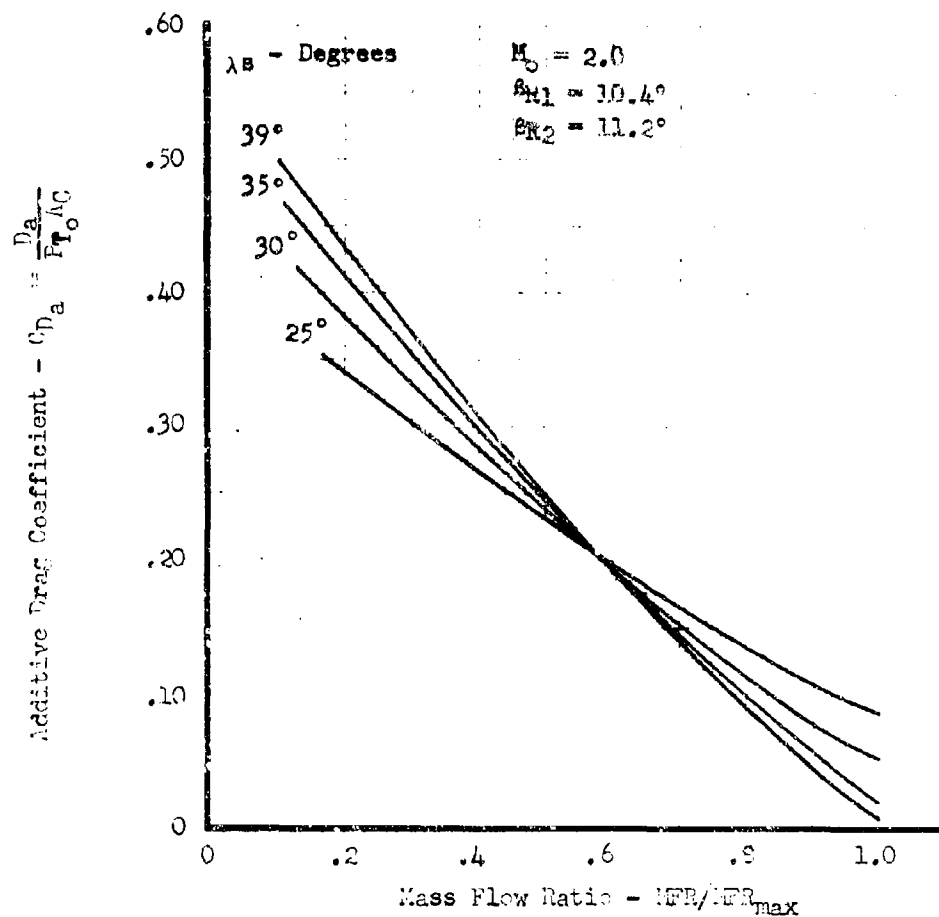
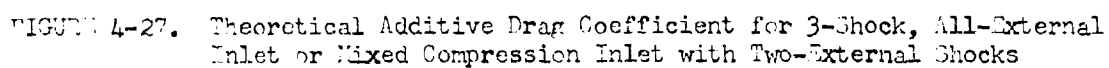


FIGURE 4-26. Theoretical Additive Drag Coefficient for 3-Shock, All-External Inlet or Mixed Compression Inlet with Two-External Shocks



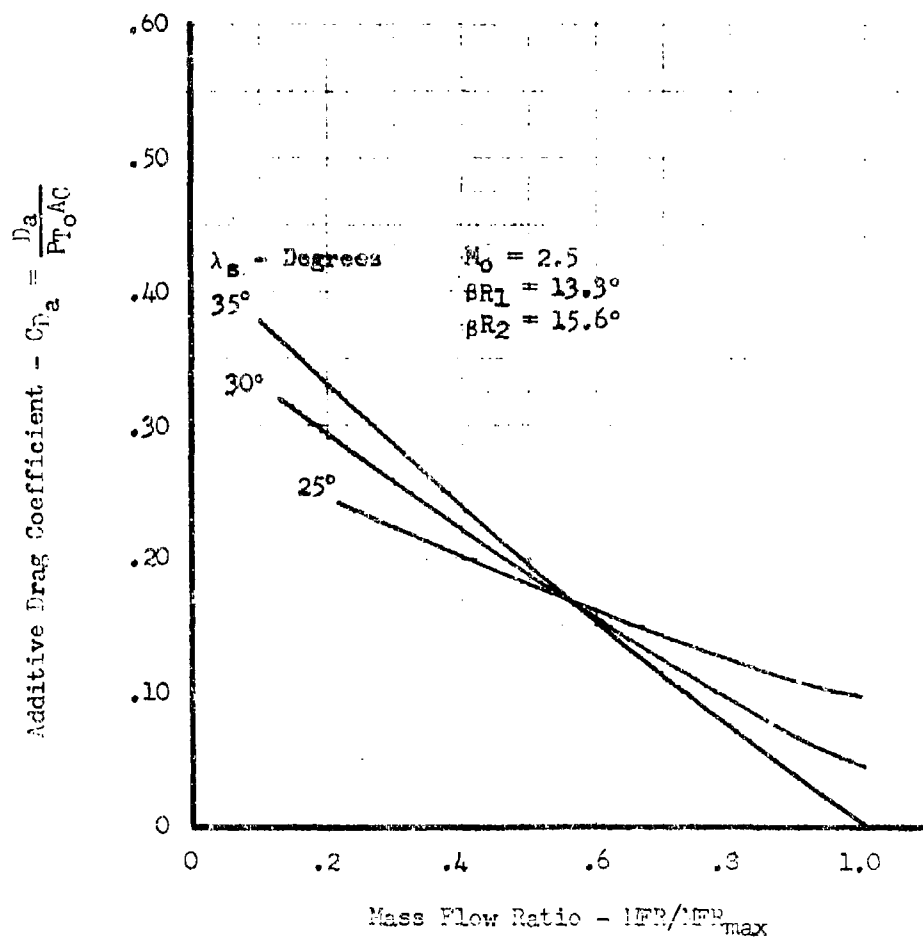


FIGURE 4-28. Theoretical Additive Drag Coefficient for 3-Shock, All-External Inlet or Mixed Compression Inlet with Two-External Shocks



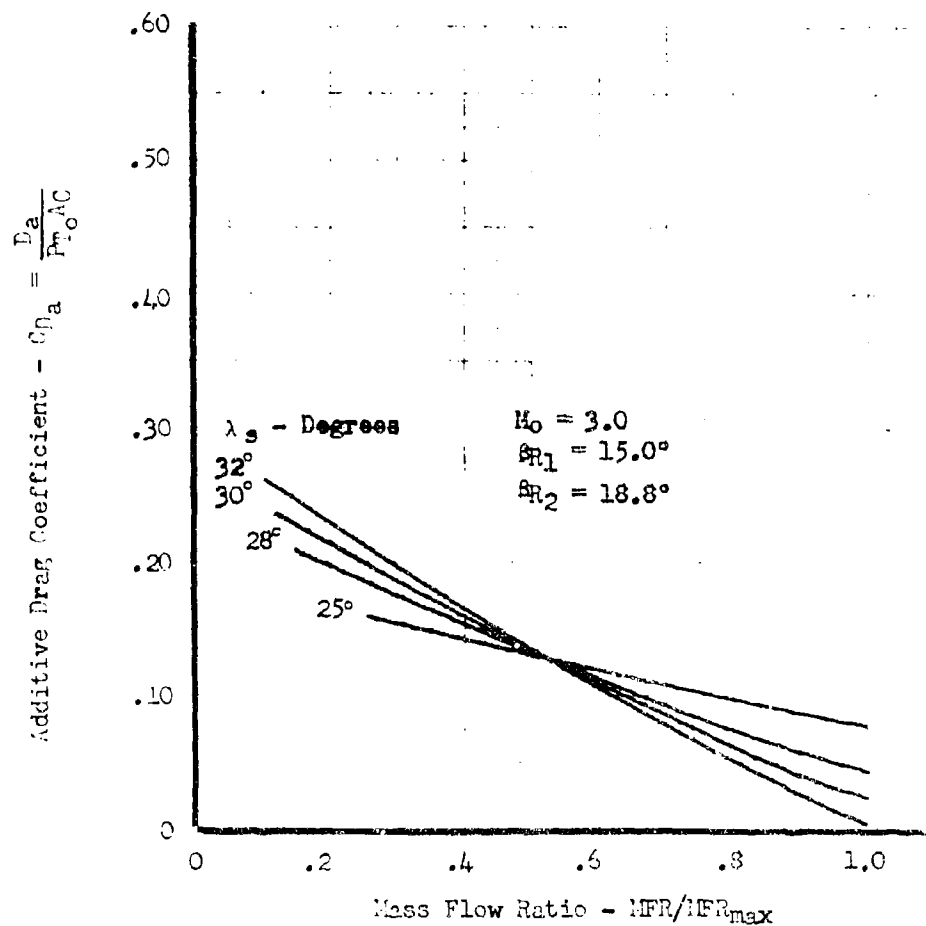


FIGURE 4-29. Theoretical Additive Drag Coefficient for 3-Shock, All-External Inlet or Mixed Compression Inlet with Two-External Shocks

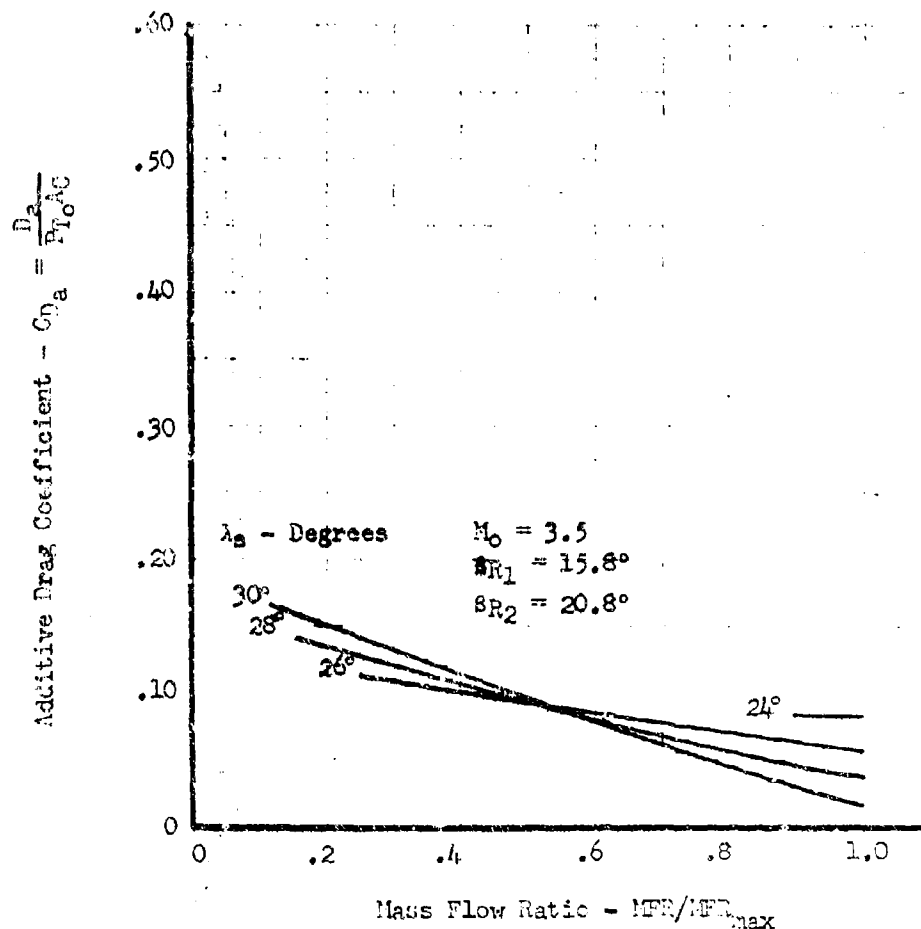


FIGURE 4-30. Theoretical Additive Drag Coefficient for 3-Shock, All-External Inlet or Mixed Compression Inlet with Two-External Shocks

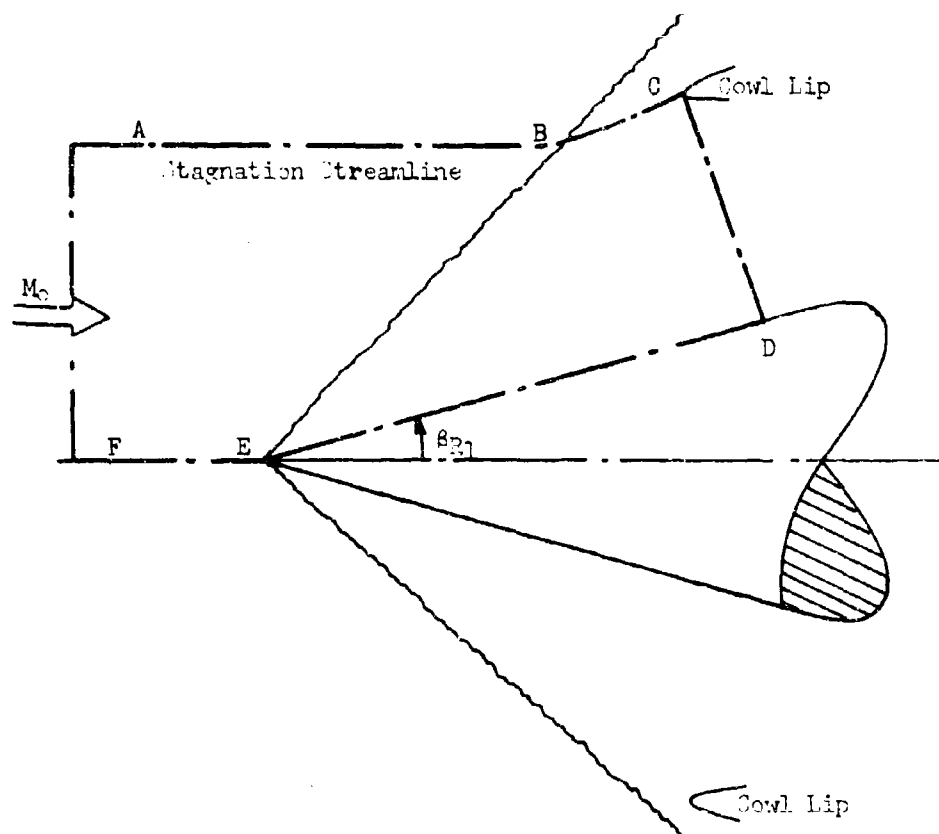


FIGURE 4-31. Illustration of Additive Drag Calculation Path for an Axisymmetric Inlet

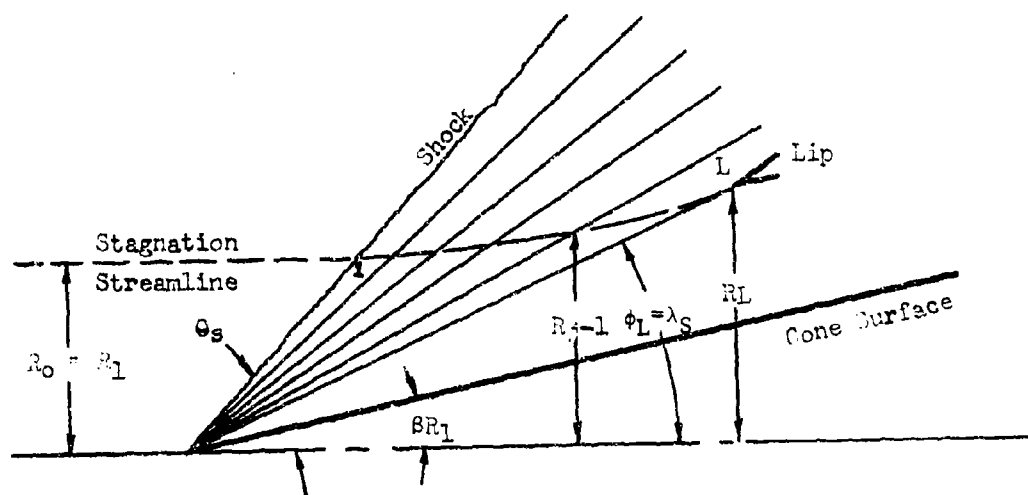


FIGURE 4-32. Diagram Showing Conical Flow Field Streamline Construction

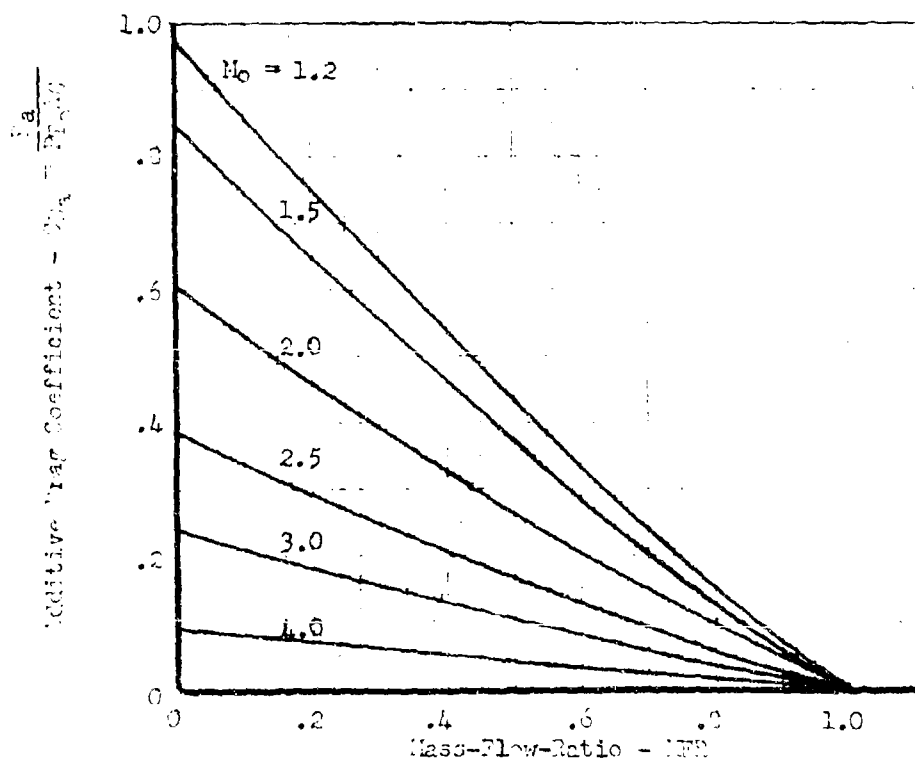
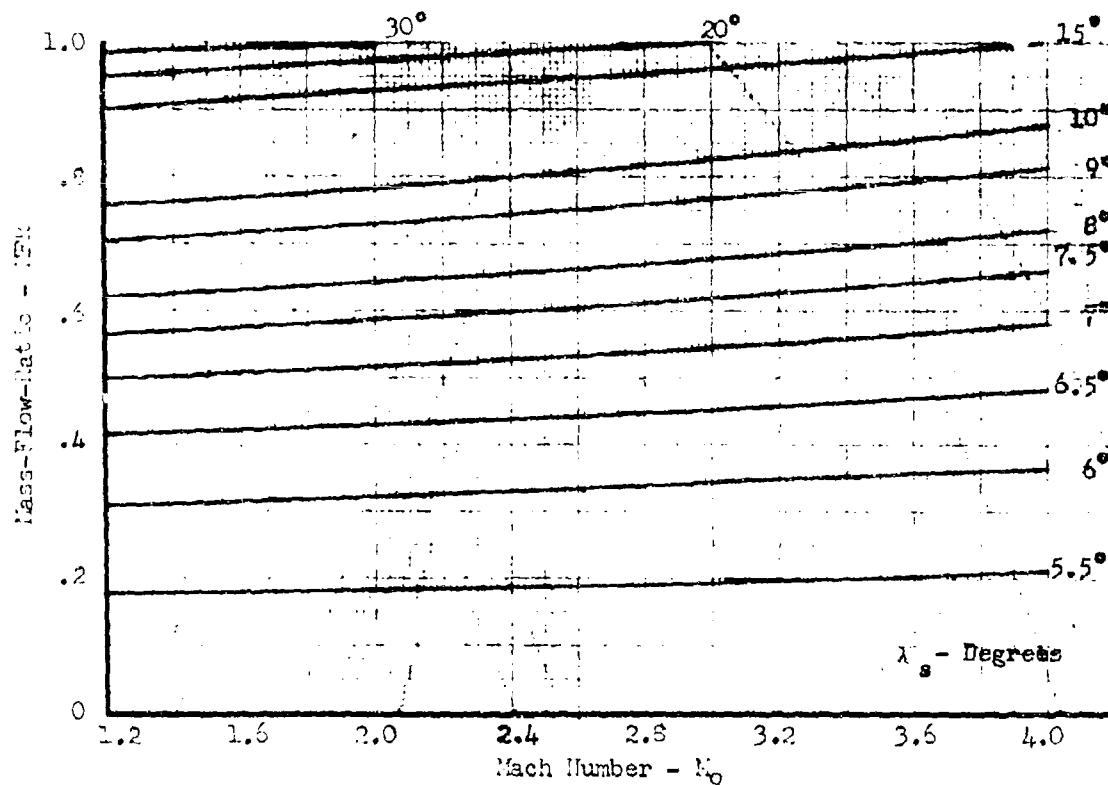


FIGURE 4-33. Theoretical Additive Drag Design Charts for Axisymmetric (Cone) Inlets  
Cone Semi-Vertex Angle  $\theta_{r1} = 5^\circ$

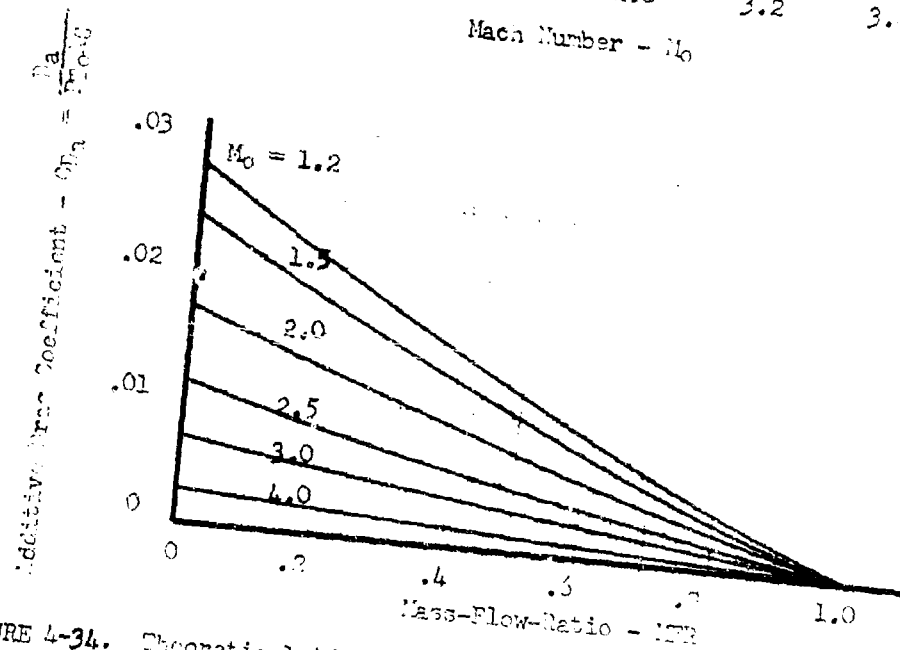
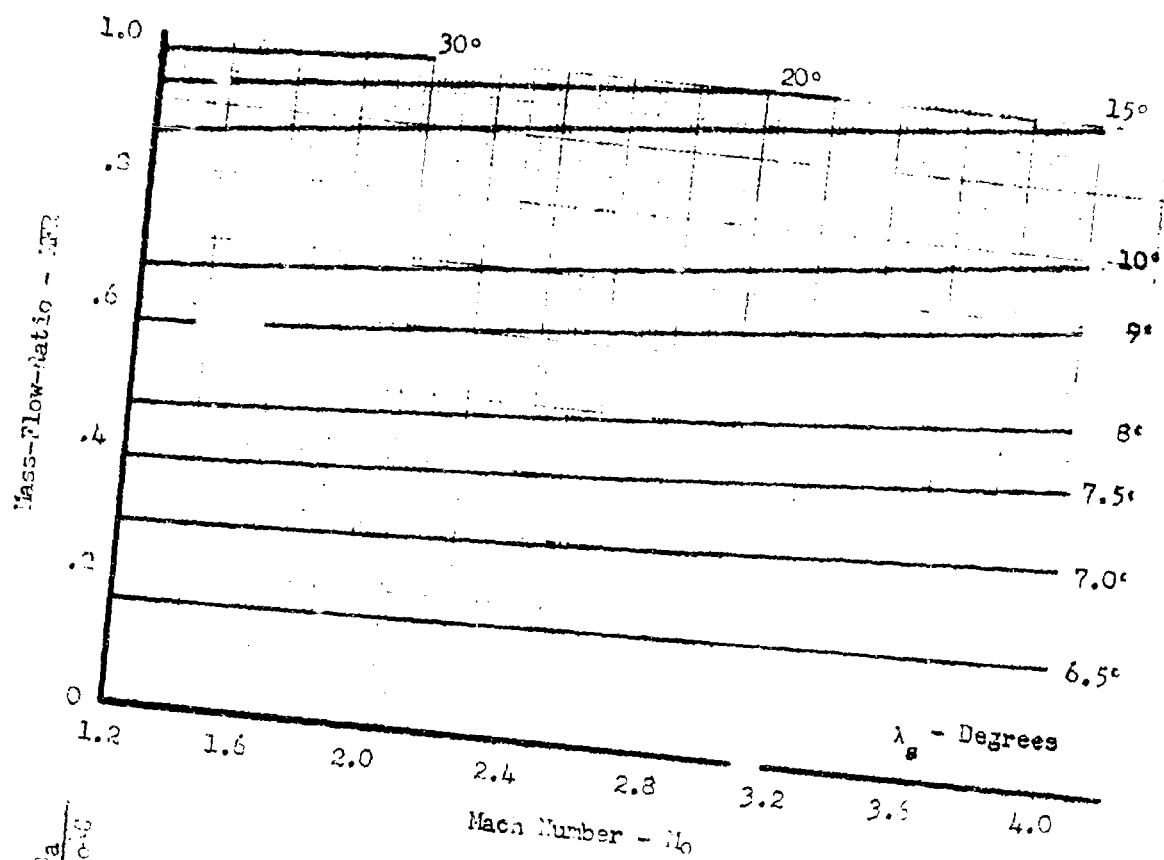


FIGURE 4-34. Theoretical Additive Drag Design Charts for Axisymmetric (Single Cone) Inlets  
Cone Semi-Vertex Angle  $\theta_{r1} = 6^\circ$

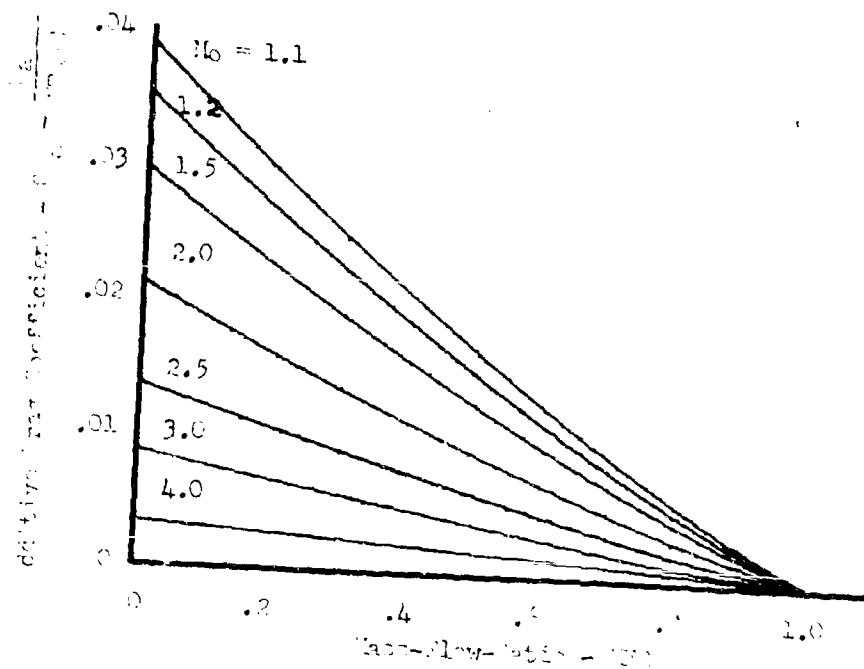
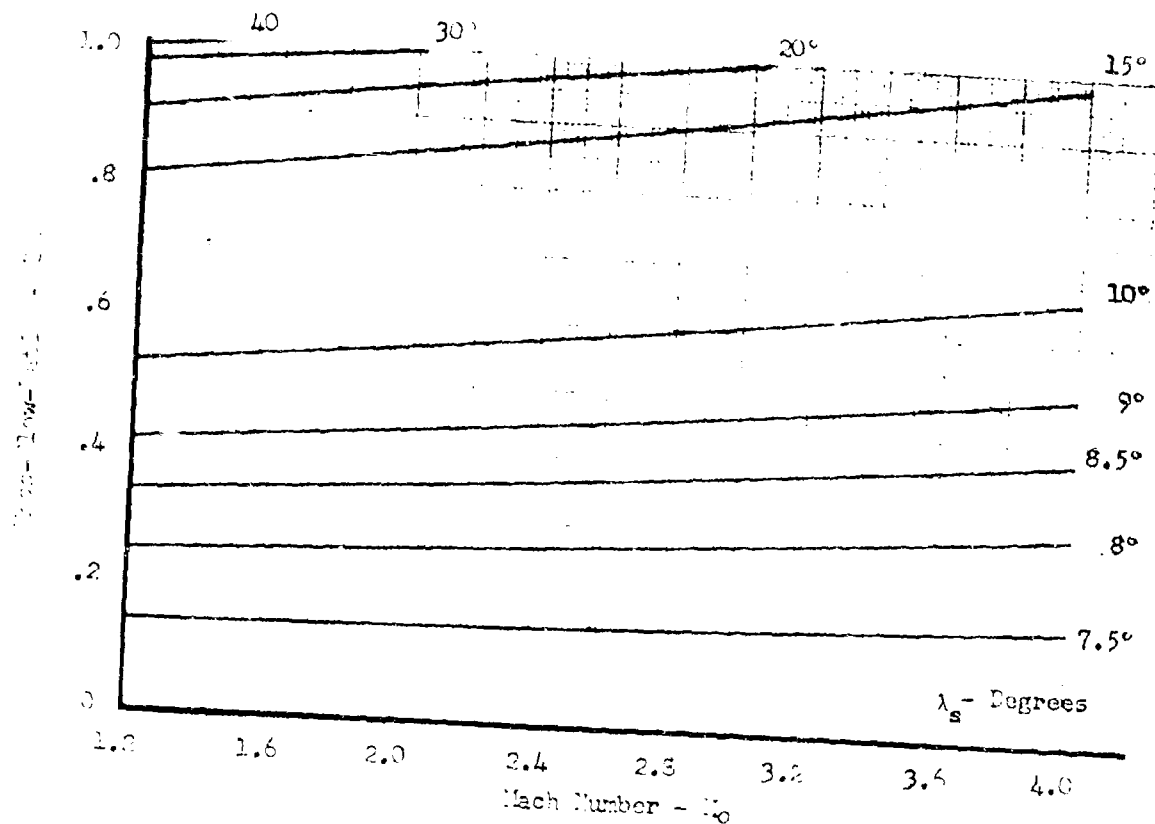


FIGURE 4-35. Theoretical Additive Drag Design Charts for Axisymmetric (Single Cone) Inlets  
Cone Semi-Vertex Angle  $\theta_{rl} = 2^\circ$

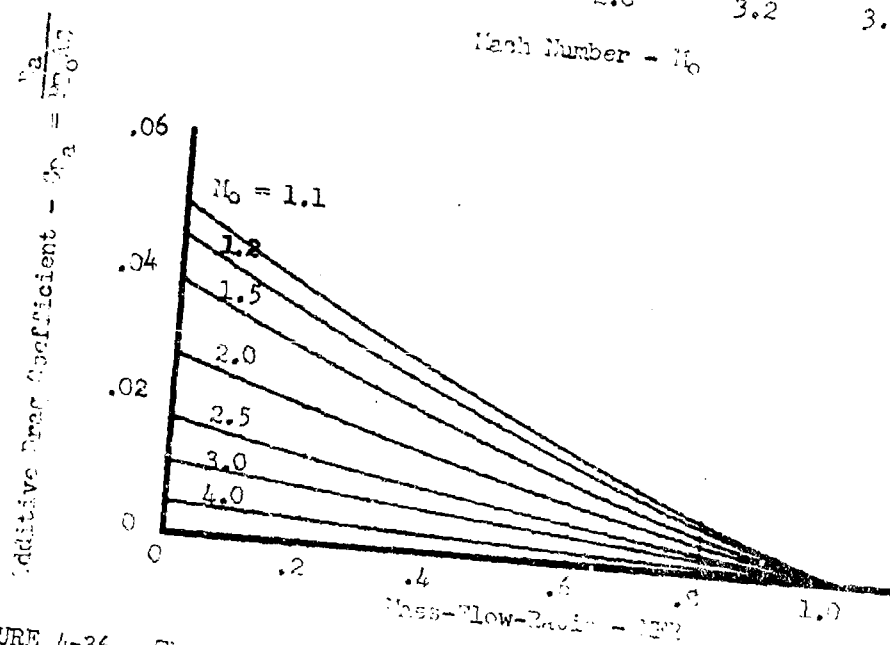
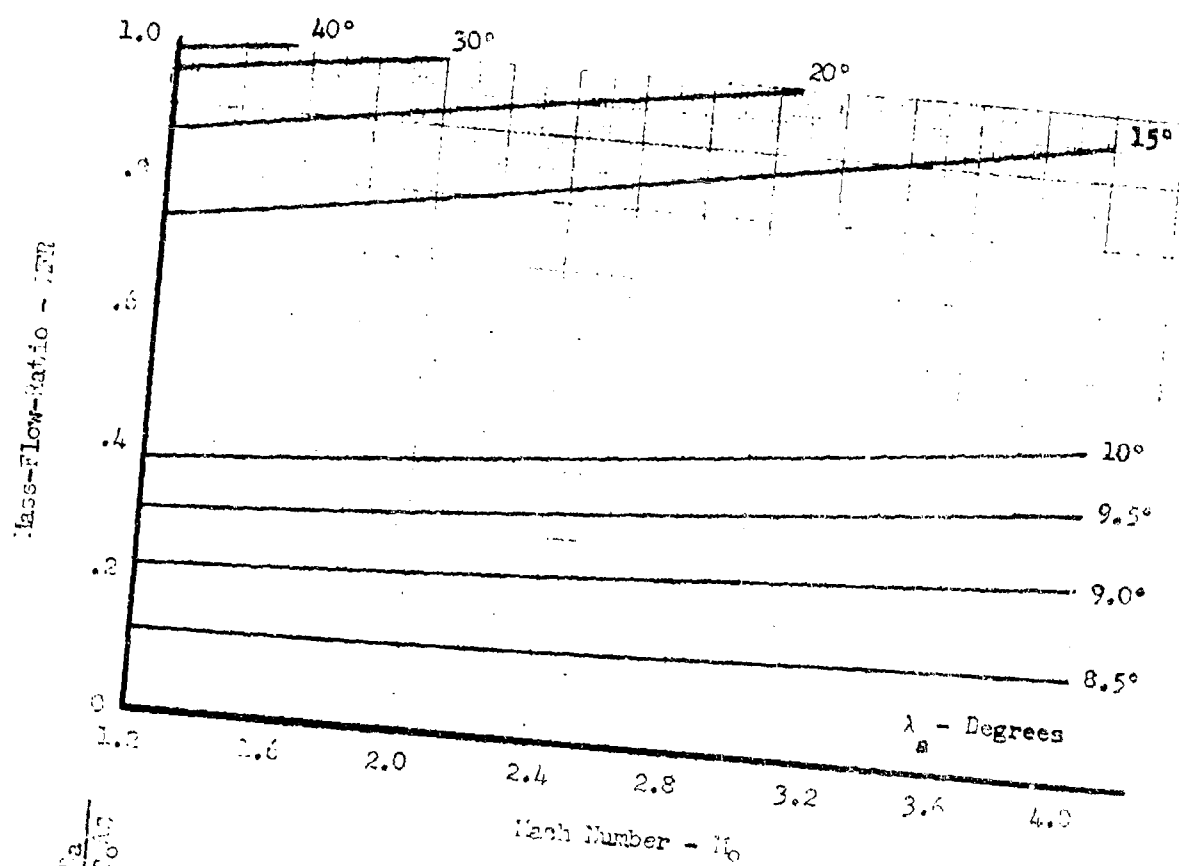


FIGURE 4-36. Theoretical Additive Drag Design Charts for Axisymmetric (Single Cone) Inlets  
Cone Semi-Vertex Angle  $\lambda_1 = 0^\circ$



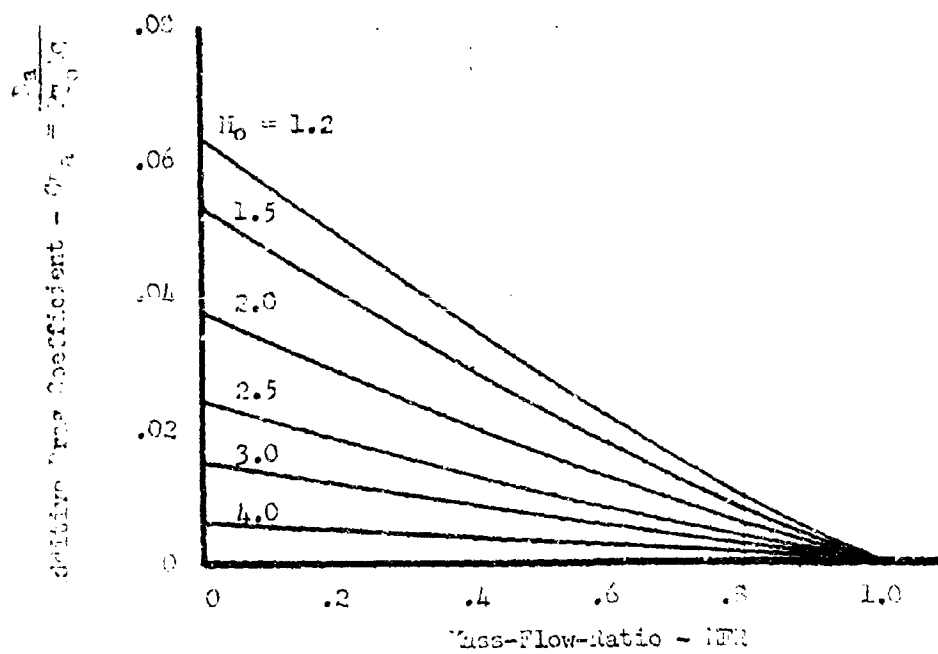
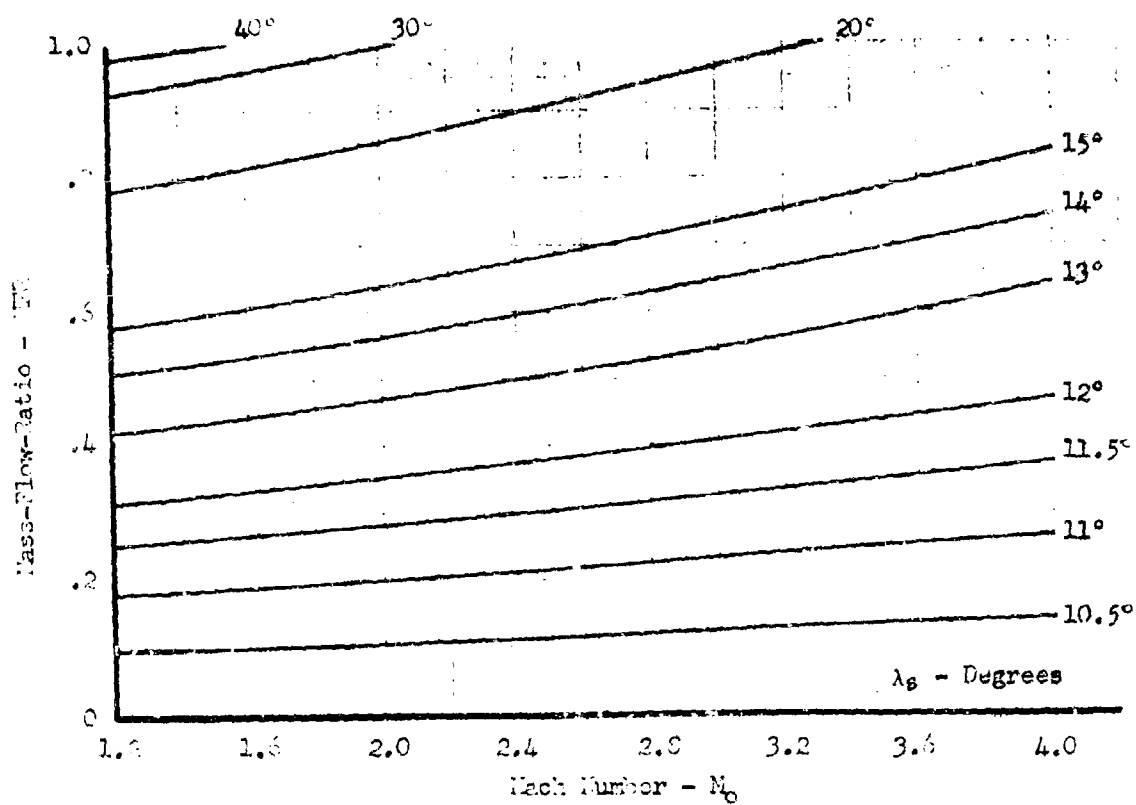


FIGURE 4-37. Theoretical Additive Trac Design Charts for Axisymmetric (Single Cone) Inlets  
Cone Vertex-Angle  $\theta_{r1} = 10^\circ$

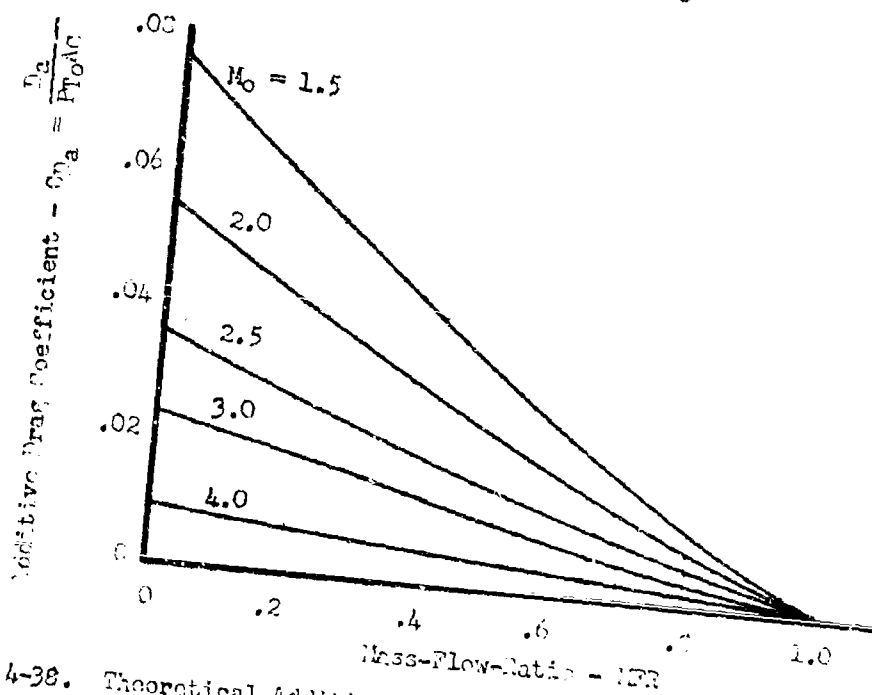
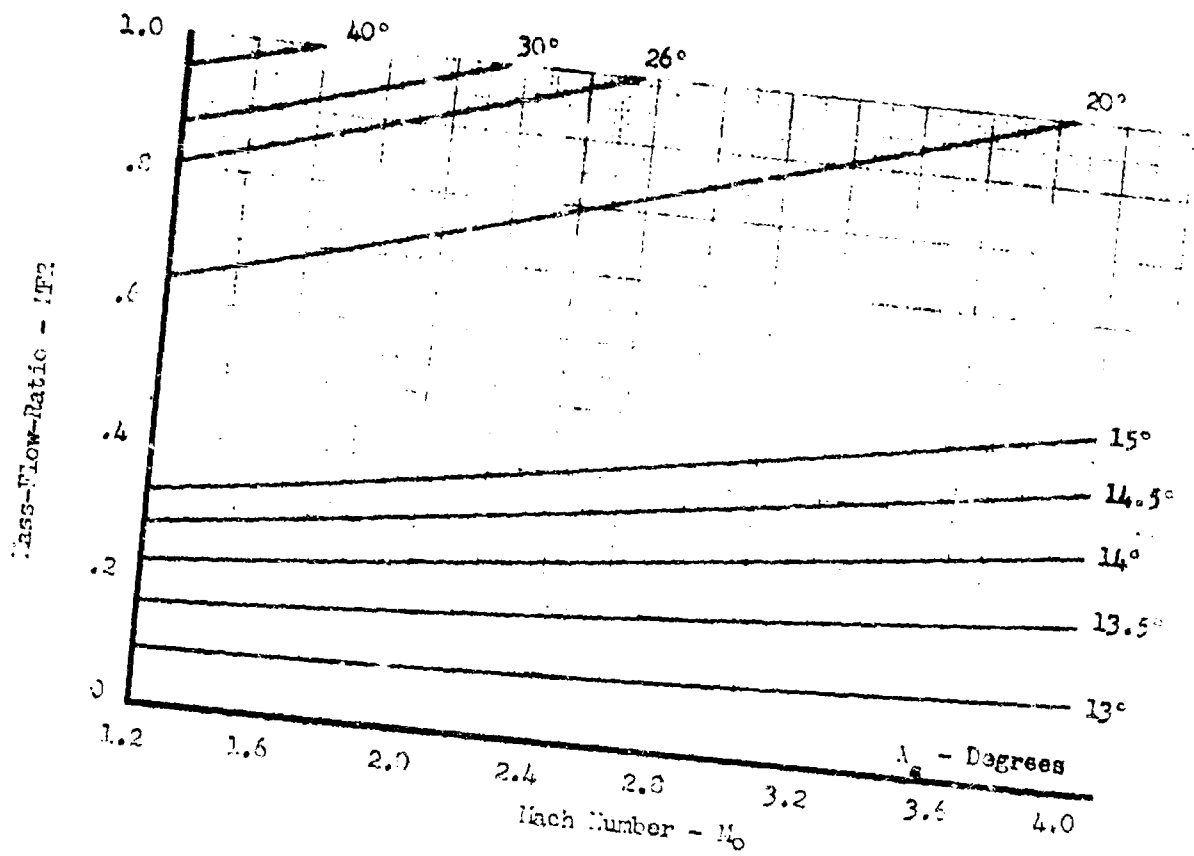


FIGURE 4-38. Theoretical Additive Drag Design Charts for Axisymmetric (Angle Cone) Inlets  
Cone Semi-Vortex Angle  $\theta_{r1} = 12.5^\circ$

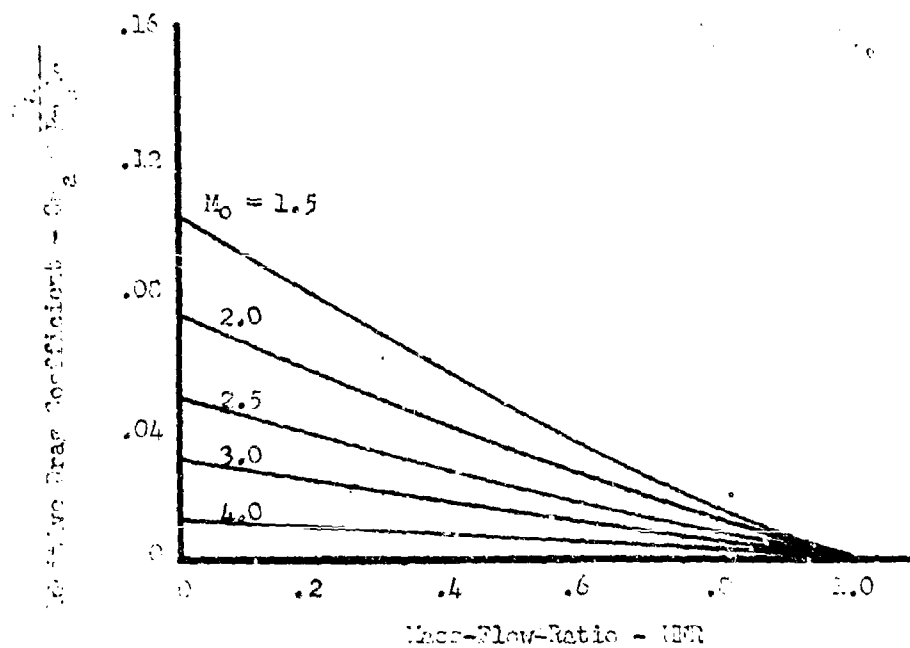
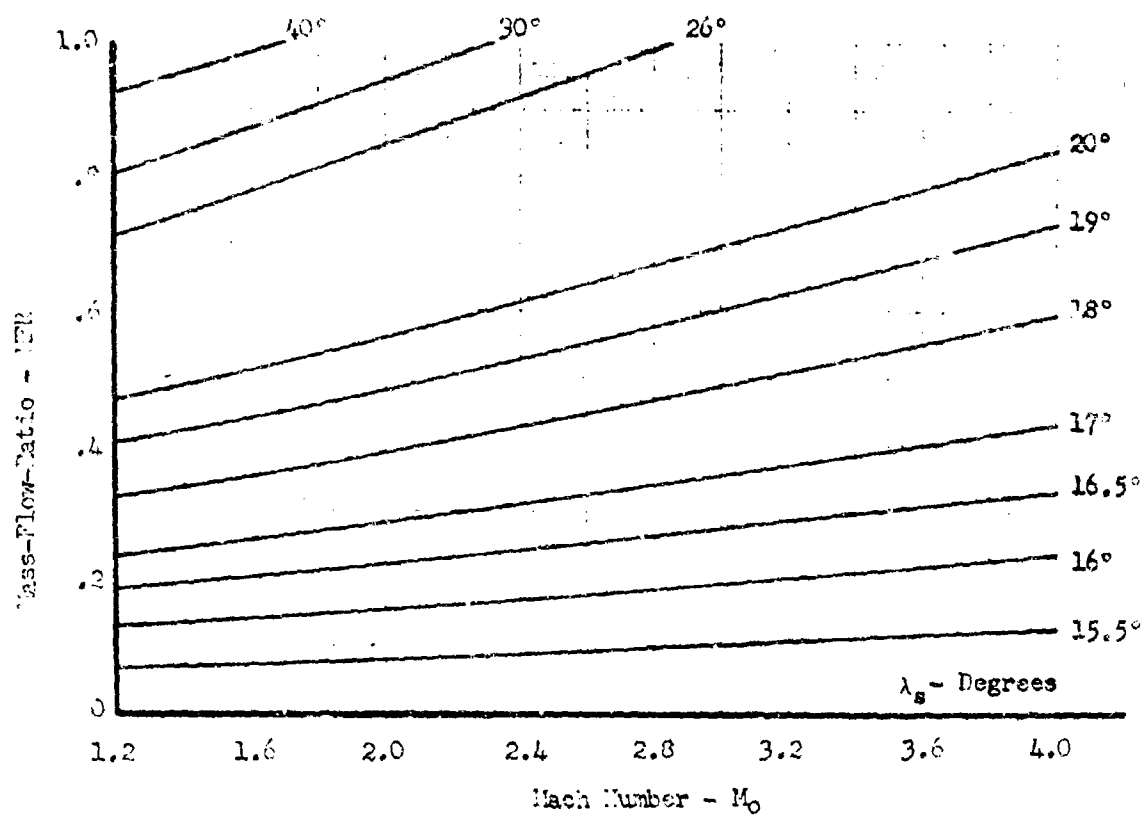


FIGURE A-39. Theoretical Additive Drag Design Charts for Axisymmetric (Single Cone) Inlets  
Cone Semi-Vertex Angle  $\theta_{r1} = 15^\circ$

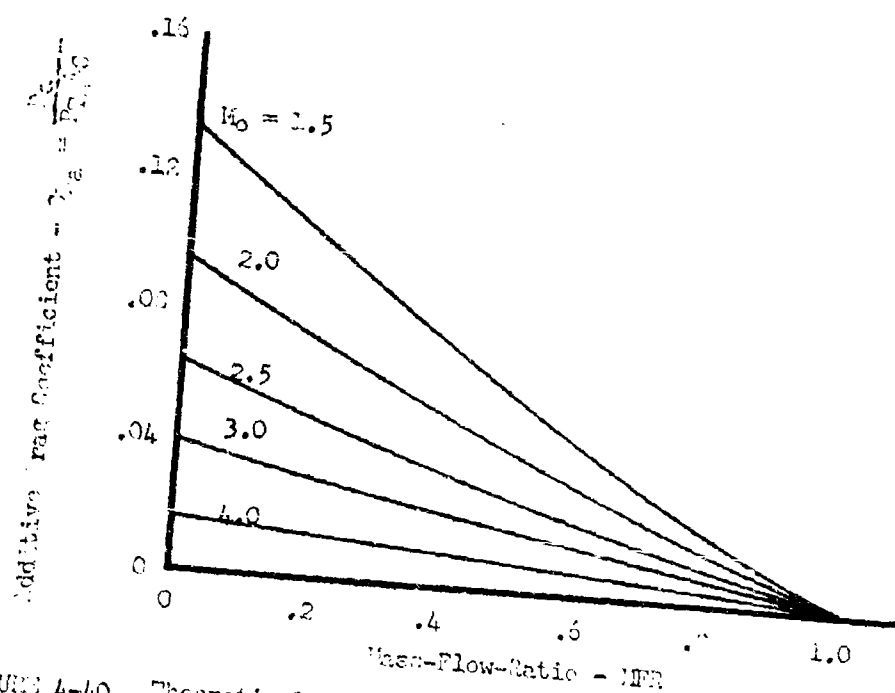
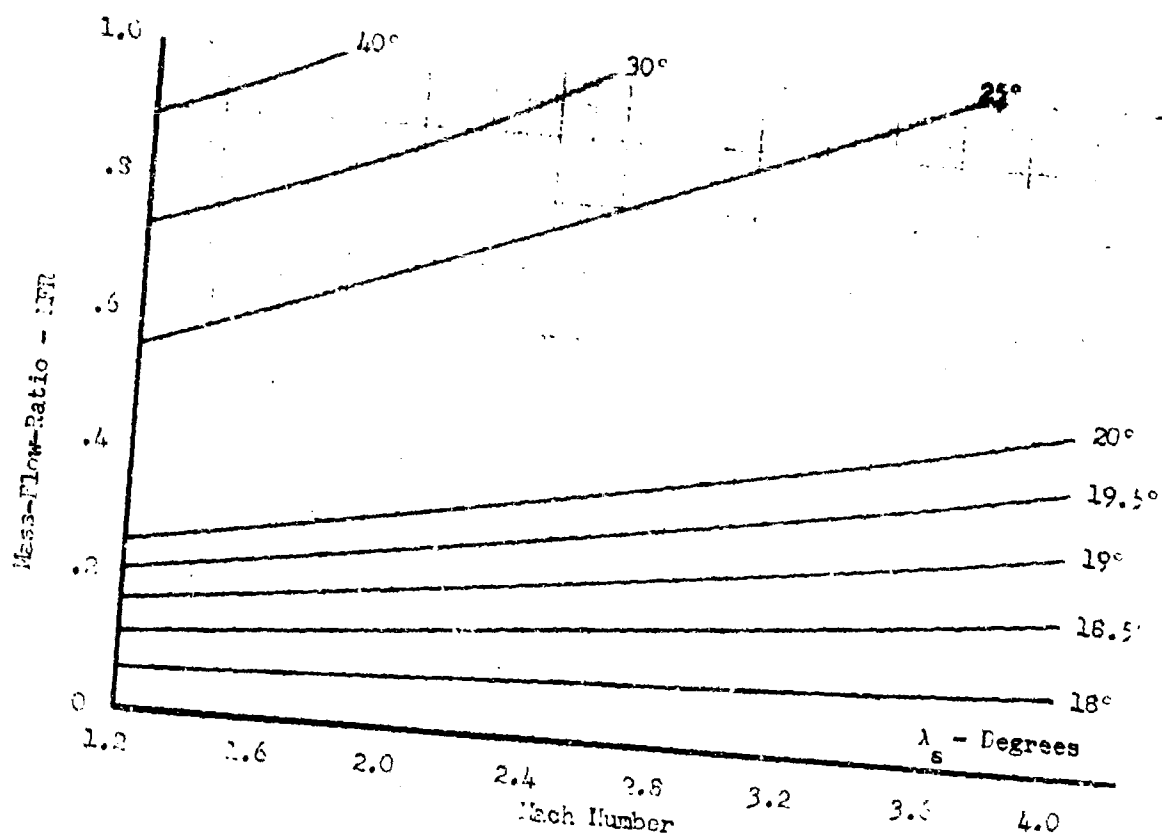


FIGURE 4-40. Theoretical Additive Drag Design Charts for Axisymmetric (Single Cone) Inlets  
Cone Semi-Vertex Angle  $\theta_{rl} = 17.5^\circ$

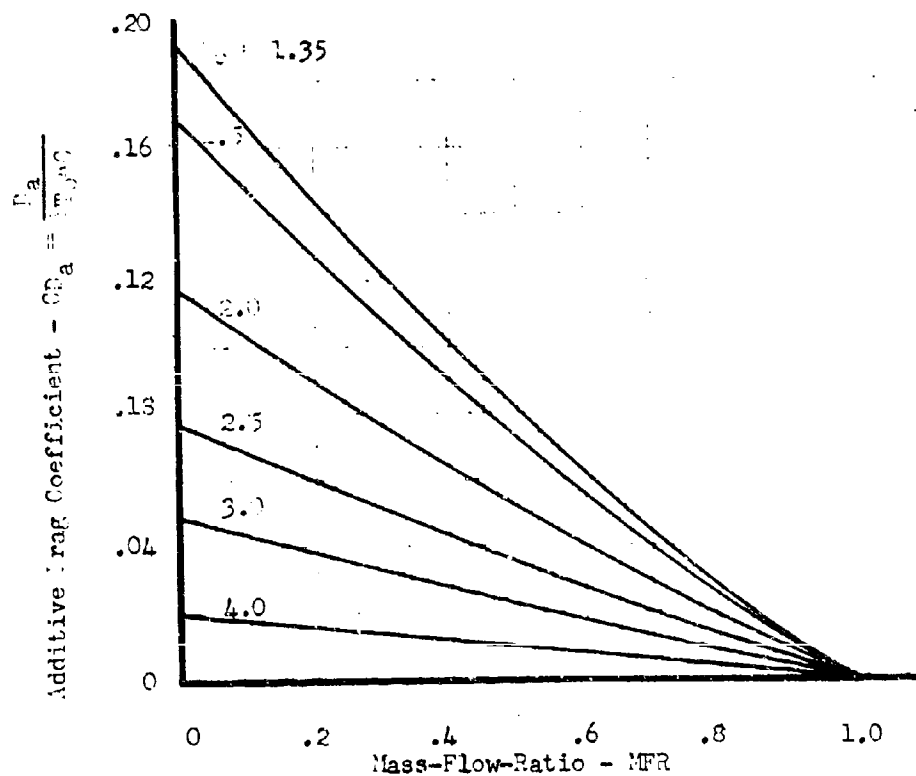
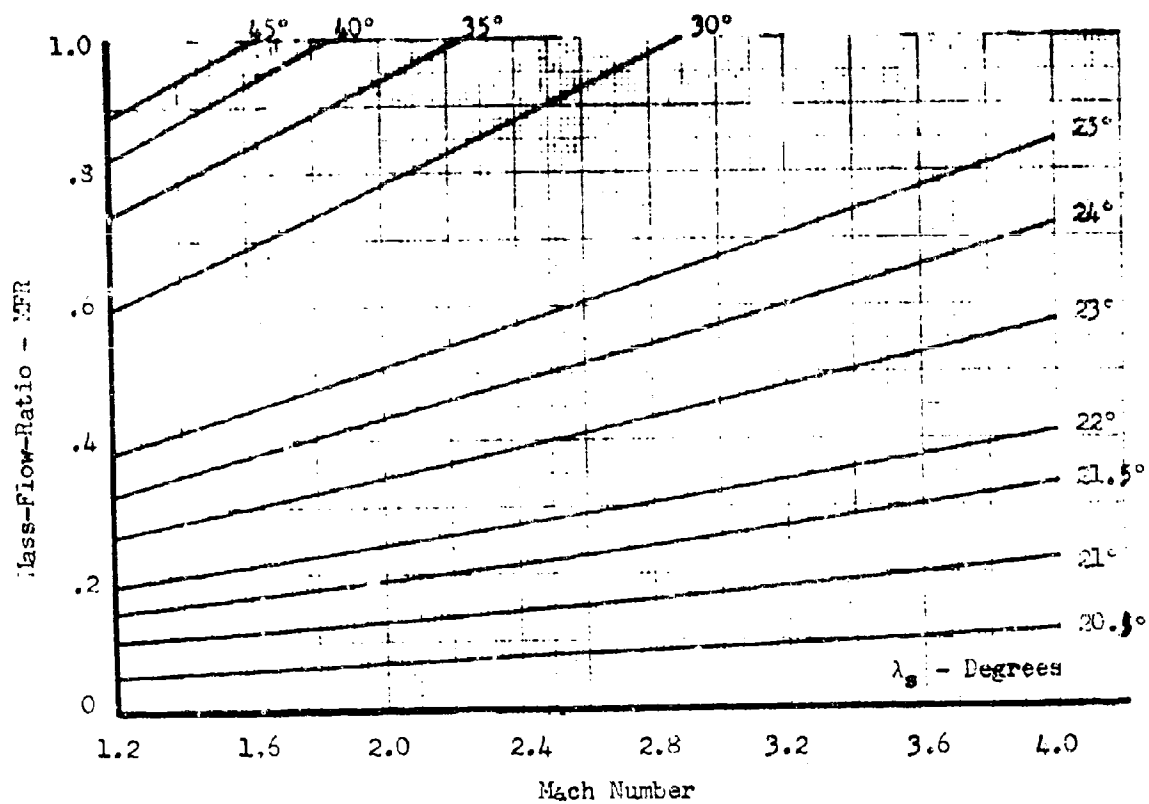


FIGURE 4-41. Theoretical Additive Drag Design Charts for Axisymmetric (Single Cone) Inlets  
Cone Semi-Vertex Angle  $\theta_{r1} = 20^\circ$

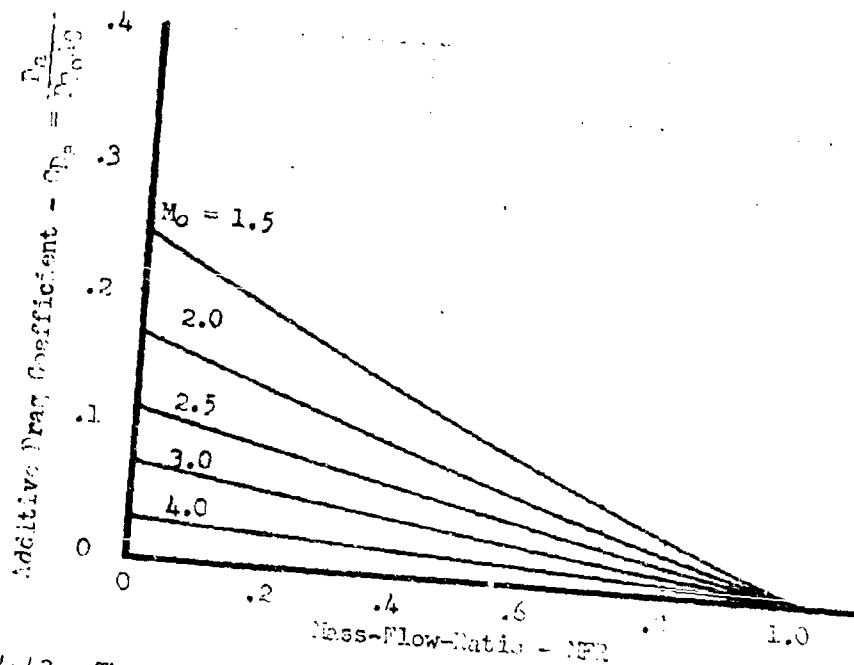
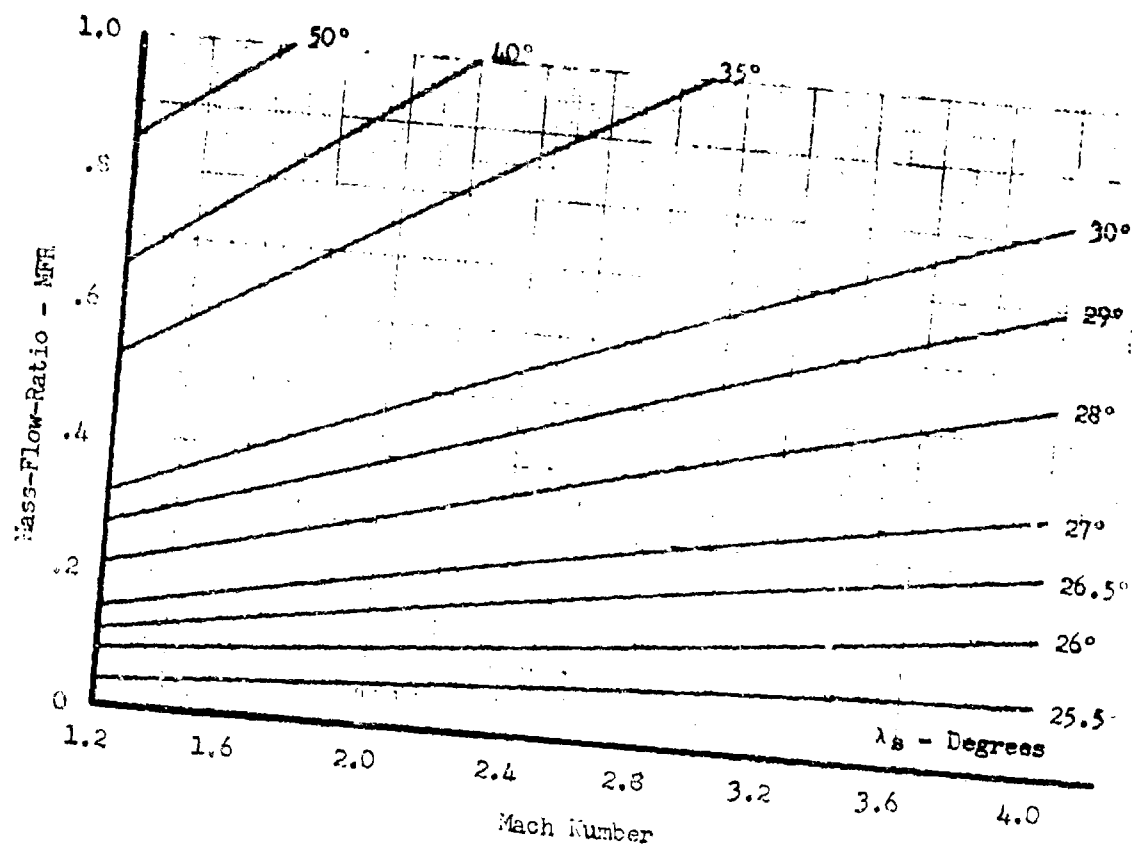


FIGURE 4-42. Theoretical Additive Drag Design Charts for Axisymmetric (Single Cone) Inlets  
Cone Semi-Vertex Angle  $\theta_{r1} = 25^\circ$

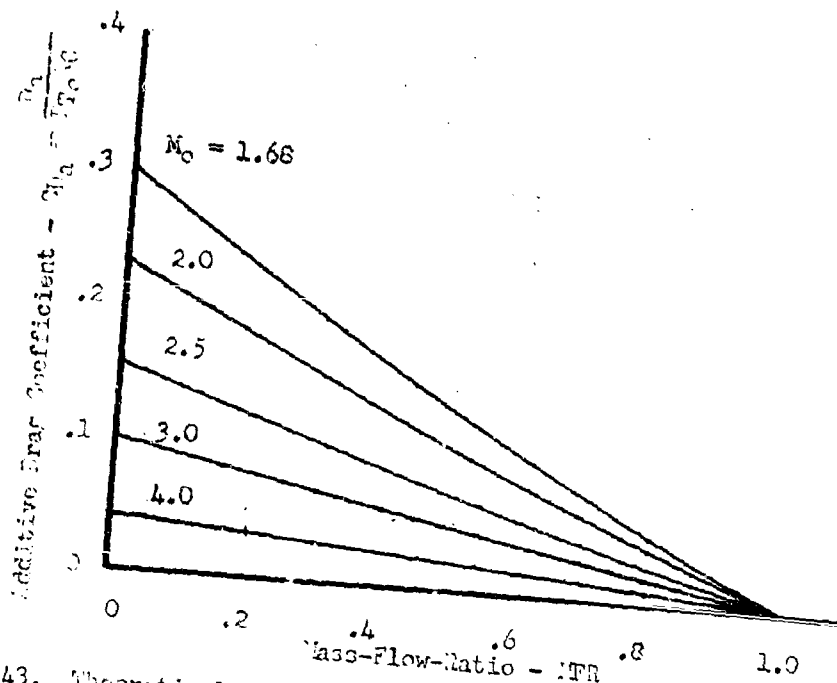
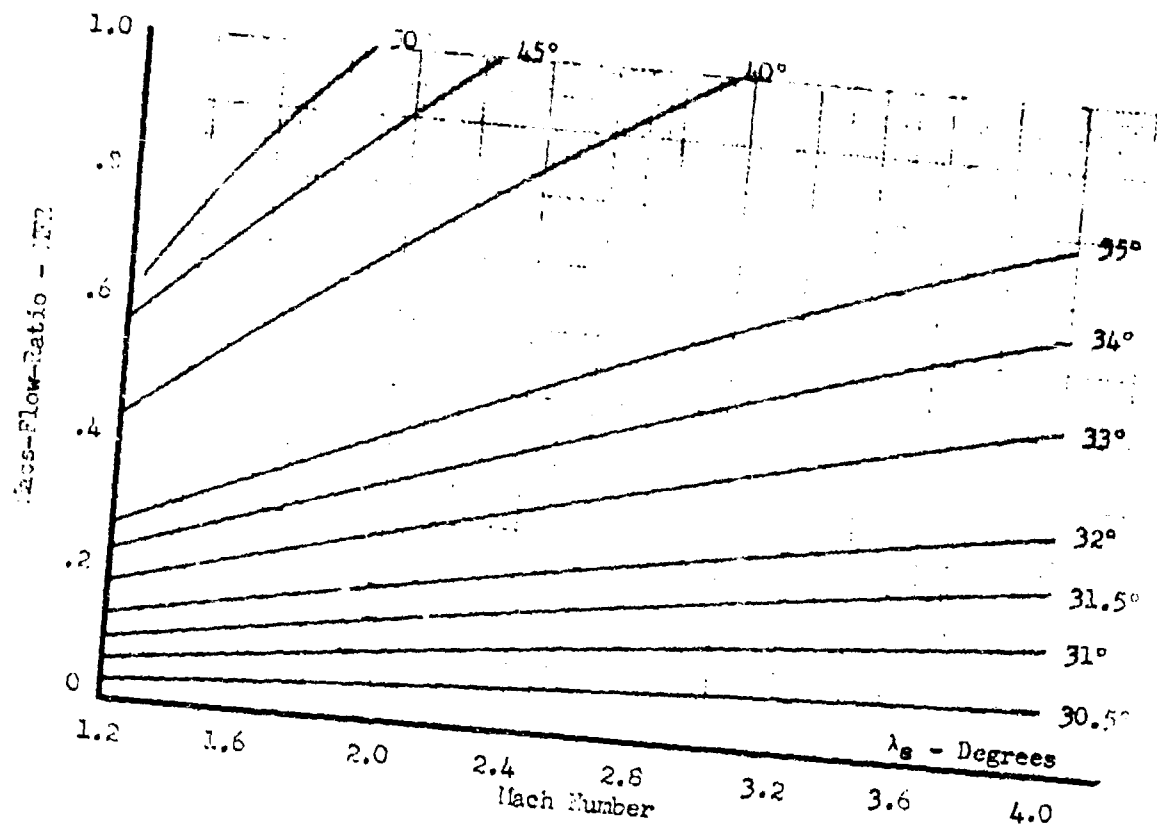


FIGURE 4-43. Theoretical Additive Drag Design Charts for Axisymmetric (Single Cone) Inlets  
Cone Semi-Vortex Angle  $\theta_{r1} = 30^\circ$

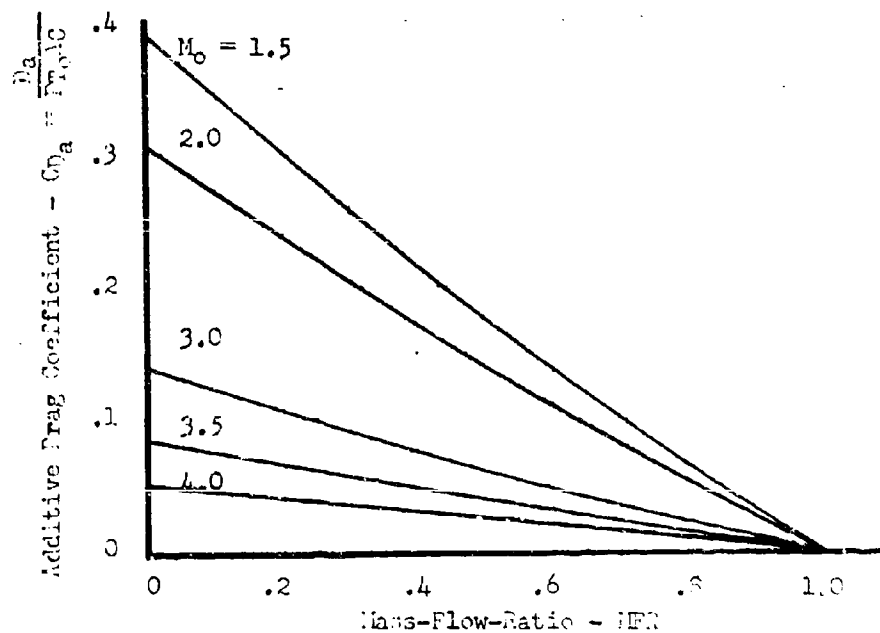
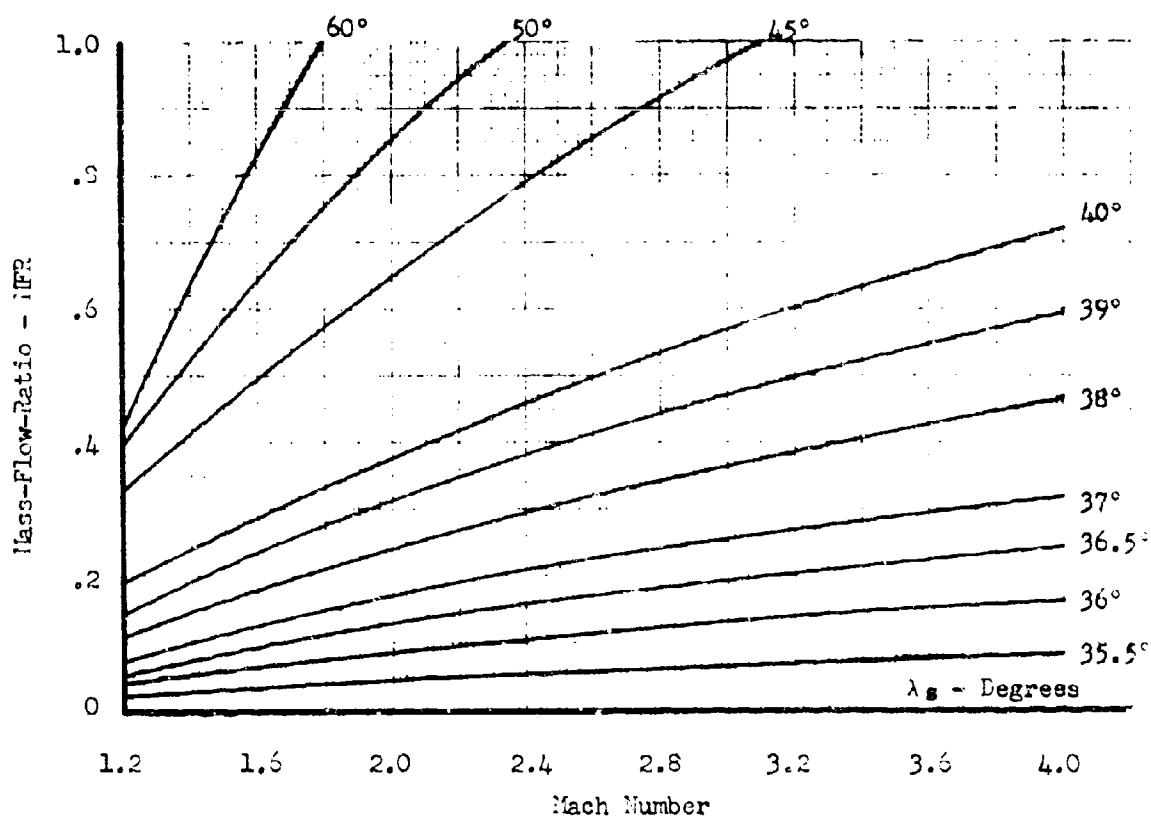


FIGURE 4-44. Theoretical Additive Drag Design Charts for Axisymmetric (Single Cone) Inlets

Cone Semi-Vertex Angle  $\theta_{r1} = 35^\circ$



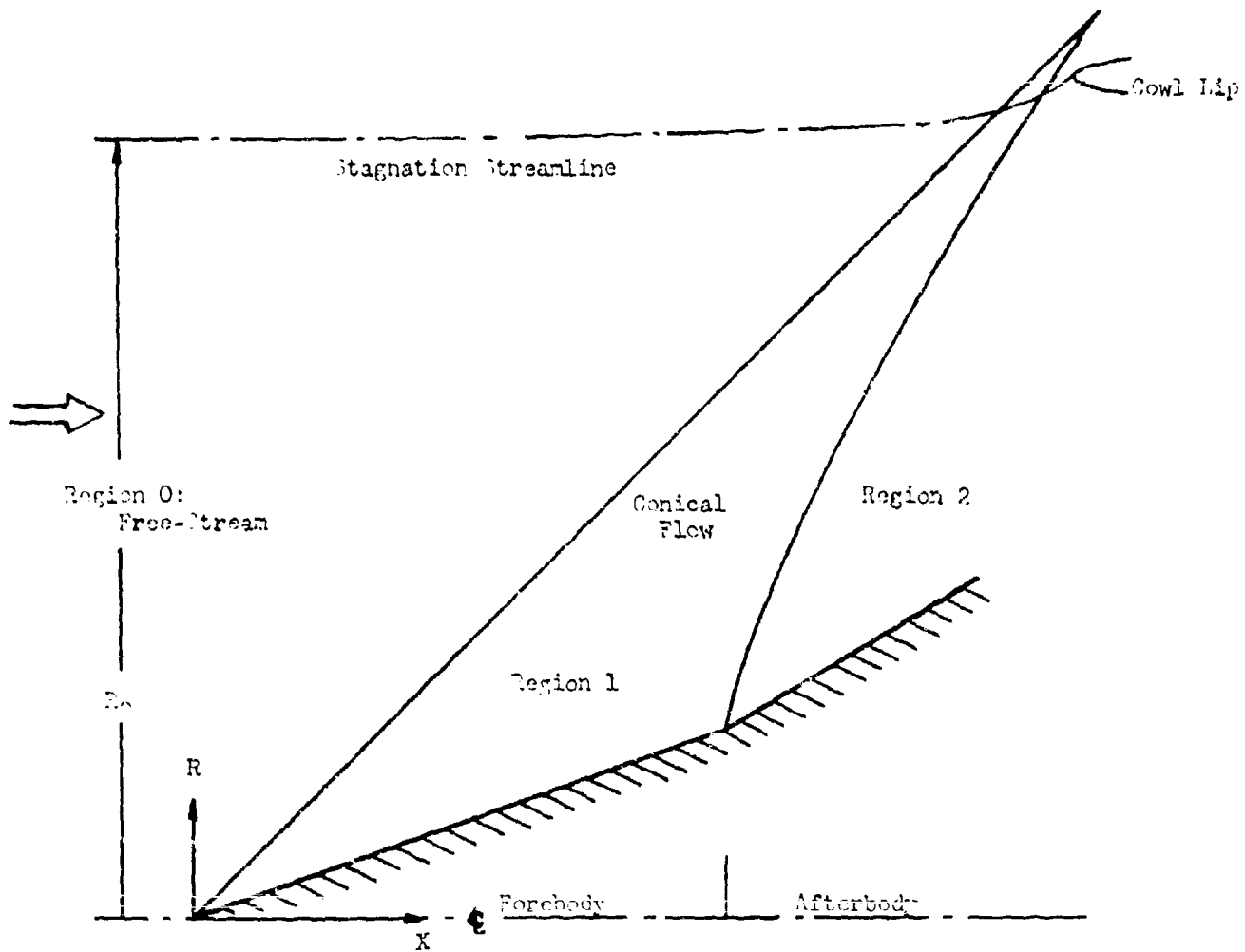


FIGURE 4-45. Illustration of Double-Cone Inlet Flow Field

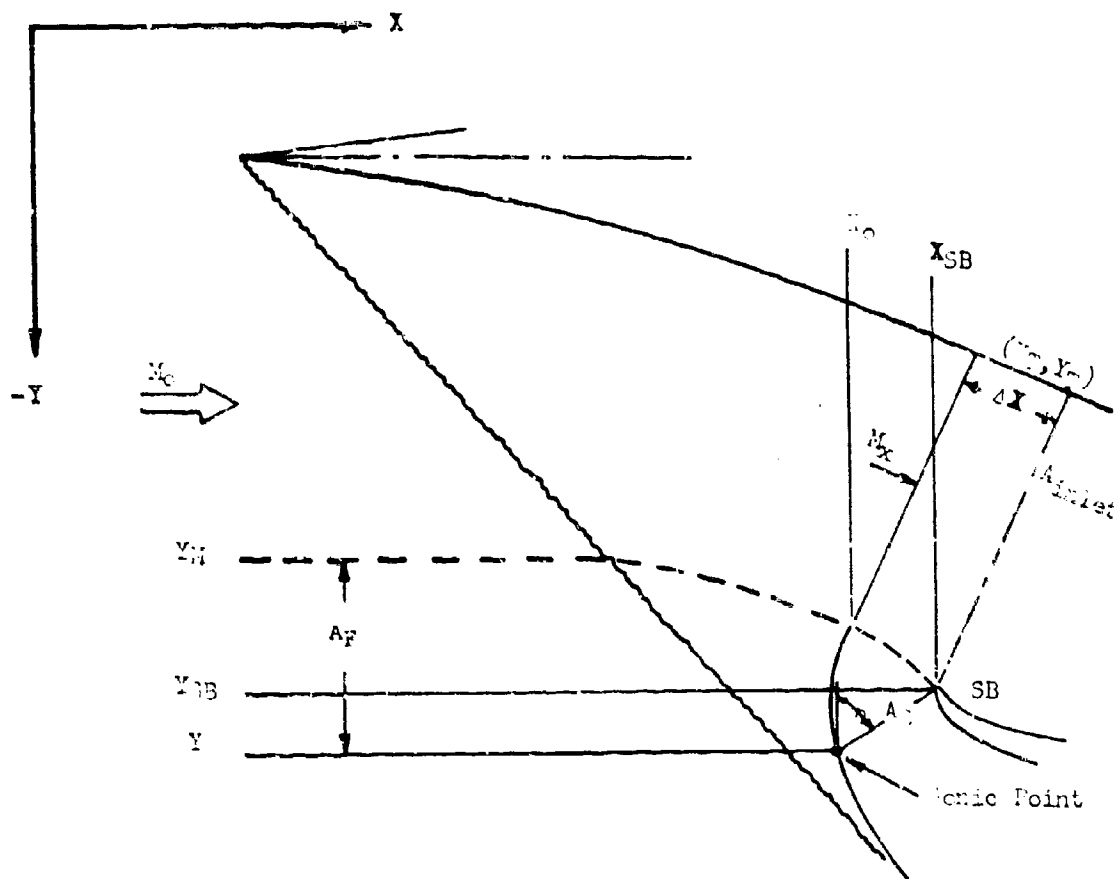


FIGURE 4-46. Illustration of Two-Dimensional Detached Shock Wave Geometry

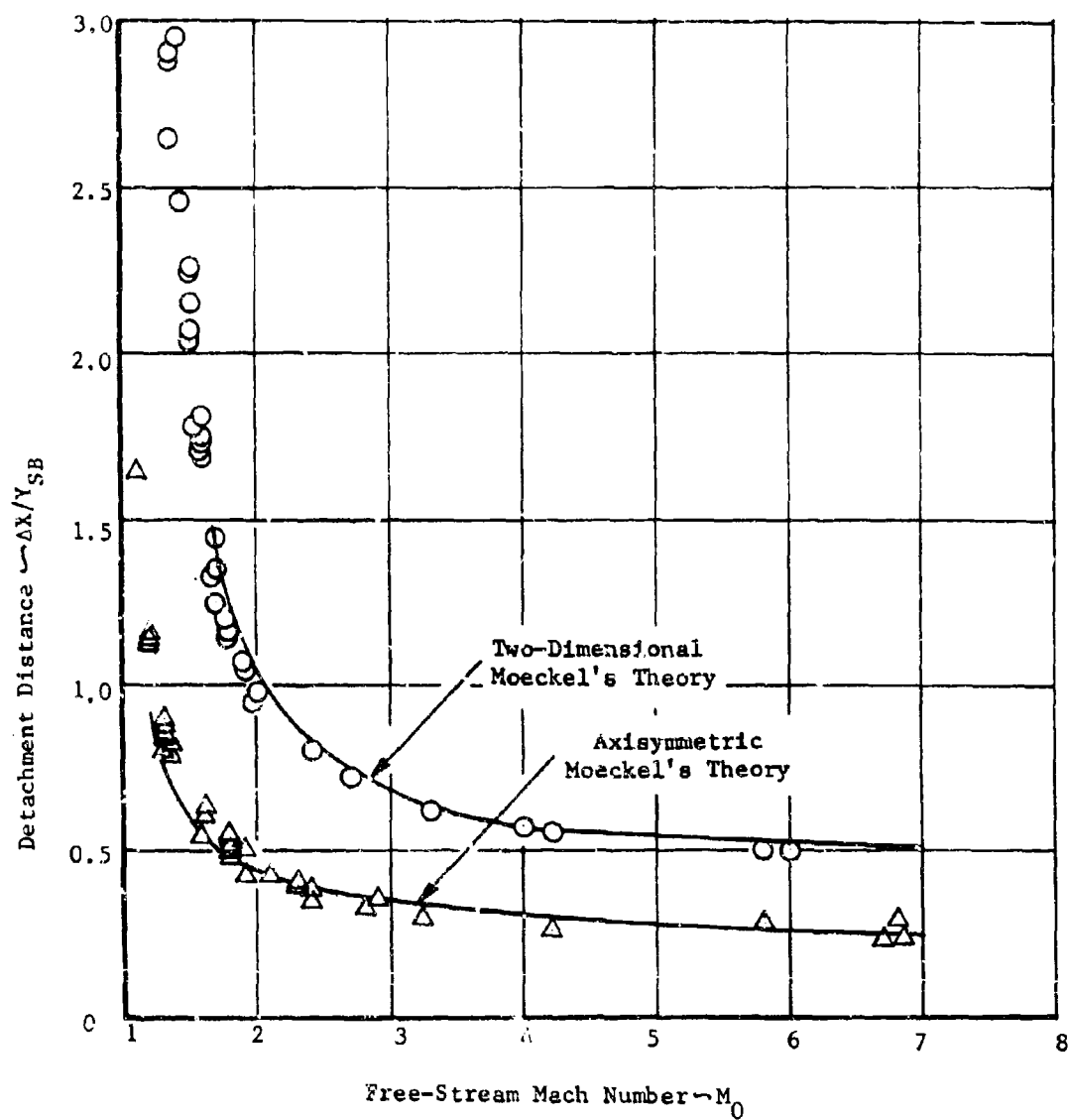


FIGURE 4-47 Compilation and General Correlation of Data on Detachment Distance for Two-Dimensional and Axisymmetric Nose Shapes (Reference 7)

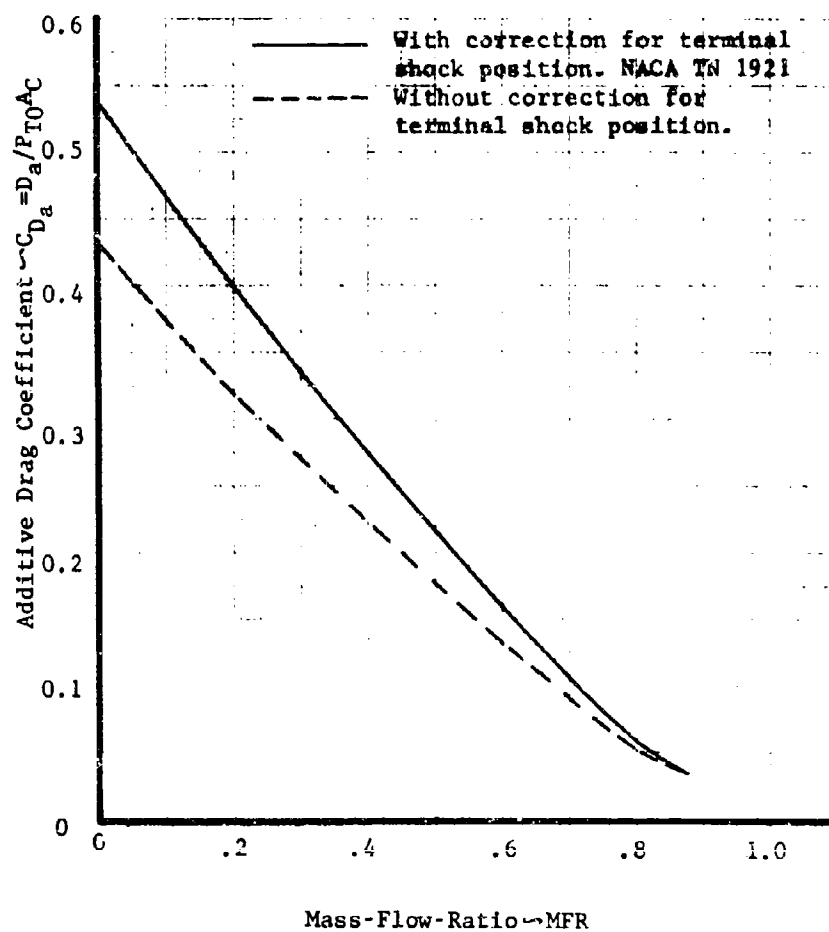


FIGURE 4-48 Illustration of Theoretical  $C_{D_a}$  Variation Resulting From "Attached" Terminal Shock Position Assumption. Mach 2.4 Design Isentropic Ramp at Mach 2.4.

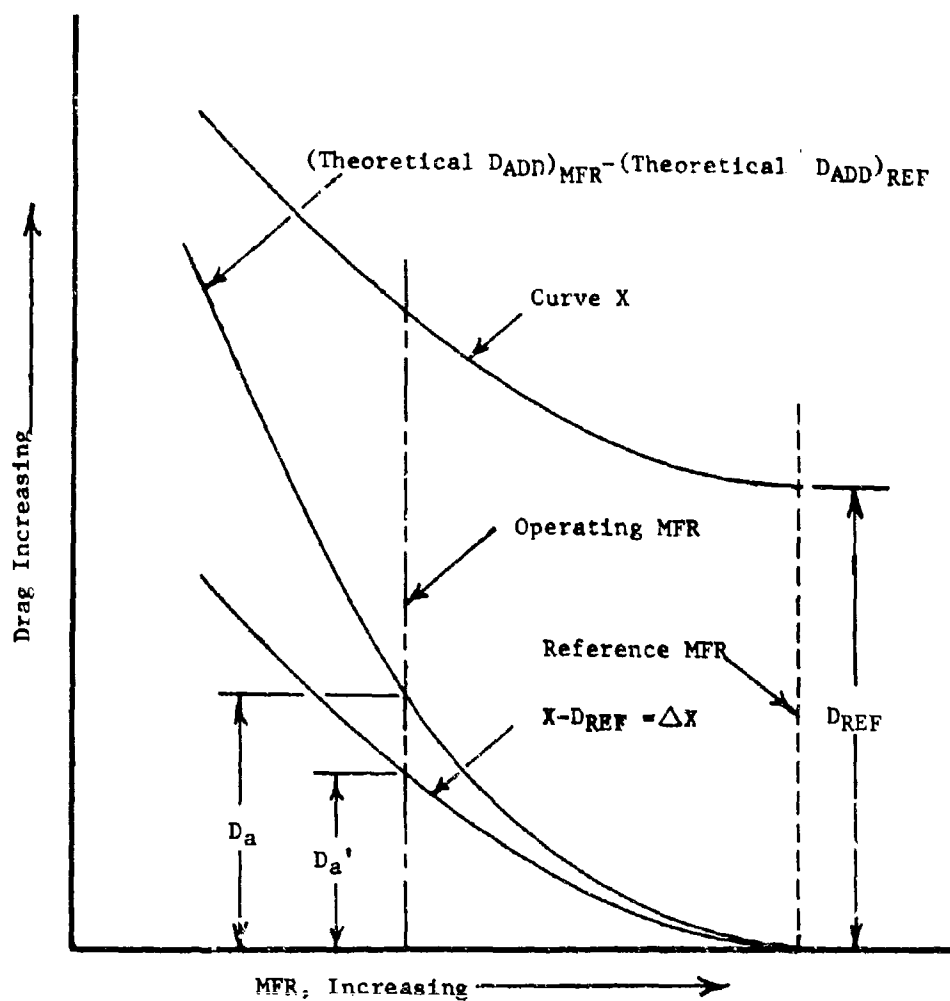


FIGURE 4-49. Illustration of Method Employed to Obtain Corrected Additive Drag

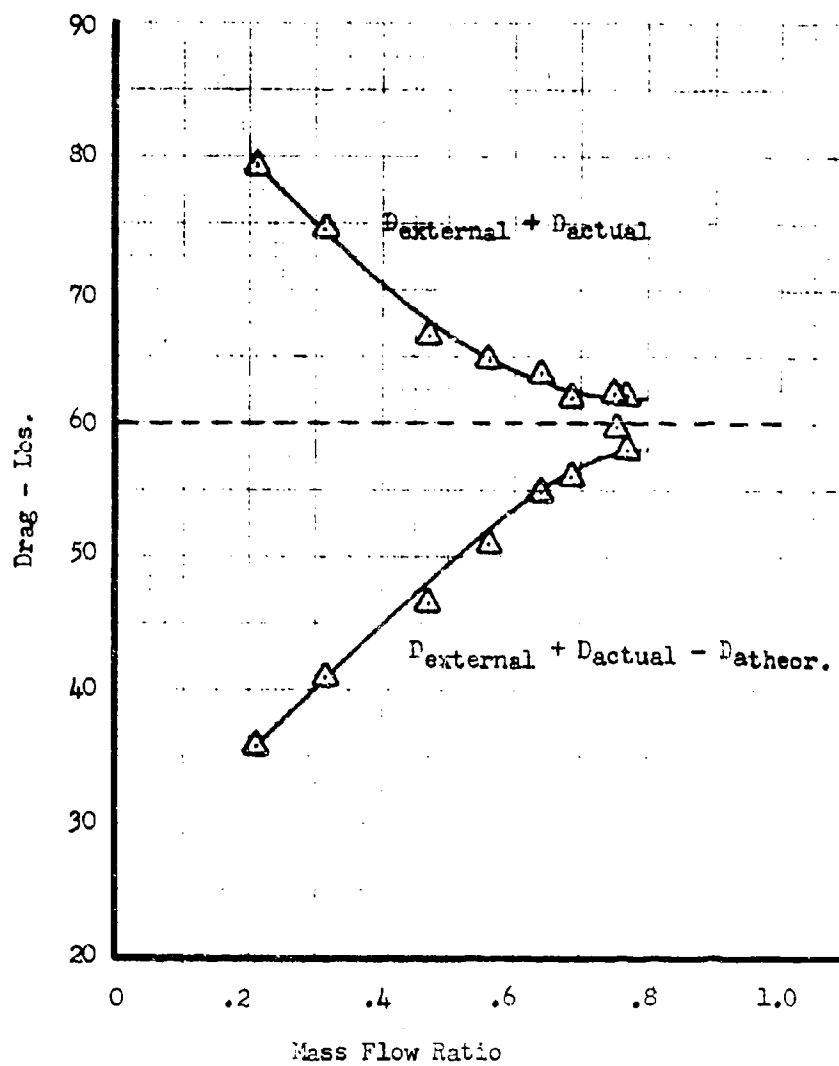


FIGURE 4-50. Drag Variation With Mass Flow Ratio  
 $M_0 = 0.9$   $\theta_{R2} = 4.5^\circ$   $\alpha = 1.5^\circ$   
 .125 Scale A-5A Inlet Model

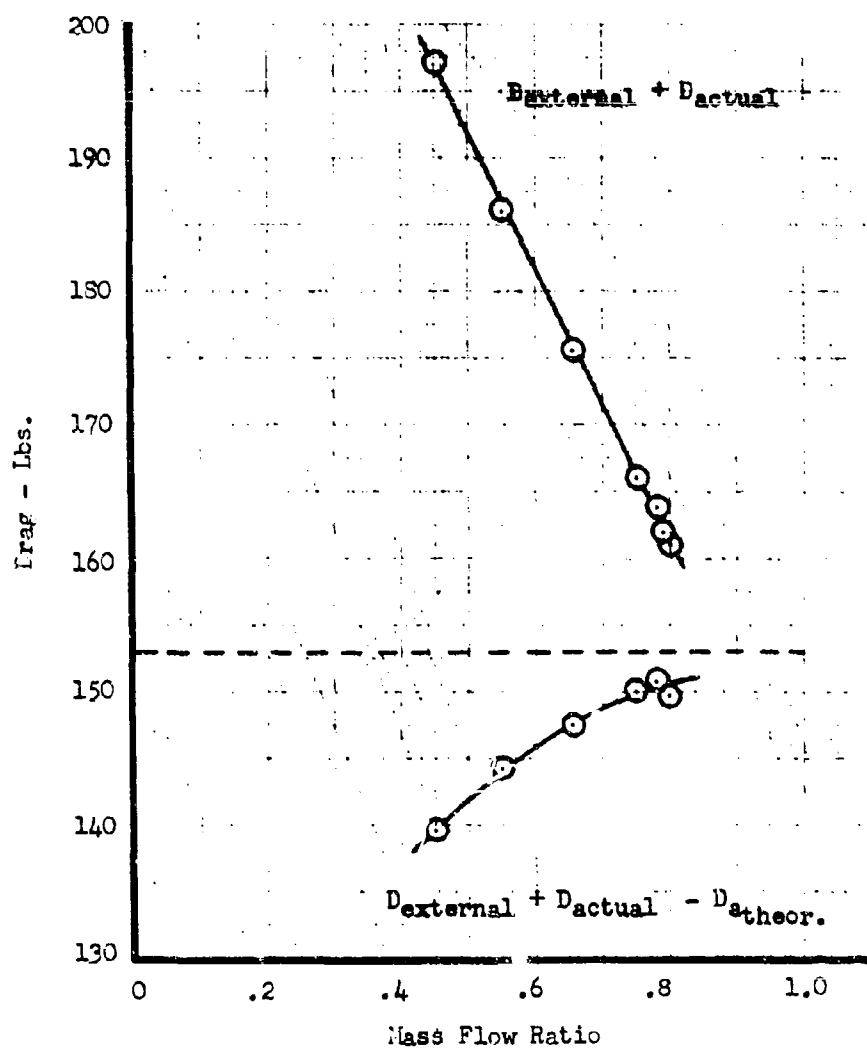


FIGURE 4-51. Drag Variation With Mass Flow Ratio  
 $M_0 = 1.57$   $\theta_{R2} = 11.5^\circ$   $\alpha = 1.5^\circ$   
 .125 Scale A-5A Inlet Model

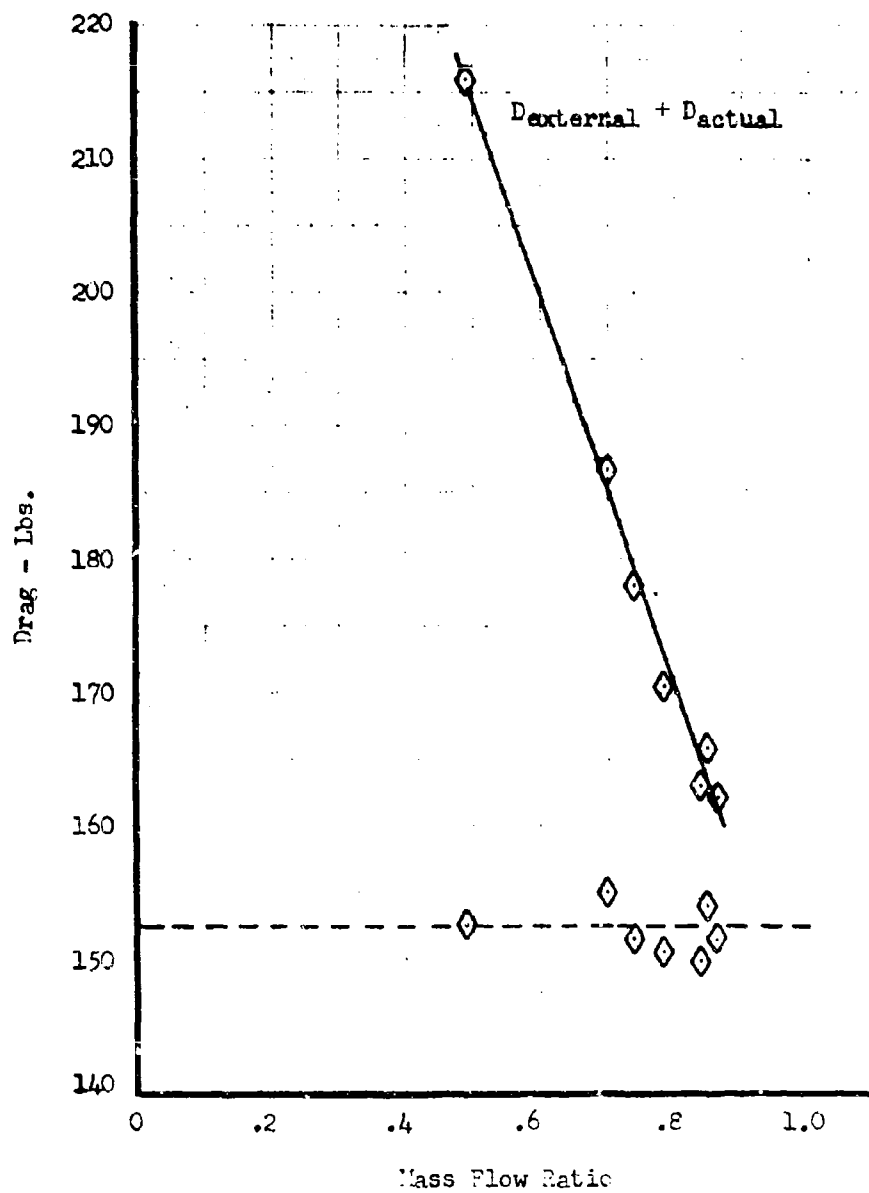


FIGURE 4-52. Drag Variation With Mass Flow Ratio  
 $M_0 = 1.97$   $\theta_{R2} = 17.5^\circ$   $\alpha = 1.5^\circ$   
 .125 Scale A-5A Inlet Model



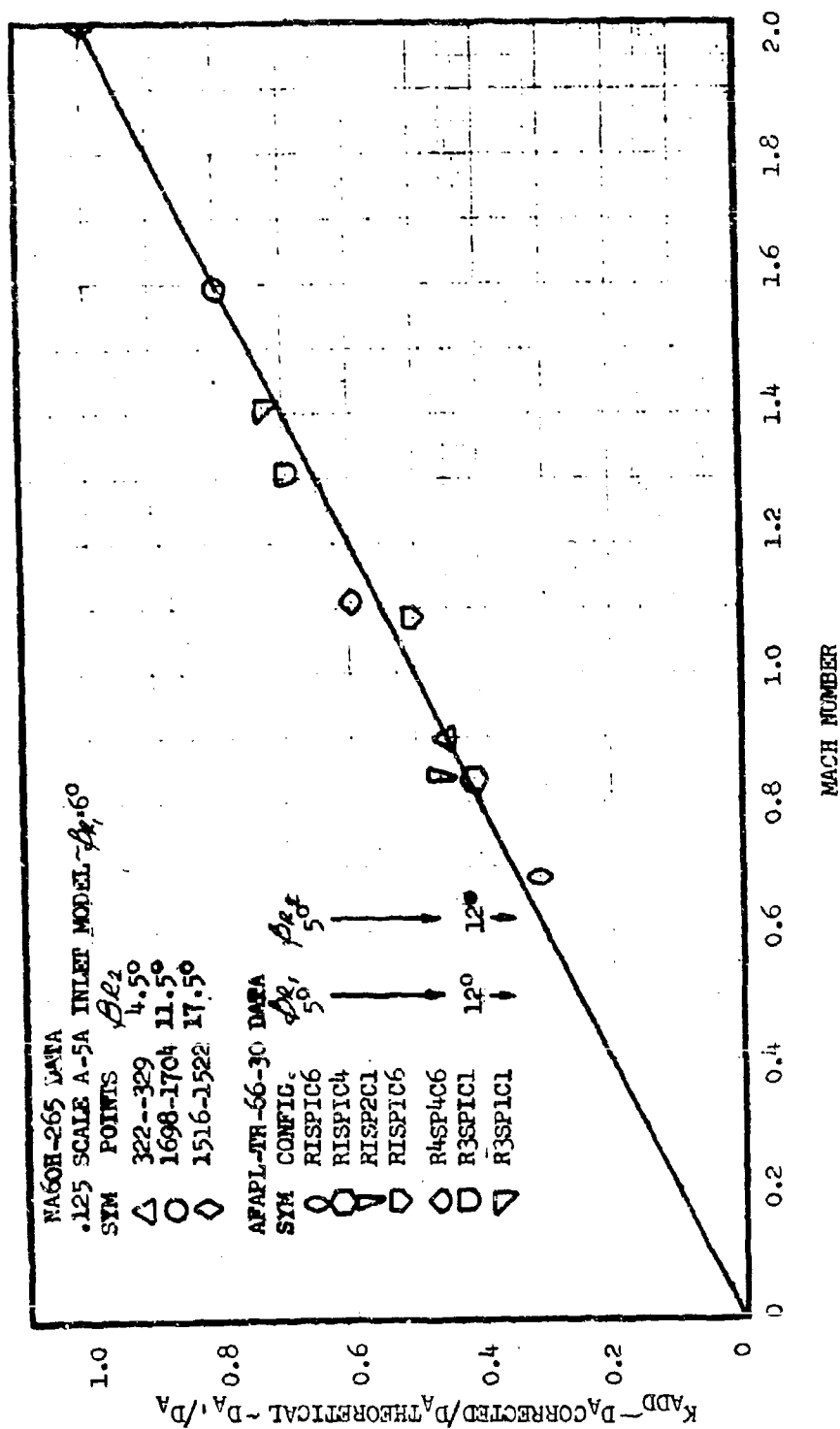


FIGURE 4-53. Variation of Corrected to Theoretical Additive Drag Ratio  
 $\beta_{R1}$  = Initial Ramp Angle --  $\beta_{R2}$  = Second Ramp Angle  
 (Reference 11)

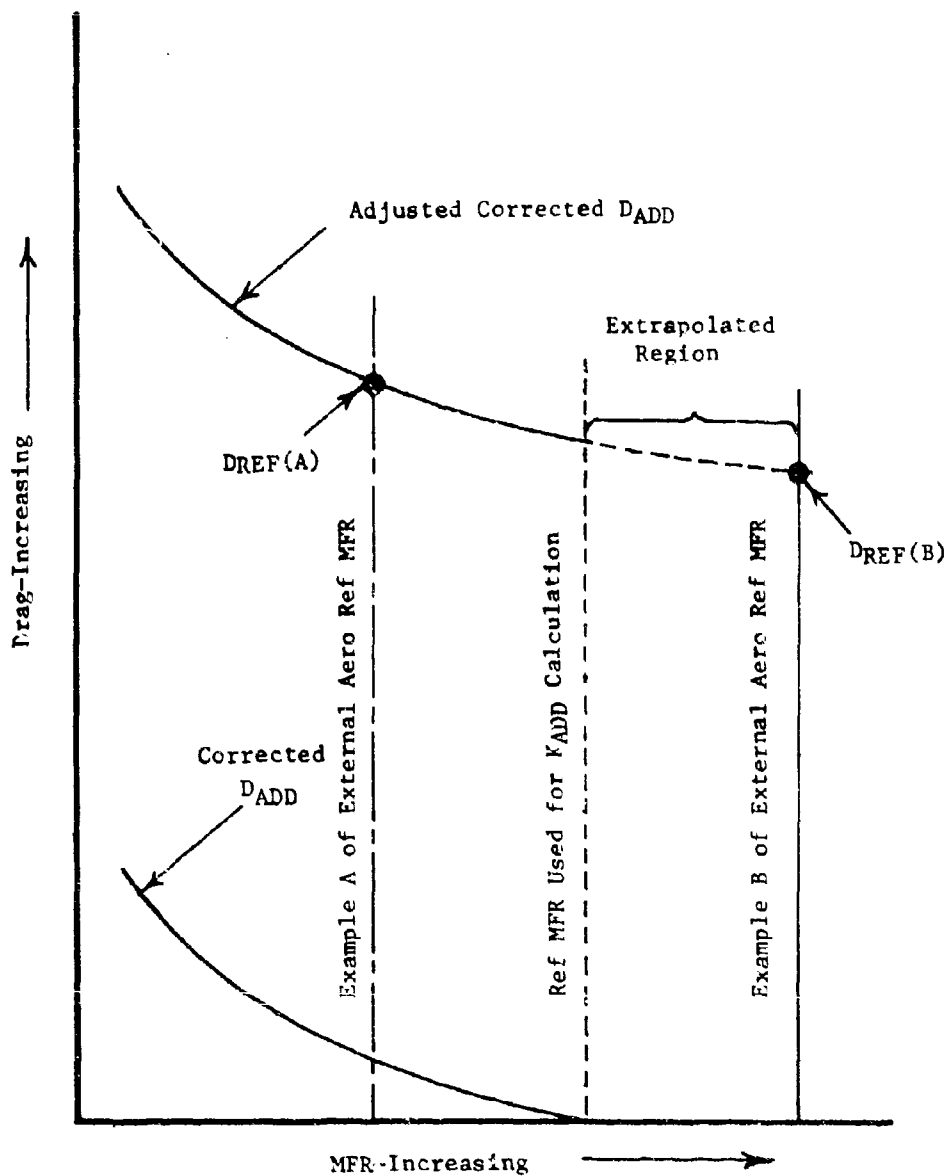


FIGURE 4-54. Combining Corrected Additive Drag With External Aircraft Drag

# AXISYMMETRIC SINGLE CONE INLET MODEL

$$\alpha = 0^\circ$$

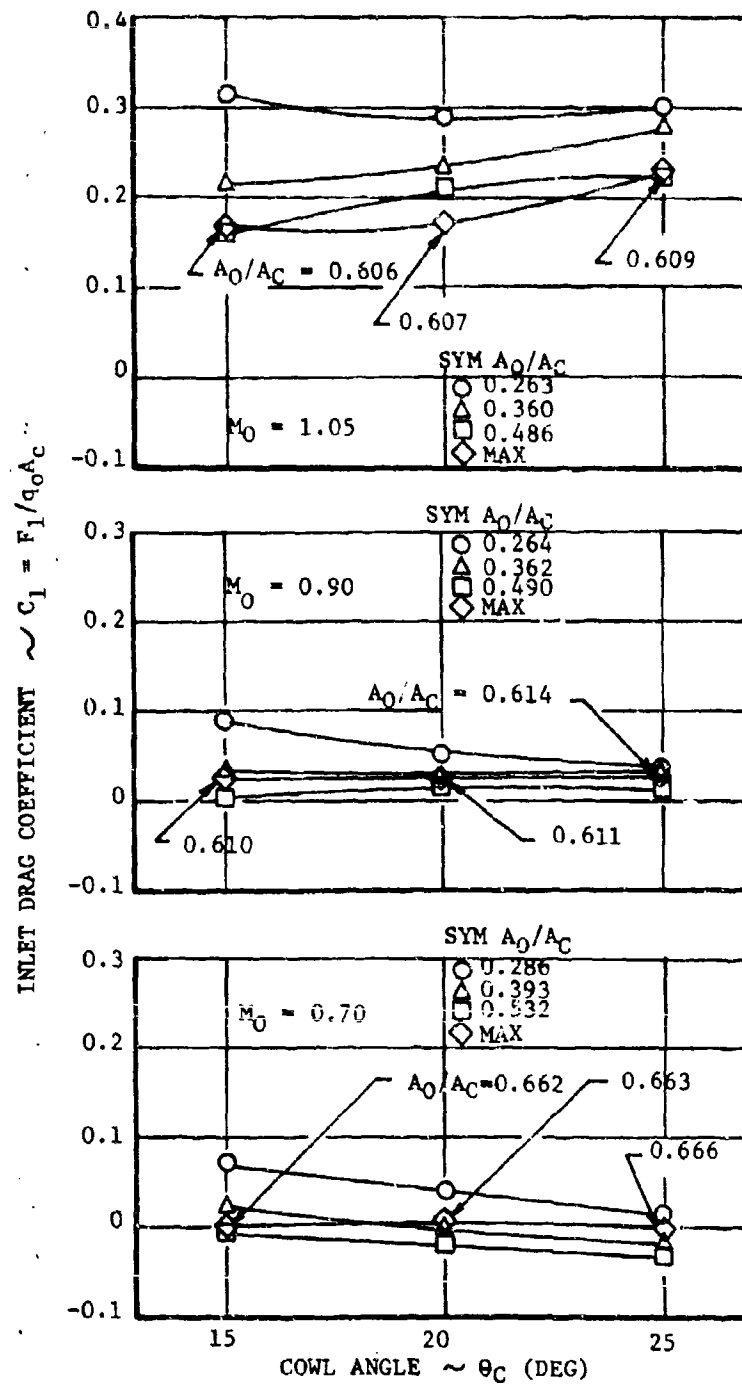


FIGURE 4-55. EFFECT OF COWL ANGLE ON INLET DRAG

# Axisymmetric Single Cone Inlet Model

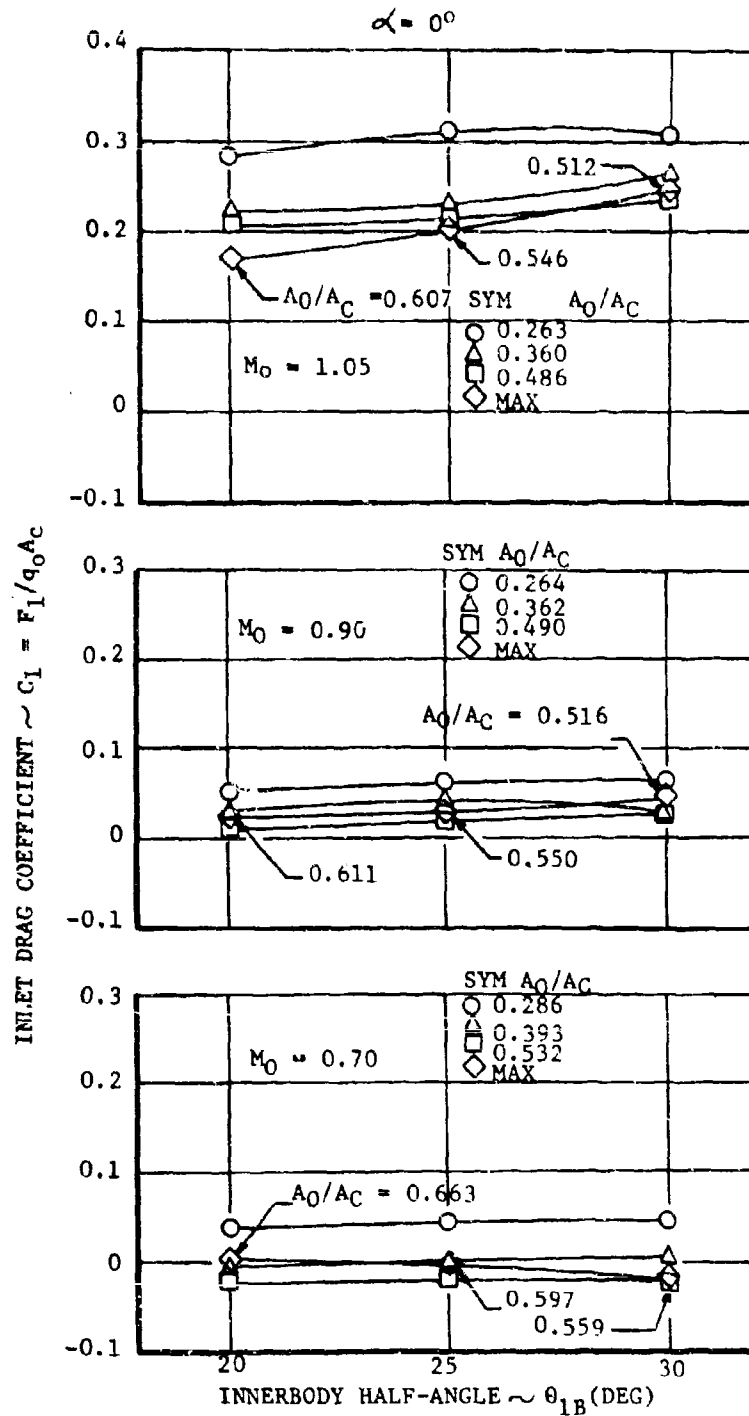


FIGURE 4-56. EFFECT OF INNERBODY HALF ANGLE ON INLET DRAG

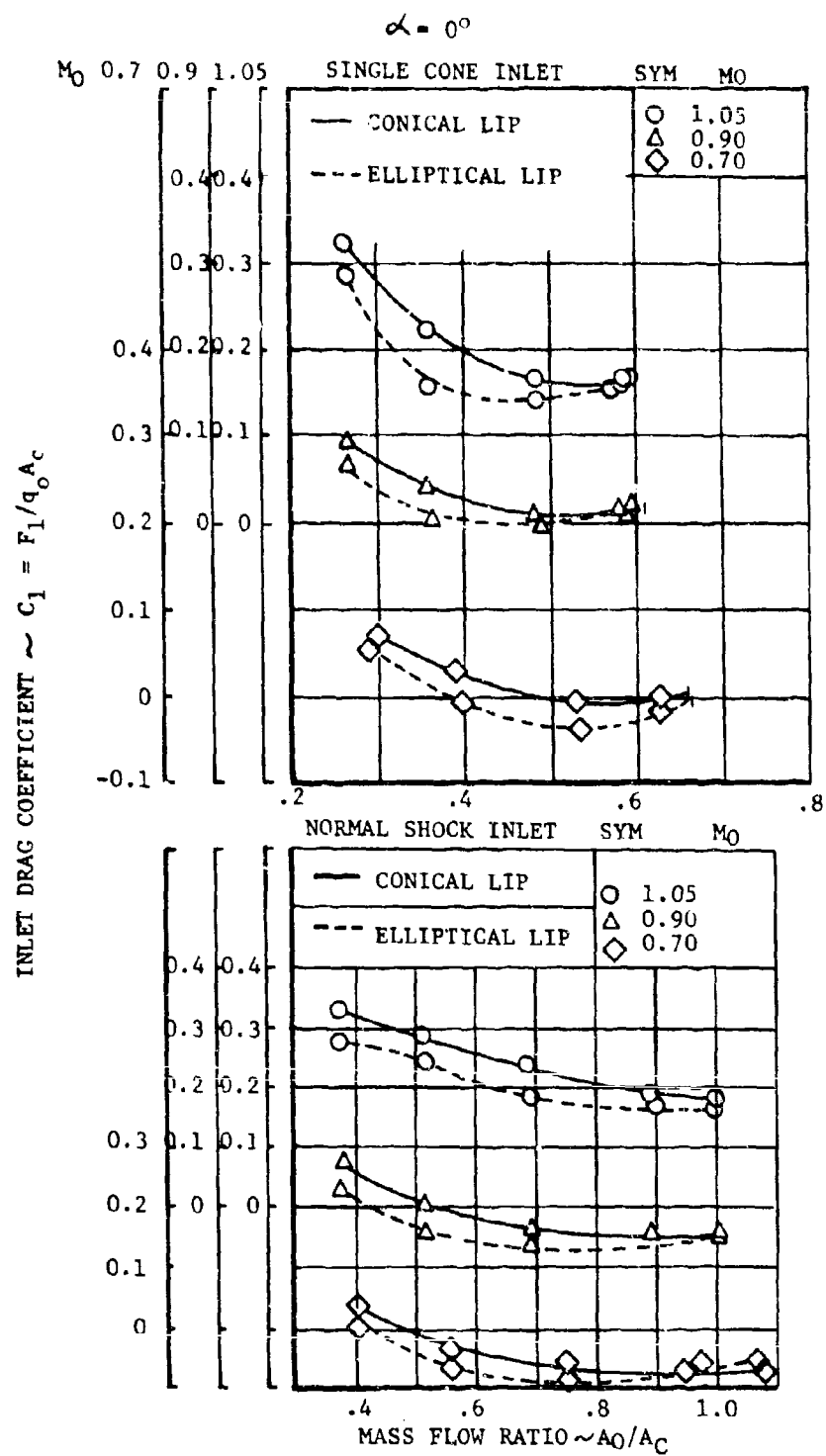


FIGURE 4-57. COMPARISON OF CONICAL AND ELLIPTICAL LIP INLET DRAG

$$\alpha = 0^\circ$$

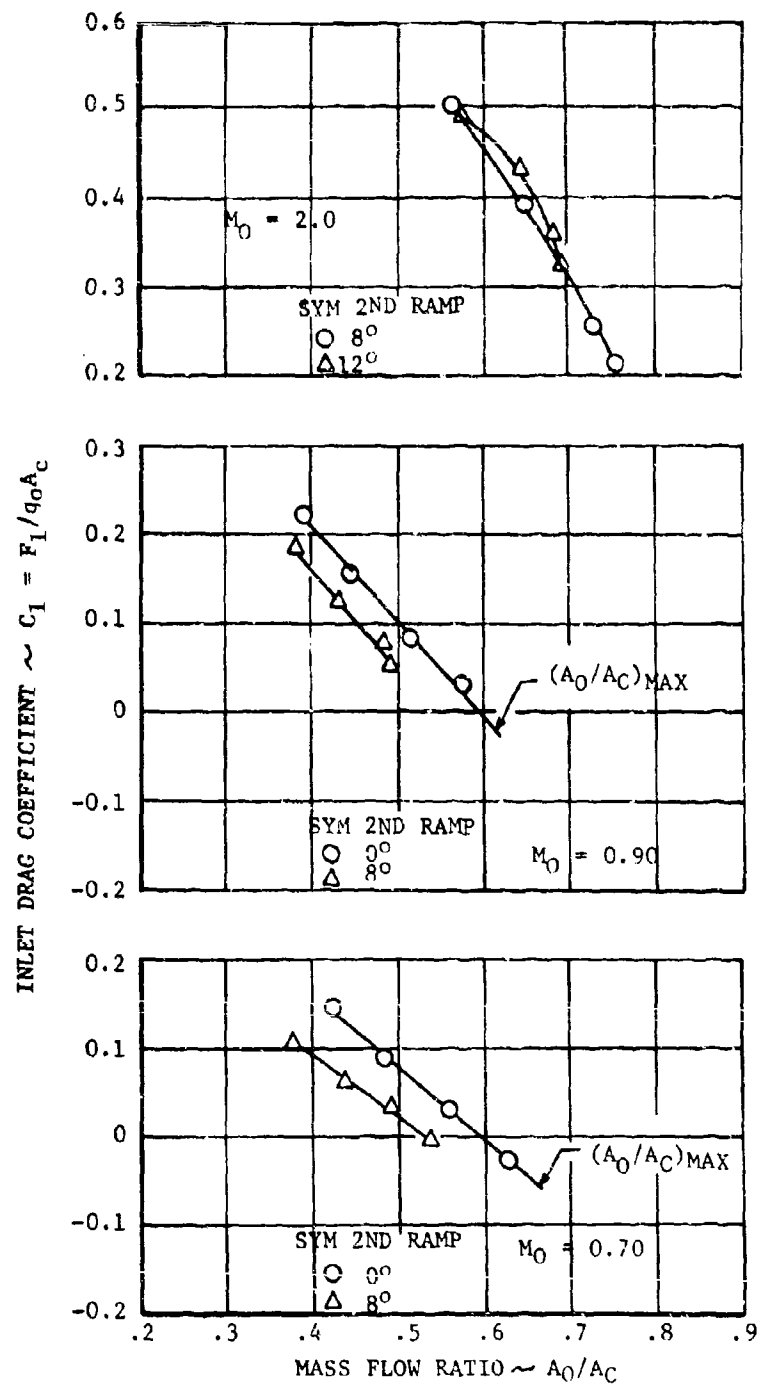


FIGURE 4-58.F-4 INLET RAMP ANGLE COMPARISON

## 5.0 Inlet Instability and Unsteady Flow Phenomena

Unsteady internal aerodynamic flow phenomena can occur in all flight regimes, both subsonic and supersonic. In most of the cases, the unsteadiness is internal to the inlet and is due to a rapid static pressure increase in the presence of a boundary layer. In this case the pressure rise causes separation of the boundary layer which usually leads to unsteady flow. If this unsteady pressure pulse is large enough to stall the engine or if the inlet-engine dynamics are such that the pressure pulse is amplified until the engine stalls, the system is termed unstable.

### 5.1 Unsteady Flow at Static and Subsonic Flight Conditions

Reference 1 points out that static pressure gradients and the initial condition of the boundary layer are important factors that affect both performance and flow steadiness. It is also pointed out that flow unsteadiness more often accompanies high diffuser entrance Mach numbers. This is because, for a given wall divergence angle that gradient in static pressure increases rapidly at high subsonic Mach numbers. To illustrate this, Figures 5 - 1, 5 - 2, and 5 - 3 are presented to show the theoretical pressure ratio in a length equal to one initial diameter for the moderate diffuser half angles of 2, 4, and 6 degrees.

Tests of a family of diffusers were reported in Reference 1. The inlets to the diffusers were bellmouth. A sketch of a representative test specimen and the instrumentation is shown in Figure 5 - 4. The measurements that were taken include static pressure fluctuations near the diffuser exit as well as performance. The diffuser shapes that were tested were described by maximum wall divergence angle. The maximum angles were 8° and 13.5°. The initial angles varied from zero to 6°. An important variable was the initial condition of the boundary layer. The initial condition was varied by trip wires placed on the bellmouth entry contour. For some of the tests, when the initial boundary layer was attached, the parameter used to express the thickness was  $\theta/r$ , the ratio of the momentum thickness to the duct radius. When the initial boundary layer was separated, the thickness was expressed in terms of  $\delta^*/r$ , where  $\delta^*$  was the displacement thickness. Data from the tests described above appear in Figure 5 - 4, 5 - 5, and 5 - 6 where the percentage static pressure fluctuation at the diffuser exit measuring station is plotted versus mass flow ratio. Also shown on the plots are amplitudes corresponding to a beat frequency that was present. This denotes that there were oscillations of more than one frequency present producing a beat of higher amplitude and lower frequency when two oscillatory disturbances came into phase to reinforce each other.

A similar phenomenon was discussed in Reference 2. The subject tests, on which most of the low speed loss methodology of Section 2.0 was based, had a total pressure probe with a transducer just upstream of the simulated compressor face. Here, as in the tests discussed above, a pressure fluctuation of lower frequency and higher amplitude was superimposed on the average periodic oscillation. Reference 2 gives a sketch like Figure 5 - 7 to illustrate the general nature of the oscillograph traces that were recorded during the tests. An aperiodic maximum total pressure fluctuation appeared along with a more periodic average fluctuation. Dynamic data for two of the eight test specimens were taken. Such data was taken for a sharp lipped inlet and one with a lip radius of 0.16 inches; the inlet diameter was slightly over 4 inches. Figure 5 - 8 shows data for the sharp lipped inlet and Figure 5 - 9 shows data for the round lipped inlet. The data shows that amplitude ratios tend to decrease as speed increases. Also, smaller amplitude ratios are shown for the round lipped inlet than for the sharp lipped inlet. These phenomena again can be related to the severity of the pressure gradient. Since the degree of separation becomes less severe with speed increase and with lip bluntness, the ratio of aerodynamic flow area between downstream and upstream decreases and hence static pressure gradient decreases. The data is presented versus the Mach number at the simulated compressor face. To facilitate more detailed study of the data as it relates to conditions at the inlet, the theoretical relationship between the inlet Mach number,  $M_1$ , and the compressor face Mach number,  $M_3$ , for the model being discussed is presented as Figure 5 - 10.

## 5.2 Duct Rumble and Twin Duct Instability

Duct rumble is an unsteady flow phenomenon that has occurred at high subsonic speeds. In Reference 3, duct rumble was associated with the Mach number region of 0.65 to 0.92 when operating at very low inlet velocity ratios when there is boundary layer present. In this case the high static pressure gradient is in front of the inlet. At the low inlet velocity ratios corresponding to an engine windmilling or idle power operating condition, the entering flow has a small free-stream tube area that expands to fill the inlet area as shown in Figure 5-11. Increasing the mass-flow-ratio decreases the static pressure gradient in the expanding stream tube and would eliminate the rumble, but this is not often possible since the inlet size is dictated by the larger flow quantities. An effective boundary layer diverter is the method most often used to alleviate the problem.

Twin duct instability is a problem that can occur when twin ducts empty into a common chamber to feed one engine. Referring to



Figure 5 - 12, if the inlet is operating at the point corresponding to the pressure peak at Point s, a disturbance such as the boundary layer interaction mentioned previously can cause the operating point of one inlet to move to Point b, and the other to move to Point a. A sufficiently effective boundary layer removal system would cause the point for peak static pressure to be at zero velocity ratio and hence the problem of twin duct instability would be eliminated. The problem of twin duct instability can, of course, occur in supersonic flight and should be avoided there too. In a supersonic application, adverse twin duct interaction was alleviated by perforating the wall between ducts upstream of the juncture to equalize the static pressure and enable the crossflow to provide viscous damping.

### 5.3 Supersonic Unsteady Flow Phenomena

Figure 5 -13 is a typical pressure recovery versus mass flow ratio curve for an external compression inlet operating supersonically. On it are noted the regions of possible instability; on the supercritical leg of the curve, normal shock oscillation and the possible buzz region occurring subcritically.

Two points of the curve are mentioned as being possibly able to create an engine stall condition. The lower of these two is not likely to happen in a practical situation since it would require a large increase in corrected weight flow demand. However, under an engine out condition, the decrease in air flow demand could cause such a condition as the point at which the intensity of buzz would be sufficient to stall the engine. The consequences of the other regions of unsteady flow and instability can range from annoying noise levels to minor aircraft structural damage.

#### 5.3.1 Supercritical Normal Shock Oscillation

What is happening here is not unlike the phenomenon that was demonstrated in the small scale low speed tests discussed in a previous section. The degree of this type of difficulty that can be experienced due to engine variations, inlet control system tolerances, etc. can be minimized by boundary layer control. However, as the inlet becomes more supercritical the normal shock moves further aft in the duct. It is impractical to remove the boundary layer along the full length of the subsonic duct. Therefore at some supercritical mass flow the normal shock will move out of the region of controlled boundary layer and into a region of sufficient boundary layer that separation occurs which usually leads to unsteady flow. This type of unsteady flow is characteristically of high frequency and is not necessarily an instability.

### 5.3.2 Inlet Buzz

Buzz is the low mass-flow-ratio phenomenon in which the normal shock moves in and out of the duct in an attempt to satisfy continuity. Separation of either duct or pre-compression surface boundary layer occurs during part of the buzz cycle. Figure 5 - 14 shows schematic sketches of two buzz triggering theories. In the upper one when the normal shock is expelled from the duct, a vortex sheet from the shock intersection impinges on the duct wall and separates the boundary layer which changes the aerodynamic flow area in such a way that the shock wants to be swallowed. After it is swallowed the vortex sheet disappears so that continuity again demands an expelled shock position.

In the lower diagram, the high diffuser pressure is being fed through the boundary layer causing separation, an altering of the aerodynamic flow area distribution, asking for shock swallowing, and then after the shock is swallowed, the physical reason for the swallowing requirements is removed, and the whole process repeats itself.

In a prototype flight test program on a supersonic aircraft, a considerable amount of data was gathered on performance, distortion, buzz, and buzz in combination with engine compressor stall. For that particular aircraft the results were summarized as follows:

1. The fundamental buzz component appeared to have a frequency near 10 cps and an amplitude on the order of  $\frac{1}{5}$  of free-stream total pressure.
2. Compressor stall often accompanied buzz with pulse frequencies on the order of 1 to 4 cps and amplitudes of up to  $\frac{2}{3}$  of free-stream total pressure.
3. That the locations of the maximum amplitudes appeared to be in the downstream portion of the diffuser.

These may be thought of as being near typical; however, the effects of distortion and stall tolerance of the compressor are important factors.

#### 5.4 Inlet/Engine Dynamic Interaction

For the design of an optimum engine/inlet system, an important interface area, it is imperative that the airframe and engine manufacturers work more closely together. Typically, the engine and airframe manufacturer each design to the maximum steady state operating condition. However, acceptable transient and off-design operation of air-breathing propulsion systems result in the scheduling of the various components below their optimum steady-state performance levels. At off-design operation, it is likely that certain inlet-engine transients would cause unstable operation. Although scheduled stability margins are required for only small portions of the mission time, they impose a performance penalty for all steady-state operations. This makes it necessary for the airframe and engine manufacturers to work closely together in this interface area and make each other aware of the off-design limitations of the components. Then, an optimum dynamically designed, air breathing propulsion system will result.

During an inlet development program, initial dynamic measurements should be made from the beginning. As the program progresses and larger scale models are tested, more complete instrumentation can be installed. The random pressure data thus obtained require random data analysis techniques such as time correlation, spatial correlation and spectral analysis in order to develop distortion design criteria.

Instrumentation requirements for propulsion system dynamic testing include extremely high response pressure transducers with frequency response capability up to 5,000 cps for scale model testing.

Air inlet-engine incompatibility has become a major problem of high speed aircraft. The phenomenon consists of inlet (or engine) induced flow distortions and pressure pulsations which may cause compressor stalls, duct unstarts, etc. One approach to the dynamic interaction problem is to mathematically model the inlet/engine combinations and then subject the system to high frequency transients. However, in most cases the pressure fluctuations are random, requiring that random data analysis techniques be utilized such as power spectral analysis. For the convenience of the reader a few of the more common terms encountered in statistical analyses of inlets are discussed below. For more rigorous definitions and discussions the reader is referred to any good text on Statistical Analysis, a good example of which is Reference 4.

Power Spectral Density (PSD) is a representation of how the mean square value of the variable being considered is distributed over the frequency range. In the case of inlet analysis the variable of interest is pressure

fluctuation and:

$$\int_0^{\infty} (\text{PSD}) \, d(\text{freq}) = \int_0^{\infty} \frac{(\Delta P_{\text{RMS}})^2}{\text{freq}} \, d(\text{freq}) = (\Delta P_{\text{RMS}})^2$$

The great utility of the PSD representation is that if "energy" is concentrated at or near particular frequencies, such concentration appear as "spikes" on the PSD graph, and the generating mechanism is hence often determined. An example PSD plot is shown at the top of Figure 5-16.

Amplitude Probability Density (APD) represents the probability of occurrence of a given amplitude at any given time. The Central Limit Theorem states that the APD for a variable that results from a succession of random events can be expected to approach a Gaussian or Normal distribution. An example APD plot is shown at the bottom of Figure 5-16. This curve is extremely useful since it displays the "randomness" of the data. Most of the tools of statistical analysis are based on the assumption of purely random variations. If this is not true then the statistical analysis is invalid. Thus if the APD curve varies very much from a Normal Distribution statistical analysis should not be used. A good example of this is an inlet in buzz. The definition of turbulence given in Section 5.4.1 can include pressure variations due to inlet buzz. However, since the buzz disturbance will tend to dominate the pressure fluctuations due to other sources the APD plot of an inlet in buzz will not be Normal. Therefore statistical analysis is not possible.

#### 5.4.1 Inlet Turbulence and Dynamic Distortion

Duct turbulence is defined in most inlet studies as the AC component of the pressure (usually engine face total) at a particular point. The source of duct turbulence can be external to the engine installation such as free stream disturbances, wing or fuselage vortices or boundary layer; or it can be internal such as a burner instability, local separation in the compressor or afterburner blow out as well as duct boundary layer instability.

A survey of the steady state engine face total pressure of any engine installation will reveal an uneven distribution of pressure across the engine face. This unevenness is called distortion. A standard parameter for the measurement of this distortion is  $(P_{\text{max}} - P_{\text{min}}) / P_{\text{average}}$ . If, instead of steady state data, a survey is made of the instantaneous absolute value of engine face total pressure this observed distortion is called instantaneous or dynamic distortion.

Much work has been done in recent years in trying to correlate turbulence, steady state distortion and dynamic distortion to degradation in engine performance and particularly to compressor stall or surge. Recent developments have brought about several more complicated parameters for measuring distortion such as ND1, KD2, K<sub>A</sub>, K<sub>RA</sub>, K<sub>C</sub>, etc. These parameters, however, are related to specific engines and are developed according to the characteristics of that engine. It has been found that there is an interrelation between engine tolerance to turbulence, steady state distortion and dynamic distortion as well as engine face total pressure recovery. For example a lower steady state average engine face recovery is usually associated with a lower tolerance to turbulence. For this reason turbulence is usually shown in the literature divided by PT<sub>2</sub>. Also a higher value of  $\Delta P_{RMS}/PT_2$  will result in a lower tolerance to distortion. An example of the manner in which this varies is shown in Figure 5-15. (It should be pointed out here that there is a slight inconsistency in the currently available turbulence data. Some of the data is in terms of  $\Delta P$  while the rest is in  $\Delta P_{RMS}$ . Since these two are not always clearly differentiated, care should be taken to determine which is being used. For a purely random distribution  $\Delta P \approx 6 \Delta P_{RMS}$ ).

Most of the current effort in this field has been concentrated on the gross parameters such as steady state distortion and  $\Delta P_{RMS}/PT_2$  because of the availability of data and ease of data acquisition as well as the amount of data required. There are those, however, who believe that these gross parameters will never show a good enough correlation to stall and that the more detailed analysis methods and parameters will have to be used such as instantaneous pressure maps, power spectral density plots and even narrow frequency band turbulence measurements throughout a wide frequency range. For example, results of Pratt & Whitney Aircraft TF-30 turbofan engine testing (Reference 5) indicates that the percent loss in compressor surge line showed some correlation with the RMS total pressure parameter  $\left(\frac{P_{TRMS}}{PT_2}\right)$  in the frequency range from zero to about the rotor's revolution (160 Hertz), however, it did not predict surge. The TF-30 test results indicate that the surge inducing event is instantaneous distortion and is predictable. The frequency range, however, had to be timed to the rotor rotation (0 to 160 Hertz) in order to predict surge. There were cases where larger dynamic distortion occurred than that which caused surge, but its time duration was evidently too short to affect the engine. P&W found that their circumferential distortion factor (K<sub>Q</sub>) plotted as a function of time for high cut rates predicted the pending surge slightly after the peak of K<sub>Q</sub> occurred in nearly every case provided that a 160 Hertz low-pass filter was used on the data prior to analysis.

The fact that the test data analysis to date has not found a parameter or combination of parameters using  $\Delta P/T_{RMS}$  and a form of steady state distortion that correlate well with the surge event does not mean that one does not exist. Much effort is still being expended to find such a correlation.

It is hoped by some that a "Universal" distortion parameter can be found that is correlatable to stall for all engines. If such a "Universal" parameter or group of parameters do exist it is more probable that they will be found in the detailed analyses methods. It will then be necessary to decide whether it is best to use a "Universal" analysis method that is very detailed or an individual empirical analysis method of more easily obtained gross parameters. There are obviously uses for each.

Another area of study in the inlet dynamics field is the problem of how to scale turbulence from model to full size. It is very important to be careful here in the use of the terms decay, dispersion, and dissipation since considerable confusion can arise if the terms are used interchangeably. As used here:

DECAY is the decline in magnitude of the turbulence kinetic energy

DISPERSION is the spreading of the turbulence kinetic energy over the range of wave numbers by inertial interaction of the eddies

DISSIPATION is the process by which the action of molecular viscosity actually converts the kinetic energy of the turbulence to heat.

Pratt & Whitney has conducted a study in this area (Reference 6). The conclusions of this study, although not yet universally accepted, give evidence that for most inlet turbulence the rate of decay of turbulence within both subscale models and full scale inlets is primarily limited by dispersion rather than by dissipation. As a consequence, the decay of inlet turbulence intensity will be independent of the inlet Reynolds number over a very broad range of Reynolds numbers. This simplifies the scaling of turbulence energy spectra. For cases where this is not true it should be pointed out that sub-scale turbulence tests will give an unduly conservative prediction of turbulence intensity at the engine face. It should also be emphasized that the above discussion is concerned with turbulence decay and not with turbulence production which can be very configuration and Reynolds number dependent.

## References

1. Scherrer, R. and Anderson, W. E., Preliminary Investigation of a Family of Diffusers Designed for Near Sonic Inlet Velocities, NACA TN 3668, February 1966.
2. Blackaby, J. R. and Watson, E. C., An Experimental Investigation at Low Speeds of the Effect of Lip Shape on the Drag and Pressure Recovery of a Nose Inlet in a Body of Revolution, NACA TN 3170, April 1954.
3. Davis, W. F. and Scherrer, R., Aerodynamic Principles for the Design of Jet-Engine Induction System, NACA RMA55F16, February 27, 1956.
4. Bendat, J. S. and Piersol, A. G., Measurement and Analysis of Random Data, John Wiley & Sons, Inc., 1966
5. Plourde, G. A. and Brimelow, B. Pressure Fluctuations Cause Compressor Instability, Pratt & Whitney Aircraft, 69-9055
6. Oatis, G. C., Sherman, D. A. and Motycka, D. L., Experimental Study of Inlet-Generated Pressure Fluctuations, Pratt & Whitney Aircraft, PWA-3682

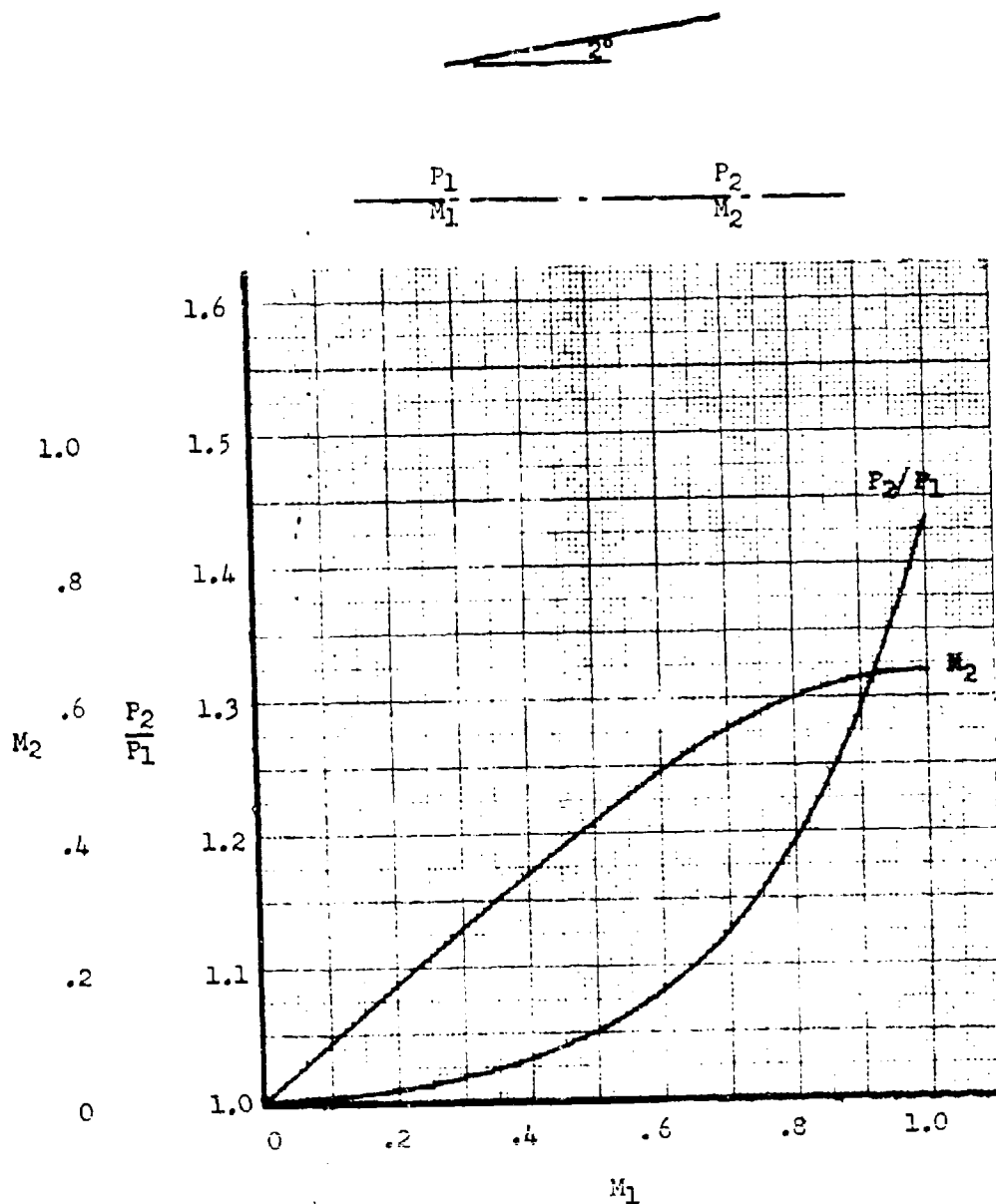


FIGURE 5-1. Theoretical Diffuser Static Pressure Rise as a Function of Initial Mach Number -  $\theta/2 = 2^\circ$



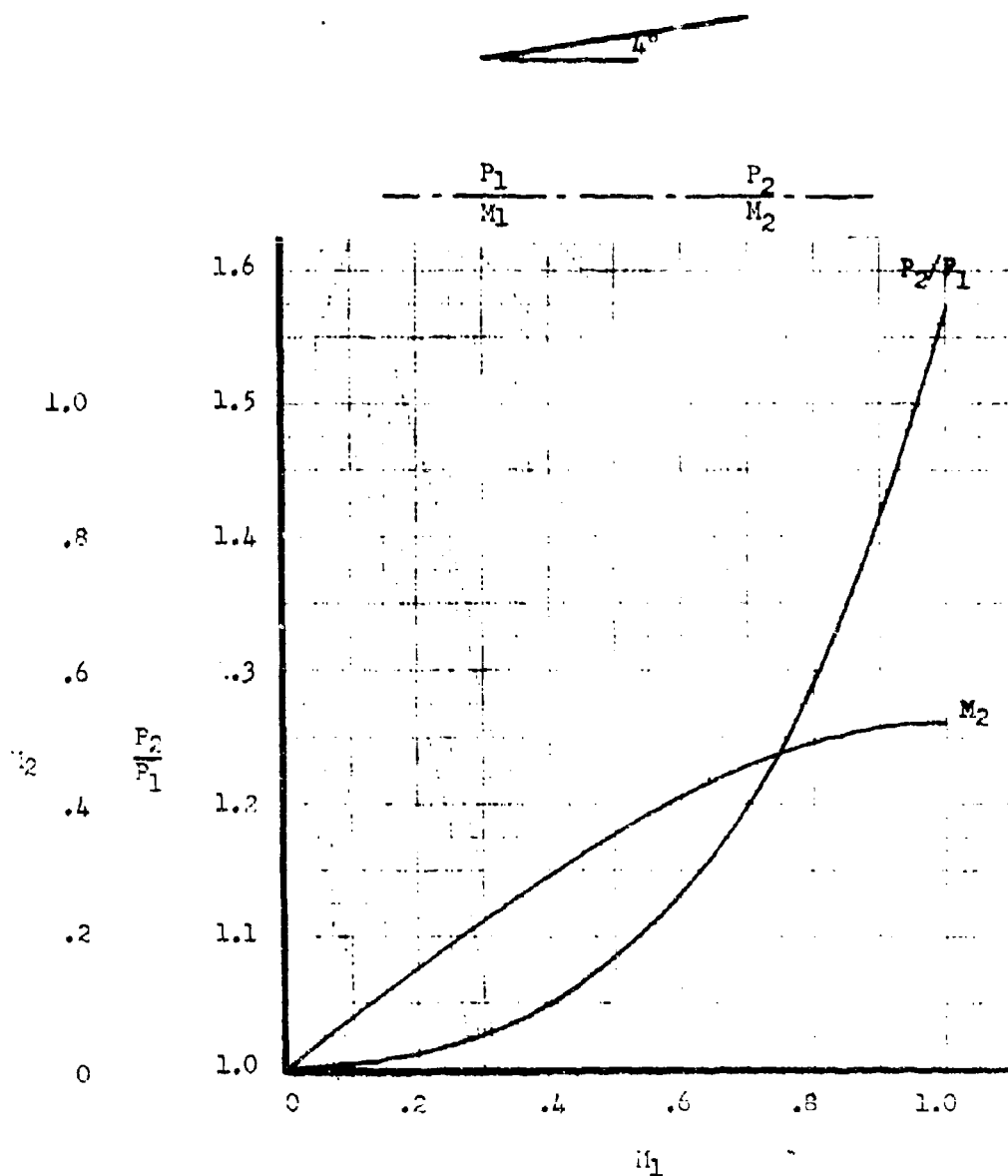


FIGURE 5-2. Theoretical Diffuser Static Pressure Rise as a Function of Initial Mach Number -  $\theta/2 = 4^\circ$

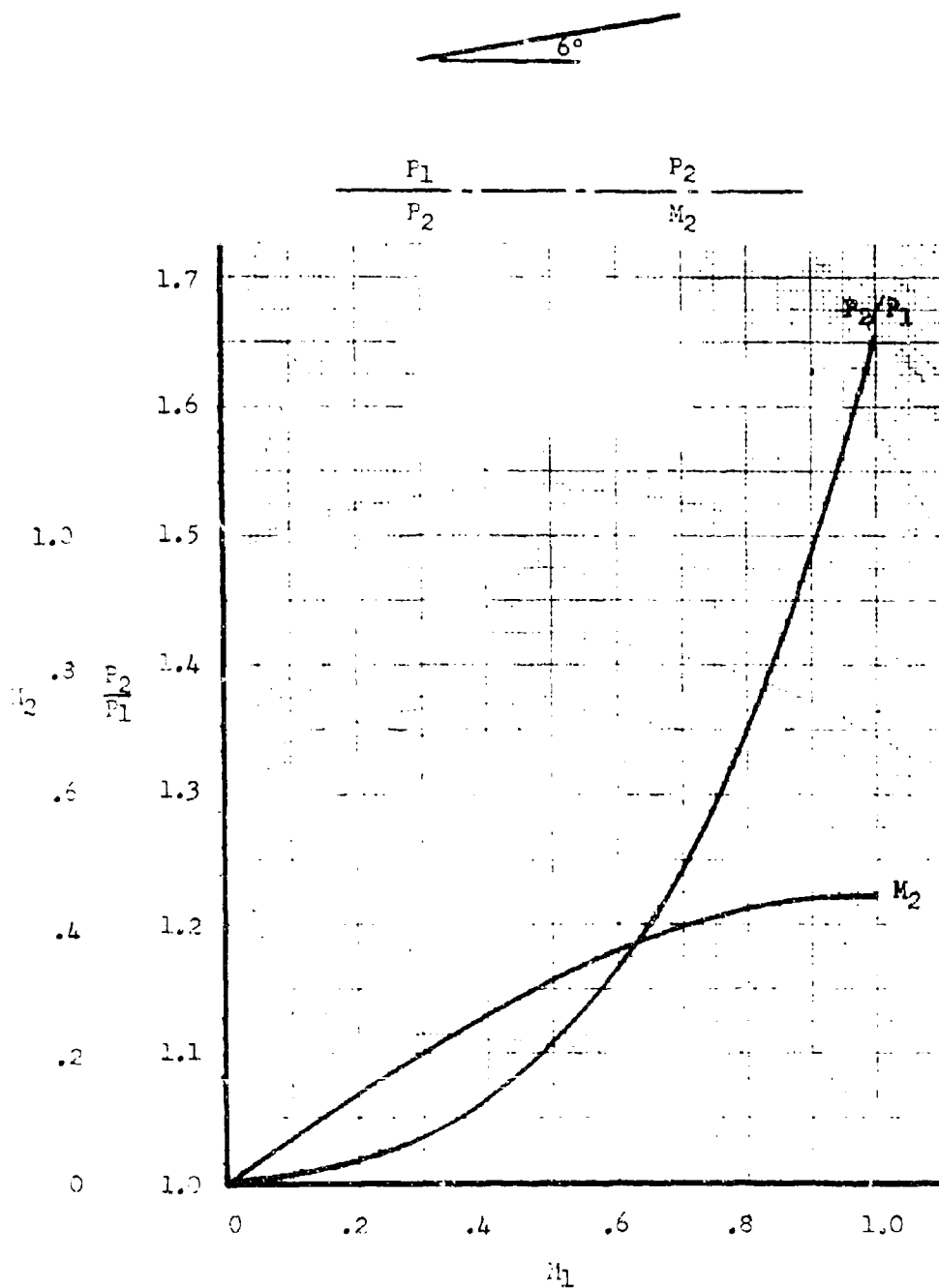


FIGURE 5-3. Theoretical Diffuser Static Pressure Rise as a Function of Initial Mach Number -  $\theta/2 = 6^\circ$

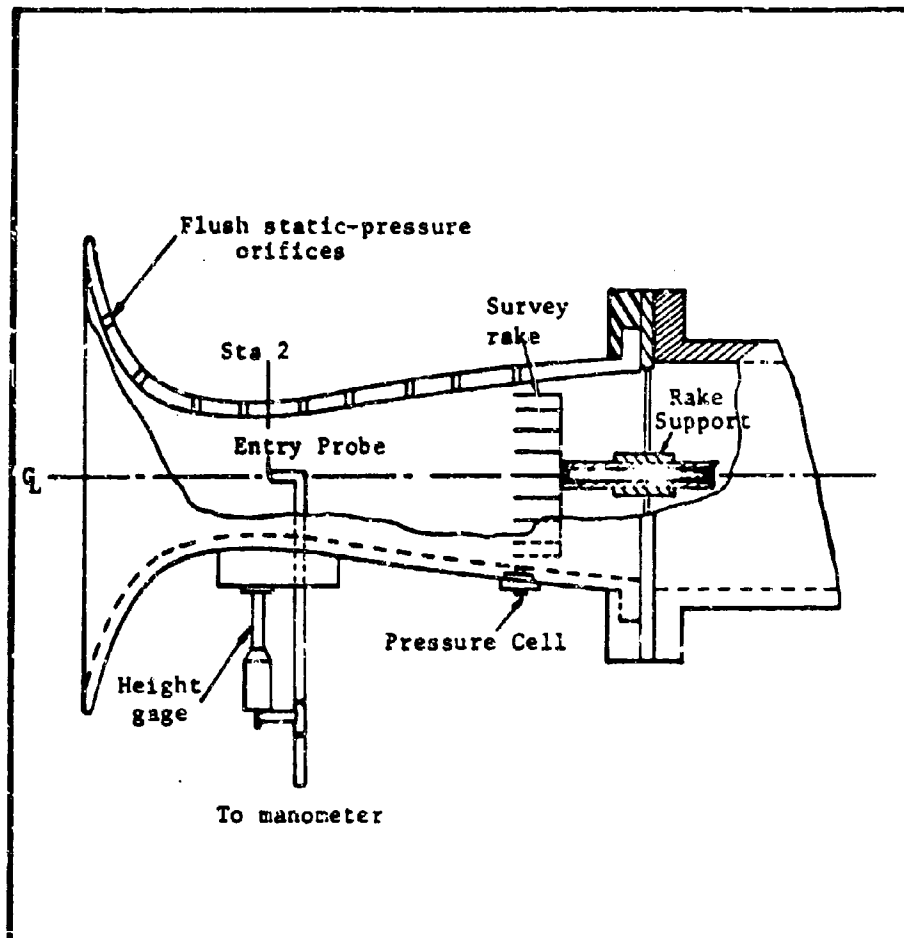


FIGURE 5-4. Sketch of Test Model

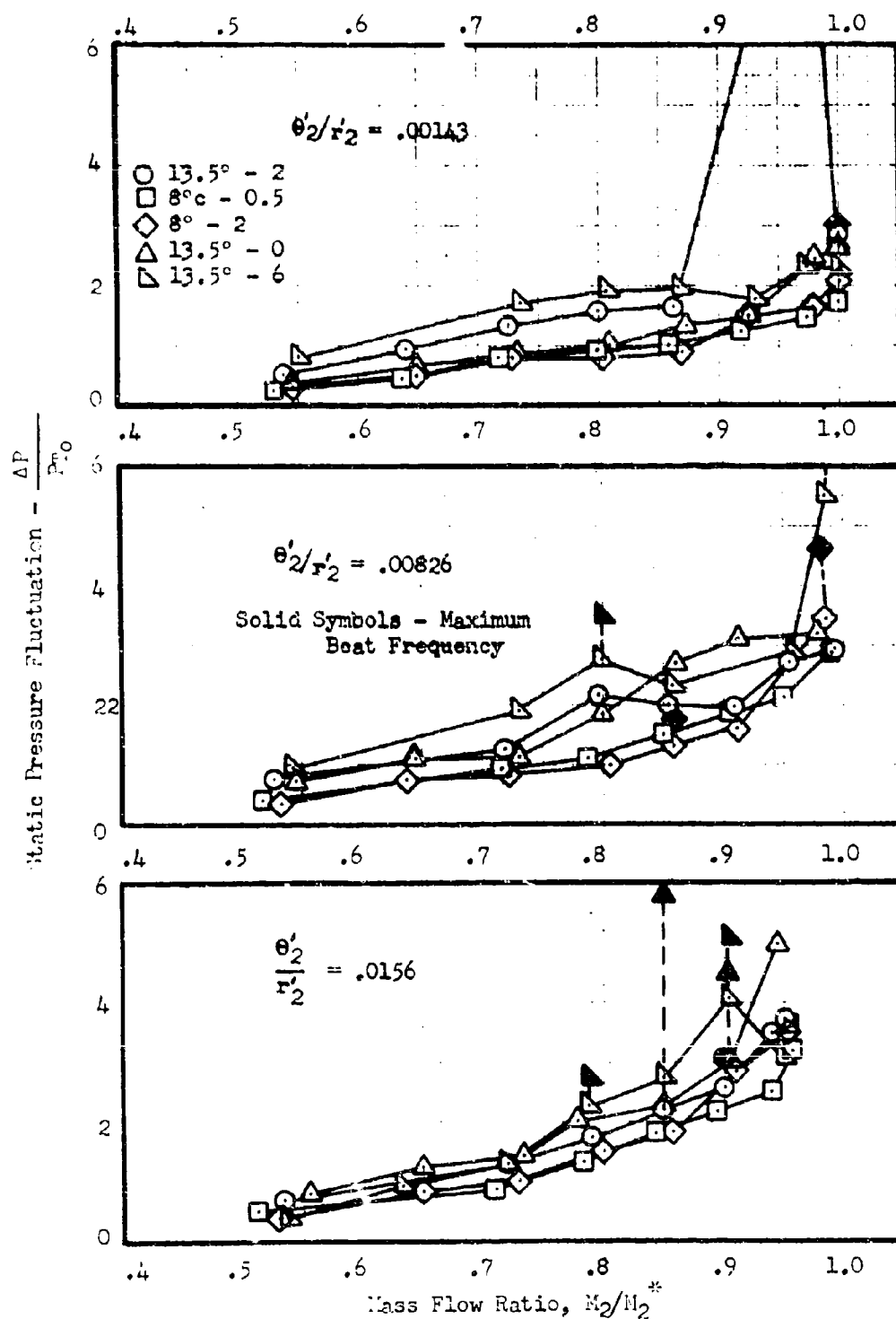


FIGURE 5-5. Static Pressure Fluctuation Characteristics of Straight Diffuser Models

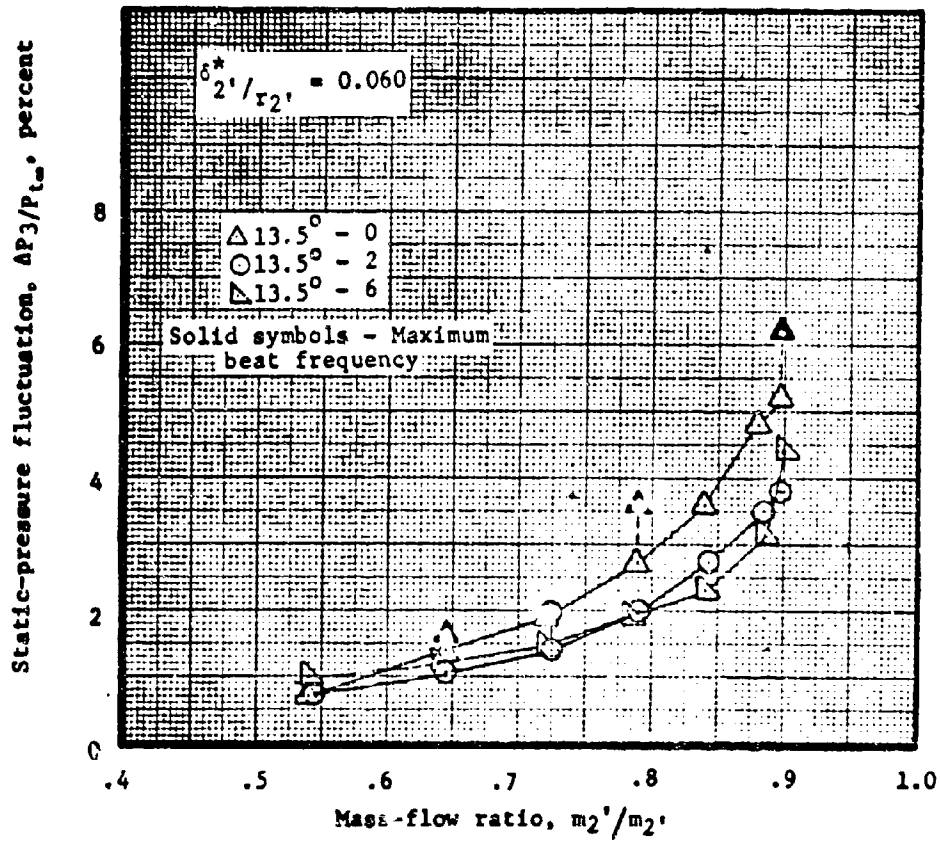


FIGURE 5-6. Diffuser Exit Static Pressure Fluctuation Data

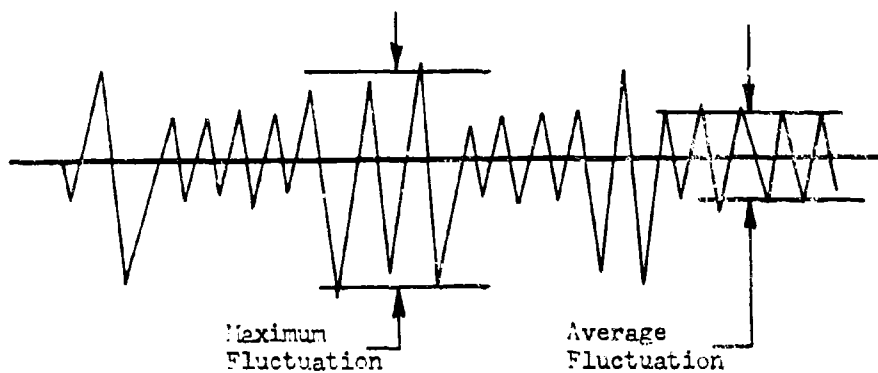


FIGURE 5-7. Representation of the Nature of Diffuser Total Pressure Fluctuations

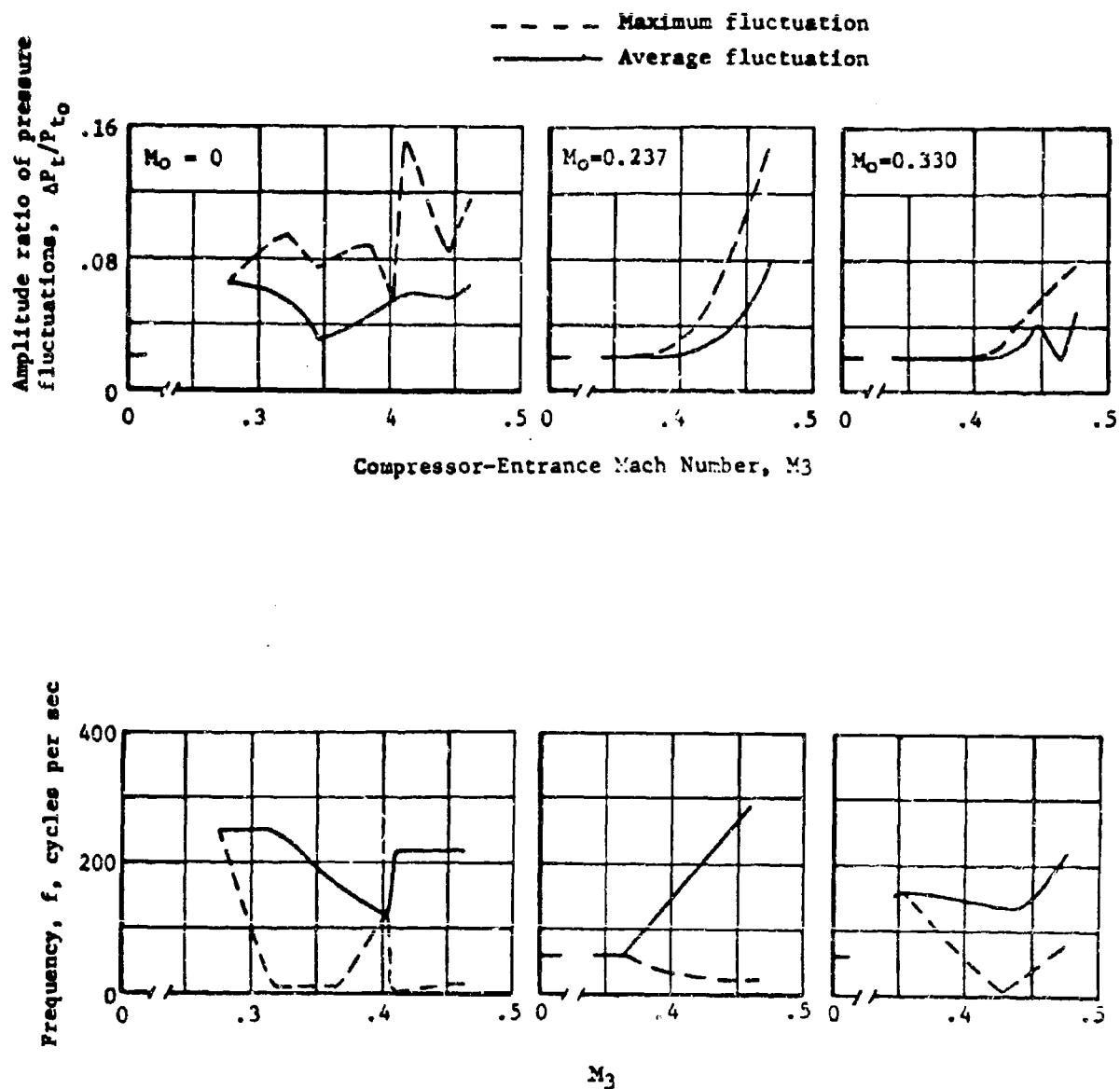


FIGURE 5-8. Amplitude and Frequency of Diffuser Exit Total Pressure of Sharp Lipped Inlet

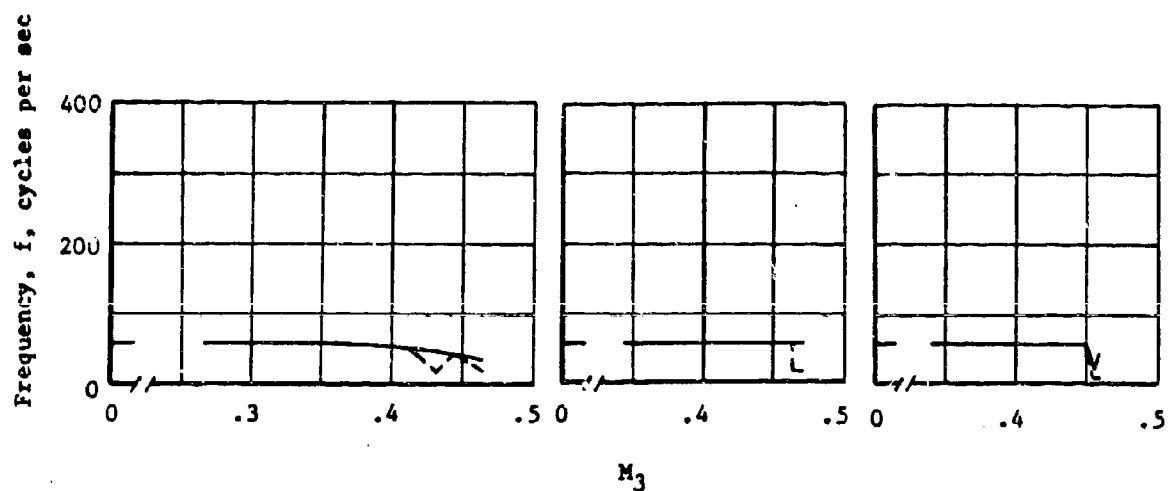
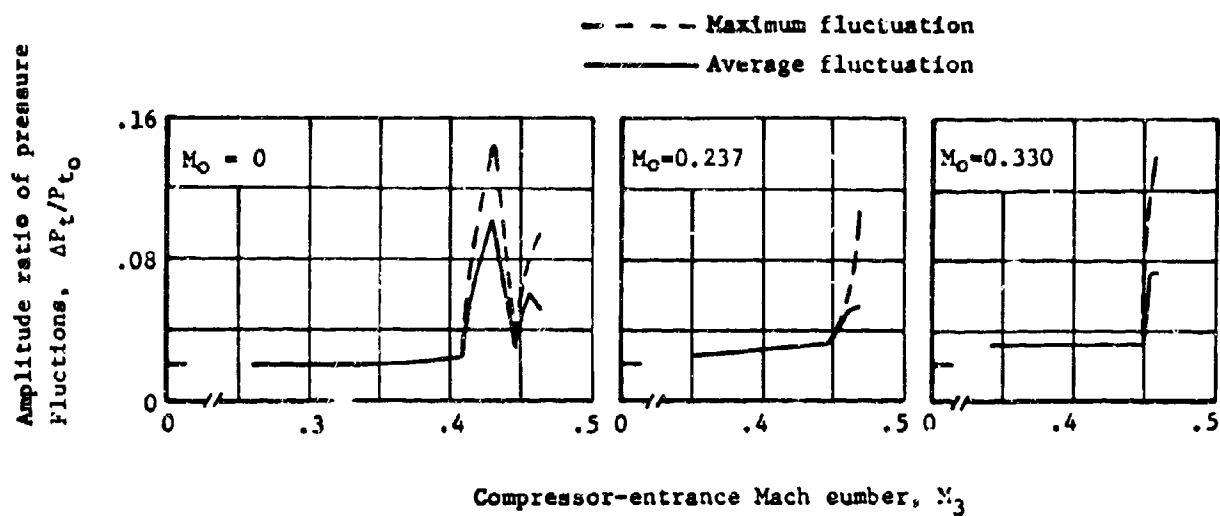


FIGURE 5-9. Amplitude and Frequency of Diffuser Exit Total Pressure of Round Flipped Inlet



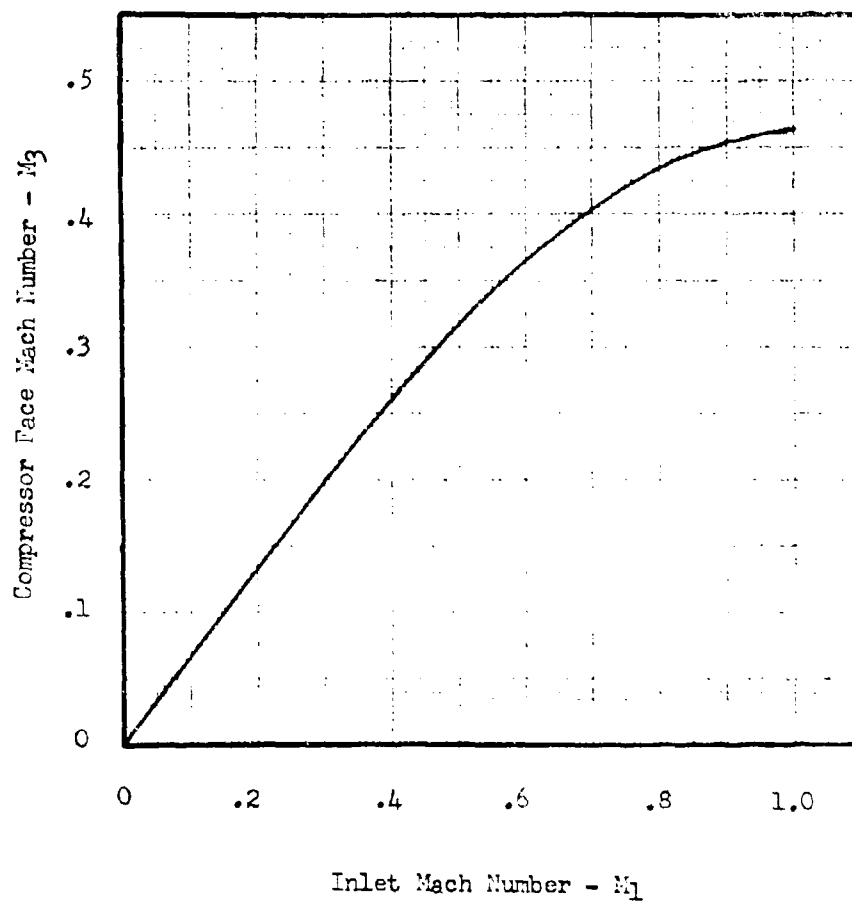


FIGURE 5-10. Theoretical Variation of Compressor Face Mach Number with Inlet Mach Number

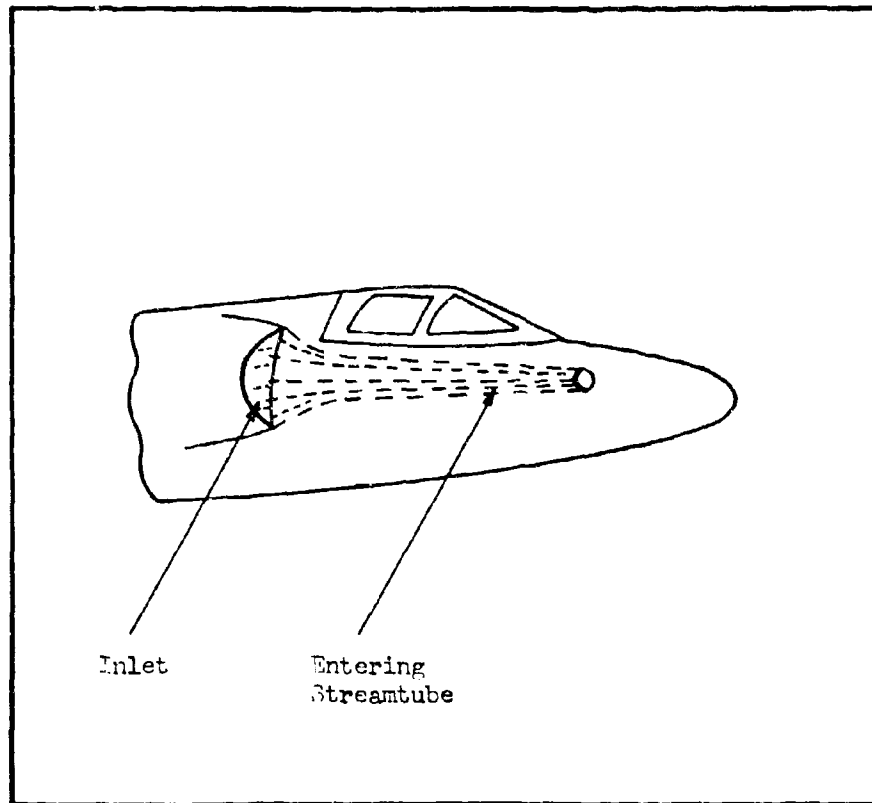


FIGURE 5-11. Streamtube at Low Inlet Mass-Flow-Ratios

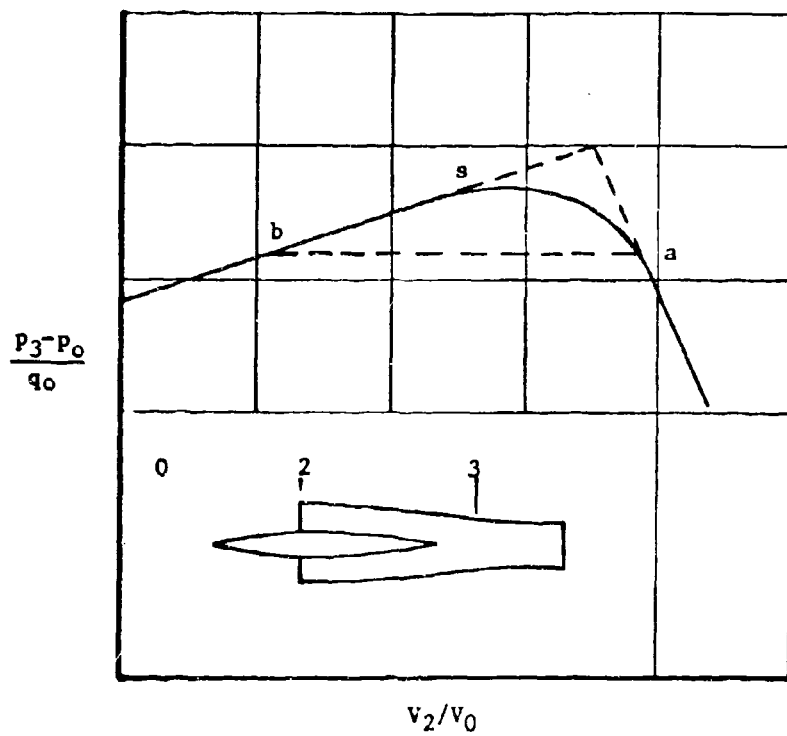


FIGURE 5-12. Twin Duct Instability

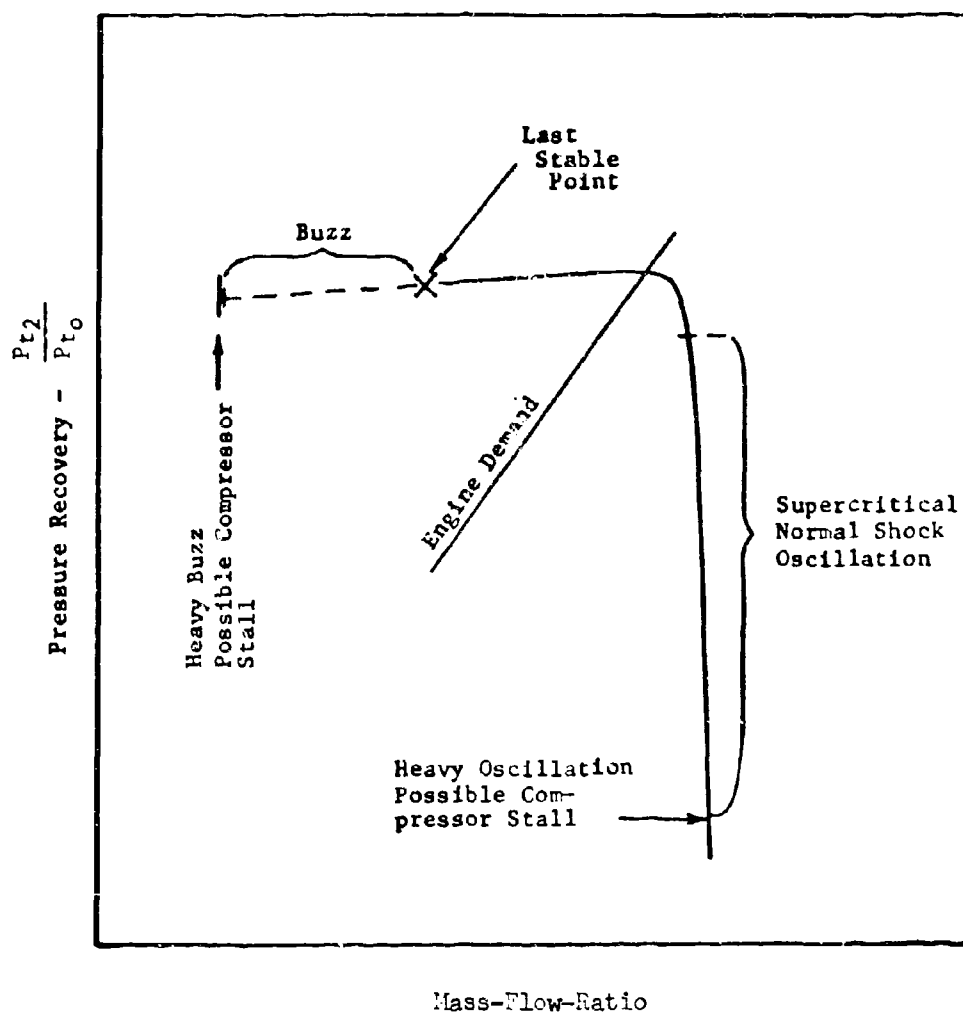


FIGURE 5-13. Typical Supersonic Inlet Performance Curve with Regions of Instability

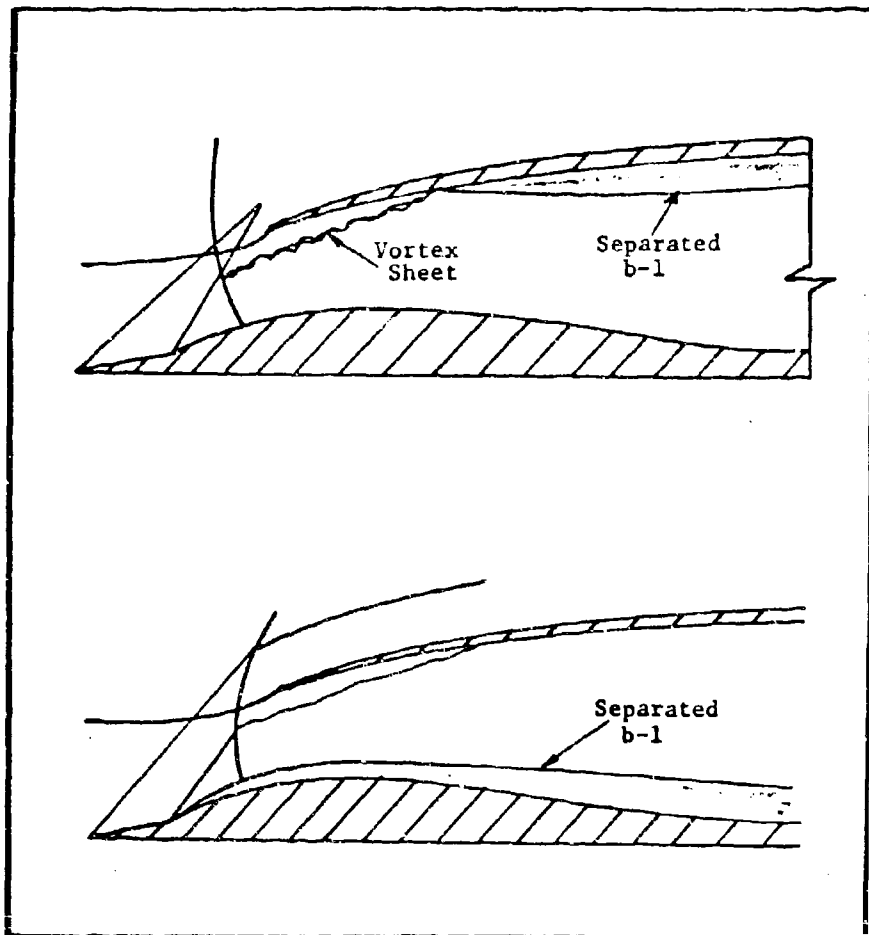


FIGURE 5-14. Schematics of Buzz Triggering Theories

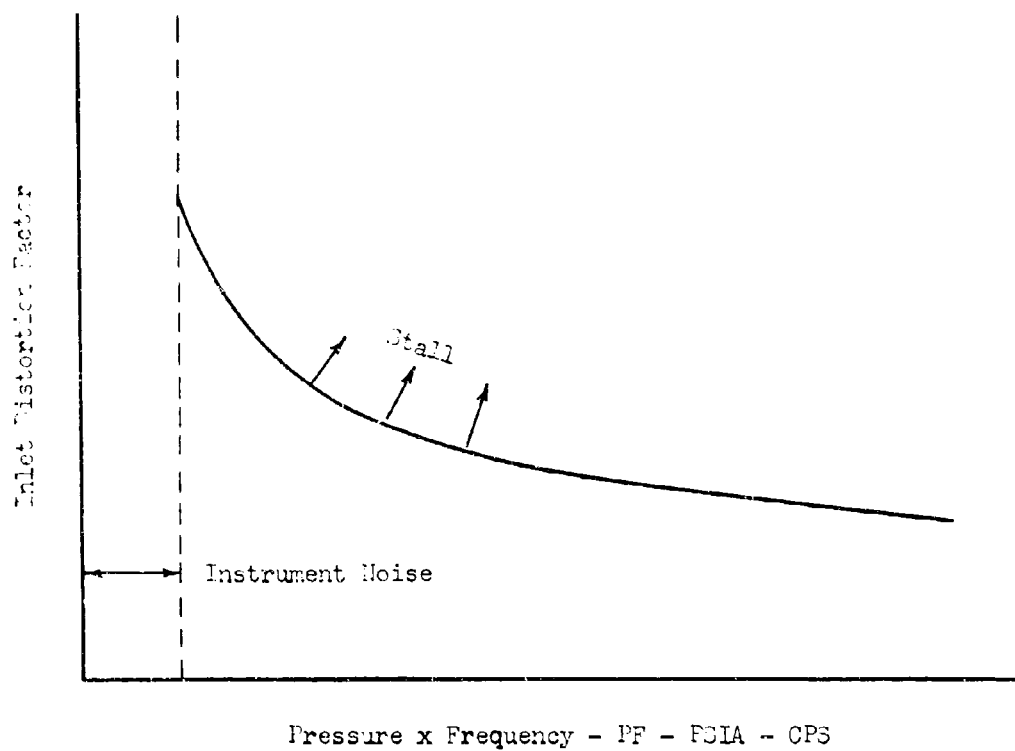


FIGURE 5-15. Effect of Inlet Pressure Fluctuation on Stall

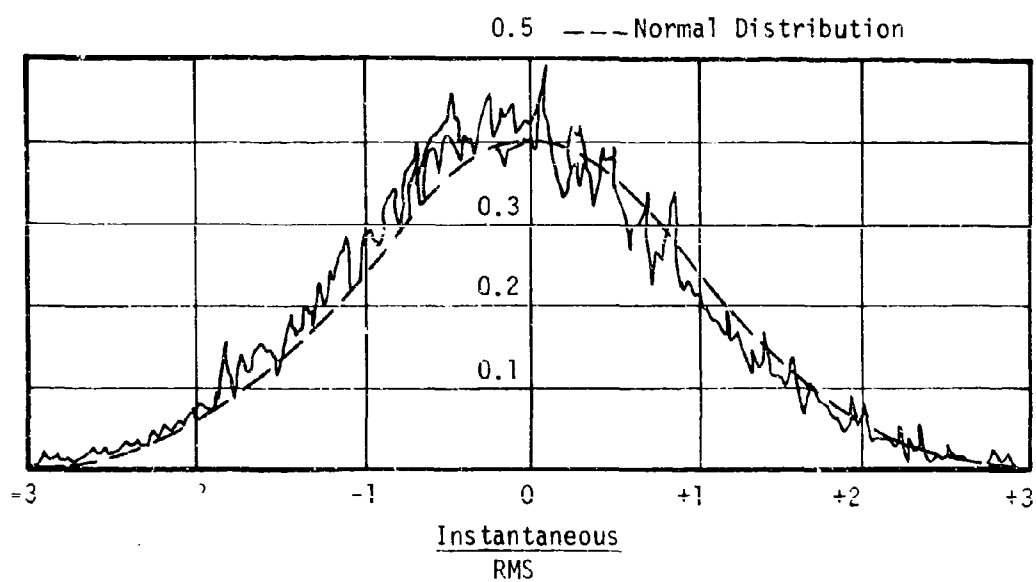
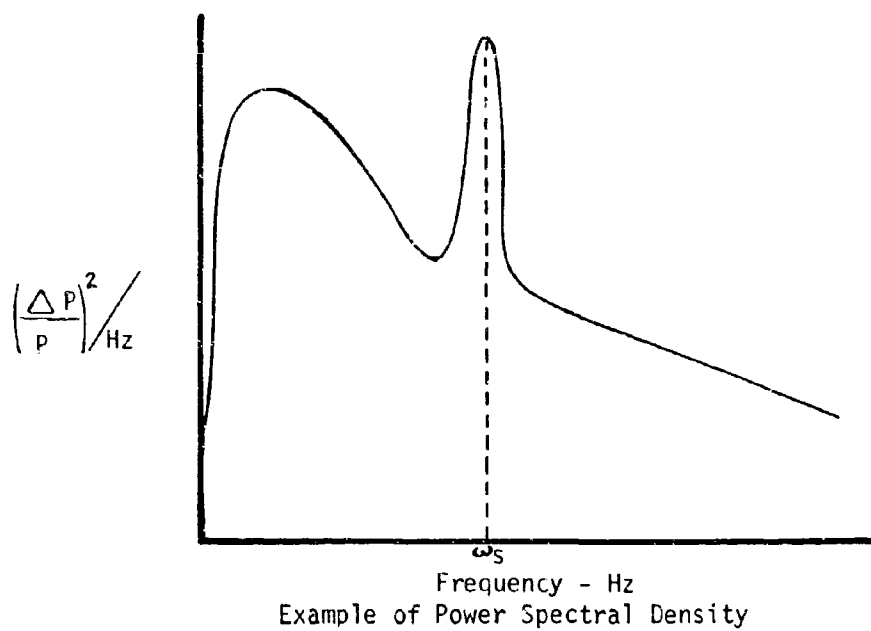


Figure 5-16. Samples of Statistical Analysis Curves

## 6.0 Inlet Control Considerations

As flight speeds increase, the role of the air induction control system becomes more important. This is a natural consequence of the increased ram compression available at supersonic flight speeds. For example, potential ram compression is greater than 7.8 at Mach 2.0, 36.7 at Mach 3.0 and 76.2 at Mach 3.5. Within the flight regime being discussed, ram pressure potential exceeds present state-of-the-art turbojet/turbofan overall compression ratios. Hence, the inlet becomes important and an integral part of the propulsion cycle.

The primary function of a supersonic inlet is to efficiently convert the kinetic energy of free-stream air to pressure. In addition, the inlet must supply the correct amount of air at velocities which the engine can accept. And it should do this with low drag over the entire range of operation. With increasing flight Mach number, the task of the inlet becomes more difficult, and inlet design becomes more sophisticated to meet a wide range of requirements. Inlets for Mach 1.5 to 2.5 aircraft all incorporate variable geometry features to provide variable precompression and engine airflow matching. These systems maintain the normal shock externally, and therefore, the control system is relatively straightforward. Aircraft above 2.5 maintain the shock internal, and are normally referred to as a "mixed compression" or "started" inlet. Needless to say, such inlets require complex control systems.

Optimum air induction system performance necessitates an inlet control system that will maximize total pressure recovery, minimize spillage drag (additive drag) and recover as much total momentum of by-passed airflow as possible. Specific topics that must be considered are:

- a) Requirements for the variable geometry inlet and the control system that must control it.
- b) Approaches to obtaining variable geometry.
- c) Closed loop vs open loop control system.
- d) Sensors.
- e) Servo-Valves.
- f) Actuators.
- g) Linkages
- h) Error Analysis



These topics will be discussed herein and their impact, both singular and cumulative, on the air induction system will be stressed.

#### 6.1 Requirements for an Air Inlet Control System

The amount of compression available from a supersonic inlet afforded by converting the kinetic energy of the air to pressure is shown in Figure 6-1 as a function of the total-to-free-stream static pressure ratio,  $P_{To}/P_o$ . Thus, for an aircraft flying at 0.9 Mach number, the theoretical ram pressure is 1.7 times the free-stream static pressure, whereas for a supersonic jet flying at Mach 3 the theoretical ram pressure is 36 times the ambient pressure, and at Mach 4 the ideal theoretical pressure is 150 times the ambient pressure. These pressure ratios are considerably greater than the sea level static compression ratio of a turbojet, and at supersonic flight conditions the turbojet compression ratio is markedly reduced making inlet compression even more significant.

Also shown in Figure 6-1 are practical limits of the total pressure for three inlet types. Type I is for subsonic and low supersonic flight speeds up to approximately Mach 1.5, a simple normal shock inlet provides very efficient compression of the air. With this inlet type the air is decelerated from supersonic to subsonic velocities through a single "normal shock". This inlet requires no control mechanism since the normal shock is stable and will adjust to varying engine airflow requirements. The F-100 employs this type of inlet. With a Type I inlet, total pressure losses increase very rapidly above Mach 1.5; thus, it is no longer a practical inlet for operation near Mach 2.0 or above. Type II is for the intermediate speed range from Mach 1.5 to 2.5, an external compression inlet can provide good pressure recovery (i.e., inlet total pressure divided by the free-stream total pressure). With an external compression inlet, supersonic flow is decelerated externally to a lower supersonic Mach number by one or more oblique shocks and/or isentropic compression turns prior to deceleration to subsonic velocities through a "normal shock" at the cowl lip station. The normal shock has a small range of stable operation and can adjust to only a small amount of engine airflow variation; however, this range can be increased by providing bleed flow in the normal shock region. Variable geometry is required with this inlet to enable it to: operate efficiently over a range of Mach numbers, to provide better engine matching characteristics, to vary the amount of external compression, and to reduce the spillage drag. Type III is a mixed compression inlet and is for high supersonic Mach numbers, 2.5 and above. As the free-stream Mach number changes, the inlet control system is required to vary the amount of turning of the free-stream air by varying the inlet components. This concept is generally referred to as a "started" or mixed compression inlet and has

both external and internal compression requirements for the free-stream air. The reason for these two compression modes is that there is a limit of approximately  $12^\circ$  that the air can be turned. If this limit is exceeded, the efficiency of the inlet is reduced, which results in both less thrust output by the engine and increased aerodynamic drag on the overall airplane. Therefore, above approximately 2.5 considerably better performance can be obtained with an external-plus-internal compression inlet. With this third inlet type, the flow is decelerated supersonically to a low throat Mach number by a series of oblique shocks. It is then decelerated to subsonic velocity through a "normal shock" located near the minimum area or throat region. Some sort of variable geometry is required to vary the amount of compression and usually to accommodate starting characteristics of the contracted internal flow passage.

#### 6.1.1 Inlet Control System Performance

The inlet pressure recoveries shown in Figure 6-1 for the different inlet types are representative of the maximum practical pressure recoveries of each inlet type and do not reflect any penalties due to control tolerances or due to mismatches with engine airflow requirements. Therefore, the inlet control system's tolerances must be compatible with the operational limits of the total propulsion system. This means that the configuration and performance of the inlet control system can vary considerably for aircraft in different speed regimes. Generally, the higher the Mach number the more accuracy and sophistication is required by the control system.

Figure 6-2 shows typical inlet performance characteristics at a given supersonic Mach number. The performance is given in terms of the inlet pressure recovery,  $P_{T1}/P_{T0}$ , the inlet mass-flow-ratio MFR--which is defined as the actual capture flow divided by the ideal flow which could pass through the inlet projected area--and the inlet spillage drag coefficient,  $C_{D\alpha}$ . During supercritical operation with the normal shock swallowed, the inlet captures constant relative weight flow. When the normal shock is downstream of the capture station (as shown by the lower sketch) the pressure recovery is low (Point A); by throttling the inlet, the pressure recovery can be driven up to a critical point (Point C) where the shock is just attached to the cowl lip. This is considered the optimum operating point for inlet pressure recovery. Further throttling of the inlet will drive the normal shock ahead of the cowl lip, spilling some flow externally (as shown by the upper sketch for Point B). The portion of the inlet performance curve above the critical Point C is called subcritical operation. Proper throttling of the inlet is the function of the control system. The

weight flow spilled during the subcritical operation results in increased drag as shown in the lower right-hand corner of the figure. On such a pressure recovery-relative weight flow plot, lines of constant engine corrected airflow are shown by straight lines radiating from the origin. The intersection of this engine corrected weight flow line with the inlet operating curves is the operating point for a specified inlet size. For a high engine corrected weight flow, the intersection may be in the supercritical portion of the inlet performance curve (Point A). For a low engine corrected weight flow, the engine operating line may intersect the inlet operating curve at Point B giving higher pressure recovery but some increased spillage drag. The optimum operating point is a trade-off between pressure recovery, mass-flow and drag. For any one flight condition, the inlet can be sized to operate at the most favorable point of the performance curve. However, at other flight conditions the engine airflow requirements may not match the inlet airflow characteristics and either a pressure recovery penalty (exemplified by Point A) or a drag penalty (exemplified by Point B) may result.

#### 6.1.2 Inlet Off-Design Point Penalties

The problem of inlet-engine matching is discussed in Figure 6-3 for two extreme cases of inlet design: (1) for an inlet having a fixed capture area in which all the compression is internal and the amount of compression is varied by varying the internal geometry and throat area; and (2) for an inlet having a fixed throat area in which the compression is external and the amount of compression is varied by varying the external flow spillage and free-stream capture area. For this example, both inlets were sized to deliver 100 percent relative weight flow ( $MFR \approx 1.0$ ) at a Mach number of 3. The relative weight flow schedules for the two inlets are shown in the upper half of Figure 6-3. The fixed capture area inlet has a constant relative weight flow of 1.0, whereas the fixed throat area inlet has a relative weight flow schedule which markedly decreases below the design Mach number, dropping to approximately 30 percent at Mach 1.0. On the lower portion of this figure is shown the corrected weight flow schedule of the fixed capture area inlet, the fixed throat area inlet, and a typical turbojet engine. Thus, the fixed throat area inlet would deliver constant corrected weight flow to the engine, whereas the fixed capture area inlet would deliver greatly increased airflow at low Mach numbers. A typical engine corrected airflow schedule falls in between and varies by a factor of 2 between Mach 1.0 and 3.0.

Since a fixed capture area inlet typically delivers more air than the engine can use, excess flow must be spilled through downstream by-pass doors and a drag penalty is incurred. On the other hand, fixed throat area inlet, which delivers too little airflow off-design, operates supercritically (with the normal shock being located downstream of

the throat, Figure 6-2) at a reduced total pressure. The loss in total pressure incurred by the fixed throat area inlet is illustrated in Figure 6-4. With this inlet, a 50 percent loss in total pressure recovery is incurred at Mach numbers between 1.0 and 2.0. In comparison, the fixed capture area inlet (by virtue of downstream flow spillage) could operate along the maximum pressure recovery potential of this inlet below the design Mach number. The drag of these two inlets is shown in the lower half of Figure 6-4. Although fixed throat area inlet requires no downstream flow spillage, the large amount of external spillage results in even higher drags than the downstream by-pass spillage of fixed capture area inlet.

#### 6.1.3 Inlet-Engine Airflow Matching

The effect of the matching loss on engine performance is shown in Figure 6-5. The upper half of this figure shows the relative net thrust which is normalized by the thrust for a perfectly matched inlet having no drag. On this basis, the fixed capture area inlet causes a small thrust penalty due to the drag of the by-pass flow spillage; however, the fixed throat area inlet with its lower airflow handling capability causes a large thrust penalty amounting to as much as 60 percent at the low Mach numbers. The relative thrust specific fuel consumption is shown on the lower half of this figure. On this basis the differences are reduced; however, they are still significant at the lower Mach numbers. As can be seen from these results, a large thrust and fuel consumption penalty is incurred when the inlet airflow is too low necessitating operation at a reduced pressure recovery. Therefore, it is extremely important to design the inlet to capture as much airflow as the engine can handle at the maximum inlet pressure recovery. Although not as severe, the airplane drag penalty due to capturing too much weight flow must be carefully considered.

#### 6.1.4 Inlet Transients, Buzz and Distortion Limits

During transient operation of the engine or aircraft, specific fuel consumption can be allowed to increase without any significant effect on range because of the short time spent in these transient conditions. However, during these transients, it is important that the inlet and engine combination does not get into any conditions which could result in engine stall or excessive aircraft roughness. For these reasons it is important to avoid operating regions which result in (1) excessive distortion at the engine face, (2) inlet buzz conditions, and (3) duct unstarts.

The definition of regions where buzz or excessive distortion can occur involves a very empirical science and, in general, test data are required to define these regions for specific applications. Wind tunnel test data provide a qualitative feel for the regions of concern. It is recognized that these regions may be influenced to some extent by the presence of the engine and, therefore, in the actual installation, these regions may change somewhat.

The buzz and distortion regions are influenced by a multitude of parameters such as Mach number, angle of attack, angle of yaw, engine airflow, spike or ramp position inlet turn angle. For buzz and distortion regions encountered during engine airflow transients, Figure 6-6 illustrates the desired operating point in terms of inlet turn angle and spike position at the nominal engine airflow at a flight Mach number of 1.8 and typical angles of attack and yaw. Also shown on this map are the regions of airflow and spike position where excessive distortion and buzz can occur at this particular turn angle.

This figure also depicts the same buzz and distortion regions at the turn angle which is scheduled for the maximum corrected engine airflow which can be obtained at this Mach number

## 6.2 Configuration of Variable Geometry Inlets

Generally, these approaches fall in two categories, the two-dimensional inlet, or commonly referred to as 2-D and the axisymmetric of 3-D. Each approach will be discussed from a control system standpoint only.

### 6.2.1 Two-Dimensional Inlets (2-D)

This type of inlet is rectangular in nature from the inlet to the throat and then as the duct approaches the engine face, it makes a transition to a circular cross-section to mate with the engine. These inlets generally require a little more distance between the entrance lip and the engine face than the 3-D types. This additional length provides a better opportunity to minimize pressure distortion at the engine face. Some of the existing airplanes, utilizing these two-dimensional inlets are F-4, RA-5C, XB-70, Concord, Russian TU-144, etc. Figure 6-7 illustrates a typical 2-D type inlet control system. The inlet control system must position two, three or four ramps, air by-pass doors, or a by-pass ring, and possibly the inlet lip; however no existing airplane varies the inlet lip.

#### 6.2.1.1 Ramps

The function of the ramps is to vary both (1) the amount of air spilled around the inlet, and (2) the throat area. In addition, they provide an area in which to bleed the inlet and provide sliding air seals at the ramp edges. Since the ramps are hinged together, their movement must be coordinated.

#### 6.2.1.1.1 Ramp Location

These ramps can be located either in a vertical or horizontal position. From a controls point of view they are desired to be located vertically, parallel to the fuselage, for the following reasons:

- 1) When two inlets are involved, it is much easier to provide synchronization and possible combinations of the powered mechanism.
- 2) Fail safe position is generally required to have the ramps in the retracted position. It is easier for the aerodynamic loads to retract the ramps because only friction forces must be overcome.
- 3) The back up structure is much more rigid because it generally is in the fuselage. This provides less structural deflection inputs to the system.

If they are located horizontally, usually additional back up structure must be added to withstand the duct internal air loads. Also, in case of control system failure, the aerodynamic loads required to blow back the ramps must be sufficient to overcome both the system friction forces and ramp weight.

The ramps are generally controlled by a Mach number schedule. The sensor may be located (1) at the inlet for a local Mach number indication, or (2) in the central air data system for the free stream Mach number. They must be positioned at any point between fully extended to fully retracted; therefore, the control system must be capable of assuming an infinite number of positions. The system can be either an open or closed loop system. A closed loop utilizes additional sensor located at the throat which detects the throat Mach number. This aerodynamic signal is fed back to the controlling mechanism. Mach 2 vehicles generally utilize a two ramp system and Mach 3 vehicles utilize either three or four. However, the fourth ramp generally is a two position ramp.

#### 6.2.1.1.2 By-Pass Ring or Doors

The function of these doors or rings is to provide a passageway for the excess air taken aboard but not required by the engine. They allow matching of the inlet duct air supply and engine air intake demand. The excess air may be utilized as secondary cooling air and then discharged overboard.

#### 6.2.1.1.2.1 By-Pass Ring

These rings are utilized just forward of the engine face as shown in View "A" of Figure 6-7, and are generally found in a type of system that does not require fast response. This means aircraft of the 1.5 - 2.5 Mach number range and generally an open loop system as mentioned above. These rings are usually mounted on the engine and translate forward to mate with a fixed airframe mounted ring. They are controlled by vehicle Mach numbers. In order to close this loop, a pressure recovery sensor may be installed in the diffuser area on the inlet.

#### 6.2.1.1.2.2 By-Pass Doors

These doors are utilized just forward of the engine face as shown in Figure 6-7, and are generally found in a system that requires fast response. This means aircraft of the 2.5 to 3.5 Mach number range, and a closed loop system. These doors are in two sizes. The smaller doors are called "trimmer" doors and are utilized to position the normal shock at pilot selected position. The larger doors are slaved off the smaller ones as shown in Figure 6-8, which is a different concept of the doors shown in Figure 6-7.

These large doors are naturally designed to handle large flows and they should be designed to discharge their air through a convergent-divergent type nozzle. This minimizes the drag penalty. The loop is closed by an aerodynamic feed back signal obtained from a unit which senses the normal shock position.

#### 6.2.2 Axially Symmetric (3-D) Inlets

These type inlets are of circular cross-section and conical longitudinally. From the inlet's entrance lip to the throat, the duct cross-sectional area diminishes and from the throat to the engine face it increases. These type inlets are generally shorter in length than the 2-D type for the same pressure distortion level. Some of the existing airplanes utilizing these 3-D inlets are: F-104, B-58, Boeing's SST, Russian MIG 21 and SR-71. This type inlet is illustrated in Figure 6-9.

The inlet control system must position the spike, air by-pass doors, or a ring.

#### 6.2.2.1 Spike

The function of the spike is to (1) control the amount of air spilled around the inlet and (2) vary the throat (minimum) area. The most common method that is utilized to obtain these variations is to translate the spike as in Figure 6-9. However, alternate methods are to translate the cowl or to collapse the spike.

The spike, of course, must house an actuator that is utilized to translate it forward and aft or collapse it. The spike must also provide an area for the boundary layer bleed and air seal at the sliding surfaces. The bleed air must be ducted from the spike to the vehicle. This generally limits the amount of bleed that can be accomplished because of the limited area allocated for air ducts. If cooling is required, this duct area limitation further constrains the design. As in the other types of systems, the sliding surface must be air sealed.

##### 6.2.2.1.1 Translating Spike

This type spike may be in either 360°, 180° or 90° segments. The sensor that controls the position of the spike is the same as the ones discussed for the 2-D ramp which sensed local Mach parameter or vehicle Mach parameter. When the 180° or 90° segment spike is utilized, they are mounted on the fuselage. This location provides more volume to house the mechanism and duct the bleed air away and simplifies the air sealing of the sliding surfaces.

The 360° type, when utilized, imposes a geometric constraint on the AICS system. The mechanism must be housed inside the spike. The actuator generally is long and slender which means its load carrying capability is limited by the poor slenderness ratio of the actuator. This type also has a control problem in angles of attack and yaw. If the inlet is not aligned with the flow the entering on the windward side experiences more compression while the air entering the leeward side experiences less compression. The inlet control system must therefore control to some average between the two conditions. This requires multiple sensors around the annular inlet.

##### 6.2.2.1.2 Collapsible Spikes

This concept has the advantage of varying the throat area more than the translating type; however, the bleeding and sealing problem is increased. This concept still requires additional inlet area for take-off.



#### 6.3 Comparison of 2-D and 3-D Inlet Control Systems

Some key factors for comparing the 2-D and 3-D inlet control system are presented in Table I and applications in Table II.

TABLE I  
COMPARISON OF 2-D AND 3-D INLETS

<u>Item</u>	<u>2-D</u>	<u>3-D</u>	
Design Pt Performance			
Percent Throat Area Variation	Good	Translating Low	Collapsing Fair
Wt & Mechanical	Fair	Good	Fair
Aux. Inlets for Off Design Pt.	Generally Not Req.	Generally Yes	
Sys. Dev. Adaptability	Good	Poor	
Sys. Stability	Good	Fair	
Sensor Signal	Fair	Difficult	
Ground Check	Fair	Good	

TABLE II  
APPLICATION OF TYPES

<u>Item</u>	<u>2-D</u>	<u>3-D</u>
Application	F-4 F-106 RA-5C Concorde XB-70	F-105 B-58 SST SR-71 MIG-21

#### 6.4 Inlet Control System

Inlet operation is characterized by pressure changes, but it can account for altitude and temperature effects by using pressure ratios for control signals. Inlet controls must sense some signal to determine if a specific operating position is the one desired, and if not, provide correction through repositioning the variable geometry and other inlet variables. The control can only achieve results consistent with the signals it receives and the variable capability of the inlet. Both open loop and closed loop controls are feasible, so each must be considered when

selecting the mode of control. The inlet control must be sensitive to sudden changes in the entering air and must also be sensitive to downstream disturbances caused by the engine. Such changes require rapid response by the inlet control to prevent disturbing and perhaps unsafe aerodynamic effects from occurring in the propulsion system. Conditions which could be encountered are buzz, shock expulsion for started inlet, engine stall, and flameout. Any of these conditions could be a flight hazard. Not only must the control react quickly, but it must measure the pressure ratio signals with precision.

Figure 6-7 is a sample of the gross information flow of a closed loop system. The control functions indicated are throat and by-pass actuator as a function of a pneumatic signal.

#### 6.4.1 Closed vs Open Loop Systems

The question of open loop versus closed loop inlet controls deserves close scrutiny. Figure 6-10 illustrates the difference between these two basic control concepts.

The open loop control schedules actuator position to predetermined values. A change in actuator position has no effect on the control input parameters, so this is termed open loop control. The system must measure each parameter which requires a change in the inlet configuration and combine these schedules and biases with actuator position feedback to achieve the desired output. Some commonly used parameters for this type of control are: local Mach number, diffuser exit Mach number, angle of attack, angle of yaw, position of other inlet geometry, and engine parameters indicative of airflow such as corrected speed and compressor pressure ratio. Overrides are often provided to account for inlet buzz, restart, severe maneuvers, or sudden engine airflow changes indicated by changes in duct pressure or fuel manifold pressure. Because the signals are unaffected by actuator position, signal characteristics have no effect on the dynamics of open loop controls.

A closed loop inlet control positions the actuator to achieve a desired aerodynamic effect. The selected input signals are indicative of inlet operation which are strongly affected by actuator position. This aerodynamic feedback gives a closed loop control. Therefore, the signal characteristic has a major effect on loop dynamics. The slope of signal pressure ratio to actuator position is a major gain in the feedback path thus contributing significantly to control stability and response. In addition to the signal characteristics, this type of control must account for inlet duct, transmission line, sensor, servo control, and actuator dynamics.

Parameters commonly used or considered for closed loop control are shock position and inlet Mach number at the lip, throat, or diffuser exit. Overrides are often required with closed loop controls, as they are with open loop controls, to achieve safe inlet operation under unusually severe operating conditions.

#### 6.4.2 Considerations for Inlet Control System Selection

A comparison of open loop and closed loop control considerations is given in Table III.

Table III

	Open Loop	Closed Loop
Signals	Insensitive to inlet changes. Fixed geometry close to desired. Less data needed. More predictable for restarts buzz and other transients.	Highly sensitive to inlet changes. Compensates for IEG tolerances temp effects on structure & engine air flow tolerance.
Manual Control	Adaptable	Feedback system needed.
Flexibility	Easy to add biasing parameters.	Limited to change of probes requires more test data.
Complexity	Hardware more complex.	Analysis more complex.
Installation	Main control actuator position feedback difficult.	Can locate sensors with actuators.
Power	Slightly more quiescent power.	Peak power same as open loop control.
Weight	Depends on redundancy & packaging.	Usually less than open loop.

6.4.2.1 Signals - Open loop control parameters measure upstream and downstream conditions. Often this is local Mach number, entrance flow angularity, and diffuser exit Mach number. The signals are normally unaffected by minor fixed inlet configuration changes, so inlet geometry would therefore be positioned as it was before the inlet was modified. Aerodynamic wind tunnel data sufficient to provide inlet performance would be adequate to define the signals and control schedules. Inlet unstart, buzz, and other transients would have little effect on the control signals so the action would be predictable.

Closed loop control depends on aerodynamic feedback. Aircraft inlet control system designers must have a clear and thorough knowledge of the signal requirements for successful inlet control. These requirements must be considered in the design and test stages of the inlet development to assure that they are obtained.

Listed below are four of the primary requirements for closed loop aerodynamic signals:

1. Single valued - This avoids possible control saturation caused by transient disturbances away from set point into multi-valued area.
2. High gain - High signal gain is necessary to maintain a small error in the scheduled parameter caused by set point shifts within the error band of the control.
3. Reasonable range - The gain characteristics must be maintained for a reasonable range to avoid gross errors and possible flight malfunction caused by a small error in the set point.
4. Consistent gain at all conditions - A consistent value of the signal gain will enable the control to be sized to have high response at all conditions. If the signal gain varies with flight conditions, stability requirements would generally require the control to be sized so that the response rate would vary according to the signal gain variation.

Figure 6 - 11 describes a signal with ideal characteristics, and a comparison of this ideal signal to four other signals with poor characteristics is shown in Figure 6 - 12.

By definition then, these signals are located close to regions of high pressure gradient such as the normal shock. Small changes in the inlet configuration usually cause gross changes in these signals which in turn can cause the inlet geometry to be far from the desired position unless there are additional changes to the control such as relocated signal probes or revised pressure ratio set points. Because the signal slopes are so important to loop dynamics, much more aerodynamic data is needed for the closed loop control. Data is needed for the full range of inlet geometry and for numerous potential probe types and locations. One advantage of closed loop control is the tendency to achieve automatic compensation for manufacturing tolerances in the inlet, temperature effects on the structure, engine airflow tolerances, and other factors of importance which are not measured.

6.4.2.2 Manual Control - The open loop control incorporates output position feedback so it is readily adaptable to manual control. A closed loop control on the other hand usually does not have this feedback, so one must be added.

6.4.2.3 Flexibility - Because the signals are outside the open loop control feedback path, other parameters can be added to bias output position schedules without upsetting system dynamics. Closed loop controls are less flexible. Usable signals generally have limited ranges of acceptable aerodynamic gain so added parameters would probably require a change of probes. Another problem is the loop dynamics which could be grossly affected by the added control loop and thus require revised control gain and compensating networks. Any change requiring new probes or large revision of pressure ratio set points will likely necessitate new test data over the entire operating range of the inlet.

6.4.2.4 Complexity - Open loop controls depend on measurement of all major parameters that affect inlet operation. There are more sensors and more computing devices, hence, there is usually more hardware than with a closed loop control. The closed loop control reduces the number of sensing and computing functions by selecting parameters which accomplish the same end by measuring the aerodynamic effect on the inlet of these major parameters of influence. Closed loop inlet control requires complex analysis of the aerodynamic and dynamic characteristics.

- 6.4.2.5 Installation - When the open loop control uses several parameters for computing output schedules, these functions are generally grouped into one main control. Space limitations and accessibility result in the main control being installed remote from the actuators. Position feedback must be routed to the main control through rather tortuous paths. Closed loop controls could locate the sensor with the actuator and thus eliminate the installation difficulties of feedback systems.
- 6.4.2.6 Power Consumption - Each sensor and computing function requires a certain power drain on the aircraft. This quiescent power is normally about 5% of peak power demands. The closed loop control uses slightly less quiescent power because of fewer elements. It must do the same work in the same time, however, so the peak power is the same as the open loop control.
- 6.4.2.7 Weight - The weight of the inlet control can vary widely depending on the environment, fail safe features, self check capability, adjustments for flexibility, complications for ease of maintenance, etc. Redundancy philosophy and packaging concepts cause direct weight increments. The hardware simplicity of closed loop controls usually provide weight savings. Whenever control system weights are discussed, the trade-off between weight and performance is the deciding factor. A heavier control that runs the inlet more efficiently enables the aircraft to achieve its flight objectives with lower fuel consumption. The weight of fuel saved can be many times the weight increment for the control.

In addition to the technical criteria delineated above, and perhaps of prime importance, is the time schedule and development status. If the period from program initiation to flight demonstration is short, then proven concepts and thoroughly developed equipment should be selected. This may also dictate an open loop control because the closed loop control requires additional wind tunnel and flight test data with more complicated analysis. Choice of a closed loop control entails a development risk but often promises better performance.

Selecting the proper inlet control mode is a task with many facets. Evaluation must be based on requirements which provide operational efficiency and flight safety in accordance with the overall functional plan of the vehicle.

## 6.5 Sensors

All the sensors detect a pressure ratio in the inlet. These ratios have various nomenclatures; however, they all boil down to and generally they are as follows:

$P_{sig}$  = signal pressure as total pressure

$P_{ref}$  = reference pressure as static pressure

The typical types of sensors utilized are as follows:

1. Mechanical - Bellows, levers, cams, pistons
2. Electronic - Linear elements, transistors, resistors, & capacitors.
3. Pure Fluid Devices - Pure fluid elements.

#### 2.2.1 Mechanical Sensors

##### 2.2.1.1 Jet Pipe Concept

Figure 1 - 13 shows a force balance type pressure ratio sensor. The device works on a balanced beam principal with forces in equilibrium, its jet pipe valve is in the null position, and both flow and pressure on both sides of the servo piston are equal. A change in either static or ambient will cause a force unbalance and deflection of the jet pipe resulting in a change in both pressure and flow to the servo position. The loop is closed through rollers providing position feedback from the servo piston. Such a sensor offers high signal gain because of the pressure and flow sensitivity developed by the jet valve and good accuracy because of the mechanical design and low displacements of the system. However, this sensor is sensitive to changes in the fluid viscosity, or temperature changes, and pressure variations from the aircraft's hydraulic system supply.

##### 2.2.1.2 Hydro-Mechanical Vector Sensor

Figure 6 - 14 shows an innovation in hydro-mechanical pressure ratio sensing - the Vector Sensor. This device offers simple internal feedback sensing mechanism. The principal of operation of the Vector Sensor is best explained by the three sets of vectors shown in the figure. The vector B-D1 indicates initial steady state operation. For a change in static pressure, the force unbalance on the bellows would produce a rotation of point A about point B as shown. This motion of point A would be fed to a double-acting servo piston rotated to bring point A back to its original position and null out the flapper valve.

It can be shown that for this type of sensor, the tangent of  $\alpha$  is proportional to the pressure ratio sensed by the two bellows. It follows that servo piston motion is proportional to  $\alpha$ , and hence we have a pressure sensing loop.

### 6.5.1.3 Force Balancing Beam Concept

Force balance sensors achieve their accuracy by the fact that the bellows operate in a force-versus-pressure regime which is generally a more linear relation than deflection-versus-pressure. Consequently, a minimum of shaping and functionalizing is required. Low hysteresis is achieved due to the principle of "balanced force" and therefore no strain is imposed on the diaphragm or bellows. All deflection-type sensors exert a strain on the diaphragm and as a result, exhibit definite hysteresis. The force balance sensor exhibits lowest possible temperature effects through extensive use of stainless steel in the elements. Vibration effects are easily eliminated by the addition of counterweights and viscous damping, because of the electrical error output signal scheme employed.

The pressure ratio transducer shown schematically in Figure 6 - 15 is a typical force balancing beam instrument, with a servo-driven shaft positioning the output synchros. A short stiff beam, pivoted on a movable fulcrum which has attached to it a differential pressure bellows ( $P_{diff} - P_B$ ) at one end and an evacuated bellows ( $P_B$ ) at the other. The bellows are attached to the beam through flexure pivots which eliminate the need for knife edges and can transmit force in either direction. The beam is free to rotate about the fulcrum by displacing the bellows slightly from their normal balanced position. Control pressure  $P_B$  is fed into the instrument case and reference pressure  $P_{ref}$  is fed into a pressure bellows. Pneumatic forces are applied to the beam by the two bellows, one evacuated bellows producing a force proportional to a  $P_B$  and one differential bellows producing a force proportional to  $P_{diff} - P_B$ . A change in either pressure causes beam unbalance. The unbalance is detected by a two-phase servo system which functions to restore beam balance. The bellows are held essentially at constant length, which avoids the large hysteresis normally associated with deflecting plates and diaphragms. The instrument is completely enclosed in a sealed case.

### 6.5.2 Electronic Sensors

An important aspect of electronic control is sensing. Similar to hydro-mechanical technology, the techniques of control have been highly developed, but packaging and sensors continue to receive development attention. Two new types of sensors which are undergoing development investigation are shown in Figures 6 - 16 and 6 - 17.



Figure 5 - 16 shows a stretched diaphragm type of sensor. This is a capacitive type transducer in which capacitance is a function of the load on the diaphragm, or on diaphragm displacement and air gap. Non-linearities in diaphragm displacement are minimized by preloading the diaphragm to a high stress level. Since the per cent change in total load with changes in pressure is very small, the effect of error is also small. This type of sensing device shows promise from the standpoint of hysteresis, linearity, and temperature sensitivity. Some material changes in the basic scheme shown also indicate promise. The ceramic plates may be replaced with quartz as it also exhibits dimensional stability with changes in temperature and stress. Thoughts are also being given to the use of crystalline diaphragm such as silica, ruby, quartz or sapphire.

Figure 6 - 17 shows another promising type of pressure transducer. This device is made up of two concentric quartz cylinders with metallized coating. It also is a capacitive type transducer and promises improvement in sensitivity to temperature and vibration. These are only two of a large variety of exotic sensors currently being investigated.

### 3.3 Pure Fluid Amplifiers

Despite a currently limited technology, the application of pure fluid amplifiers to advanced air inlet control concepts are anticipated. Pure fluid amplifiers, as the name implies, are devices which control the flow of a fluid medium, either gaseous or liquid, much in the same way that vacuum tubes and transistors control electron flow. Figure 6 - 18 shows two typical configurations for pure fluid amplifiers.

Basically, two types of pure fluid amplifiers exist. One, the bistable element is dependent upon the tendency of a fluid flow stream to attach itself to a wall (the COANDA effect). In the sketch shown, a flow stream from the power nozzle will attach itself to the wall of one output arm and will remain in that condition until a control input pressure signal is provided to break the attachment and divert the flow to the opposite arm where the stream becomes attached to that wall. This type of digital element is obviously equivalent to a "flip-flop" electronic circuit and is applicable to logical computing tasks.

Externally biased bistable elements can also be used as "and/or" gates. In the "and" gate pure fluid device, the flow stream remains attached to the wall of the "no output" arm and will remain in this

state until input pressure signals are present at all the control input ports. In a similar manner, the "or" element is biased so that the flow stream is diverted to the output arm when a pressure signal is present at any one or more of the input ports.

The second type of pure fluid amplifier is the proportional or analog fluidic element in which the flow stream is prevented from attaching itself to a wall by the presence of wall vents. In this device the flow stream is diverted proportionally to the two output legs by the pressure differential at the two control ports. This device is equivalent to a proportional electronic amplifier.

At this time, bistable elements are sufficiently well developed to be applied to logic circuitry and are incorporated in a few commercial control applications, including a shock position sensor being developed by Minneapolis - Honeywell.

Figure 6 - 19 is a pure fluid proportional element used to produce an output  $\Delta P$  proportional to the ratio of two input pressures. This device, at a fixed pressure level, has an output characteristic as shown, but requires the addition of successive stages for pressure level compensation.

The pure fluid pressure ratio sensor could be applied to a simple air inlet control loop, providing acceptable threshold levels can be attained.

## 6.6 Servo Valve

This portion will discuss hydraulic servo-valves only.

A hydraulic servo-mechanism is a closed loop system containing a controller (Servo-Valve) and a feedback element or elements load (actuator).

The servo valve varies the rate as well as the direction of flow of fluid to an actuator by metering the hydraulic fluid through controlled orifices. There are three types of hydraulic servo-valves, a seating, a sliding, and a jet pipe type.

In the seating or poppet type of servo valve, the control member moves in the same direction as the static pressure force which is acting on the member. In other words, the fluid and the control

member move in the same direction. The principal disadvantages of this arrangement are that large forces are required to move the control member when anything but very small flows are controlled, and that the total valve motion must be within the clearance between the controlling member and the seats. If additional clearance is used, a high quiescent leakage results.

The two principal advantages of the seating- or poppet-type valves are that, in general, they are simpler devices than the slide type, and that they can be built with considerably less stiction on the controlling member. The principal use of the seating-type valve, for servo-valves, is in pilot stages, like the flapper valve commonly used in the first stage of the hydraulic amplifier.

The sliding type of servo valve employs a controlling member that moves in a direction perpendicular to the static pressure force, or perpendicular to the flow of fluid. The sliding-type valve has considerably less leakage than the seating-type and can be built with much higher power gains. Of course, stiction forces are greater, and slide valves can be more easily jammed by dirt and impurities. There are many varieties of slide valves, such as spool types and flat plates, which either slide or rotate, but the sliding spool is the most commonly used for AIC.

A Jet-pipe Valve consists of a nozzle and a receiver block. The nozzle, or jet pipe, is arranged on a pivot so that it may be displaced from a neutral position, as shown in Figure 6 - 26(a). The jet pipe serves to convert pressure energy into the kinetic energy of a jet and direct this jet toward two receiver holes in the receiver block. When the jet of oil strikes the flat receiver block, its kinetic energy is recovered in the form of pressure. If the stream is directed exactly halfway between the receiver holes, the pressure in the two holes will be equal; the differential pressure, therefore, is zero. As the jet pipe is deflected, more oil will be directed at one hole than the other, raising the pressure in that hole and decreasing the pressure on the other, and thus creating a differential-pressure output.

Figure 6 - 25 shows the idealized pressure-flow curves, or characteristic curves, of a servo valve plotted from Equation (6.1). These curves are analogous to the torque speed curves of an electric motor or to the characteristic plate curves of a vacuum tube. For different values of  $x$  there are different curves; they are all parabolas which pass through the points where  $P_L = P_S$  in either direction. Above the  $Q = 0$  line the flow is through the other set.

#### 6.6.1 Output Power of Servo Valve

In a valve-controlled system, part of the power is sacrificed for the privilege of maintaining precise control. This can be demonstrated by calculating the maximum output power which can be passed through the valve. The power output is flow multiplied by load pressure drop.

$$H = P_L \times Q$$

$$H = P_L \times C_z x \sqrt{P_S - P_L} \quad (6.1)$$

To maximize,

$$\frac{dH}{dP_L} = C_z x \left[ \sqrt{P_S - P_L} - P_L \times \frac{1}{2} \times (P_S - P_L)^{-\frac{1}{2}} \right] = 0$$

$$(P_S - P_L)^{\frac{1}{2}} = \frac{P_L}{2} (P_S - P_L)^{-\frac{1}{2}}$$

$$P_S - P_L = \frac{P_L}{2}$$

and

$$P_S = P_L + \frac{P_L}{2} = \frac{3P_L}{2}$$

or  $P_L = 2/3 P_S$  when  $H$  is maximum

where

$Q_L$  = flow through load

$C$

$C_z$  = valve constant

$x$  = displacement of control element

$P_S$  = supply pressure

$P_L$  = pressure drop across load piston

Thus, the maximum-area rectangle which will fit under each curve has  $P_L = 2/3 P_S$ . Usual design practice is to establish the maximum required actuator load and velocity, then to use a piston area such that this load can be carried with  $P_L = 2/3 P_S$ , and provide for sufficient flow to move the piston at the desired velocity, Figure 6-25. This, of course, is done only in the interest of obtaining optimum efficiency as far as the use of hydraulic power is concerned. There may be other sets of conditions which would call for other methods of fitting the power-available curves to the power-required conditions.

#### 6.1.1 Two-Stage Hydraulic Servo Valves

Most two-stage electro-hydraulic servo valves use a nozzle flapper valve for the first, or primary, stage, and it is well suited for such use. It has an extremely lightweight moving element, requiring only very small magnetic forces; therefore, less electrical input power is required for any given response characteristic. The nozzle flapper valve can be used as a pressure (force) controller with a spring-loaded spool as a second stage. Used in this fashion it is not an integrator; thus, the valve can be used open-loop. It has comparatively high neutral leakage, but since the first stage need not be large, its flow consumption may be held within 1 to 10 per cent of the total flow across the power spool. This arrangement makes it possible to build valves up to 15 horsepower in capacity with inputs of as little as 10 mmw into the torque motor, and with outputs of up to 20 gpm with time constants of 3 to 5 msec. A two-stage valve of this type is practically insensitive to accelerations and vibrations because the forces available to drive the spool are many times greater than the weight of the spool itself.

Figure 6-26 shows a typical two-stage valve of the open-loop type. The first stage has a calibrated pressure output which is applied to a spring-loaded second-stage spool.

Another type of two-stage electro-hydraulic valve, one with a flapper pilot stage, is shown in Figure 6-27. This valve has a mechanical

feedback from the spool of the power stage to the flapper of the pilot stage. A three-way valve whose output feeds into one end of the power-stage spool is used as the first stage. Supply pressure is applied to half the area of the other end of the spool, and the remaining balancing force is developed in the feedback spring. This spring applies the feedback force to the flapper. The spool will always move in such a manner as to keep the control pressure (inside the nozzle and on the full area of the end of the spool) at one-half the supply pressure. This creates a displacement of the spool which corresponds to the flapper position, greatly magnified.

Figure 6 - 28 illustrates a valve which also has feedback around the first stage. A four-way flapper valve is used for the first stage. The flapper is extended in the form of a leaf spring, the end of which fits into a groove in the spool. As the spool moves, it deflects this spring and applies a force upon the flapper to bring the pressure back to neutral.

Figure 6 - 29 shows a more recent valve in which a jet-pipe valve is employed for the first stage and a special feedback spring connects the power spool with the first-stage armature.

Force feedback, as used in the last three valves described above, causes the spool to follow the first-stage armature position. Force feedback makes possible extremely high first-stage gains; thus, the valve is less susceptible to spool friction induced by contamination. It can also assist the making of a valve with good linearity.

## 6.7 Actuators

The preliminary design of actuators is discussed in this section. The data represents an actuator, consisting of an aluminum body and a steel piston and piston rods with normal operating pressure of 3,000 psi. The maximum pressure that these units can withstand are 7,500 psi,  $2\frac{1}{2}$  times the operating pressure per Mil H 5440 bursting pressure. That is the material can have permanent deformation but the actuator will still hold pressure. The unit must also withstand 4,500 psi surge pressure with no permanent deformation.

### 6.7.1 Design Considerations

The following assumptions for this preliminary design and weight estimation are as follows:

- (a) The piston rod diameter is  $\frac{1}{2}$  the bore diameter.
- (b) The hinge moment is maximum at the midpoint of the stroke and equal at the retracted extended positions.

Correction for configurations other than in (b) above may be made by selecting a larger deflection angle,

#### Design Formulae

See Figure 6 - 30 for Actuator Geometry and Legend

#### Bore Design

- (1) Tandem Actuator (2 hydraulic systems)

$$A = \frac{\pi}{4} (d^2 - d_1^2) \times 2 \quad d_1 = \frac{d}{2}$$

$$A = \frac{\pi}{4} (d^2 - \frac{d^2}{4}) \times 2$$

$$A = \frac{6\pi}{16} d^2 = \frac{M}{PL \cos \frac{\phi}{2}}$$

$$d = \frac{.0163}{\sqrt{\cos \frac{\phi}{2}}} \sqrt{\frac{M}{L}} \quad \text{for } P = 3,000 \text{ psi}$$

See curves, Figure 6 - 31

- (2) Parallel - Single Rod End Actuator (2 hydraulic systems)

$$A = \frac{2\pi d^2}{4} = \frac{M}{PL \cos \frac{\phi}{2}}$$

$$d = \frac{.0145}{\sqrt{\cos \frac{\phi}{2}}} \sqrt{\frac{M}{L}} \quad \text{for } P = 3,000 \text{ psi}$$

See curves, Figure 6 - 32

(3) Single Rod End Actuator (1 system)

$$\Delta = \frac{\pi d^2}{4} = \frac{M}{PL \cos \frac{\phi}{2}}$$

$$d = \frac{.0206}{\cos \frac{\phi}{2}} \sqrt{\frac{M}{L}} \quad \text{for } P = 3,000 \text{ psi}$$

See curves, Figure 6 - 33

Stroke Determination

$$S = 2L \sin \frac{\phi}{2}$$

See curves, Figure 6 - 34

6.7.2 Weight Formulae and Curves

(1) Plain, Single Rod End Actuator

A formula obtained from Reference 8 was used to plot the curves shown on Figure 6 - 35. This formulae is for a plain aluminum alloy cylinder and a steel rod. No valve is included in this weight. Rod dia. =  $\frac{1}{2}$  bore dia.

The formula follows:

$$\begin{aligned} W = & 2.64 \times 10^{-5} d^2 P + (.00028) d^3 p \left( \frac{20,000 + P}{20,000 - P} \right) \\ & + 2.31 \times 10^{-3} P^2 d^3 \left( \frac{20,000 - P}{20,000 + P} \right)^{\frac{1}{2}} + .0248 d^3 + .0392 d^2 \\ & + .0122 d^3 + (.02633 + .0305) d^2 + .8 \times 10^{-9} d^4 P^2 \\ & + [.012 d^3 + (.07355 + .0447) d^2] \frac{2P}{20,000 - P} \\ & + .0036 d^3 + .0436 d^2 + .1097 d + .0478 \end{aligned}$$



where:

W = weight, lbs.

d = bore dia., inches

S = stroke, inches

P = pressure, psi

For P = 3,000 psi the formula becomes  $W = .0478 + .1097d + (.208 + .054S)d^2 + .245d^3 + .0072d^4$

See curves, Figure 6 - 35.

#### (1) Dual System Actuator and Valve

The A3J longitudinal, directional and lateral actuators were used to arrive at the curves shown in Figure 6 - 36. Corrections for various strokes were made by calculations of the weight change for various lengths.

#### 6.7.3 Design Summary

Data required:

Hinge moment, M, in. lbs. (max.)

Deflection of Surface or component,  $\phi$ , degrees (max.)

Lever arm length, L, inches

1. Using lever arm length, L, and deflection angle,  $\phi$ , determine actuator stroke from Figure 6 - 34.
2. Calculate the force gradient,  $\frac{M}{L}$ ; hinge moment divided by lever arm.
3. Select type of actuator to be used, i.e., balanced dual tandem, or single rod end, dual, parallel, or single rod end, single system.
4. Using the curves Figures 6 - 31, 6 - 32 and 6 - 33, for the type of actuator selected determine the bore diameter from the force gradient and deflection angle.

5. Using curves Figure 6 - 35 or 6 - 36 determine weight of actuator from the bore and stroke.

## 6.8 Linkages

Linkages are utilized as the connectors between the surfaces to be controlled and the controlling mechanism. In the AICS system they are the connecting link between the system, generally actuators, and servo valves and the moveable ramps or spikes and doors or range for the throat and by-pass functions, respectively. These linkages are divided up into two categories: one is the power linkage and the others are follow up or control linkages.

### 6.8.1 Power Linkages

All power linkages distribute the load of the actuators to various points or point on the moveable unit (ramp, spike, door or ring). If the load is low or the surface is rigid, then only a few points are required to distribute the load. However, if the surface is flexible, several points are required to distribute the load. The trade-off here is the number of attach points versus the rigidity of the moving surface..i.e. several attach points, which is complexity, for a light weight but flexible surface; or few attach points, which are simple for a rigid, heavy surface.

Figure 6 - 8 shows this linkage in schematic form.

### 6.8.2 Follow-up Linkage

All follow-up linkages are designed to transmit position only, and generally null out some balancing mechanism. Therefore, they are lightly loaded and rigid enough to withstand the ambient vibratory loads. The mechanical follow up linkages are generally push pull rods or teleflex (flexible shaft) cable.

The systems also utilize an electrical follow-up also. These are in the form of a potentiometer, some are linear and some are rotary.

The location of this follow-up mechanism in the vehicle is extremely important. It is desirable to have short runs for accuracy of the mechanism itself with a minimum number of joints and minimum structural feed back.

It is also desirable to locate it directly on the surface that the system is controlling and at a position that has minimum deflection under load.

## 6.9 Error Analysis

An error analysis must be related to a specific propulsion system so the errors can be evaluated in terms of aircraft performance. When comparing more than one type system for the specific propulsion system, performance gains of one system over another must be traded against such factors as weight, reliability, maintainability, cost, etc., to best satisfy total weapon system requirements. Therefore, the inlet control system selected for a vehicle with a specific propulsion system may differ considerably from another vehicle with a similar propulsion system (same engine) but a different inlet control system.

One vehicle may have open loop throat and bypass control and a competing vehicle may utilize an open loop for the throat control and closed loop for the bypass control. Still a third competing vehicle may utilize closed loop control for both the throat and bypass control.

As a result of these variations discussed above, a critical evaluation must be accomplished by the weapons system evaluators and determine if the inlet control and propulsion system selected for the total weapons system will perform as proposed.

A key factor in determining if an inlet control system will perform as proposed is a detail error analysis of the system with regards to total vehicle propulsion efficiency and duct spillage drag throughout the complete flight envelope.

The following paragraphs will analyze an assumed inlet control system and provide sample of a simplified error analysis for a ramp system.

### 6.9.1 Control System Errors

Errors in the control system can be grouped as sensor errors, computing errors, and feedback errors.

#### 6.9.1.1 Sensor Characteristics

Accurate sensors are prime requirements for accurate inlet control. The beam balance sensors shown schematically in Figure 6-13 provide about 0.8% of point accuracy at the lowest pressure levels and with the most adverse environment. Typical pressure range of the local Mach

static signal is 0.5 to 20 psia. At the low pressure condition the total error would be 0.004 psi which is only 0.02% of full scale. Considering that sensor threshold is a part of the total error, one can see that the sensors are precision instruments with accuracies comparable to some of the best laboratory equipment available. Figure 6-37 is a graph to indicate how the percent error variation of a specific sensor capability varies with altitude. This situation applies because in sensing a pressure ratio at altitude the absolute pressures are so low. In order to achieve this accuracy in a force balance sensor, careful attention is given to every detail of the system. The pressure sensing bellows must exhibit a linear force-pressure characteristic from 0.25 to 35 psia. These are evaluated on a specific deadweight tester built for this purpose using graduated weights accurate to 0.01%. Force balance linkage mechanism must be rugged to withstand the environment of an engine nacelle but yet so precise that it must be assembled to tolerances less than 0.0001 inch. The jet pipe valve develops sufficient pressure differential on the servo piston to start it in motion with only 0.000010 inch displacement of the input arm and presents only a 0.0002 pound load on the sensor linkage to accomplish this. The overall force amplification from the jet pipe input arm to the servo piston output is 100,000 to 1. The sensor assembly is mass balanced to better than 0.0005 inch-pounds making it insensitive to acceleration, attitude changes and vibration. Thermal effects are eliminated by a packaging concept that creates equal heat flow paths to critical points in the mechanism through material with equal thermal resistance.

#### 6.9.1.2 Computer Characteristics

Computer errors include manufacturing tolerances on the scheduling cams and minor control shifts or wear which appear as null shifts in the control valve. To determine the result of these errors in terms of ramp angle, the errors can be transposed to increments of reference ramp angle or actual ramp angle. The computer errors are as follows:

(1) Scheduling Cam - The manufacturing tolerance on the radial dimension of the scheduling cam is 0.0005 inch. This gives an error in the ramp angle reference scheduled into the ramp position control. Although it is desirable to use large cams to minimize the errors contributed by manufacturing tolerances, compromises in cam size are necessary. The cam rise (change in radial dimension) determines linkage travel which in turn sets linkage lengths to avoid serious non-linearities. Linkage stiffness is affected by the loads and lengths. Cam rise thus has a significant effect on the weight and size of the control unit. A quarter of an inch (0.25 in.) cam rise is usually a reasonable compromise between control weight and accuracy.

(2) Control Shifts - Minor shifts in the computing linkage, control valve, or control housing can occur from wear, temperature expansion, erosion, and other sources. These can be combined and considered as a shift in the null point of the control valve. A reasonable assignment of error to these sources is 0.0002 inch of null shift.

### 6.9.1.3 Feedback Characteristics

Backlash in the mechanical transmission of ramp position to the control unit is directly related to error in ramp position. Typical values for this backlash is equivalent to 0.050 inch of actuator position.

### 6.9.2 Sample Error Analysis

The following paragraphs describe a ramp system, other systems are similar.

#### 6.9.2.1 Local Mach Sensor Error

The sensing error is, in general, related to the inverse of sensed static pressure level. Hence, the higher the static pressure, the lower the error. Under conditions of typical maximum speed at high altitude, total errors experienced with the present state-of-the-art sensors are  $\pm 0.8\%$  of local Mach pressure ratio ( $\Delta P_{RLM}/P_{RLM}$ ). The resultant error in ramp position depends on the slope of the ramp schedule with  $M$  number, the higher the slope the larger the signal.

$$\Delta\theta_2 = (\text{local Mach sensing error}) (\text{slope of ramp schedule})$$

$$\Delta\theta_2 = (\Delta P_{RLM}/P_{RLM} \times P_{RLM}) (\partial\theta_2/\partial P_{RLM})$$

#### Sample Calculations

The local Mach static pressure ( $P_{SLM}$ ) is 0.5 psia and the total pressure ( $P_{TLM}$ ) is 2.70 psia. The error in ramp angle ( $\theta$ ) contributed by the local Mach sensor is the error in reference ramp angle scheduled into the computer and 2 degrees/local Mach pressure ratio.

$$\Delta\theta_2 = (0.008 \times 5.4 \text{ units}) (2^\circ/\text{unit } P_{RLM})$$

$$\Delta\theta_2 = (0.0432 \text{ units}) (2^\circ/\text{unit}) = 0.086^\circ$$

#### 6.9.2.2 Scheduling Cam Error

Utilizing manufacturing data described in paragraph 6.9.1.2 (1) the scheduling cam error is as follows:

$$\Delta\theta_2 = (\Delta \text{cam radius}) (\text{cam rise})$$

$$\Delta\theta_2 = (\Delta X_R) \left( \frac{\partial\theta_2}{\partial X_R} \right)$$

### Sample Calculation

$$\Delta\theta_2 = (0.0005 \text{ inch radius}) \left( \frac{60^\circ \theta_2}{\text{inch radius}} \right) = 0.03^\circ$$

### 6.9.2.3 Control Shifts

Utilizing data described in paragraph 6.9.1.2 (2) the control shift error is as follows:

In terms of reference ramp angle the 0.0002 inch shift must be reflected back to an equivalent change in cam radius and thus a given error is scheduled ramp position.

$$\Delta\theta_2 = (\Delta \text{ valve position}) \left( \frac{1}{\text{forward linkage gain}} \right) (\text{cam rise})$$

$$\Delta\theta_2 = (0.0002 \text{ inch valve}) \left( \frac{1}{\frac{1.28 \text{ inch valve}}{\text{inch cam radius}}} \right) \left( \frac{60^\circ \theta_2}{\text{inch cam radius}} \right)$$

$$\Delta\theta_2 = 0.0094^\circ$$

This same error could have been reflected to actual ramp angle through the forward control path. Displacement of the ramp control valve transmits hydraulic pressure and flow to the ramp actuator. The actuator moves in response to the loads applied and the flow available. In the dynamic sense it is an integrator that moves until the input error to the control valve is reduced to zero. Actuator position is fed back to the control valve so that displacement of the actuator gives a proportional displacement of the control valve in the direction to null the valve. Output position of the actuator is thus proportional to the valve position. Ramp angle is related to actuator position through the kinematics of the connecting linkage and ramp mechanism. The following calculation uses typical values for component relationships:

$$\Delta\theta_2 = (\Delta \text{ valve position}) \left( \frac{1}{\text{feedback linkage gain}} \right) (\text{ramp linkage gain})$$

$$\Delta\theta_2 = (\Delta X_{RV}) \left( \frac{1}{\partial X_{RV} / \partial X_{RFB}} \times \frac{1}{\partial X_{RFB} / \partial X_{RA}} \right) \left( \frac{\partial \theta_2}{\partial X_{RA}} \right)$$

### Sample Calculations

$$\Delta\theta_2 = (0.0002 \text{ inch}) \left( \frac{1}{\frac{1.5 \text{ inch valve}}{\text{in feedback}}} \times \frac{1}{0.03 \frac{\text{inch feedback}}{\text{inch actuator}}} \right)$$

$$\left( \frac{2.12^\circ \theta_2}{\text{inch actuator}} \right)$$

$$\Delta\theta_2 = 0.0094^\circ \text{ just as shown with this error reflected to the reference ramp position}$$

#### 6.9.2.4 Feedback Error

Utilizing data described in paragraph 6.9.1.3 of 0.050 inch of actuator position, the feedback error is as follows:

$\Delta\theta_2 = (\text{equivalent } \Delta X_{RA}) (\text{ramp linkage gain})$

$$\Delta\theta_2 = (\Delta X_{RA}) \left( \frac{\partial\theta_2}{\partial X_{RA}} \right)$$

#### Sample Calculation

$$\Delta\theta_2 = (0.050 \text{ inch actuator}) \left( \frac{2.12^\circ \theta_2}{\text{inch actuator}} \right) = \underline{0.106^\circ}$$

Summary of Ramp Control Errors - The overall accuracy to be experienced with this equipment is a statistical summary of the contributing parts. Good correlation has been achieved using the square root of the sum of the squares. Applying this formula to the ramp control errors yields the following:

$$\Delta\theta_2 \text{ total} = \sqrt{\Sigma(\text{component errors})^2}$$

$$\Delta\theta_2 \text{ total} = \sqrt{(0.086)^2 + (0.03)^2 + (0.0094)^2 + (0.106)^2}$$

$$\Delta\theta_2 \text{ total} = \underline{0.14^\circ}$$

#### 6.9.3 Vehicle Impact

The hypothetical control system analyzed will weight about 70 pounds per inlet. The trade-off between weight and performance is dependent on the vehicle mission. However, if we assume 80,000 pound vehicle with two inlets with 20,000 pounds of fuel aboard, and a SFC inlet pressure recovery ratio of 1 to 1.8, then an increase of 1% in pressure recovery can be evaluated as follows:

0.018 x 20,000 = 360 pounds of fuel  
plus vehicle growth reduction of 25% when fuel is involved

equals 360 x 1.25 = 450 pounds

for this vehicle 1% inlet pressure recovery is equivalent to  
a reduction in Take-Off-Gross Weight of 450 pounds.

Now assume this inlet control system makes an improvement of 4% in inlet pressure recovery over a fixed inlet. Then the reduction in T.O.G.W. will be as follows:

$$\begin{aligned} (450 \times 4\%) - (70 \times 2) &= 1800 - 140 \\ &= 1660 \text{ lbs.} \end{aligned}$$

When evaluating competing inlet control systems, then of course the inlet pressure recovery ratio remains the same for all systems; but this ability to provide delta inlet pressure recovery and their corresponding weight are the determining factors.

#### 6.9.4 Type III Characteristics (Mach 2.5 and above)

Figure 6-38 indicates maximum pressure ratio error of the local Mach sensor over the flight envelope. This curve indicates the largest error at approximately Mach 2.0.

Figure 6-39 indicates sensor Mach error vs airplane Mach number. This curve indicates that the Concorde has a higher tolerance Mach number than most existing air data computers.

Figure 6-40 shows the variation of the shock position signal with inlet pressure recovery for a typical Mach 2.5 and above aircraft.

Figure 6-41 and 6-42 are cross plots of typical type III data. These curves indicate pressure recovery error and sensor full scale accuracy versus signal pressure ratio errors for a typical sensor. These curves are applicable to an aerodynamically closed loop system with only sensor errors included.



## References

1. Kepler, G. Edward, Inlets for Supersonic Flight, United Aircraft Research Laboratories, 1967.
2. Harner, Kermit I., Dynamic Response Requirements for Inlet Controls, Hamilton Standard Division of United Aircraft Corporation, 1967.
3. Flanders, Theodore, Methods of Inlet Control, Hamilton Standard Division of United Aircraft Corporation, 1967.
4. Hayes, John J., Advanced Inlet Control Techniques, Hamilton Standard Division of United Aircraft Corporation, 1967.
5. Kahoun, Frank, Signal Probe Characteristics, Hamilton Standard Division of United Aircraft Corporation, 1967.
6. Morse, Allen C., Electro-Hydraulic Servo Mechanisms, McGraw-Hill Book Company, Inc., New York, 1963.
7. Hilburger, E. A., Electro-Mechanical Systems Preliminary Design, NASOH-171, 1960.
8. Cooke, C., Gessner, E. and Smith, R. L., Optimum Pressure for a Hydraulic System, WADC TR54-189, January, 1954.

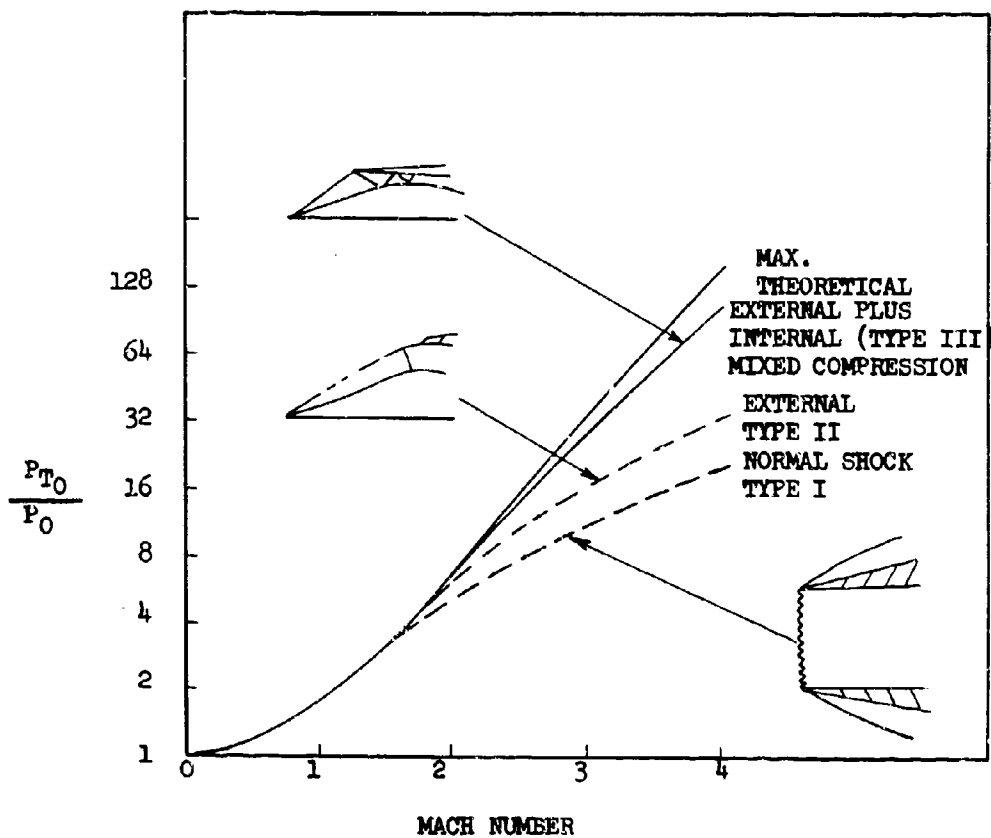


FIGURE 6-1. COMPARISON OF REPRESENTATIVE INLET PERFORMANCE

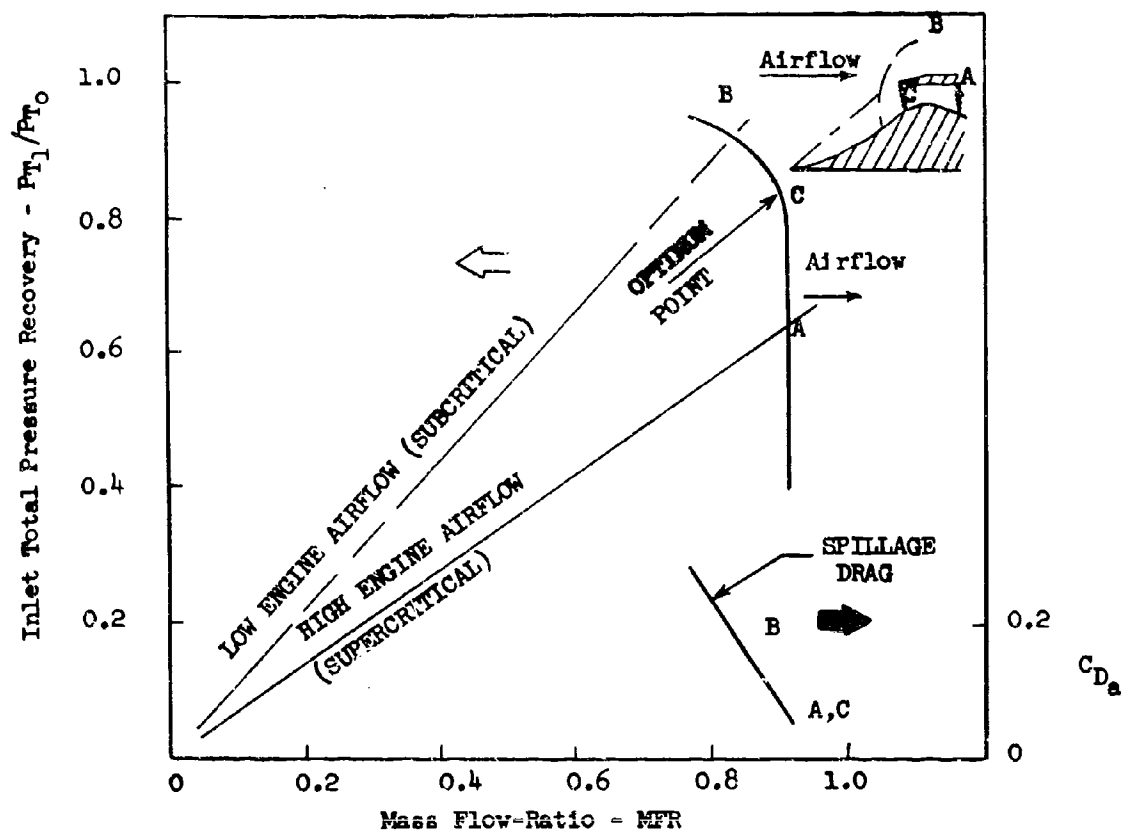


FIGURE 6-2. Typical Performance Characteristics

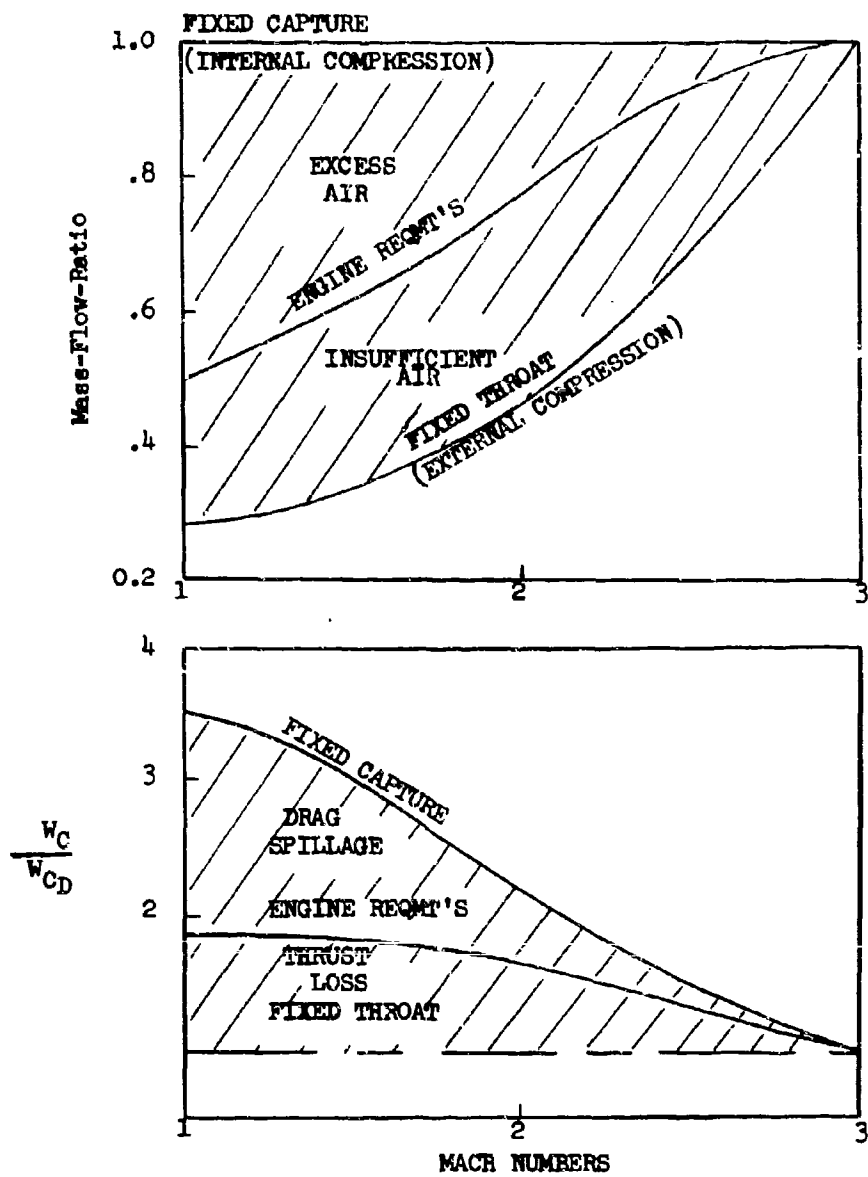


FIGURE 6-3. Engine Airflow Matching

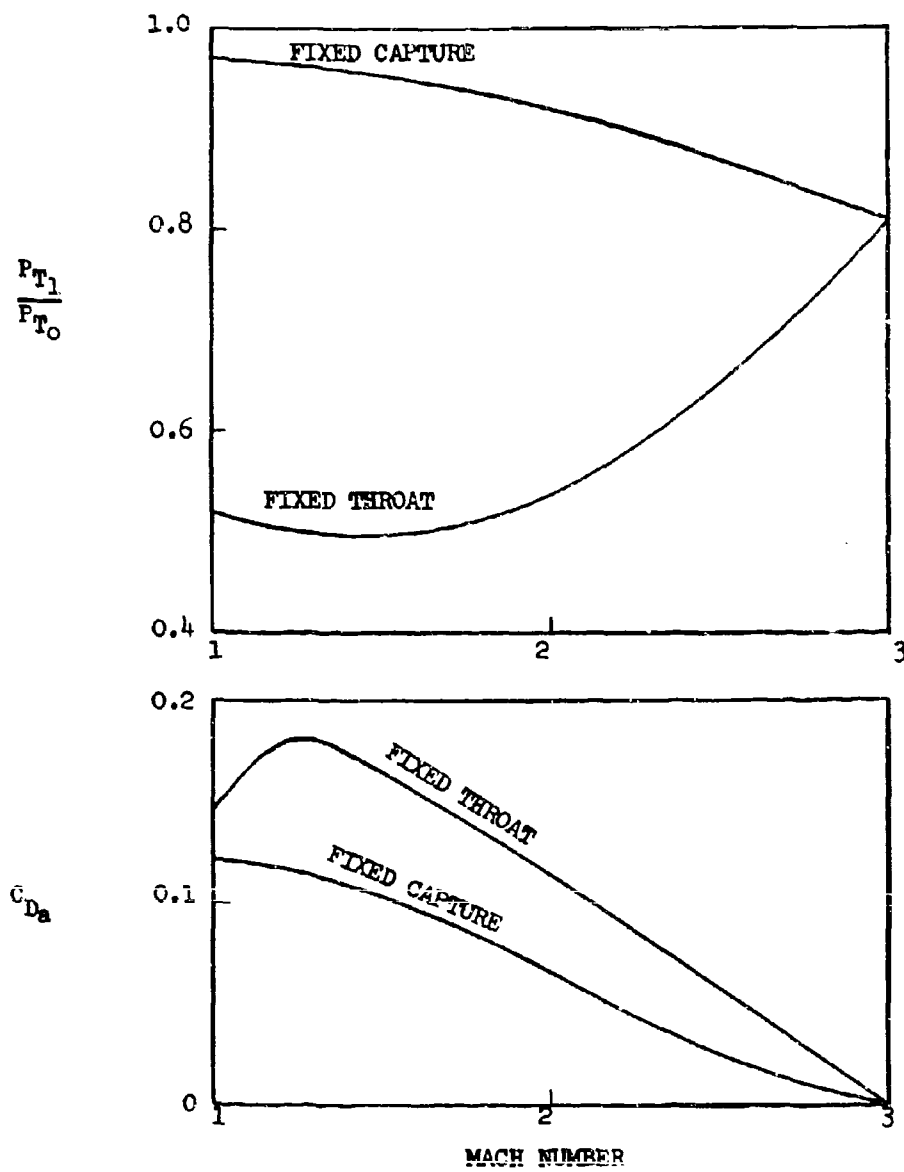
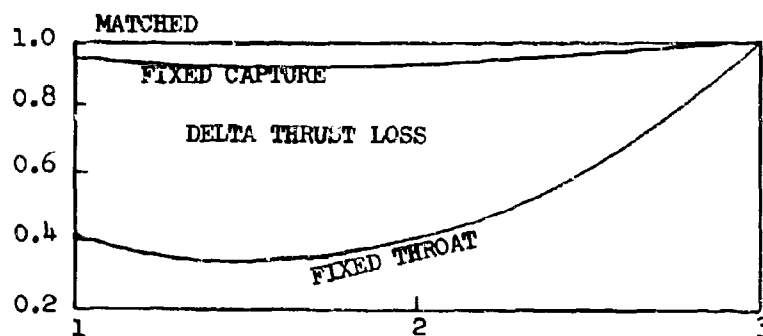


FIGURE 6-4. Off-Design Inlet Performance

$$\frac{T}{T_{Match}}$$



$$\frac{TSFC}{TSFC_{Match}}$$

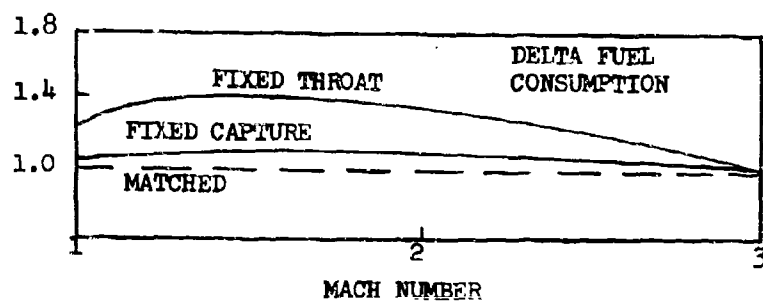


FIGURE 6-5. Off-Design Engine Performance

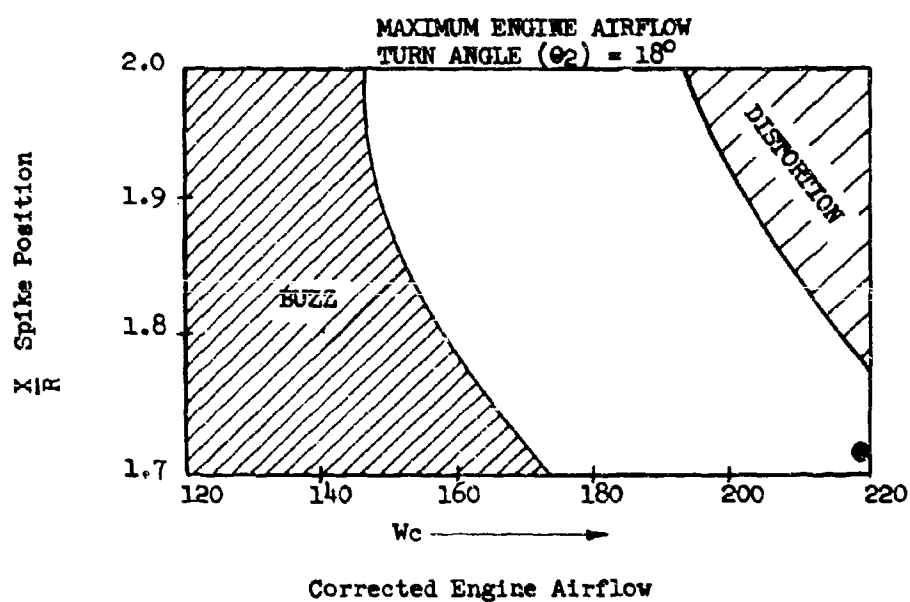
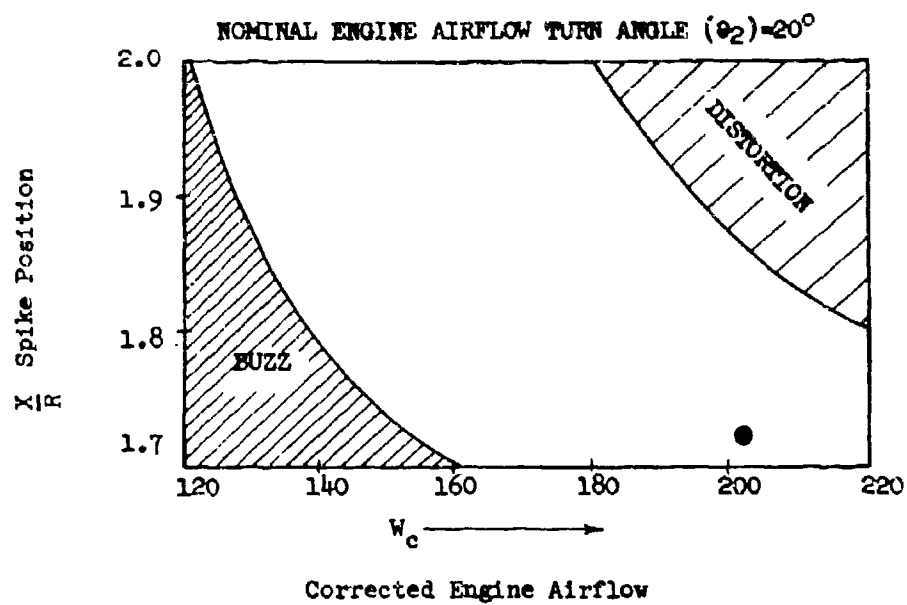


FIGURE 6-6. Buzz and Distortion Regions with Varying Engine Airflow

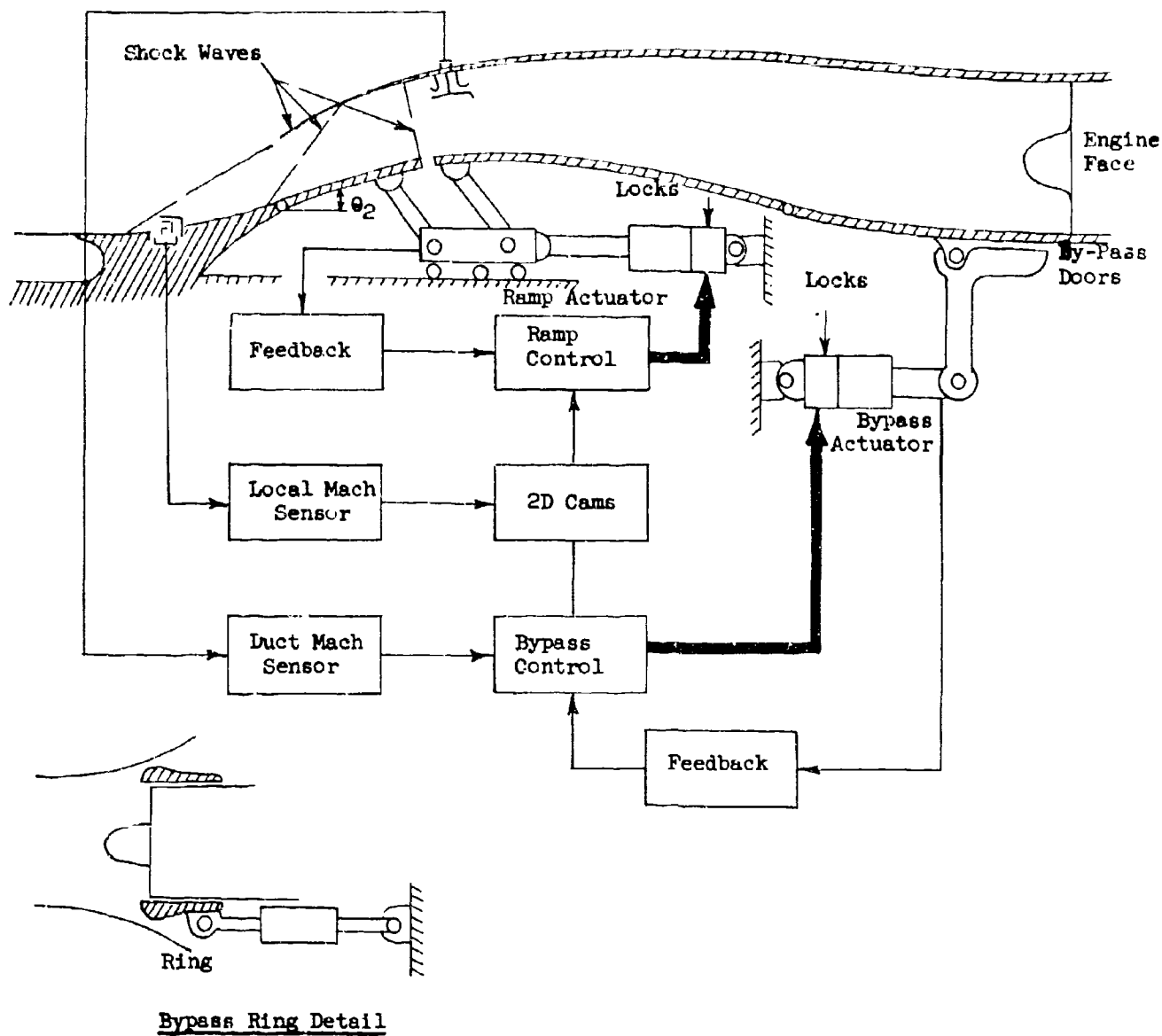


FIGURE 6-7. Typical Two-Dimensional Inlet Control System



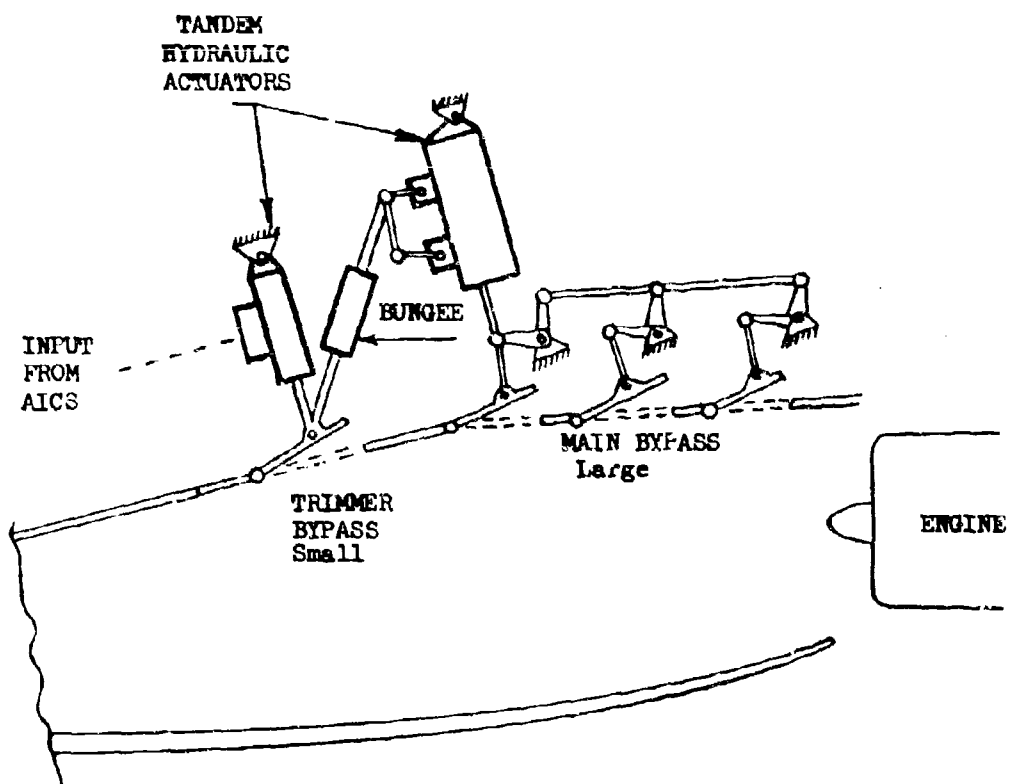


FIGURE 6-8. Bypass Door Configuration

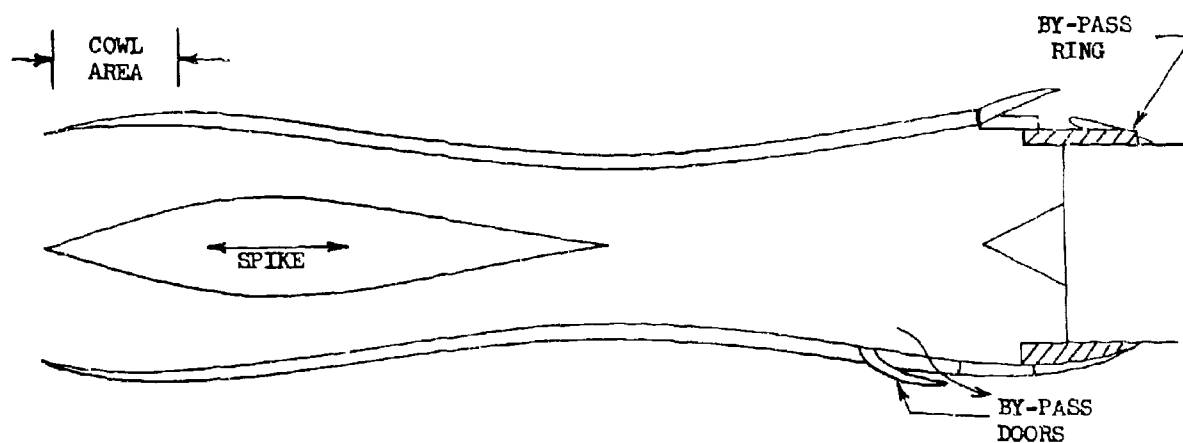


FIGURE 6-9. Illustration of a Conical Spike Inlet Control System.

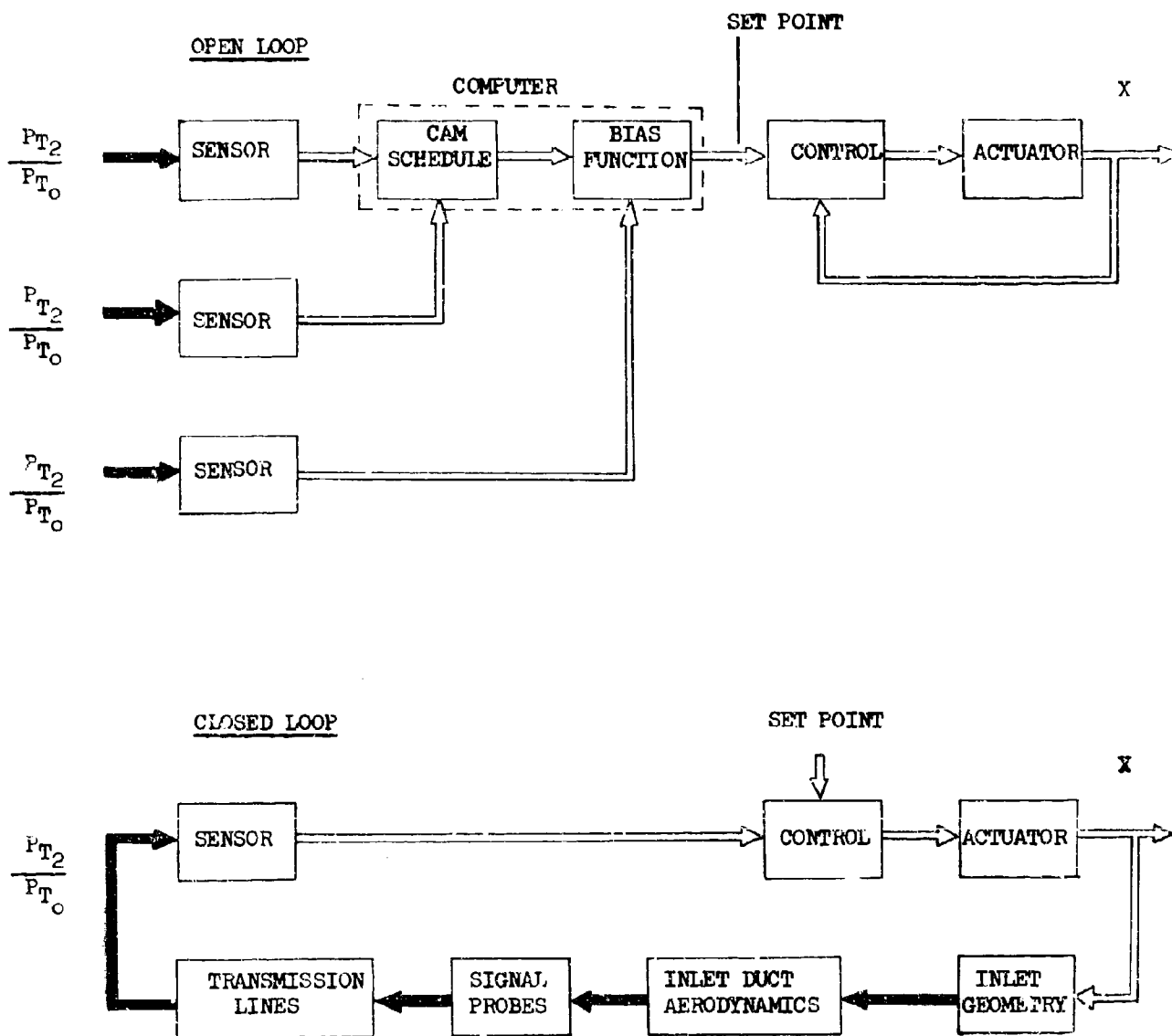


FIGURE 6-10. Inlet Control Concepts

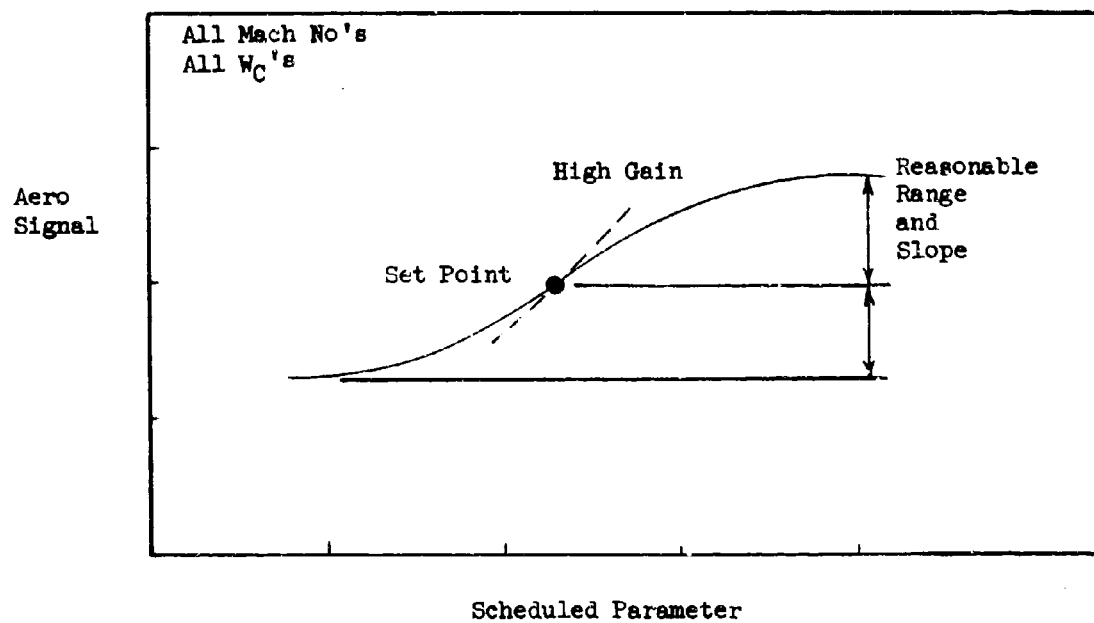


FIGURE 6-11. Signal with Ideal Control Characteristics

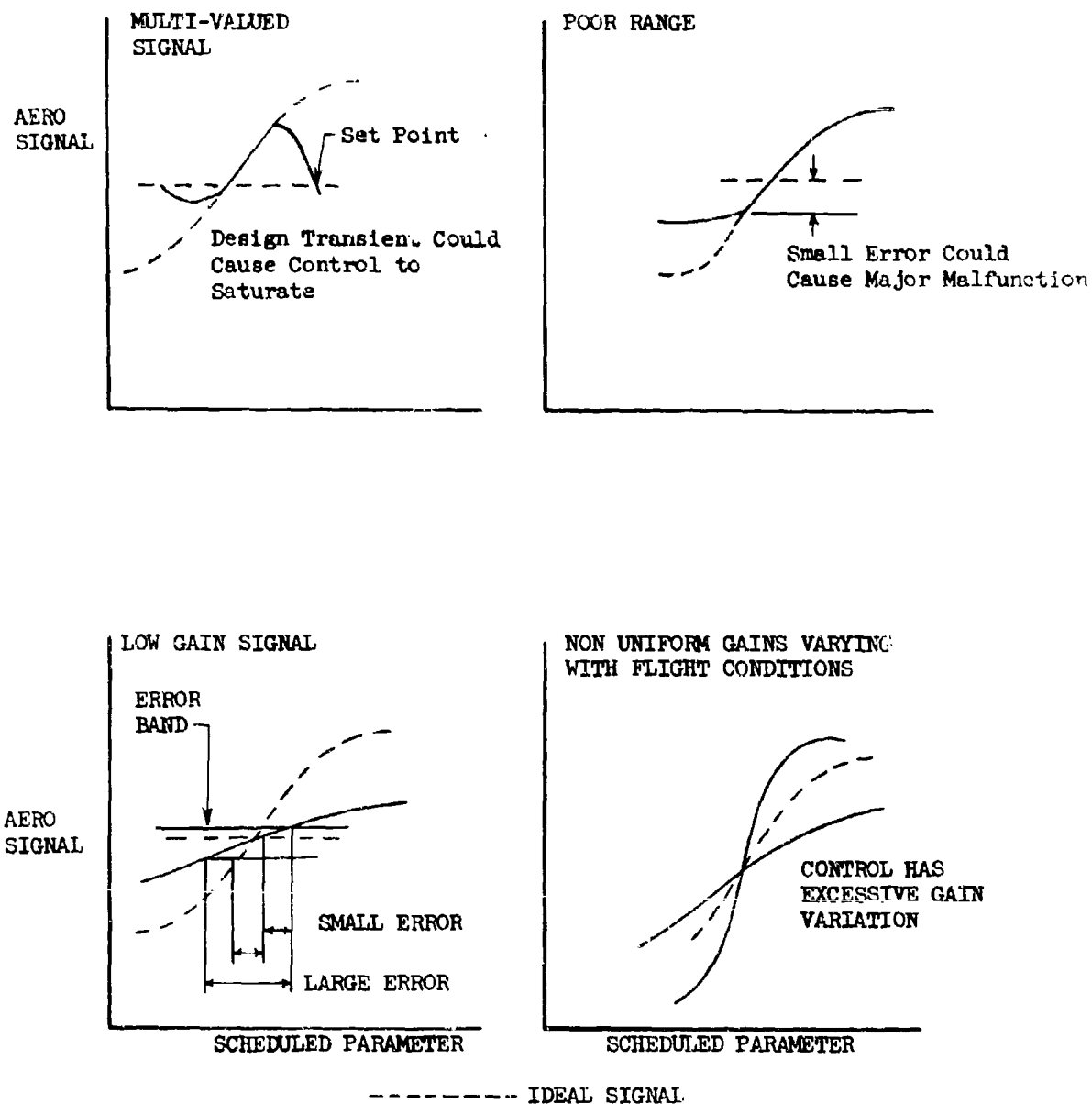
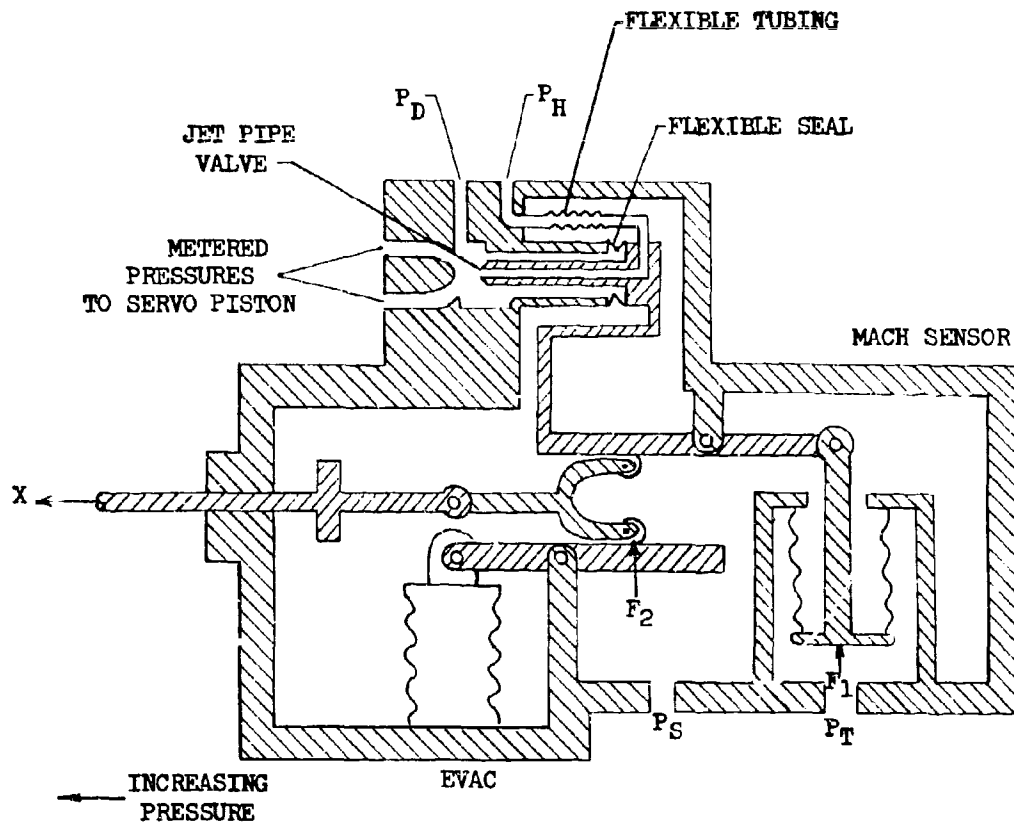


FIGURE 6-12. Signal with Poor Control Characteristics



$$F_1 = f(P_T - P_S)$$

$$F_2 = f(P_S, X)$$

$P_S$  = Static Pressure

$P_T$  = Total Pressure

$P_H$  = A High Pressure Source

$P_D$  = A Low Pressure Dump

FIGURE 6-13. Jet Pipe Pressure Ratio Sensor

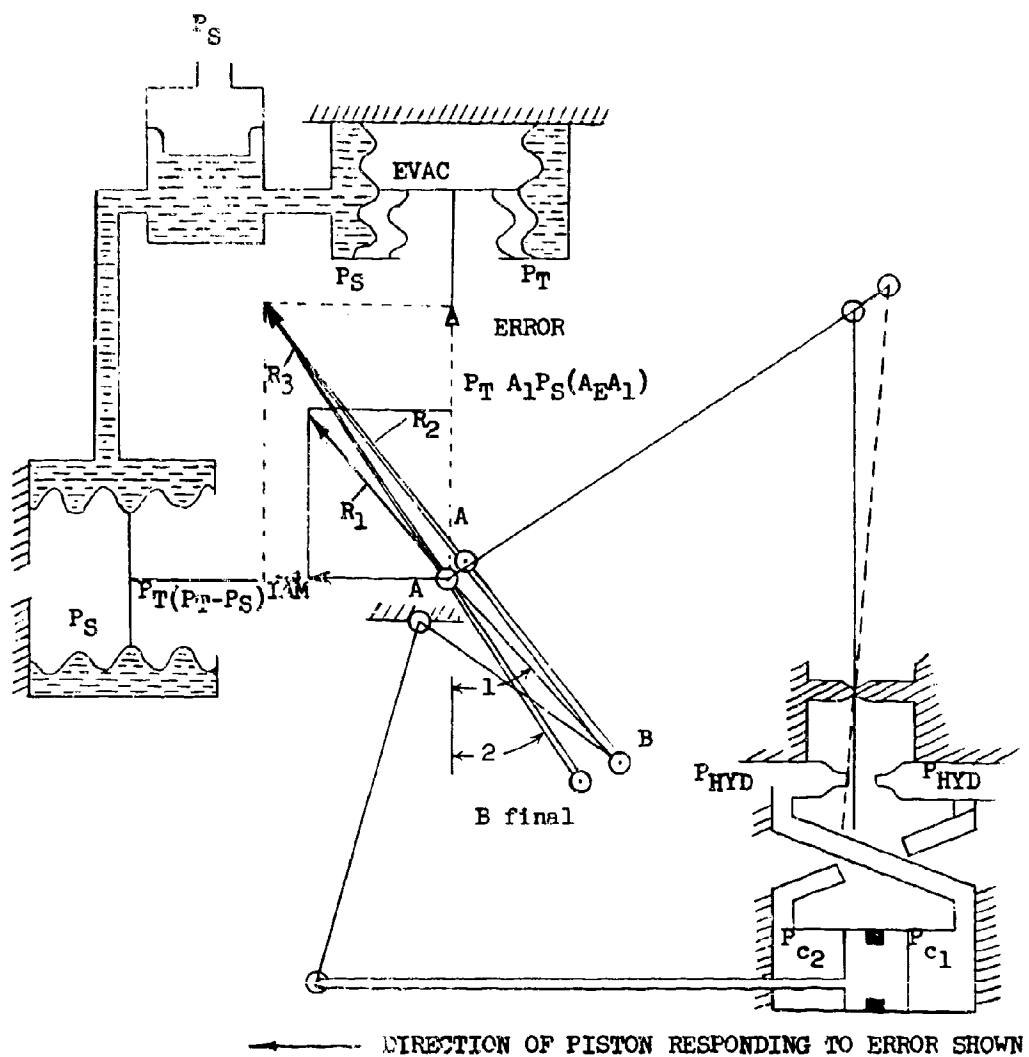


FIGURE 6-14. Force Vector - Pressure Ratio Sensor

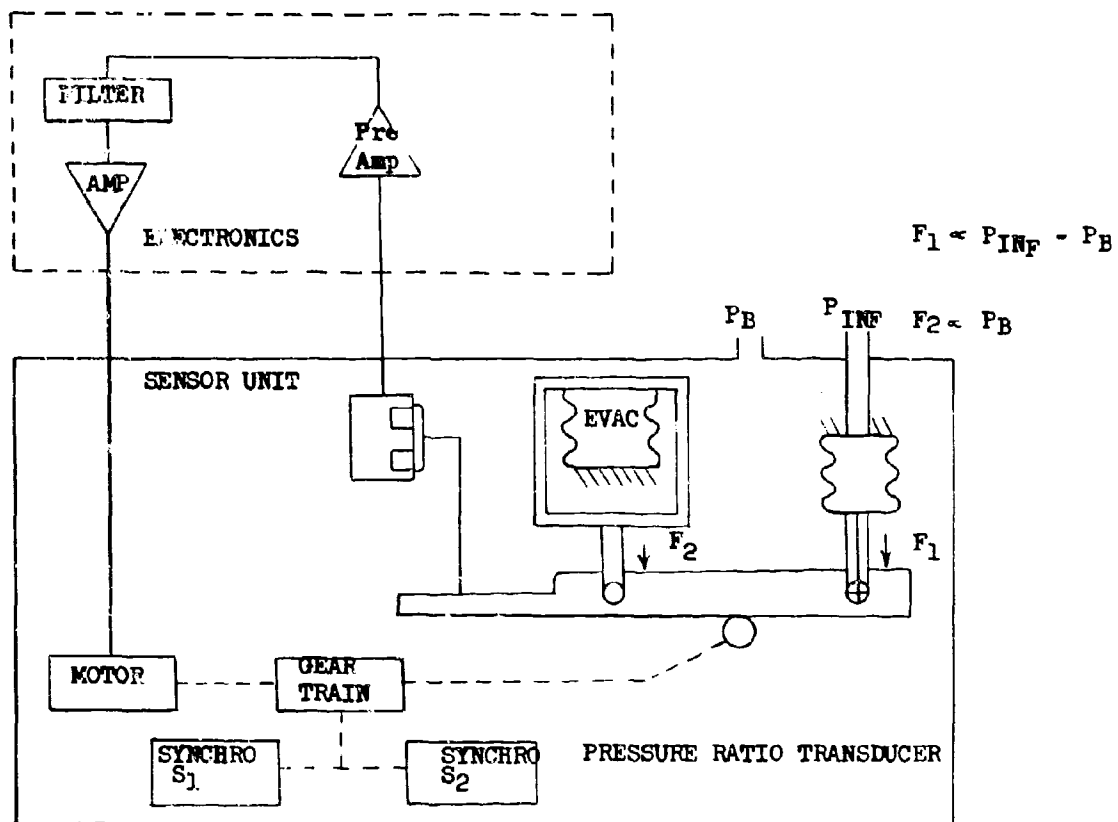


FIGURE 6-15. Pressure Ratio Sensor Block Diagram.

Compliments of AiResearch Mfg. Div.



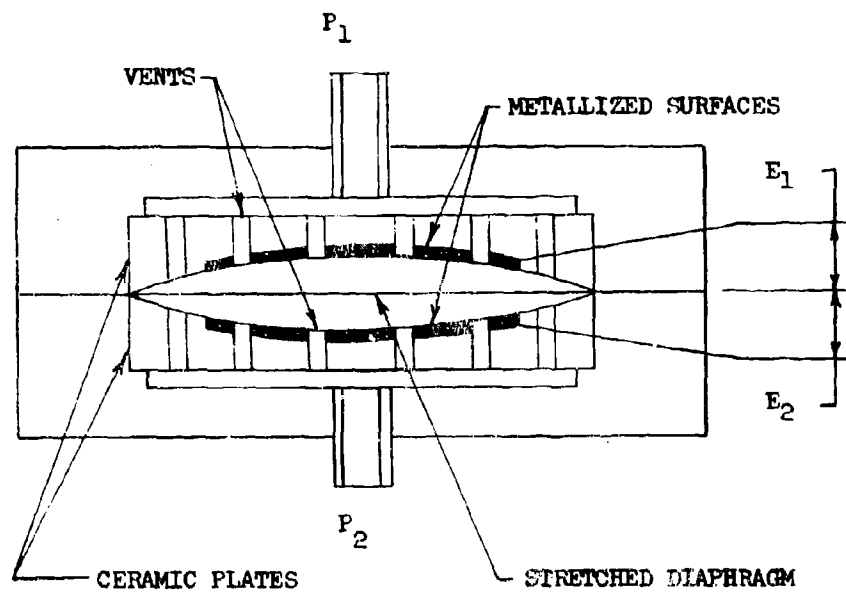


FIGURE 6-16. Stretched Diaphragm Pressure Sensor

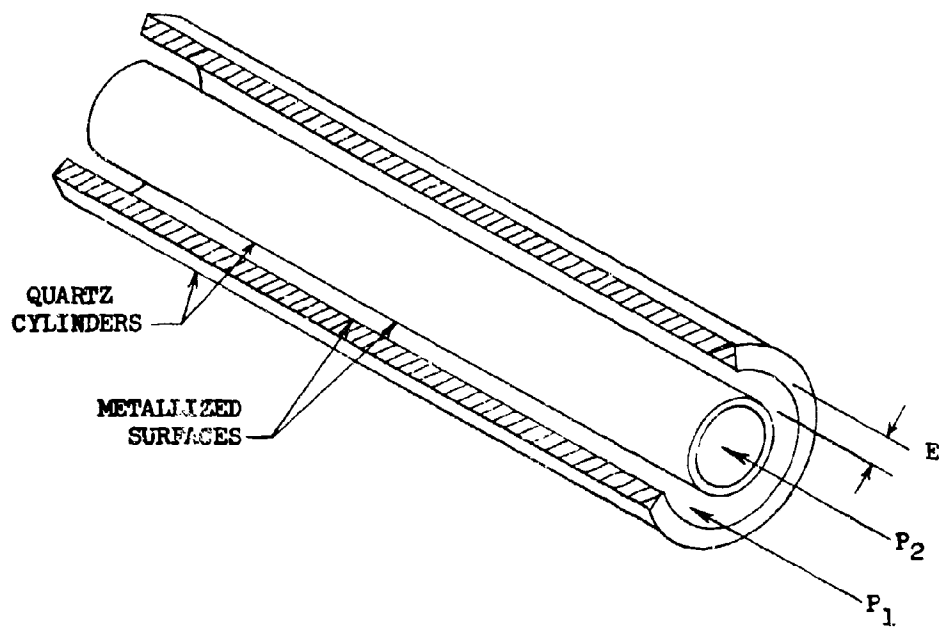


FIGURE 6-17. Variable Capacitance Concentric Cylinder Pressure Sensor

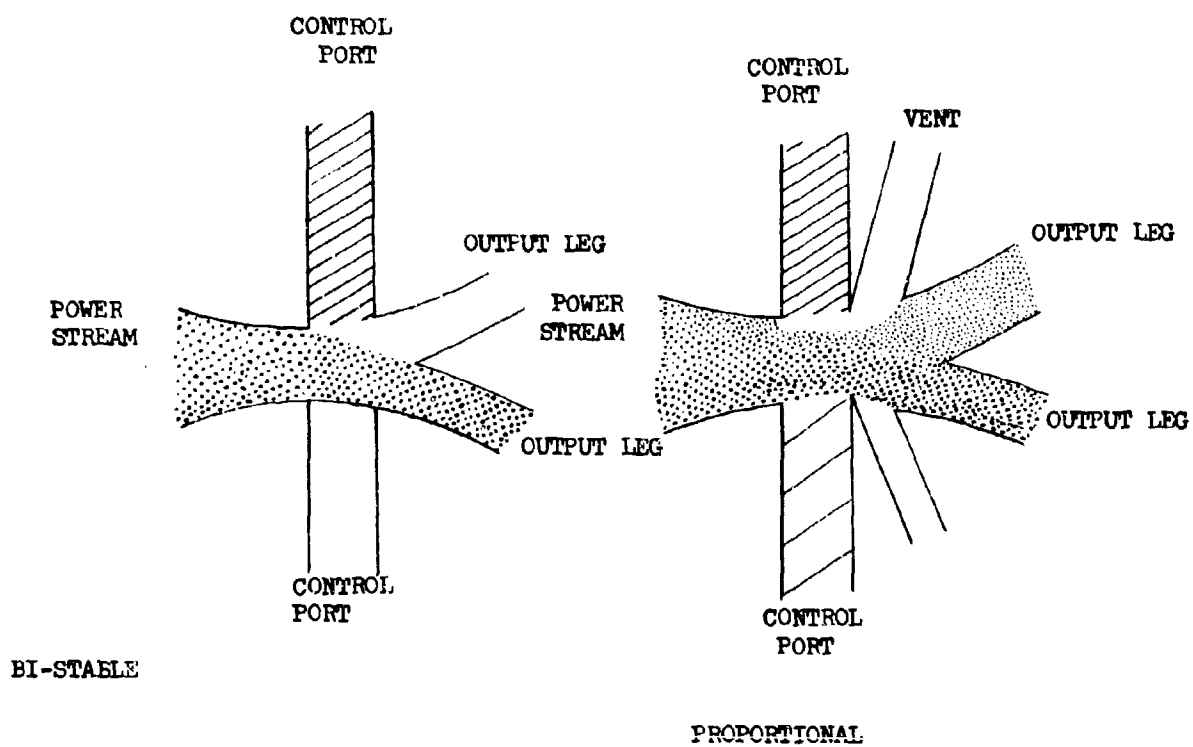


FIGURE 6-18. Pure Fluid Amplifiers

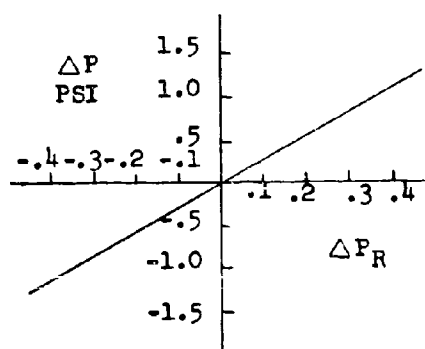
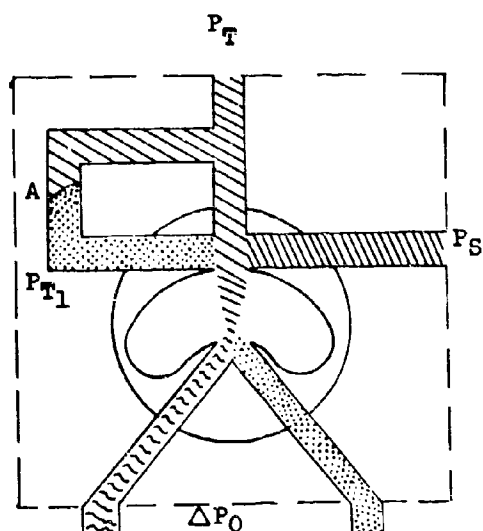


FIGURE 6-19. Pressure Ratio Sensor

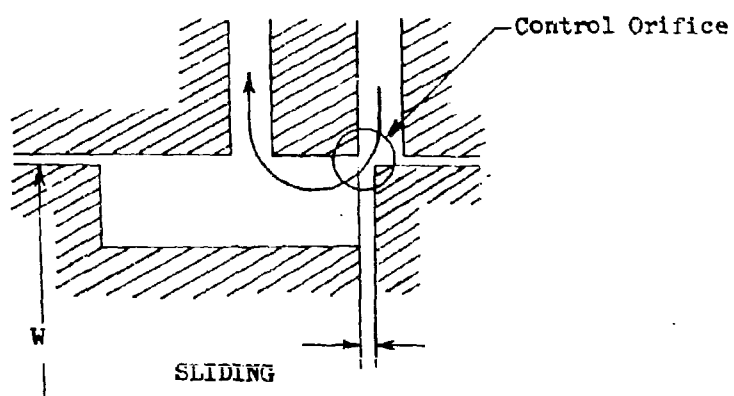
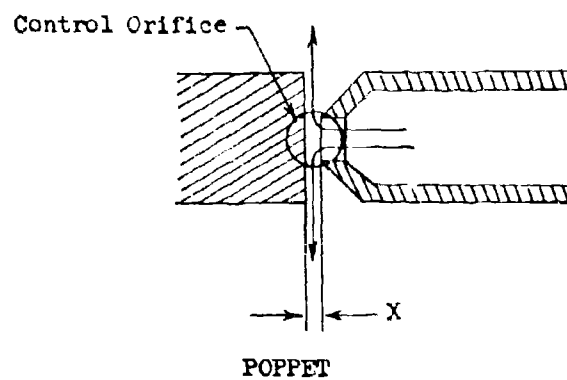


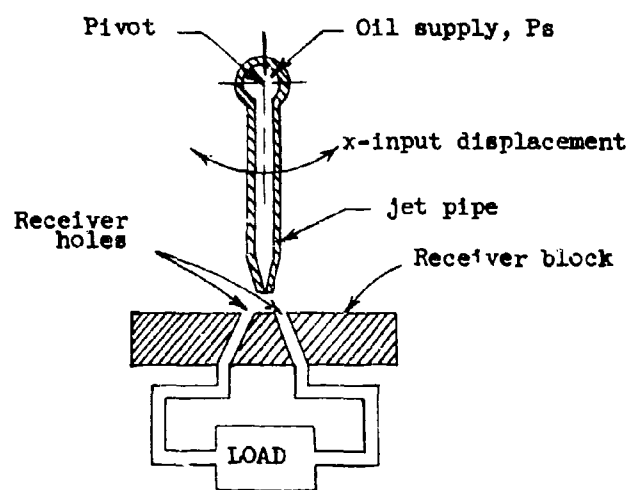
FIGURE 6-20. General Configuration of Valve Ports Showing Control Dimensions

FIGURE 21 INTENTIONALLY OMITTED

FIGURE 22 INTENTIONALLY OMITTED

FIGURE 23 INTENTIONALLY OMITTED





(a) Jet-pipe valve.

FIGURE 6-24. Illustration of Jet Pipe Valve Characteristics

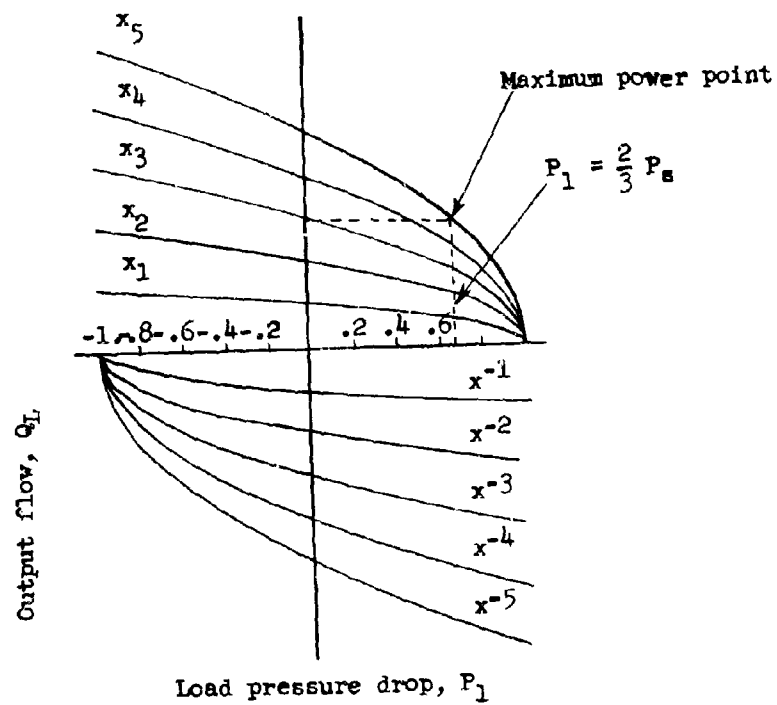


FIGURE 6-25. Idealized characteristics of a hydraulic servo valve.

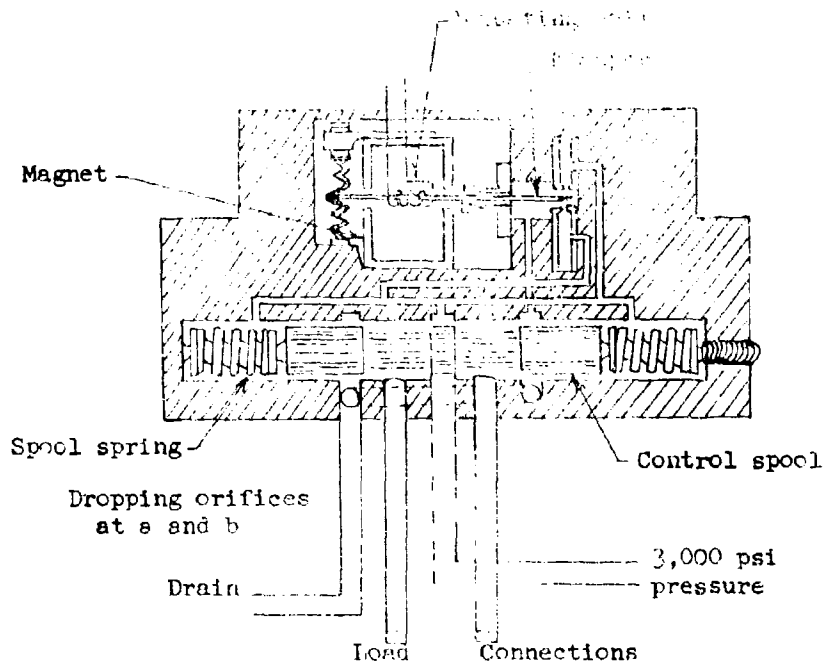


FIGURE 6-26. Two-stage electrohydraulic servo valve. The first stage is a four-way flapper valve with a calibrated pressure output, driving a second stage spring-loaded four-way spool valve.

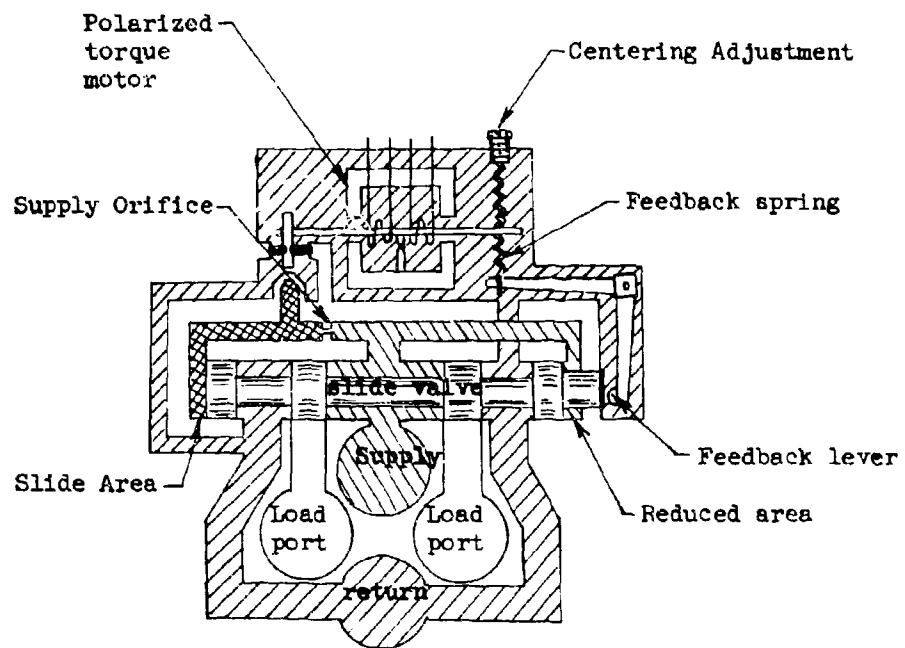


FIGURE 6-27. Two-stage servo-valve with mechanical feedback.

The first stage is a three way flapper valve, the second stage is a four way spool valve.

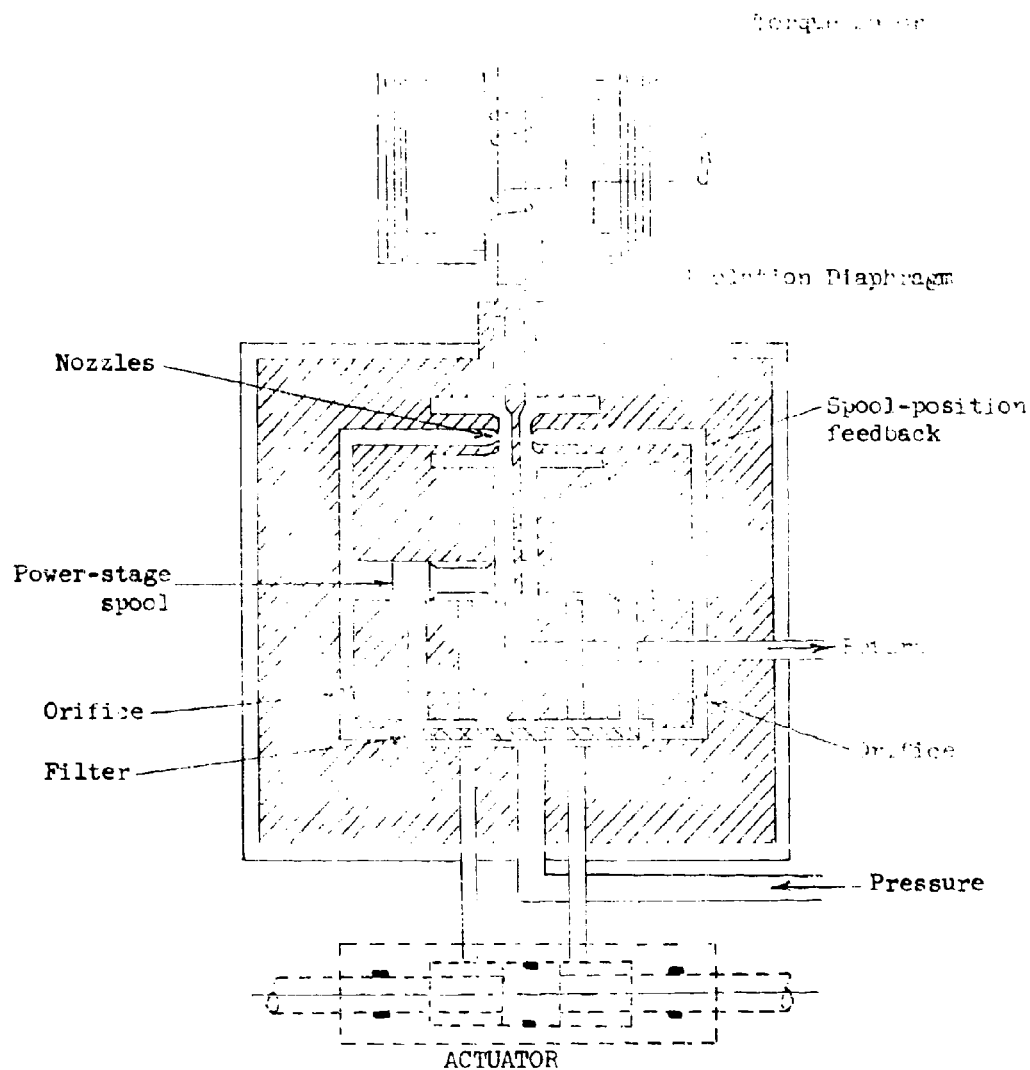


FIGURE 6-28. Two-stage servo valve with mechanical feedback. The first stage is a four-way flapper valve. The second stage is a four-way spool valve. The extension of the flapper into a leaf spring acts as the feedback element.

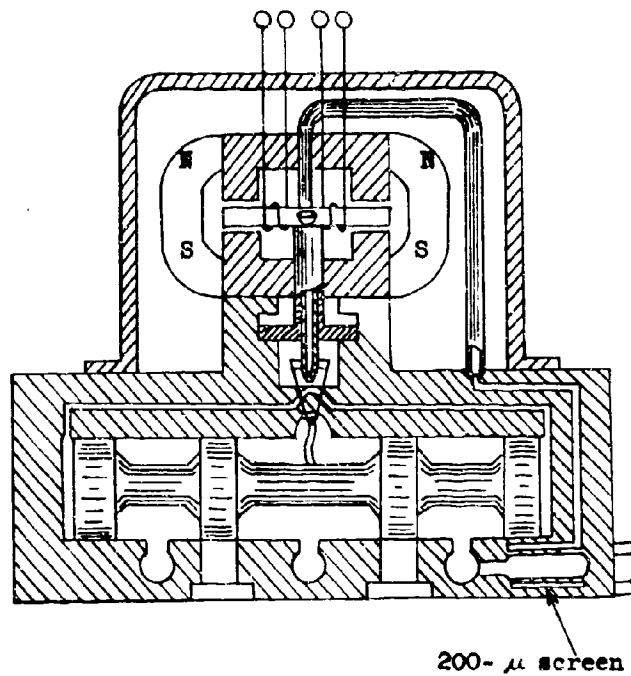
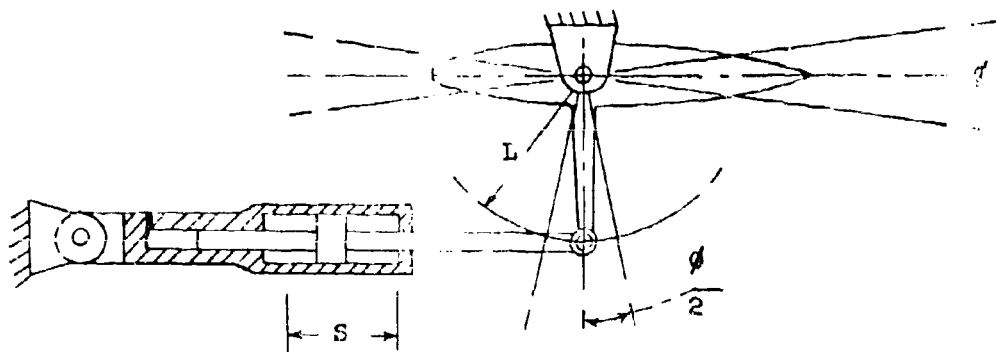
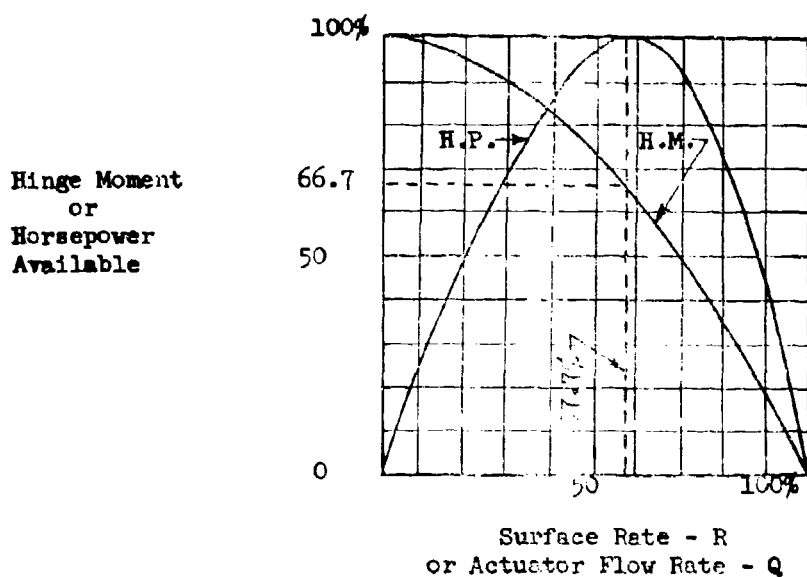


FIGURE 6-29. Two-Stage servo valve with a jet-pipe first stage and mechanical feedback. The second stage is a four-way spool valve attached to the first-stage nozzle by a special feedback spring.



Actuation Geometry



Typical Performance Curve  
Surface Control Actuator

FIGURE 6-30. Actuation Geometry and Legend

**Legend:**

System

- $L$  = lever arm, inches
- $M$  = hinge moment, in. lbs.
- $\phi$  = deflection angle, degrees
- $R$  = max surface rate, deg/sec.

Actuator

- $A$  = actuator area, in<sup>2</sup>
- $d$  = bore diameter, inches
- $d_1$  = rod diameter, inches
- $F$  = force, lbs.
- $P$  = hydraulic pressure, psi
- $Q$  = flow, in #/sec. or gpm
- $S$  = actuator stroke, inches
- $v$  = piston velocity, in/sec.

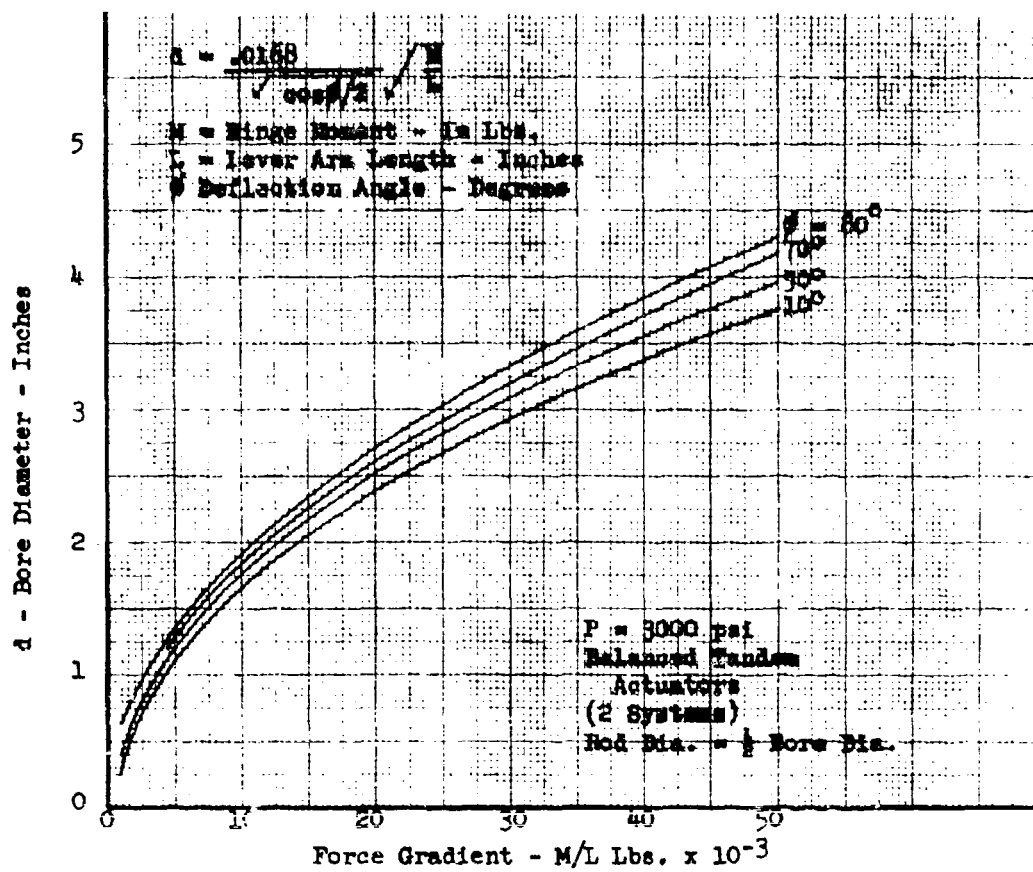


FIGURE 6-31. Actuator Bore Vs Force Gradient -  $M/L$



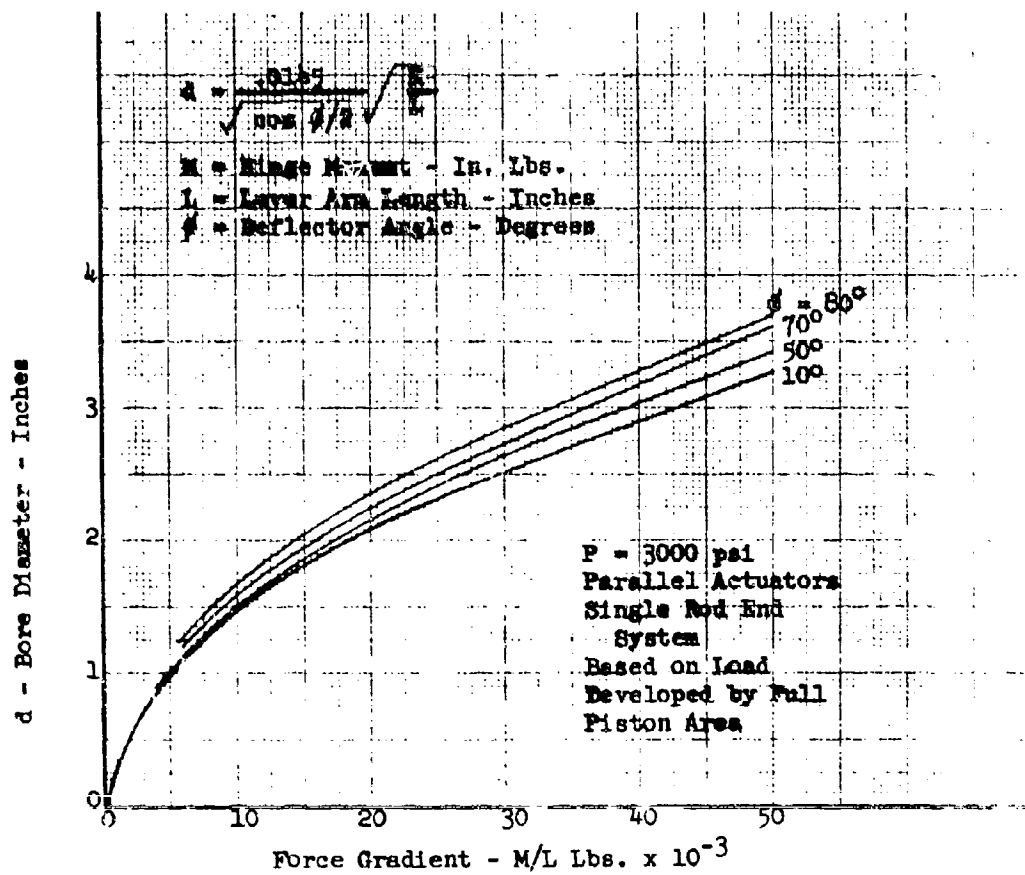


FIGURE 6-32. Actuator Bore Vs Force Gradient -  $M/L$

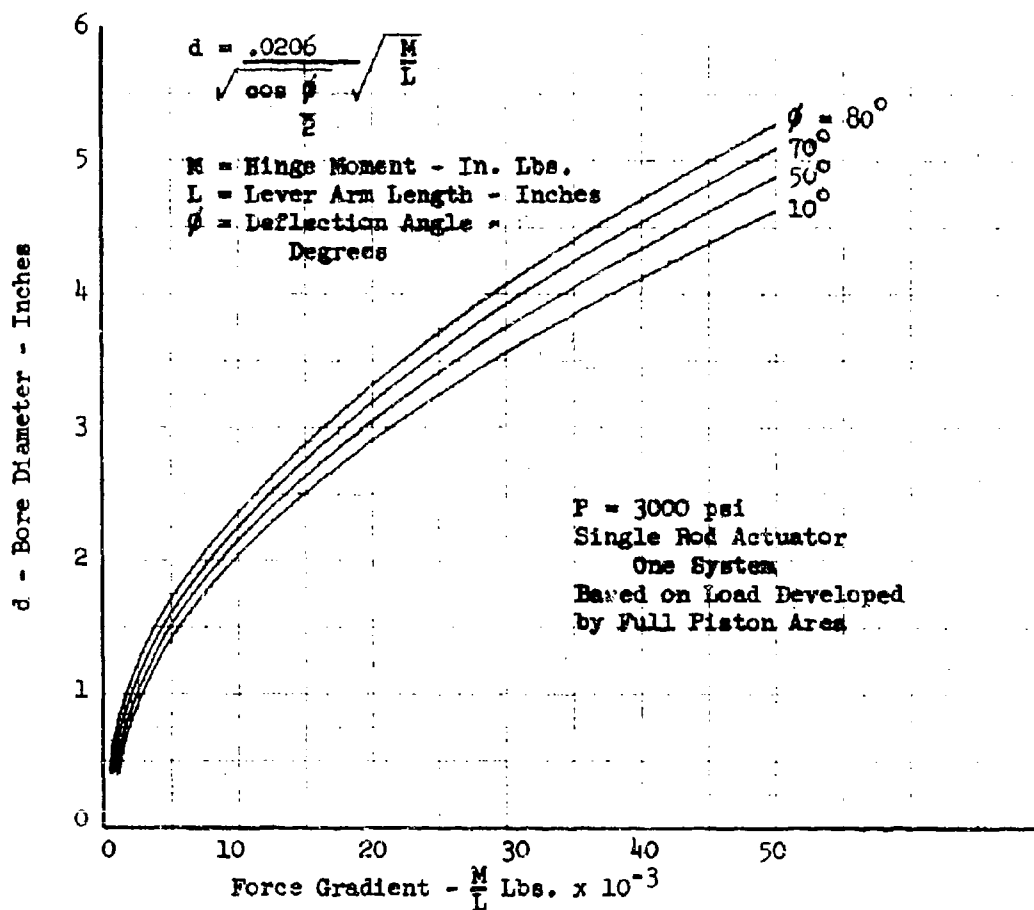


FIGURE 6-33. Actuator Bore

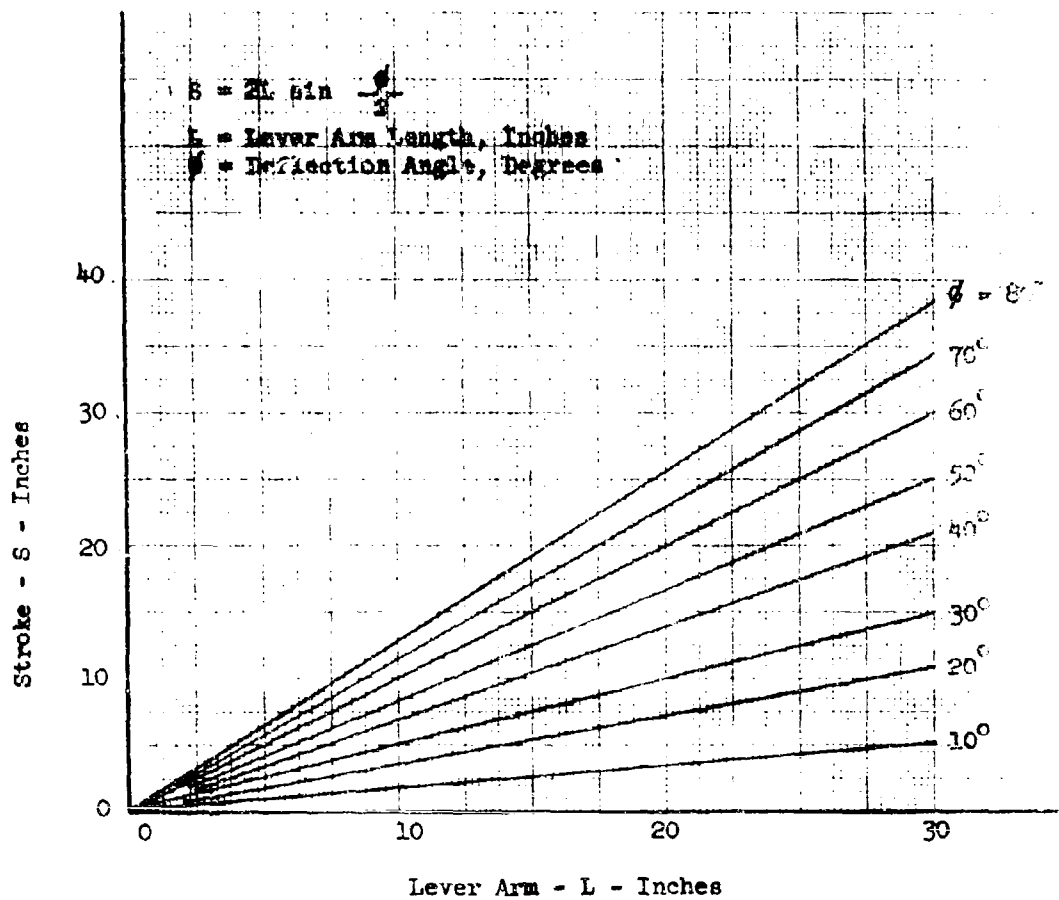


FIGURE 6-34. Actuator Stroke Vs Lever Arm and Deflection

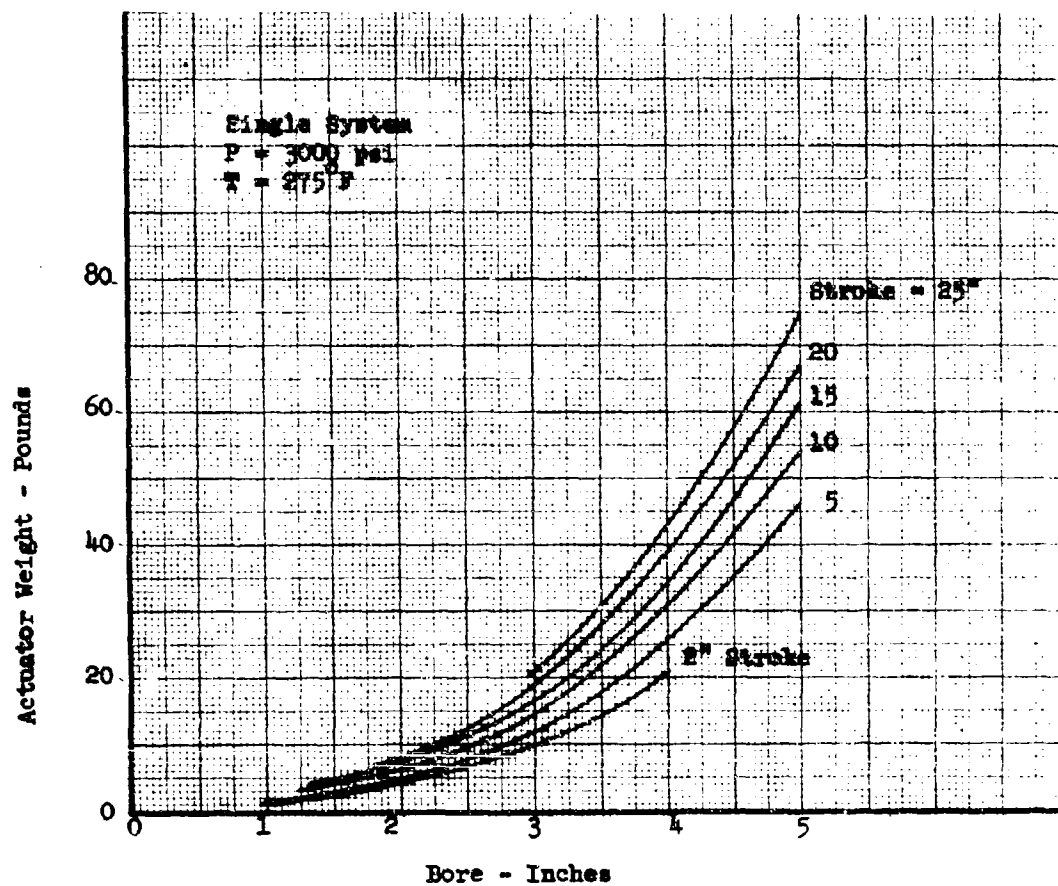


FIGURE 6-35. Weights of Plain, Single Rod End Actuator Assemblies

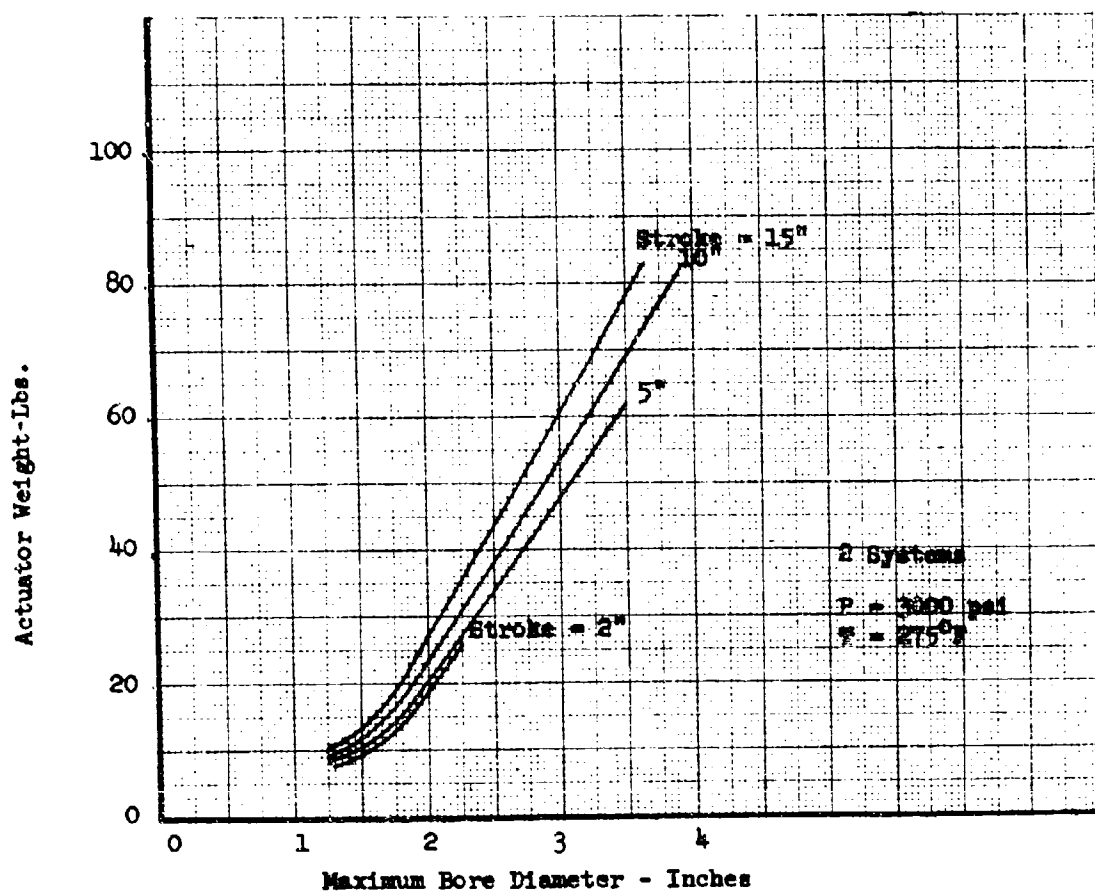


FIGURE 6-36. Weights of Tandem or Parallel Actuators and Valve Assemblies

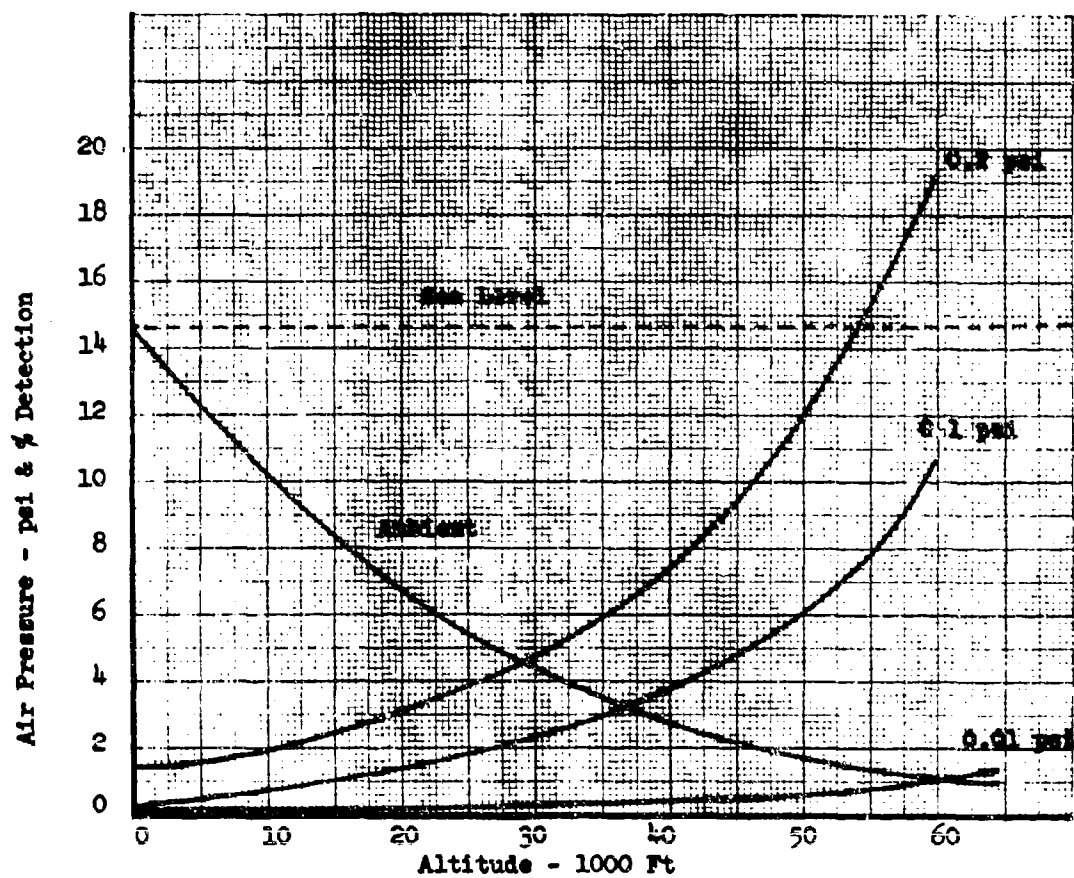


FIGURE 6-37. Signal Variations

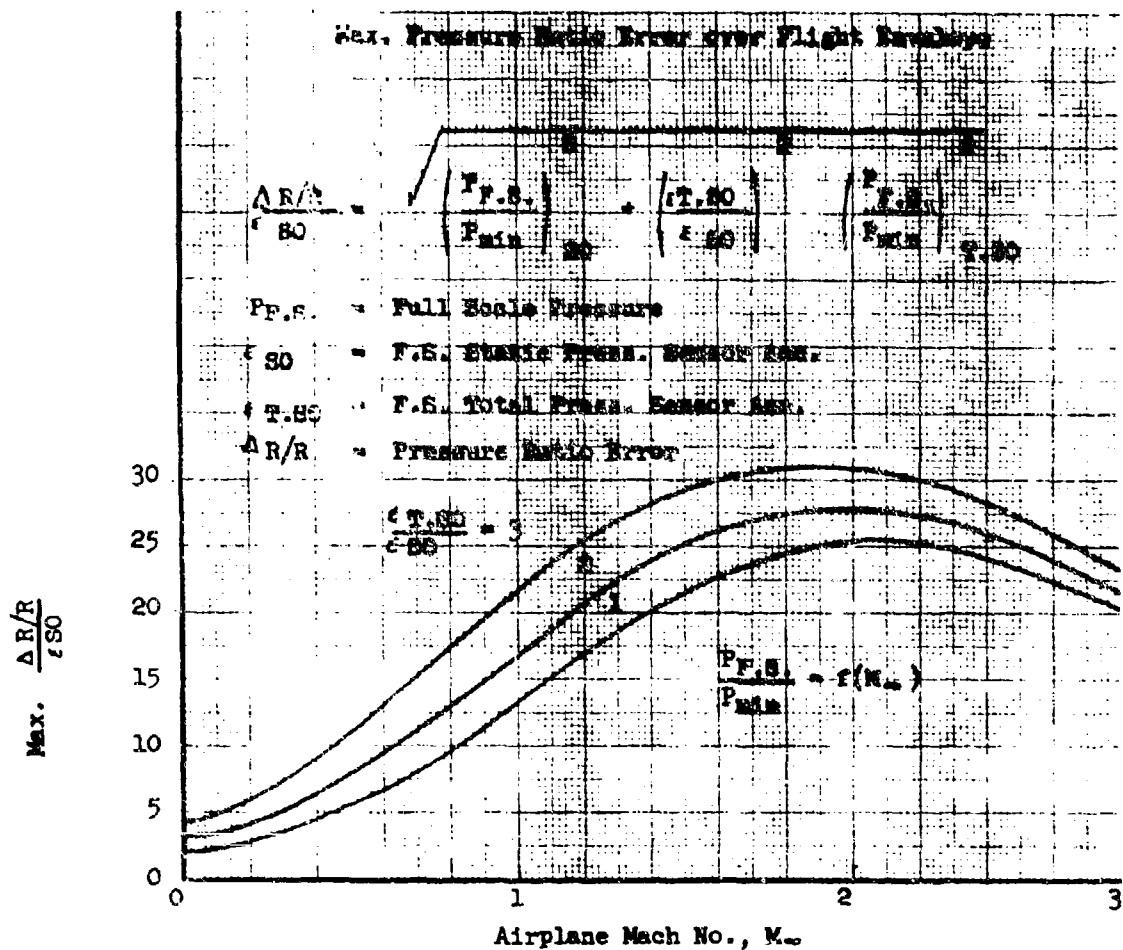


FIGURE 6-38. Local Mach Sensor - Pressure Ratio Error vs.  $M_{\infty}$

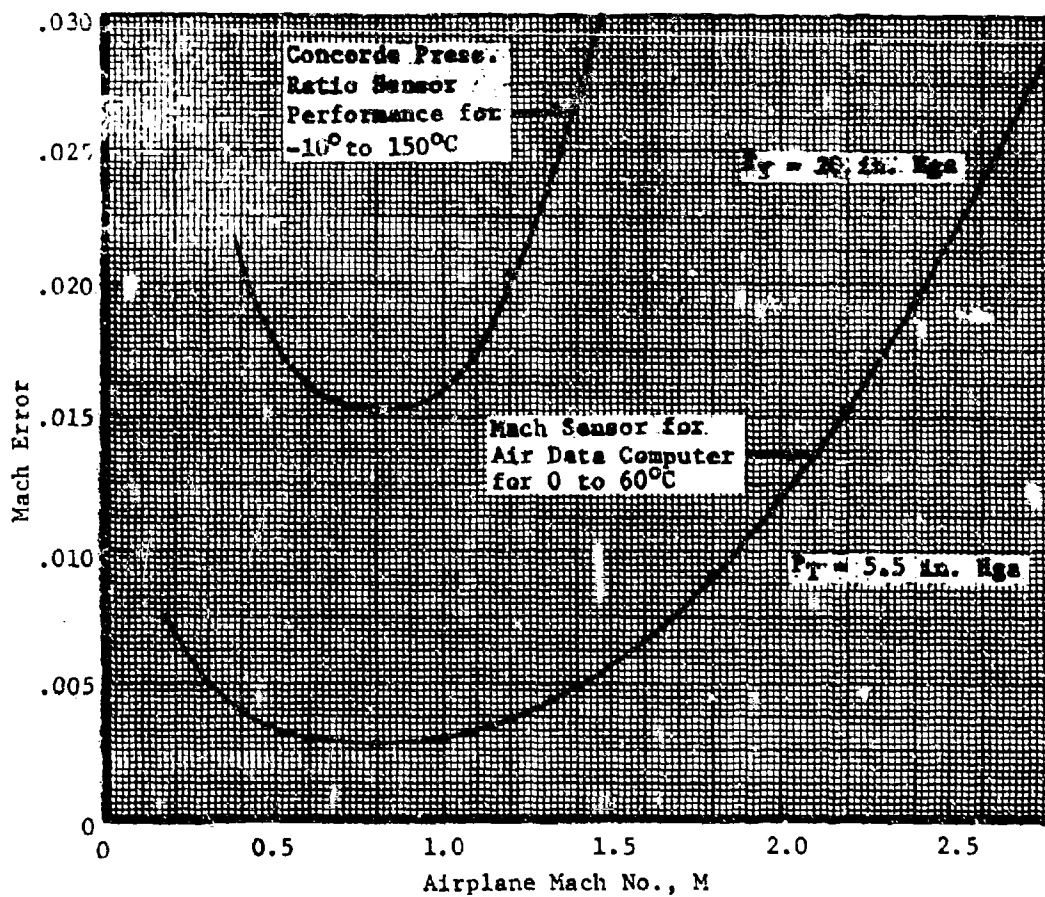


FIGURE 6-39. Performance of Pressure Ratio Sensor



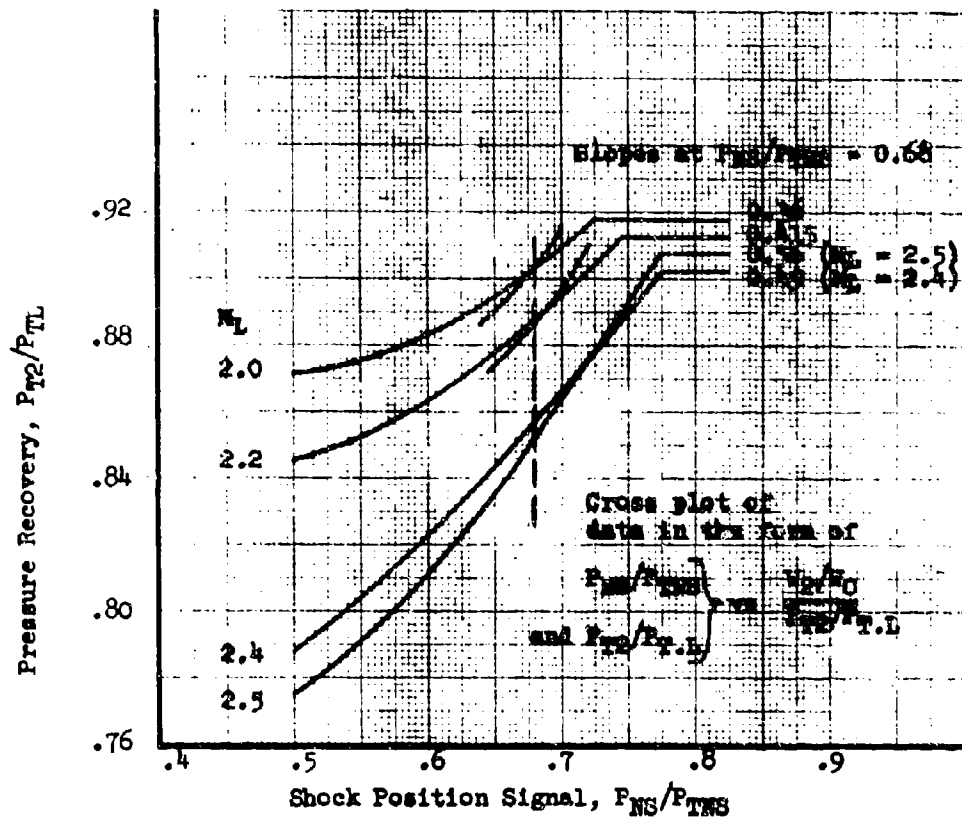


FIGURE 6-40. Bypass Door Control Loop Pressure Recovery vs. Signal Pressure Ratio

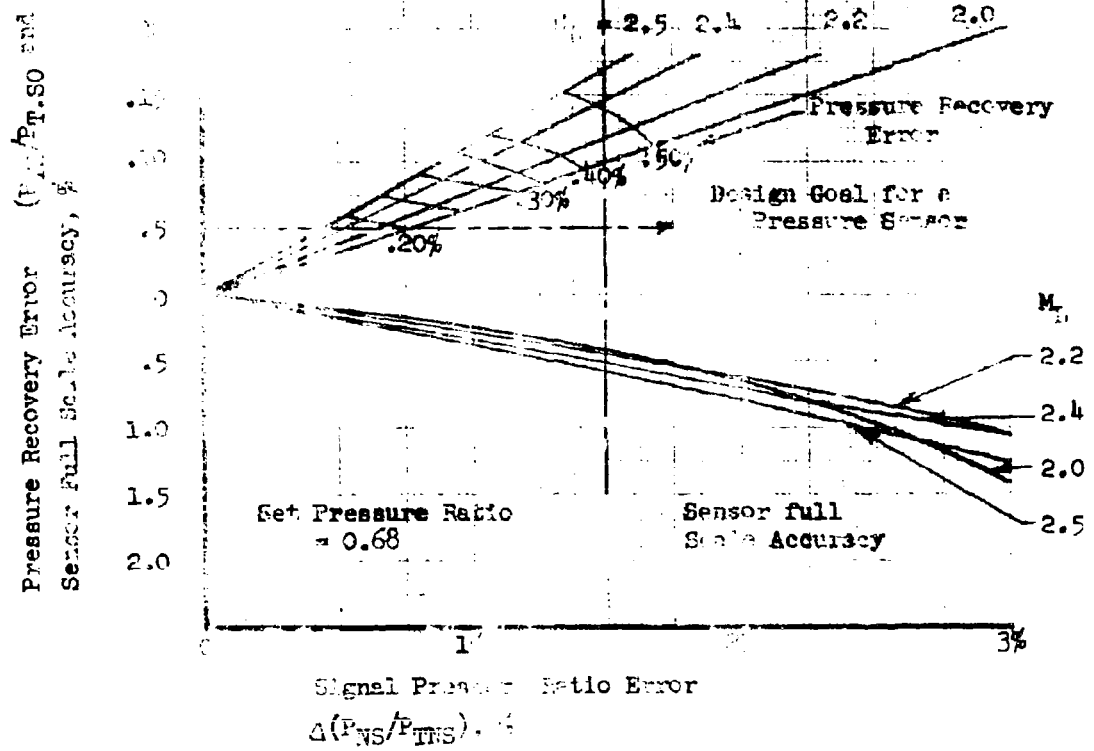


FIGURE 4-10. Ingress Design Limitation - Typical Sensor Accuracy Requirements

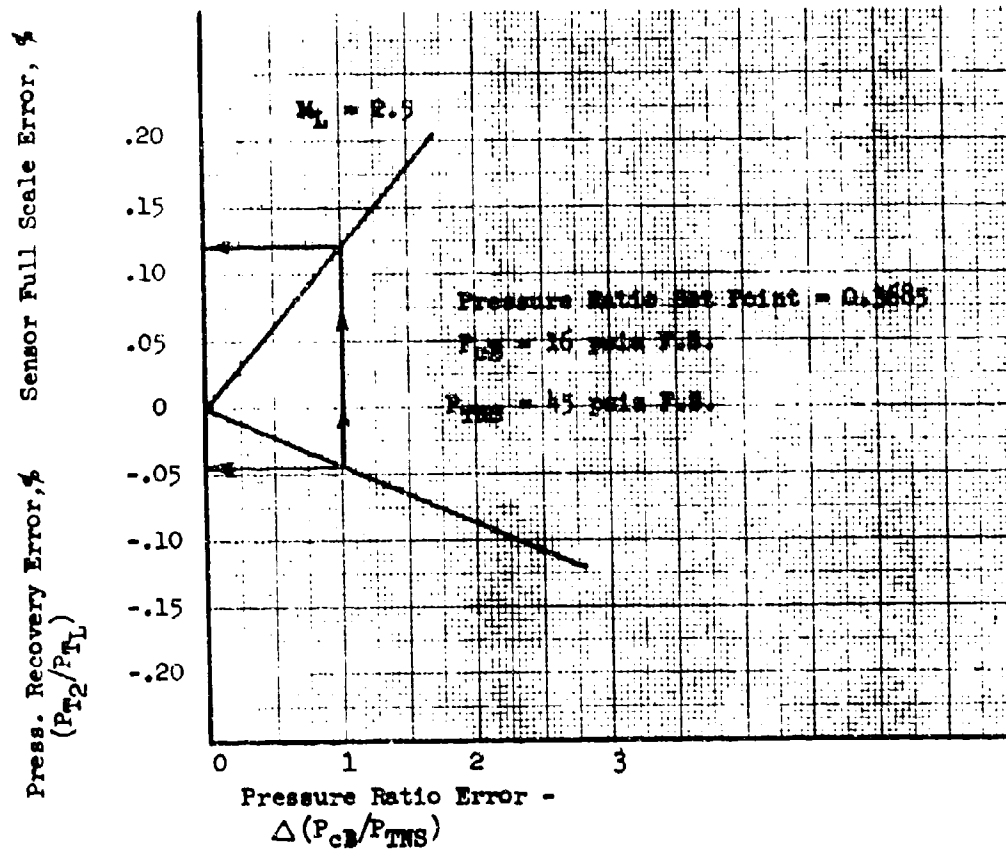


FIGURE 6-42. Centerbody Control Loop - Sensor Accuracy Requirements

**NOTE:** This chart states that if the requirements are to maintain a 0.05% pressure recovery error, the sensor full scale accuracy must be 0.12% error.

## 7.0 Secondary Airflow Systems Performance

### 7.1 Introduction

#### 7.1.1 Definition of Secondary Airflow

Secondary air is that quantity of air which is taken onboard the aircraft either through the engine inlet duct or external scoops, passes between the engine and the surrounding aircraft structure, and is either ducted through an engine ejector exhaust nozzle or dumped overboard through openings in the aircraft structure.

#### 7.1.2 Purposes

Secondary airflow serves several useful purposes;

1. Engine and Accessory Cooling
2. Engine Inlet Airflow Matching
3. Improve Ejector Exhaust Nozzle Performance

### 7.2 Engine Cooling

#### 7.2.1 Cooling Configurations

Practically all turbine engine installations utilize secondary airflow for cooling the engine, engine accessories, and surrounding aircraft structure. Figure 7-1 presents two typical cooling configurations. Figure 7-1A represents the T2B installation which has a fire-wall separating the hot sections from the area of combustible fluids. For normal flight conditions, air which is taken from the inlet duct near the compressor face, flows through the forward compartment, and is dumped overboard. Air for the aft compartment is taken aboard through scoops in the side of the fuselage. It passes through the compartment and passes overboard through an ejector nozzle. For ground and very low speed flight operation, the ejector nozzle is capable of pumping sufficient quantities of cooling through the aft compartment. In the forward compartment the inlet duct pressure is below ambient and this causes reverse flow through the compartment. As flight speed increases there is null point when the duct pressure equals ambient pressure and there is no flow through the compartment. This null point is a function of airspeed and power setting as shown on Figure 7-2. It is usually a transient condition and does not cause over-temperature problems. However, if the null point would occur

during a loiter condition, either the air intake at the inlet duct or the overboard dump could be modified to change the pressure balance and cause a positive flow of cooling air.

Figure 7-1B is a flow-through type installation employed in the RA-5C. Air is taken from the inlet at the compressor face through a modulated gap. The air flows through the engine compartment and is utilized in the ejector nozzle. For ground and low speed operation, the ground cooling door is opened and air enters the compartment, divides, with part of it flowing forward through the gap and into the inlet duct. The remainder flows aft through the ejector nozzle. It is theoretically possible for a null point to occur in the forward portion of the engine compartment with this installation, but no cooling problem has ever been discovered. The only over-temperature problem that has been encountered is when the engine bleed duct leaked.

These are only two configurations. There are no doubt many variations of these two installations plus completely different configurations. Methods for calculating the quantity of secondary airflow will be presented in subsection 7.5 that should be applicable to many configurations.

#### 7.2.2 Structural Temperatures

The quantity of cooling air required to cool the engine is generally less than that required to cool the surrounding aircraft structure. If the structure is cooled, the engine will be sufficiently cooled.

For any particular flight condition the structural temperatures will be a function of secondary airflow as shown on Figure 7-3. The quantity of secondary airflow should be sufficient to operate at point A on the curve so that variations in secondary airflow will have only a slight effect on structural temperatures. If the airflow is reduced to point B, slight variations in airflow cause large changes in structural temperatures. It must be remembered that the quantity of secondary airflow decreases with altitude; therefore, the structural temperature will increase with altitude. The three flight conditions that are usually critical for structural temperatures are: 1. Ground operation, 2. High altitude cruise, 3. High altitude supersonic flight.

#### 7.3 Inlet Matching

Supersonic inlets are sized to obtain the best performance at the design condition. At off-design points the inlet usually has excess flow capacity and this additional capacity causes increased additive drag.

The additive drag can be reduced by increasing the inlet flow which means increasing the secondary airflow. Additional secondary airflow also increases ram drag. The net effect may or may not be an increase in thrust.

Figure 7-4A presents a typical inlet duct operating line with the duct airflow operating line superimposed. The duct airflow consists of engine airflow, secondary airflow, and any other miscellaneous airflow that may be extracted from the duct. The duct airflow operating line is to the left of the knee of the inlet curve for off-design operation but usually the optimum engine performance is obtained when the duct airflow line is at the knee. The duct airflow operating line can be moved to the right by increasing secondary airflow. Utilizing the pressure recovery where the duct airflow operating line crosses the inlet duct operating line, the net thrust of the engine can be calculated by the following equation

$$F_{Ne} = F_N - D_{ADD}$$

where

$F_{Ne}$  = Installed net propulsive effort

$F_N$  = Installed net thrust including the ram drag of the secondary airflow

$D_{ADD}$  = Additive Drag

Figure 7-4B shows the result of increasing secondary airflow. Point A has excessive additive drag. Point B is close to optimum. At Point C and D the inlet is probably supercritical and the additive drag is constant at its minimum value but the pressure recovery is decreasing.

#### 7.4. Nozzle Performance

##### 7.4.1 Effects of Secondary Airflow

Ejector nozzles are employed on turbine engines for two purposes:

1. To pump cooling air through the engine compartment,
  2. To provide additional thrust for engines operating at high nozzle pressure ratios (usually at Mach numbers greater than 1.4).
- For subsonic aircraft ejector nozzles have very little effect on thrust and are only required to pump cooling air through the engine compartment. For supersonic aircraft the ejector not only pumps cooling air but also increases the engine thrust at low nozzle pressure ratios by decreasing losses due to overexpansion of the exhaust gasses.

The secondary flow affects the thrust of the engine by controlling the expansion of the primary flow. This effect reflects itself in the nozzle gross thrust coefficients as shown on Figure 7-5. As secondary airflow increases the nozzle gross thrust coefficient increases. As the secondary airflow and the gross thrust coefficient increase, the ram drag of the additional secondary airflow also increases. The net effect can be determined by plotting net thrust versus secondary airflow. For comparison purposes, the effect of secondary airflow on net thrust has been determined for two types of convergent-divergent ejector nozzles employed on the J79 family of engine. Figure 7-6A is a sketch of the conical ejector on the J79-8/-15 and Figure 7-6B the guided expansion nozzle on the J79-16/-17. Figures 7-7, -8 and -9 presents the effects of secondary airflow at 35,000 feet maximum A/B at Mach No. = 0.9, 1.6, 2.0. Results show that for the conical ejector an increase in secondary airflow increases net thrust except at large secondary airflows at  $M_0 = 2.0$ . For the guided expansion nozzle, secondary airflow decreased net thrust slightly at  $M_0 = 1.6$  and 2.0. For a more detailed explanation of the differences between the two nozzles, please refer to Figure 7-10 which presents the gross thrust coefficients for both nozzles. The thrust coefficient for the guided expansion nozzle is at a higher level than the conical nozzle at zero secondary airflow, but the thrust increment for increasing secondary airflow is less. The magnitude of the ram drag term is greater than the thrust increment for the guided expansion nozzle at the higher Mach numbers. For this same reason the conical nozzle loses performance at high secondary airflows at  $M_0 = 2.0$ .

These are only two examples of ejector nozzles. Nozzle performance varies considerably with types of nozzle and dimensional relationships so that no general statement can be made regarding the effects of secondary airflow on performance. Each type and configuration of nozzle must be evaluated individually. A more complete description of nozzles is given in Section 8.3.

#### 7.4.2 Engine Compartment Pressure

Increasing secondary airflow increases gross thrust but it also increases the pressure required to pass the air through the ejector. Figure 7-11 presents the required secondary airflow pressure ratio across the nozzle to pump a given quantity of air. This secondary airflow pressure has a bursting effect upon the engine compartment. The external pressure on the compartment may be slightly higher or lower than ambient depending upon the flow field around the aircraft. The delta pressure between the inside and outside skin of the compartment will be one of the design loads that the compartment must withstand. If the

delta pressure becomes excessive the compartment may fail, but on the other hand to design the compartment to withstand all possible pressure loads would require excessive weight. The engine compartment should be designed to withstand the pressures for all level flight conditions for the mission requirements of the aircraft. For transient conditions such as a throttle chop or a dive at high speed, a pressure relief device may be necessary to dump the excess secondary air overboard in order to maintain the engine compartment pressures within the structural design limitations.

Early in the development of the A-5A aircraft, a design study revealed that under certain transient flight conditions the engine compartment pressures would exceed the design pressure of the engine compartment. One of these transient conditions was a throttle chop from max A/B power setting to military power setting at the maximum Mach number guarantee condition. Another condition was a high speed dive at lower altitudes.

At the maximum aircraft Mach number, the engine compartment pressure varied as the secondary airflow modulated gap varied as shown on Figure 7-12. The engine compartment was designed for 8 PSID, so the gap setting selection was 30 in<sup>2</sup>. This setting was also influenced by inlet sizing conditions. Figure 7-13 presents the engine compartment pressure at this max Mach condition at the 30 in<sup>2</sup> gap position for various power settings. As the throttle is retarded the pressure increases to a peak at military power, then decreases to a very low value at idle. Also shown on Figure 7-13 are the pressures at various power settings during a high speed dive at lower altitudes. For power settings above 80% RPM the engine compartment design pressure will be exceeded.

It was obvious that some type of pressure relief system must be incorporated in the engine compartment to dump the excess air overboard. The first consideration was blow-out panels. However, once the panel blew out, the aircraft performance would be reduced because of the loss of secondary airflow for the ejector nozzle and second, the engine compartment probably would over-temperature. This condition dictated that the pressure relief mechanism would have to close after the transient overpressure condition subsided. Since a throttle chop can occur very rapidly the pressure relief device must also react rapidly. It was decided to combine the pressure relief door with the ground cooling door. For ground cooling operation, an electrical actuator opens and closes the door in conjunction with the operation of the landing gear. For pressure relief operation, the door is held closed with an overcenter-linked bungee. As the engine compartment pressure exceeds 8 PSID, the door moves overcenter and the bungee opens the door. As the pressure in the compartment drops below 6 PSID, the



electrical actuator extends, grips the door, closes the door, and resets the bungee. This entire operation requires approximately 30 seconds.

Flight test results have shown excellent results with the pressure relief door. The door has opened as predicted during high speed dives on many occasions. The steady state pressure in the engine compartment have been approximately 0.5 psi lower than estimated. This is probably due to leakage in the engine compartment.

This was an example of one type of engine with one particular secondary airflow system. Other aircraft with different exhaust nozzles may pose other types of overpressure problems. The main point to stress here is to evaluate various flight conditions, both transient and steady state, at various power settings to determine if an overpressure condition exists.

## 7.5 Estimating Secondary Airflow Quantities

### 7.5.1 Method of Calculation with Overboard Dump

Airflow through a system can be calculated if the boundary conditions are known, such as pressure and temperature, and the flow losses between the two points. Airflows are calculated from the airflow parameter  $\frac{W \sqrt{\theta}}{A \delta_T}$ .

The airflow parameter is defined by this equation:

$$\frac{W_T \sqrt{\theta_T}}{A \delta_T} = \frac{(.59316) (\text{Mach})}{(1.0 + 0.2 \text{ Mach}^2) (2.993)} ; \gamma = 1.4$$

$W_T$  = theoretical airflow - lb/sec

$\theta_T = T_T/518.7$  (Total temperature - °R)

$A$  - Area - in<sup>2</sup>

$\delta_T = P_T/14.696$  (Total pressure - lb/in<sup>2</sup>)

The Mach number is related to the pressure ratio by the following equation:

$$\frac{P_T}{P_S} = (1.0 + 0.2 \text{ Mach}^2)^{3.5}; \quad \gamma = 1.4$$

$P_S$  = Static Pressure

Tables of pressure ratio and airflow parameter and airflow parameter versus Mach number are presented in Appendix A and E, respectively.

In the definition of the airflow parameter, the term  $W_T$  was defined as the theoretical airflow. To calculate the airflow through an area at given pressure and temperature conditions, the airflow is a direct function of the area. This will give the airflow without any regard to the boundary layer effects. If the boundary layer effects are ignored, the calculations will be the theoretical airflow that can flow through the area. The actual airflow will be less due to the boundary layer effects. The ratio of the actual flow to the theoretical flow is defined as the flow coefficient (K).

$$K = \frac{W_A}{W_T}$$

$W_A$  = Actual airflow

$W_T$  = Theoretical airflow

By substituting the actual airflow for the theoretical airflow in the airflow parameter:

$$\frac{W_A \sqrt{\theta_T}}{K A \delta_T} = f (\text{Mach})$$

The flow coefficient (K) is usually determined by experimental means. Data are available in the literature for K values for orifices, venturi tubes, etc., and for overboard dumps which will be discussed in detail in subsection 7.5.4, but for many cases the K factor must be estimated from a similar configuration where data are available or a lab test must be obtained to obtain the K factors.

To illustrate the method of estimating secondary airflow, the sketch of a secondary airflow compartment, as shown on Figure 7-14, will be analyzed. The flow coefficient for the two areas ( $A_G, A_P$ ) will be assumed to be 1.0 for this example. The known boundary conditions are the compressor face total and static pressure, the total temperature, the flow areas, and the ambient pressure at the exit.

There are two unknowns, the secondary airflow ( $W_S$ ) and the secondary airflow compartment pressure. This requires an iteration process to solve for the two unknowns. The best method is to assume values of  $P_{T_S}$  and solve for the airflow at the entrance and the exit. The airflow can be plotted versus  $P_{T_S}$  and where the two lines cross, both entrance and exit conditions will be satisfied.

First, consider the entrance to the compartment. The total and static pressure must be known in the gap ( $A_G$ ) in order to calculate the airflow. Unless experimental data are available,  $P_{T_G}$  can be estimated by assuming that  $P_{T_G}$  equal the static pressure in the duct ( $P_{S_2}$ ). This is a good assumption and amounts to a 1 q loss in total pressure from the duct to the gap. The term q is the compressible dynamic pressure:

$$q = P_T - P_S$$

Assuming the velocity of the secondary airflow in the compartment is such that the total pressure in the compartment is approximately equal to the static pressure  $P_{S_S}$ , the gap static pressure ( $P_{S_G}$ ) is equal to the compartment pressure ( $P_{T_S}$ ). This is valid because the static pressure in a duct with subsonic flow entering a plenum chamber must equal the pressure in the plenum chamber. By assuming various values of  $P_{T_S}$ , the flow through the gap can be calculated by means of the airflow parameter for each value of  $P_{T_S}$ . The total temperature is constant, since essentially no heat is added or lost by the secondary airflow at this point. For this example there will be no loss in the secondary airflow compartment pressure from the entrance to the exit, but if there were any restrictions in the passage, the pressure loss could be estimated and the  $P_{T_S}$  value reduced at the exit. At the exit  $P_{T_S}$  will be the total pressure ( $P_{T_P}$ ) and the static pressure ( $P_{S_P}$ ) will be equal to the ambient pressure ( $P_0$ ) since the air is dumping into a "plenum" chamber. Exit airflows can be calculated for various secondary compartment pressures. The values of airflow for the entrance and exit areas versus  $P_{T_S}$

can be plotted and the actual airflow determined. The following is a typical calculation of a given flight condition:

Mach = 0.9; 20,000 ft.; Standard Day

$$P_0 = 6.75 \text{ psia } P_{T_0} = 11.42 \text{ psia } T_{T_0} = 519.9 \text{ } ^\circ\text{R } \sqrt{\theta_{T_0}} = 1.001$$

$$\text{Pressure Recovery} = .98 \quad P_{T_2} = (.98)(P_{T_0}) = 11.19$$

$$A_G = 20 \text{ in}^2 \quad A_D = 30 \text{ in}^2$$

Assume Mach number in duct = 0.4

From isentropic flow theory for  $M_{\text{duct}} = 0.4$

$$P_{T_2}/P_{S_2} = 1.117 \quad P_{S_2} = 11.19/1.117 = 10.02$$

$$P_{T_G} = P_{S_2} = 10.02 \quad P_{S_G} = P_{T_S}$$

Assume  $P_{T_S}$  then:

$P_{T_S}$	$P_{T_G}/P_{S_G}$	$M_G$	$\frac{W\sqrt{\theta}}{A \delta_T}$
9 psia	$10.02/9 = 1.113$	.394	.213
8	$10.02/8 = 1.253$	.577	.282
7	$10.02/7 = 1.431$	.734	.320

$$W_G = \left[ \frac{W\sqrt{\theta}}{A \delta_T} \right] \left[ A_G \right] \left[ \frac{P_{T_G}}{14.7} \right] \left[ \frac{1}{\sqrt{\theta_{T_0}}} \right]$$

Hence:

$P_{T_S}$	$W_G$
9 (.213) (20) (10.02/14.7) (1/1.001)	= 2.90 lb/sec
8 (.282) (20) (10.02/14.7) (1/1.001)	= 3.84
7 (.320) (20) (10.02/14.7) (1/1.001)	= 4.36

At the exit assume the air temperature increased  $50^\circ$

$$T_{TD} = 519.9 + 50 = 569.9 \sqrt{\theta_{TD}} = \frac{569.9}{518.7} = 1.048$$

$$P_{TD} = P_{TS} \quad P_{SD} = P_0 = 6.75$$

Assume  $P_{TS}$  then:

$P_{TS}$	$P_{TD}/P_{SD}$	$M_1$	$\frac{W\sqrt{\theta}}{A \delta T}$
9	$9/6.75 = 1.333$	.654	.303
8	$8/6.75 = 1.185$	.498	.255
7	$7/6.75 = 1.037$	.228	.1311

So that:

$P_{TS}$	$W_D$
9	$(.303)(30)(9/14.7)(1.048) = 5.31$
8	$(.255)(30)(8/14.7) = 3.97$
7	$(.1311)(30)(7/14.7) = 1.79$

Figure 7-15 presents a plot of the gap airflow and the exit airflow versus secondary airflow total pressure. The two lines cross at a secondary airflow of 3.9 lb/sec and a pressure of 7.95 psia. At this point the gap and exit airflow match and this will be the secondary airflow for this particular flight condition and configuration. By varying gap and exit area, various combinations of secondary airflow and pressure can be obtained.

#### 7.5.2 Method of Calculation with Flow Through Compartment

The method of calculating secondary airflows for a flow through compartment can apply to both the RA-5C type where the secondary airflow is obtained from a gap at the engine face or the air can be obtained through an external scoop as shown for the aft compartment of the T-2B.

The method of calculating secondary airflows with a flow through compartment is very similar to the method presented in the previous subsection, with the exception that instead of an overboard dump, there is an ejector nozzle. The flow capability of the nozzle is obtained from the pumping characteristics discussed

previously. By assuming various values of  $P_{T5}$ , the secondary airflows can be calculated for any particular flight condition. The gap airflows can be calculated as presented in the previous subsection and both airflows plotted versus  $P_{T5}$  and the match point determined.

For the RA-5C, it was decided to construct a 0.25 scale model and measure the pressure losses through the engine compartment. Two sets of losses were recorded. One set was from the inlet duct total pressure at the compressor face to the secondary air modulating gap. The other set was from the secondary gap total pressure to the nozzle inlet total pressure. The average pressure loss from the inlet duct to the gap was 5%. The pressure loss from the gap to the nozzle was mainly the result of the sudden expansion from the gap into the secondary compartment, and there was very little loss through the engine compartment itself. Assuming a one "q" loss from the gap to the engine compartment and no losses in the engine compartment will give essentially the same result as that measured on the model.

From the model data and the performance of the ejector the secondary airflow can be calculated for various gap settings and engine power settings. Figure 7-16 presents secondary airflows versus gap area at given Mach numbers at max A/B power settings for the RA-5C.

For ground and low speed flight conditions, the ground cooling door is opened and cooling air is taken aboard through the door, with part of the air going forward through the gap into the inlet duct - the remaining air going aft through the ejector nozzle as shown on Figure 7-17. For this case the cooling door flow must equal both the gap flow and the nozzle flow. The method is similar to the previously discussed method. Various values of  $P_{T5}$  are assumed and the flows calculated and plotted. The total pressure of the air flowing through the door will be equal to ambient pressure ( $P_o$ ). The static pressure will be equal to  $P_{T5}$  since the flow is not choked at the door. At the gap, the total pressure is equal to  $P_{T5}$  and the static pressure is equal to the inlet duct static pressure. The nozzle flow is calculated from the nozzle pumping curves for each value of  $P_{T5}$ . Figure 7-18 presents the ground cooling door airflow, the gap airflow, the nozzle airflow and the total of gap and nozzle versus secondary airflow pressure. Where the door airflow and the total of the gap and nozzle airflow cross is the path point. The door flow is 29.4 lb/sec, and the secondary pressure is 13.3.

Reading the gap flow curve and nozzle flow curve at  $P_{Tg} = 13.3$  gives 19.7 and 9.7 lb/sec flow, respectively.

#### 7.5.3 Engine Compartment Bursting Loads

In the course of calculating secondary airflows, the secondary airflow pressure in the engine compartment is also calculated. From aerodynamic data the pressure coefficients on the external surface of the engine compartment can be obtained and the external static pressure determined. The differential between the internal pressure and the external pressure will be the bursting load of the engine compartment. The engine compartment is designed to withstand a given load and the bursting pressures must not exceed this value. Figure 7-19 presents the differential across the engine compartment for various gap settings and Mach numbers at max A/B power setting for the RA-5C. The design pressure is 8.0 psid; therefore at higher Mach numbers the gap area must be limited or the design pressure will be exceeded.

For conditions where the design pressure is exceeded the pressure relief door opens and the pressure is decreased. The question then arises as to what size pressure relief door is required? For most cases for the RA-5C the secondary airflow gap is choked when the pressure relief door is required to open. When the gap is choked, a constant secondary airflow is flowing into the engine compartment regardless of the compartment pressure. Assuming values of secondary pressure ( $P_{Tg}$ ), the nozzle flow and the door flow can be calculated and plotted versus  $P_{Tg}$  to determine at what value of  $P_{Tg}$  the pressure relief door flow and the nozzle flow match the gap flow. This will be the engine compartment internal pressure. If the differential pressure is above the design pressure, a larger pressure relief door is required.

The most important item to consider in these calculations is the flow coefficient for the pressure relief door. For supersonic flight the flow coefficient could be considerably reduced, which would then require a larger door opening to reduce the engine compartment pressures. The following subsection will present flow coefficients for the RA-5C pressure relief door.

#### 7.5.4 Overboard Exits

This discussion of the flow coefficient and the thrust performance of overboard exits applies not only to secondary airflow compartment

exits but also to any other airflow exit required on the aircraft, such as heat exchanger cooling airflows, ramp boundary layer bleed airflows, etc. References 1 through 4 present performance data for overboard exits for various types of exits and flow conditions. A discussion of the results of these reports will be presented herein.

The airflow through an overboard exit is generally calculated from the total pressure in the exit and the ambient pressure at the given aircraft altitude. From this pressure ratio the Mach number can be determined and hence the airflow parameter and the actual airflow. However, the interaction of the exit airflow with the free stream airflow may cause a static pressure rise at the exit. The actual pressure ratio will be less than the assumed ratio and the actual airflow will be less than the theoretical calculated value. The flow coefficient (K) is not only influenced by the boundary layer effects but also by the static pressure rise due to the interaction of the two mixing streams. Figure 7-20 presents a sketch of this interaction of the free stream air with the exit air in supersonic flow.

Figures 7-21 through 7-24 present the sonic flow coefficient and the thrust coefficient for four flush exits with varying exhaust angles. The sonic flow coefficient is very similar to the flow coefficient previously defined in this lecture except that the actual flow is referenced to the maximum theoretical sonic flow which would pass through the exit area at the same pressure and total temperature. For pressure ratios greater than 1.893, the sonic flow coefficient is identical to the flow coefficient (K) defined in this lecture. The thrust coefficient is defined as the actual thrust of the exit air divided by the isentropic thrust of the air at the same pressure and temperature.

From these figures, it is readily apparent that the flow coefficient is independent of pressure ratio and free-stream Mach number above pressure ratios of approximately 3.0. Unfortunately, most of the air dumped overboard from an aircraft is usually at a low pressure level and the flow coefficients in this range have considerable scatter and poor accuracy.

The thrust coefficients show the best performance at the shallower discharge angles which is what would be normally expected.



Reference 3 presents a performance comparison between flush and shielded inlets. A sketch of the two types of exits is shown on Figure 7-25. A thrust comparison of the two exits is presented on Figure 7-26. The shielded exit has better performance than the flush exit at supersonic Mach numbers. Some unpublished test work performed in the Thermo Lab at North American several years ago indicated that shielded exits had very high flow coefficients. This can be expected because there is very little interaction between the exit stream and the free stream. For no exit flow the pressure at the exit will be reduced below ambient. It is possible under some subsonic flow conditions to actually have a flow coefficient greater than one because the external static pressure is below ambient.

It is very difficult to find good data for performance and flow coefficients for overboard exits for a complete range of Mach numbers and exit pressure ratios.

When the pressure door problem came along on the RA-5C, it was decided that sufficient data were not available to accurately predict the flow coefficients for the pressure relief door. The pressure relief door extended into the air stream as shown on Figure 7-27. The additional shock waves generated by the door complicated the flow field at the exit so that it was very difficult to predict the flow coefficient. The thrust or drag produced when the door was open was of no concern since the door would only be open during transient flight conditions.

A lab test was initiated to measure the flow coefficients of this type of exit in a supersonic stream. The results of this test are presented on Figure 7-28. The maximum flow coefficients are approximately 0.8 at pressure ratios of 4. The flow coefficients presented on Figures 7-21 through 7-24 were approximately 0.95 at a pressure ratio of 4. Apparently the addition of the door in the exit stream created additional shock waves and increased the static pressure at the exit, thereby decreasing the flow coefficient.

## 7.6 Secondary Airflow Losses

### 7.6.1 Inlets and Diffusers

About the same components compose each of the miscellaneous systems. Each has an inlet. It could be a perforated plate, a ram air scoop, or a flush inlet. Variations exist in each major category. Ram air scoops may be submerged in the boundary layer or exposed to free stream. The flush inlets could be slots or NACA submerged inlets.

### 7.6.1.1 Flush Inlet Losses

Flush inlets may take the form of perforations, flush holes or slots, and inclined holes or slots. Perforations have low flow coefficients and a large number of holes may be necessary to bleed off the boundary layer air. To stabilize a normal shock, the boundary layer air should be bled ahead and downstream of the shock. A porous bleed system lends itself well to this requirement. Airflow is low, as is the bleed air pressure recovery. However, many boundary layer bleed systems utilize this method of removing the low energy air.

In designing a porous surface removal system, pressure drop across the material and flow rate are the quantities of interest. Usually, the free-stream boundary layer is being removed from flows parallel to the porous plate. This results in a reduction in the flow coefficient of the holes in the surface. It is convenient to utilize normal flow data by modifying the porosity of the plate to account for the reduction in flow coefficient. A correlation of the existing porous material flow characteristics has been accomplished in Reference 5. Figure 7-27 shows the correlation of various data for flow normal to a porous plate. The data for the curves was taken from References 13 through 15. The equation governing the flow for hole aspect ratios of .64 and greater is shown on the plot. Since this is for flow normal to the plate, another correlation is required to determine the effect of flow parallel to the plate. The equations allowing the correlation are stated below.

$$\frac{\sigma_A}{\sigma_o} = 1 + (.0562 \frac{L}{D_h} + .2289 \frac{\Delta P}{P_o} - f(\sigma_o))(M_o)^g \frac{L}{D_h} \quad (7.1)$$

$$\text{where: } g\left(\frac{L}{D_h}\right) = 1.461 - .8948\left(\frac{L}{D_h}\right) + .3165\left(\frac{L}{D_h}\right)^2 \quad (7.2)$$

$$\text{and } f(\sigma_o) = .3978 + 2.561\sigma_o - 6.352\sigma_o^2 \quad (7.3)$$

The last two equations are plotted in Figure 7-30.

The above equations are valid in the following ranges:

$$\begin{aligned} 0 &\leq M_o \leq 1.4 \\ .02 &\leq \sigma_o \leq .20 \\ .89 &\leq L/D_h \leq 2.5 \end{aligned}$$

The nomenclature is described in Figure 7-31.

If the porous material is used in an area where the Mach number changes, the area should be broken down into strips and average properties used over that area.

Figure 7-32 illustrates the method of obtaining the flow characteristics as a function of porosity. A number of Mach numbers would fill out the spectrum for the complete aircraft envelope. The minimum loss would be selected. At some critical mission condition, the porosity would be chosen to minimize the losses.

An example of the use of the equations and curves follows. Assume a bleed flow. Compute  $(W \sqrt{\theta_{to}})/(\delta_o A_o)$  from the Mach number along the surface and the average properties of the stream. Assume a hole aspect ratio  $L/D_h = 1$  for this example and assume a corrected bleed flow rate of .1. Using equation (7.1) and Figure 7-2, compute  $\sigma_a/\sigma_o$  for various values of  $\sigma_o$  and  $P/P_o$ . Plot the results as shown in the upper portion of Figure 7-32. Then, using the equation shown on Figure 7-29, calculate  $\sigma_a$  for several values of  $\Delta P/P_o$  versus  $\sigma_o$ .

$$\frac{W \sqrt{\theta_{to}} \frac{x1}{\sigma_a}}{\delta_o A_o} = \sqrt{.3049 \frac{\Delta P}{P_o} - .2591 \left( \frac{\Delta P}{P_o} \right)^2}$$

for the given airflow and Mach number. Repeat the above until a map of Mach numbers and/or weight flows are covered and then choose the best compromise for the aircraft.

If one is asked to evaluate a given system, the following procedure is recommended. Choose the conditions and determine the Mach number,  $M_o$ . From the design, determine the porosity ( $\sigma_o$ ) and the hole aspect ratio ( $L/D_h$ ). Determine  $f$  ( $\sigma_o$ ) and  $g$  ( $L/D_h$ ) from Figure 7-31. Substitute the values in Equation (7.1). This results in an equation  $\sigma_a = f \cdot (\Delta P/P_o)$ . Assume a  $\sigma_a$  and solve for  $\Delta P/P_o$ . Choose a typical value of bleed flow from the table below.

TABLE I

Inlet Type	$W_{b1}/W_{Duct}$
External Compression	3 - 5%
Mixed Compression	6 - 8%
	10 - 12% (if higher recovery desired)
All Internal Compression (Pitot Type)	(25 - 30%)

Calculate  $(W_{b1} \sqrt{\theta_{t0}}) / \dot{q}_0 A_0$  and divide by the assumed  $c_a$ . Find the value of the corrected weight flow on the abscissa of Figure 7-29 and determine the loss through the porous plate on the ordinate. Compare this value with the one previously assumed. Iterate until a  $\Delta P/P_0$  is found that satisfies both conditions. Using the methods described later, the exiting momentum and drag will be determined.

#### 7.6.1.2 Flush Slots

Perforations have poor flow coefficients in supersonic flow and require a large number of holes to bleed the required airflow. A flush slot can bleed moderate amounts of air with good bleed pressure recovery. The bleed area requirement is much less for the flush slot.

In general, for flush inlets, the inclination of the inlet axis with the surface is the major geometric parameter influencing recovery. Smaller angles with respect to the surface, offer superior performance. For low mass flow ratios, an NACA submerged inlet offers improved recoveries. Deep, narrow inlets have lower drag than wide shallow ones at Mach numbers greater than .9, but at lower Mach numbers the wider inlets prove superior. The width to depth ratio affects the performance of inlets by allowing more high energy air to enter with the low width to depth inlets. Both pressure recovery and mass flow will increase.

Figures 7-33 through 7-43 are typical performance parameters for flush slots at varying angles of inclination. Both Mach number and mass-flow-ratio affect the performance of the inlets. Figures 7-44,-45 show similar parameters for an NACA type submerged inlet. The initial ramp is  $7^\circ$  and the sides diverge to meet the inlet. Included also are drag coefficients based upon freestream  $q$  and inlet area for each configuration.

Figure 7-46 presents the inlet area required for equal mass flow and drag for various ramp inclination angles. The principle effect of small initial inclination of the ramp is to reduce the inlet area required significantly.

In the analysis of flush inlets, the total pressure recovery is used instead of the static pressure drop as in the perforated plates. With flush inlets, the area is large enough to allow turning the flow and improving the pressure recovery.

Reference 7 shows the effects of yawing the axis of the flush inlet on inlet performance. Needless to say, the axis of the inlet should be aligned with the flow direction for maximum performance.

Having the mass flow and pressure recovery characteristics of a flush inlet, an iterative process utilizing the flow elements of the remainder of the system is required to size the inlet. This will be illustrated in an example later.

### 7.6.1.3 Ram Scoops

Ram scoops have good recovery, but they are rather inflexible. A ram scoop is another inlet and must be sized properly, otherwise it will spill and separate boundary layer ahead of it. Good recovery is obtained from it however, and flow area can be minimized using it.

With this type of inlet, a theoretical approach for analysis is available from Reference 8. The position of the scoop with respect to the boundary layer determines the maximum theoretical pressure recovery possible. A scoop in the boundary may be analyzed utilizing the curves shown in Figures 7-47 through 7-50 taken from Reference 7. The figures shown are for a boundary layer profile that follows the 1/7 power law  $u/U = (y/\delta)^{1/7}$ . This approximation will serve for most applications and will be within  $\pm 5\%$  accuracy.

Steps are outlined below in the design or evaluation of a boundary layer scoop. The boundary layer thickness must first be calculated. The equation commonly used for computing a turbulent boundary layer is:

$$\delta/x = 0.376/(R_{ex})^{0.2}$$

where  $R_{ex}$  = Surface Reynolds Number

The length of the body to the station is used for the length. This gives a boundary layer thicker than actual, but is sufficiently accurate for analysis of the inlet. Forebody shape and initial laminar flow would reduce the thickness, but these refinements are not necessary for this application. From the design conditions, the Mach number and scoop height are obtained. The scoop height to boundary layer thickness ratio is computed and Figures 7-47 through 7-50 are entered for boundary mass-flow-ratio, momentum ratio, and pressure recovery. For a boundary layer scoop of height equal to the boundary layer at a Mach = 2.0, the maximum theoretical mass that can be captured is 76% of what is available in an equal area in the free stream. The maximum recovery is 51.6% of free-stream total pressure. These are theoretical values based upon a 1/7 law velocity profile. Reference 9 is a test of a submerged and ram scoop inlet in a relatively thick boundary layer ( $r/\delta = 1.0$ ) (Figure 7-51). The recovery at Mach = 2. was 28% at the critical mass-flow-ratio, Figure 7-52. The maximum mass flow the inlet could pass was 52% of that available in the free-stream of the same area. The theoretical

values were computed for a  $1/7$  velocity profile boundary layer, however Reference 10 indicates that the profiles may vary from  $1/11$  to  $1/5$  and even be laminar without a discrepancy of more than 2% in total recovery.

The actual scoop performance is seen to be inferior to the theoretical. An approach to the design of boundary layer ram scoop would be, first, to determine the mass flow and recovery theoretically. Second, the recovery and mass-flow-ratio can be modified by ratios formed from the data of Figures 7-51 and 7-52. These ratios are shown in Figures 7-53 and 7-54 for  $r/\delta = 1$ . These data should be valid for scoop heights in the range of  $r/\delta = .8$  to 1.5. For scoops of smaller  $r/\delta$ , the data presented may be optimistic and wind tunnel data of the particular design should be obtained. The modified data represents the performance that can be expected from an actual boundary layer inlet.

## 7.7 Heat Exchanger Drag

Miscellaneous drag systems can each be viewed as miniature propulsion systems. Each has an inlet, diffuser, energy change and exit. The propulsion system increases the energy of the working fluid, the other systems reduce the energy. With a heat exchanger in the circuit, there is an addition of energy to the system in the form of heat and a pressure loss through the heat exchanger core. The net effect is a loss, but the off-setting effect of heat addition must be considered in the analysis.

### 7.7.1 Heat Exchanger Types

In general, the addition of heat to the working fluid is accomplished by extended surfaces of some nature. Most common heat exchanger designs are tubular and plate fin. The tubular heat exchanger provides less restriction on the cooling air side and allows higher cooling air flow than a plate fin heat exchanger. Where sufficient pressure drop is available, a plate fin heat exchanger is more effective because more heat transfer surface is provided.

Examples of heat exchanger use include oil coolers used on engine lubrication systems and primary and secondary heat exchangers for cabin and avionics conditioning systems. Most critical operating conditions for the heat exchanger are chosen for sizing the surface and ducting components. An air oil cooler for a turboprop power plant would be sized for ground operation at idle speed. For a supersonic aircraft other critical operating conditions exist. In maximum afterburning at high speed, fuel is used for a heat sink. For overload conditions, an auxiliary air oil cooler must be used. The cooling medium, however,

ic at high temperature and the heat exchange surfaces tend to get large in order to reject the heat. For a hot day sea level loiter, the pressure head available for cooling is small and the cooling air temperature high. This problem is sometimes solved by utilizing a jet ejector pump to aspirate air through the heat exchanger core. There are many examples of heat exchanger use. The losses are generally charged against the propulsion system.

#### 7.7.2 Heat Exchanger Drag Estimation

The drag of the heat exchanger system must include the loss characteristics of all the components. For heat exchangers curves of the type shown in Figures 7-55 and 7-56 are necessary. Usually the cabin or avionics heat rejection is known. The effectiveness curves (Figure 7-55) are entered and a heat balance struck between the two fluids. The average temperature and pressure in the core determine the pressure loss through the heat exchanger (Figure 7-56).

An example of the use of the curves is shown below:

Altitude = 50,000 feet      Hot Day  
 Bleed Air Temperature = 1370°R  
 Bleed Air Pressure = 80 PSIA  
 Ambient Air Temperature = 421°R (-39°F)  
 Ram Air Temperature = 710°R (250°F)

Heat exchanger cooling air

Inlet total pressure = 9.9 PSIA (20.2" Hg)  
 Outlet static pressure = 2.5 PSIA  
 Distance to inlet from lip = 100 inches  
 Duct Mach No. = .55  
 Inlet Dimensions = 3 inch deep x 8 in wide  
 Duct Reynolds No. =  $10^5$

The heat exchanger inlet is a slot in the duct at an angle of 15° from the duct surface. From Figures 7-33 obtain the total pressure recovery (.92). Calculate the boundary layer thickness from

$$\delta/x = \frac{.376}{(R_{ex})^{0.2}} ; \text{ so that } \delta = 100 \left[ \frac{.376}{(10^5)^{0.2}} \right] = 3.76$$

and  $r/\delta = .8$ . The  $r/\delta$  for Figure 7-33 are on the order of 1.4. This total pressure recovery must be modified by the data of Figure 7-50.

So that

$$\left[ P_{t2}/P_{t0} \right]_{\text{modified}} = \left[ \left( P_{t2}/P_{t0} \right) \left( \text{from Figure 7-33} \right) \left( \frac{P_{t2}}{P_{t0}} \right)_{r/\delta=.8} \right] /$$

$$\left( \frac{P_{t2}}{P_{t0}} \right)_{r/\delta=1.4}; \text{ where } P_{t2}/P_{t0} = \frac{.92(.95)}{.97} = .90$$

The mass flow is taken to be critical and is modified in a similar calculation to that for pressure recovery using Figure 7-47.

$$m/m_i = (m/m_o)_{\text{Figure 7-33}} (m/m_o) / (m/m_o)_{r/\delta=1.4} = \frac{1.02 (.845)}{.895} = .96$$

where  $m$  - mass flow  
 $o$  - free stream conditions  
 $i$  - inlet conditions

A curve of pressure drop through the heat exchanger is now devised. Assume that the engine bleed flow is known to be 40#/min. Set up the following table:

$W_{\text{bleed}}$ #/Min	$W_{\text{cooling}}$ #/Min	$\epsilon$	$t_{\text{Bleed}}$ in	$t_{\text{cool}}$ in	$\Delta t$	$Q$	$\Delta t_{\text{Bleed}}$	$t_{\text{bleed}}$ out	$\Delta t_{\text{cooling}}$
40	40	.77	1370°R	710°R	660°F	2032	211 F	1160°R	211°F
40	60	.875	1370°R	710°R	660°F	2310	240	1130	160
40	80	.93	1370°R	710°R	660°F	2455	255	1115	128
40	100	.96	1370°R	710°R	660°F	2534	264	1106	106
40	120	.975	1370°R	710°R	660°F	2574	268	1102	89

$W_{\text{cooling}}$	$t_{\text{cool}}$	$t_{\text{avg}}$	$\sigma \Delta P$	$\Delta P$ ("Hg)
40	920°R	815°R	3"H <sub>2</sub> O	.5 "Hg
60	870	790	7	1.24
80	838	774	13	2.2
100	816	763	20	3.5
120	799	755	28	5.1



The following equations were utilized in the calculations above.

$$Q = (W C_p) (\text{smallest } c) (t_1 \text{ in} - t_2 \text{ in})$$

$$c = 17.35 \frac{P_{\text{avg}}}{T_{\text{avg}}} \quad \begin{matrix} (P \text{ in "Hg}) \\ (T \text{ in } ^\circ\text{R}) \end{matrix}$$

$$\Delta P = (c \Delta P) \frac{T_{\text{avg}}}{17.35 P_{\text{avg}}} = \frac{c \Delta P T_{\text{avg}}}{(17.35) (P_{\text{in}} - \frac{\Delta P}{2})(13.6)}$$

$$c = \text{effectiveness} = \frac{\text{actual heat transfer}}{\text{maximum possible heat transfer}}$$

The actual heat transfer may be computed by calculating the energy lost by the hot fluid or the energy gained by the cold fluid. The fluid that undergoes the most temperature change has a minimum value of  $(W C_p)$  and is the one used to compute the heat transferred. This is evident since the heat absorbed by one fluid must equal the heat rejected by the other.

The results of the above Table are plotted on Figure 7-57. A short cut to the above method would be to compute only one of the points, plot it on log-log paper and construct a line with slope = 2. This will produce the typical loss curve shown. The pressure is known at the inlet and suppose there is a diffuser of  $A_2/A_1$  of 2 immediately aft of the flush inlet. Having determined the total pressure recovery and mass flow at the inlet station, a corrected weight flow is now computed at that point assuming the maximum mass flow.

Following is an iterative method of matching the air flow through the system chosen for this example.

$$\text{For } M_1 = .55; \text{ the corrected airflow parameter } \frac{W_0 \sqrt{\sigma_{t0}}}{\sigma_{t0} A_1} = .2735$$

$$A_1 = 24 \text{ in}^2$$

$$\sigma_t = 9.9/14.7 = .673$$

$$\sqrt{\sigma_{t0}} = \sqrt{710/579} = 1.17$$

$$W_0 = \frac{.2735 \times 24 \times .673}{1.17} = 3.77 \text{ \#/sec.}$$

$$m/m_0 = .96 \text{ (Figure 7-47)}$$

$$m_{act} = .96 \times 3.77 = 3.62 = W_1 = 218 \text{ lb/min}$$

$$P_{t1}/P_{t0} = 0.9$$

$$P_{t1} = (.9)(9.9) = 8.9 \text{ psi} \quad \delta_{t1} = 8.9/14.7 = .605$$

$$\frac{W_1 \sqrt{\theta_{t1}}}{\delta_{t1} A_1} = \frac{(3.62)(1.17)}{(.605)(24)} = .292$$

$$M_1 = .611, P_{t1} = 1.286, P_1 = 8.9/1.286 = 6.92 \text{ psi}$$

$$q_1 = .7 \text{ PM}^2 = (.17)(6.92)(.611)^2 = 1.81 \text{ psi}$$

The next step is to determine the losses in the diffuser. The configuration looks like a 60° transition bend and a loss coefficient may be determined from data presented in Reference (11).

A  $\Delta P_t/q = 0.8$  is calculated

$$P_t = (1.81)(0.8) = 1.45$$

$$P_{t_{in}} = 8.9 - 1.45 = 7.45 \text{ psi}$$

$$T_{in} = 7.45/14.7 = .506$$

$$\frac{W_{in} \sqrt{\theta_{t_{in}}}}{\delta_{in} A} = \frac{(3.62)(1.17)}{(.506)(48)}$$

$$M_{in} = .312, P_{T_{in}}/P_{in} = 1.07$$

$$P_{in} = 6.96$$

From Figure 7-57 at 218 lb/min airflow, a  $P_s$  of 18" Hg. is read.

$$P = 8.84 \text{ psi}$$

$$P_{s_{out}} = 6.98 - 8.84 = -2 \text{ psi}$$

This does not match the exit condition of 2.5 psi. It means the initial estimate of maximum airflow is not correct. The mass flow is now reduced and the above procedure repeated until the mass flow selected produces a pressure that matches the exit conditions.

The exit momentum is now determined. The exit is a  $15^\circ$  slot. From Figure 7-57 a velocity coefficient and flow coefficient are found. Knowing the mass flowing through the system determining the total pressure at the exit, and having the exit area and temperature, the exit mass flow parameter is found. This is matched against the data of Section 7.5.

A better approach to this inlet, heat exchanger, exit matching problem is to begin with a number of flows through the system solving for the losses and an exit area. By plotting the cooling flows against the exit area, one is able to enter the curve with the known exit area and find the cooling airflow. The exit momentum is found from the figures of Section 7.5.

This term is recovered momentum that is added to the thrust of the aircraft. A series of these recovery values for a typical mission are found and plotted against Mach number. This generalization is then used for other portions of the envelope.

#### 7.8 Auxiliary Cooling Drag

The devices included in this section are those that have no published loss curves readily available from a manufacturer. Additional cooling scoops such as those required for cooling generators or compartments add very little energy to the exiting stream. Usually the losses associated with these auxiliary openings are small compared with the net propulsive effort. The conventional method of estimating the losses is to assume a total momentum loss from the free stream condition to the exit. For example, the T-2B has a lateral firewall across the engine bay that separates the compressor from the burner compartment. Air for cooling the burner area is introduced to the bay with ram scoops that extend out into the free stream. The losses are calculated to be the total momentum of the entering stream ( $\frac{W}{g} V_0$ ). Air flow ( $W$ ) is calculated from the air flow

parameter ( $W_0 \sqrt{\theta} / (\delta/A)$ ), the airplane free stream conditions and the physical area of the scoop. The losses are higher than actual, but corrections would unduly complicate the procedure. For generator cooling, a similar calculation to that outlined in the heat exchanger section will have to be followed to check for adequate generator cooling. However, for the drag estimation, the total inlet momentum is considered lost.

#### 7.9 Boundary Layer Bleed Drag

Boundary layer that has accumulated on inlet surfaces must be removed to provide optimum pressure recovery for maximum thrust and maximum inlet

stability. Three methods of removing the boundary layer are commonly used. The perforated plate, flush scoop, and ram scoop. Each of these inlet types have been discussed previously. A means of estimating the pressure recovery and mass flow has been devised. Minimizing the losses through the system is the main problem. The A-5A originally had porous-ramps to remove the boundary layer growth along the inlet surfaces. Several problems arose. The holes were difficult to drill because each was centered in the middle of a honeycomb backup structure. The holes could not be protectively coated after machining and corroded after service use. The cost was high. The first moveable ramp had a porosity of about 10%. Typical bleed rates are shown on Figure 7-58. The effect upon recovery is shown on Figure 7-59. The flow emptied into a chamber behind the ramp and was compartmentized from the other bleed areas. The flow exited through a 15° flush exit. The boundary layer bleed drag is the momentum change of the bleed air through the system. The incoming momentum was accounted for in the inlet ram drag by increasing the airflow by the bleed percentage.

$$F_{ram} = \frac{W_e}{g} V_o \left[ 1 + \frac{W_{BLEED}}{W_e} + \frac{W_{HX}}{W_e} + \frac{W_{BYPASS}}{W_e} \right]$$

To analyze the boundary layer bleed system an item by item loss analysis determines the pressure drop to the exit. Since the mass is known a corrected weight flow parameter may be computed. From the pressure ratio at the exit, flow and velocity coefficients may be determined and the exit momentum calculated. The recovered momentum in the flight direction is added to the aircraft thrust.

The problems mentioned before for the perforated ramps forced the substitution of slotted ramps for the perforations on the RA-5C. Both boundary layer bleed systems have performed well, however, the slotted ramps are easier to manufacture. An example of the method analysis for the boundary bleed drag follows. Assume a flight condition such as Mach 1.8, 35,000 feet, and standard atmosphere. Fixed first ramp is 8.5° second movable ramp is at 14°. Second ramp Mach number is approximately 1.3. The slot is 50 inches behind the leading edge. The boundary layer is calculated to be .50 inches. The throat height for the slot is 1.0 inch and  $r/\delta$  is therefore 2.0. The slot is at an angle of about 30°. From the curves on Figure 7-35, one obtains the total pressure recovery. The recovery is modified by the recovery values of Figure 7-50. The recovery is  $.44 \times .87 + .83 = .46$ . The mass flow ratio is .43 and must be modified by the  $r/\delta$  ratios for the different boundary layers ( $m/m_o = .448$ ).

The free stream corrected airflow is modified by the recovery and mass flow factors.

$$\text{Since } \left( \frac{W_o \sqrt{\theta_{T_o}}}{\delta_{T_o} A_1} \right) \left( \frac{P_{T_1}}{P_{T_o}} \right)_{\text{corrected}} \left( \frac{m}{\dot{m}_o} \right)_{\text{corrected}} = \frac{W_1 \sqrt{\theta_{T_1}}}{\delta_{T_1} A_1}$$

$$\text{so that } \frac{W_1 \sqrt{\theta_{T_1}}}{\delta_{T_1} A_1} = \frac{(.322)(.448)}{(.46)} = .314$$

$$\text{Given } A_1 = 20 \text{ in}^2, \quad \sqrt{\theta_{T_1}} = 1.12 \quad \delta_{T_1} = .62$$

$$\text{then } W = \frac{W \sqrt{\theta_{T_1}}}{\delta_{T_1} A_1} \left( \frac{A_1 \delta_{T_1}}{\sqrt{\theta_{T_1}}} \right) = 3.46 \text{ lbs/sec}$$

and from isentropic tables the slot entrance Mach number is found to be:

$$M_L = .702$$

Determine  $q_L$ :

$$q_L = \frac{\gamma}{2} P_{\text{static}} M_L^2 = .7(6.46)(.702)^2 = 2.23 \text{ lb/in}^2$$

The dumping loss from reference (11) is computed assuming total loss of  $q$ .

$$\frac{\Delta P}{q} = 1.0 \text{ so } \Delta P = 2.23 = 6.74 \text{ lbs/in}^2$$

so that bleed air total pressure is:

$$P_{T_2} = P_{T_0} \left( \frac{P_{T_1}}{P_{T_0}} \right) - \Delta P = 8.97 - 2.23 = 6.74 \text{ lbs/in}^2$$

The internal total to exit static pressure ratio is formed again and the flow coefficient determined. The air flow that the exit can pass is determined from the figures in Section 7.5 on exits. For a  $15^\circ$  exit angle Figure 7-57 is used. The flow coefficient is .93 and the maximum flow (choked conditions) that can pass is 2.6. The exit flow is less than was assumed for the inlet conditions. The inlet flow now must be modified and the process repeated until the exit flow matches that assumed for the inlet.

## 7.10 Boundary Layer Diverter

### 7.10.1 Sizing Considerations

In the final design phases of a configuration study, the boundary layer thickness must be determined and the boundary layer diverter sized. The results of a study (Reference 12), have yielded an accurate means of determining the boundary layer thickness on bodies of revolution. The pertinent equations are shown below.

$$\delta^* = .0475 \frac{(1+.35Mo^2)}{(1+.176Mo^2)} .44 \frac{\bar{S}_t}{(Re_t)^{0.2}}$$

Where  $S_t$  = equivalent flat plate distance from origin of the turbulent flow to the point in question.

$$Re_{ot} = \left( \frac{\rho V}{\mu} \right)_o \bar{S}_t$$

Rearranging the equation above

$$\delta^* = \phi_1(M) \frac{\bar{S}_t^{0.8}}{\left( \frac{\rho V}{\mu} \right)_o^{0.2}} ; \quad \delta = \delta^* \frac{\delta}{\delta^*} = \phi_1(M) \frac{\bar{S}_t^{0.8}}{\left( \frac{\rho V}{\mu} \right)_o^{0.2}}$$

where  $\delta/\delta^*$  is shown on Figure 7-62

$\phi_1(M)$  is shown on Figure 7-63

$(\rho V/\mu)_o$  is shown on Figure 7-64

$\bar{S}_t$  is determined from Figure 7-65

The distance  $S_t$  is determined by finding the transition point surface location  $S_{tr}$  and subtracting this from the total surface length  $S$  to the point in question, then  $S_t = S - S_{tr}$  and  $S_{tr} = Re_{tr}/(\rho V/\mu)_o$ . The transition Reynolds number ( $Re_{tr}$ ) is shown in Figure 7-65. When  $S_t$  is calculated, it must be modified to reduce  $S_t$  to its equivalent flat plate distance  $S_t$ . This modifier accounts for the thinning out of the boundary layer on forebodies where the cross sectional area is increasing in the downstream direction. The forebody may be divided into about 2 cone frustrums and the equivalent flat plate surface length determined from Figure 7-65.

An approximate method that yields a conservative boundary layer thickness is to assume complete turbulent flow from the nose of the forebody to the inlet and considers it a flat plate. The common expression

$$\delta/x = 0.2 \cdot .376/(Re)$$

yields the boundary layer thickness. It has been industry practice to remove 70% of the boundary layer determined by the above expression by a boundary diverter. With the more exact expression, it is recommended that all the boundary layer be removed.

Other design parameters that influence the diverter drag are the wetted area of the system, the deflection angles in the diverter and the divergence angle of the passage. Design criteria for diverter systems is found in Reference 16). In brief, the leading edge of the boundary plate should be swept back, when this is consistent with the inlet shock configuration, and the diverter apex should be at least one diverter height back of the boundary plate apex. To reduce the pressure and friction drag and to minimize the deflection angles (and lateral velocity), the included angle of the diverter wedge should be  $20^\circ$  or less. To prevent vortex formation in the diverter channel, the corners should have generous radii. The passage height must diverge both longitudinally and laterally to minimize flow resistance and prevent choking.

#### 7.10.2 Drag Estimation

The diverter system drag may be divided into two parts (1) the pressure drag of the wedge and (2) the skin friction drag from the system consisting of portions of the wedge, splitter plate, and body. The method presented here yields the total drag on the diverter, and the additional wetter surfaces within the shadow of the splitter plate. Figure 7-60 defines the total wetted area  $A_w$  for a typical boundary layer diverter system. Pressure drag is in parametric form in Figures 7-66 through 7-68. Skin friction drag is calculated from Figures 7-69 through 7-70. Figure 7-71 is a comparison of experimental results and the method outlined. Although the data presented is shown for a diverter apex indentation of zero, the drag estimation technique may be applied to indentation distances of  $2\delta$ .

The area considered for the skin friction calculations include the sides of the diverter wedge, the wetted underside of the splitter plate from the lip to the diverter base, and the wetted surface of the main body that lies in the shadow of the diverter. Figure 7-60 calculates the wetted area of a system with a rectangular splitter plate.

Skin friction depends upon Reynolds number as well as Mach number. Reynolds numbers may be obtained from Figure 7-64 by multiplying the distance to the inlet. Friction coefficients are obtained from Figure 7-69. Figure 7-70 shows the correlation of some experimental data used in the presented method.

The following procedure is recommended: (1) Given:  $M_0$ , Altitude, diverter geometry, boundary layer thickness. (2) Calculate parameters needed for Figures 7-66 to 7-68. These parameters are Mach number, Reynolds number,  $\theta$ ,  $h/\delta$ ,  $d/\delta$ ,  $A_{wetted}$ ,  $A_{projected}$ . Use free stream Mach number, and Reynolds number based on surface distance to the inlet. (3) Calculate  $C_{DP}$  from Figures 7-66 through 7-68. This coefficient is based on projected frontal area. (4) Calculate  $C_{DF}$  from Figures 7-70 and 7-71.

$$C_{DF} \text{ (Based on } A_w) = (C_{fw}) \frac{C_{DF}}{C_{fw}}$$

$$C_{DF} \text{ (Projected Area)} = C_{DF} \text{ (wetted area, } A_w) \left( \frac{A_w}{A_{projected}} \right)$$

(5) Calculate total drag coefficient based on projected area.

$$C_{Dt} = C_{DP} + C_{DF} \text{ (Project Area)}$$

#### 7.11 Bypass Door Drag

Bypass door drag is calculated in a manner similar to the heat exchanger and boundary layer bleed drag. There is an additional item of drag that must be considered and that is the pressure drag on the door that is exposed to the free-stream. Some designs may not expose the door to the free-stream and the drag would not be present. A conservative estimate is to assume a drag coefficient of 1.17 based upon projected frontal area.

#### 7.12 Miscellaneous Drags

##### 7.12.1 Screen Drag

Occasionally, openings must be screened to prevent foreign object ingestion by engines. Much data are available for determining losses and loads. Figure 7-72 shows a curve that may be used to determine the pressure drop through such a screen and the drag of the screen based upon the free area ratio and the approaching Mach numbers.



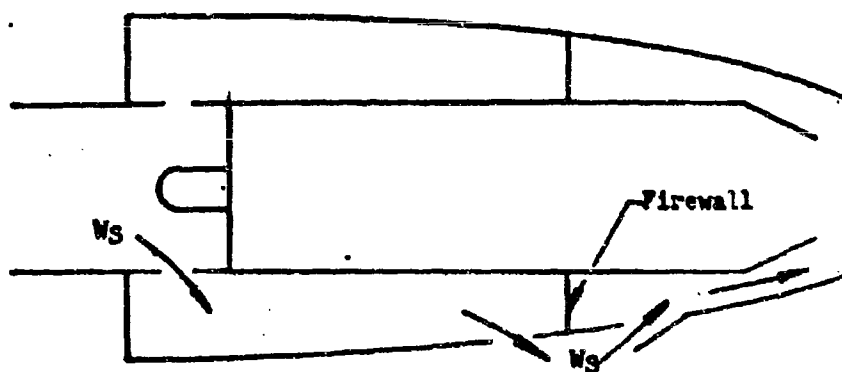
7.13 Internal Ducting Losses

Pressure losses incurred by ducting the air internal through the aircraft are fully discussed in Section 2.6 which contains information on inlet duct pressure losses.

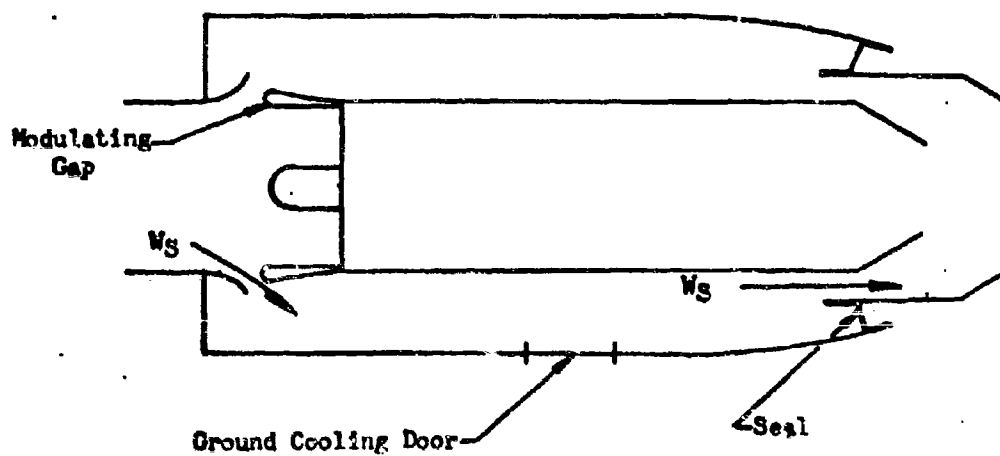
## References

1. Dewey, Paul E., A Preliminary Investigation of Aerodynamic Characteristics of Small Inclined Air Outlets at Transonic Mach Numbers, NACA Report No. TN 3442, May, 1955.
2. Vick, Allen R., An Investigation of Discharge and Thrust Characteristics of Flapped Outlets for Stream Mach Numbers from 0.40 to 1.30, NACA Report No. 4007, July, 1957.
3. Abdalla, Kaleel L., Performance Characteristics of Flush and Shielded Auxiliary Exits at Mach Numbers of 1.5 to 2.0, NACA Memo 3-18-59 E, June, 1959.
4. McLafferty, G. H., Krasnoff, E. L., Ranard, F. D., Rose, W. G., Vergara, R. D., Investigation of Turbojet Inlet Design Parameters, United Aircraft Corporation Research Department Report No. R-0790-13, December, 1955.
5. Schrello, D. M., A Method for Estimating the Flow Characteristics of Permeable Material Suitable for Boundary Layer Control Applications, NA58H-354, July, 1958.
6. Pennard, John S., The Total Pressure Recovery and Drag Characteristics of Several Auxiliary Inlets at Transonic Speeds, NACA Memo, December, 1958.
7. Pennard, John S., A Transonic Investigation of the Mass Flow and Pressure Recovery Characteristics of Several Types of Auxiliary Air Inlets, NACA RML57B07.
8. Simon and Kowalski, Charts of Boundary Layer Mass Flow and Momentum for Inlet Performance Analysis Mach Number Range, 0.2 to 5.0, NACA TN 3583.
9. Pennington and Simon, Internal Performance at Mach Numbers to 2.0 of Two Auxiliary Inlets Immersed in Fuselage Boundary Layer, NACA RM E53L28b.
10. McLafferty, George, The Theoretical Pressure Recovery Through a Normal Shock in a Duct with Initial Boundary Layer, Journal of Aeronautical Sciences, March, 1953.
11. GAT Aero Space Applied Thermodynamics Manual.
12. Hessman, F., Drag of Boundary Layer Diverter Systems at Supersonic Speeds, NA64H-913.

13. Donnenberg, Gambucci, and Weiberg, Perforated Sheets as a Porous Material for Distributed Suction and Injection, NACA TN 3669, April, 1956.
14. Donnenberg, Weiberg, and Gambucci, The Resistance to Air Flow of Porous Materials Suitable for Boundary Layer Control Applications Using Area NACA TN 3094, January, 1954.
15. Yates, L. C., On the Permeability of Porous Materials, NACA TN 3596, January, 1956.
16. Davis and Scherrer, Aerodynamic Principles for the Design of Jet Engine Induction Systems, NACA RM A55F16, February, 1956.



1A T2B Cooling Configuration



1B RA-5C Cooling Configuration

FIGURE 7-1. Typical Engine Compartment Cooling Configuration

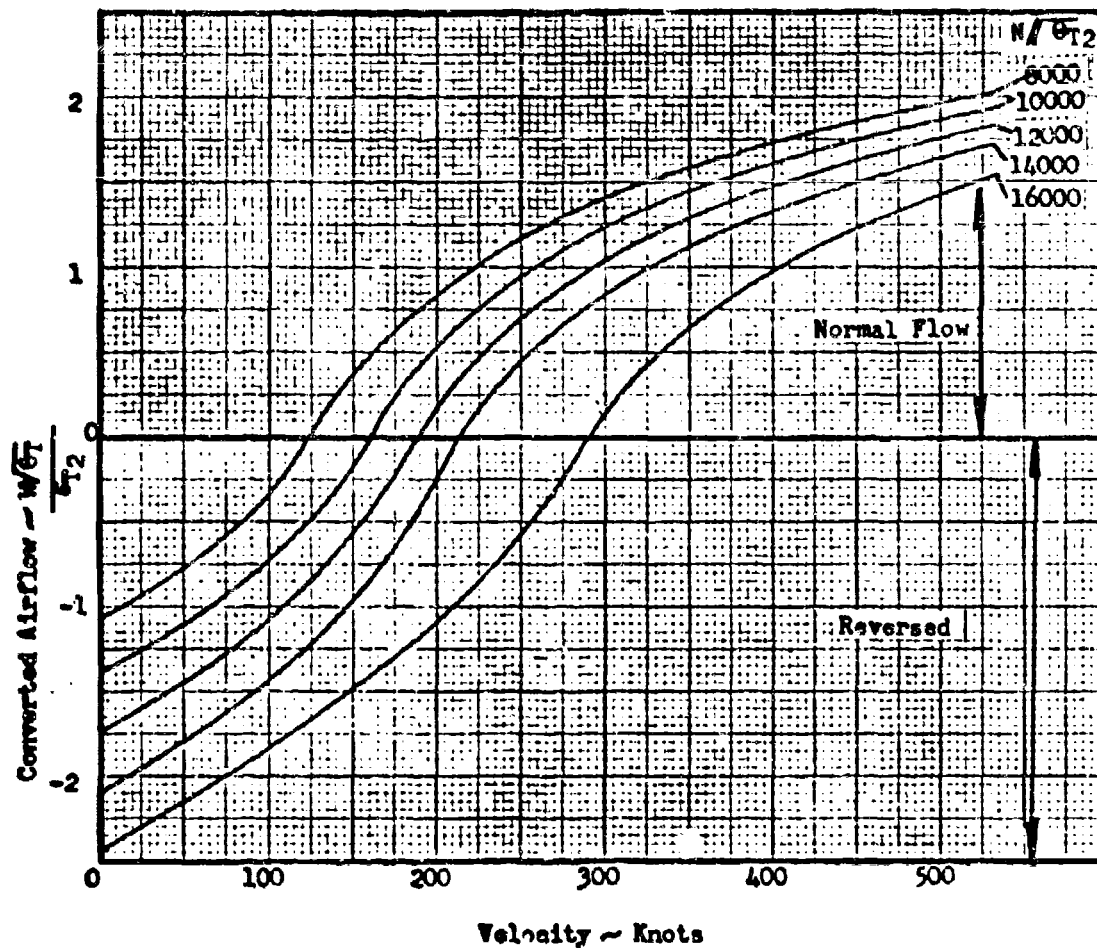


FIGURE 7-2. Estimated T2B Forward Engine Compartment Secondary Airflow

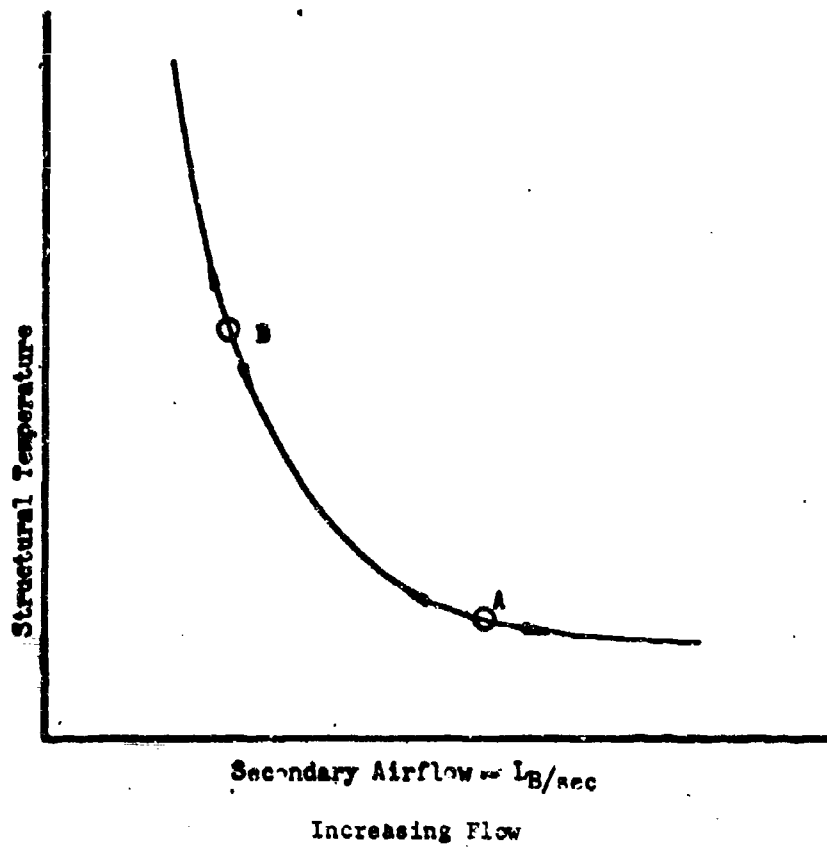


FIGURE 7-3. Structural Temperature Variation with Secondary Airflow

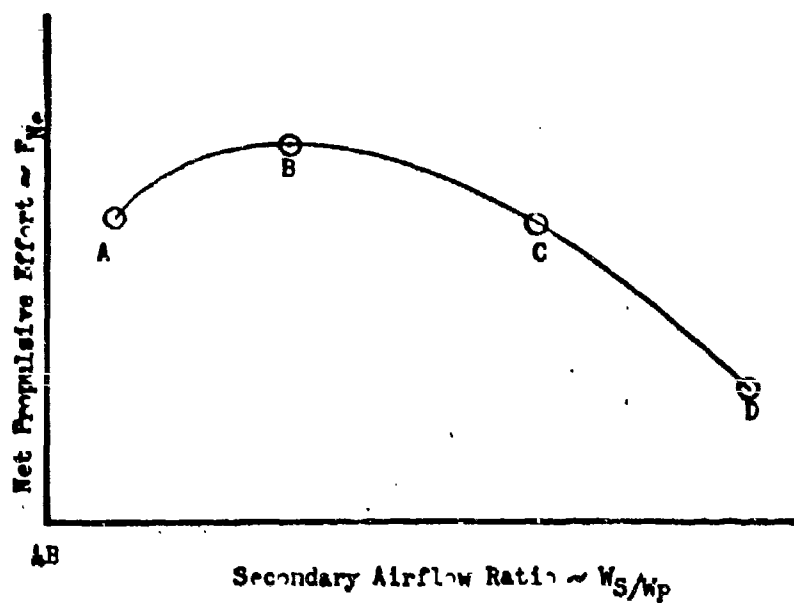
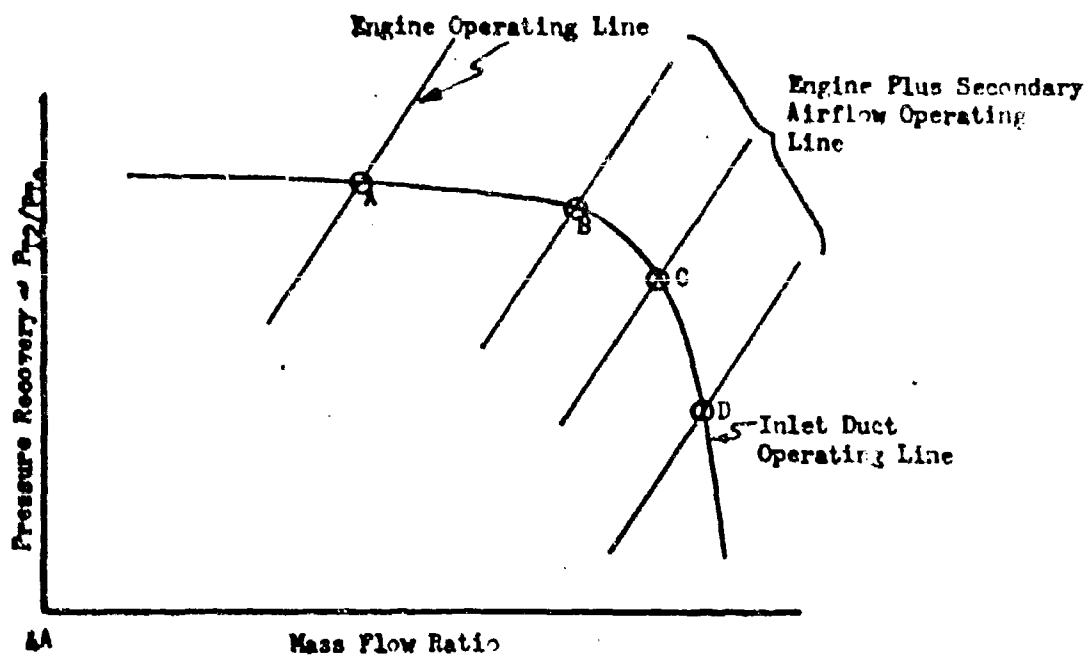


FIGURE 7-4. Inlet Optimisation

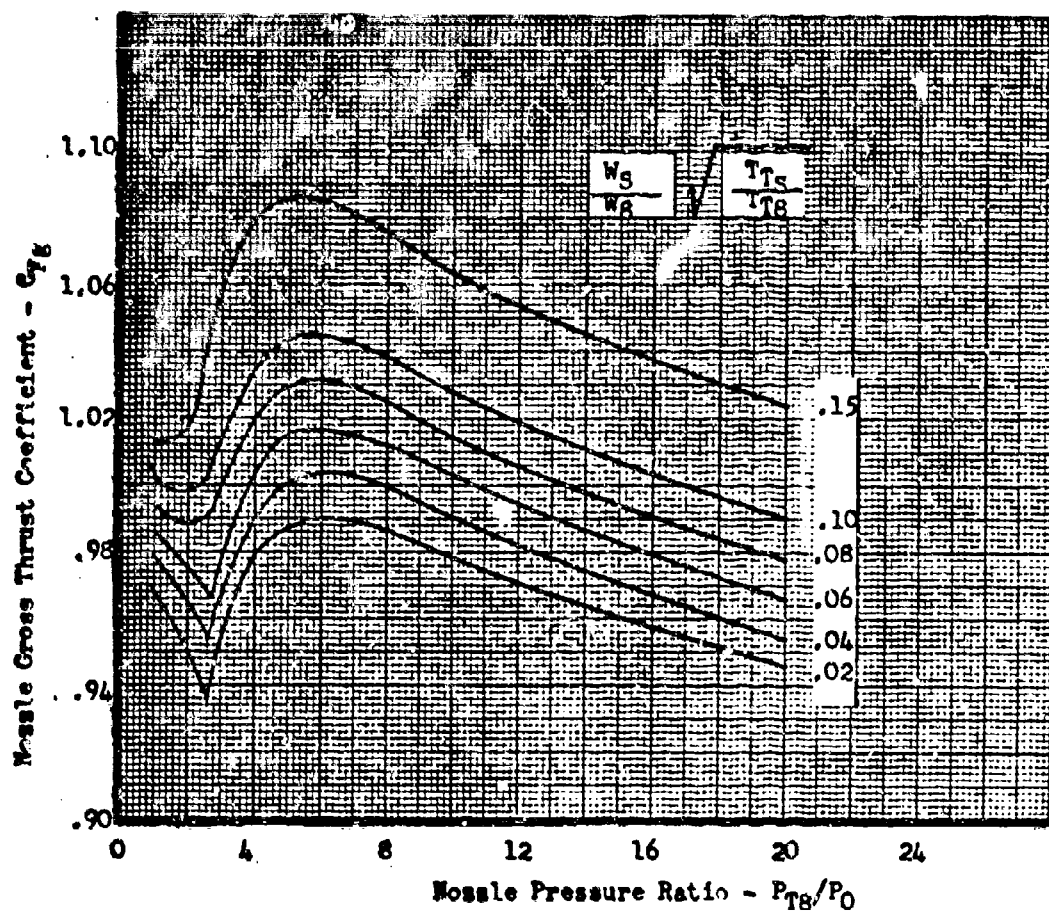


FIGURE 7-5. Typical Plot of Nozzle Gross Thrust Coefficient





6A Conical Ejector



6B Guided Expansion Ejector

FIGURE 7-6. Sketch of Ejector Configurations

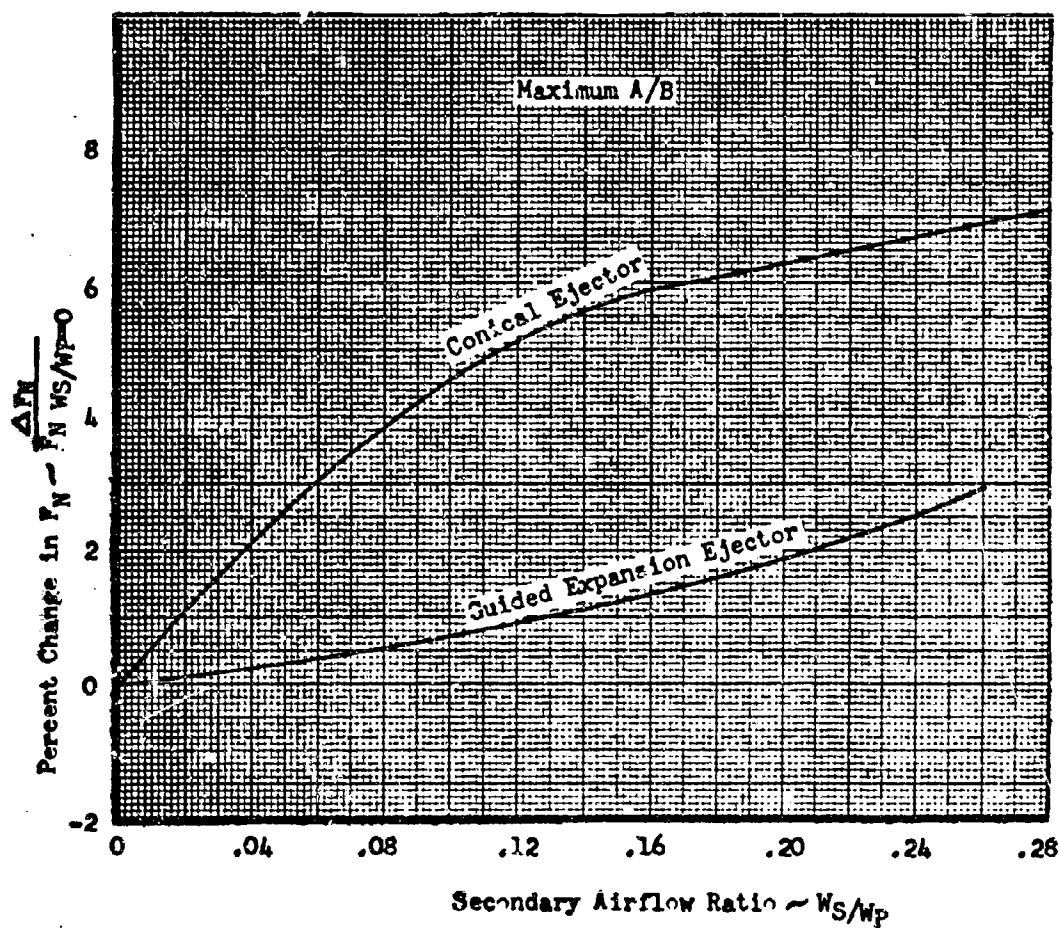


FIGURE 7-7. Effect of Secondary Airflow on Ejector Performance  
 -  $M_0 = 0.9$ , 35000 Ft.

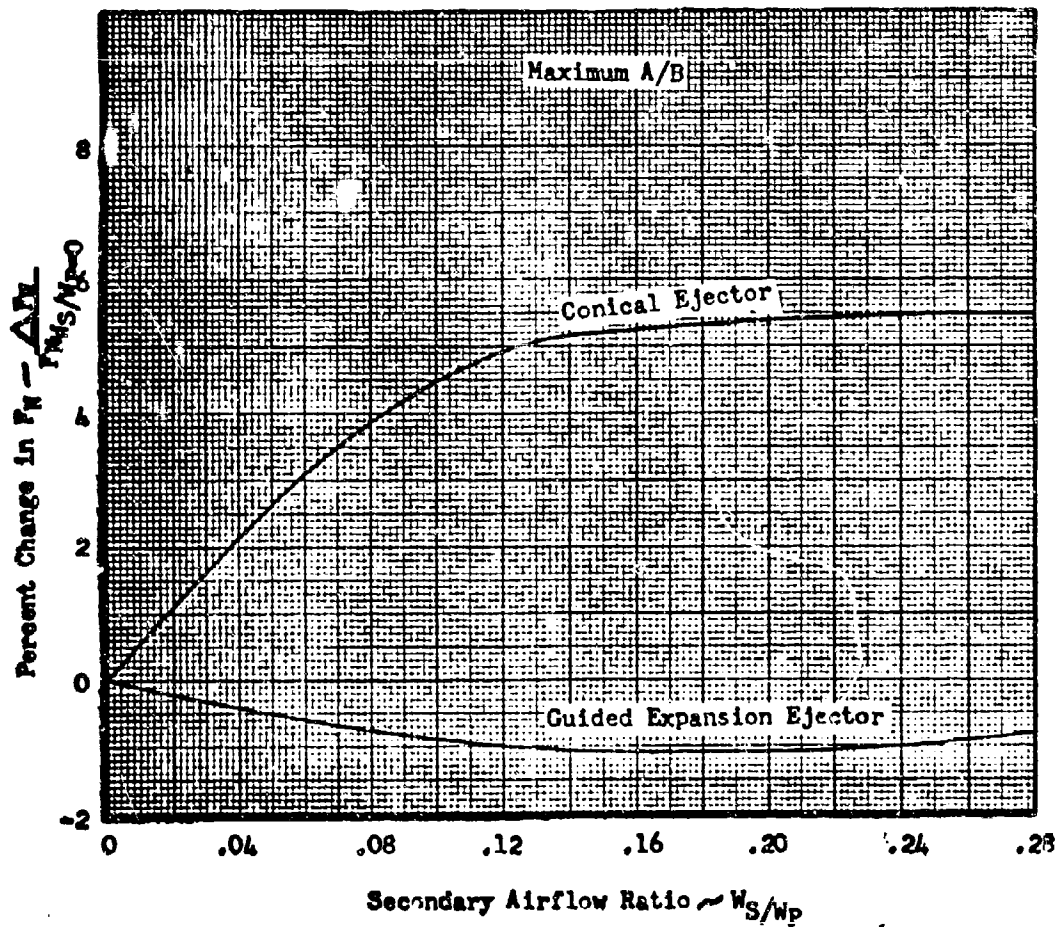


FIGURE 7-8. Effect of Secondary Airflow on Ejector Performance  
 -  $M_p = 1.6$ , 35000 Ft.

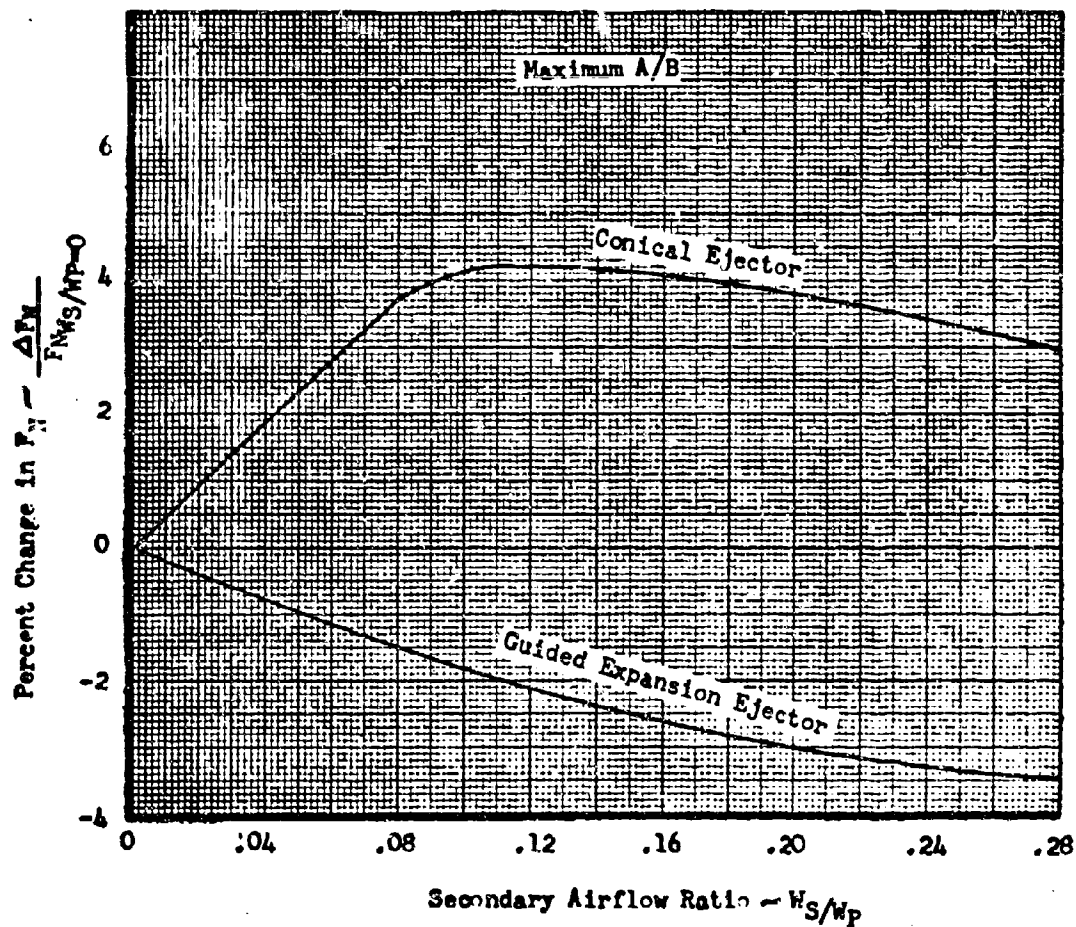


FIGURE 7-9. Effect of Secondary Airflow on Ejector Performance  
 -  $M_0 = 2.0$ , 35000 Ft.

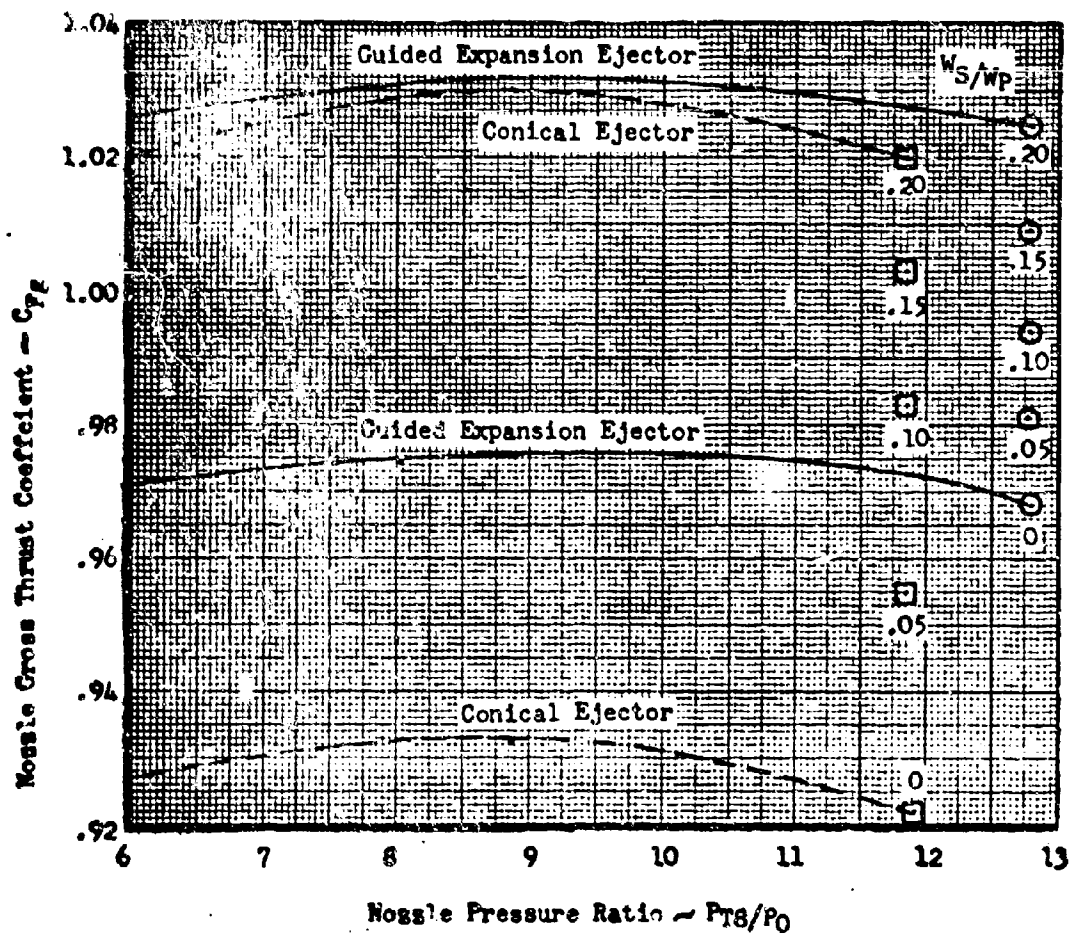


FIGURE 7-10. Comparison of Nozzle Gross Thrust Coefficients

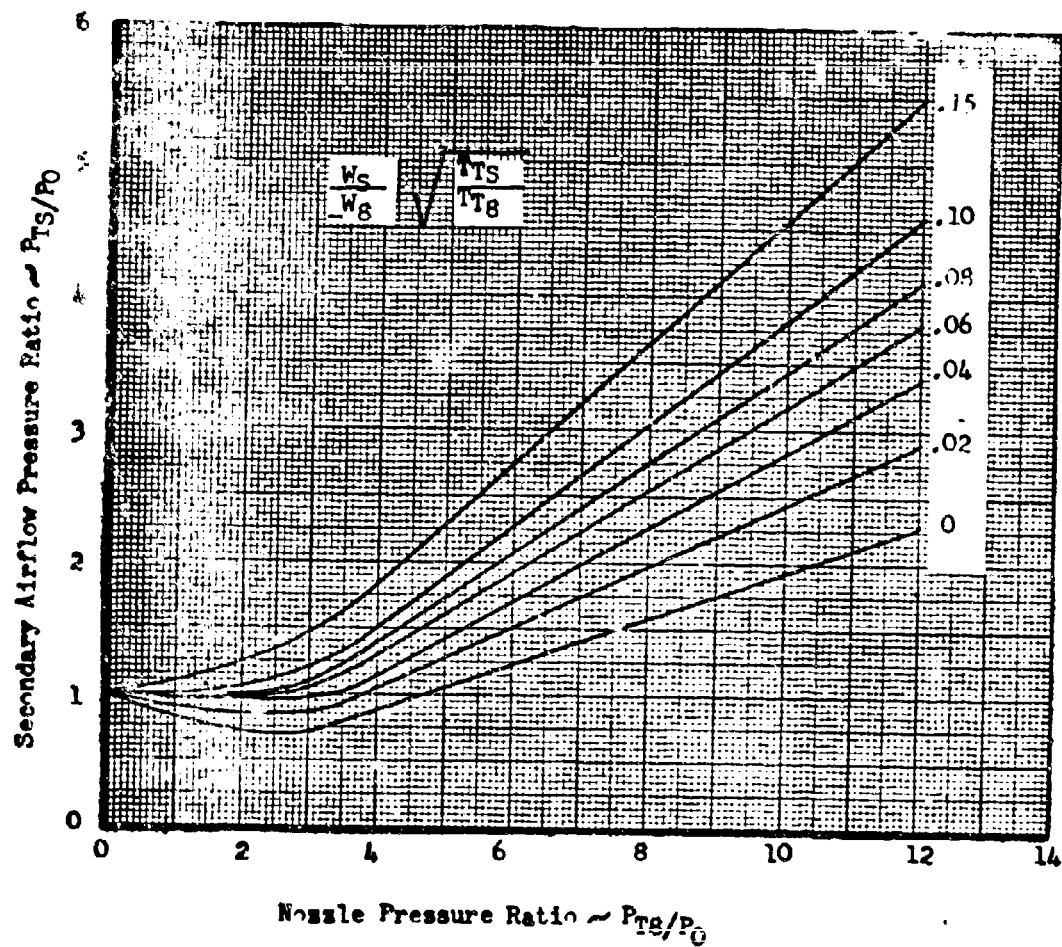


FIGURE 7-11. Nozzle Pumping Characteristics

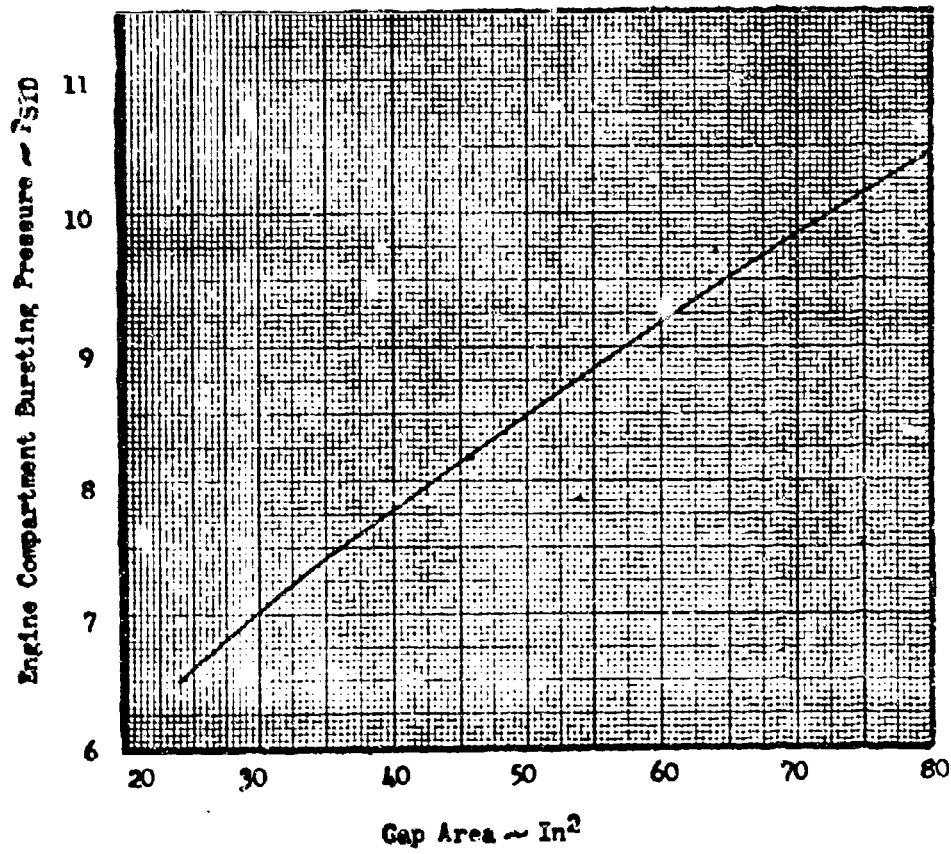


FIGURE 7-12. Engine Compartment Pressure at Mach No. = 2.0

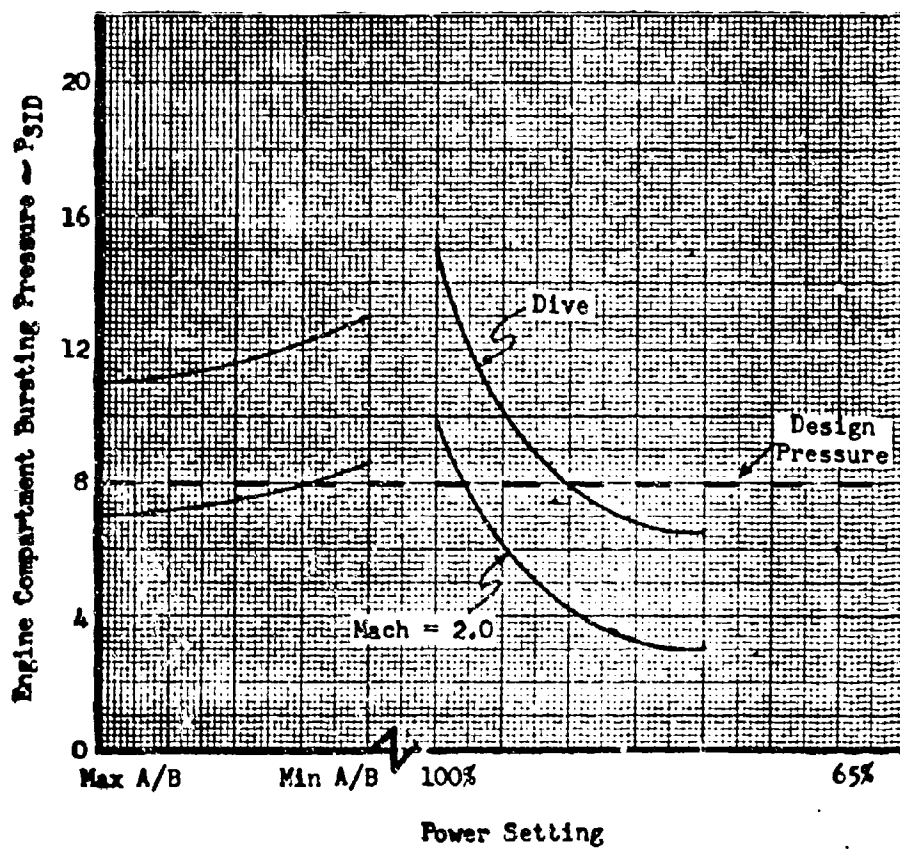


FIGURE 7-13. Engine Compartment Bursting Pressure Versus Power Setting



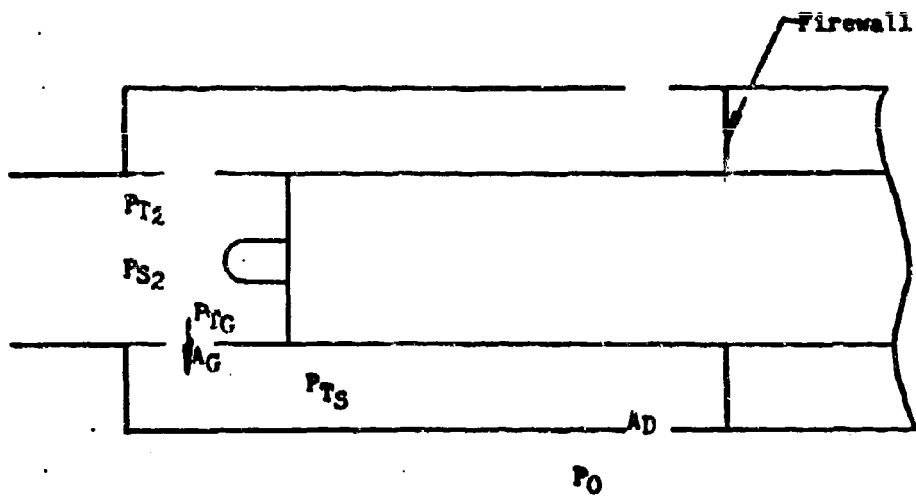


FIGURE 7-14. Sketch of Cooling Configuration

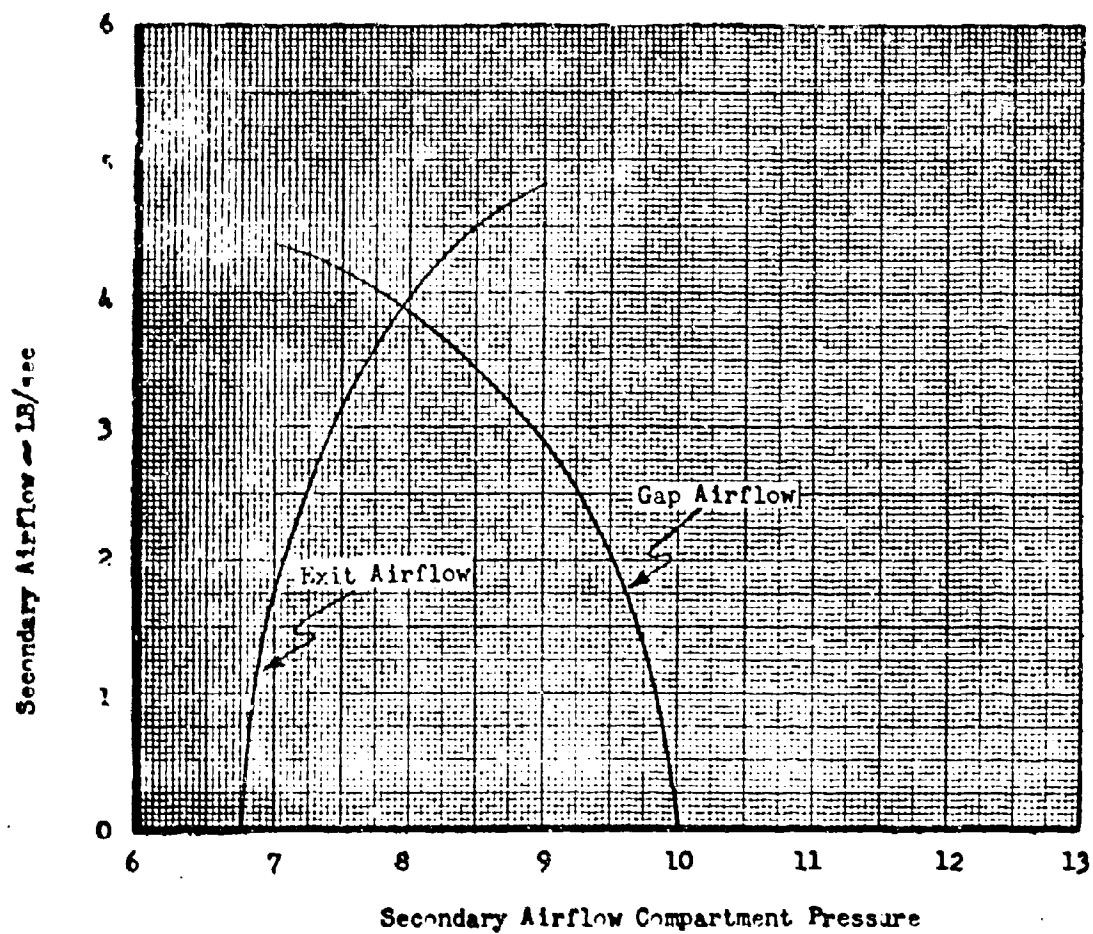


FIGURE 7-15. Secondary Airflow Matching

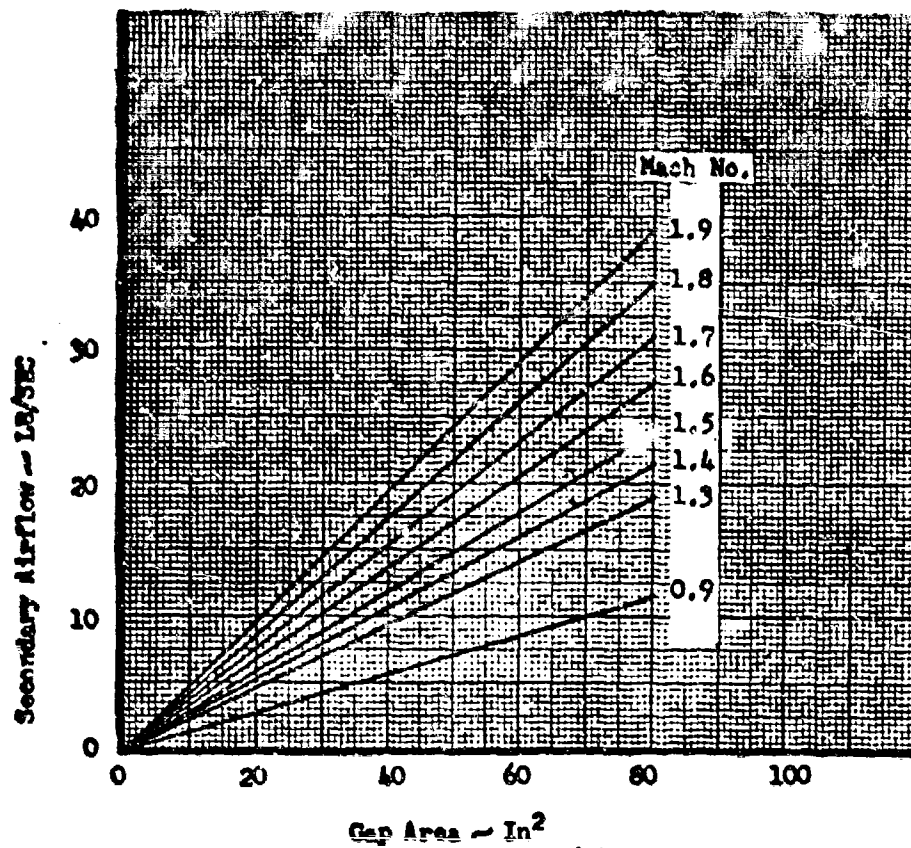


FIGURE 7-16. Secondary Airflows Versus Gap Area

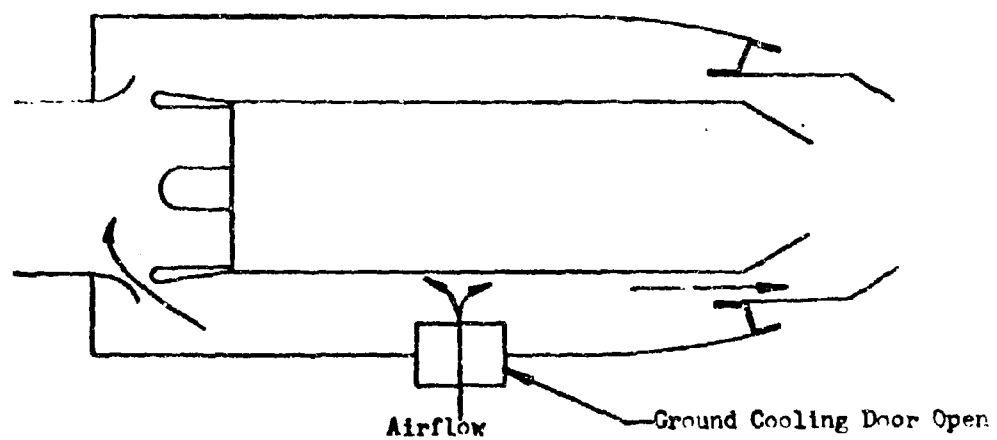


FIGURE 7-17. Sketch of RA-5C Ground Cooling Configuration

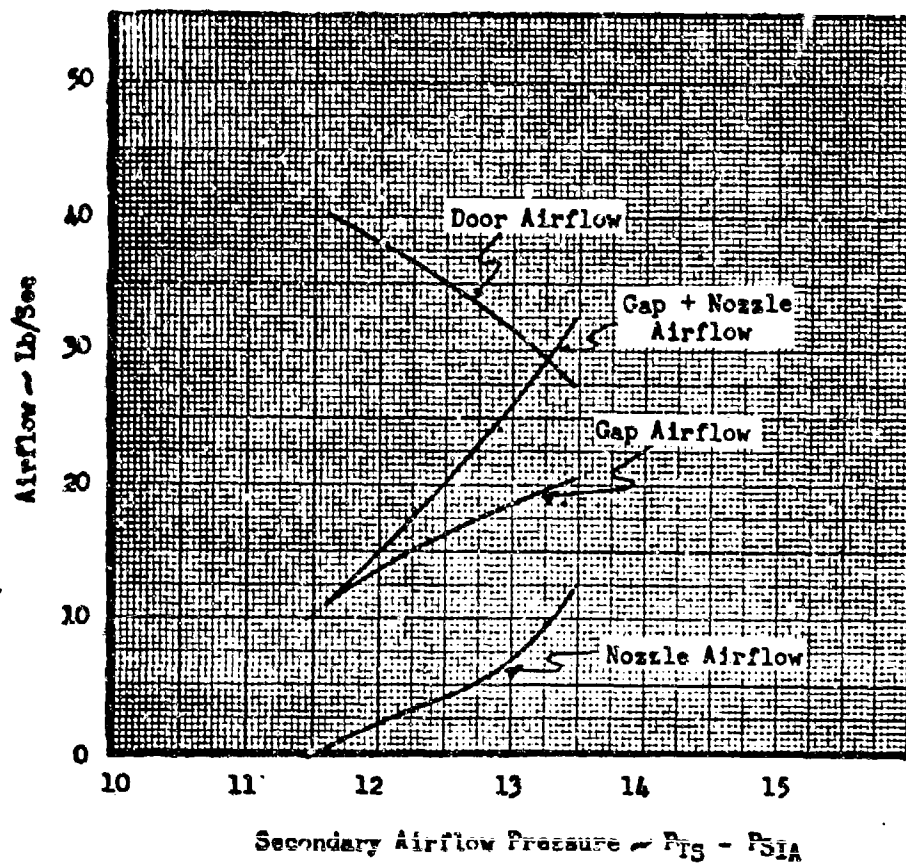


FIGURE 7-18. Ground Cooling Airflow Matching

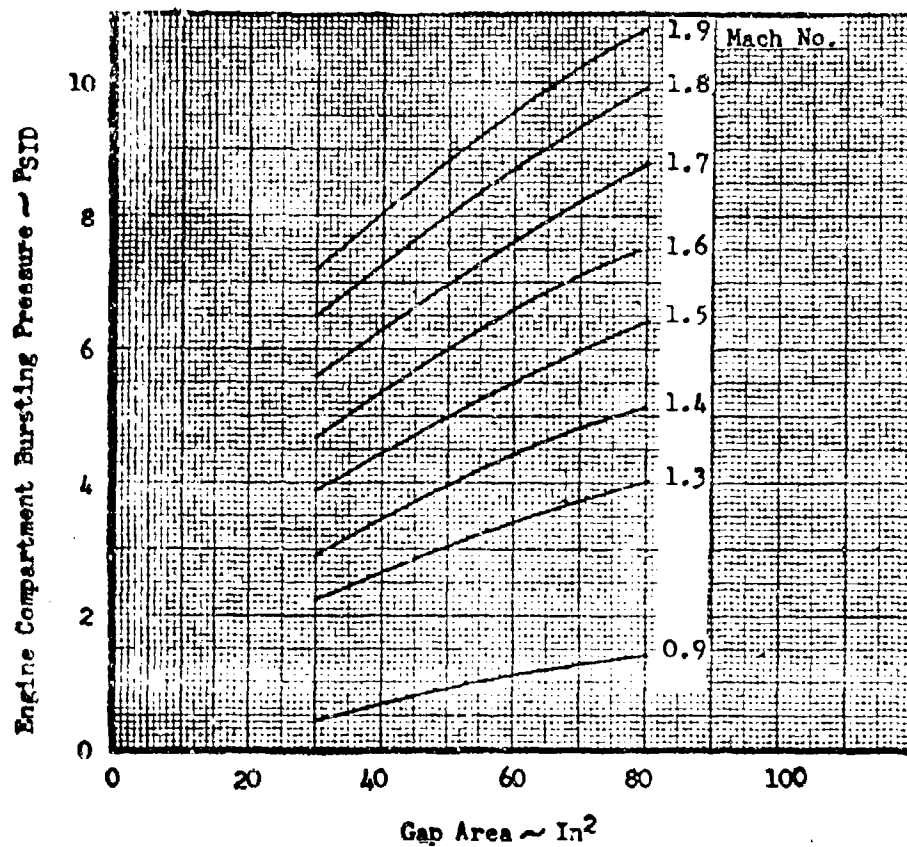


FIGURE 7-19. Engine Compartment Bursting Pressures

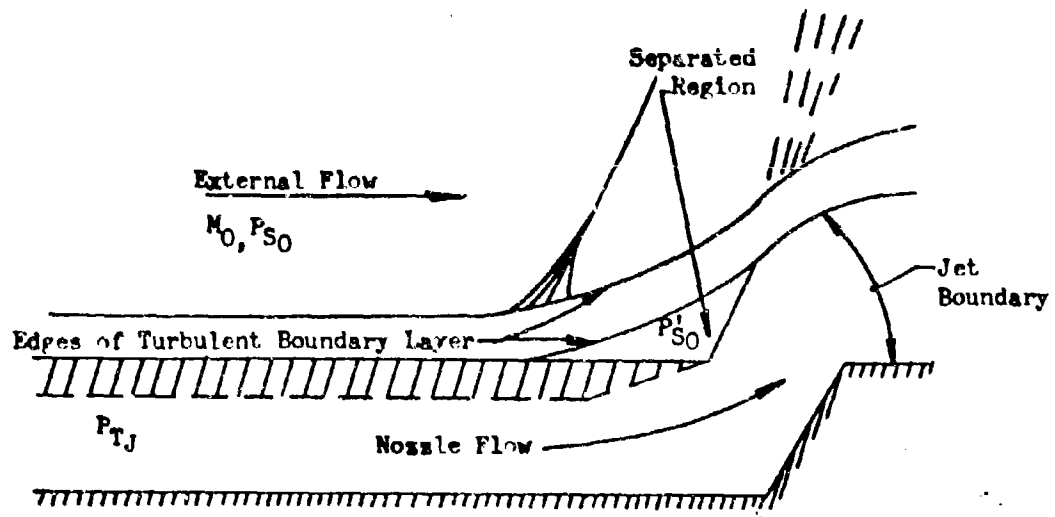


FIGURE 7-20. Sketch of Interaction between Exit Flow and Free Stream Flow

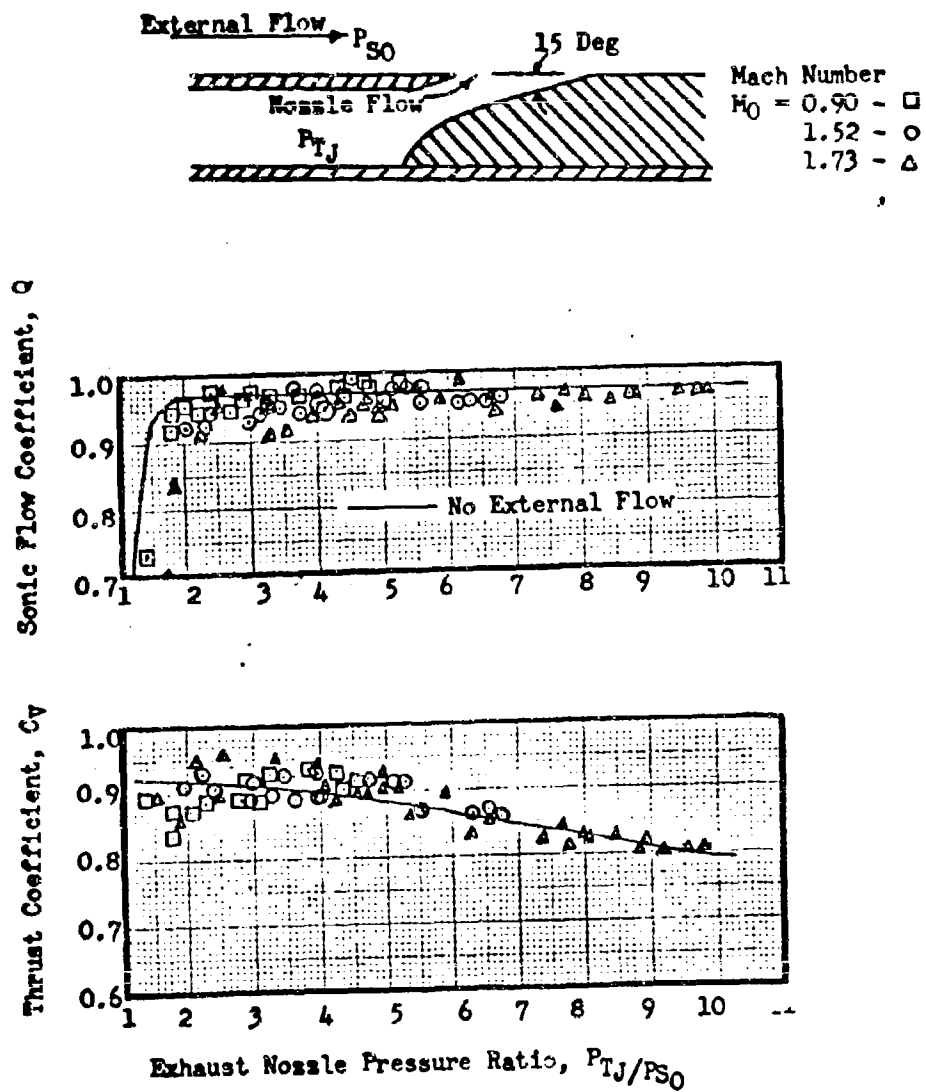


FIGURE 7-21. Performance of the 15-Deg Oblique Exhaust Nozzle with External Flow



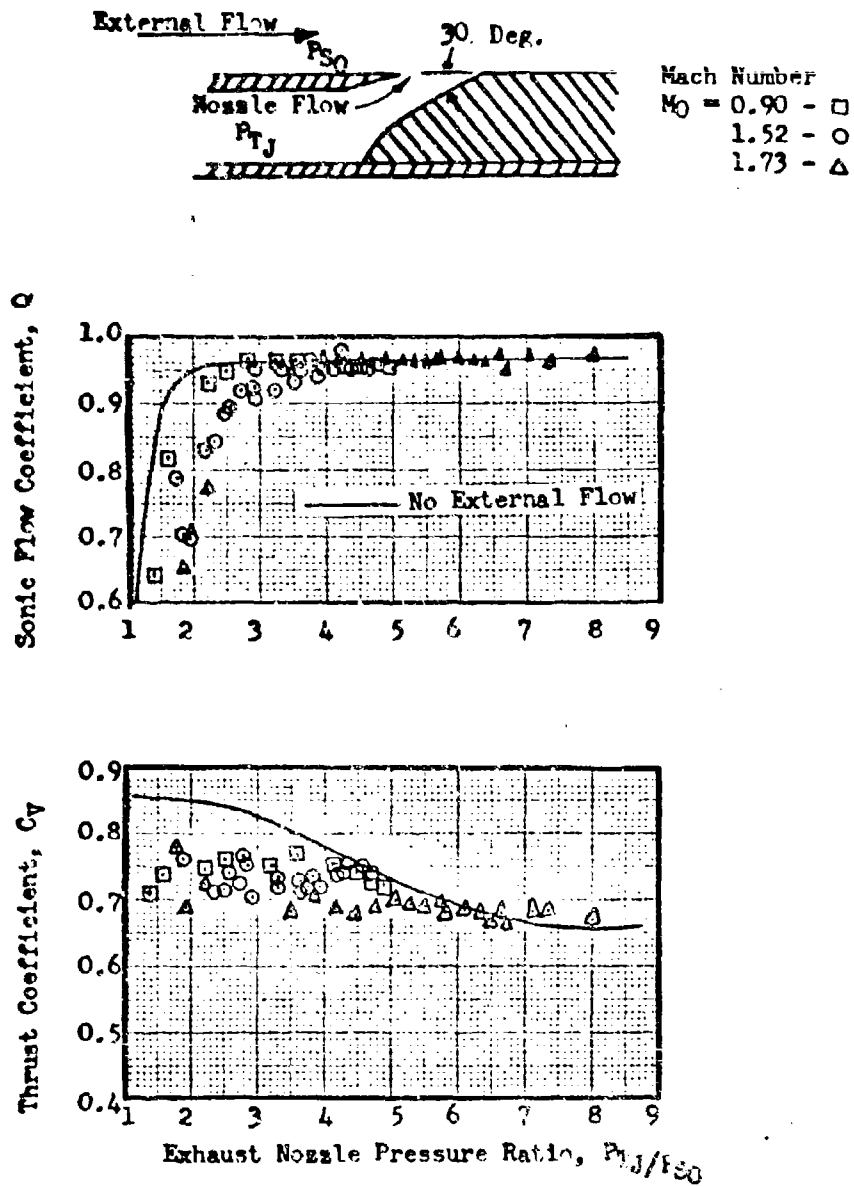


FIGURE 7-22. Performance of the 30-Deg Oblique Exhaust Nozzle with External Flow

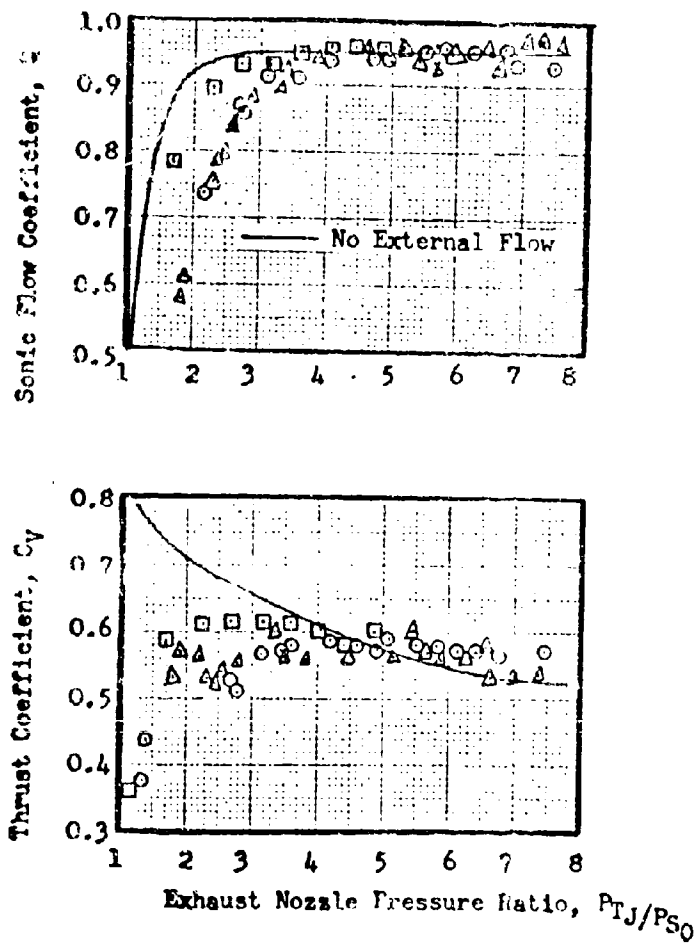
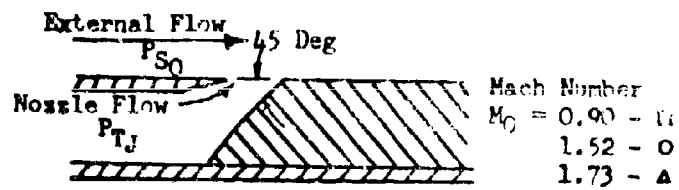


FIGURE 7-23. Performance of the 45-Deg Oblique Exhaust Nozzle with External Flow

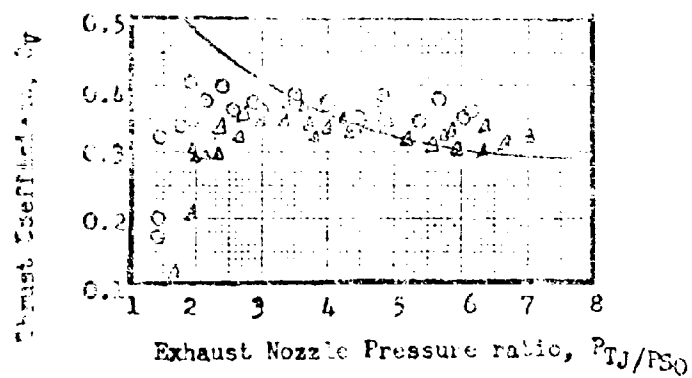
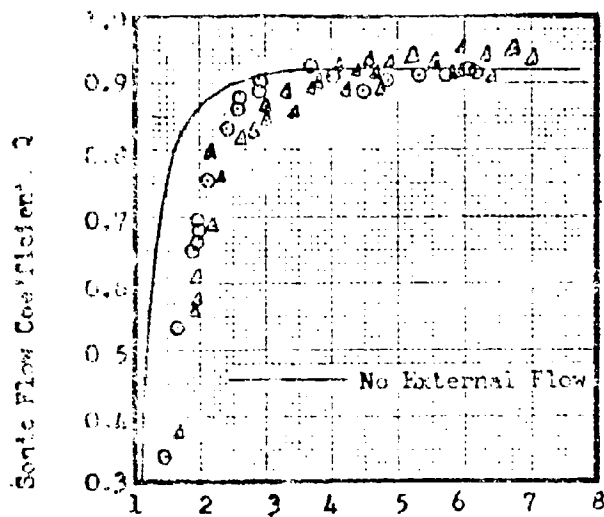
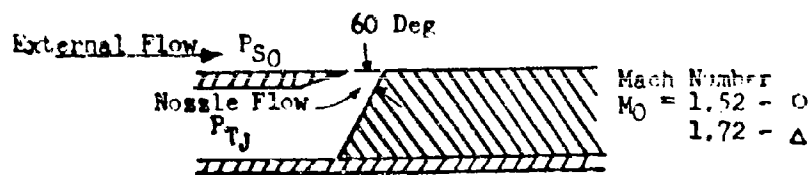
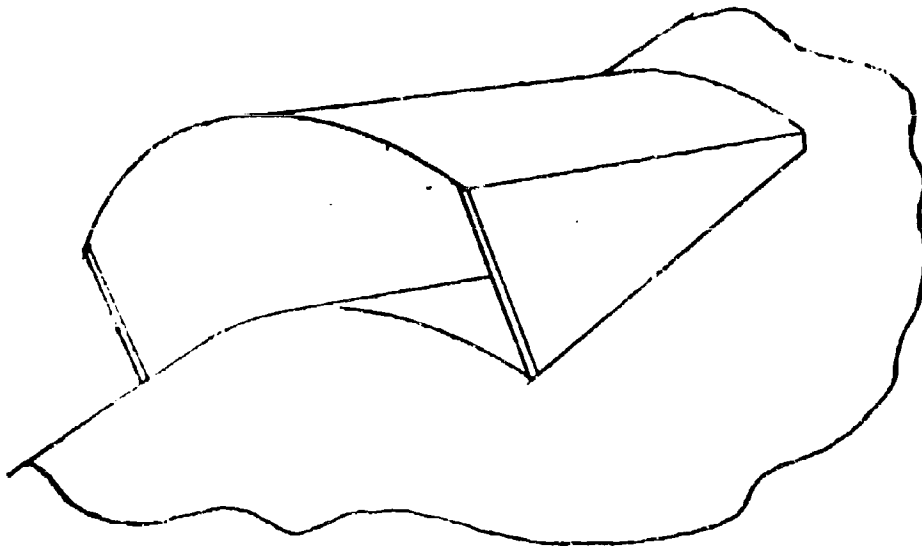
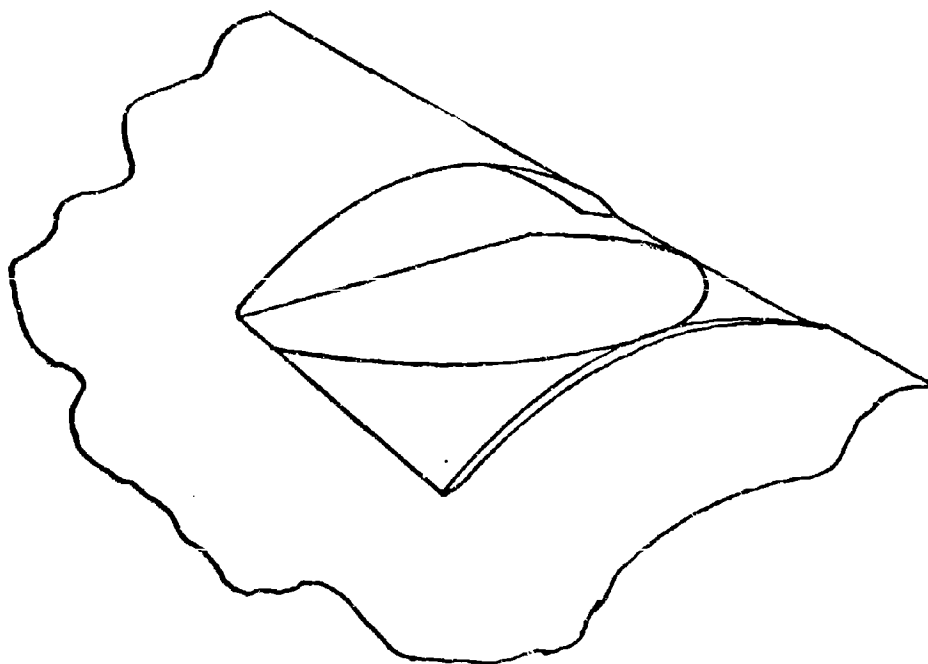


FIGURE 7-24. Performance of the 60-Deg Oblique Exhaust Nozzle with External Flow



**Shielded Exit**



**Flush Exit**

**FIGURE 7-25. Sketch of Flush and Shielded Exits**

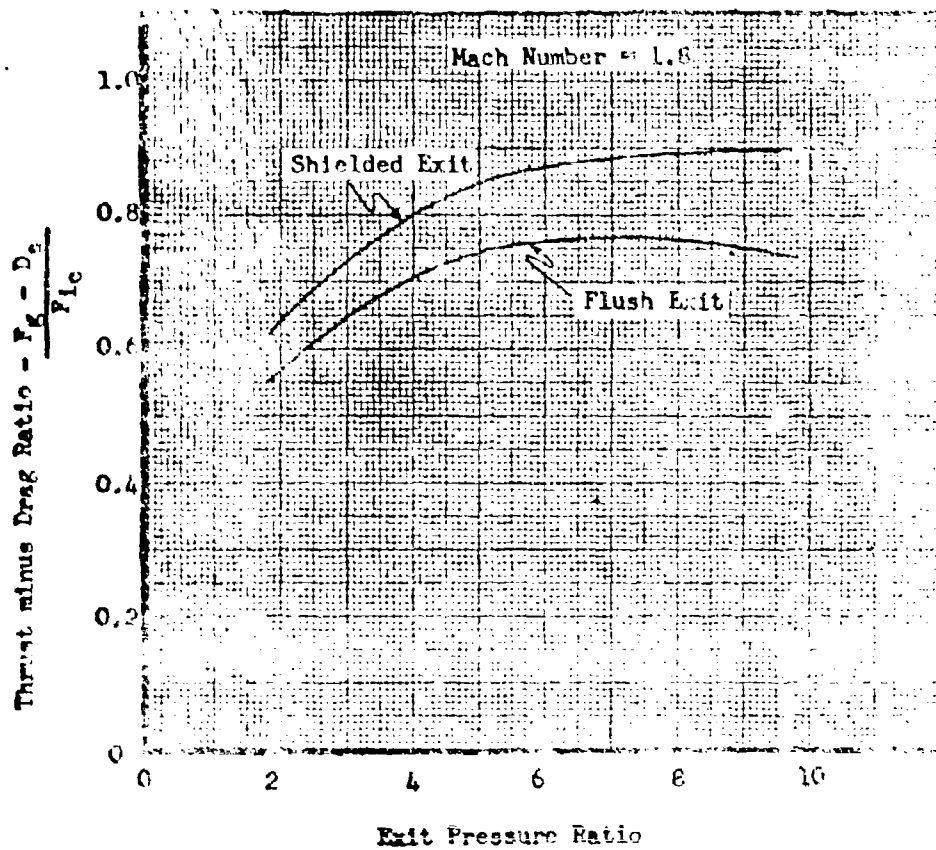


FIGURE 7-26. Performance Comparison of Flush and Shielded Exits

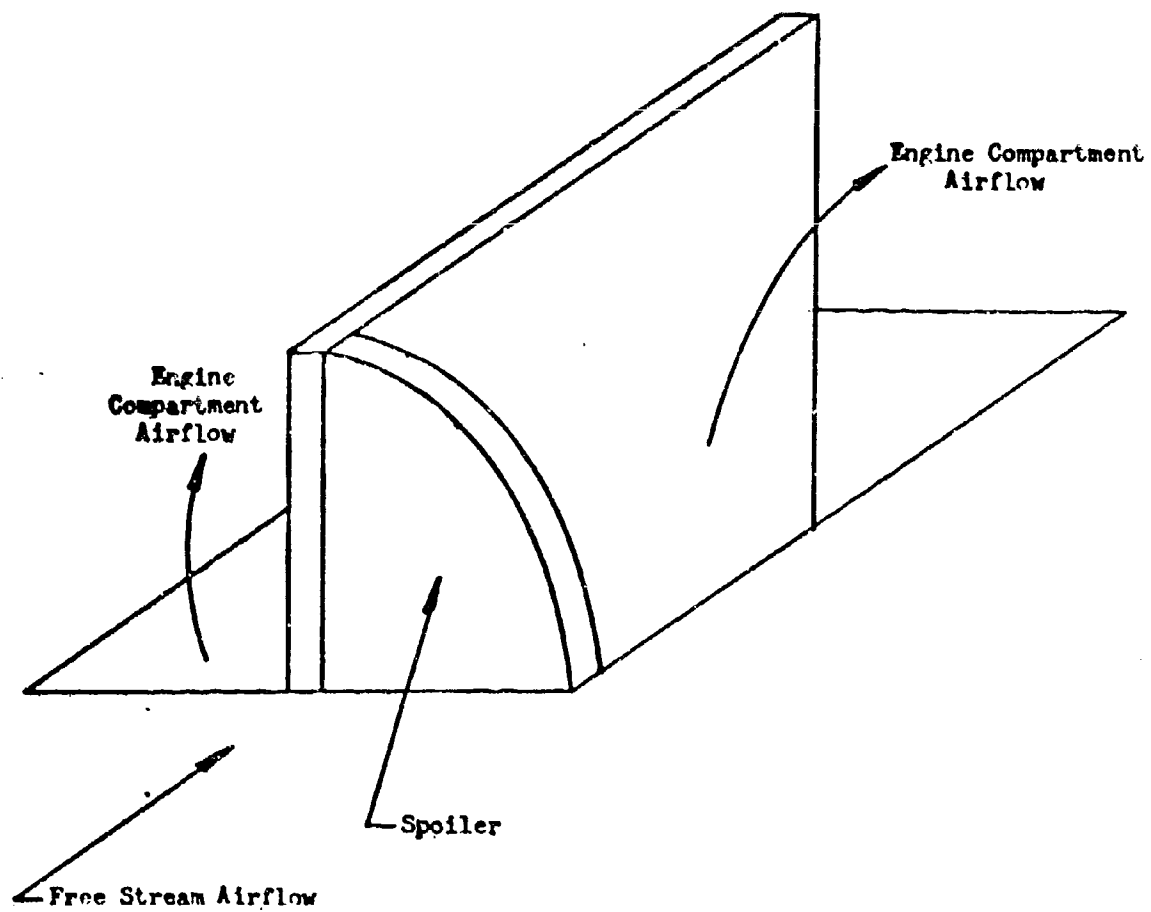


FIGURE 7-27. Sketch of RA-5C Engine Compartment Pressure Relief Door

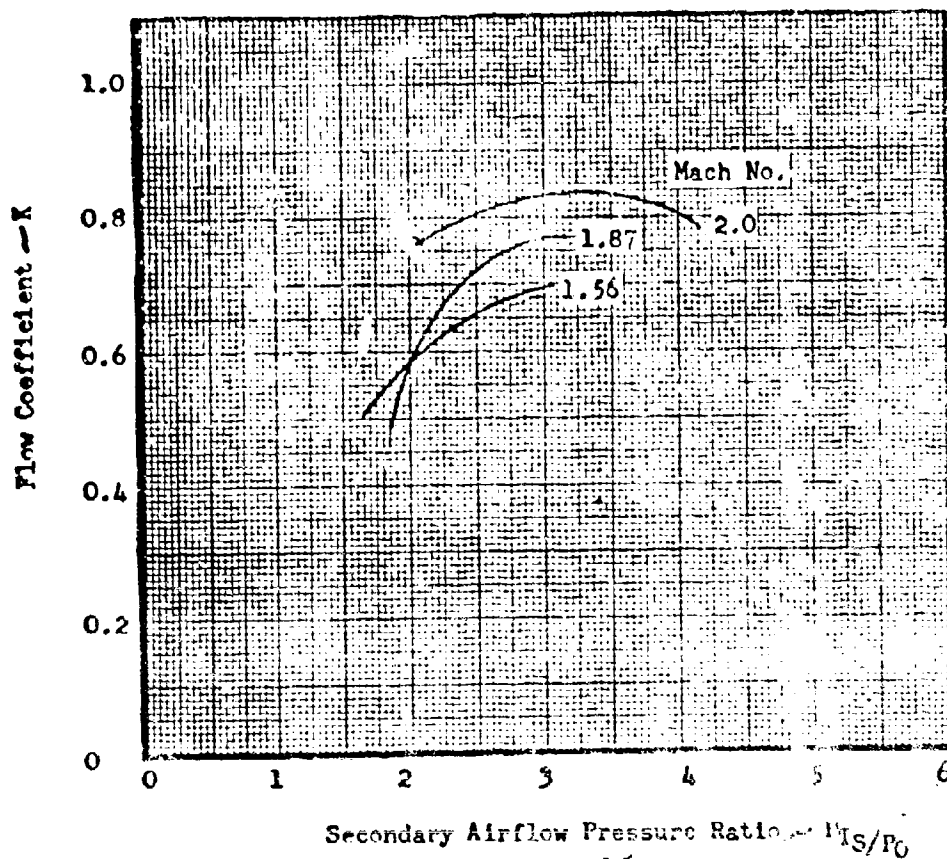


FIGURE 7-28. Flow Coefficients for RA-5C Engine Compartment Pressure Relief Door

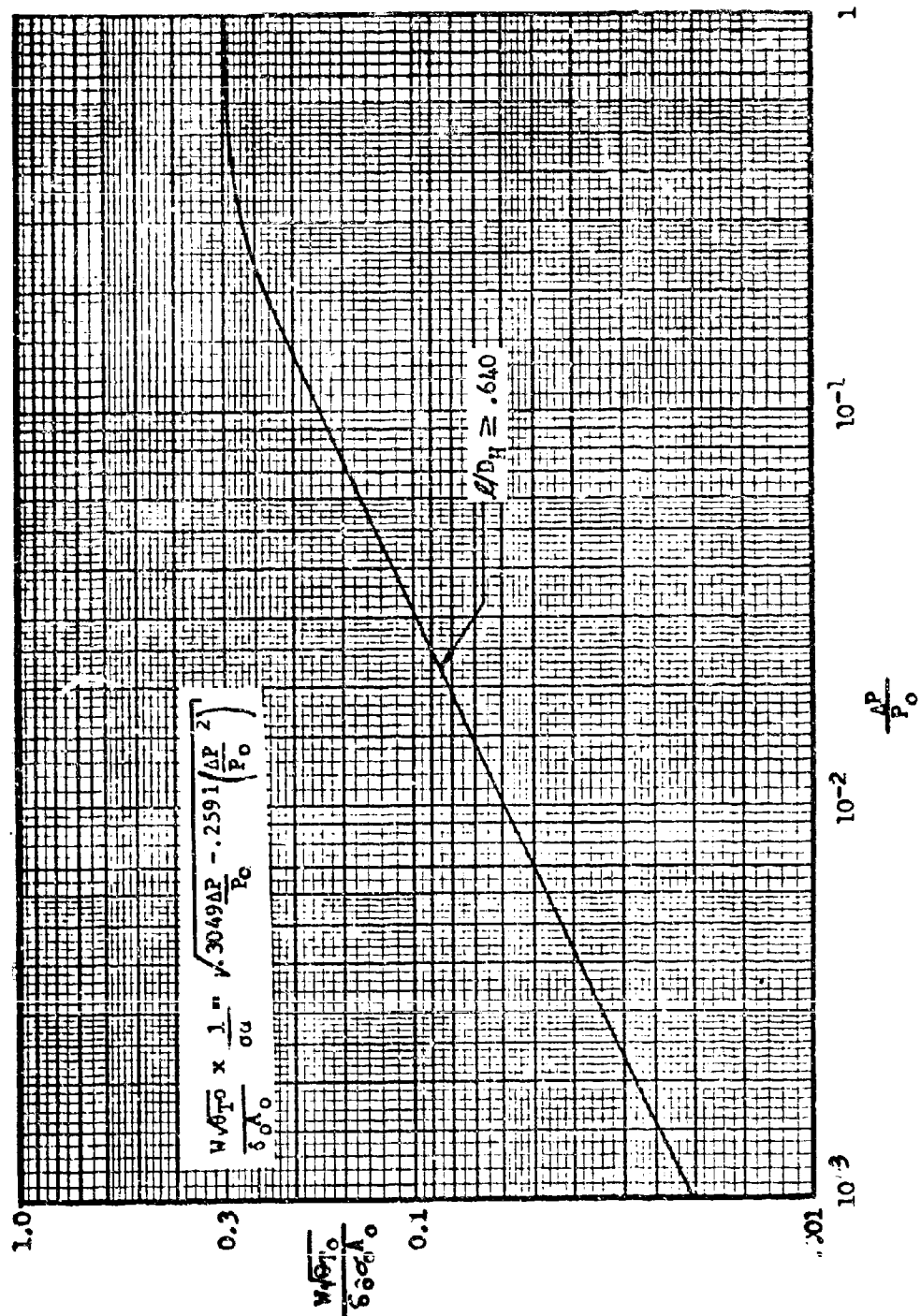
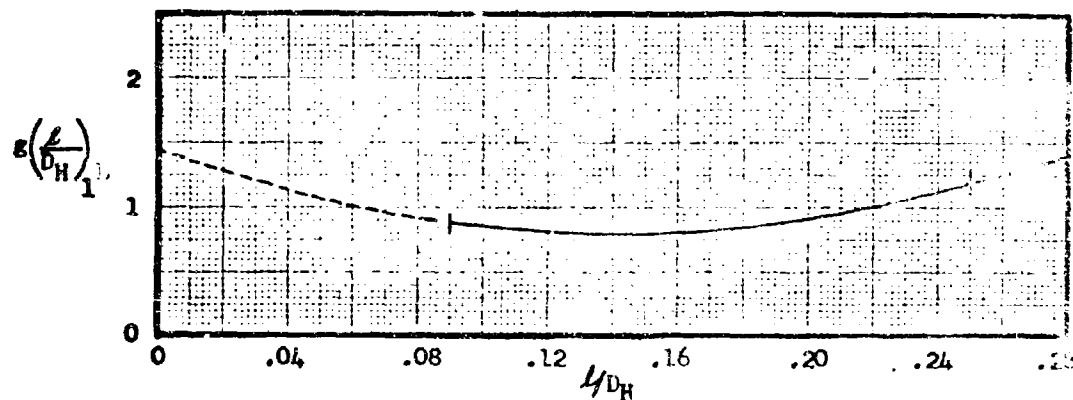
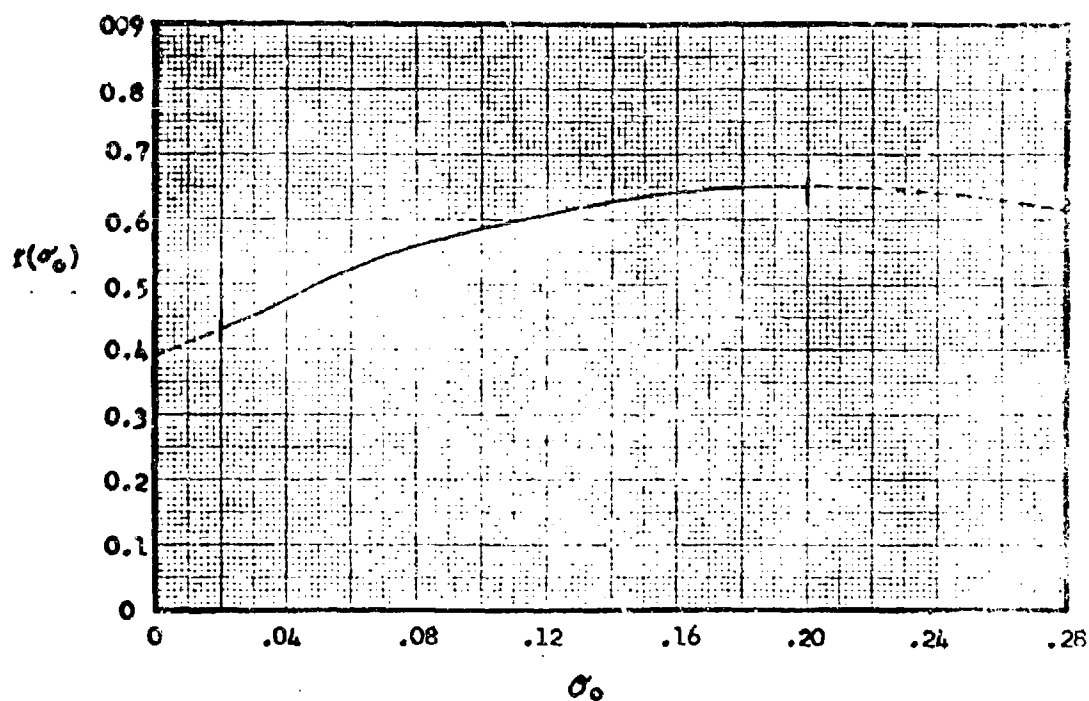


FIGURE 7-29. Correlated Characteristics of Drilled Materials in Normal Flow:  $1/D_H \approx .64$





$$f(\sigma_0) = .3978 + 2.561 \sigma_0 - 6.352 \sigma_0^2$$

$$g(L/D_H) = 1.461 - .8948 L/D_H + .3165 \left(\frac{L}{D_H}\right)^2$$

FIGURE 7-30.  $g(L/D_H)$  and  $f(\sigma_0)$  for Drilled Materials in Parallel Flow from Equation 1.

### NOMENCLATURE

- $A_o$  - Total Plate Area, Sq. In.
- $D_H$  - Mean Hydraulic Diameter of a Flow Passage, In.
- $f$  - Function of  $\sigma_o$  Defined by Equation 1.
- $L$  - Mean Length of a Flow Passage, In.
- $M_o$  - Parallel Mach Number Over Material.
- $P_o$  - Static Pressure Above Material, PSF.
- $\sigma_o$  - Porosity, Ratio of Total Open Area to Plate Area.
- $\sigma_A$  - Apparent Porosity Defined by Equation 2.
- $T_{T_o}$  - Absolute Total Temperature, Degrees Rankine.
- $W$  - Mass Rate of Flow Through Material, Lb/Sec.
- $\xi_o$  - Static Pressure Ratio to Standard  $P_o/2116$ .
- $\theta_{T_o}$  - Total Temperature Ratio to Standard  $T_{T_o}/518.7$ .
- $g$  - Function of  $L/D_H$ ,  $\sigma_o$ ,  $\Delta P/P_o$  Defined by Equation 2.

FIGURE 7-31

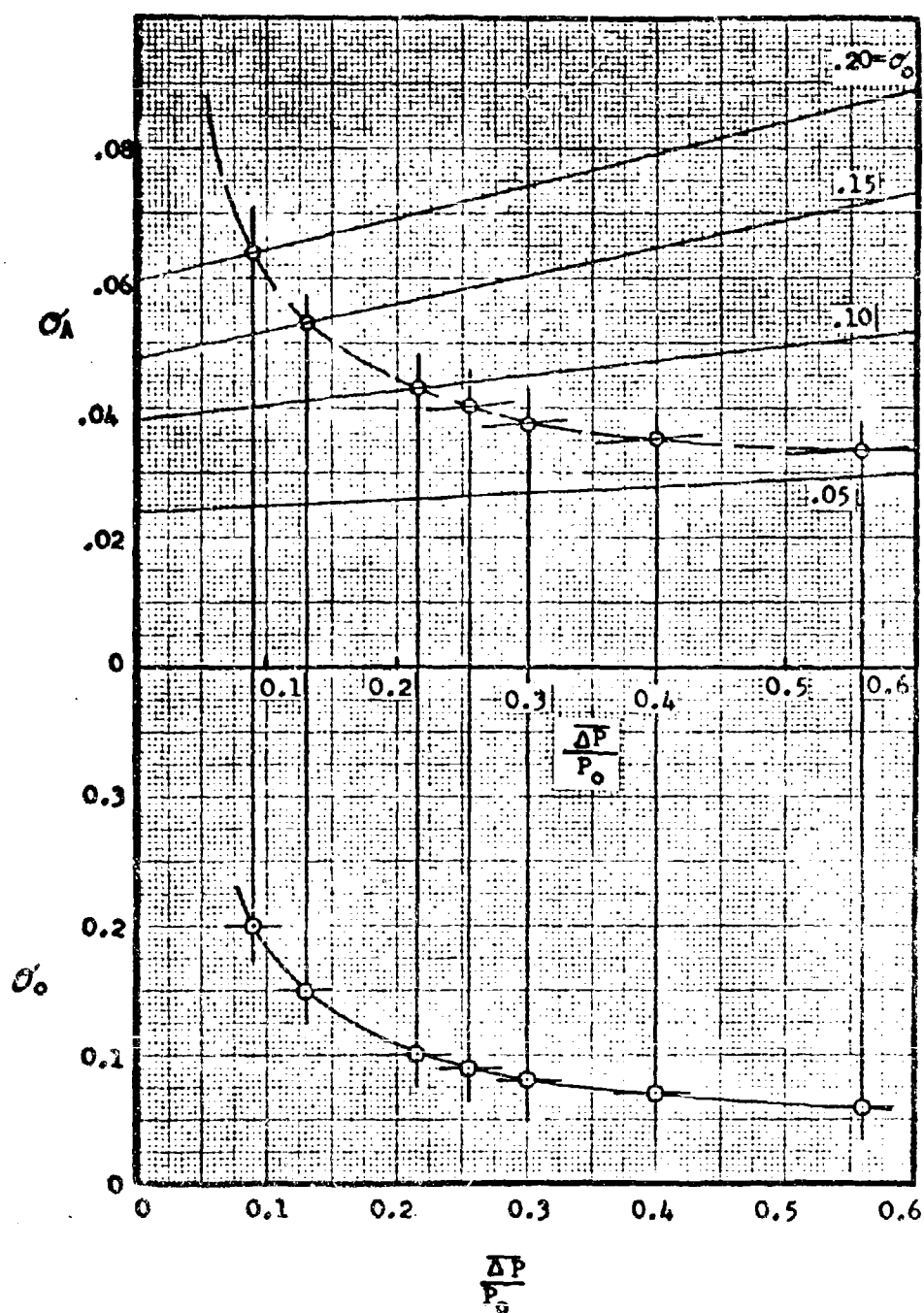


FIGURE 7-32. Sample Determination of  $\sigma_0$  as a Function of

$\frac{\Delta P}{P_0}$  for the Case of:

$$\frac{W/\sigma_{T_0}}{\sigma_0 A_0} = .010; M_0 = 1.20; l/D_H \approx 1.00$$

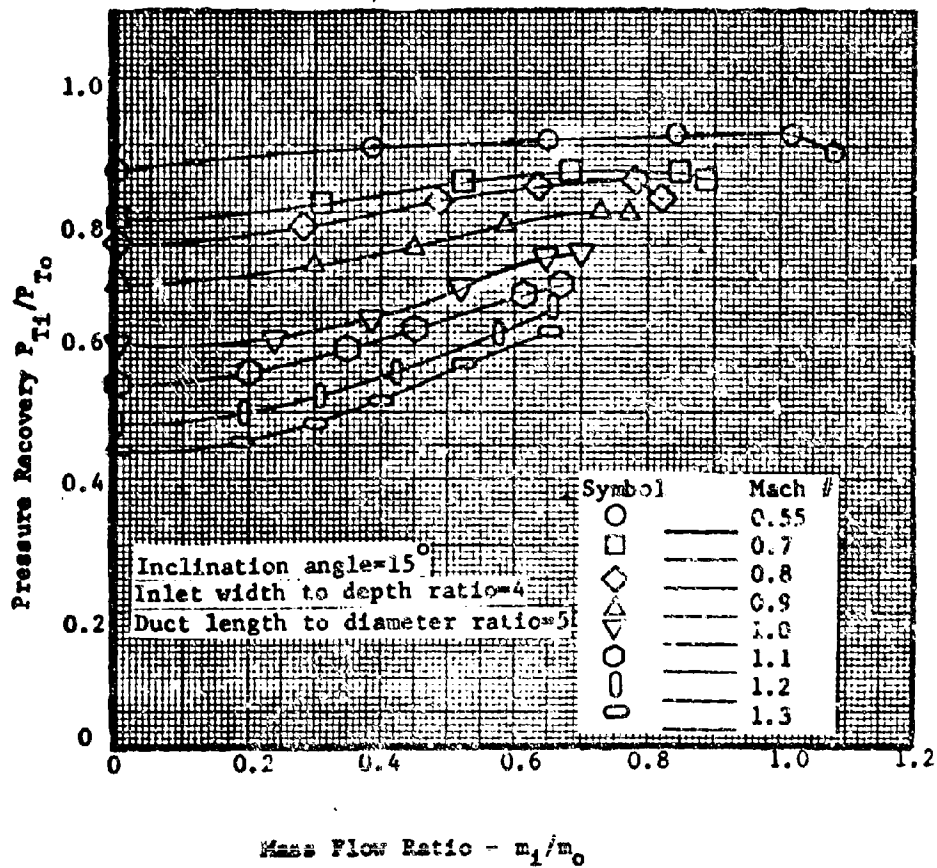


FIGURE 7-33. Recovery Characteristics of a Flush Rectangular Inlet.  
 Reference: (NASA MEMO 12-21-58L)

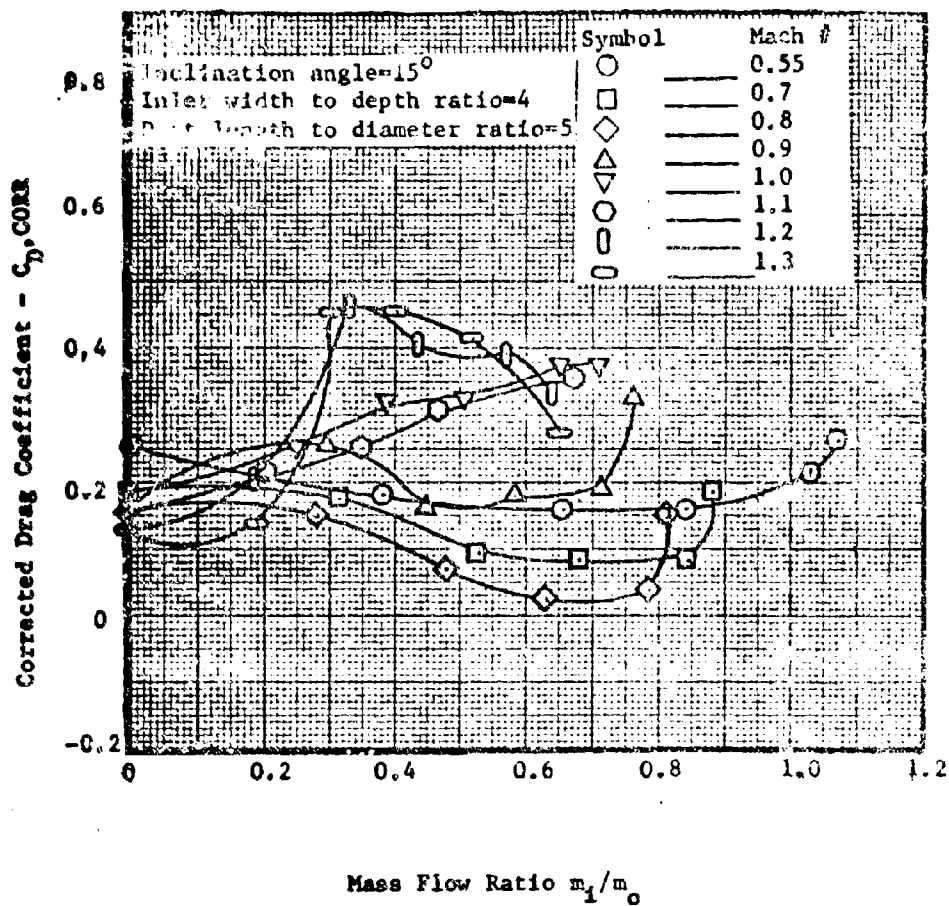


FIGURE 7-34. Drag characteristic of a flush Rectangular inlet .

Reference: (NASA MEMO 12-21-58L)

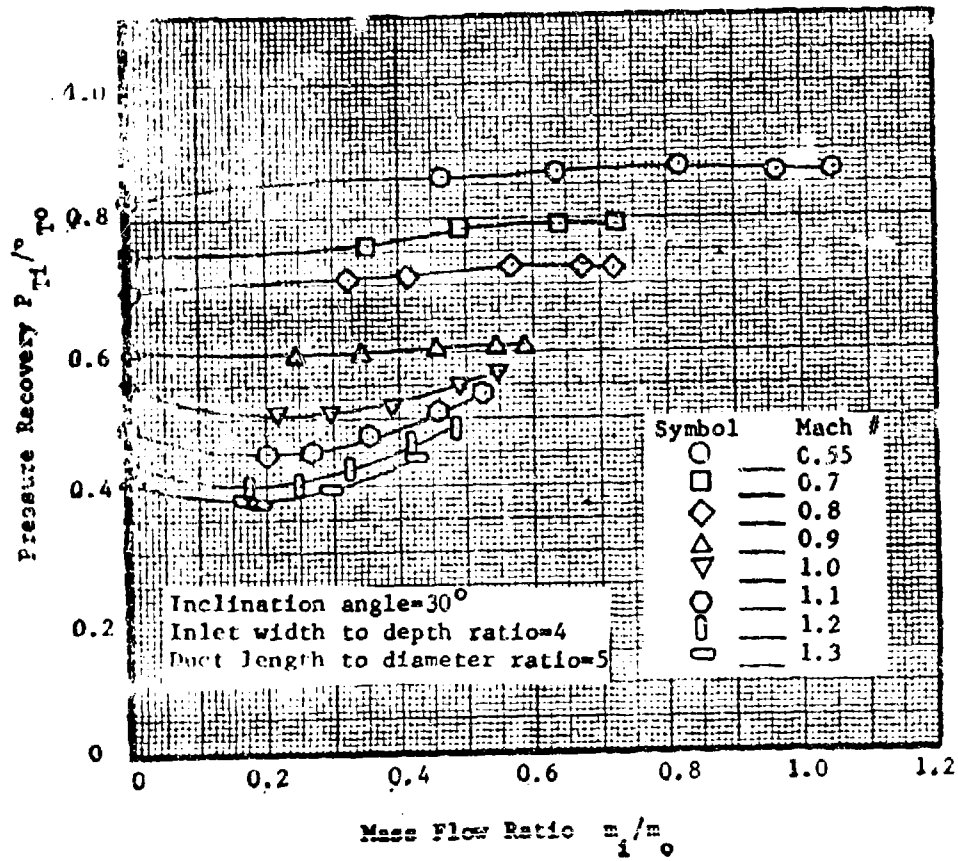


FIGURE 7-35. Recovery Characteristic of a Flush Rectangular Inlet.  
 Reference: (NASA MEMO 12-21-58L)

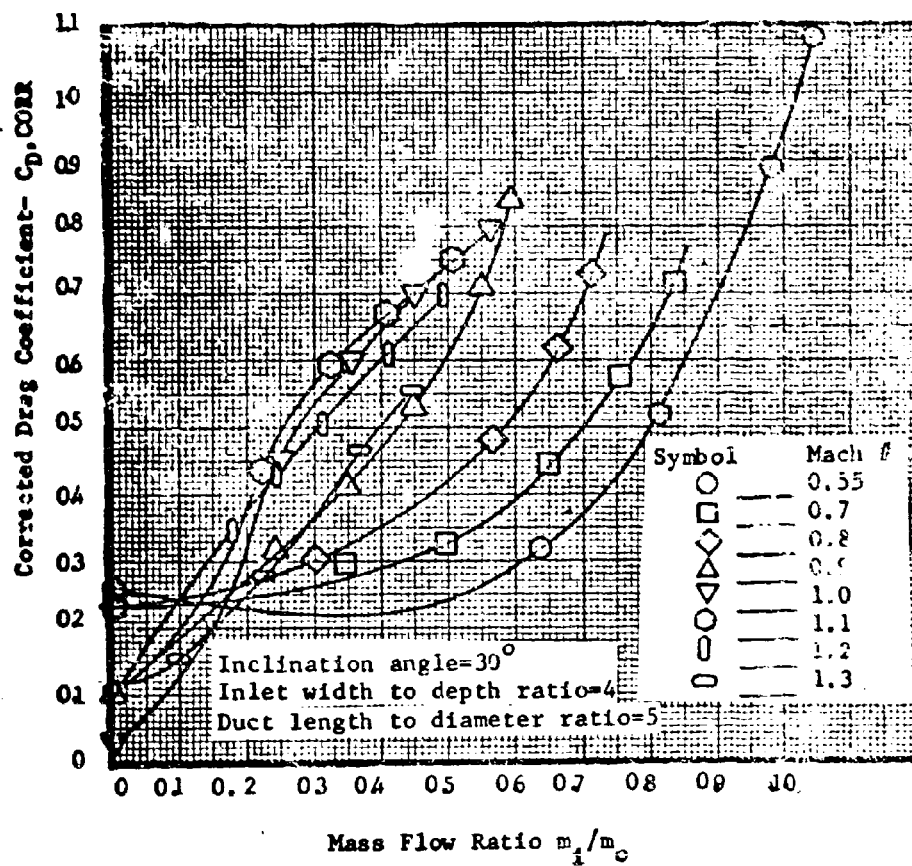


FIGURE 7-36 Drag characteristic of a flush Rectangular inlet.

Reference: (NASA MEMO 12-21-58L)

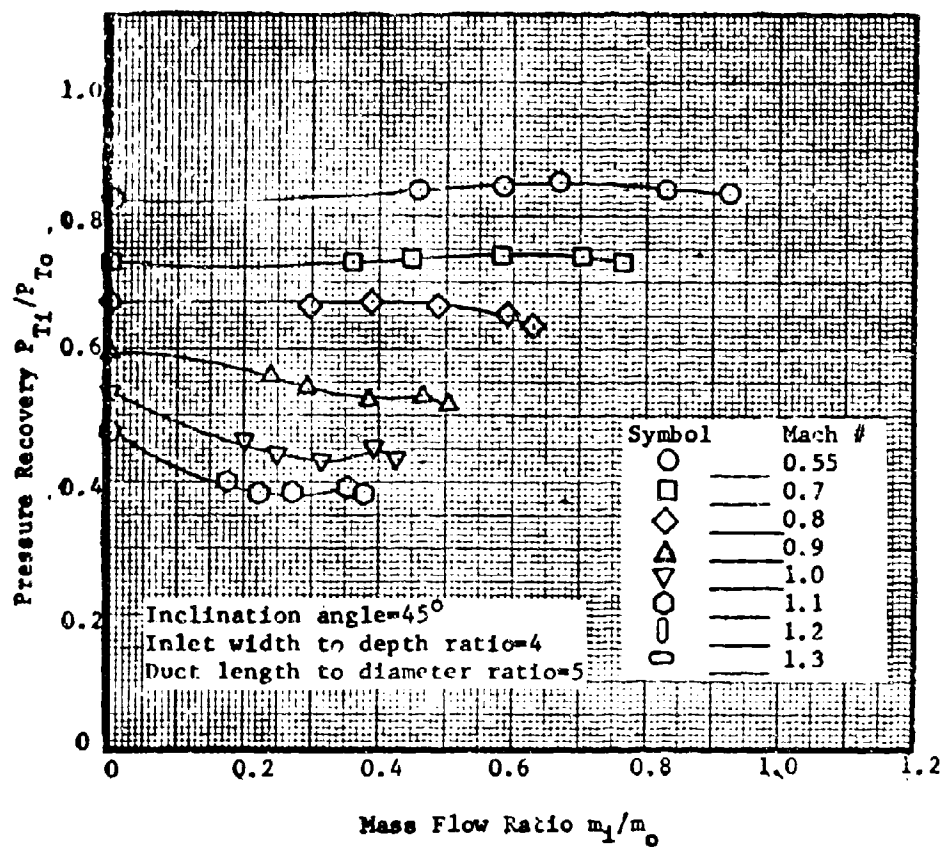


FIGURE 7-38. Recovery Characteristic of a Flush Rectangular Inlet.  
 Reference: (NASA MEMO 12-21-58L)



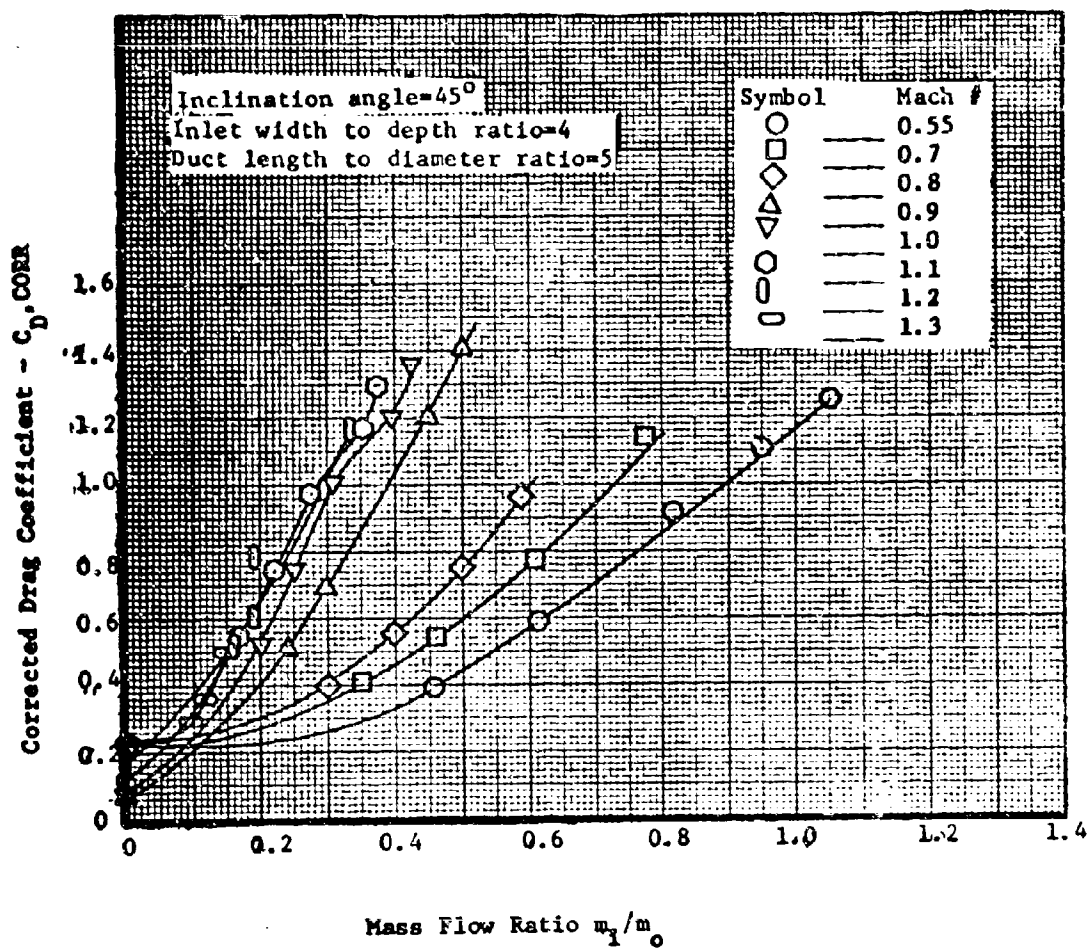


FIGURE 7-39. Drag characteristic of a flush Rectangular inlet.

Reference: (NASA MEMO 12-21-58L)

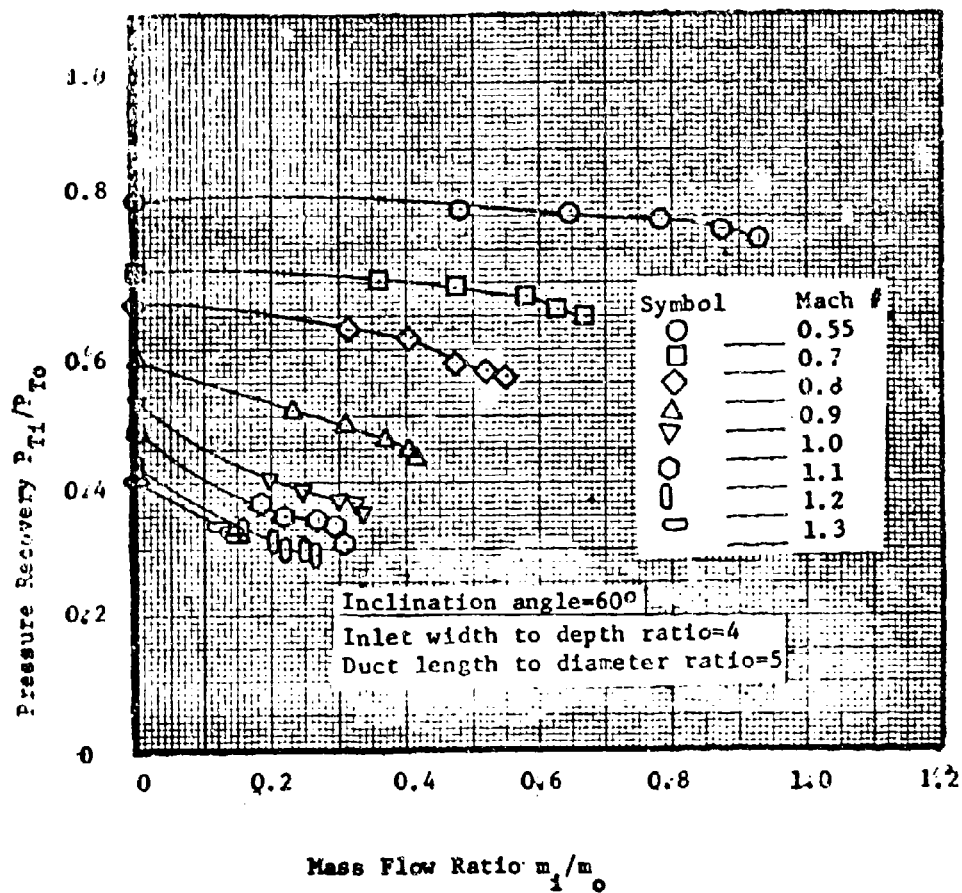


FIGURE 7-40. Recovery Characteristic of a Flush Rectangular Inlet.

Reference: (NASA MEMO 12-21-58L)

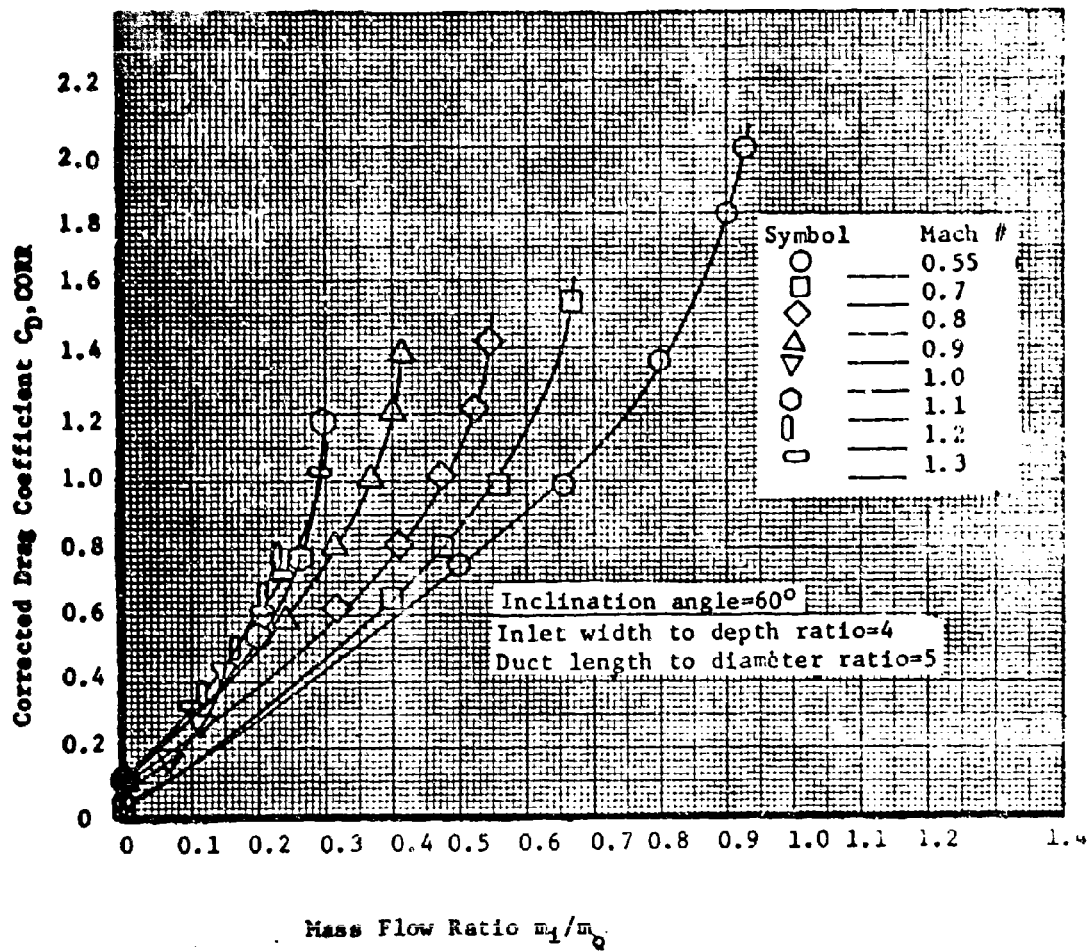


FIGURE 7-41. Drag characteristic of a flush Rectangular inlet.

Reference: (NASA MEMO 12-21-58L)

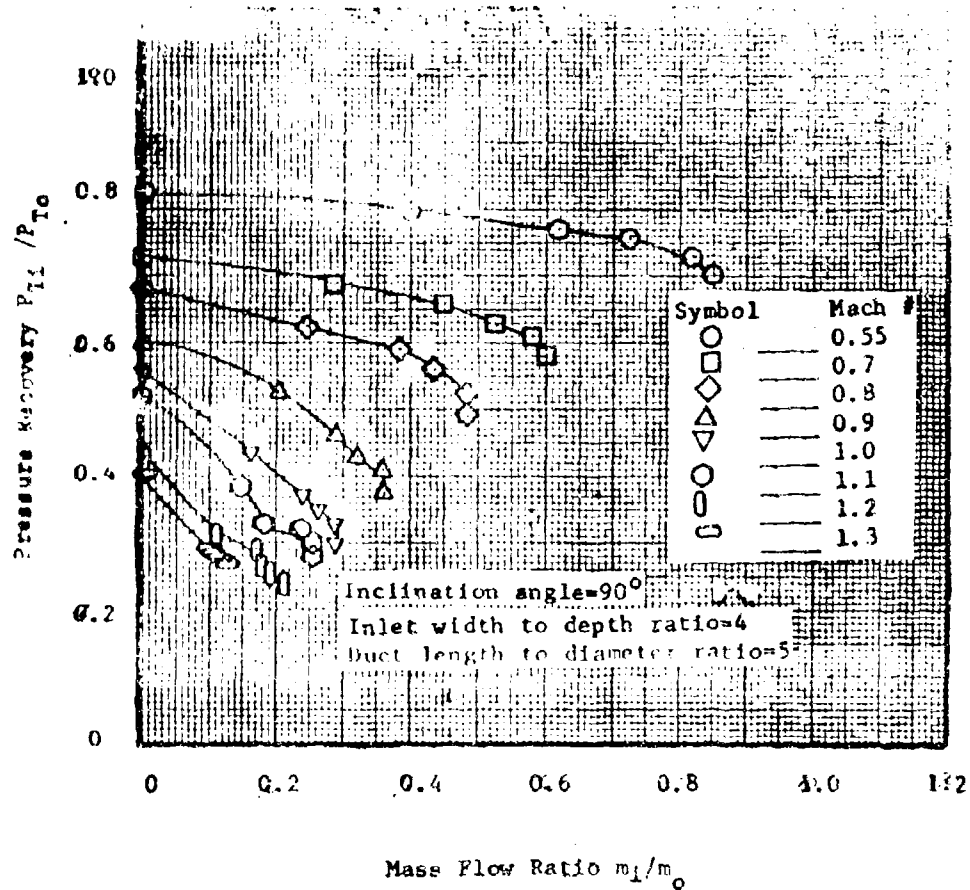


FIGURE 7-42. Recovery Characteristic of a Flush Rectangular Inlet.  
 Reference: (NASA MEMO 12-21-58L)

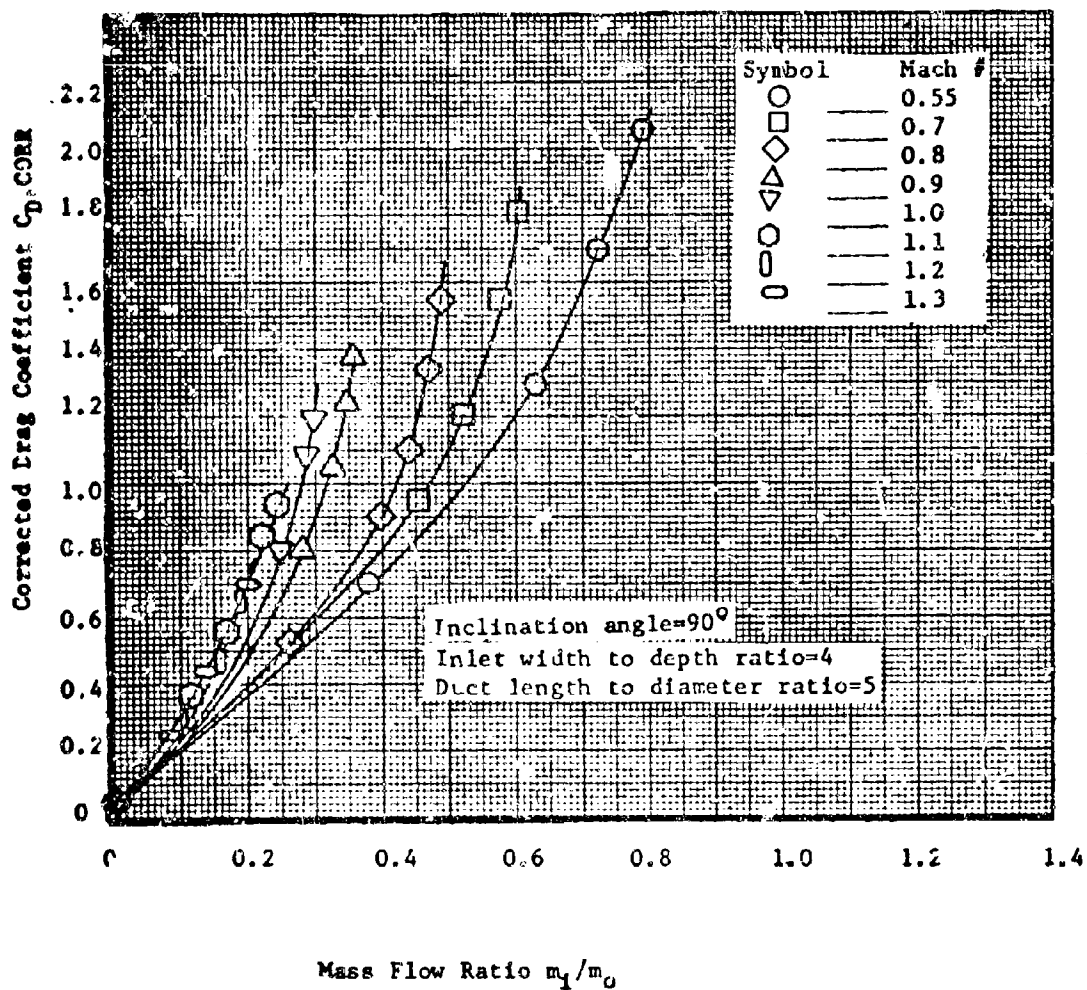


FIGURE 7-43. Drag characteristic of a flush Rectangular inlet.

Reference: (NASA MEMO 12-21-58L)

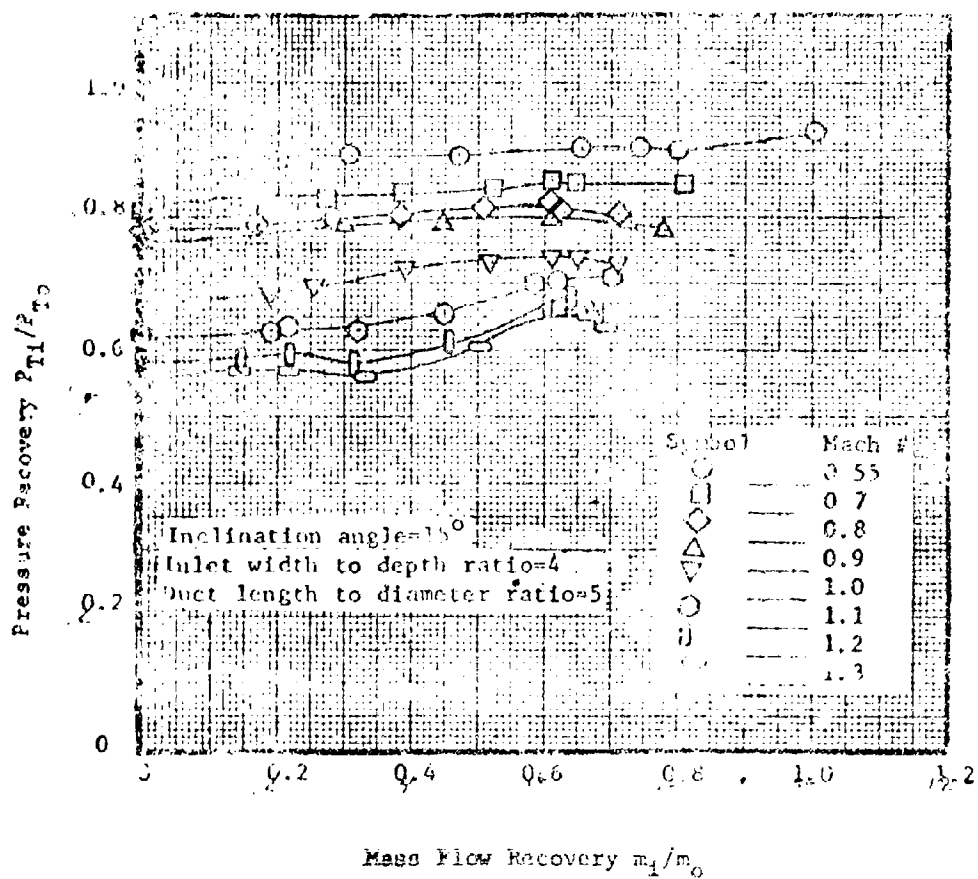


FIGURE 7-44. Pressure Recovery Characteristic of Flush Rectangular Inlet using a  $7^\circ$  approach ramp with diverging walls. (NASA submerged inlet.)  
 Reference: (NASA MEMO 12-21-58L)

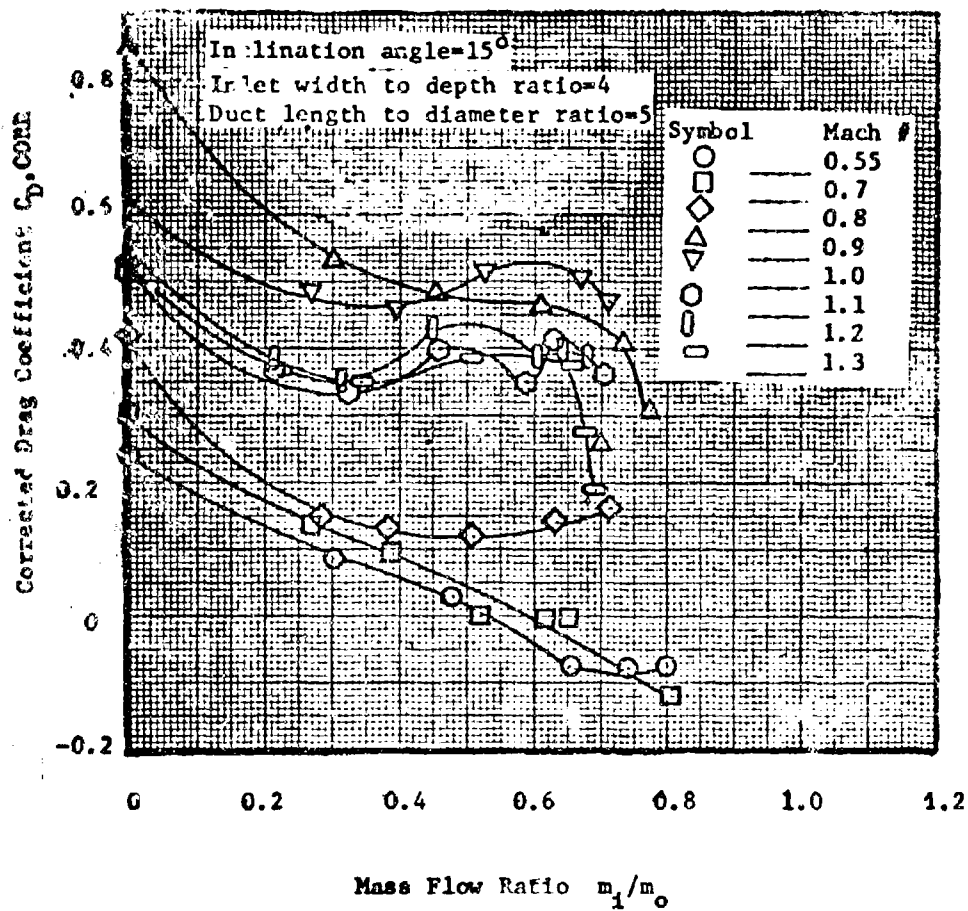


FIGURE 7-45. Drag Characteristics of a Flush rectangular inlet using a  $7^\circ$  approach ramp with diverging walls. (NACA Submerged Inlet.)

Reference: (NASA MEMO 12-21-58L)

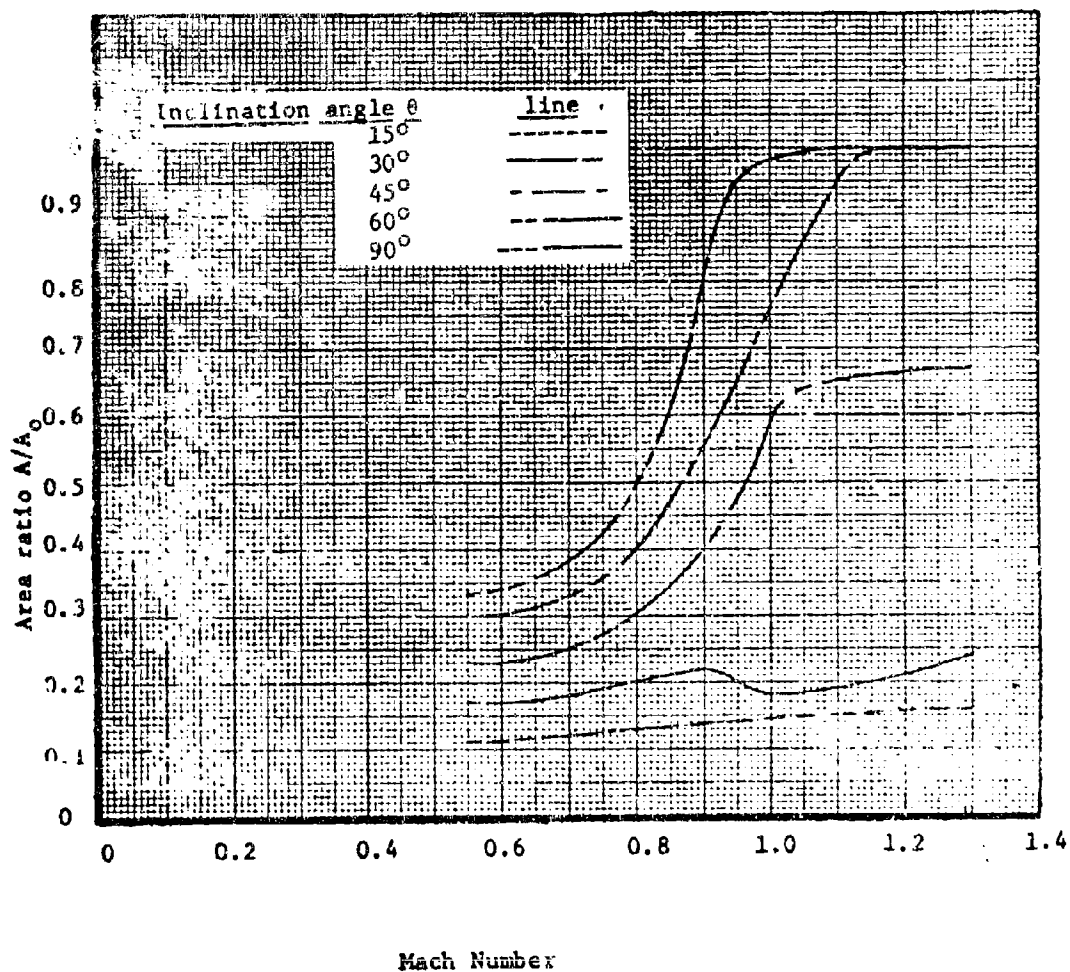


FIGURE 7-46. Variation of required inlet area with mach number for operation at equal mass flows and minimum drag for each flush rectangular inlet.



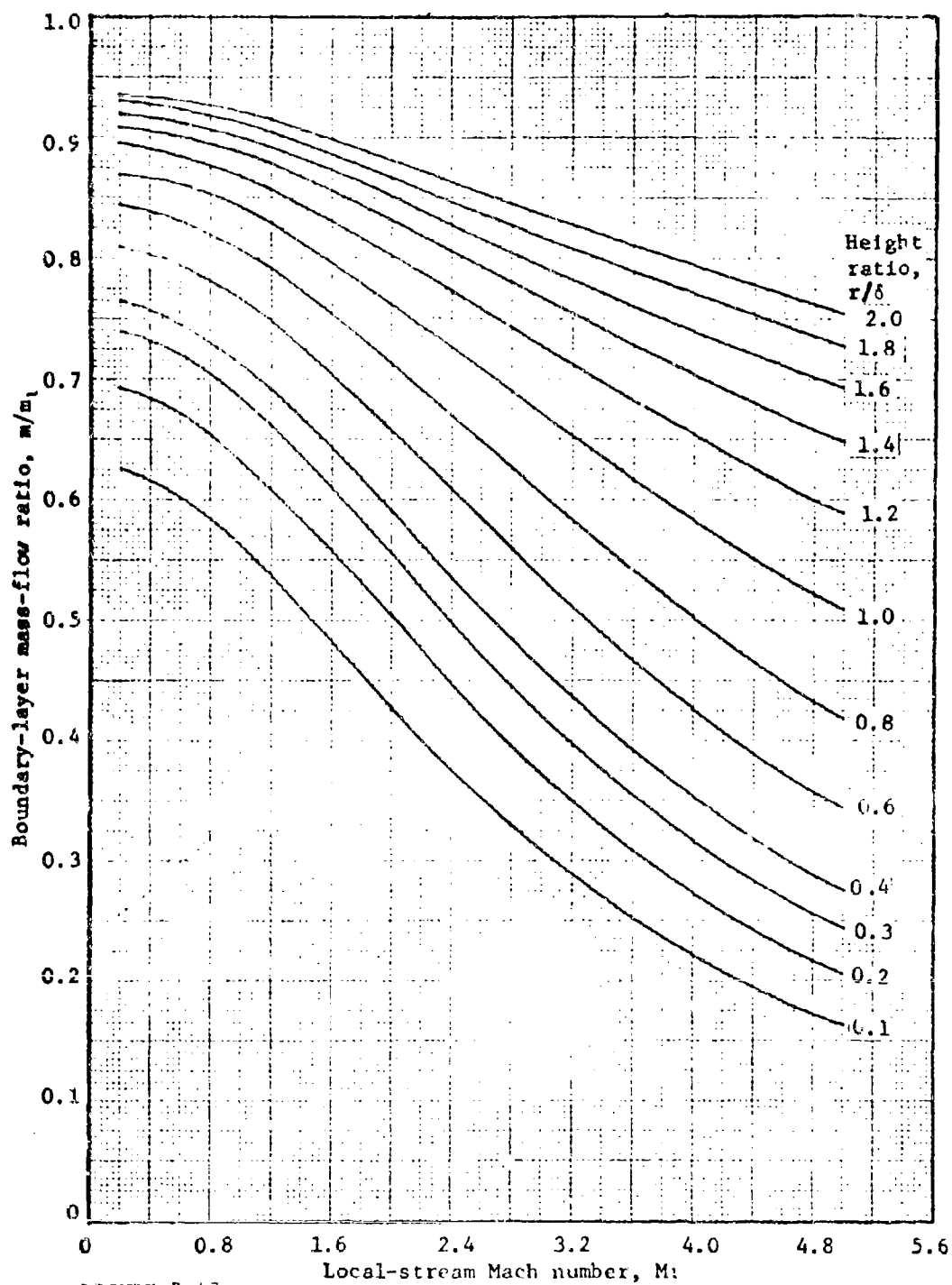


FIGURE 7-47.

Mass flow ratio for various fractions of boundary layer

Velocity profile parameter  $N=7$

Reference: NACA TN 3583

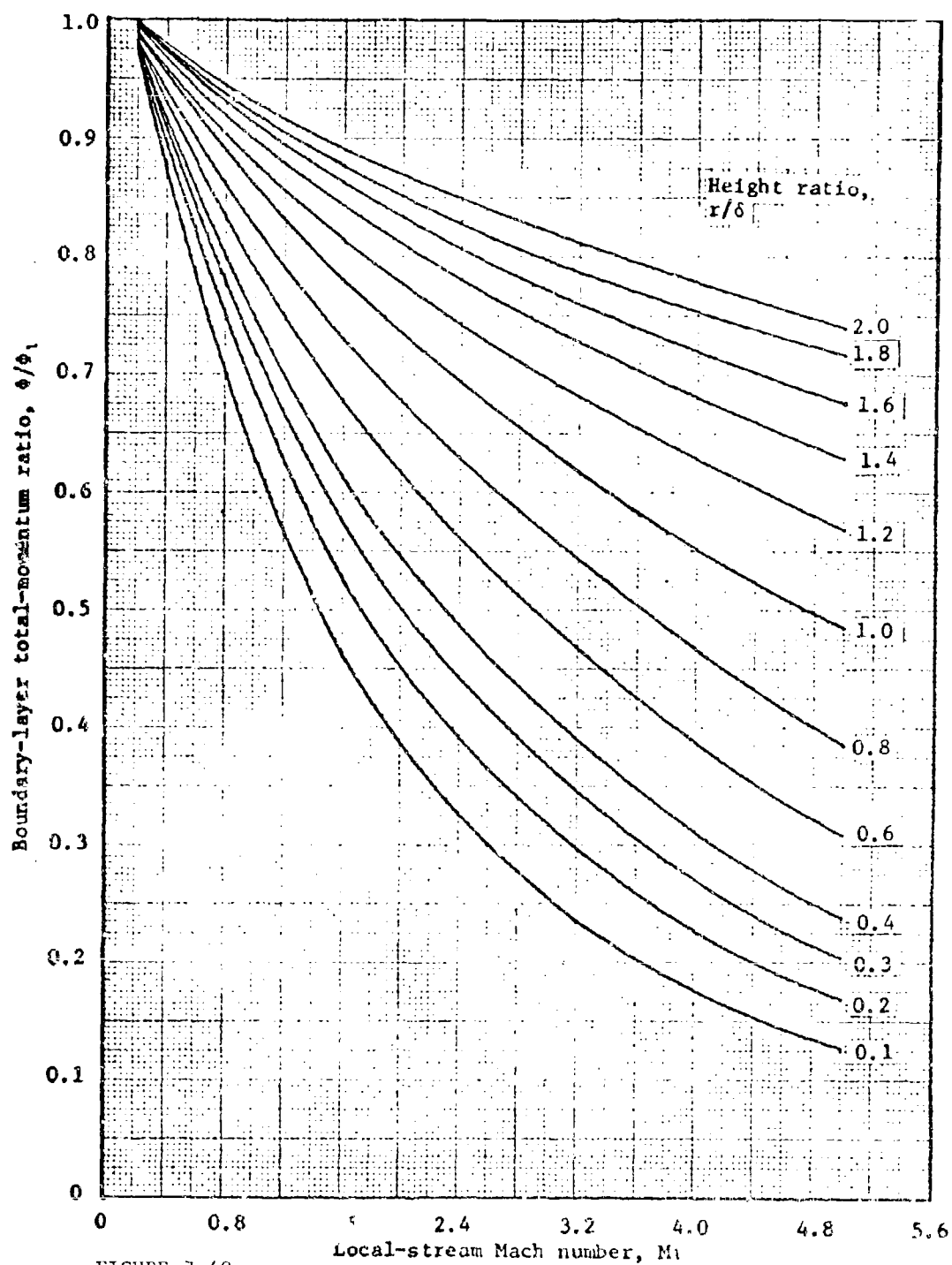


FIGURE 7-48.

Total Momentum Ratio for various fractions of boundary layer.  
Velocity Profile parameter  $N=7$ .

Reference: NACA TN3583

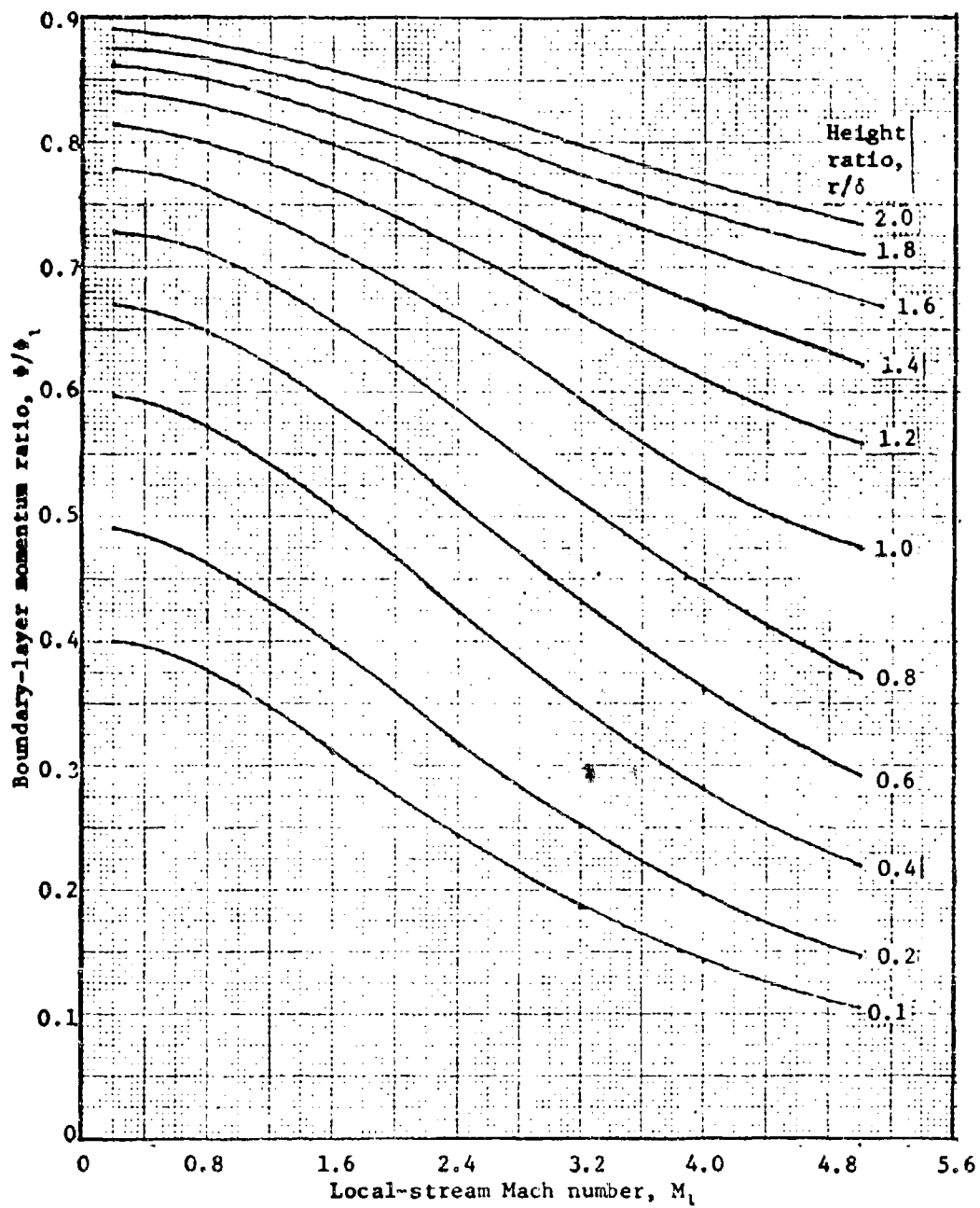


FIGURE 7-49.

Momentum ratio for various fractions of boundary layer.  
Velocity profile parameter  $N=7$ .

Reference: NACA TN 3583

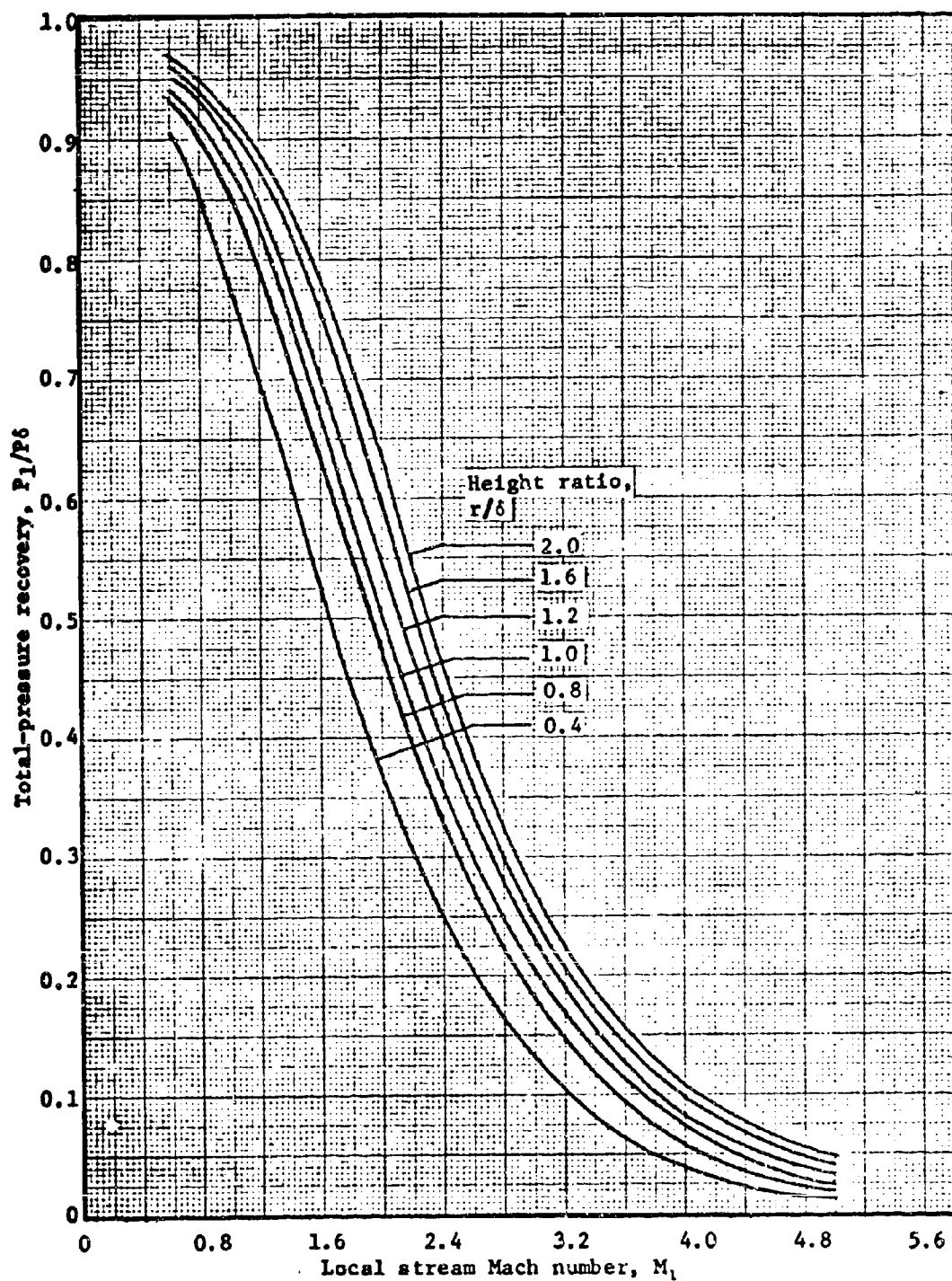
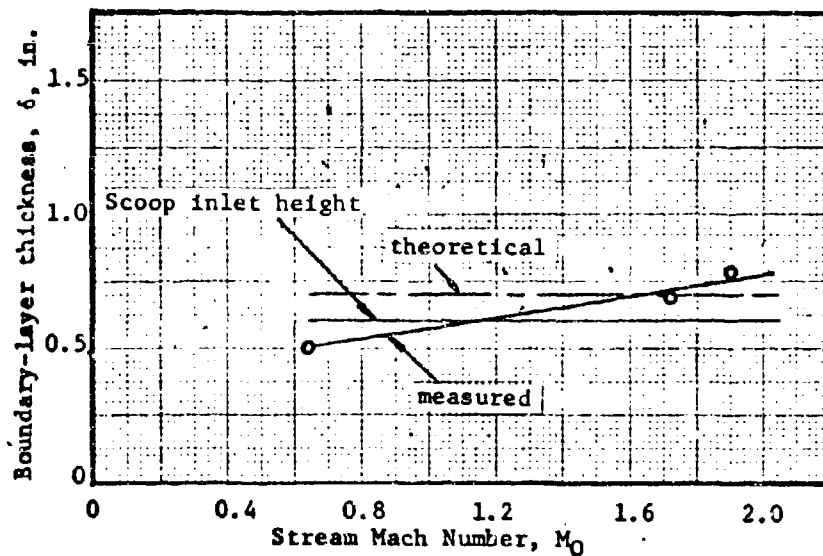


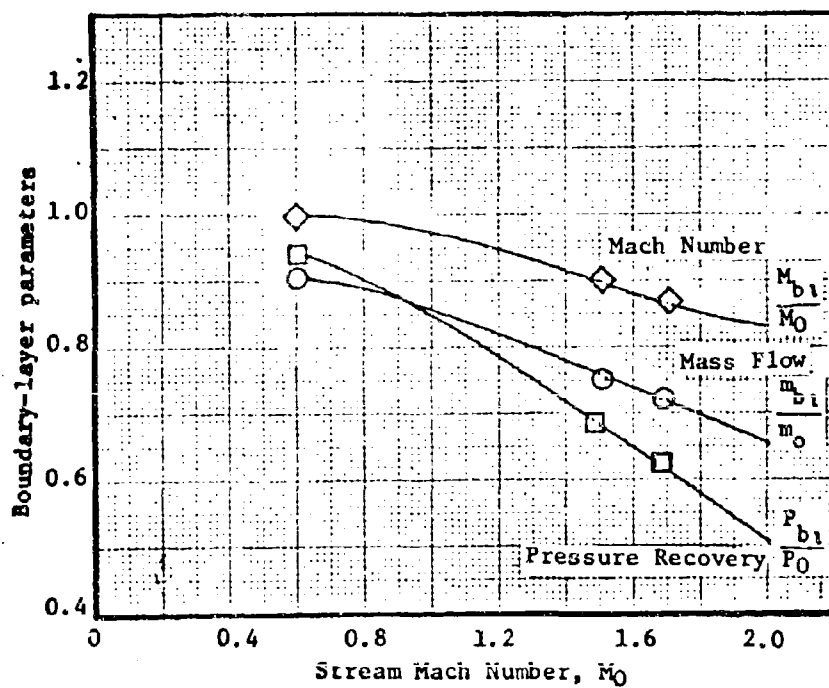
FIGURE 7-50.

Total pressure recovery of attached rectangular boundary layer inlets for various inlet heights. Velocity profile parameter  $N=7$ .

Reference: NACA TN 3583



Boundary layer thickness ahead of inlets.



Ratio of average Boundary layer values to free stream parameters.

FIGURE 7-51. Test of Submerged and Scoop Inlet.

Reference: NACA RM E53L28b

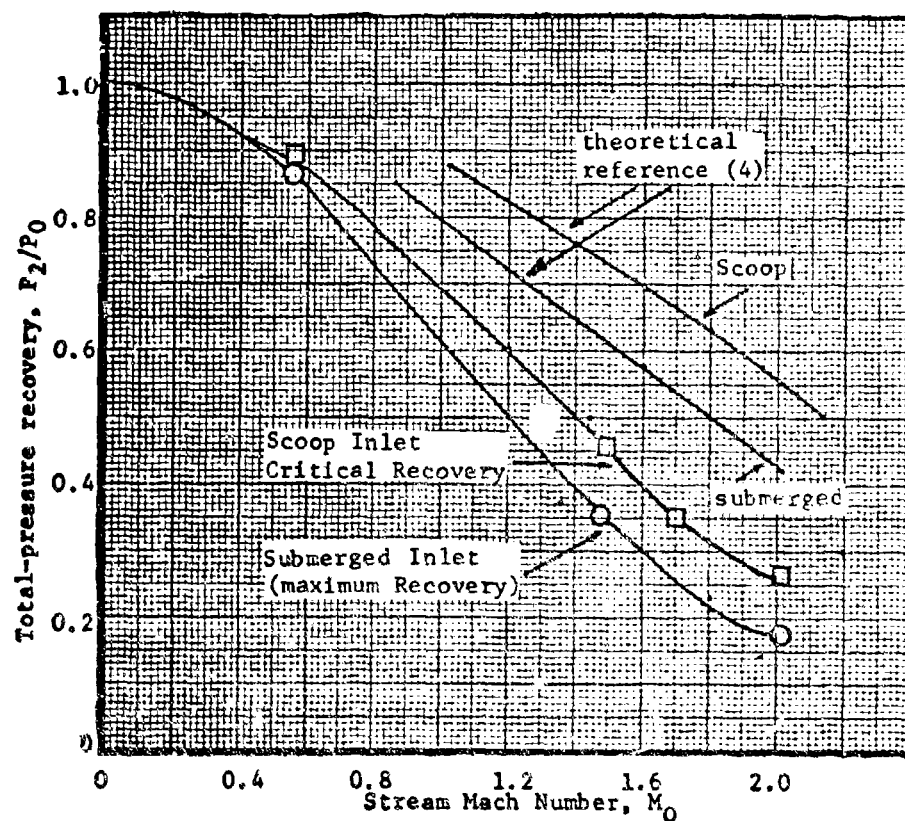


FIGURE 7-52. Total pressure Recovery of Submerged and scoop inlets.

Reference: NACA RM E53L28b

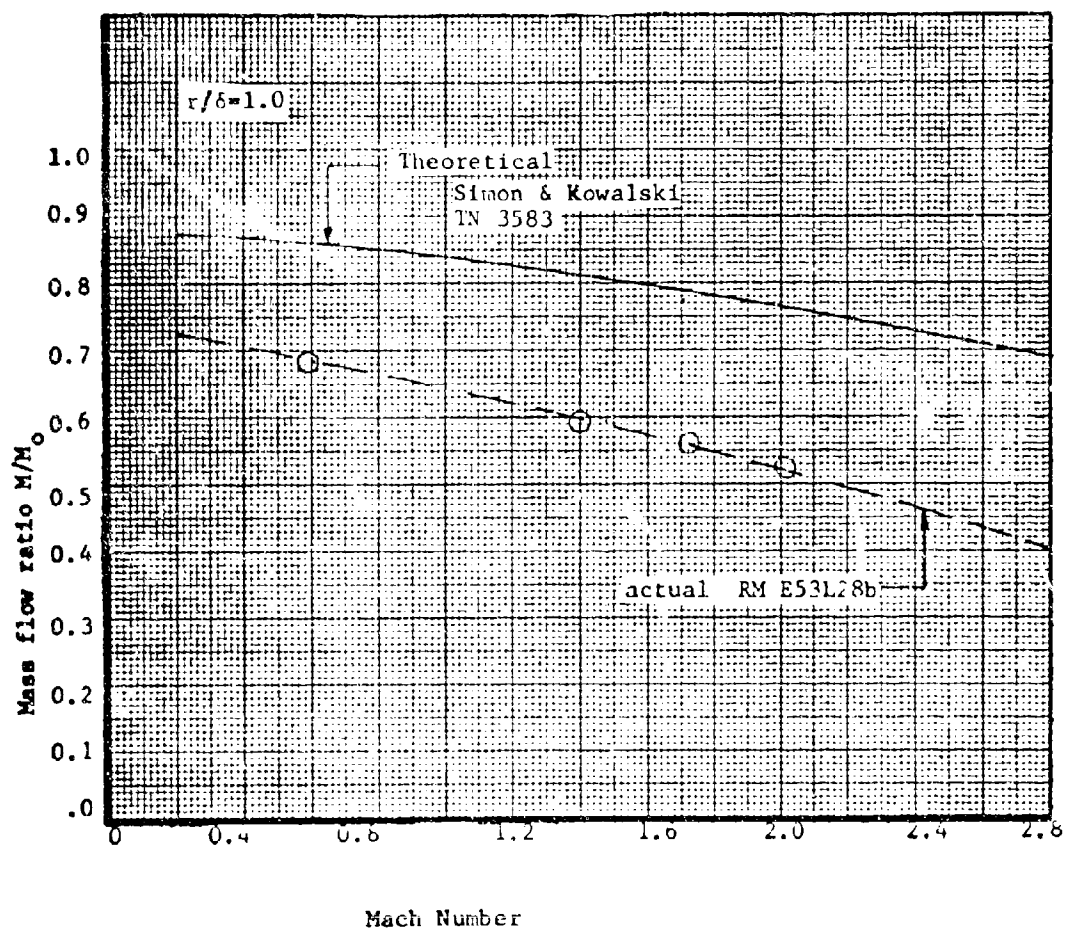


FIGURE 7-53. Mass flow characteristics of a scoop inlet.

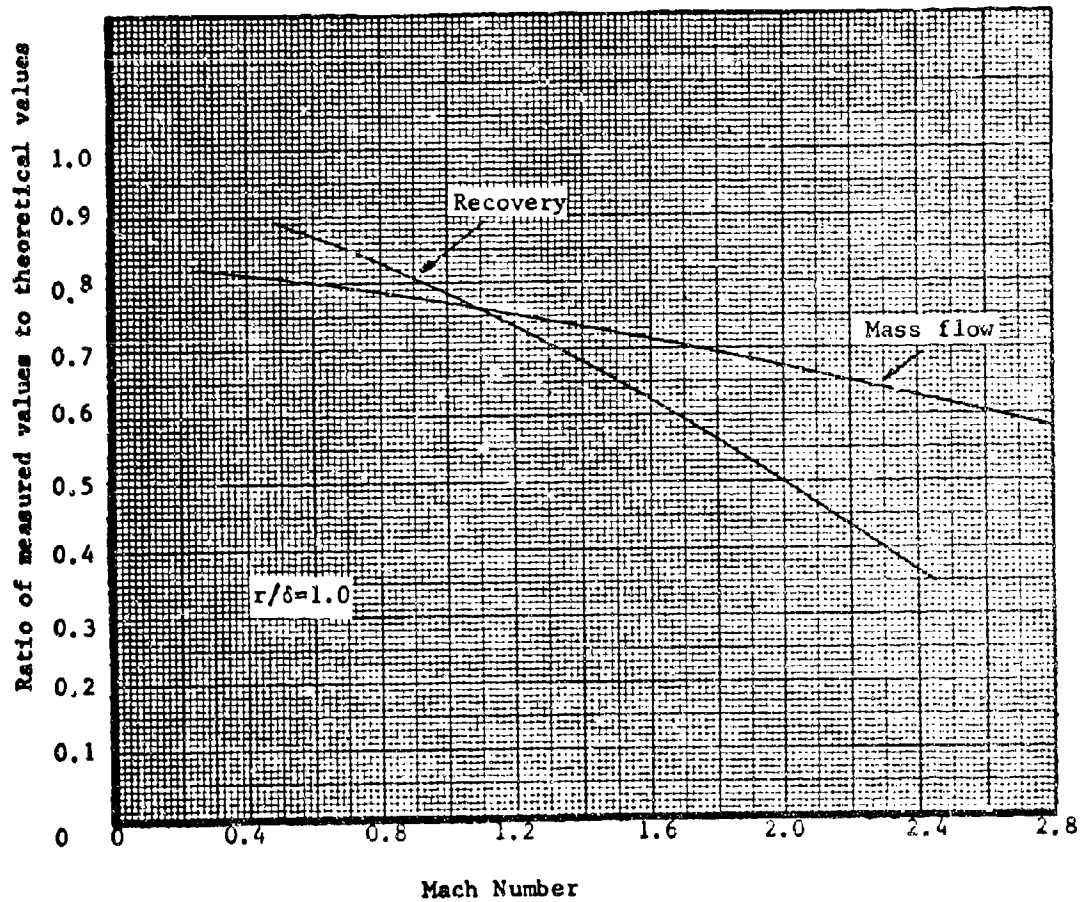


FIGURE 7-54. Estimated actual to theoretical mass flow and recovery characteristics of a scoop inlet.



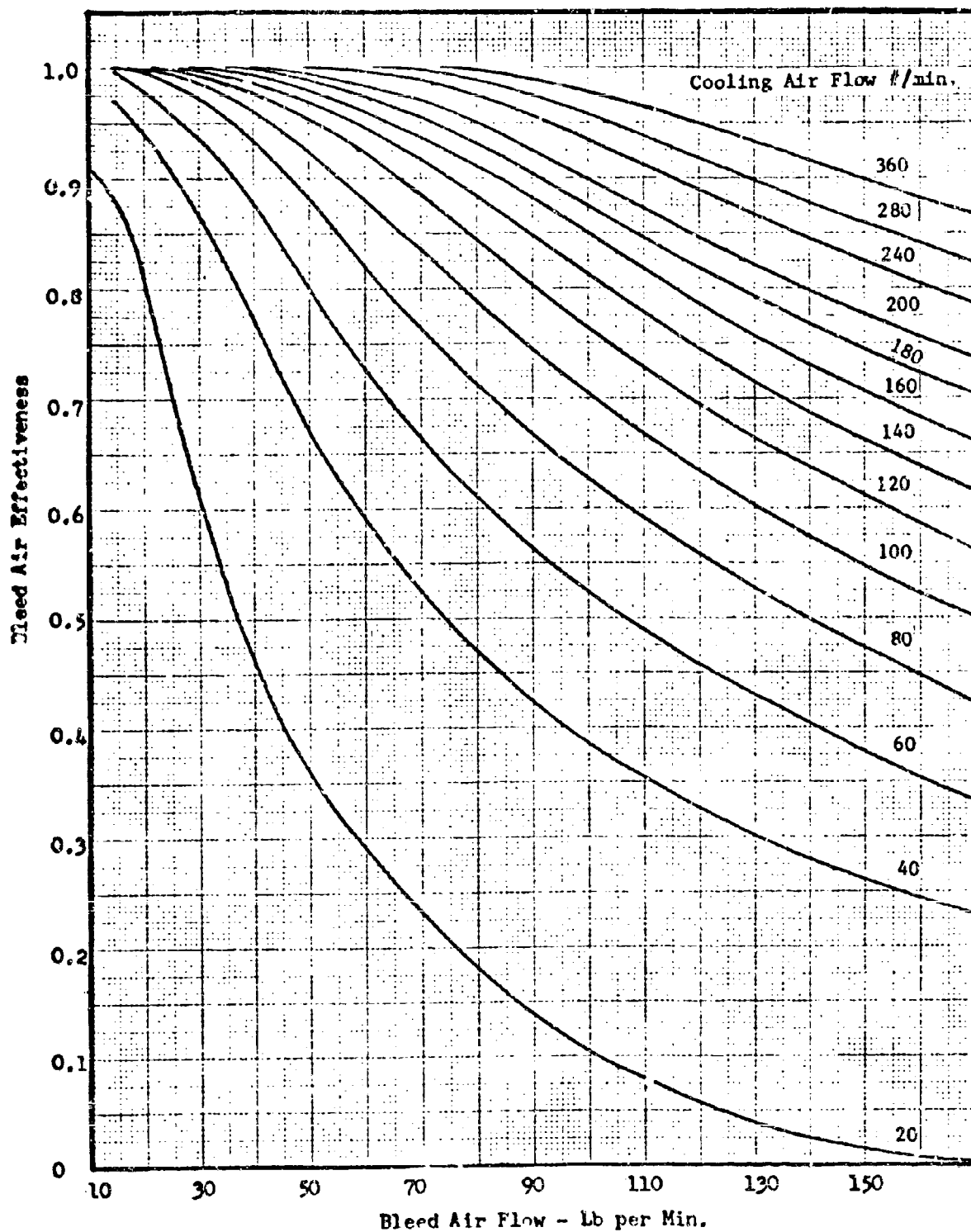


FIGURE 7-55. Typical Heat Exchanger Effectiveness Curves.

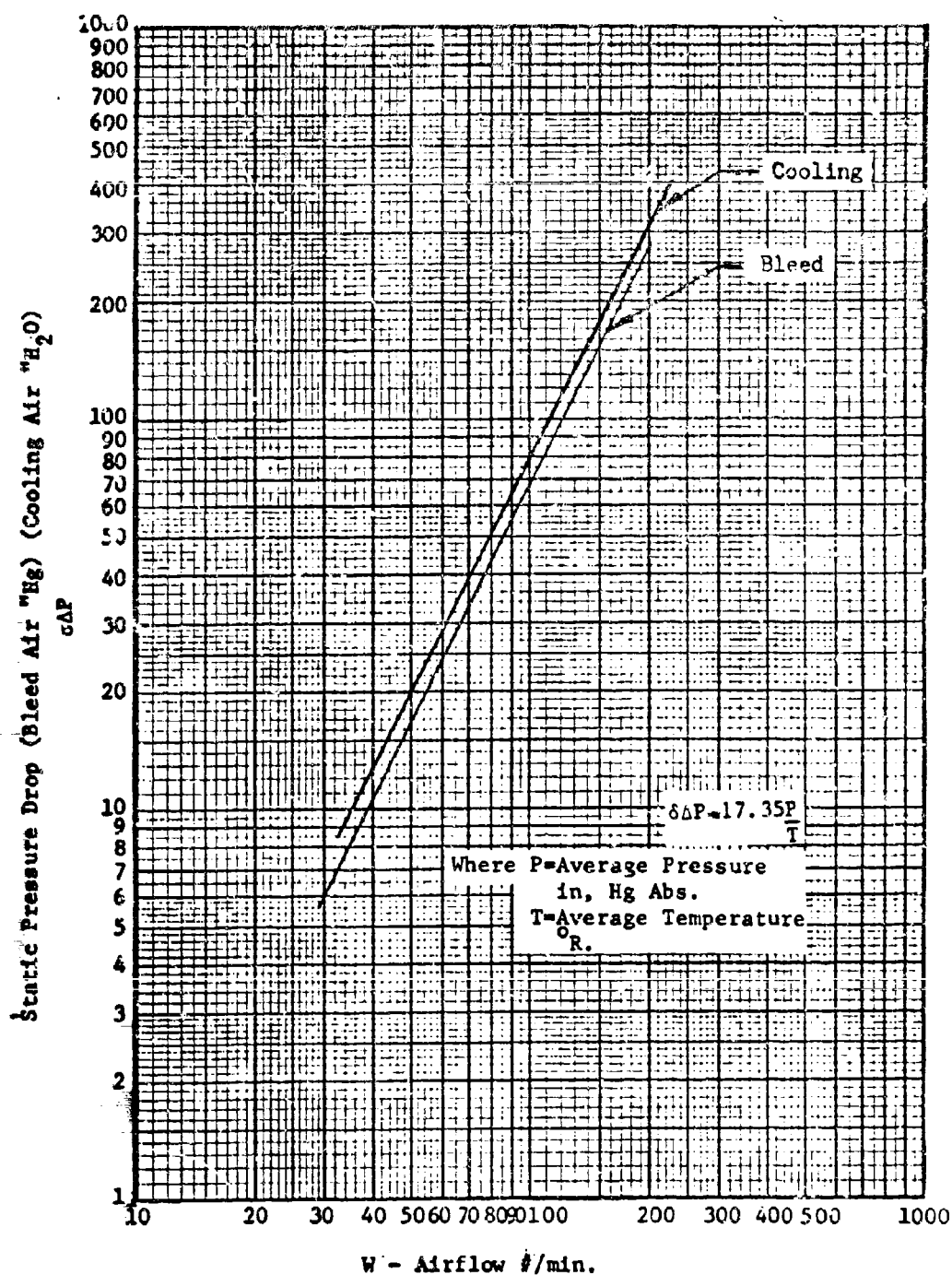


FIGURE 7-56. Typical Heat Exchanger Pressure Drops.

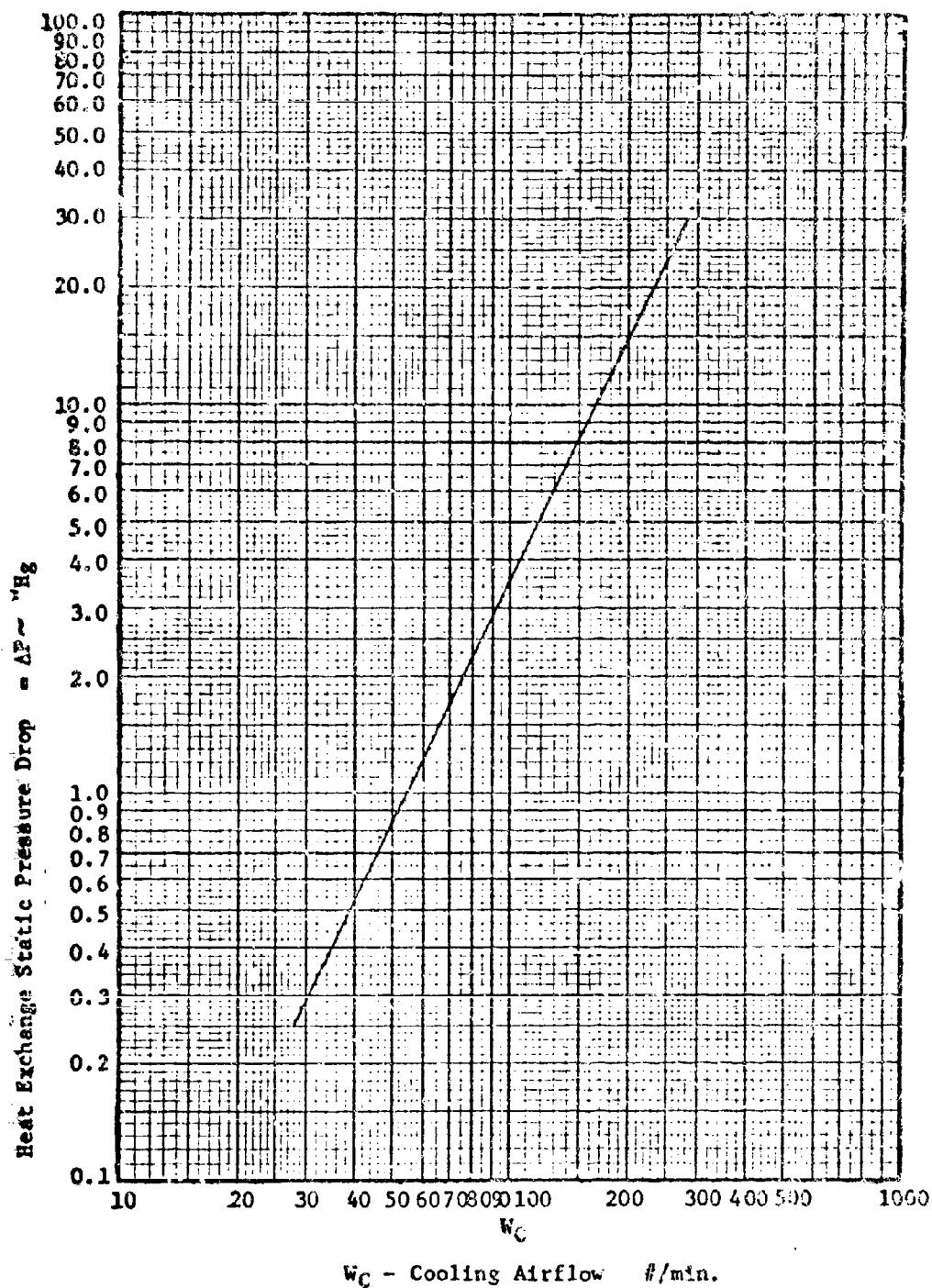


FIGURE 7-57. Pressure loss through heat exchanger used in example.

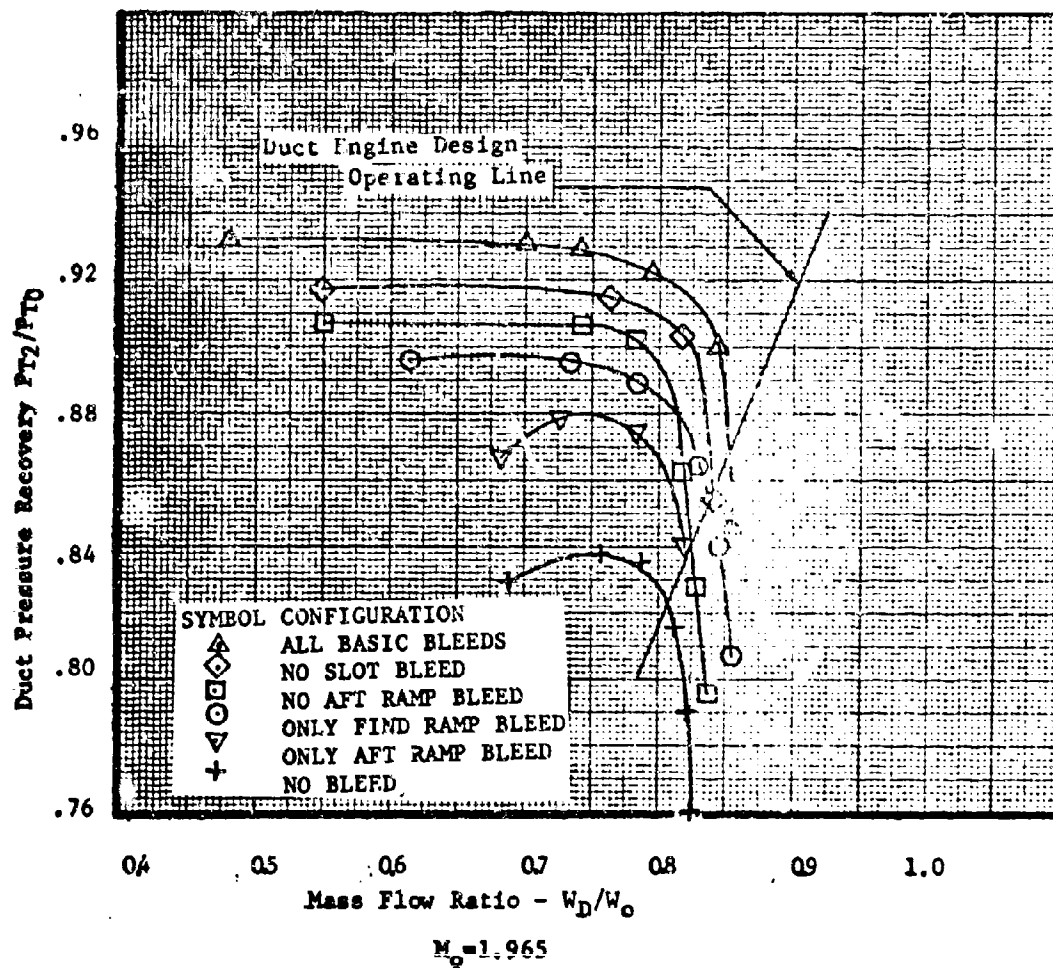


FIGURE 7-58. Effect of Ramp Bleed on Inlet Duct Performance.

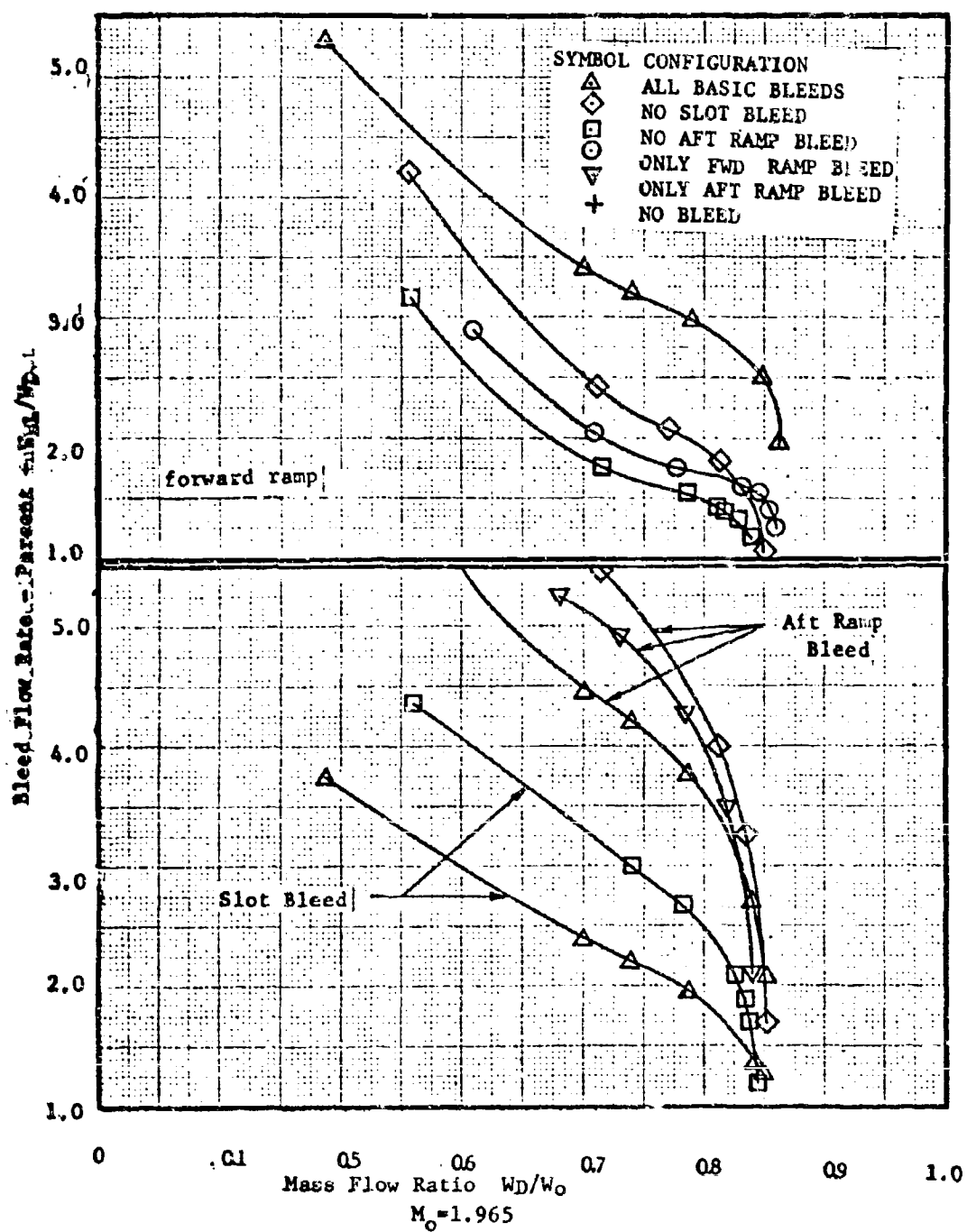


FIGURE 7-59. Ramp Bleed Flow Rates

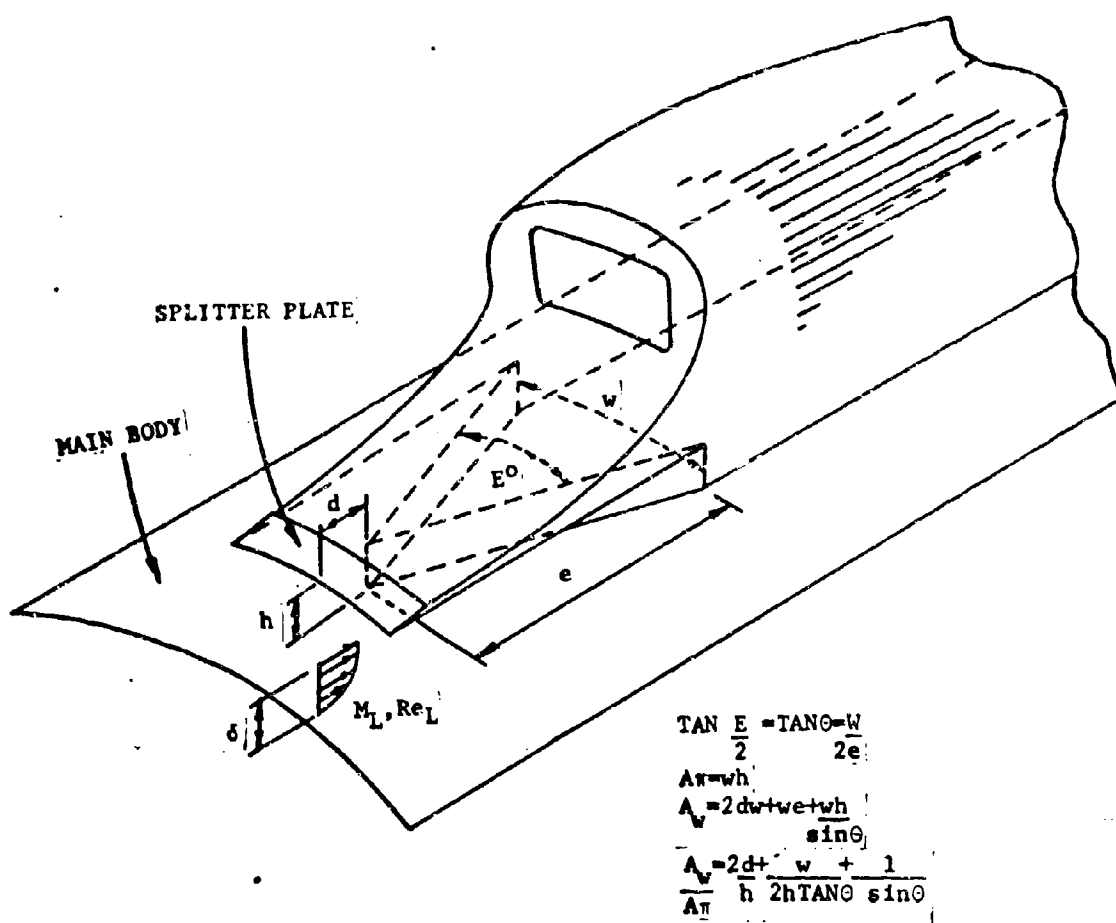


FIGURE 7-60. Boundary Layer diverter geometry.

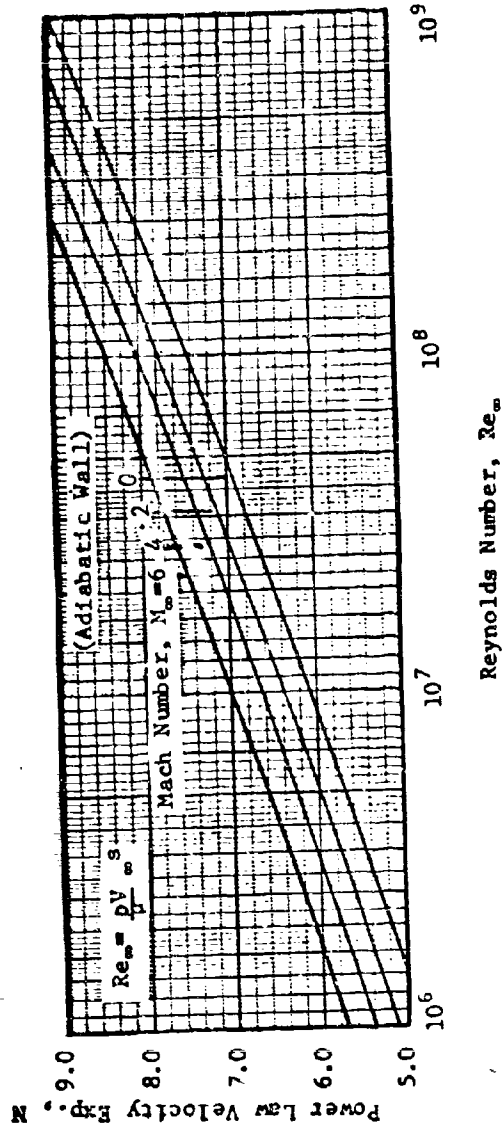


FIGURE 7-51. Turbulent Boundary Layer Profile Characteristics.

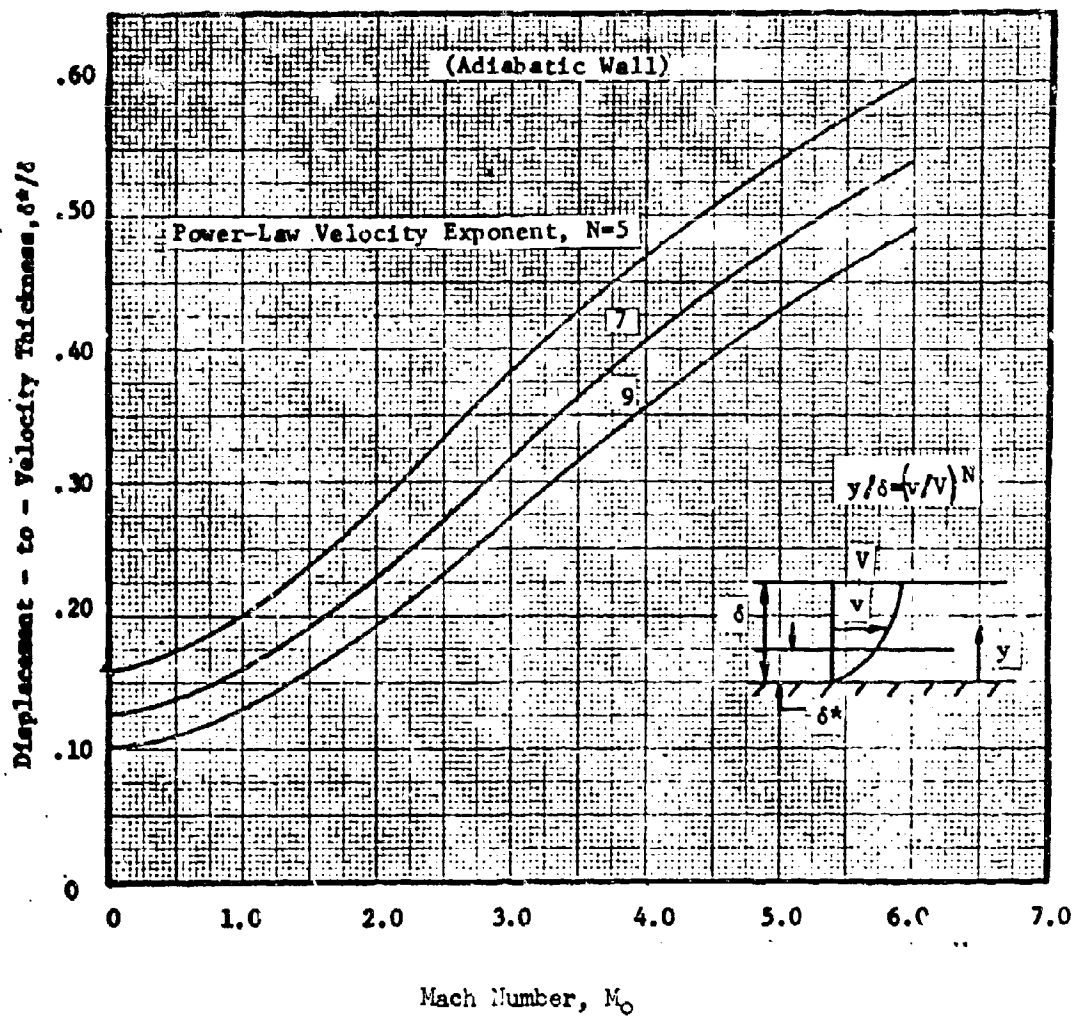


FIGURE 7-62. Turbulent Boundary Layer Profile Characteristics.



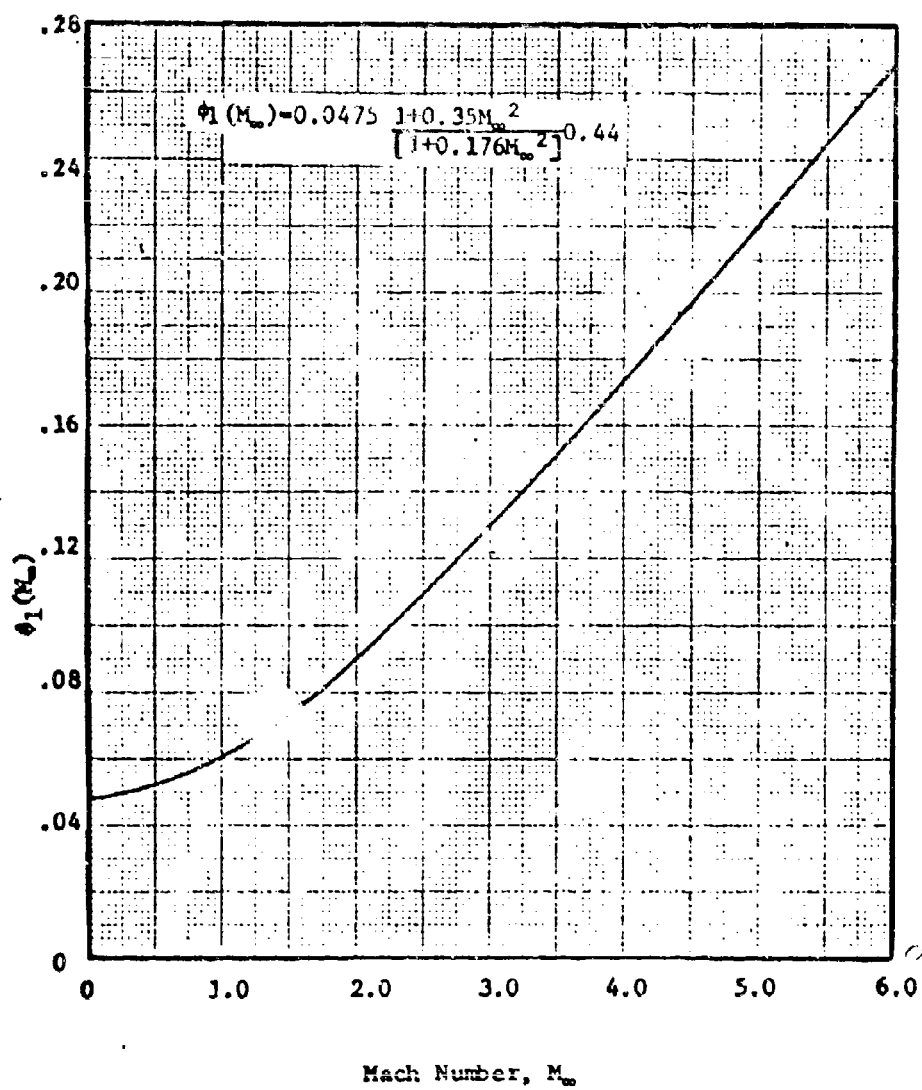


FIGURE 7-63. Mach Number Function For Turbulent Boundary Layer.

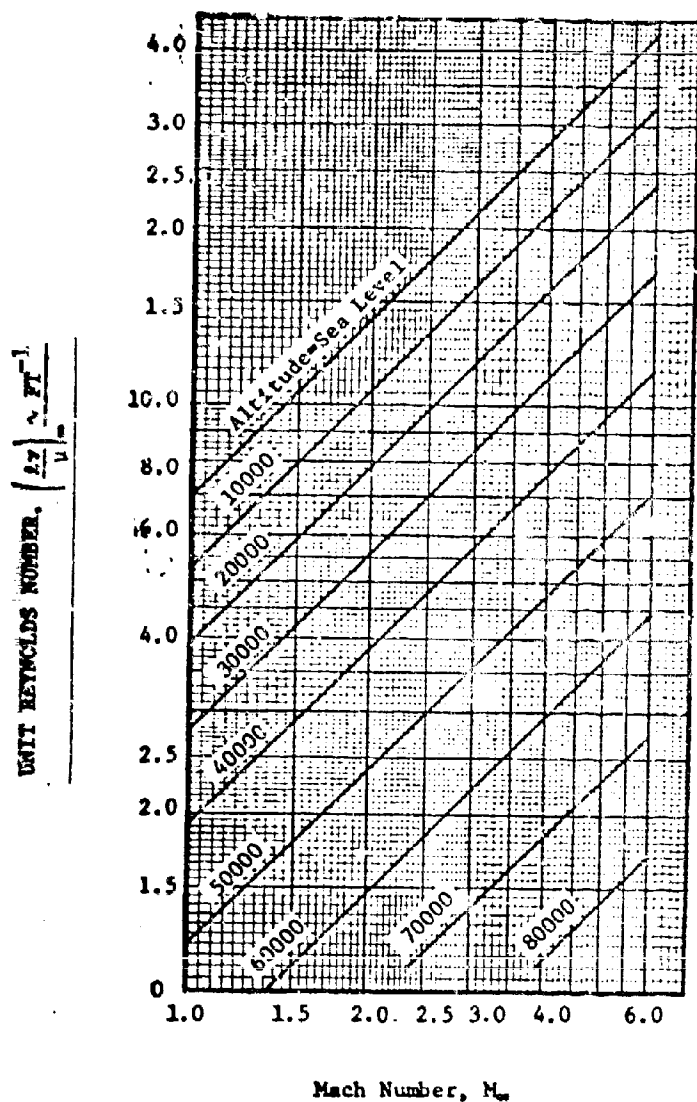


FIGURE 7-64. Free-stream Reynolds Number Per Unit Length.

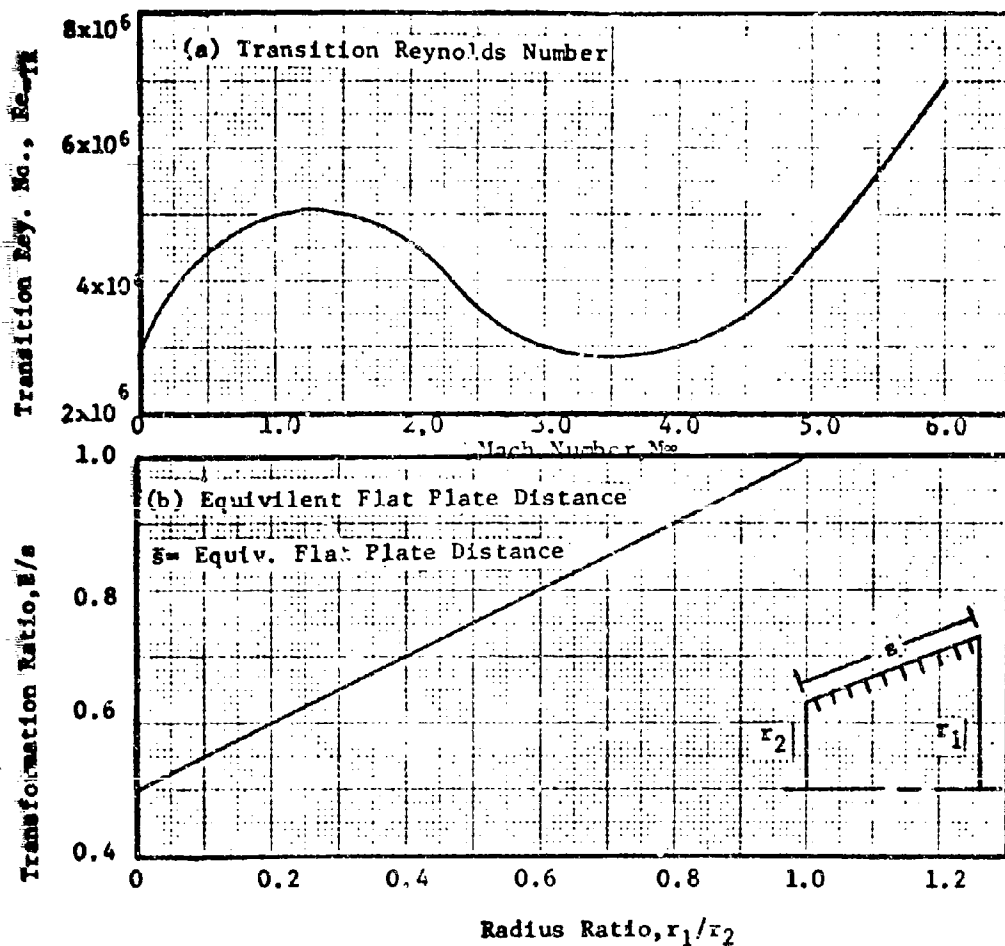
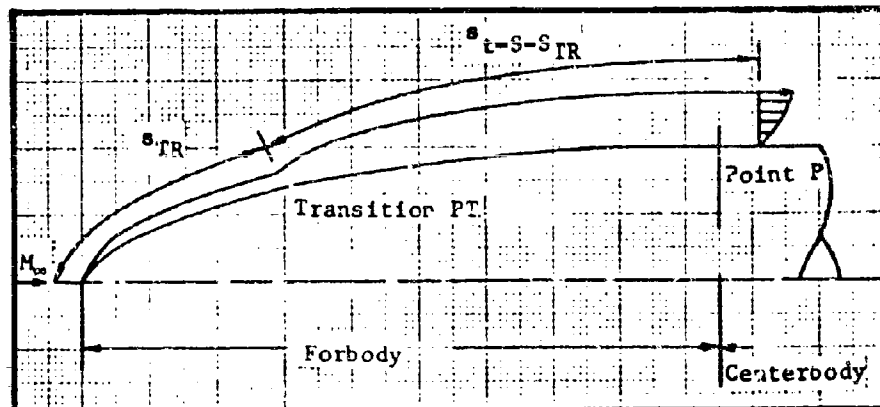


FIGURE 7-65. Equivalent Flat Plate Distance For Turbulent Boundary Layers.

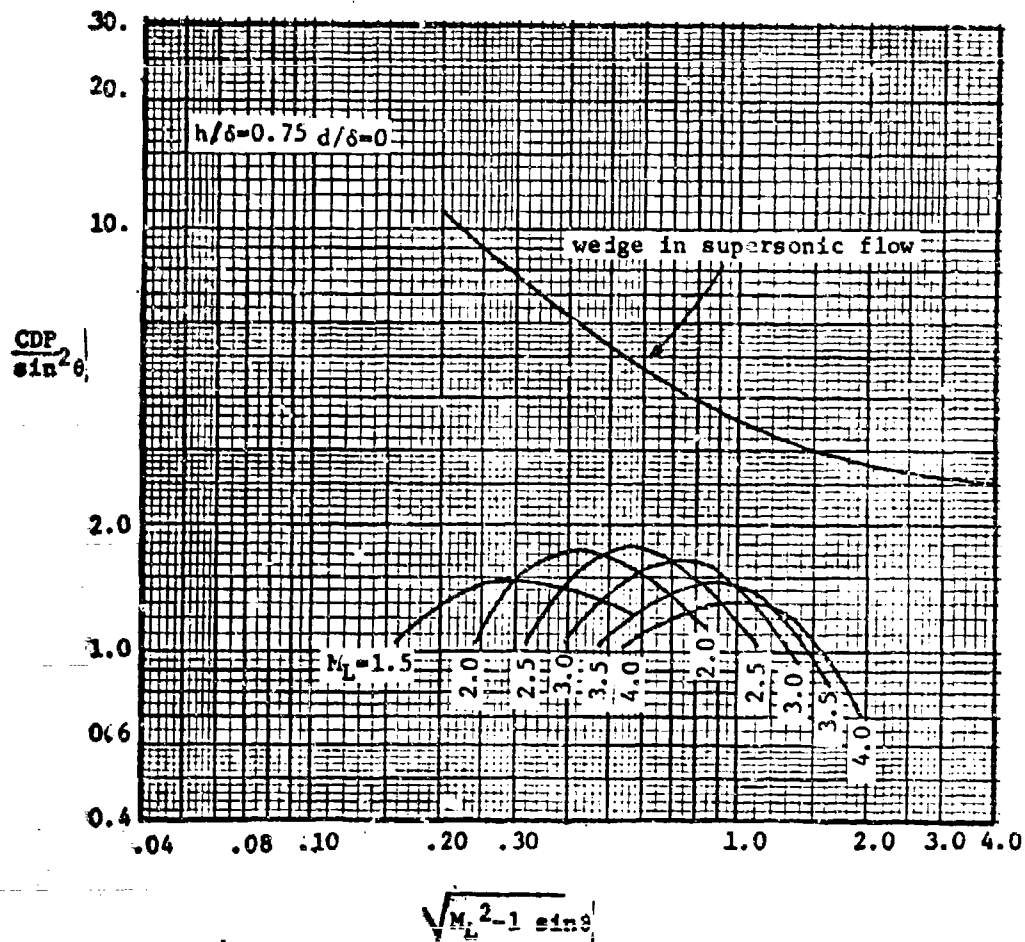


FIGURE 7-66. Wedge diverter pressure drag coefficient.

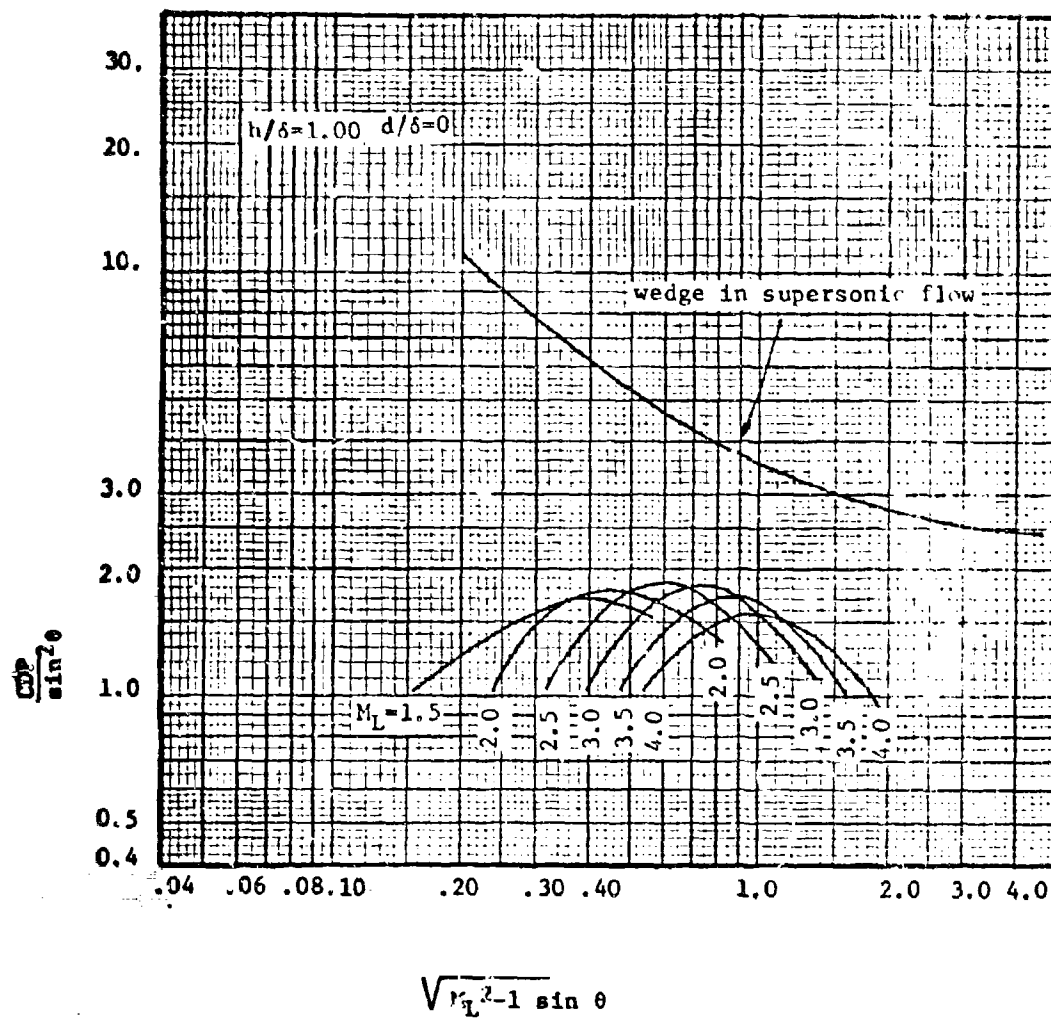


FIGURE 7-67. Wedge diverter pressure drag coefficient.

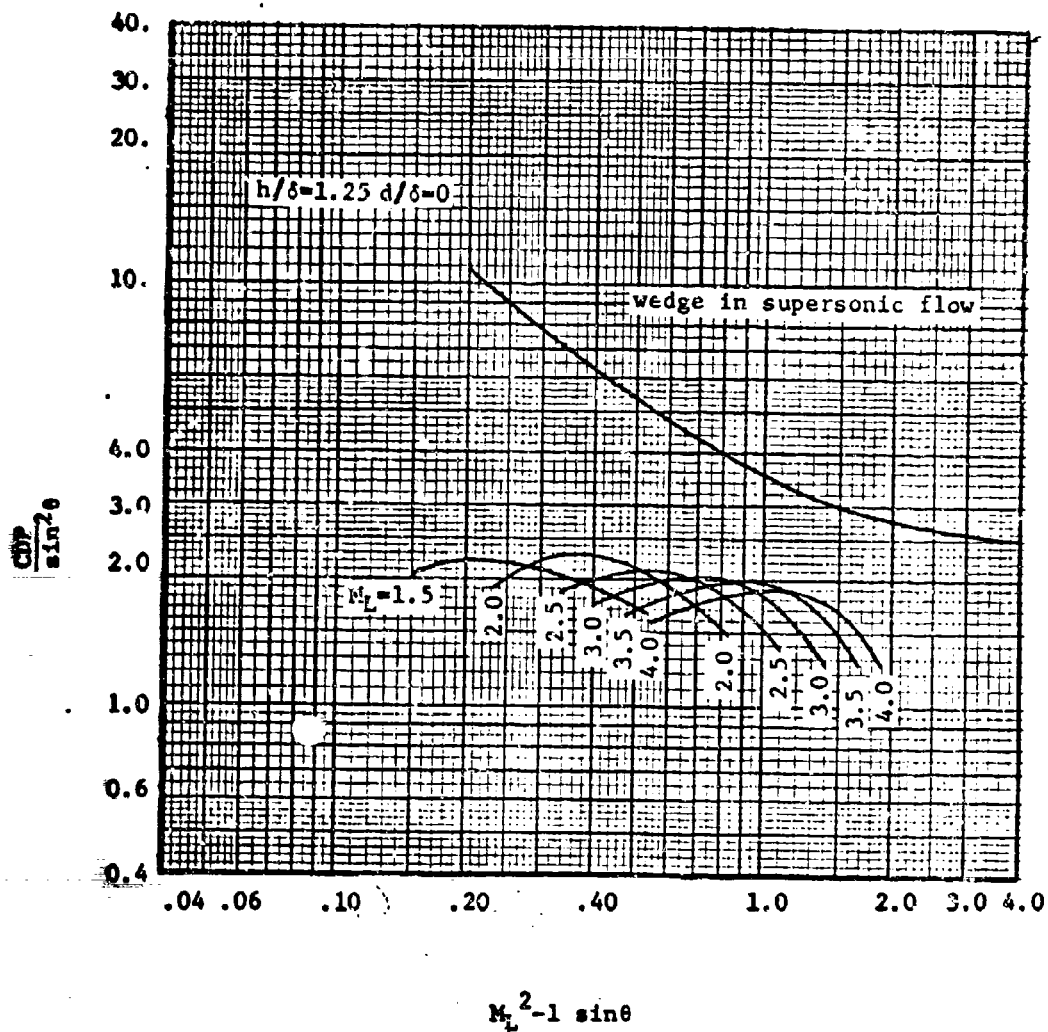


FIGURE 7-68. Wedge diverter pressure drag coefficient.

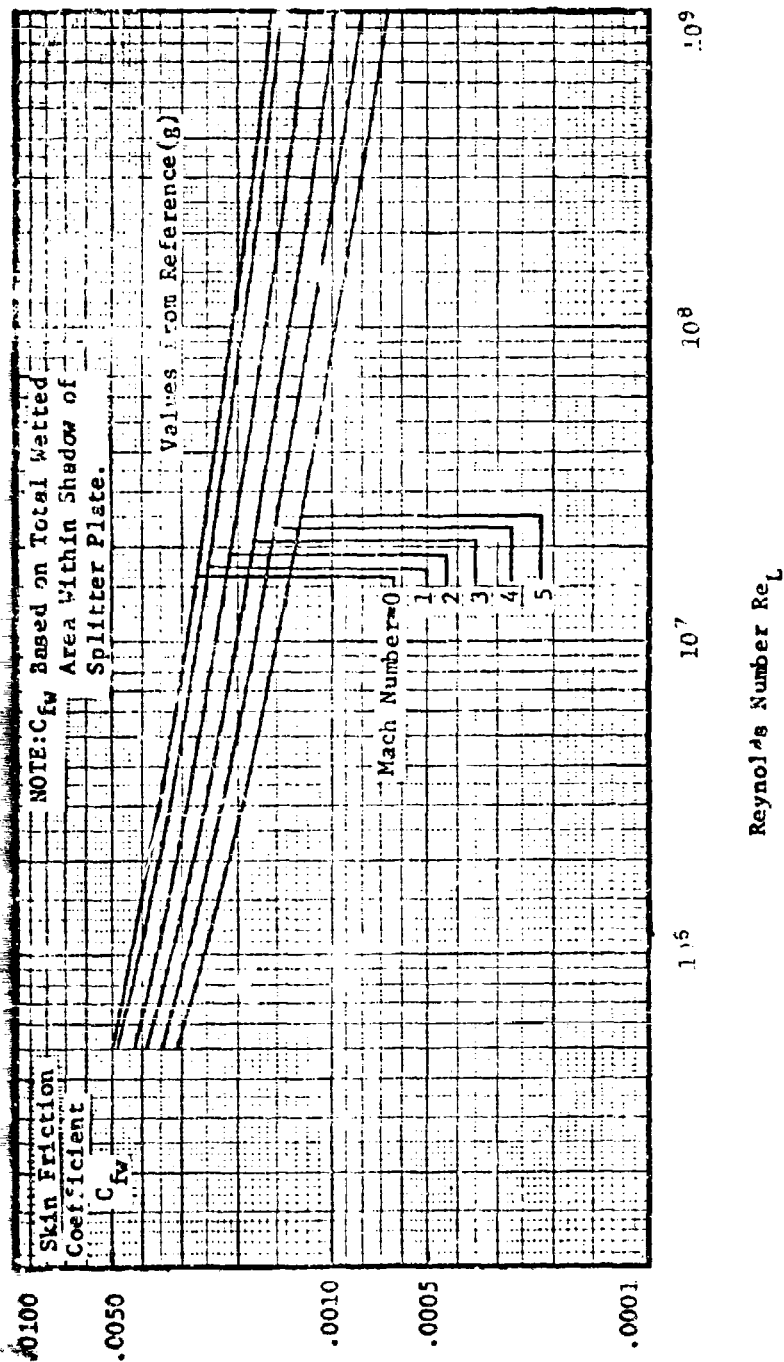


FIGURE 7-69. Wedge Diverter Skin-Friction Coefficient (Turbulent Flow)

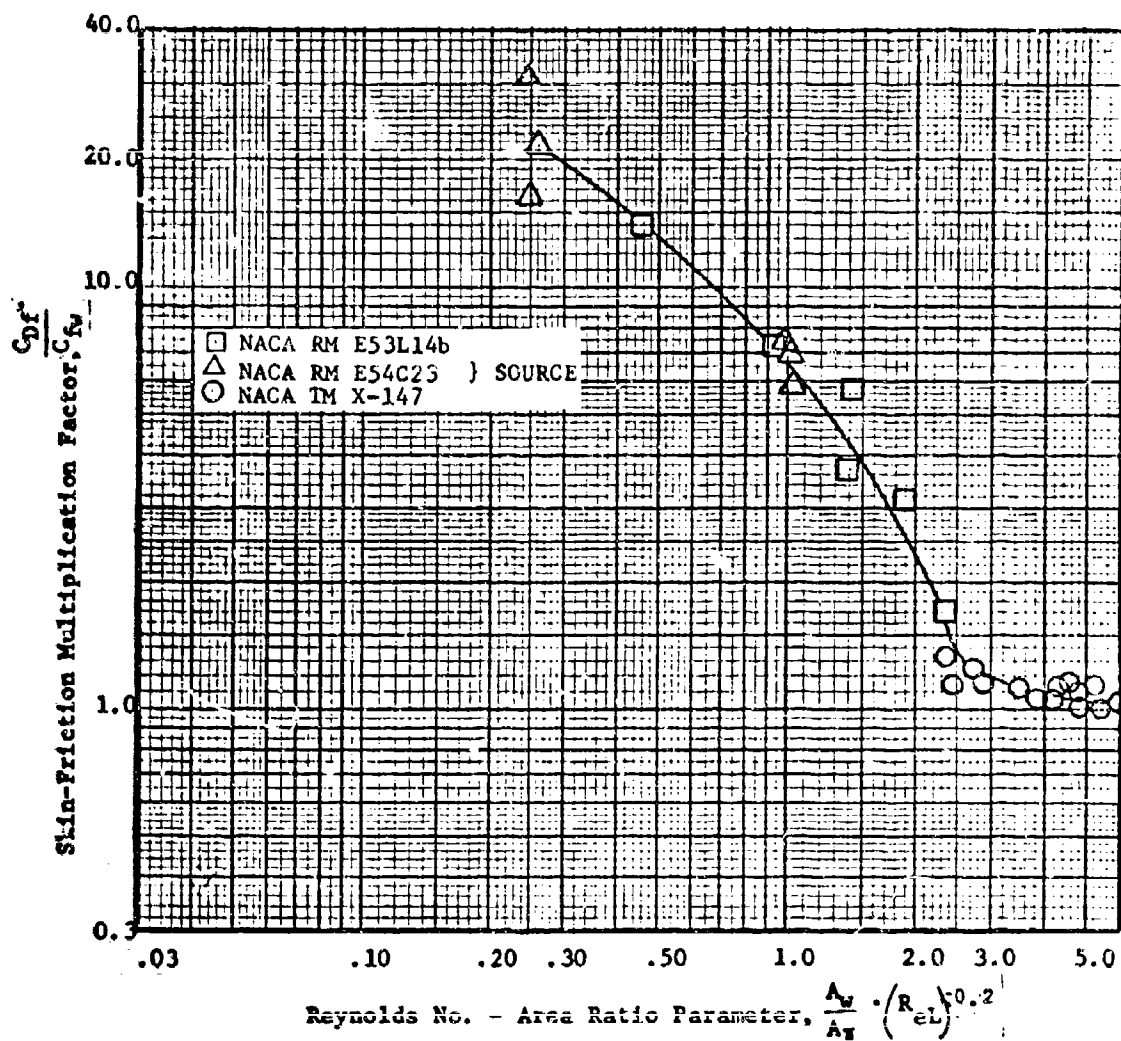


FIGURE 7-70. Wedge Diverter Skin-Friction Multiplication Factor.



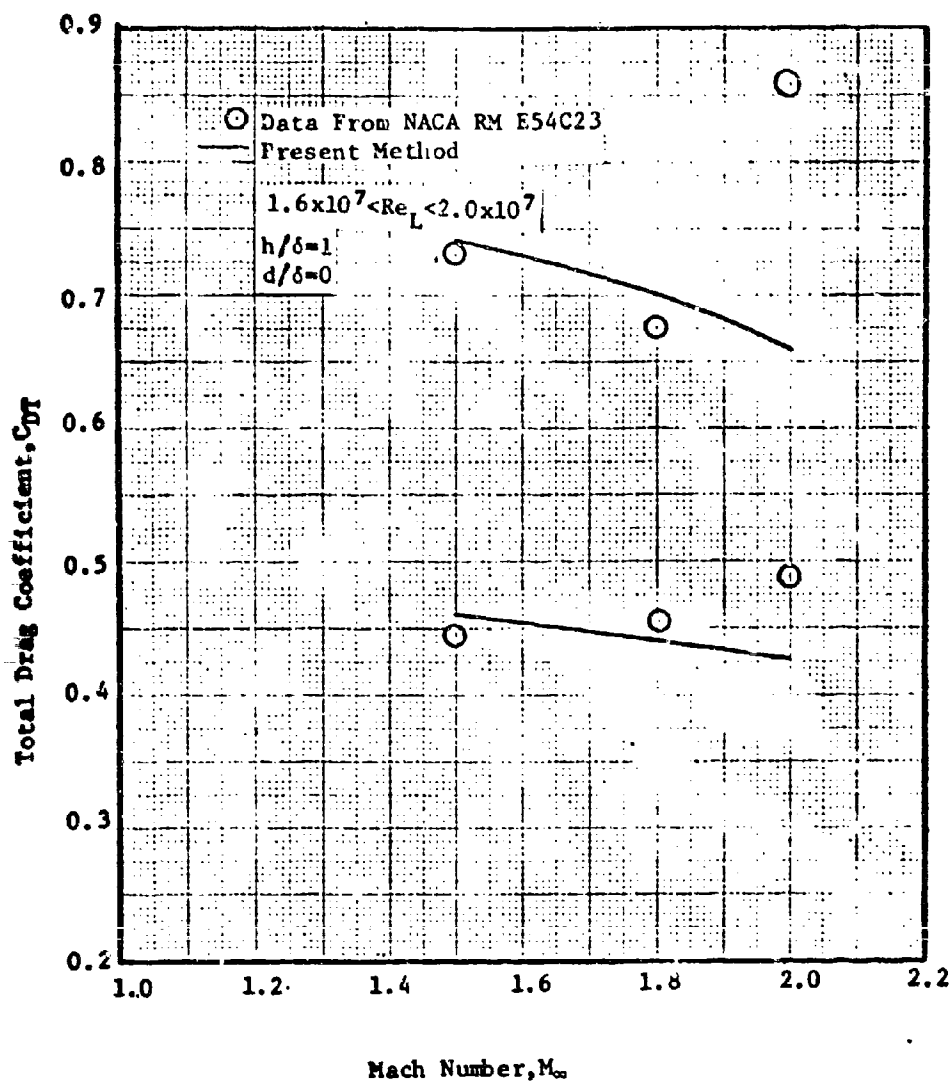


FIGURE 7-71. Comparison of Results to Experimental Data.

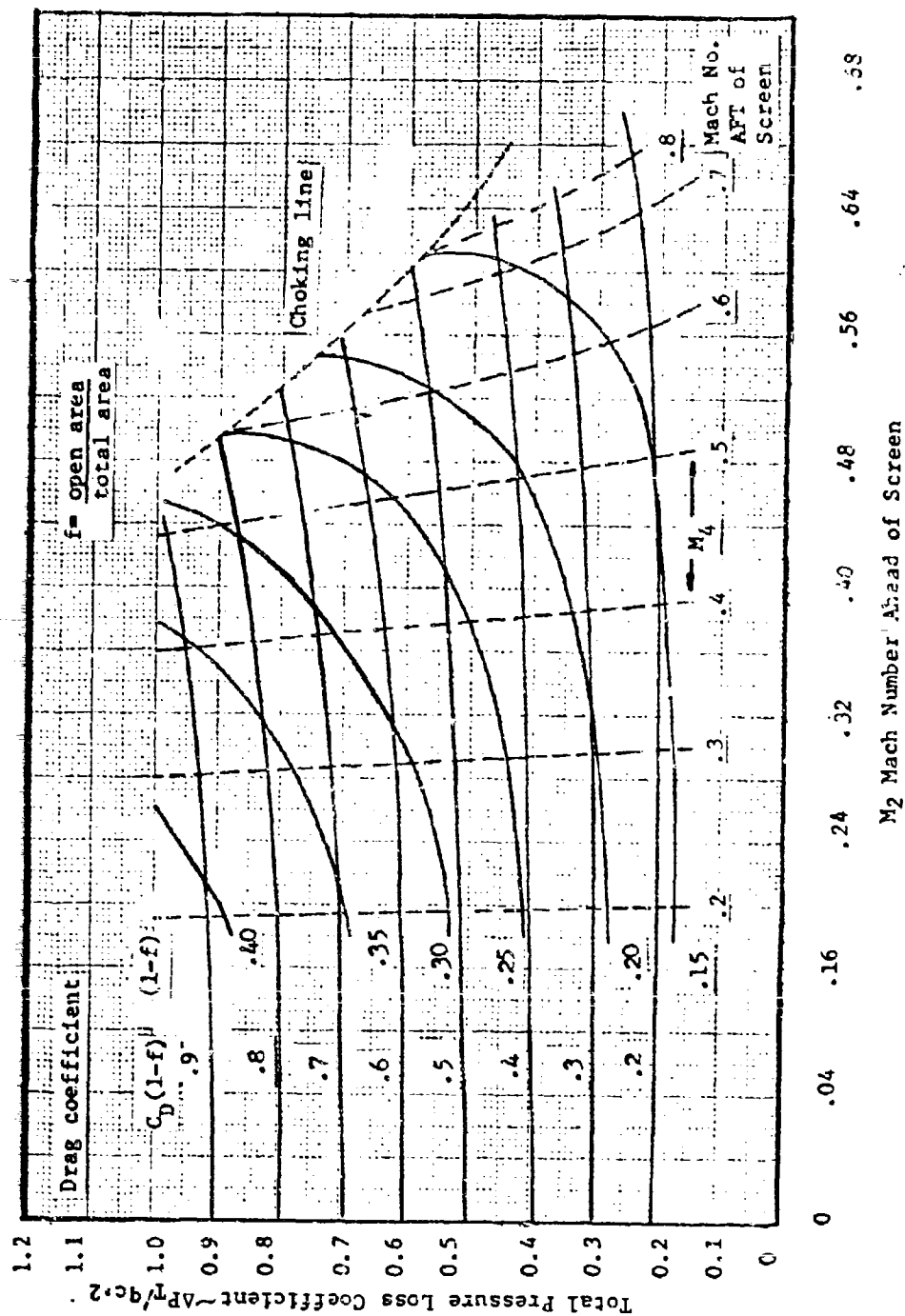


FIGURE 7-72. Total-pressure-loss coefficient design chart for straight screens for values of loss coefficient from 0 to 1.0.